Non-Equilibrium Self-Assembly:
Formation and Function of Meso-Structures with Applications in Biology and Material Science

Andrés Arango-Restrepo

Dissertation

Non-Equilibrium Self-Assembly: Formation and Function of Meso-Structures with Applications in Biology and Material Science

Author

Andrés Arango-Restrepo

Advisor

Prof. Dr. Miguel Rubi

UNIVERSITAT DE
BARCELONA

Non-Equilibrium Self-Assembly: Formation and Function of Meso-Structures with Applications in Biology and Material Science

Memoria presentada para optar por el grado doctor en la
Universitat de Barcelona

Programa de Doctorado en Física

Autor
Andrés Arango-Restrepo
Andres Arango R

Director
Prof. Dr. Miguel Rubi

Tutor
Prof. Dr. Giancarlo Franzese

UNIVERSITAT DE
BARCELONA

Declaration

I here by declare that the thesis entitled *Nonequilibrium self-assembly: formation and function of mesostructures with applications in biology and material science* submitted by me, for the award of the degree of Philosophiae Doctor in Pyhsics to the Universitat de Barcelona (University of Barcelona) is a record of bonafide work carried out by me under the supervision of Prof. J. Miguel Rubi, Departament de Física de la matèria condensada, Facultat de Física, Universitat de Barcelona, Barcelona, Spain.

I further declare that the work reported in this thesis has not been submitted and will not be submitted, either in part or in full, for the award of any other degree or diploma in this institute or any other institute or university.

When you get free from certain fixed concepts of the way the world is, you find it is far more subtle, and far more miraculous, than you thought it was, (...) parts exist only for purposes of figuring and describing, and as we figure the world out we become confused if we do not remember this all the time, (...) we are a function of what the whole universe is doing in the same way that a wave is a function of what the whole ocean is doing.

Alan Watts

A short tale in Gaia

In a future that already happened in another galaxy, little Marie, with her indomitable and persevering spirit, full of curiosity, one day felt dissatisfied with the answers of her friends and parents.

A short time later, on a family visit to the mountain where her father's old aunt lived, late at night, she heard Selene, the moon. She asked the little girl: why was her sight lost in the immensity of the sky, which you are looking for? Little Marie only told her that she didn't understand how and why so many atrocious things and so many wonderful things were happening on Gaia, her planet, that she felt fuller seeing her and the stars! Selene replied that everything followed a natural flow, that no being could oppose it, not even her sister Gaia or her brother Helios, nor the stars that her soul longed for so much.

With her answer, she gave light to the unsatisfied soul of the girl and immediately lit again her inner fire. Marie asked her if she knew what that natural flow was and why it existed. The moon, showing solemnity, recognized that it was not for her to know why, but she knew that the natural flow was any action that fulfilled an equivalent exchange of energy. What do you mean,.[a]sked the little girl. Well, simple, if you want something, you must give something of yourself, if you climb that great mountain, you must breathe a lot and use your inner energy, if the tree wants to grow, it must take water and nutrients from the soil if the river flows, it is because the form of its energy changes, it gives its potential energy so that it becomes kinetic energy, even the river that you see coming down from the mountain must exchange something. My little one, this flow of nature is nothing more than a balance of energies, conservation because even my brother sun does it because he spends his most condensed energy - mass - to give me shine and to warm Gaia and all the beings that live in her.

Marie felt her heart shaking, her hair standing up, her eyes watering and her stomach creating a vacuum. She probably had a moment of joy and full realization, which many people do not even manage to live in their lives with such purity and strength.

Wait! someone said it on the horizon, you missed something to tell the little one! The sun was rising, and this voice was that of Helios, Selene's brother. He said: Marie, life and the universe is not just equivalent exchange, it is not just a balance of energy or efforts, never forget that you must always give more, you must always give your best even though what you get is not proportional to what you give for something specific. I understand that this may not be easy to understand, but not every step you take to climb a mountain is the energy that you spend to get to the top .... Much of that energy, of that effort, is being transformed into something else, learning, and experience, having the opportunity to observe beautiful things, or simply taking a little detour that does not take you to the top. But remember, everything is necessary, and it is not wrong to give more than you think you can give, because, the more general universal law says that everything happens in order, and what happens must happen because there is always profit, always the universe, with every action of each being increases its information or that something ineffable, and for this, we must always give more than what is required in each of our actions.

The little one, astonished, did not understand entirely what Helios was telling her with so much passion and wisdom, and just asked who and why had established such an unbalanced law. Helios, with immeasurable calm, replied: Perhaps it is the greatest god that a mortal can imagine, or perhaps it is the very essence that gives sense to everything, even time and space depends on it. This god always grows after every human, animal, vegetal, and microbial action. This god has been associated with the disorder, but the truth is that because he always grows and grows, it generates order, life, art, is destruction and creation, is storm and calm. Perhaps, even humans and you are not prepared to know it completely, but some day they will do it and perhaps you are the first or who will give more of itself so that this god is not so misunderstood by all beings that inhabit Gaia.

The little one, after such a praiseworthy and fascinating story, had a light in her eyes and an infinite determination to undertake a long journey, where, looking at the stars, she would like to meet companions who could be as fascinated as she is to understand many mysteries that this universe and this misunderstood god called entropy.

A couple of years later, one day when she woke up in an ocean of conviction where she was gently rocked by waves of calm, realization, and tranquility, she felt a fire in her heart and only managed to ask with all the strength of her soul: Stars! Please, tell me if there is an energy that we cannot observe, I want to know if there is an energy that we still see with our eyes, but do not recognize. Why do I have this feeling that it is like magic, how can such wonderful things happen? I understand that everything is energy, but is everything energy that we can see? Is it right to say that this energy does not exist if we cannot even prove that it does not exist?

Our little, answered a small group of stars, there are energies that you will never see, but that is always there and will be there. There are phenomena, which you call magic, which mortals try to justify with intricate relationships based on their toy theories, but which in themselves are all related since this energy is the intermediary of all the processes of the universe. Remember, energy evokes energy, and remember that a bird does not always fly because it can, but because it wants to, if you have the conviction you can understand what that energy is and open your eyes to a dimension where you see that everything is connected by that energy. Thus, you will know some of the principles of how this ineffable and intricate network of space, time, and energy that you call the universe works.

Preface

How and why can disorder give way to order? This basic question has attracted the interest of scientists from different disciplines. In order to answer it, various theories and models have been proposed. Self-assembly is currently a field of great interest because of its numerous applications in physical chemistry, biology, materials science and nanoscience. It is also fundamental to the understanding of the origin of life. We understand the cell as a self-organised structure in which functional self-assembly takes place, which could be the starting point for the design of artificial self-assembled structures and for tissue engineering. In technology, self-assembly is used to produce nanostructures for nanotechnology development. It is common to many dynamic, multi-component systems, from smart materials and self-healing structures to networked sensors and computer networks.

A wide variety of self-assembly processes, such as gelation, crystallisation, active particles organisation, magneto-hydrodynamic structure formation, protein synthesis among others, take place under non-equilibrium conditions. Despite such a large casuistry, there is currently no general theory that provides a detailed explanation of such processes. We only know results about the stability of such systems from dynamical systems theory. We understand very little about the role of energy dissipation in the formation of ordered structures from disordered components. But we do know that they are of vital importance for example in the functionality of the cell. Such facts constitute a strong motivation for the study of out-of-equilibrium self-assembly.

To study non-equilibrium self-assembly systems, it is necessary to characterise the possible structures, describe their formation and transport mechanisms, and consider the energetic changes involved in the formation processes. Since a wide variety of factors are involved in self-assembly processes, it is essential to reduce the description by proposing models. We therefore aim to formulate a mesoscopic theory capable of explaining the formation of self-assembled structures. The theory is based on non-equilibrium mesoscopic thermodynamics, from which we will obtain the kinetics and thermodynamics of the processes.

The objectives of this thesis are summarized as follows:

- To develop a general formalism to describe the non-equilibrium dynamics of self-assembly processes based on non-equilibrium mesoscopic thermodynamics.
- We will validate the formalism through experimental data for gelation and Liesegang pattern formation.
- To analyse the behaviour of the entropy production in the study cases.
- To formulate a thermodynamic criterion for the formation of self-assembled structures production of entropy in the process.

- We will study the influence of external forces and structural parameters on self-assembly in order to find optimal conditions for structure formation in biology and materials science.

The thesis is divided into three parts dealing with how to model out-of-equilibrium self-assembly in concrete examples (Part I), the role of entropy production in the process of structure formation and maintenance (Part II), and the thermodynamics and dynamics of self-assembled mesostructures under the action of external forces (Part III).

The Introduction contains our review article on the emergence of non-equilibrium self-assembled structures. In it, we propose a classification of the different non-equilibrium processes that give rise to self-organising and self-assembling structures. We define the preliminary process concepts and discuss the types of interactions, the hierarchical structures, the energy involved and the structure formation mechanisms that have been proposed so far. The main topic of this part is the discussion of some models proposed to describe the formation and maintenance of structures. We also raise the question of whether the behaviour of entropy production could explain the emergence of self-assembling and self-organising structures.
In Part I, we address the modelling of two case studies: gelation and Liesegang band formation, as out-of-equilibrium self-assembly processes. We propose a mechanism that gives rise to a set of equations describing the formation dynamics. This mechanism is related to the entropy production of the process, which will allow us to further discuss the relationship between this quantity and the shape of the structures.

The main part of the thesis aims to answer the questions of why under the same conditions and precursors some structures are more probable than others, and whether there is a criterion capable of determining the type of structures that form in a non-equilibrium self-assembly process. In Part II, we shed light on these questions by showing that the role of entropy production is key not only in the proposition of models but also in the formulation of an effective potential to estimate the probability of structure emergence as a function of a structural parameter.

Part III analyses the effect of external forces on the assembly and function of structures in biology and materials science. We show how initial and external conditions lead to different entropy production regimes that induce and amplify symmetry breaking in self-assembled crystals. We explore the transition between different regimes in tissues, from healthy to cancerous, by considering the tissue as a self-assembled structure. We relate the structural evolution of enzymes to the search for the optimal activation energy that minimises/maximises the work lost in an enzymatic process. We analyse the breakage of a set of organised fibres in which energy dissipation dictates the critical deformations of the whole structure. Finally, we consider how the organisation and distribution of surfactant in a droplet affects the motion of the droplet under an external temperature gradient.

In the Conclusions, we highlight our main findings of the work and present perspectives in multidisciplinary areas.

The following is a list of the articles that have been published in international peer-reviewed journals that have resulted from the thesis:

- Arango-Restrepo, A., Rubi, J. M., & Barragán, D. (2018). Kinetics and energetics of chemical reactions through intermediate states. *Physica A: Statistical Mechanics and its Applications*, **509**, 86-96.

- Arango-Restrepo, A., Rubi, J. M., & Barragán, D. (2018). Understanding gelation as a nonequilibrium self-assembly process. *The Journal of Physical Chemistry B*, **122**(18), 4937-4945.
- Arango-Restrepo, A., Barragán, D., & Rubi, J. M. (2018). Nonequilibrium self-assembly induced Liesegang rings in a non-isothermal system. *Physical Chemistry Chemical Physics*, **20**(7), 4699-4707.
- Arango-Restrepo, A., Barragán, D., & Rubi, J. M. (2019). Self-assembling outside equilibrium: emergence of structures mediated by dissipation. *Physical Chemistry Chemical Physics*, **21**(32), 17475-17493.
- Arango-Restrepo, A., Rubi, J. M., & Barragán, D. (2019). The role of energy and matter dissipation in determining the architecture of self-assembled structures. *The Journal of Physical Chemistry B*, **123**(27), 5902-5908.
- Arango-Restrepo, A., & Rubi, J. M. (2019). The Soret coefficient from the Faxén theorem for a particle moving in a fluid under a temperature gradient. *The European Physical Journal E*, **42**(5), 55.
- Arango-Restrepo, A., & Rubi, J. M. (2020). Role of Interfacial Entropy in the Particle-Size Dependence of Thermophoretic Mobility. *Physical Review Letters*, **125**(4), 045901.
- Arango-Restrepo, A., Barragán, D., & Rubi, J. M. (2020). Modelling non-equilibrium self-assembly from dissipation. *Molecular Physics*, **118**, 1-7.
- Arango-Restrepo, A., & Rubi, J. M. (2020). Entropic transport in a crowded medium. *The Journal of Chemical Physics*, **153**(3), 034108.
- Arango-Restrepo, A., Rubi, J. M., & Pradhan, S. (2021). A Thermodynamic Framework for Stretching Processes in Fiber Materials. *Frontiers in Physics*, **98**.
- Arango-Restrepo, A., Barragan, D., & Rubi, J. M. (2021). A Criterion for the Formation of Nonequilibrium Self-Assembled Structures. *The Journal of Physical Chemistry B*, **125**(7), 1838-1845.
- Arango-Restrepo, A., Rubi, J. M., Kjelstrup, S., Angelsen, B. A. J., & de Lange Davies, C. (2021). Enhancing carrier flux for efficient drug delivery in cancer tissues. *Biophysical Journal*, **120**(23), 5255-5266.

In addition, the resulting articles in preparation are:

- Arango-Restrepo, A., Rubi, J. M. & Barragan, D.. Enzymatic evolution driven by entropy production. *bioRxiv*, 319814.
- Arango-Restrepo, A., Arteaga, O., Barragan, D., & Rubi, J. M.. Breaking and amplification of the chiral symmetry from energy dissipation.
- Arango-Restrepo, A. & Rubi, J. M.. Energy dissipation unveils the transition from healthy to carcinogenic tissues.

Acknowledgments

To Prof. Miguel Rubi, it has been an amazingly exceptional experience working with you over the years, especially for your involvement, enthusiasm, ambition and attention to every little detail. Thank you for the real supervision.

To Prof. Daniel Barragán, I acknowledge and deeply appreciate his true support and motivation for introducing me to the wonderful world of physical chemistry, non-equilibrium thermodynamics and self-organisation. Also, for his time and energy, for all the discussions we have had throughout my PhD, discussions that push us beyond the limits of understanding thermodynamics and self-organisation.

To Prof. Signe Kjelstrup and Prof. Dick bedeaux, thank you both for the excellent help and warm welcome during my stay at PoreLab. Especially for having fostered, during the Covid time, an amazing and indescribable experience in the academic and personal sense in cold but magical Norway.

To my colleagues and friends at PoreLab and the UB Condensed Matter Department: I have enjoyed many interesting discussions on natural and social sciences. Special thanks to Ivan Latella who helped and supported me from the first day to the last day. The more intense and longer academic discussions on thermodynamics with you really impacted the way I now understand statistical physics. Anna, with whom I spent most of my time in Barcelona, I am deeply grateful for the interesting discussions on thermodynamics and social sciences. Luis and Juan, for making my time in the office much more interesting with discussions about all aspects of academia and life. To Michael, who made my second stay at PoreLab very exciting, always pushing me to think deeper and showing a wonderful German sense of humour. Finally, I am sincerely grateful for Ailo's friendship, both in Barcelona and in Norway, sharing time and thoughts with you was an absolute pleasure.

I want to thank MICIU, Spanish Government and the Catalan Government for granting me the opportunity to pursue this PhD under Grant No. PGC2018-098373-B-I00 and Grant 2017-SGR-884.

I thank my parents, siblings and Melissa, without their support it would not have been possible to have started this long journey. I would also like to thank my new family, my soul sisters, Silvia and Inés for giving me unconditional support in all aspects during these last years. To Valen and Gloria, for helping me to wake up from the illusion of the endless final year.

...I am grateful to all the people I have met throughout my life because without them, the entropy I have produced, efficiently and not so efficiently, would not have been enough to obtain information to build, rebuild and maintain my complex being. I am deeply grateful to all of them and their teachings because then I was able to flow spontaneously and let myself get caught up in the philosophy of science and thermodynamics to understand myself and thus the universe itself a little more.

Abstract

A set of disordered interacting building blocks may form ordered structures via self-assembly. External intervention in the system through the addition of chemical species or the application of forces leads to different self-assembly scenarios with the appearance of new structures. For instance, the formation of microtubules, gels, virus capsids, cells and living beings among others takes place by self-assembly under non-equilibrium conditions. A general evolution criterion able to determine the type of structures formed in a non-equilibrium self-assembly process is lacking. Under equilibrium conditions, we know that structures emerge at minimum free energy values. Experiments, however, have shown that when self-assembly takes place outside equilibrium the structures do not appear at free energy minima but rather at optimal values of some structural parameters. We show how the architecture of self-assembled structures can be determined from the knowledge of the energy and matter dissipation inherent to its formation. When the amount of dissipation, quantified by the total entropy produced in the process, is represented in terms of parameters characterising the shape of the assembled structures its extremes correspond to structures found in experimental situations such as gelation and Liesegang ring formation. From the connection between the entropy produced and the type of structures formed, we formulate a selection criterion that shows why a set of disordered units can give rise to a certain self-assembled structure. The criterion establishes that the minima of a non-equilibrium free energy depend on structural parameters and on the entropy produced. The criterion is able to predict the formation and configuration of structures such as Liesegang rings and patterns in magnetic colloids and could constitute a powerful tool to understand the synthesis of advanced materials, enantiomers, and nanoparticles. From the knowledge of the intimate mechanisms leading to the formation of structures and the thermodynamic criteria for the emergence of self-assembled structures, we might make possible the implementation of re-configurable and bio-inspired materials as well as give a more straightforward perspective to the understanding of the emergence of life.

Key words: Condensed Matter, Dissipation, Entropy Production, Mesoscopic Structures, Non-Equilibrium Thermodynamics, Self-Assembly, Self-Organisation, Symmetry-breaking.

Content

INTRODUCTION

1. Self-assembling outside equilibrium: emergence of structures mediated by dissipation

A collection of disordered building blocks interacting with each other can form ordered structures through a process of self-assembly. These structures can be modified by the addition of a chemical species or the application of external forces. For example, the formation of microtubules, gels, virus capsids and cells takes place by self-assembly under non-equilibrium conditions. A general evolutionary criterion for why nature selects some non-equilibrium structures and not others is lacking. However, progress has been made in understanding the mechanisms of non-equilibrium self-assembly (NESA) by formulating models to analyse particular situations. The main concepts, mechanisms and models proposed for the study of non-equilibrium self-assembly systems and their applications in different disciplines are reviewed, and the role of dissipation in the emergence and maintenance of structures is analysed. This chapter aims to lay the foundations for the development of models and experimental studies of NESA systems.

This introduction is based on the review article published in *the Journal of Physical Chemistry Chemical Physics*, **21**, 17475-17493, (2019). Ref. [1]

1.1. Thermodynamics for self-organised systems

How can we explain the emergence of order in nature? What is the mechanism by which homogeneous systems can form ordered structures? Researchers such as Ilya Prigogine [2] and Adrian Bejan [3, 4] have already pointed out that the transition from an ordered to a disordered state is irreversible and therefore entails a production of entropy.

Turing's seminal work on the formation of spatio-temporal patterns [5, 6], together with the works of Belouzov and Zhabotynski on pattern formation in chemical reacting systems [7] and those of Lorenz on climate unpredictability [8, 9, 10], shown that structures, far from being static and completely predictable, where adaptable, i.e., dynamically stable under large fluctuations. These phenomena are called self-organisation, which is not only observed in nature but also in human society. If, according to thermodynamics, the ultimate goal of the universe is the increase of entropy and its irreversible production, the best way to achieve this could be through the self-organisation of its parts by complex dissipative processes.

How could thermodynamics contribute to explaining the self-organisation of systems? Self-assembly processes are essential in the formation of self-organised structures that arise under non-equilibrium conditions with consequent energy dissipation. Understanding the relationship between structure formation and energy dissipation is therefore of vital importance for the understanding of the mechanisms of self-assembly. This is the main objective of this thesis. We will propose a model that explains why certain structures appear with higher probability and why others that could in principle occur are never observed.

1.2. From equilibrium to non-equilibrium self-assembly

Self-assembly (SA) is the process through which a disordered set of constituents interact with one another to form organized structures [11]. The constituents, the building blocks (BB), are the smallest discrete entities required to build the structure. They can be as small as atoms and as large as planets [12]. The nature of the BB as to their chemical composition, geometry, mass and charge is crucial to determine the type of emerging structures and the processes leading to them [13]. Contrarily, pattern formation in continuous media such as Benard cells [14], chemical waves [15] and Turing structures [5] results from the existence of a dynamic instability where the nature of the BB is not essential to determine the organization process.

When self-assembly takes place outside equilibrium, the system can adapt its organization mode in response to external stimuli, thus it can self-heal its structures when wounded and even self-replicate [16]. Contrarily, equilibrium SA has a limited adaptability [17] and cannot show multiple length scale structures [18]. Non-equilibrium self-assembly (NESA) (illustrated in Fig.**1-1**) leads to the transient formation of an active material [19] in which properties such as lifetime, stiffness and self-regeneration capability are determined by the assembly pathway [20], reaction kinetics and fuel levels rather than by equilibrium compositions [21]. Active materials built from NESA processes show a nonlinear dynamic behavior and constitute a key step in the development of synthetic self-organization in out-of-equilibrium systems [22]. Prominent examples include GTP-fueled microtubule assembly[23, 24] and ATP-driven actin assembly[25]. Nevertheless, while synthetic counterparts may in principle exist, such complex responses have not been observed [26] because of the lack of feedback mechanisms [27] that increase the strength of the correlations, as occurs in self-organized criticality [28].

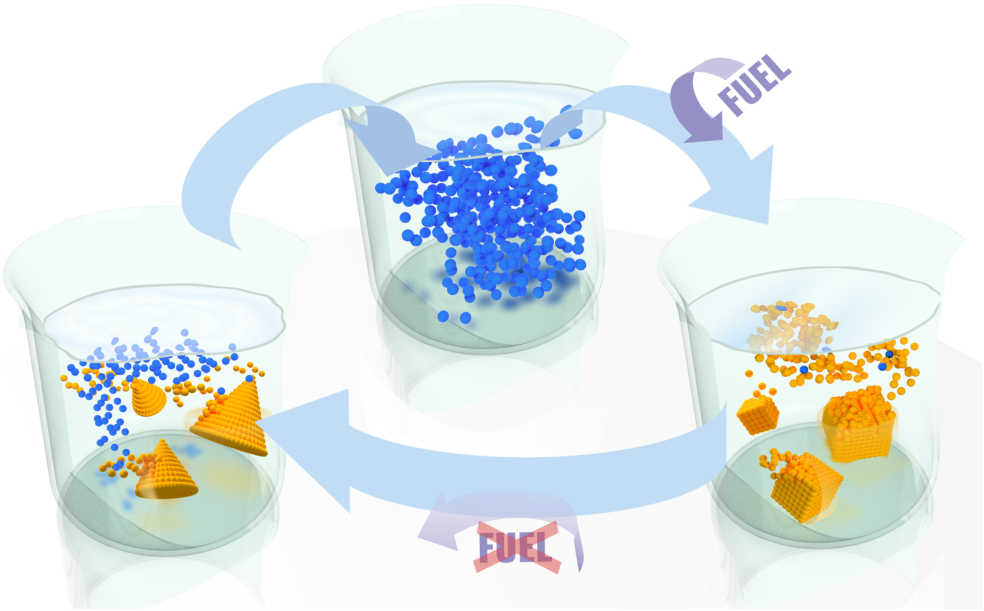

Fig. 1-1.: General scheme of a non-equilibrium self-assembly process. The system is initially in a disordered state in which the building blocks (blue particles) are deactivated. After addition of fuel, the components become activated and form stationary structures (golden cubes) in which the assembling and dissasembling of the blocks balance each other out. When fuel addition ceases, the structures may reach a kinetically trapped or metastable state represented by conical structures of golden particles. These structures may in general persist for long periods or may, due to small perturbations, again return to the initial state.

Currently, there is a great deal of interest in the control of NESA structures such as hydrogels for medical applications [29, 30, 31, 32, 33, 34, 35, 36, 37] and in the synthesis of self-assembled particles for technological applications [38, 39, 40] as well. In material science, there is a high interest in the design and control of structures to yield mesoparticles of a well-defined size [41]. Some efforts have been devoted to develop novel synthesis methods based on the bottom-up approach to produce organic nanomaterials with well-defined shapes for potential medical applications under non-equilibrium conditions [42, 43].

Non-equilibrium self-assembly is accompanied by energy dissipation and entropy production [26]. The process leads to the formation of stationary, kinetically trapped or even equilibrium structures. Due to the non-equilibrium nature of the process, in general there is no thermodynamic potential having minima at the states in which structures are formed. How energy dissipation may explain the emergence of ordered structures from a set of disordered components and how the formation of the structures is governed by the laws of thermodynamics [44, 45] remains an unanswered question [44]. The lack of a general framework for the description of self-assembled structures under non-equilibrium conditions has promoted the development of computational approaches. These approaches, however, are not always easy to implement since the number of particles needed to explain the formation of the structures must be extraordinarily large [46, 47].

A practical performance may be carried out by means of coarse-grained particles [47] and implicit solvent models [48, 38] such as phase-field approaches [49, 45], coarse-grained molecular dynamics [50], mesoscopic dynamics [51, 52, 53], Langevin dynamics [54, 55, 56] and kinetic Monte Carlo [38, 57, 51, 52, 58, 59]. Additionally, kinetic models based on balance equations [60, 61, 62, 63, 64, 65, 66, 67, 68, 69], hydrodynamic equations [44, 70, 71], and mesoscopic non-equilibrium thermodynamic formalisms [72, 73, 53] brings ways to understand the dynamics of the formation of NESA structures. On the other hand, thermodynamic approaches based on information [74, 44, 75, 76, 77, 78, 79, 80, 81, 82, 83, 84, 85] and Gibbs [2, 72, 86, 87, 88, 89, 90, 53] entropies have been proposed to characterize and understand the NESA processes and the assembled structures.

The amount of energy dissipated in the assembly process plays an important role in the characterization of the final state of the emerging structure and in its resulting properties. Under this perspective, we review the main concepts, mechanisms and models proposed to study non-equilibrium self-assembly systems and their applications in different disciplines and to analyze the role played by dissipation in the emergence and maintenance of the structures. This chapter intends to set up the basis for the development of models and experimental studies of NESA systems. Some key concepts used throughout the manuscript are: An assembled structure is understood as an arrangement of BB into a material object that integrates a heterogeneous system; SA is the organization of discrete elements into patterns or structures; Equilibrium SA is a process leading to the formation of stable structures through quasi-equilibrium steps; NESA is a process leading to the formation of stable, metastable, kinetically-trapped and stationary structures mediated by dissipation, being the knowledge of the nonequilibrium intermediate structures and their kinetics crucial in the understanding of the process; NESA processes are the previous steps in the formation of SO structures; SO is the formation of highly hierarchical structures induced by the existence of a network of feedback loops; By adding a network of feedback loops to NESA processes we may obtain SO structures. Finally, pattern formation in continuous media without aggregation of components is a kind of SO but not of SA.

The chapter is organized as follows. In section 2, we define and discuss NESA and SO as a processes leading to the formation of ordered structures, as well as their relation. In Section 3, we focus on the concept of structure and present some examples of kinds of NESA. In section 4 we discuss mechanism, processes and energetics of NESA systems. In section 5, we discuss the most common models to describe the dynamics and/or the thermodynamics of the assembly processes. In section 6, we highlight the importance of distinguishing different non-equilibrium structures in ordered states. In section 7, we point out an open question related to a general non-equilibrium potential. Finally, in Section 8 we present the main conclusions and perspectives about NESA and propose some open problems which could be of interest to more deeply understand NESA systems.

1.3. Processes generating non-equilibrium structures

To identify the mechanisms governing the formation of structures constitutes the starting point in the formulation of robust computational, kinetic and thermodynamic models able to explain SA processes.

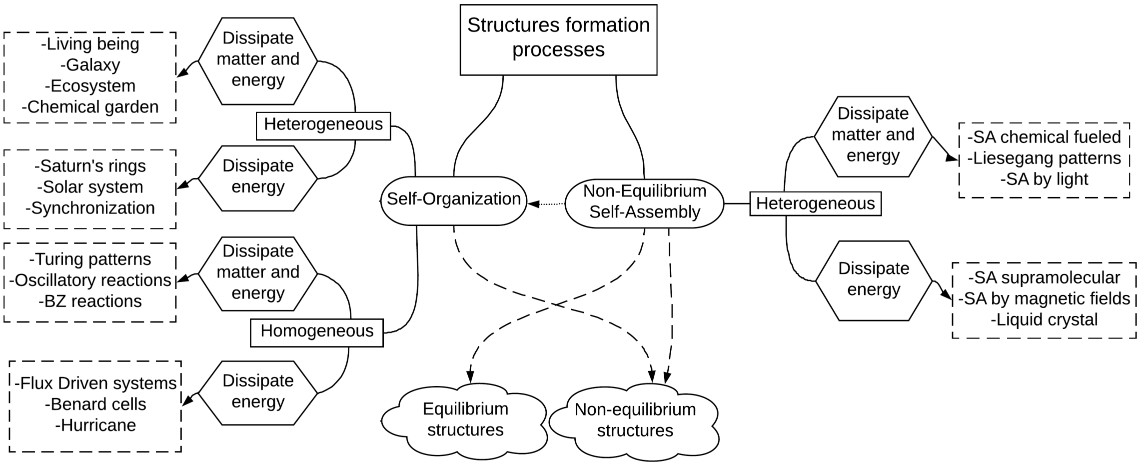

Fig. 1-2.: Structure formation processes. Equilibrium and non-equilibrium structures are formed through self-assembling processes whereas self-organizing processes only lead to non-equilibrium structures. Non-equilibrium self-assembly processes may give rise to self-organization if feedback loops are added to the system. The resulting structures are heterogeneous, composed of building blocks, or homogeneous emerging in continuous media. These structures dissipate only energy or energy and matter. Examples are given in the dashed squares.

Self-assembly processes yield non-equilibrium and equilibrium structures, depending on if energy and matter are supplied to the system or not, whereas self-organization processes always lead to non-equilibrium structures. In Fig.**1-2**, we give examples of structure formation via both types of processes.

1.3.1. Nonequilibrium self-assembly and self-organization

Two are the processes leading to the formation of nonequilibrium structures: NESA processes in which structures emerge by sequential addition of their elementary constituents, and spatio-temporal instabilities leading to SO whose origin may be direct self-catalysis, indirect self-catalysis (positive feedback) and end-product inhibition (negative feedback) [91]. In this subsection, we will mention some characteristics of these processes.

SO is understood as the appearance of spatio-temporal ordering that manifest itself through the formation of non-equilibrium spatio-temporal structures or patterns. [92, 93, 94, 95]. The most elementary steps in the evolution of living beings are based on self-organization [96, 2, 97, 98, 99, 100]. These processes are frequently observed in flocking birds, swimming bacteria, microtubules assemblies as a major constituent of the cellular cytoskeleton [24, 23] and in actin filament networks [17]. Galaxies and structures composing them can also be viewed as SO structures dissipating matter and energy [101, 102, 103, 104, 105]. Chemical gardens are self-organized structures in which many different chemical species can form structures having a great disparity of scales, ranging from nanometers to meters [106].

Additionally, self-organization is frequently observed in hydrodynamic systems with the formation of patterns resulting from the existence of instabilities such as those occurring in thermal convection in pure fluids and binary mixtures, Taylor-Couette flow, parametric-wave instabilities[14], solidification fronts [60], nonlinear optics[14], oscillatory chemical reactions [107, 108] and plankton colonies [109] to mention just a few. Self-organization also takes place in many diverse soft-condensed-matter systems such as lipid membranes or vesicles, Langmuir and Langmuir-Blodgett films, thin liquid films on solid surfaces and adsorbate layers in metals [110] and in electrode-electrolyte interfaces [111]. SO also takes place when a system having a large number of degrees of freedom evolves towards a state that exhibits spatial and/or temporal scale-invariance. This type of SO has been referred to as self-organized criticality [28].

On the other hand, nonequilibrium self-assembly processes have been analyzed when the system is subjected to external fields and templates, as in directed assembly [112] and when molecular building blocks are engineered, as in controlled self-assembly[113]. The process has also been studied at supramolecular scales [114, 115, 116, 117] and in the presence of dissipation [44].

SA processes under nonequilibrium conditions has been subdivided into two categories: dissipative and metastable [18, 26]. Dissipative SA [11] is the organization of a system due to a continuous input of energy from the environment. Metastable SA is the organization of a system which dissipates energy around a local equilibrium or around a kinetically trapped state [26]. Both processes are ubiquitous in biology, driven by irreversible chemical reactions and leading to the formation of structures unavailable under equilibrium conditions [56]. Disassembly (DA) refers to the reverse of SA, the dismantling of the original crystalline, liquid crystalline or amorphous state of the material prior to self-assembly [117].

In Fig. **1-3**, we show some representative SO and NESA structures. Figs.**1-3**(a) and (b) are NESA structures, while Figs.**1-3**(c) and (d) are SO structures.

1.3.2. From non-equilibrium self-assembly to self-organization

NESA structures may evolve towards adaptable, spatio-temporally controlled and self-healing structures but their formation cannot explain the inherent complexity of natural systems such as a biological cell [22]. In the cell, self-assembled structures are organized in hierarchical levels in which different kinds of structures interact and affect the formation and maintenance of other structures. This higher degree of organization is referred to as self-organization [118]. The concept of SO is clearly illustrated by the diversity of the architectures observed in cytoskeletal microtubule networks [24, 23].

We can interpret NESA processes as the first step in the formation of a self-organized system. In fact, NESA is a specific case of SO in which fundamental and discrete entities make up structures. The coupling of the relevant variables of NESA processes may give rise to the appearance of feedback loops which increase the complexity of the structure and endows it with a hierarchical nature, thus leading to a self-organized state,as shown in Fig.**1-2**. This fact brings advantages and opportunities because properties of biological self-organized structures, such as the spatial and temporal control over the assembly, highly adaptability, and self-healing can also be reached using NESA man-made counterparts [26]. NESA and chemical systems that use chemical reaction networks and transport processes to achieve various types of oscillatory behaviors illustrate the way to go from NESA to SO [119, 44].

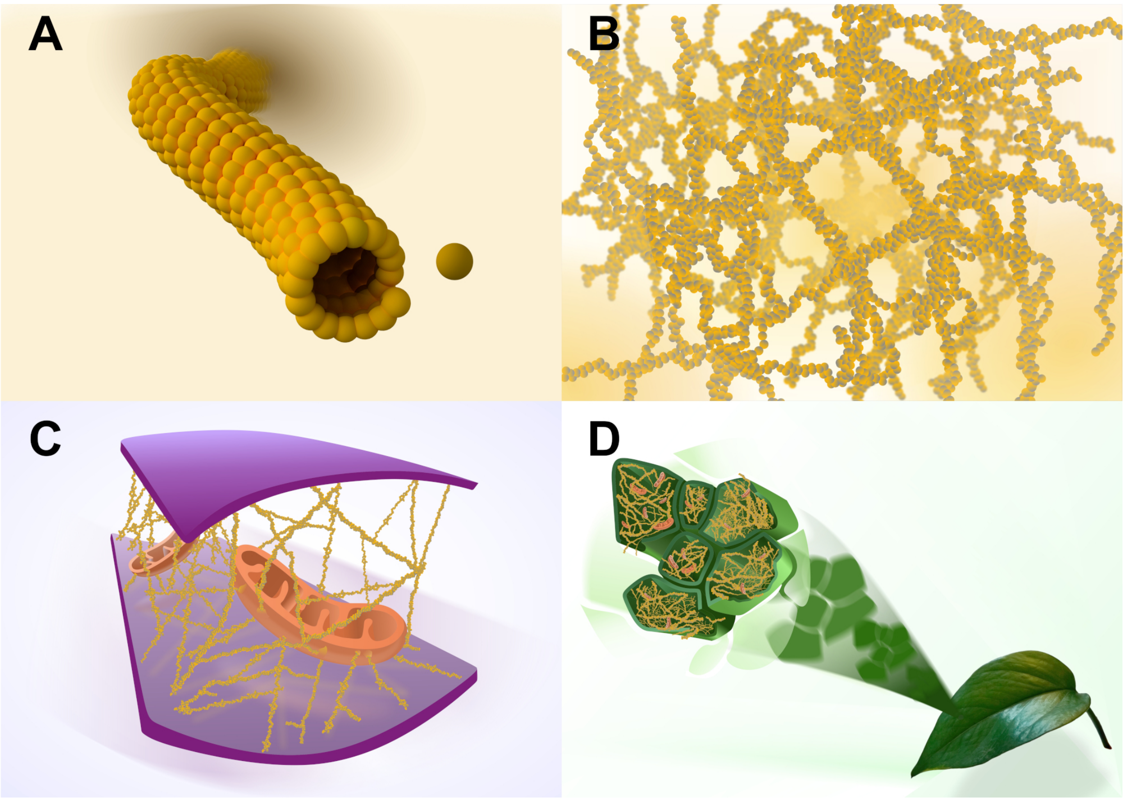

Fig. 1-3.: Self-organized and non-equilibrium self-assembled structures. a) Microtubule, assembled from tubulin dimers. b) Gel, assembled from fibers or microtubules. c) Plant cells, assembled from microtubules assemblies. d) Leaf, assembled from plant cells.

1.4. Non-equilibrium self-assembled structures

1.4.1. Interactions and building blocks

The BB have specific active zones where covalent non-covalent interactions may take place. The location of the active zones determines the final shape of the resulting structures such as fibers, branched fibers, cubes, spheres, sheets, rings, icosahedra, square pyramids, tetrahedra and twisted and staircase structures [120]. For instance, in the formation of linear fibers (polymers based on chromophoric azobenzene [121] or dibenzoyl-(l)-cystine, *DBC* [122]), the BB have two spatially opposed assembly centers. In the formation of micro-tubules (polymers based on tubuline) [24] and non-linear fibers [123], the BB have two assembly centers not spatially opposed. In the case of light-induced self-assembly structures from BB of nano-particles coated with photo-switchable molecules [124], particles have more than two assembly centers. Monomers having two or more functional groups, i.e., BB having more than two assembly centers, trigger the formation of branched polymers and a competition between ordered self-assembly and non-linear random polymerization[125]. A special case of BB are patchy particles, such as Janus particles [126, 127] which can be synthesized by using different techniques [128].

1.4.2. Hierarchical nature of the interactions

The transition from an initial disordered state to a final structure [129, 22] takes place progressively, proceeding through intermediates steps. The appearance of these structures depends on their precursors [22], on the strength of the interactions [130] and on the sequentiality of the assembly processes [13]. Hierarchical order of the structures results from the different interactions taking place in every stage of the assembling process. We differentiate the simple structures formed from the assembly of BB from those which result from the assembly of the simpler structures that can be viewed as precursors.

For instance, during the SA process we identify first-, second- and higher-order structures depending on the nature of the interactions and material precursors. First-order structures result from activated precursors which interact strongly by means of covalent interactions giving rise to matter dissipation, high magnetic forces or hydrogen bonds with energy dissipation [121], triggering an ordered assembly called sequential or non-vectorial assembly[13]. Second-order structures result from previously activated first-order structures which interact more weakly than the fundamental activated BB, triggering a non-sequential or vectorial assembly [13]. Higher-order structures may assemble from lower-order structures due to van der Waals and other weak forces [131]. An example of how the presence of hierarchical interactions may give rise to the formation of hierarchical structures is gelation [122, 132].

1.4.3. Examples of self-assembly under non-equilibrium conditions

Application of an external force or a matter input may trigger the self-assembly process giving rise to the formation of non-equilibrium self-assembled structures in closed and open systems. The emerging structures in open systems are stationary structures shown in Fig.**1-4** while those emerging in closed systems are metastable or stable structures as Fig.**1-5** indicates.

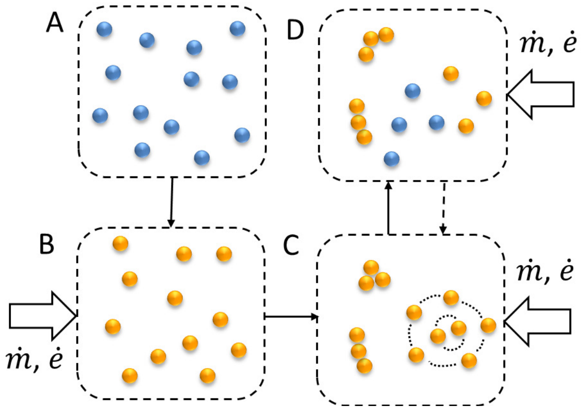

Fig. 1-4.: Scheme of NESA in open systems. a) A system composed of deactivated BB (blue particles). b) A constant input of matter and/or energy activates the BB (yellow particles). c) Structures assemble. d) A system composed of stationary structures and instantaneous presence of disassembled and deactivated BB. Dotted lines indicate particle trajectories.

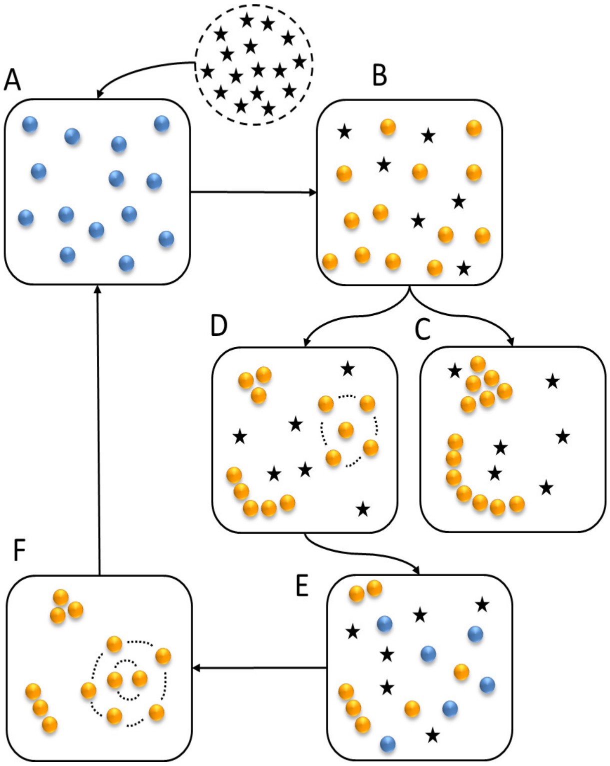

Fig. 1-5.: Scheme of NESA in closed systems. a) A system composed of deactivated BB (blue particles). b) Addition of activator (black stars) yields activated BB (yellow particles). c) Assembly of activated BB triggers the formation of equilibrium structures, or d) metastable structures. Metastable structures may reach another energetically more stable state, but before they must pass through transition states e) in which some BB are disassembled and deactivated. f) If there is enough activator, the system could reach another metastable configuration. In the absence of more activator, the BB disassemble and deactivate, the system thus adopts the equilibrium configuration a) unless more activator is added.

Typical cases in which NESA structures are observed are the following:

Bottom-up chemical fueled assembly

The bottom-up approach is used to synthesized NESA structures from well defined small units and chemical fuel. Processes such as gelation and reactive-crystallization are examples where the small units suffer sequential transformation to finally yield kinetically trapped or metastable structures [18], for instance virus capsids [133, 134, 135, 136, 137]. Furthermore, polymerization is a key process to identify NESA structures such as those observed in the polymerization of vinyl monomers that contain an enzymatic activated substrate, triggering an SA of colloidal nanostructures [138], diblock semiflourinaded n-alkanes aggregation and gels[139], and assembly of micellar aggregates [140].Another prominent example of chemical-fueled SA is active gels [141] such as bio-filaments, associated to motor proteins, and the cytoskeleton of living cells [142, 143, 144, 145].

Transient assembly in reaction-diffusion processes

Transient assembly of active materials fueled by a chemical reaction [21] combines reaction-diffusion and assembly processes in which lifetime, stiffness and self-regeneration capabilities of the self-assembly of synthetic molecules is determined by the interconversion rate between inactive and active monomers and the amount of reactant [122]. One common characteristic of these reaction-diffusion assisted SA processes is that a reaction is not always required to maintain the nanostructures once they are formed. When the reaction stops, order may remain [146]. Reaction-diffusion processes can be used to generate closely monodisperse, often sophisticated SA nanostructures [146], as is the case of Liesegang patterns in which reaction-diffusion-agglomeration take place [66, 60, 67, 147, 68, 148, 132].

Active particles assembly

Dynamical clustering and pattern formation of active particles which present induced self-phoresis and chemorepulsion by surface effects [149, 150, 151] may give rise to NESA structures. Furthermore, active particles tend to form different metastable structures with different shapes [152] or stationary structures characterized by segregation coefficients [153]. Also, self-thermophoresis of Janus particles [126, 128, 127] can lead to structure formation, as in the case of Au-capped colloidal particles [154]. In Addition to phoretic forces, Marangoni stresses can also generate particle propulsion [155, 156, 157]. Finally, it has been shown that self-propulsion may also promote synchronization of particles and dynamic clusters [158, 159].

Light-induced assembly

Light may induce reversible switching of a molecular system between aggregated and non-aggregated states, leading to the emergence of NESA structures which at the macroscopic level manisfest a fully reversible sol-gel phase. The aggregation and the photochemically induced NESA structures also lead to dynamic pattern formation [123]. Another example of NESA induced by light are nanoparticles (NPs) decorated with ligands combining photo-switchable dipoles and covalent cross-linkers, forming three-dimensional supra-structures of various types and sizes. NPs covered with only a few photoactive ligands form metastable crystals that may assemble and disassemble on demand by using light of different wavelengths [38]. Doted NPs may also organize themselves into permanently cross-linked structures including robust supracrystals and spherical aggregates[124]. The simplest case is found in a system based on dithienylcyclopentene photochromic which under light exposure gets excited, triggering the formation of extended aggregates in solution and allowing the control of the media viscosity by light [160]. Another example of light-induced assembling is photo-switchable catalysis controlled by reversible aggregation/dispersion of catalytic nanoparticles [161]. Reversible SA of NPs induced by light does not require that the particles be functionalized with light-responsive ligands. Instead, one can use a photo-switchable medium that responds to the light modulating the interparticle interactions [39].

Self-assembly induced by magnetic fields

Magnetic colloidal dispersions suspended at the interface of a liquid constitute a rich terrain to explore the fundamental mechanisms of out-of-equilibrium dynamics and self-assembly [58]. One of the first studies on magneto-hydrodynamic SA systems was performed in [46] by using millimeter-sized objects rotating at a liquid-air interface to observe a pattern in the distribution of the particles [46]. Other examples are magnetic droplets on superhydrophobic surfaces [162], lanes of colloidal particles under the influence of external fields [163, 164], clusters of active colloids [165], swarms of self-propelled particles [166] and self-assembly of superparamagnetic colloids [167], paramagnetic particles [168, 169] and ellipsoidal particles [170] under the presence of a magnetic field. We can also mention in this context the formation of chain-like aggregates from very small (10 nm diameter) maghemite nanoparticles and the subsequent aggregation of these chains into complex-ordered super-structures upon evaporation of the solvent under an applied magnetic field [171].

Self-assembly on surfaces

NESA can be observed in surfaces such as self-cleaning super-hydrophobic surfaces [172]. The careful placement of functional groups, such as Porphyrin molecules, that are able to participate in directed non-covalent interactions will allow the rational design and construction of a wide range of supramolecular architectures absorbed on surfaces (gold NPs surfaces) forming monomers, trimers, tetramers or extended wire-like structures [173].

1.5. Non-equilibrium self-assembly mechanism and energetics

1.5.1. Mechanism

Three main steps are involved on the formation of NESA structures: activation[174, 22, 123, 160], assembly and disassembly [16, 122, 132]. Activation of the BB provides the energy required to trigger the process. BB and even intermediate structures can also be activated when concentration, temperature or size surpass a certain threshold value and by means of phase-changes. BB and intermediate structures may also be activated by chemical reactions, light [160] and rotating magnetic fields [46]. A mechanism for structures in metastable and kinetically trapped states is discussed in [20].

Assembly and disassembly processes may take place sequentially (block-by-block) or non-sequentially as in the case of non-oriented assembly [53, 16]. The type of process which may occur depends on the nature and characteristics of the building blocks. While assembly may be reversible, disassembly is irreversible [122] because the disactivated BB must be activated again to proceed with the formation of NESA structures [44]. Studies on supramolecular polymers are important for the understanding of the assembly mechanism where an intrinsic mechanism for supramolecular polymerization can be seen as a sequence of monomer (BB) association and dissociation steps [175]. A theoretical formulation for the sequential assembly processes of monomeric units was presented in [176]. Alternatively, a mechanism considering competition under thermodynamic control between self-assembly and nonlinear random polymerization was proposed in [125].

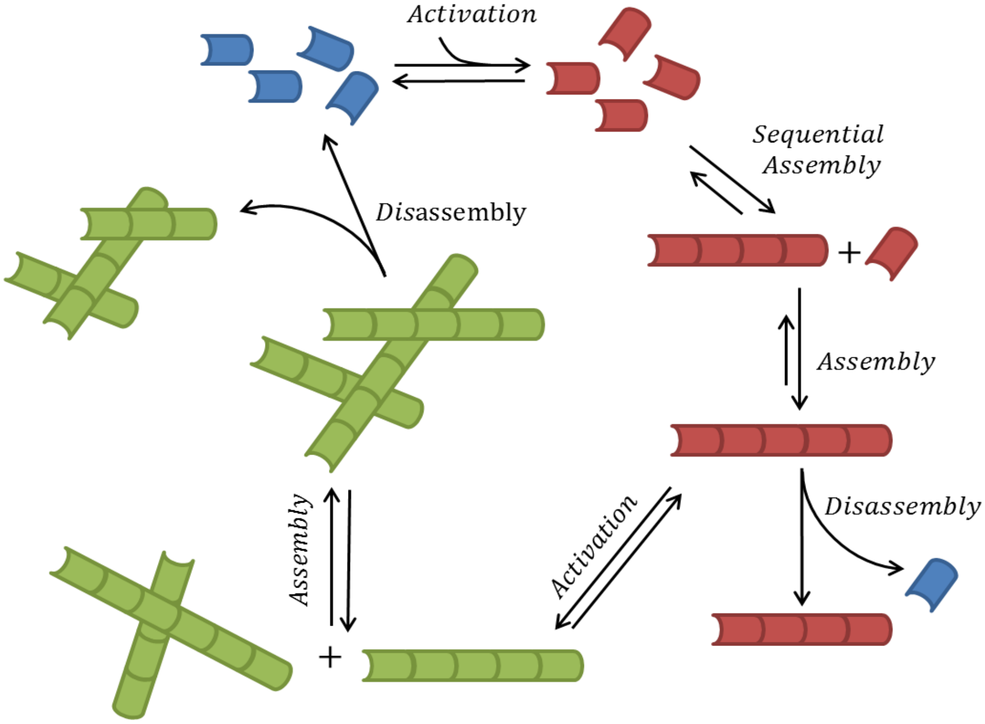

Fig. 1-6.: NESA mechanism. Building blocks (blue squares) are activated (red squares) and assemble to produce red cylinders. Red cylinders in turn may disassemble giving shorter red cylinders and building blocks (blue squares). Eventually, the red cylinders could be activated (green cylinders which are able to interact with other green cylinders) to form a more complex structure that in turn may disassemble yielding multiple building blocks and smaller complex structures.

As mentioned in section 3.2, the existence of a hierarchy in the interactions allows the differentiation of the kinds of hierarchical structures formed. Following the example of gelation [132], we illustrate in Fig.**1-6** a general mechanism considering two types of components (blue squares and red cylinders) and two kinds of structures: red cylinders and overlapping green cylinders. The fundamental components denoted by blue squares are activated becoming red squares that assemble to form red cylinders. These cylinders in turn are activated yielding green cylinders which may interact among themselves to form more complex structures: green overlapping cylinders. The structures may also disassemble to back into the original components.

1.5.2. Energetics

In kinetically trapped and metastable structures, the system may be confined around a local minimum of the free energy landscape whose time evolution depends on the shape of the energy landscape around that minimum[175, 11]. The formation of self-assembled structures in a stationary state requires the presence of a constant influx of energy or matter e.g., chemical fuel or light and the removal of waste products to be kept in a dissipative non-equilibrium state. The main differences between equilibrium and non-equilibrium SA have been pointed out in [13] and in [16].

There is a growing evidence that the properties of NESA structures largely depend on the conditions under which SA takes place and that the process can end at different final basins of the free energy landscape [177]. Different local minima may coexist in the free energy landscape where, in some cases, self-assembled structures cannot be reached due to the presence of high potential barriers [178]. In NESA processes, the system tends to minimize its free energy by forming structures thus increasing order and decreasing the entropy. Due to the second law, entropy must then be produced during the process and released to the environment. In equilibrium, structures tend to lie at the minima of the free energy. Outside equilibrium, this is not necessarily so due to the lost of entropy due to dissipation.

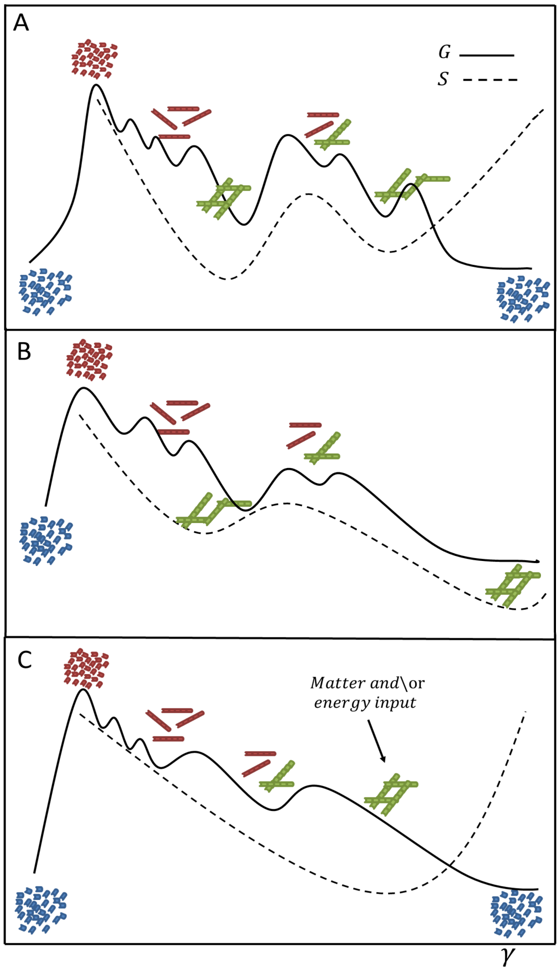

Fig. 1-7.: Equilibrium free energy G and entropy S of NESA systems as a function of the reaction coordinate γ. Final self-assembled structures are represented as overlapping (and aligned) green bars. NESA structures correspond to states of local or global minimum of the entropy. a) Kinetically trapped and metastable NESA structures. The free energy of the state is close to a local minimum. b) Equilibrium NESA structure. Energetic instead of entropic effects dominate. c) Steady-state NESA structure. They do not lie in a local or global minimum of the free energy of the system. This is only observed when there is a constant input of matter and/or energy to the system.

In Fig.**1-7**, we sketch typical equilibrium free energy and entropy landscapes for the structure formation. In Fig.**1-7**(a), the kinetically trapped NESA structure corresponds to the lowest value of the entropy of the possible structureswhich is close to a free energy local minimum. To reach this state, the system has to evolve through different intermediate metastable states represented by red bars. The free energy barrier between kinetically trapped and a metastable NESA structure is high. However, the structure could be reorganized into another metastable structure which has a higher tendency to minimize the free energy of the system and return to a disordered equilibrium state. Fig.**1-7**(b) shows that the NESA structure lies in a state of minimum free energy with the lowest entropy. To reach this state, the system passes through different metastable states represented by the red bars and a different configuration of overlapped green bars. In Fig.**1-7**(c), we represent the stationary NESA structures which do not lie in a local minimum of the free energy but rather in the lowest entropy of the system. Likewise, the system may evolve through different intermediate and metastable states composed of intermediate structures such as the red bars and a different configuration of overlapping green bars until a stationary NESA structure is reached.

1.6. Non-equilibrium self-assembly models

Reaction-diffusion equations proposed in [179, 180] and aggregation equations based on the law of mass action [181] are basic in the formulation of models for the formation dynamics of NESA structures [182]. Diverse models have been proposed to describe the formation of non-equilibrium structures at multiple length scales [13, 12], from atomistic to mesoscopic scales. Computational models perform atomistic descriptions whereas mean-field and coarse-grained models [183] have been used to overcome the inherent complexity of atomistic models [47]. On the other hand, kinetic models are proposed to describe macroscopic dynamics and even to connect microscopic and macroscopic dynamics. Additionally, thermodynamic models have been used to characterize thermodynamically the emerging structures.

1.6.1. Computational models

Molecular dynamics and Montecarlo methods have been used to simulate the formation of NESA structures. Multiscale methods combine coarse-grained and atomistic or Monte Carlo and molecular descriptions [51, 52, 47]. Additionally, Langevin dynamics is frequently used to describe hydrodynamic and assembled structures in the mesoscale [183].

Monte Carlo and molecular dynamics

One of the first attempts to understand the formation of structures through Monte Carlo (MC) simulations was the study of the dynamics of diffusion-limited cluster-cluster aggregation [184] and reaction-limited cluster-cluster aggregation [185, 186, 187].MC simulations have been performed, for example, to describe assembled structures of truncated-conical shape forming cylindrically shaped nanofibers. These simulations are very useful to study self-assembly at the nanoscale but not so much so for larger scales.

The form of the simulation potentials is crucial to implement such methods. A family of simple potentials that give rise to the assembly of chain-like, random surfaces, tubular and hollow icosahedral structures similar in many respects to viruses was proposed in [188, 189, 190]. For instance, one of the potentials used to compute the dipole interactions U_d between a pair of particles has the form

$$U_d = (\vec{\mu}_i \cdot \vec{\mu}_j)/r_{ij}^3 - 3(\vec{\mu}_i \cdot r_{ij})(\vec{\mu}_i \cdot r_{ij})/r_{ij}^5 \tag{1-1}$$

where $\vec{\mu}_i$ is the dipole moment of particle i while r_{ij} is the distance between the particles i and j. Interactions between elongated particles have been modelled by including quadrupolar contributions to the potentials [59].

Contrary to conventional MC, Kinetic Monte Carlo (KMC) computes the transition probabilities from a set of possible transition rates rather than from a set of possible configurations. Additionally, KMC algorithm gives the correct time scale for the evolution of the system [191] and can be used as a tool to describe non-equilibrium phenomena [192] in terms of long-time self-assembly dynamics, as performed in biochemical reaction networks taking place in cell [193]. Scaling arguments and KMC simulations have been performed to study the reversible formation of aggregates [194, 195]. The solution of the master equation by KMC works in a similar way to Guillespi Algorithm [196]. The transition probabilities in the KMC scheme are derived from a renormalized master equation of the diffusion process, having a similar form as the one proposed in Glauber dynamics [197]. The recipe of the KMC simulation using Glauber dynamics is similar to the Metropolis scheme [198] but with the transition probability for the change of state s_i into state s_j, with energies E_i and E_j, given by

$$P(s_i \rightarrow s_j) = \left[1 + \exp((E_j - E_i)/k_B T)\right]^{-1}, \tag{1-2}$$

This scheme was implemented for a system of nanoparticles interacting through Lennard-Jones pair potentials that change their nature from repulsive to attractive depending on light exposure (activation) [38]. This method does not allow the study at several length scales; however, it avoids the use of a stochastic noise term therefore this method is particularly relevant for cases where the magnitude of the driving force is comparable to the stochastic noise, such as in Brownian dynamics.

Langevin dynamics

By using Langevin dynamics, it has been shown that internal and external forces, such as electrostatic, local temperature gradients, magnetic, electric or temperature fields, underlying non-equilibrium segregation can be used to control the SA of particles that lack attractive interactions. It has also been demonstrated that the segregated structures can range from compact clusters to elongated and string-like patterns [55]. To show the formation of such structures one can use the potential of mean force

$$U(\vec{r}) = k_B T \ln\left(\frac{P_F(\vec{r})}{P_0(\vec{r})}\right) \tag{1-3}$$

where $P_F(\vec{r})$ is the particle distribution function in the presence of a force $\vec{F}$ acting on the particles and P_0 is the corresponding distribution at $\vec{F} = 0$. In the absence of inertial effects, Brownian dynamics simulations have been performed for a binary mixture of particles coated by weak acids and weak bases under externally controlled pH oscillations [56] to explain the emerging structures. Brownian dynamics simulations of polar microtubule ensembles driven by cross-linking motors have allowed the study of microscopic organization and stresses[183].

Langevin dynamics has also been implemented to analyze the random motion of active particles, self-propelled objects susceptible to assemble to form structures of diverse shape [199, 200]. For instance, for self-propelled particles moving with velocity v and rotating an angle ϕ, the corresponding stochastic differential equations for translation and rotation are

$$\frac{d\vec{x}}{dt} = v\cos\phi + \sqrt{2D}\vec{\xi} \tag{1-4}$$

$$\frac{d\phi}{dt} = \sqrt{2D_\phi}\,\xi_\phi \tag{1-5}$$

Here $\vec{x}$ is the position vector, D the translational diffusion coefficient and D_ϕ the rotational diffusion coefficient. The terms $\vec{\xi}$ and ξ_ϕ define independent white noise stochastic processes with zero mean and correlation $\langle \xi_i(t)\xi_i(t')\rangle = \delta(t-t')$ [201]. In Fig.**1-8**, we present a particular case in which Brownian dynamics could be applied to describe the behavior of hemicylindrical like-plates covered with platinum on one surface and that float at the surface of an aqueous solution of hydrogen peroxide, exhibiting ordered assembly [149].

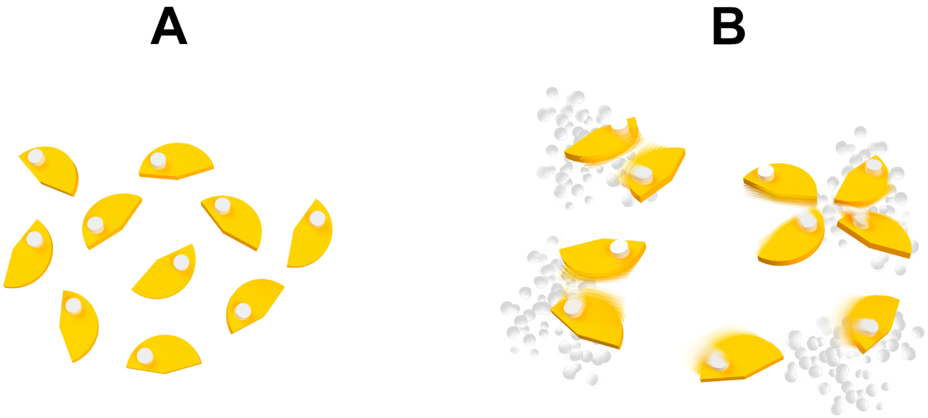

Fig. 1-8.: Self-propelled particles may self-assemble due to the presence of chemical reactions thus forming pairs or even aggregates such as rotating asters[149].

1.6.2. Kinetic models

Kinetic models based on conservation equations have been proposed to avoid conventional computational limitations found in classic Monte Carlo, Molecular Dynamics and Langevin methods, such as long computational time, limited length scales, use of noise term, among others. Conventional kinetic models cannot give enough microscopic information about the NESA structures. But some of these models allow us to establish a link between microscopic and macroscopic dynamics, as is the case of magneto-hydrodynamic, reaction-diffusion and mesoscopic non-equilibrium thermodynamic (MNET) models.

Reaction-Diffusion models

The starting point of these models is a set of deterministic nonlinear partial differential equations [14, 61] describing the time evolution of the systems exhibiting patterns and structures. Anomalous diffusion modelled by diffusion-like equations containing fractional derivatives has also been used to explain pattern formation such as Turing or Liesegang structures that appear in reaction-diffusion systems [202]. Additionally, there are found reaction-diffusion models describing the emergence of Liesegang patterns composed of NESA structures [41, 132].

Reaction-diffusion processes yield Liesegang [60, 64, 132] and Turing [203, 204, 205, 206, 207, 5, 75] patterns. In the case of Liesegang patterns, several models have been proposed to consider different growth/precipitation kinetics [66, 208, 148, 209, 210, 211, 63, 212, 64, 213]. A key element in these models is the kinetic expression for solids nucleation, growth and/or precipitation, which is a step function depending on the precursor concentration. For instance, in [132] the growing rate of the solid particles R_s, composing the Liesegang patterns, is divided into two steps and is represented by the Heaviside function:

$$R_s = \begin{cases} k(T)C_oC_s^2 & \text{if} \quad C_o < C_{lim} \\ k(T)C_oC_s^2 + k(T)C_eC_o(C_s - C_{lim}) & \text{if} \quad C_o \geq C_{lim} \end{cases} \tag{1-6}$$

where k_T is a kinetic constant function of the local temperature T, C_e is the electrolyte concentration, C_o the solid nuclei concentration, C_s the concentration of solid particles and C_{lim} the threshold concentration of the solid nuclei which determines the growing mode. We also mention that Liesegang pattern formation was studied by using the hyperbolic version of the reaction-diffusion equations [69].

Magneto-hydrodynamic models

Models defined through boundary value problems involving magneto-hydrodynamic equations for magnetic colloidal dispersion have been used to describe non-equilibrium self-assembly under the influence of a magnetic field. These models can also be applied to a variety of interfacial particle systems driven out of equilibrium by external energy fluxes [58]. Numerical schemes and analytical methods are used to calculate the energy dissipation rates in a prototypical magneto-hydrodynamic NESA system composed of metal particles suspended on a liquid-air surface in which a rotating magnetic field is applied [46, 214]. This method is based on the Navier-Stokes equation that considers multi-body interactions and includes the force f exerted on the fluid due to the rotations of the magnetic particles

$$\rho \left[\frac{\partial \vec{u}}{\partial t} + \vec{u} \cdot \nabla \vec{u} \right] = -\nabla p + \mu \nabla^2 \vec{u} + \vec{f}, \tag{1-7}$$

Here ρ is the fluid density, μ the fluid viscosity, $\vec{u}$ the velocity field and $\vec{f}$ a local body force that transmits the perturbation to the fluid caused by the rotation of the particles [215]. Using the Force Coupling Method, $\vec{f}$ can be expressed as:

$$f_i = \sum_n^N F_i^{(n)} \Delta[x - y^{(n)}] + G_{ij}^{'(n)} \tag{1-8}$$

where N is the number of particles, $y^{(n)}$ represents the position of the n-th particle, $F^{(n)}$ is the force that the particle exerts on the fluid and Δ is a density function that accounts for the finite size of the particle. This first term on the right-hand corresponds to a force monopole while the second $G_{ij}^{'(n)}$ is a force dipole term [215]. This method has been useful in finding the distribution of magnetic particles on the surface of a fluid under a rotatory magnetic field and to understand the relation between energy dissipation and kind of structure.

Hydrodynamic equations were also used to study the organization of microtubules assemblies driven by cross-linking motors [216, 72, 217, 218] which reproduce the hydrodynamic flows generated by polarity-dependent active stresses and which relate local polar structure to flow structures and defect dynamics [183].

Kinetic master equations

Chemical-kinetic master equations have been used to describe the assembly and disassembly of protofilaments and microtubules built from α- and β tubulin BB [219, 220, 221, 222]. These models may account for the microscopic structure and interaction between proto-filaments, where an important approach to describe the assembly dynamics is that the growth of the structures is reaction-limited rather than diffusion-limited [219]. This last fact was shown *in vivo* and *in vitro* conditions for microtubules assembly [223].

The steady mean velocity of growth given by these models can be written as:

$$r = \frac{d}{R_N}\left(1 - \prod_{j=1}^{N} \frac{w_j}{u_j}\right) \tag{1-9}$$

where d is the size of the BB (α-, β-tubulin), N the number of protofilament composing the microbutule and R_N a factor that depends on the rates of attachment and deattachment to the protofilament j, u_j and w_j, respectively. The ratio between these rates is given by

$$\frac{u_j}{w_j} = \exp\left[-(g_v + g_h + g_i)/k_B T\right] \tag{1-10}$$

Here g_v is a bond energy related to head-to-tail binding, g_h the energy of lateral interactions between protofilament and g_i the free energy of the attachment of a BB to the protofilament.

Mesoscopic non-equilibrium thermodynamic models

Mesoscopic nonequilibrium thermodynamics (MNET) is used to obtain the nonlinear kinetics of nonequilibrium systems in the presence of fluctuations [73, 224]. It provides kinetic equations of the Fokker-Planck type, compatible with the second law of thermodynamics, which describe the evolution of the probability density of the relevant quantities of the system. It has been used to analyze the kinetics of chemical and biochemical reactions [225, 226, 227], transport processes such as ion translocation through protein channels [228], electro-dynamic processes [229] and nucleation phenomenon [230, 231]. MNET can also be applied to study cross-linked motor-filament and active gels at different length scales. The latter have only been analyzed through linear non-equilibrium thermodynamics [232, 233, 234, 235].

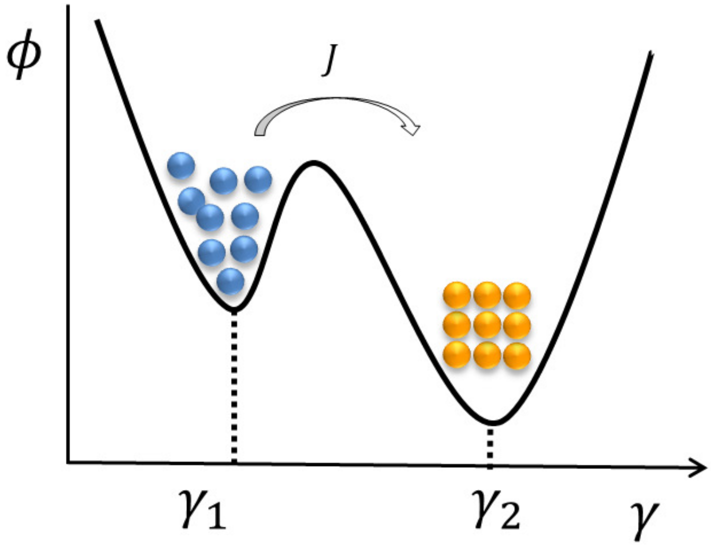

Fig. 1-9.: Illustration of a simple bi-stable potential ϕ for self-assembly modelling. In the initial state, the building blocks are already activated but disordered. The final state corresponds to the self-assembled structure.

Self-assembly processes can be viewed as activated processes which can be modelled by the crossing of a free-energy barrier that separates the disordered state from the assembled state that corresponds to the local minima of the barrier [73], as shown in Fig.**1-9**. To cross the barrier, the system needs to acquire energy in order that the assembly of the building blocks may take place. If we consider the process at shorter time scales, the state of the system progressively transforms by passing through successive structural configurations. These different configurations can be characterized by a reaction coordinate γ. In this situation, one may assume that the state of the system undergoes a diffusion process along the reaction coordinate crossing the potential barrier. The local entropy production is [73]

$$\sigma(\gamma) = -\frac{1}{T} J(\gamma) \frac{\partial \mu}{\partial \gamma} \tag{1-11}$$

where J is the diffusion current and μ the chemical potential. From the entropy production, one can derive the linear law [73] between the current J and the thermodynamic force $\partial\mu/\partial\gamma$

$$J = -\frac{L}{T}\frac{\partial \mu}{\partial \gamma} \tag{1-12}$$

in which L is an Onsager coefficient and the chemical potential μ is given by

$$\mu = k_B T \ln(p) + \phi \tag{1-13}$$

with ϕ the potential barrier shown in Fig.**1-9**. Using the expression of the current in the continuity equation ($\partial p/\partial t = -\partial J/\partial\gamma$), we can obtain the Fokker-Planck equation describing the evolution in time of the probability distribution $p(\gamma,t)$

$$\frac{\partial p(\gamma,t)}{\partial t} = D\left(\frac{\partial^2 p}{\partial \gamma^2} + \frac{p}{k_B T}\frac{\partial \phi}{\partial \gamma}\right) \tag{1-14}$$

in which the Onsager coefficient is given by $L = Dp/k_B$ with D the diffusivity along the potential barrier.

It is often the case that, at the time scales of interest, the system is mostly found in the states 1 and 2, which correspond to the minima at γ_1 and γ_2, respectively as shown in Fig.**1-9**. The probability distribution is sharply peaked at these values and almost zero everywhere else. This happens when the energy barrier is much higher than the thermal energy and intra-well relaxation has already taken place. Under these conditions and re-writing Eq.(1-12), the kinetic equation is:

$$J = -\mathscr{D}\frac{dz}{d\gamma} \tag{1-15}$$

in which the diffusion coefficient is $\mathscr{D} = L/zT$, and the fugacity is $z = \exp(\mu/k_B T)$. We now assume $\mathscr{D}$ as a constant and integrate from 1 to 2, obtaining the effective kinetic equation

$$\bar{J} \equiv \int_{\gamma_1}^{\gamma_2} J d\gamma = \mathscr{D}(z_1 - z_2). \tag{1-16}$$

in which the difference of fugacities is the driving force of the processes. This model has been applied to thermodynamically analyze [129] and dynamically explain [132] the formation of gels from the self-assembling of monomers. The entropy production of the process [224, 73] consisting of activation, assembly, disassembly and rotation is

$$\sigma = -\frac{1}{T}\sum_j J_j \frac{\partial \mu_j}{\partial \Gamma_j}, \tag{1-17}$$

where Γ is the phase-space in which the processes takes place, j refers to the j^{th} elementary process, Γ_j is the corresponding reaction coordinate of the j^{th} elementary process and J_j is the associated current. The Fokker-Plank equation describing the dynamics of the NESA structure is

$$\frac{\partial p(\Gamma,t)}{\partial t} = \sum_j D_j \frac{\partial}{\partial \Gamma_j}\left[\frac{\partial p_j}{\partial \Gamma_j} + \frac{p_j}{k_B T}\frac{\partial \phi_j}{\partial \Gamma_j}\right] \tag{1-18}$$

in which ϕ_j is the potential barrier related to the j^{th} process and D_j is the diffusivity along the j^{th} internal coordinate.

1.6.3. Information entropy

Information entropies may provide a measure of the complexity of a physical system [236]. Information entropies have been proposed to characterize the non-equilibrium structures. These entropies are computed from the dynamics of the self-assembling process given by kinetic and computational models.

Kolmogorov-Sinai entropy

Through the Kolmogorov-Sinai entropy, one can obtain a relationship between the system dynamical entropy S_{KS} and the energy dissipated in a NESA system, thus connecting the microscopic dynamics with the energetics of NESA processes. S_{KS} is computed from the Lyapunov exponents spectra λ_i that depend on a set of state variables C describing the system. The dynamic entropy is then expressed as

$$S_{KS} = \sum_i \lambda_i(C,t). \tag{1-19}$$

It has been found that for NESA states composed of clusters formed by light-activated particles [74], this entropy is larger than for non-organized states [44].

Configuration entropy

Configuration entropy [237] H is a measure of the local fluctuations of some morphological variable [238]. It is computed from Shannon entropy and has been used to characterize Turing patterns [75, 76, 77]. Pattern characterization requires the use of binary images that consider whether a pattern appears or not [237, 239]. Thus, in a pixel-by-pixel analysis on binary patterns, the configurational entropy is defined as

$$H = -P_w \ln P_w - P_b \ln P_b \tag{1-20}$$

where P_b and P_w are the probabilities of finding a pattern (black) or not (white) a pattern in a given spot of the system. It was found that steady state Turing patterns showing higher degree of order (direct spots) have the lower Shannon entropy. These more ordered patterns are the ones that dissipate the minimum amount of energy [75].

Assuming that the pixel-by-pixel analysis of binary patterns can be arranged into a data string, BiEntropy [240] may be used to quantify order in pattern-forming systems. Computable information density [241] may also estimate the degree of order of the pattern.

Maximum entropy production principle

The maximum entropy production (MEP) principle states that a flow system subject to various gradients will tend towards a steady state of maximum dissipation determined by the thermodynamic entropy production σ [78, 79, 82, 83, 84]. The MEP principle has been observed in the Earth's climate system [80, 81, 85], thermal (Benard) convection [242], electrical currents [243], crystalline solids [244], ecological systems[245] and biochemical processes [246, 247]. MEP selects the highest allowable entropy production σ consistent with the set of allowable bulk net fluxes J and bulk thermodynamic forces F in and between subdomains Γ of the system

$$MEP \equiv max_{\Omega}\sigma(F(\Gamma;\Omega), J(\Gamma;\Omega)) \tag{1-21}$$

where the fluxes and forces depend on a set of subdomain-wide adjustable parameters Ω.

It has been stated that by increasing the number of internal states, the system begins to respond easily (i.e., make transitions between states) to variations of the environment. Each transition necessarily involves generation of entropy (transitional entropy) over and above that associated with maintaining a state [248]. In this case a higher entropy production is expected for organized states than for non-organized ones. In this way, the organized states increase the ability of the system to interact with the surrounding environment and exhibit goal-oriented behavior associated with transitional entropy production [248]. This behavior could open the discussion about a general free energy which drives these kind of systems to specific states. For instance, it was shown that SO in a voltage-driven nonequilibrium system, consisting of conducting beads immersed in a viscous medium, gives rise to a dynamic tree structure that exhibits worm-like motion. The complex motion of the beads driven by the applied field results in a time evolution of the tree structure towards states of lower resistance or higher rates of entropy production with the purpose of receiving more energy, and avoiding conditions that decrease the available energy [249].

Life and evolution is based on SO [96, 2, 97, 98, 99, 100] and of course in out-of-equilibirum SA of cellular components [250]. The origin and evolution of life can be understood as resulting from the natural thermodynamic imperative of increasing the entropy production of the Earth in its interaction with its solar environment [251]. It could be concluded that a living being or complex ecosystem seen as a SO system tends to change its structural and energetic configuration to become complex and survive for a determined set of conditions. This complexification leads to an increase of the hierarchy (hierarchogenesis) of the structures [252, 253] and therefore also an increment of the entropy production of the SO system[254, 248].

1.6.4. Gibbs entropy-based models

Different approaches based on the formulation of the Gibbs entropy have been proposed to show the relation between entropy production, quantifying dissipation, and the formation of non-equilibrium structures. Some of these models are presented in this section.

Minimum entropy production principle

The Onsager variational principle of the least energy dissipation [255, 256] provides a useful framework to obtain the nonlinear dynamics of processes taking place in soft condensed matter systems [72, 257, 258, 259] such as phase separation in solutions, gel dynamics and molecular modeling for viscoelasticity nemato-hydrodynamics and self-assembly under non-equilibrium conditions [132, 53] to mention just a few . These dynamics describe the evolution of a state variables X_i as

$$\frac{dX_i}{dt} = \sum_j L_{ij}^{-1} \frac{\partial U}{\partial X_i} \tag{1-22}$$

where U is a potential and L_{ij} is the matrix of Onsager coefficients. Furthermore, keeping the linear relationships between fluxes and thermodynamic forces, as in Eq.(1-22), it was shown that systems exhibiting spatiotemporal patterns and a certain degree of organization, minimize the entropy production rate in steady states [2].

For instance, in surfaces where frictional processes take place, it was shown from the stability conditions, that when the entropy production rate fulfill the condition $\delta^2\sigma \geq 0$[260], the system reaches a degree of organization leading to the reduction of the friction and wear, i.e, to a minimum entropy production rate state [86, 87]. This friction reduction has been observed as the result of the self-healing and self-cleaning of a surface [88] where the energetic efficiency increases [261].

Min/Max duality of the entropy production

The evolution of some systems may fulfill maximum or minimum principles. To understand this duality, an analysis of fluxes and forces was performed by using Legendre transformations [89]. There a non-linear relation flux-force was used to describe the motion of fluids and plasmas, where two types of organized motion were observed. The total entropy production rate is maximized if the system follows a like-series flow (F_s), and is minimized if the systems follow a like-parallel flow (F_p) configuration [262]. The entropy production for this system fulfills the condition:

$$\left(\frac{\partial\sigma}{\partial F}\right)_{F=F_s^*,F_p^*} = 0 \tag{1-23}$$

$$\left(\frac{\partial^2\sigma}{\partial F^2}\right)_{F=F_s^*} < 0; \quad \left(\frac{\partial^2\sigma}{\partial F^2}\right)_{F=F_p^*} > 0 \tag{1-24}$$

in which a star denotes the value of the parameter corresponding to the stable solutions. In this example, we have patterns in continua media related to a different dynamical operation mode; however, it could be interesting to find a corresponding example for NESA systems.

Non-extrema entropy production regimes

The existence of dynamic, energetic and structural operation modes explain the fact that NESA and SO processes may display a high or a low entropy production. For instance, NESA, self-repairing, self-healing and self-replicating processes require a big amount of energy and therefore exhibit a high entropy production. In contrast, systems which are not subjected to a great diversity of external inputs may partially decouple from the energy sources thus reaching a low entropy production [263, 90] which leads to an increase of the energetic efficiency. For a nanowire self-assembly process in presence of external noise (artificially created by an ultrasound source)[90], it is found that at small noise level the entropy production first reaches its maximum value and subsequently slowly approaches a low entropy production state thus exhibiting an efficient energetic operational mode. When increasing the noise level, nanowires progressively disassemble and assemble which results in an increase of the entropy production showing that the dynamic operation mode requires a large amount of energy to maintain the structure.

In systems with an oscillatory pH, a transition between NESA structures having different degrees of order has been observed for a particular value of the oscillation frequency ω. The most ordered NESA structures are favored by fast oscillations while other structures emerge at slow oscillations [264]. The most disordered state emerges at the transition frequency ω^*, in which the entropy production reaches a maximum value and thus fulfills the conditions

$$\left(\frac{d\sigma}{d\omega}\right)_{\omega=\omega^*} = 0; \quad \left(\frac{d^2\sigma}{d\omega^2}.\right)_{\omega=\omega^*} < 0 \tag{1-25}$$

1.7. Entropy production for different types of structures

Why a particular NESA structure and not others comes up under specified conditions is an important question yet to be answered due to the lack of a nonequilibrium potential whose minima determines the structures, as occurs in equilibrium [44]. Nevertheless, it is known that the amount of energy and matter dissipated by the system reflected in the entropy production plays an important role in the selection of a NESA structure [11]. In this section, we will exemplify cases in which for similar or even the same conditions different NESA structures are observed and we will show how the entropy production can provide information about the type of structure formed.

1.7.1. Polymorphs in magneto-hydrodynamics systems

Polymorphic NESA structures illustrated in Fig.**1-10** have been found in magneto-hydrodynamic systems [46, 214, 71]. Two distinct stationary NESA structures may emerge for the same values of the system parameters, producing both low and high energy dissipation states in which the probability P of observing these structures behaves in terms of the entropy production rate σ as [71]

$$P(\sigma) \sim \exp(-k\sigma), \tag{1-26}$$

where k is a fitting constant. These results show that while nature prefers to form less dissipative (more energetically efficient) assemblies, it also chooses more wasteful structures[71].

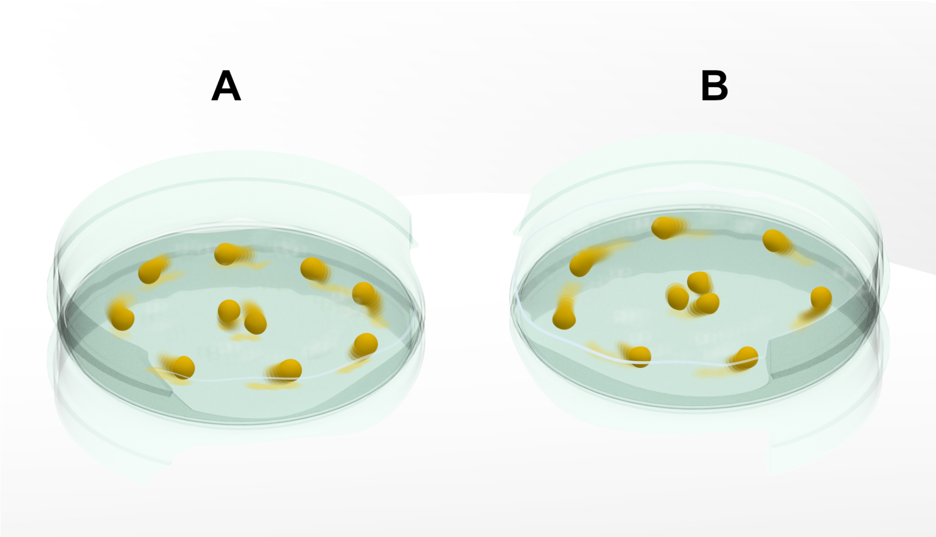

Fig. 1-10.: Polymorphs in magneto-hydrodynamic systems. For a system composed of 10 magnetic particles under the influence of a rotating magnetic field, two polymorph structures are observed: a) with 2 central particles and b) with 3 central particles [214, 71].

The relation between distinct structures and entropy production was analyzed in [65, 60] and in[264] concluding that a general principle governing the formation of NESA structures is needed.

1.7.2. Pattern formation in reaction-diffusion systems

In reaction-diffusion systems exhibiting pattern formation, the entropy production is lower for chaotic (aperiodic) patterns than for periodic patterns. The dimensionless reaction-diffusion number $N_{rd} \equiv \sqrt{m_1 m_2 / D_1 D_2 k^2}$ characterizes the structures formed [65, 60] and depends on the mass m and diffusivity D of the components and on the kinetic constant k.

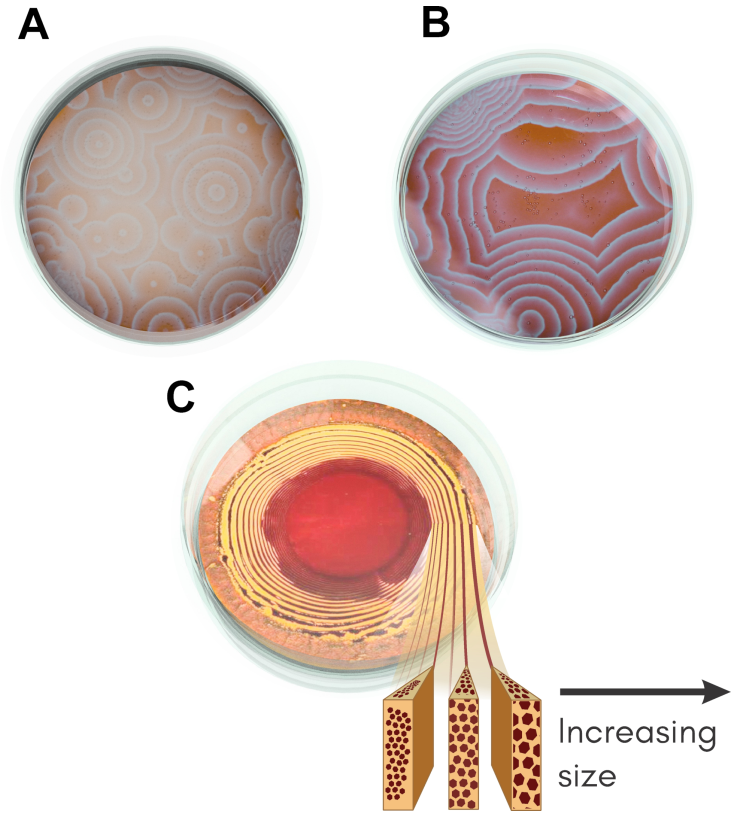

Fig. 1-11.: Patterns in reaction-diffusion systems. a) and b) correspond to Belousov-Zhabotinsky patterns with different periodic structures. Adapted from commons.wikimedia.org with license CC-BY-2.0. c) Liesegang patterns composed of particles with a predictable and progressive variable size. Adapted from commons.wikimedia.org with license CC-BY-SA-3.0.

Figs.**1-11**(a)-(b) show two different patterns having different values of the reaction-diffusion number. Low values of N_{rd} correspond to periodic patterns while high N_{rd} values are typical of periodic patterns. The entropy production is not necessarily a monotonic function of N_{rd} [65, 60], due to the relation between structure and dissipation.

In Liesegang patterns, particle size distribution was measured over the constituent bands, as illustrated in Fig.**1-11**(c). The pattern evolves toward fewer but larger particles as we go through the bands from top to bottom, as is observed upon time aging during an Ostwald ripening evolution [265]. In the bottom-up approach, the building blocks self-assemble into spatially well separated domains with controllable and predictable particle sizes [41]. It was found that the entropy production as a function of the ratio between the size change and precursor concentration change behaves non-monotonically [132, 266].

1.7.3. Fiber and microtubule assembly

Understanding how microtubules adopt specific spatial arrangements is a central issue to explain some cellular processes and properties. For instance, structures built from microtubules called spindles are responsible for chromosome segregation [267]. Furthermore, microtubules shape the cytoplasm, nucleus and organelles, and constitute the principal structural element of flagella and cilia [24].

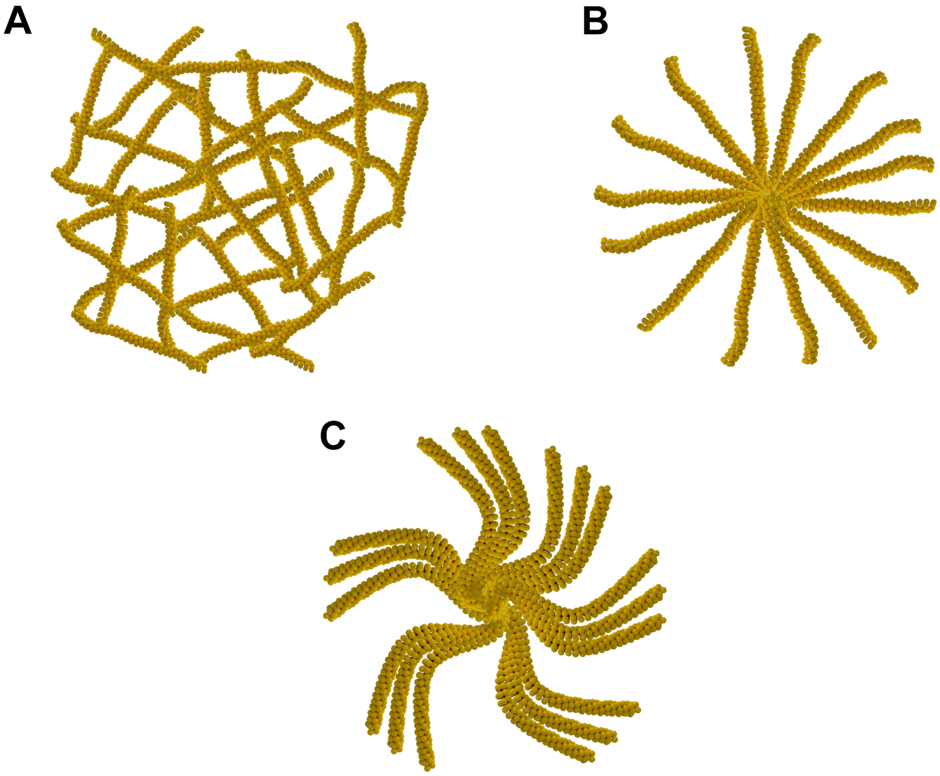

Fig. 1-12.: Microtubule assembly illustration. Microtubule-based structures: a) network, b) aster, c) vortex.

Hierarchical and spontaneous assembly of microtubules triggers the formation of molecular motors [268] having different shapes such as asters, vortices and networks of interconnected poles [142], as illustrated in Fig. **1-12**. These assembled structures show collective and self-organized behavior. Brownian dynamics and entropy production-based models show how local structures such as asters and vortices yield spatial patterns [183]. In microtubule-based structures, parameters determining the generation of these structures have been identified [142]. These parameters could be linked to the entropy production [53] of the system, as in the case of the synthetic counterparts [122]. These synthetic structures are obtained through the transient self-assembly of organic molecules driven by the consumption of a chemical fuel [21, 122]. In this case, the entropy production results from fiber orientation, gel formation and even gel porosity [53].

Actin filaments and filaments of myosin motors self-assemble into bundles with contractile elements that transmit forces to cellular length scales [269]. In these structures, the bundle length takes optimal values for an efficient transmission of the contractile force at which the entropy production may reach extreme values.

1.7.4. Planetary organization

It has been shown that entropy production gives information [270] as to the organization of the different components of cosmological systems [101, 102, 103, 104, 105]. For instance, a planetary system is in general unstable unless the planets' orbits are synchronized and their dynamics is periodic. When periods between the radially adjacent planets are synchronized, the mean orbital distance is found to follow a geometric and general progression, the same as observed in our solar system. In principle, however, there is no a priori reason of why all planets show synchronous behavior in the organized state [104]. As in the magneto-hydrodynamic system, entropy production could shed some light on this particular distribution [44].
Planetary rings, especially Saturn's rings, are structures whose formation is still not well understood [271]. The explanation of why different types of rings can be observed is an open question [272] probably related to Liesegang rings [44]. In Fig.**1-13** we illustrate a NESA (Saturn's rings) planetary system.

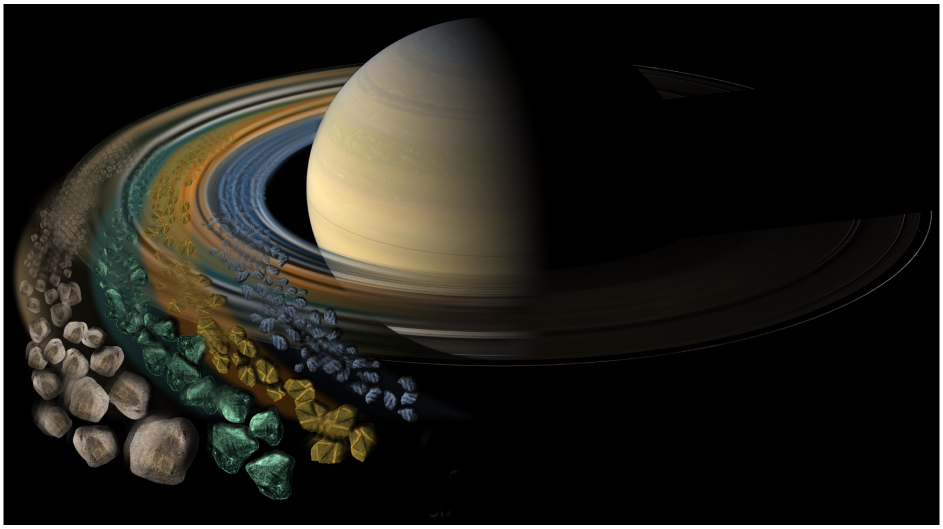

Fig. 1-13.: NESA planetary systems. Saturn's rings, in this case, the BB are rocks. Notice the similarity with Liesegang patterns shown in Fig**1-11** (C).

1.8. Searching for a general non-equilibrium principle

The search for a non-equilibrium free energy potential able to predict the formation of non-equilibrium structures, in the same way as free energy does for equilibrium systems, is an open problem in the physics of systems outside equilibrium [134, 135, 136, 137]. For instance, microtubules and microtubules-based structures are dynamically assembled under non-equilibrium conditions and their free energy is not necessarily a minimum. These structures, however, may result from the optimization of kinetic or structural parameters to improve their functional response [24, 267, 142]. Specifically, it is found that the ratio between two kinetic parameters describing the assembly of an active gel dictates the form of the final structure and as a consequence the functionality of the gel [273]. The entropy produced in the response of the gel could then set the basis to construct a non-equilibrium potential able to determine the optimal value of the kinetic parameters ratio.

Which parameters governs the formation of structures is a key question in order to understand the multiplicity of NESA structures observed. Nevertheless, the reason behind the multiplicity may lie in that every particular structure is formed depending on the dissipative nature of NESA intermediate structures [274, 275, 249]. In this section, we briefly discuss the possible existence of a function or potential which may shed some light about the relation between entropy production and structure formation.

Some first attempts to formalize a nonequilibrium potential were made in [276] and in [277, 278]. Although these potentials predict stationary states of nonequilibirum systems under some conditions, they do not show the emergence of ordered structures. On the other hand, the constructal theory may explain the formation of some structures [3]. This theory states that nature does not necessarily maximize or minimize entropy production, but maximizes the fluxes coming and passing through the system, thus facilitating the maintenance of the structure and the efficiency of the processes. However, it seems that large incoming fluxes (large entropy production) or large unused energy (low entropy production) depend on the external conditions and requirements of the system to maintain a specific structure [263, 90]. Therefore from our point of view, it is not enough to consider the maximization of the fluxes passing through the system as stated in the constructal theory. Additionally, as to the energetic efficiency in NESA and SO systems, at least we can state that there does not exist a correlation between the efficiency of living systems and the entropy production rate. This is because kinetic aspects are also relevant for establishing optimal functioning. This can be seen through examples such as molecular motors, circadian cycles and sensory adaptation, whose performance in some regimes is indeed spoiled by increasing the entropy production [279].

As we reviewed in the last two sections, minima and maximum principles of entropy production are fulfilled in different systems, but it is not possible to establish a general extrema entropy production principle. We realize that although entropy production seems to be an important quantity [89, 280] it does not enable one to predict the evolution of organized systems. Therefore, we visualize that there may be a principle which depends on the entropy production which unveil the emergence of ordered structures. The possibility of an underlying variational principle for a general free energy is highlighted in [44, 74]. Additionally, as mentioned by several authors [21, 26, 281, 19, 103], one of the keys of SO is the complex network of feedback loops in the system. Here, considering the control theory of dynamic systems, there should be a goal variable which is expected to be constant in order to maintain the system in some desired behavior [282]. Another option emerges with the optimal control theory [283, 284] in which entropy production is used to compute a like-Hamiltonian of the non-conservative system and thus minimize it as a function of a control variable [285].

We are still wondering as to which is the main variable and which is its value. We ponder the possibility that this variable may be a general nonequilibrium potential or if this desired behavior is related to an extrema principle. Maybe this potential or extrema principle could be related to the entropy production as a function of a structural parameter for different external conditions imposed over the system and respond in the dynamic, energetic and structural mode of operation of the NESA or SO systems.

1.9. Conclusions and perspectives: Dissipation and thermodynamic criteria?

Non-equilibrium self-assembly is ubiquitous in physico-chemical and biological systems and is manifested at different scales ranging from molecular to cosmological. The formation of microtubules, gels, cells and living beings among many others take place by self-assembly under non equilibrium conditions.

Despite many efforts devoted to the study of the phenomenon, a general evolution criterion able to understand why nature selects some structures and not others is lacking. This difficulty is inherent to the nonequilibrium nature of the process for which equilibrium thermodynamic potentials such as the free energy when used far from equilibrium cannot associate their minima to the structures formed. This is observed for example in the formation of microtubules and microtubule-based structures for which the free energy does not necessarily correspond to a minimum. These structures appear, however, at certain values of some kinetic and architectural parameters at which the system responds coherently.

Despite this limitation, progress in the understanding of the NESA mechanisms has been made thanks to the formulation of models to study particular situations. Computational and kinetics models are useful to describe the formation dynamics of NESA structures. Computational models unveil information about their architecture. These models are, however, restricted to the description of microscopic systems with few components therefore being unable to describe more complex systems with different hierarchical structures. Kinetic models account for the kinetics of systems with different hierarchical structures but most of them are unable to reproduce the form of the structures.

The formation of NESA structures entails matter and/or energy dissipation generated in activation, assembly and disassembly processes. During these processes intermediate metastable structures may emerge. The entropy production rate is an important quantity to describe the emergence of the structures and to determine their shape. Mesoscopic non-equilibrium thermodynamic models consider the entropy production as a starting point to reproduce the dynamics and micro-architecture of NESA structures [73, 53].

Some of the results obtained from thermodynamic models suggest a connection between the entropy production rate and NESA structures. Nevertheless, there is up to now no general consensus for the characterization of NESA systems from the entropy production. The possibility of the existence of a variational principle involving a general free energy able to reproduce the structures was discussed in [44, 74, 83]. The formation of NESA structures could be driven by an end-directed evolution criterion [281].

It is imperative that a general model of a general and a thermodynamic principle be proposed in order to allow the evaluation of different kinds of structures as a function of structural parameters as well as the functional properties of the resulting systems. Proposed models and thermodyamic principle may be checked in systems and processes in which experimental data are available. Some of these systems are: magneto-hydrodynamic system [71, 214, 46], Liesegang patterns [41], gels [160, 123, 122, 21, 124], microtubules assemblies [23, 24, 268, 183, 142]and planetary assemblies [270, 104].

The question of why different structures may emerge for similar initial conditions of the system is of great importance to establish a general evolution criterion. In magneto-hydrodynamic systems, a given initial condition may give rise to the formation of different structures [71] (see Fig.**1-10**). In these systems, a relationship between the probability of the appearance of a structure with the entropy production was experimentally found. To find different cases which show a similar feature constitutes a major current challenge.

The knowledge of the intimate mechanisms leading to the formation of structures will make the implementation of adaptive and reconfigurable materials possible with applications to sensors, tunable optical elements, microdevices [44], self-erasing inks and patterns, self-healing supramolecular gels and catalysts with tunable lifetime and activity [26] among others. It could also be useful to provide a deeper understanding of the emergence of life [286].

We hope that this chapter may offer a reference to link several current concepts and to help in the development of new models and experimental studies able to reveal hidden relations in organized systems dissipating matter and energy.

Bibliography

[1] A. Arango-Restrepo, D. Barragán, and J. M. Rubi. Self-assembling outside equilibrium: emergence of structures mediated by dissipation. *Phys. Chem. Chem. Phys.*, 21:17475–17493, 2019.

[2] Ilya Prigogine and G Nicolis. *Self organization in non equilibrium systems*. John wiley & sons, 1 edition, 1977.

[3] Adrian Bejan and Sylvie Lorente. Constructal law of design and evolution: Physics, biology, technology, and society. *J. Appl. Phys.*, 113(15):6, 2013.

[4] Adrian Bejan and Peter Zane. *Design in Nature: How the Constructal Law Governs Evolution in Biology, Physics, Thecnology and Social Organization.* Doubleday, 1 edition, 2012.

[5] Alan Mathison Turing. The chemical basis of morphogenesis. *Phil. Trans. R. Soc. Lond. B*, 237(641):37–72, 1952.

[6] A Turing. â€™nonlinear reaction-and diffusion-a key to morphology. *Phil. Trans. Roy. Society*, 237:32–40, 1952.

[7] BP Belousov. Collection of short papers on radiation medicine for 1958, chapter a periodic reaction and its mechanism. *Moscow: Med. Publ.[in Russian]*, 1959.

[8] Edward N Lorenz. The statistical prediction of solutions of dynamical equations. In *Proceedings of the International Symposium on Numerical Weather Prediction, 1962*. Meteor. Soc. Japan, 1962.

[9] Edward N. Lorenz. Deterministic nonperiodic flow. *Journal of Atmospheric Sciences*, 20(2):130 – 141, 1963.

[10] Colin Sparrow. *The Lorenz equations: bifurcations, chaos, and strange attractors*, volume 41. Springer Science & Business Media, 2012.

[11] Bartosz A Grzybowski, Christopher E Wilmer, Jiwon Kim, Kevin P Browne, and Kyle J.M Bishop. Self-assembly : from crystals to cells. *Soft Matter*, 5:1110–1128, 2009.

[12] George M Whitesides and Bartosz Grzybowski. Self-assembly at all scales. *Science*, 295(5564):2418–2421, 2002.

[13] Stephen Mann. Self-assembly and transformation of hybrid nano-objects and nanostructures under equilibrium and non-equilibrium conditions. *Nat. Mater.*, 8(10):781–792, 2009.

[14] M. C. Cross and P. C. Hohenberg. Pattern Formation Outside of Equilibrium. *Rev. Mod. Phys.*, 65(3):851–1112, 1993.

[15] Irving R Epstein and John A. Pojman. *An introduction to nonlinear chemical dynamics: Oscillations, Waves, Patterns, and Chaos*. Oxford University Press, 1 edition, 1998.

[16] Helmut Cölfen and Stephen Mann. Higher-Order Organization by Mesoscale Self-Assembly and Transformation of Hybrid Nanostructures. *Angew. Chem. int. Ed*, 42(21):2350–2365, 2003.

[17] Sriram Ramaswamy. The mechanics and statistics of active matter. *Annu. Rev. Condens. Matter Phys.*, 1:323–345, 2010.

[18] D Krishna Kumar and Jonathan W Steed. Supramolecular gel phase crystallization: orthogonal self-assembly under non-equilibrium conditions. *Chem. Soc. Rev.*, 43(7):2080–2088, 2014.

[19] Flavio della Sala, Simona Neri, Subhabrata Maiti, Jack LY Chen, and Leonard J Prins. Transient self-assembly of molecular nanostructures driven by chemical fuels. *Curr. Opin. Chem. Biol.*, 46:27–33, 2017.

[20] Stephen Whitelam and Robert L Jack. The statistical mechanics of dynamic pathways to self-assembly. *Annu. Rev. Phys. Chem.*, 66:143–163, 2015.

[21] Job Boekhoven, Wouter E Hendriksen, Ger JM Koper, Rienk Eelkema, and Jan H van Esch. Transient assembly of active materials fueled by a chemical reaction. *Science*, 349(6252):1075–1079, 2015.

[22] Job Boekhoven. *Multicomponent and Dissipative Self-Assembly Approaches: toward functional materials*. PhD thesis, Delft University of Technology, 2012.

[23] Cyril Papaseit, Nathalie Pochon, and James Tabony. Microtubule self-organization is gravity-dependent. *PNAS*, 97(15):4–8, 2000.

[24] Arshad Desai and Timothy J Mitchison. Microtubule Polymeriztion Dynamics. *Annu. Rev. Cell Dev. Biol.*, 13:83–117, 1997.

[25] Richard J Williams, Andrew M Smith, Richard Collins, Nigel Hodson, Apurba K Das, and Rein V Ulijn. Enzyme-assisted self-assembly under thermodynamic control. *Nat. Nanotechnol.*, 4(1):19, 2009.

[26] Susan A. P. van Rossum, Marta Tena-Solsona, Jan H. van Esch, Rienk Eelkema, and Job Boekhoven. Dissipative out-of-equilibrium assembly of man-made supramolecular materials. *Chem. Soc. Rev.*, 46:5519–5535, 2017.

[27] Benedikt Riess, Caren Wanzke, Marta Tena-Solsona, Raphael K. Grotsch, Chandan Maity, and Job Boekhoven. Dissipative assemblies that inhibit their deactivation. *Soft Matter*, 14:4852–4859, 2018.

[28] Per Bak, Chao Tang, and Kurt Wiesenfeld. Self-organized criticality. *Phys. Rev. A*, 38:364–374, Jul 1988.

[29] Allan S Hoffman. Hydrogels for Biomedical Applications. *Adv. Drug Deliv. Rev.*, 64:18–23, 2012.

[30] Nasim Annabi, Jason W Nichol, D Ph, Xia Zhong, and Chengdong Ji. Controlling the Porosity and Microarchitecture of Hydrogels for Tissue Engineering. *J. Tissue Eng.*, 16(4):371–383, 2010.

[31] Zulma A. Jiménez and Ryo Yoshida. Temperature Driven Self-Assembly of a Zwitterionic Block Copolymer That Exhibits Triple Thermoresponsivity and pH Sensitivity. *Macromolecules*, 48(13):4599–4606, 2015.

[32] Jinxing Jiang and Kenji Sakurai. Formation of Ultrathin Liesegang Patterns. *Langmuir*, 32(36):9126–9134, 2016.

[33] Yukikazu Takeoka and Masayoshi Watanabe. Tuning Structural Color Changes of Porous Thermosensitive Gels Through Quantitative Adjustment of the Cross-Linker in Pre-Gel Solutions. *Langmuir*, 19(22):9104–9106, 2003.

[34] Marta Tena-Solsona, Benedikt Rieß, Raphael K Grötsch, Franziska C Löhrer, Caren Wanzke, Benjamin Käsdorf, Andreas R Bausch, Peter Müller-Buschbaum, Oliver Lieleg, and Job Boekhoven. Non-equilibrium dissipative supramolecular materials with a tunable lifetime. *Nat. Commun.*, 8:15895, 2017.

[35] Yiming Wang, Robin M de Kruijff, Matija Lovrak, Xuhong Guo, Rienk Eelkema, and Jan H van Esch. Access to metastable gel states using seeded self-assembly of low molecular weight gelators. *Angew. Chem. Int. Ed.*, 2018.

[36] Alison M Douglas, Alexandros A Fragkopoulos, Michelle K Gaines, L Andrew Lyon, Alberto Fernandez-Nieves, and Thomas H Barker. Dynamic assembly of ultrasoft colloidal networks enables cell invasion within restrictive fibrillar polymers. *Proc. Natl. Acad. Sci.*, 114(5):885–890, 2017.

[37] Jeffrey C Gaulding, Michael H Smith, John S Hyatt, Alberto Fernandez-Nieves, and L Andrew Lyon. Reversible inter-and intra-microgel cross-linking using disulfides. *Macromolecules*, 45(1):39–45, 2011.

[38] Prateek K. Jha, Vladimir Kuzovkov, Bartosz A. Grzybowski, and Monica Olvera de la Cruz. Dynamic self-assembly of photo-switchable nanoparticles. *Soft Matter*, 8(1):227–234, 2012.

[39] P. K. Kundu, D. Samanta, R. Leizrowice, B. Margulis, H. Zhao, M Börner, T Udayabhaskararao, Debasish Manna, and Rafal Klajn. Light-Controlled Self-Assembly of Non-Photoresponsive Nanoparticles. *Nat. Chem.*, 7(8):646–652, 2015.

[40] Keitaro Sou, Li Yan Chan, and Chi-lik Ken Lee. Photo-Switchable and Self-Erasable Fluorescent Nanoprobe. *J. Photochem. Photobiol. A. chem.*, 332:25–31, 2016.

[41] Roché M. Walliser, Florent Boudoire, Eszter Orosz, Rita Tóth, Artur Braun, Edwin C. Constable, Zoltán Rácz, and István Lagzi. Growth of Nanoparticles and Microparticles by Controlled Reaction-Diffusion Processes. *Langmuir*, 31(5):1828–1834, 2015.

[42] Larken E Euliss, Julie A Dupont, Stephanie Gratton, Joseph Desimone, James D Martin, and Stephanie Gratton. Imparting size , shape , and composition control of materials for nanomedicine. *Chem. Soc. Rev.*, 35:1095–1104, 2006.

[43] Andrew Z Wang, Robert Langer, and Omid C Farokhzad. Nanoparticle Delivery of Cancer Drugs. *Annu. Rev. Med*, 63:185–198, 2012.

[44] Marcin Fialkowski, Kyle J M Bishop, Rafal Klajn, Stoyan K Smoukov, Christopher J Campbell, and Bartosz A Grzybowski. Principles and Implementations of Dissipative (Dynamic) Self-Assembly. *J.Phys. Chem. B*, 110:2482–2496, 2006.

[45] Rashmi C Desai and Raymond Kapral. *Dynamics of Self-organized and Self-assembled Structures*. Cambridge University Press, 1 edition, 2009.

[46] Bartosz A Grzybowski, Howard A Stone, and George M Whitesides. Dynamic self-assembly of magnetized, millimetre-sized objects rotating at a liquid–air interface. *Nature*, 405(6790):1033, 2000.

[47] Martin McCullagh, Tatiana Prytkova, Stefano Tonzani, Nicolas D. Winter, and George C. Schatz. Modeling self-assembly processes driven by nonbonded interactions in soft material. *J. Phys. Chem. B*, 112(34):10388–10398, 2008.

[48] Martin Kröger. Simple models for complex nonequilibrium fluids. *Phys. Rep.*, 390(6):453–551, 2004.

[49] Katsuyo Thornton, John Ågren, and PW Voorhees. Modelling the evolution of phase boundaries in solids at the meso-and nano-scales. *Acta Mater.*, 51(19):5675–5710, 2003.

[50] C Reichhardt and CJ Olson Reichhardt. Dynamical ordering and directional locking for particles moving over quasicrystalline substrates. *Phys. Rev. Lett.*, 106(6):060603, 2011.

[51] Helgi I Ingólfsson, Cesar A Lopez, Jaakko J Uusitalo, Djurre H de Jong, Srinivasa M Gopal, Xavier Periole, and Siewert J Marrink. The power of coarse graining in biomolecular simulations. *Wiley Interdiscip. Rev. Comput. Mol. Sci.*, 4(3):225–248, 2014.

[52] Mingyang Hu. *Designing polymer-tethered membrane-nanoparticle composites*. PhD thesis, Carnegie Mellon University, 2013.

[53] Andrés Arango-Restrepo, J Miguel Rubi, and Daniel Barragán. Understanding gelation as a nonequilibrium self-assembly process. *J. Phys. Chem. B*, 122(18):4937–4945, 2018.

[54] Scott H Northrup, Stuart A Allison, and J Andrew McCammon. Brownian dynamics simulation of diffusion-influenced bimolecular reactions. *J. Chem. Phys*, 80(4):1517–1524, 1984.

[55] Michael Grünwald, Simon Tricard, George M Whitesides, and Phillip L Geissler. Exploiting nonequilibrium phase separation for self-assembly. *Soft Matter*, 12(5):1517–1524, 2016.

[56] Mario Tagliazucchi, Emily A Weiss, and Igal Szleifer. Dissipative self-assembly of particles interacting through time-oscillatory potentials. *Proc. Natl. Acad. Sci.*, 111(27):9751–9756, 2014.

[57] Stefan Tsonchev, George C. Schatz, and Mark A. Ratner. Electrostatically-directed self-assembly of cylindrical peptide amphiphile nanostructures. *J. Phys. Chem. B*, 108(26):8817–8822, 2004.

[58] Alexey Snezhko. Non-equilibrium magnetic colloidal dispersions at liquid–air interfaces: dynamic patterns, magnetic order and self-assembled swimmers. *J. Phys.: Condens. Matter*, 23(15):153101, 2011.

[59] Eric P. Lewandowski, Marcello Cavallaro, Lorenzo Botto, Jorge C. Bernate, Valeria Garbin, and Kathleen J. Stebe. Orientation and self-assembly of cylindrical particles by anisotropic capillary interactions. *Langmuir*, 26(19):15142–15154, 2010.

[60] Mazen Al-Ghoul and Byung Chan Eu. Hyperbolic reaction-diffusion equations and irreversible thermodynamics: II. Two-dimensional patterns and dissipation of energy and matter. *Physica D: Nonlinear Phenomena*, 97:531–562, 1996.

[61] András Volford, Ferenc Izsák, Mátyás Ripszám, and István Lagzi. Pattern formation and self-organization in a simple precipitation system. *Langmuir*, 23(3):961–4, 2007.

[62] István Lagzi, Bartlomiej Kowalczyk, and Bartosz a. Grzybowski. Liesegang rings engineered from charged nanoparticles. *J. Am. Chem. Soc.*, 132(1):58–60, 2010.

[63] Mahmoud M Ayass, Andrew Abi Mansour, and Mazen Al-Ghoul. Alternating metastable/stable pattern in the mercuric iodide crystal formation outside the ostwald rule of stages. *J. Phys. Chem. A*, 118(36):7725–31, 2014.

[64] István Lagzi. Formation of Liesegang patterns in an electric field Â´. *Phys. Chem. Chem. Phys.*, 4:1268–1270, 2002.

[65] Mazen Al-ghoul and Byung Chan Eu. Hyperbolic reaction-diffusion equations and irreversible thermodynamics. *Physica D*, 90:119–153, 1996.

[66] M. Al-Ghoul and R Sultan. Front Propagation in Patterned Precipitation. 1. Simulation of a Migrating Co(OH) 2 Liesegang Pattern. *J. Phys. Chem. A*, 105(34):8053–8058, 2001.

[67] M. Al-Ghoul and R. Sultan. Front propagation in patterned precipitation. 2. Electric effects in precipitation-dissolution patterning schemes. *J. Phys. Chem. A*, 107(2):1095–1101, 2003.

[68] Mazen Al-Ghoul. Generalized hydrodynamics of reaction-diffusion systems and dissipative structures. *Philos. Trans. Royal Soc. A*, 362(1821):1567–81, 2004.

[69] Andrew Abi Mansour and Mazen Al Ghoul. Scaling and crossover dynamics in the hyperbolic reaction-diffusion equations of initially separated components. *Phys. Rev. E: Stat. Phys., Plasmas, Fluids,*, 84(2):026107, 2011.

[70] Bartosz a. Grzybowski, Bartlomiej Kowalczyk, István Lagzi, Dawei Wang, Konstantin V. Tretiakov, and David a. Walker. Inorganic salts direct the assembly of charged nanoparticles into composite nanoscopic spheres, plates, or needles. *Faraday Discuss.*, 159:201, 2012.

[71] Konstantin V Tretiakov, Igal Szleifer, and Bartosz A Grzybowski. The Rate of Energy Dissipation Determines Probabilities of Non- equilibrium Assemblies. *Angew. Chem. int. Ed*, 52:10304–10308, 2013.

[72] Masao Doi. Onsager's variational principle in soft matter. *J. Phys.: Condens. Matter*, 23(28):284118, 2011.

[73] D Reguera, JM Rubi, and JMG Vilar. The mesoscopic dynamics of thermodynamic systems. *J. Phys. Chem. B*, 109(46):21502–21515, 2005.

[74] Jason R Green, Anthony B Costa, Bartosz A Grzybowski, and Igal Szleifer. Relationship between dynamical entropy and energy dissipation far from thermodynamic equilibrium. *Proc. Natl. Acad. Sci.*, 110(41):16339–16343, 2013.

[75] Horacio Serna, Alberto P Munuzuri, and Daniel Barragán. Thermodynamic and morphological characterization of turing patterns in non-isothermal reaction-diffusion systems. *Phys. Chem. Chem. Phys.*, 19:14401–14411, 2017.

[76] Cosma Rohilla Shalizi and James P Crutchfield. Computational mechanics: Pattern and prediction, structure and simplicity. *J. Stat. Phys.*, 104(3-4):817–879, 2001.

[77] Eugene Kagan. Turing systems, entropy, and kinetic models for self-healing surfaces. *Entropy*, 12(3):554–569, 2010.

[78] Roderick C Dewar, Charles H Lineweaver, and Robert K Niven. *Beyond the Second Law: Entropy Production and Non-equilibrium Systems.* Springer-Verlag Berlin Heidelberg, 1 edition, 2014.

[79] Roderick Dewar. Information theory explanation of the fluctuation theorem, maximum entropy production and self-organized criticality in non-equilibrium stationary states. *J. Phys. A: Math. Gen.*, 36(3):631, 2003.

[80] Garth W Paltridge. Global dynamics and climate-a system of minimum entropy exchange. *Q. J. Royal Meteorol. Soc.*, 101(429):475–484, 1975.

[81] GW Paltridge. The steady-state format of global climate. *Q. J. Royal Meteorol. Soc.*, 104(442):927–945, 1978.

[82] Robert K. Niven. Steady state of a dissipative flow-controlled system and the maximum entropy production principle. *Phys. Rev. E: Stat. Phys., Plasmas, Fluids, - Statistical, Nonlinear, and Soft Matter Physics*, 80(2):1–15, 2009.

[83] R. K. Niven. Minimization of a free-energy-like potential for non-equilibrium flow systems at steady state. *Philos. Trans. Royal Soc. B*, 365(1545):1323–1331, 2010.

[84] Robert K Niven. Simultaneous extrema in the entropy production for steady-state fluid flow in parallel pipes. *J. Non-Equilib. Thermodyn.*, 35(3):347–378, 2010.

[85] A. Kleidon and R.D. Lorentz. *Non-equilibrium Thermodynamics and the Production of Entropy: Life, Earth, and Beyond.* Springer-Verlag Berlin Heidelberg, 1 edition, 2004.

[86] Michael Nosonovsky and Bharat Bhushan. Thermodynamics of surface degradation, self-organization and self-healing for biomimetic surfaces. *Philos. Trans. Royal Soc. A*, 367(1893):1607–1627, 2009.

[87] Michael Nosonovsky and Bharat Bhushan. Surface self-organization: From wear to self-healing in biological and technical surfaces. *Appl. Surf. Sci.*, 256(12):3982–3987, 2010.

[88] Bharat Bhushan, Yong Chae Jung, and Kerstin Koch. Micro-, nano-and hierarchical structures for superhydrophobicity, self-cleaning and low adhesion. *Philos. Trans. Royal Soc. A*, 367(1894):1631–1672, 2009.

[89] Y. Kawazura and Z. Yoshida. Entropy production rate in a flux-driven self-organizing system. *Phys. Rev. E: Stat. Phys., Plasmas, Fluids, - Statistical, Nonlinear, and Soft Matter Physics*, 82(6):1–8, 2010.

[90] Alfred Hubler, Andrey Belkin, and Alexey Bezryadin. Noise induced phase transition between maximum entropy production structures and minimum entropy production structures? *Complexity*, 20(3):8–11, 2015.

[91] John J Tyson. Classification of instabilities in chemical reaction systems. *J. Chem. Phys.*, 62(3):1010–1015, 1975.

[92] Jean-Marie Lehn. Towards complex matter: supramolecular chemistry and self-organization. *Eur. Rev.*, 17(2):263–280, 2009.

[93] Werner Ebeling and Rainer Feistel. *Physics of Self-organization and Evolution*. John Wiley & Sons, 1 edition, 2011.

[94] Gardner C Quarton, Theodore Melnechuk, and Francis O Schmitt. *The neurosciences. A study program*. Rockefeller Univ. Press, 1 edition, 1967.

[95] Tom Misteli. The concept of self-organization in cellular architecture. *J. Cell Biol.*, 155(2):181–186, 2001.

[96] Paul Glansdorff, Ilya Prigogine, and Robert Nyden Hill. Thermodynamic theory of structure, stability and fluctuations. *Am. J. Phys.*, 41:147–148, 1973.

[97] Hermann Haken and Robert Graham. Synergetik-die lehre vom zusammenwirken. *Umschau*, 6(191):178, 1971.

[98] Hermann Haken. Synergetics: an introduction. non-equilibrium phase transition and self-selforganisation in physics, chemistry and biology, 1983.

[99] Ilya Prigogine, Gregoire Nicolis, and Agnes Babloyantz. Thermodynamics of evolution. *Physics today*, 25:23, 1972.

[100] Grégoire Nicolis and J Portnow. Chemical oscillations. *Chem. Rev.*, 73(4):365–384, 1973.

[101] V Krinsky. *Self-organization*. Springer, 1 edition, 1984.

[102] Joseph Silk. Dissipative Processes in Galaxy Formation. *PNAS*, 90(June):4835–4839, 1993.

[103] G Bodifee. Star formation regions as galactic dissipative structures. *Astrophys. Space Sci.*, 122(1):41–56, 1986.

[104] Renato Pakter and Yan Levin. Stability and self-organization of planetary systems. *Phys. Rev. E: Stat. Phys., Plasmas, Fluids,*, 97(4):042221, 2018.

[105] Toshiya Nozakura and Satoru Ikeuchi. Formation of Dissipative Structures in Galaxies. *Atrophys. J*, 279:40–52, 1984.

[106] Leroy Cronin, Anne De Wit, Ivria J Dolobo, Bruno Escribano, Raymond E Goldstein, Florence Haudin, David E H Jones, Alan L Mackay, Jerzy Maselko, Jason J Pagano, J Pantaleone, Michael J Russell, C Ignacio Sainz-d, Oliver Steinbock, David A Stone, Yoshifumi Tanimoto, and Noreen L Thomas. From chemical gardens to chemobrionics From Chemical Gardens to Chemobrionics. *Chem. Rev*, 115:8652–8703, 2015.

[107] Irving R. Epstein, John A. Pojman, and Oliver Steinbock. Introduction: Self-organization in nonequilibrium chemical systems. *Chaos*, 16(3):037101, 2006.

[108] Tongxin Wang, An Wu Xu, and Helmut Cölfen. Formation of self-organized dynamic structure patterns of barium carbonate crystals in polymer-controlled crystallization. *Angew. Chem. Int. Ed.*, 45(27):4451–4455, 2006.

[109] JMG Vilar, RV Solé, and JM Rubi. On the origin of plankton patchiness. *Physica A*, 317(1-2):239–246, 2003.

[110] Francesc Sagués and Irving R. Epstein. Nonlinear chemical dynamics. *Dalton Transactions*, (7):1201–1217, 2003.

[111] Marek Orlik. *Self-Organization in Electrochemical Systems I*. Springer Science & Business Media, 1 edition, 2012.

[112] Marek Grzelczak, Jan Vermant, Eric M. Furst, and Luis M. Liz-Marzán. Directed self-assembly of nanoparticles. *ACS Nano*, 4(7):3591–3605, 2010.

[113] Jean-Marie Lehn. Beyond chemical synthesis: Self-organization?! *Isr. J. Chem.*, 58(1-2):136–141, 2018.

[114] Jean-marie Lehn. Perspectives in Supramolecular Chemistry-From Molecular Recognition towards Molecular Information Processing and. *Angew. Chem. int. Ed. Engl*, 29:1304–1319, 1990.

[115] Anders E C Palmqvist. Synthesis of ordered mesoporous materials using surfactant liquid crystals or micellar solutions. *Curr. Opin. Colloid Interface Sci.*, 8:145–155, 2003.

[116] Kelly Hales and Darrin J. Pochan. Using polyelectrolyte block copolymers to tune nanostructure assembly. *Curr. Opin. Colloid Interface Sci.*, 11(6):330–336, 2006.

[117] Brad M Rosen, Christopher J Wilson, Daniela A Wilson, Mihai Peterca, Mohammad R Imam, and Virgil Percec. Dendron-mediated self-assembly, disassembly, and self-organization of complex systems. *Chem. Rev.*, 109(11):6275–6540, 2009.

[118] Eric Karsenti. Self-organization in cell biology: a brief history. *Nat. Rev. Mol. Cell Biol.*, 9(3):255, 2008.

[119] Kyle JM Bishop, Rafal Klajn, and Bartosz A Grzybowski. The core and most useful molecules in organic chemistry. *Angew. Chem. Int. Ed.*, 45(32):5348–5354, 2006.

[120] Zhenli Zhang and Sharon C Glotzer. Self-assembly of patchy particles. *Nano Lett.*, 4(8):1407–1413, 2004.

[121] Goutam Palui and Arindam Banerjee. Fluorescent gel from a self-assembling new chromophoric moiety containing azobenzene based tetraamide. *J. Phys. Chem. B*, 112(33):10107–10115, 2008.

[122] Job Boekhoven, Aurelie M. Brizard, Krishna N. K. Kowlgi, Ger J. M. Koper, Rienk Eelkema, and Jan H. van Esch. Dissipative Self-Assembly of a Molecular Gelator by Using a Chemical Fuel. *Angew. Chem.*, 122(28):4935–4938, 2010.

[123] Jaap J.D De Jong. Light-Driven Dynamic Pattern Formation. *Angew. Chem. int. Ed*, 44:2373–2376, 2005.

[124] Rafal Klajn, Kyle J M Bishop, and Bartosz A Grzybowski. Light-controlled self-assembly of reversible and irreversible nanoparticle suprastructures. *PNAS*, 104(25):10305–10309, 2007.

[125] Gianfranco Ercolani. A model for self-assembly in solution. *J. Phys. Chem. B*, 107(21):5052–5057, 2003.

[126] C Casagrande, P Fabre, E Raphael, and M Veyssié. Janus beads: realization and behaviour at water/oil interfaces. *EPL*, 9(3):251, 1989.

[127] Andreas Walther and Axel HE Müller. Janus particles. *Soft Matter*, 4(4):663–668, 2008.

[128] Amar B Pawar and Ilona Kretzschmar. Fabrication, assembly, and application of patchy particles. *Macromol. Rapid Commun.*, 31(2):150–168, 2010.

[129] G. J M Koper, J. Boekhoven, W. E. Hendriksen, J. H. Van Esch, R. Eelkema, I. Pagonabarraga, J. M. Rubí, and D. Bedeaux. The Lost Work In Dissipative Self-Assembly. *Int. J. Thermophys.*, 34(7):1229–1238, 2013.

[130] Jin Zhang, Haiqiao Wang, Xiaoyang Li, Shasha Song, Aixin Song, and Jingcheng Hao. Two gelation mechanisms of deoxycholate with inorganic additives: Hydrogen bonding and electrostatic interactions. *J. Phys. Chem. B*, 120(27):6812–6818, 2016.

[131] Yan Qiao, Yiyang Lin, Zhiyi Yang, Huanfa Chen, Shaofei Zhang, Yun Yan, and Jianbin Huang. Unique temperature-dependent supramolecular self-assembly: From hierarchical 1d nanostructures to super hydrogel. *J. Phys. Chem. B*, 114(36):11725–11730, 2010.

[132] Andrés Arango-Restrepo, Daniel Barragán, and J Miguel Rubi. Nonequilibrium self-assembly induced liesegang rings in a non-isothermal system. *PCCP*, 20(7):4699–4707, 2018.

[133] Robijn F Bruinsma, William M Gelbart, David Reguera, Joseph Rudnick, and Roya Zandi. Viral Self-Assembly as a Thermodynamic Process. *Phys. Rev. Lett*, 90(24):1–4, 2003.

[134] Michael F Hagan and David Chandler. Dynamic pathways for viral capsid assembly. *Biophys. J .*, 91(1):42–54, 2006.

[135] Eduardo Sanz, Chantal Valeriani, Daan Frenkel, and Marjolein Dijkstra. Evidence for out-of-equilibrium crystal nucleation in suspensions of oppositely charged colloids. *Phys. Rev. Lett.*, 99(5):055501, 2007.

[136] Artem Levandovsky and Roya Zandi. Nonequilibirum assembly, retroviruses, and conical structures. *Phys. Rev. Lett.*, 102(19):198102, 2009.

[137] Tristan S Ursell, Jeffrey Nguyen, Russell D Monds, Alexandre Colavin, Gabriel Billings, Nikolay Ouzounov, Zemer Gitai, Joshua W Shaevitz, and Kerwyn Casey Huang. Rod-like bacterial shape is maintained by feedback between cell curvature and cytoskeletal localization. *Proc. Natl. Acad. Sci.*, page 201317174, 2014.

[138] Roey J Amir, Sheng Zhong, Darrin J Pochan, and Craig J Hawker. Enzymatically triggered self-assembly of block copolymers. *J. Am. Chem. Soc.*, 131(39):13949–13951, 2009.

[139] Lorenzo Tattini, Pierandrea Lo Nostro, Luca Scalise, Barry W. Ninham, and Piero Baglioni. Gels from a semifluorinated n-alkane in fluorinated solvents as a probe for intermolecular interactions. *J. Colloid Interface Sci.*, 339(1):259–265, 2009.

[140] Christophe B. Minkenberg, Louw Florusse, Rienk Eelkema, G. J M Koper, and Jan H. Van Esch. Triggered self-assembly of simple dynamic covalent surfactants. *J. Am. Chem. Soc.*, 131(32):11274–11275, 2009.

[141] Frank Schweitzer. *Brownian agents and active particles: collective dynamics in the natural and social sciences*. Springer, 1 edition, 2007.

[142] Thomas Surrey, Francois Nédélec, Stanislas Leibler, and Eric Karsenti. Physical Properties Determining Self-Organization of Motors and Microtubules. *Science*, 292:1167–1171, 2001.

[143] Karsten Kruse, Jean-Francois Joanny, Frank Jülicher, Jacques Prost, and Ken Sekimoto. Generic theory of active polar gels: a paradigm for cytoskeletal dynamics. *Eur. Phys. J. E*, 16(1):5–16, 2005.

[144] Frank Juelicher, K Kruse, J Prost, and J-F Joanny. Active behavior of the cytoskeleton. *Phys. Rep.*, 449(1-3):3–28, 2007.

[145] M Cristina Marchetti, Jean-François Joanny, Sriram Ramaswamy, Tanniemola B Liverpool, Jacques Prost, Madan Rao, and R Aditi Simha. Hydrodynamics of soft active matter. *Rev. Mod. Phys.*, 85(3):1143, 2013.

[146] Irving R Epstein and Bing Xu. Reaction–diffusion processes at the nano-and microscales. *Nat. Nanotechnol.*, 11(4):312, 2016.

[147] Mazen Al-Ghoul, Manal Ammar, and Rabih O Al-Kaysi. Band propagation, scaling laws and phase transition in a precipitate system. I: Experimental study. *J. Phys. Chem. A*, 116(18):4427, 2012.

[148] Mazen Al-Ghoul and Tarek Ghaddar. Theoretical Modeling of Front Propagation of CdS Nanoparticles in a Gel. *Journal of Nano Research*, 11:19–24, 2010.

[149] Rustem F Ismagilov, Alexander Schwartz, Ned Bowden, and George M Whitesides. Autonomous movement and self-assembly. *Angew. Chem. Int. Ed.*, 41(4):652–654, 2002.

[150] Walter F Paxton, Ayusman Sen, and Thomas E Mallouk. Motility of catalytic nanoparticles through self-generated forces. *Chem. Eur. J.*, 11(22):6462–6470, 2005.

[151] Benno Liebchen, Davide Marenduzzo, Ignacio Pagonabarraga, and Michael E Cates. Clustering and pattern formation in chemorepulsive active colloids. *Phys. Rev. Lett.*, 115(25):258301, 2015.

[152] Joakim Stenhammar, Raphael Wittkowski, Davide Marenduzzo, and Michael E Cates. Activity-induced phase separation and self-assembly in mixtures of active and passive particles. *Phys. Rev. Lett.*, 114(1):018301, 2015.

[153] Xingbo Yang, M Lisa Manning, and M Cristina Marchetti. Aggregation and segregation of confined active particles. *Soft matter*, 10(34):6477–6484, 2014.

[154] Hong-Ren Jiang, Hirofumi Wada, Natsuhiko Yoshinaga, and Masaki Sano. Manipulation of colloids by a nonequilibrium depletion force in a temperature gradient. *Phys. Rev. Lett.*, 102(20):208301, 2009.

[155] Ziane Izri, Marjolein N Van Der Linden, Sébastien Michelin, and Olivier Dauchot. Self-propulsion of pure water droplets by spontaneous marangoni-stress-driven motion. *Phys. Rev. Lett.*, 113(24):248302, 2014.

[156] Maximilian Schmitt and Holger Stark. Swimming active droplet: A theoretical analysis. *EPL*, 101(4):44008, 2013.

[157] Shashi Thutupalli, Ralf Seemann, and Stephan Herminghaus. Swarming behavior of simple model squirmers. *New J. Phys.*, 13(7):073021, 2011.

[158] Demian Levis, Ignacio Pagonabarraga, and Benno Liebchen. Activity induced synchronization. *arXiv preprint arXiv:1802.02371*, 2018.

[159] Jean-Baptiste Delfau, Cristóbal López, and Emilio Hernández-García. Active cluster crystals. *New J. Phys.*, 19(9):095001, 2017.

[160] Linda N Lucas, Jan van Esch, Richard M Kellogg, and Ben L Feringa. Photocontrolled self-assembly of molecular switches. *Chem. Commun.*, (8):759–760, 2001.

[161] Yanhu Wei, Dow Chemical, Shuangbing Han, Dow Corning, and Shuangbing Han. Photoswitchable Catalysis Mediated by Dynamic Aggregation of Nanoparticles. *J. Am. Chem. Soc.*, 132:11018–11020, 2010.

[162] Jaakko VI Timonen, Mika Latikka, Ludwik Leibler, Robin HA Ras, and Olli Ikkala. Switchable static and dynamic self-assembly of magnetic droplets on superhydrophobic surfaces. *Science*, 341(6143):253–257, 2013.

[163] Mirjam E Leunissen, Christina G Christova, Antti-Pekka Hynninen, C Patrick Royall, Andrew I Campbell, Arnout Imhof, Marjolein Dijkstra, Rene Van Roij, and Alfons Van Blaaderen. Ionic colloidal crystals of oppositely charged particles. *Nature*, 437(7056):235, 2005.

[164] Dirk Helbing, Illés J Farkas, and Tamás Vicsek. Freezing by heating in a driven mesoscopic system. *Phys. Rev. Lett.*, 84(6):1240, 2000.

[165] Ivo Buttinoni, Julian Bialké, Felix Kümmel, Hartmut Löwen, Clemens Bechinger, and Thomas Speck. Dynamical clustering and phase separation in suspensions of self-propelled colloidal particles. *Phys. Rev. Lett.*, 110(23):238301, 2013.

[166] Nguyen HP Nguyen, Eric Jankowski, and Sharon C Glotzer. Thermal and athermal three-dimensional swarms of self-propelled particles. *Phys. Rev. E: Stat. Phys., Plasmas, Fluids,*, 86(1):011136, 2012.

[167] Jordi Faraudo, Jordi S Andreu, Carles Calero, and Juan Camacho. Predicting the self-assembly of superparamagnetic colloids under magnetic fields. *Adv. Funct. Mater.*, 26(22):3837–3858, 2016.

[168] Pietro Tierno, Ramanathan Muruganathan, and Thomas M Fischer. Viscoelasticity of dynamically self-assembled paramagnetic colloidal clusters. *Phys. Rev. Lett.*, 98(2):028301, 2007.

[169] Pietro Tierno. Magnetically reconfigurable colloidal patterns arranged from arrays of self-assembled microscopic dimers. *Soft Matter*, 8(45):11443–11446, 2012.

[170] Fernando Martinez-Pedrero, Andrejs Cebers, and Pietro Tierno. Orientational dynamics of colloidal ribbons self-assembled from microscopic magnetic ellipsoids. *Soft matter*, 12(16):3688–3695, 2016.

[171] Chiara Neto, Massimo Bonini, and Piero Baglioni. Self-assembly of magnetic nanoparticles into complex superstructures: Spokes and spirals. *Colloids Surf. A*, 269(1-3):96–100, 2005.

[172] Sampath Srinivasan, Vakayil K Praveen, Robert Philip, and Ayyappanpillai Ajayaghosh. Bioinspired superhydrophobic coatings of carbon nanotubes and linear π systems based on the "bottom-upÂ´Â´ self-assembly approach. *Angew. Chem. Int. Ed.*, 47(31):5750–5754, 2008.

[173] Takashi Yokoyama, Shiyoshi Yokoyama, and Toshiya Kamikado. Selective assembly on a surface of supramolecular aggregates with controlled size and shape. *Nature*, 413:619–621, 2001.

[174] Soumen De and Rafal Klajn. Dissipative Self-Assembly Driven by the Consumption of Chemical Fuels. *Adv. Mater.*, 1706750:1706750, 2018.

[175] Alessandro Sorrenti, Jorge Leira-Iglesias, Albert J Markvoort, Tom FA de Greef, and Thomas M Hermans. Non-equilibrium supramolecular polymerization. *Chem. Soc. Rev.*, 2017.

[176] Alexander V. Popov, Galen T. Craven, and Rigoberto Hernandez. Nonequilibrium structure in sequential assembly. *Phys. Rev. E: Stat. Phys., Plasmas, Fluids, - Statistical, Nonlinear, and Soft Matter Physics*, 92(5):1–5, 2015.

[177] Baiyong Ding, Ying Li, Meng Qin, Yin Ding, Yi Cao, and Wei Wang. Two approaches for the engineering of homogeneous small-molecule hydrogels. *Soft Matter*, 9(18):4672–4680, 2013.

[178] Ying Li and Yi Cao. The physical chemistry for the self-assembly of peptide hydrogels. *Chin. J. Polym. Sci.*, pages 1–13, 2017.

[179] Ronald Aylmer Fisher. The wave of advance of advantageous genes. *Annals of eugenics*, 7(4):355–369, 1937.

[180] A Kolmogorov. A. kolmogorov, i. petrovsky and n. piskunov, bull. univ. moscow, ser. int. a 1, 1 (1937). *Bull. Univ. Moscow, Ser. Int. A*, 1:1, 1937.

[181] Marian V Smoluchowski. Über brownsche molekularbewegung unter einwirkung äußerer kräfte und deren zusammenhang mit der verallgemeinerten diffusionsgleichung. *Annalen der Physik*, 353(24):1103–1112, 1916.

[182] Henryk Galina and Jaromir B Lechowicz. Mean-field kinetic modeling of polymerization: the smoluchowski coagulation equation. In *Grafting/Characterization Techniques/Kinetic Modeling*, pages 135–172. Springer, 1998.

[183] Tong Gao, Robert Blackwell, Matthew A Glaser, Meredith D Betterton, and Michael J Shelley. Multiscale polar theory of microtubule and motor-protein assemblies. *Phys. Rev. Lett.*, 114(4):048101, 2015.

[184] Paul Meakin, Tamás Vicsek, and Fereydoon Family. Dynamic cluster-size distribution in cluster-cluster aggregation: Effects of cluster diffusivity. *Phys. Rev. B*, 31:564–569, Jan 1985.

[185] M Kolb and R Jullien. Chemically limited versus diffusion limited aggregation. *J. Physique Lett.*, 45(20):977–981, Oct 1984.

[186] R Jullien and M Kolb. Hierarchical model for chemically limited cluster-cluster aggregation. *J. Phys. A*, 17(12):L639–L643, aug 1984.

[187] Paul Meakin and Fereydoon Family. Structure and kinetics of reaction-limited aggregation. *Phys. Rev. A*, 38:2110–2123, Aug 1988.

[188] K VanWorkum, Jack F Douglas, and Wolfgang Losert. Schematic models of molecular self-organization. In *Macromolecular Symposia*, 2005.

[189] Kevin Van Workum and Jack F Douglas. Symmetry, equivalence, and molecular self-assembly. *Phys. Rev. E: Stat. Phys., Plasmas, Fluids,*, 73(3):031502, 2006.

[190] Jacek Dudowicz, Karl F Freed, and Jack F Douglas. Flory-huggins model of equilibrium polymerization and phase separation in the stockmayer fluid. *Phys. Rev. Lett.*, 92(4):045502, 2004.

[191] Santiago A. Serebrinsky. Physical time scale in kinetic monte carlo simulations of continuous-time markov chains. *Phys. Rev. E*, 83:037701, Mar 2011.

[192] B. Meng and W. H. Weinberg. Monte carlo simulations of temperature programmed desorption spectra. *J. Chem. Phys.*, 100:5280–5289, 1994.

[193] Alexander Slepoy, Aidan P. Thompson, and Steven J. Plimpton. A constant-time kinetic monte carlo algorithm for simulation of large biochemical reaction networks. *J. Chem. Phys.*, 128:05B618, 2008.

[194] G Odriozola, A Schmitt, Arturo Moncho-Jorda, J Callejas-Fernandez, R Martinez-Garcia, R Leone, and Roque Hidalgo-Alvarez. Constant bond breakup probability model for reversible aggregation processes. *Phys. Rev. E*, 65(3):031405, 2002.

[195] Matthias Thorn and Markus Seesselberg. Dynamic scaling in colloidal aggregation: Comparison of experimental data with results of a stochastic simulation. *Phys. Rev. Lett.*, 72(22):3622, 1994.

[196] Asawari Samant and Dionisios G Vlachos. Overcoming stiffness in stochastic simulation stemming from partial equilibrium: a multiscale monte carlo algorithm. *J. Chem. Phys*, 123(14):144114, 2005.

[197] Roy J Glauber. Time-dependent statistics of the ising model. *J. Math. Phys*, 4(2):294–307, 1963.

[198] Daan Frenkel and Berend Smit. *Understanding molecular simulation: from algorithms to applications*, volume 1. Elsevier, 1 edition, 2001.

[199] Tamás Vicsek, András Czirók, Eshel Ben-Jacob, Inon Cohen, and Ofer Shochet. Novel type of phase transition in a system of self-driven particles. *Phys. Rev. Lett.*, 75(6):1226, 1995.

[200] Pawel Romanczuk, Markus Bär, Werner Ebeling, Benjamin Lindner, and Lutz Schimansky-Geier. Active brownian particles. *Eur. Phys. J. Special Topics*, 202(1):1–162, 2012.

[201] Clemens Bechinger, Roberto Di Leonardo, Hartmut Löwen, Charles Reichhardt, Giorgio Volpe, and Giovanni Volpe. Active particles in complex and crowded environments. *Rev. Mod. Phys.*, 88(4):045006, 2016.

[202] V. V. Gafiychuk and B. Yo Datsko. Pattern formation in a fractional reaction-diffusion system. *Physica A*, 365(2):300–306, 2006.

[203] P Gray and SK Scott. Autocatalytic reactions in the isothermal, continuous stirred tank reactor: Oscillations and instabilities in the system a+ 2bâ†’ 3b; bâ†’ c. *Chem. Eng. Sci.*, 39(6):1087–1097, 1984.

[204] Jia-Chen Hua, Lijian Chen, Liberty Falcon, Joseph L McCauley, and Gemunu H Gunaratne. Variable diffusion in stock market fluctuations. *Physica A*, 419:221–233, 2015.

[205] UK Rößler, AN Bogdanov, and C Pfleiderer. Spontaneous skyrmion ground states in magnetic metals. *Nature*, 442(7104):797, 2006.

[206] Jelena Raspopovic, Luciano Marcon, Laura Russo, and James Sharpe. Digit patterning is controlled by a bmp-sox9-wnt turing network modulated by morphogen gradients. *Science*, 345(6196):566–570, 2014.

[207] Norbert Stoop, Romain Lagrange, Denis Terwagne, Pedro M Reis, and Jörn Dunkel. Curvature-induced symmetry breaking determines elastic surface patterns. *Nat. Mater.*, 14(3):337, 2015.

[208] Rabih F. Sultan. Propagating fronts in periodic precipitation systems with redissolution. *PCCP*, 4(8):1253–1261, 2002.

[209] Andrew Abi Mansour and Mazen Al-Ghoul. Band Propagation, Scaling Laws, and Phase Transition in a Precipitate System. 2. Computational Study. *J. Phys. Chem. A*, 119(35):9201–9209, 2015.

[210] Ilya M Lifshitz and Vitaly V Slyozov. The kinetics of precipitation from supersaturated solid solutions. *J. Phys. Chem. Solids*, 19(1-2):35–50, 1961.

[211] Wilhelm Ostwald. Studien über die bildung und umwandlung fester körper. *Zeitschrift für physikalische Chemie*, 22(1):289–330, 1897.

[212] Wolfgang Ostwald. Ueber die geschwindigkeitsfunktion der viskosität disperser systeme. i. *Kolloid-Zeitschrift*, 36(2):99–117, 1925.

[213] Ferenc Molnár, Ferenc Izsák, and István Lagzi. Design of equidistant and revert type precipitation patterns in reaction-diffusion systems. *Phys. Chem. Chem. Phys.*, 10(17):2368–73, 2008.

[214] Konstantin V. Tretiakov, Kyle J. M. Bishop, and Bartosz a. Grzybowski. The dependence between forces and dissipation rates mediating dynamic self-assembly. *Soft Matter*, 5(6):1279, 2009.

[215] Eric Climent, Kyongmin Yeo, Martin R Maxey, and George E Karniadakis. Dynamic self-assembly of spinning particles. *J. Fluids Eng.*, 129(4):379–387, 2007.

[216] M.Doi and S.E.Edwards. *The Theory of Polymer Dynamics*. Oxford University Press, 1 edition, 1986.

[217] David Saintillan and Michael J Shelley. Instabilities and pattern formation in active particle suspensions: kinetic theory and continuum simulations. *Phys. Rev. Lett.*, 100(17):178103, 2008.

[218] David Saintillan and Michael J Shelley. Theory of active suspensions. In *Complex Fluids in biological systems*, pages 319–355. Springer, 2015.

[219] Evgeny B Stukalin and Anatoly B Kolomeisky. Simple growth models of rigid multifilament biopolymers. *J. Chem. Phys.*, 121(2):1097–1104, 2004.

[220] Evgeny B Stukalin and Anatoly B Kolomeisky. Polymerization dynamics of double-stranded biopolymers: chemical kinetic approach. *J. Chem. Phys.*, 122(10):104903, 2005.

[221] Evgeny B Stukalin and Anatoly B Kolomeisky. Atp hydrolysis stimulates large length fluctuations in single actin filaments. *Biophys. J.*, 90(8):2673–2685, 2006.

[222] Ranjith Padinhateeri, Anatoly B Kolomeisky, and David Lacoste. Random hydrolysis controls the dynamic instability of microtubules. *Biophys. J.*, 102(6):1274–1283, 2012.

[223] D.J. Odde. Estimation of the diffusion-limited rate of microtubule assembly. *Biophys. J.*, 73(1):88 – 96, 1997.

[224] José MG Vilar and J M Rubi. Thermodynamics “beyond” local equilibrium. *PNAS*, 98(20):11081–11084, 2001.

[225] I Pagonabarraga, A Pérez-Madrid, and JM Rubi. Fluctuating hydrodynamics approach to chemical reactions. *Physica A*, 237(1-2):205–219, 1997.

[226] JM Rubi, D Bedeaux, S Kjelstrup, and I Pagonabarraga. Chemical cycle kinetics: removing the limitation of linearity of a non-equilibrium thermodynamic description. *Int. J. Thermophys.*, 34(7):1214–1228, 2013.

[227] A Arango-Restrepo, J.M Rubi, and D Barragán. Kinetics and energetics of chemical reactions through intermediate states. *Physica A*, 509:86–96, 2018.

[228] JM Rubí, Anders Lervik, Dick Bedeaux, and Signe Kjelstrup. Entropy facilitated active transport. *J. Chem. Phys.*, 146(18):185101, 2017.

[229] JM Rubi and Signe Kjelstrup. Mesoscopic nonequilibrium thermodynamics gives the same thermodynamic basis to butler- volmer and nernst equations. *J. Phys. Chem. B*, 107(48):13471–13477, 2003.

[230] David Reguera and JM Rubi. Homogeneous nucleation in inhomogeneous media. i. nucleation in a temperature gradient. *J. Chem. Phys.*, 119(18):9877–9887, 2003.

[231] David Reguera and JM Rubi. Homogeneous nucleation in inhomogeneous media. ii. nucleation in a shear flow. *J. Chem. Phys.*, 119(18):9888–9893, 2003.

[232] Fred C MacKintosh and Alex J Levine. Nonequilibrium mechanics and dynamics of motor-activated gels. *Phys. Rev. Lett.*, 100(1):018104, 2008.

[233] Alex J Levine and FC MacKintosh. The mechanics and fluctuation spectrum of active gels. *J. Phys. Chem. B*, 113(12):3820–3830, 2009.

[234] Natsuhiko Yoshinaga, J-F Joanny, Jacques Prost, and Philippe Marcq. Polarity patterns of stress fibers. *Phys. Rev. Lett.*, 105(23):238103, 2010.

[235] Shiladitya Banerjee and M Cristina Marchetti. Instabilities and oscillations in isotropic active gels. *Soft Matter*, 7(2):463–473, 2011.

[236] Clinton DeW. Van Siclen. Information entropy of complex structures. *Phys. Rev. E*, 56:5211–5215, Nov 1997.

[237] C. Andraud, A. Beghdadi, and J. Lafait. Entropic analysis of random morphologies. *Physica A*, 207(1):208 – 212, 1994.

[238] C. Andraud, A. Beghdadi, E. Haslund, R. Hilfer, J. Lafait, and B. Virgin. Local entropy characterization of correlated random microstructures. *Physica A*, 235(3):307 – 318, 1997.

[239] R. Piasecki. Entropic measure of spatial disorder for systems of finite-sized objects. *Physica A*, 277(1):157 – 173, 2000.

[240] Grenville J. Croll. Bientropy - the approximate entropy of a finite binary string. *CoRR*, abs/1305.0954, 2013.

[241] Stefano Martiniani, Paul M. Chaikin, and Dov Levine. Quantifying hidden order out of equilibrium. *Phys. Rev. X*, 9:011031, Feb 2019.

[242] Hisashi Ozawa, Shinya Shimokawa, and Hirofumi Sakuma. Thermodynamics of fluid turbulence: A unified approach to the maximum transport properties. *Phys. Rev. E: Stat. Phys., Plasmas, Fluids,*, 64(2):026303, 2001.

[243] Paško Županović, Davor Juretić, and Srećko Botrić. Kirchhoff's loop law and the maximum entropy production principle. *Phys. Rev. E: Stat. Phys., Plasmas, Fluids,*, 70(5):056108, 2004.

[244] Leonid Mikhailovich Martyushev and EG Axelrod. From dendrites and s-shaped growth curves to the maximum entropy production principle. *J. Exp. Theor. Phys*, 78(8):476–479, 2003.

[245] Filip JR Meysman and Stijn Bruers. A thermodynamic perspective on food webs: quantifying entropy production within detrital-based ecosystems. *J. Theor. Biol*, 249(1):124–139, 2007.

[246] Davor Juretić and Paško Županović. Photosynthetic models with maximum entropy production in irreversible charge transfer steps. *Comput. Biol. Chem.*, 27(6):541–553, 2003.

[247] Andrej Dobovišek, Paško Županović, Milan Brumen, Željana Bonačić-Lošić, Domagoj Kuić, and Davor Juretić. Enzyme kinetics and the maximum entropy production principle. *Biophys. Chem.*, 154(2-3):49–55, 2011.

[248] Dilip Kondepudi. Self-organization, entropy production, and physical intelligence. *Ecol. Psychol.*, 24(1):33–45, 2012.

[249] Dilip Kondepudi, Bruce Kay, and James Dixon. End-directed evolution and the emergence of energy-seeking behavior in a complex system. *Phys. Rev. E: Stat. Phys., Plasmas, Fluids, - Statistical, Nonlinear, and Soft Matter Physics*, 91(5):1–5, 2015.

[250] A Lazcano. Complexity, self-organization and the origin of life: The happy liaison? *Origins of Life: Self-Organization and/or Biological Evolution?*, pages 13–22, 2009.

[251] K Michaelian. Thermodynamic dissipation theory for the origin of life. *Earth Syst. Dynam.*, 2:37–51, 2011.

[252] George E Mikhailovsky and Alexander P Levich. Entropy, information and complexity or which aims the arrow of time? *Entropy*, 17(7):4863–4890, 2015.

[253] Robert Stone, Tom Portegys, George Mikhailovsky, and Bradly Alicea. Origins of the embryo: self-organization through cybernetic regulation. *BioSystems*, 173:73–82, 2018.

[254] Olivier Toussaint and Eric D Schneider. The thermodynamics and evolution of complexity in biological systems. *Comp. Biochem. Physiol., Part A Mol. Integr. Physiol.*, 120(1):3–9, 1998.

[255] Lars Onsager. Reciprocal relations in irreversible processes. i. *Physical review*, 37(4):405, 1931.

[256] Lars Onsager. Reciprocal relations in irreversible processes. ii. *Physical review*, 38(12):2265, 1931.

[257] Sybren Ruurds De Groot and Peter Mazur. *Non-equilibrium thermodynamics*. Dover Publications Inc., 1985.

[258] Georgy Lebon, David Jou, and José Casas-Vázquez. *Understanding non-equilibrium thermodynamics*, volume 295. Springer, 1 edition, 2008.

[259] Signe Kjelstrup and Dick Bedeaux. *Non-equilibrium thermodynamics of heterogeneous systems*, volume 16. World Scientific, 1 edition, 2008.

[260] Mikhail Nosonovsky and George G Adams. Vibration and stability of frictional sliding of two elastic bodies with a wavy contact interface. *Journal of applied mechanics*, 71(2):154–161, 2004.

[261] Noel De Nevers and JD Seader. Lost work: A measure of thermodynamic efficiency. *Energy*, 5(8-9):757–769, 1980.

[262] Yohei Kawazura and Zensho Yoshida. Comparison of entropy production rates in two different types of self-organized flows: Bénard convection and zonal flow. *Phys. Plasmas*, 19(1):012305, 2012.

[263] Alfred W Hübler. Which forces reduce entropy production? *Complexity*, 19(5):6–7, 2014.

[264] Mario Tagliazucchi and Igal Szleifer. Dynamics of dissipative self-assembly of particles interacting through oscillatory forces. *Faraday Discuss.*, 186:399–418, 2016.

[265] L. Mandalian, M. Fahs, M. Al-Ghoul, and R. Sultan. Morphology, particle size distribution, and composition in one- and two-salt metal oxinate Liesegang patterns. *J. Phys. Chem. B*, 108(4):1507–1514, 2004.

[266] Andrés Arango-Restrepo. Non-equilibrium self-assembly processes: thermodynamics of structures formation out of equilibrium. Master's thesis, Universidad Nacional de Colombia, Mayo 2017.

[267] Torsten Wittmann, Anthony Hyman, and Arshad Desai. The spindle: a dynamic assembly of microtubules and motors. *Nat. Cell Biol.*, 3(1):E28, 2001.

[268] Tim Sanchez, Daniel TN Chen, Stephen J DeCamp, Michael Heymann, and Zvonimir Dogic. Spontaneous motion in hierarchically assembled active matter. *Nature*, 491(7424):431, 2012.

[269] Todd Thoresen, Martin Lenz, and Margaret L. Gardel. Reconstitution of contractile actomyosin bundles. *Biophys. J.*, 100(11):2698 – 2705, 2011.

[270] Calvin A Fracassi Farias, Renato Pakter, and Yan Levin. Entropy production and vlasov equation for self-gravitating systems. *J. Phys. A*, 51(49):494002, 2018.

[271] Michele Dougherty, Larry Esposito, and Stamatios Krimigis. *Saturn from Cassini-Huygens*. Springer Science & Business Media, 1 edition, 2009.

[272] Richard Greenberg and André Brahic. Planetary rings-a dynamic, evolving subject. In *IAU Colloq. 75: Planetary Rings*, pages 3–11, 1984.

[273] D. A. Head, W. J. Briels, and Gerhard Gompper. Nonequilibrium structure and dynamics in a microscopic model of thin-film active gels. *Phys. Rev. E*, 89:032705, Mar 2014.

[274] Volker Schaller, Christoph Weber, Christine Semmrich, Erwin Frey, and Andreas R. Bausch. Polar patterns of driven filaments. *Nature*, 467(7311):73–77, 2010.

[275] Syoji Ito, Hiroaki Yamauchi, Mamoru Tamura, Shimpei Hidaka, Hironori Hattori, Taichi Hamada, Keisuke Nishida, Shiho Tokonami, Tamitake Itoh, Hiroshi Miyasaka, and Takuya Iida. Selective optical assembly of highly uniform nanoparticles by doughnut-shaped beams. *Sci. Rep.*, 3:21–23, 2013.

[276] DN Zubarev and AG Bashkirov. Statistical theory of brownian motion in a moving fluid in the presence of a temperature gradient. *Physica*, 39(3):334–340, 1968.

[277] R Graham and H Haken. Generalized thermodynamic potential for markoff systems in detailed balance and far from thermal equilibrium. *Zeitschrift für Physik A Hadrons and nuclei*, 243(3):289–302, 1971.

[278] R. Graham and A. Schenzle. Non-equilibrium potentials and stationary probability distributions of some dissipative models without manifest detailed balance. *Zeitschrift für Physik B Condensed Matter*, 52(1):61–68, 1983.

[279] Marco Baiesi and Christian Maes. Life efficiency does not always increase with the dissipation rate. *Journal of Physics Communications*, 2(4):045017, 2018.

[280] Michael Nguyen and Suriyanarayanan Vaikuntanathan. Design principles for nonequilibrium self-assembly. *Proc. Natl. Acad. Sci.*, 113(50):14231–14236, 2016.

[281] Dilip Kondepudi, Bruce Kay, and James Dixon. Dissipative structures, machines, and organisms: A perspective. *Chaos*, 27(10):104607, 2017.

[282] Katsuhiko Ogata and Yanjuan Yang. *Modern control engineering*, volume 4. Prentice hall India, 1 edition, 2002.

[283] Yu-Chi Ho. *Applied optimal control: optimization, estimation, and control*. Hemisphere Publishing Corporation, distributed by Halsted Press, 1 edition, 1975.

[284] RV Gamkrelidze, Lev Semenovich Pontrjagin, and Vladimir Grigor'evic Boltjanskij. *The mathematical theory of optimal processes*. Macmillan Company, 1 edition, 1964.

[285] Signe Kjelstrup, Dick Bedeaux, Eivind Johannessen, and Joachim Gross. *Non-equilibrium thermodynamics for engineers*. World Scientific, 1 edition, 2010.

[286] Editorial. Self-assembling life. *Nat. Nanotechnol.*, 11:909, 2016.

PART I. Non-Equilibrium Self-Assembly Processes

2. Understanding gelation as a non-equilibrium self-assembly process

Gel formation is described by a non-equilibrium self-assembly mechanism which considers the presence of precursors. Assuming that non-equilibrium structures appear and are maintained by entropy production, we developed a mesoscopic non-equilibrium thermodynamic model that describes the dynamic assembly of the structures. In the model, the evolution of the structures from the initially inactivated building blocks to the final agglomerates is governed by kinetic equations of the Fokker-Planck type. From these equations, we get the probability densities which enable one to know measurable quantities such as the concentrations of the different components and the dynamic structure factor obtained in light-scattering experiments. Our results obtained are in very good agreement with the experiments. The model proposed can in general be used to analyze the kinetics of formation of non-equilibrium self-assembly structures usually found in biomedicine and advanced materials.

This chapter was published in *the Journal of Physical Chemistry B*, **122**, 4937-4945, (2018). Ref.[1]

2.1. Introduction: Non-equilibrium self-assembly (NESA)

Non-equilibrium self-assembled (NESA) structures [2, 3] are thermodynamic systems sustained by a continuous dissipation [4] of matter and/or energy [5] and they are composed of fundamental building blocks [6, 2]. NESA structures dissipate matter and energy until they reach states which can either be stationary (dissipative self-assembled structures [3]) or metastable (kinetically trapped self-assembled structures[6]) [7, 8]. NESA structures may constitute precursors of self-assembled equilibrium structures as occurs in the formation of Liesegang patterns [9, 10]. The concept of NESA structure enables us to analyze the overall self-assembly process instead of subdividing it into different steps in which dissipative, kinetically trapped and equilibrium structures may emerge [7], thereby simplifying the description.

As dynamic systems, NESA structures are versatile and exhibit some features peculiar to biological forms such as adaptability, hierarchical organization, self-replication, compartmentalization [11, 6], and even self-organization [12, 13, 14, 15] in the case that the process is controlled by a complex network of feedback loops [16, 8]. Examples of NESA structures in biological systems are microtubules [17], molecular motors [15], membranes and cells [8], to mention just a few. Moreover, self-assembled structures are used to design new materials, such as nanoparticles, polymeric materials and monolayers [18, 19, 20, 21, 22, 23]. Gelation and crystallization are typical processes involving NESA structures in non-living systems [9]. The self-assembly of these structures must be driven either by light [20, 21, 22], chemical fuel [24, 25, 16] or magnetic fields [3, 26] since building blocks must be activated (their energy must be increased) in order to trigger the assembly process [6, 8]. Formation of intermediate NESA structures are key to the characterization of the micro-architecture of the final structure [9, 27, 28, 2, 7].

How energy dissipation may explain the emergence of ordered structures from a set of disordered components [2] remains an unanswered question. In the lack of a general framework for the description of NESA structures, computational approaches have been proposed. These approaches, however, are not easy to implement since the number of particles needed to explain the mesoscale behavior must be extraordinarily large [26, 29]. A practical performance may be carried out by means of numerical schemes based on continuum, coarse-grained particle [29] and implicit solvent models [30, 23] such as phase-field approaches [31], coarse-grained molecular dynamics[32], Brownian dynamics methods [33] and scaling theory with kinetic Monte Carlo [23]. These methods allows for the simulation of larger systems for longer times but they do not in general directly quantify the dissipation or the entropy production and cannot describe the internal micro-architecture of the structures. In the case of a magneto-hydrodynamic system exhibiting NESA structures, however, the viscous dissipation function and the entropy production follow from the solution of the Navier-Stokes equations for the fluid motion [3].

It is known that the assembly rates are of high importance to determine NESA structures [6]. The formulation of kinetic models could contribute to the knowledge of the pathways leading to the formation of the structures [7, 34]. Despite the fact that one has a broad knowledge on functionality, synthesis, and characterization of many NESA structures, the formation kinetics of these structures and how it is subjected to the laws of thermodynamics is still an open question [35, 2].

In this chapter, we present a mechanism and theory to explain the formation of NESA structures, exemplified in a gelation process for which experimental data have been reported [16]. The theory, based on mesoscopic non-equilibrium thermodynamics [36, 37], provides values for the dissipation inherent to irreversible processes taking place at the mesoscale and formulates kinetic equations of the Fokker-Planck type for the probability of finding particular NESA structure architectures, such as agglomerated fibers forming a gel, branched structures and polyhedral forms to mention some examples. Specifically, we want to find the probability distribution of the spatial orientation of the fibers composing the gel (the case in this present study) as a function of time which defines the internal micro-architecture of the gel. To this purpose, we propose three fundamental NESA processes which are described by means of a mesoscale entropy production [36] resulting from the dissipation inherent to the emergence of ordered structures.

2.2. NESA structures: Mechanism

NESA processes are dynamic processes that entail dissipation [2]. To trigger the formation of complex structures, the intervention of an activator able to activate the building blocks (BB) is necessary [8, 6]. These BB own multiple characteristics which give rise to different structures with different complexity. These structures may be classified as a function of the processes and forces acting in the formation of them, in which fundamental processes are proposed to understand deeply the whole NESA phenomena as a function of the intermediates structures. Through this section we illustrate the energetics and fundamental processes of NESA structures in the context of the gelation process.

2.2.1. Building blocks characteristics

The BB have specific active zones where covalent or non-covalent interactions may take place. The location of the active zones determines the final shape of the structures, i.e. fibers, branched fibers, cubes, spheres, etc. For instance, in the formation of linear fibers (polymers based on chromophoric azobenzene [38] or dibenzoyl-(l)-cystine, *DBC* [16]), the BB have two spatially opposed assembly centers. In the formation of micro-tubules (polymers based on tubuline) [17] and non-linear fibers [21], the BB blocks have two assembly centers not spatially opposed. Light-induced self-assembly structures from BB of nano-particles coated with photo-switchable molecules [22] have more than two assembly centers. Monomers having two or more functional groups, triggers in BB owing more than two assembly centers, giving rise to the formation of branched polymers and to a competition between ordered self-assembly and non-linear random polymerization[39].

2.2.2. Hierarchy of the structures

The transition from the BB to the complex final structures [40, 8] takes place progressively, proceeding through NESA intermediates structures which may be first, second and higher-order structures, as is exemplified in Figure **2-1**. The appearance of these structures depends on their precursors [8], on the internal strength of the interactions [41] and on how the assembly process proceeds (sequentially or non-sequentially) [28]. First-order structures are composed of fundamental activated BB which are expected to interact strongly by means of covalent interactions (in the case of matter dissipation), high magnetic forces or hydrogen bonds [38] (in the case of only energy dissipation), triggering an ordered assembly called sequential assembly (non-vectorial [28]). Second-order structures result from previously activated first-order structures which

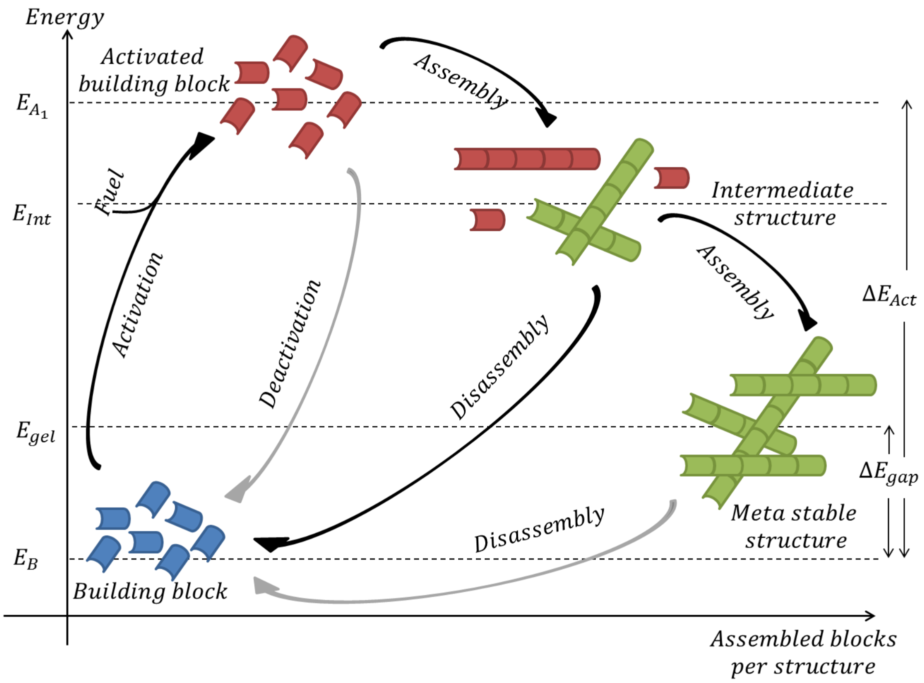

Fig. 2-1.: NESA process energetics for gelation: Unactivated building blocks (in blue) having an energy E_B become activated (in red) with an energy E_{A_1}. Self-assembly of activated blocks yields first-order structures (in red). Assembly of first-order structures gives rise second-order structures (in green), both intermediates having energy E_{int}. The aggregation process precedes the most stable structure emergence, the gel, with an energy E_{gel}.The energy profile is completed with dis-assembly steps and BB deactivation.

interact more weekly than the fundamental activated BB thus triggering their non-sequential assembly (vectorial [28]). Higher order structures may assemble from lower order structures due to van der Waals forces and other weak forces [42].

2.2.3. Fundamental NESA processes

The previously mentioned structural elements are involved in three basic processes: activation, self-assembly (SA) and disassembly (DA). These processes for each kind of structure are represented in Figure **2-2**. Activation of the BB plays a main role because it provides the energy required to trigger the assembly process (see Figure **2-1**). It may also be a sequential process. The first, second and higher-order structures become activated when concentration, temperature or size surpass certain thresholds and by means of phase-changes and processes promoting secondary interactions among the structures. While SA may be reversible, DA is irreversible [16] because the disactivated BB must be activated again to proceed with the formation of NESA structures [2].

2.2.4. Mechanism for gelation

Figure **2-2** shows a scheme for the NESA mechanism for the assembly of a gel structure. The scheme shows the mechanism composed of several steps exemplified by the proposed gelation process: BB activation,

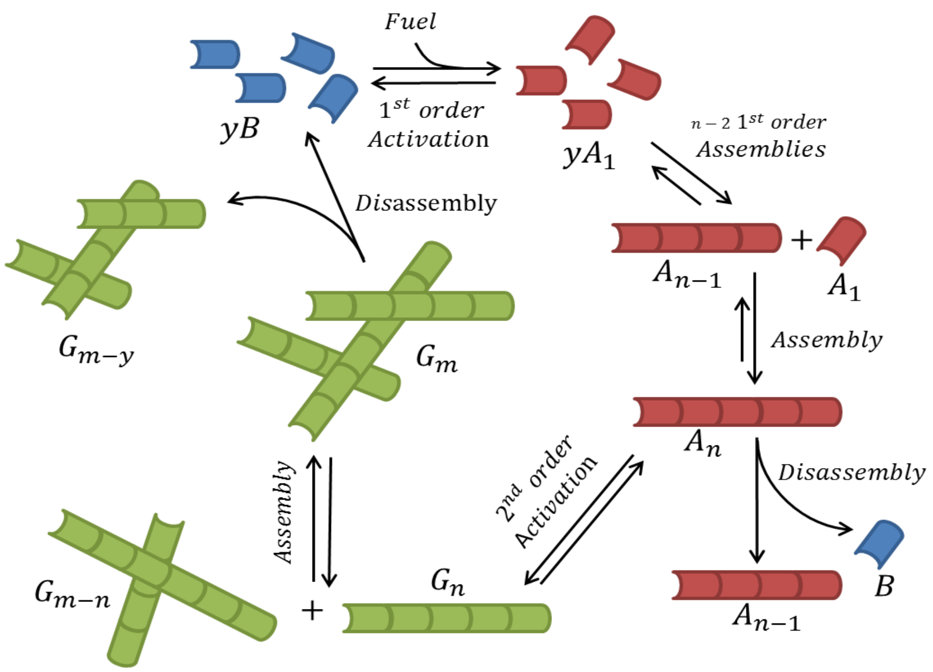

Fig. 2-2.: Sketch of the NESA process. The first-order structure is built from activated building blocks (red blocks), which are obtained from fundamental building blocks (blue blocks) by means of the first-order activation. The A_n structure (red cylinder) emerges from the self-assembly: $\mathrm{CH}_4 A_{n-1} + A <=> A_n$, with $n = 2, ..., N$, N being the maximum size of the structures. The second-order structure (green cylinders), denoted by G_n, is formed by a second-order activation process: $\mathrm{CH}_4 A_n <=> G_n$. The agglomeration (or non-ordered self-assembly of second-order structures) is quite similar to the Smoluchowski coagulation process scheme: $\mathrm{CH}_4 G_{m-n} + G_n <=> G_m$, with $n = 2, ..., \lfloor m/2 \rfloor$ because $n > \lfloor m/2 \rfloor$ takes into account again all possible combinations to form the n-th second-order structure. First-order structure disassembly: $\mathrm{CH}_4 A_n - > A_{n-1} + B + 2H^+ + 2W$ may also occur, where W is a residue and H^+ the hydrogen-ion. As long as first-order structure disassembly is sequential, proceeding one-by-one, second-order structure disassembly: $\mathrm{CH}_4 G_n - > G_{n-y} + yB + 2yH^+ + 2yW$ is not sequential, as it admits the production of y disactivated fundamental blocks, with $y = 1, ..., n-1$. Dissassembly is an irreversible process since the BB need to be activated again before new self-assembling takes places.

sequential assembly and disassembly of first-order structures, first-order structure activation (second-order structure emergence) and second-order structure assembly-disassembly. Intermediate structures may appear regardless of the type of self-assembly process, as shown in Figure **2-1**. Notice that we propose two activation of different nature: BB activation by covalent interactions and first-order structure activation by van der Waals forces once first-order structures reach certain length, concentration, area, etc.

2.2.5. Gelation experiment

As an application of the proposed mechanism, we analyze the formation of a fibrous network (gel) that uses a chemical fuel as an activator, to compare our results with the experiments presented by *Boekhoven et.al* [16]. In the experiments, the fundamental BB is N,N-dibenzoyl-(L)-cystine (DBC), the activator is Methyl Iodide (MeI), the activated block is $DBC - Me_2$, the intermediate activated building block is $DBC - Me$, the first-order structures are the linear fibers formed from DBC by sequential reaction and the second-order structure is the gel formed by agglomeration of linear fibers. Disassembly takes place because of hydrolysis which produces H^+; so in order to control the pH level, OH^- is added [16].

In the experiments, there is no continuous feeding, i.e. the system is closed and the activator is added at two different times which gives rise to the existence of two stages in the whole process. The first takes place at the beginning of the process at $t = 0h$ when there is an initial amount of activator up to $t = 400h$ when the activator is totally consumed. The second stage takes place at $t = 400h$ when the activator is added again until it is consumed completely at $t = 900h$.

The semi-continuous feeding of activator promotes the assembly of intermediate dissipative structures [16, 8, 40, 6] but not the assembly of steady-state dissipative structures. The experiments show the presence of two maxima in the concentration of agglomerated fibers. These maxima are found when the assembly and disassembly rates are equal and when the assembled BB reach the lowest possible energy in the process. Therefore, the maxima in agglomeration correspond to metastable structures (see Figure **2-1**).

In the experiments, energy dissipation is inherent to the BB activation by means of a chemical activator (chemical fuel) which triggers assembly and disassembly process dissipating more energy. The process takes place under isothermal conditions and pH is regulated through the addition of OH^-. In Figure **2-1**, it is shown the energy changes accompanying each step in the process appears as a function of the number of assembled blocks. As shown, a NESA process brings about a decrease in energy from the activated BB to the complex structure. Depending on the experimental conditions, each structural element involved in the process may disassemble thus yielding unactivated blocks.

2.3. NESA structures: Model

In this section, we model the kinetics of NESA processes by means of diffusion through a potential barrier along a reaction coordinate which can be identified from the knowledge of the internal architecture of the structures. The model is based on mesoscopic non-equilibrium thermodynamics [36, 37] and is then compatible with the thermodynamic laws. Computation of the entropy production in the space of the reaction coordinates leads to the expression of the currents (fluxes or rates) which used in the probability conservation law yield the kinetic equations for the first and second-order structures. These equations, of the Fokker-Planck (FP) type, are coupled through boundary conditions, thus describing the NESA structures dynamics. We apply our model to study the kinetics of a gelation process and to explain experimental results obtained in a bidimensional case in which hydrodynamic effects can be neglected [16].

Figure **2-3** presents the reaction coordinates and rates intervening in each step of the gelation process, from pre-activated states (BB) to first- and second-order order structures.

2.3.1. First-order structures

To describe the first-order structures composed of n BB, denoted A_n, we assume that the system is homogeneous and that the BB have two spatially opposed assembly centers (active zones) which give rise to the formation of linear structures oriented at an angle (θ_n) measured with respect to an axis perpendicular to the fiber. The first-order structures composed of n BB can be described in terms of the probability density $p_n(\mathbf{\Gamma}_n,t)/N$, where N is the maximum number of assembled blocks. Here $\mathbf{\Gamma}_n = (\gamma_n, \gamma'_n, \lambda_n, \theta_n)$ represents a

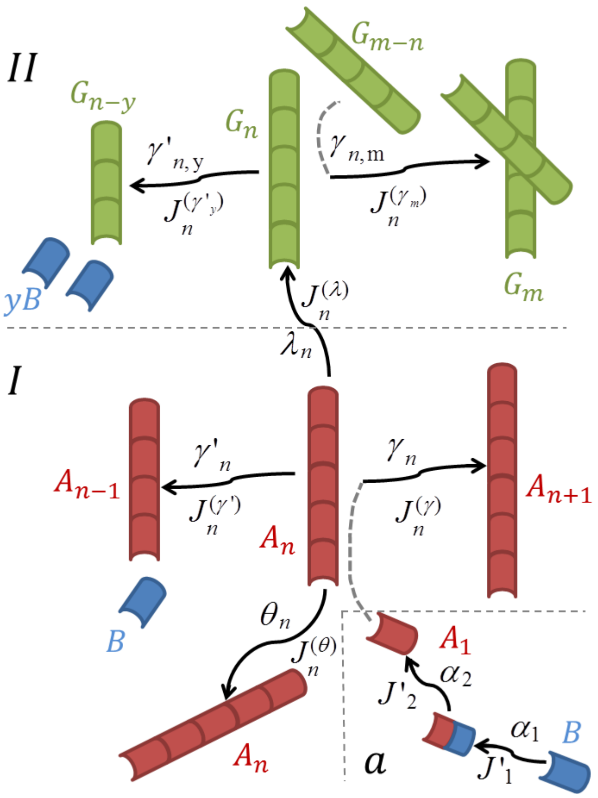

Fig. 2-3.: Reaction coordinates and rates in the proposed model. Zone ***a*** refers to the activation process taking place through the reaction coordinates α_1 and α_2 to produce activated BB (red block A_1) from non-activated BB (blue block). The fluxes through each coordinate are J'_1 and J'_2 respectively. Zone ***I*** shows those quantities for processes involving first-order structure composed of n BB (red cylinder A_n). This structure could assemble to yield A_{n+1} and disassemble giving rise to A_{n-1}. It can also rotate or become activated to generate a second-order structure G_n (green cylinder). These processes take place through the reaction coordinates γ_n, γ'_n, θ_n and λ_n being the corresponding fluxes $J_n^{(\gamma)}$,$J_n^{(\gamma')}$, $J_n^{(\theta)}$ and $J_n^{(\lambda)}$. Zone ***II*** shows the reaction coordinates $\gamma_{n,m}$, $\gamma'_{n,y}$ and λ_n and the corresponding fluxes $J_n^{(\gamma_m)}$,$J_n^{(\gamma'_y)}$ and $J_n^{(\lambda)}$ involved in the formation of second-order structures composed of n BB. These structures can also assemble, disassemble or become deactivated yielding a first-order structure composed of n BB.

phase space point which includes the assembly (γ_n) and disassembly (γ'_n) reaction coordinates, the second-order activation coordinate (λ_n) and the rotation angle of the linear structure (θ_n). Since first-order structures are assembled and disassembled sequentially, block after block, γ_n and γ'_n are scalars. First-order structure activation is carried out in one step, therefore λ_n is a scalar as well.

The evolution over time of the probability density of the structure A_n is described by the probability conservation law:

$$\frac{\partial p_n(\mathbf{\Gamma}_n,t)}{\partial t} = -\nabla_{\mathbf{\Gamma}_n} \cdot \boldsymbol{J}_n(\mathbf{\Gamma}_n,t) \tag{2-1}$$

where $\boldsymbol{J}_n(\mathbf{\Gamma}_n,t) \equiv [J_n^{(\gamma)},J_n^{(\gamma')},J_n^{(\lambda)},J_n^{(\theta)}]$ is a current in $\mathbf{\Gamma}_n$-space. In Figure **2-3**, we see how the structure A_n may transform into A_{n+1}, A_{n-1} or may become activated yielding G_n, driven by the currents $J_n^{(\gamma)}$,$J_n^{(\gamma')}$

and $J_n^{(\lambda)}$, respectively. The evolution of the system can then be assimilated to a diffusion process in $\mathbf{\Gamma}_n$-space. Since a single A_n structure cannot simultaneously follow two trajectories in phase space [43], the i^{th} component of the current $J_n^{(i)}$, only depends on its conjugated variable: $J_n^{(i)} = J_n^{(i)}(\Gamma_n^{(i)}, t)$.

The local equilibrium existence in the $\mathbf{\Gamma}_n$-space enables us to use the Gibbs relation [36]:

$$\delta S_n = -\frac{1}{T}\int_{\mathbf{\Gamma}_n} \mu_n \delta p_n d\mathbf{\Gamma}_n, \tag{2-2}$$

Taking the derivative with respect to time in Eq.(2-2), using the continuity equation (Eq.(2-1)) and integrating by parts we obtain the entropy production rate corresponding to the formation of first-order structures [36, 37].

$$\sigma_n = -\frac{1}{T}\sum_{i=1}^{4}\int_{\Gamma_n^{(i)}} J_n^{(i)}\frac{\partial \mu_n^{(i)}}{\partial \Gamma_n^{(i)}} d\Gamma_n^{(i)}, \tag{2-3}$$

It consists of contributions of the diffusion currents $J_n^{(i)}$ and the chemical potential $\mu_n^i(\Gamma_n^{(i)}, t)$ involved in the i^{th} process. Coupling linearly the currents $\boldsymbol{J}_n^{(i)}$ with its conjugated thermodynamic force $\frac{\partial \mu_n^{(i)}}{\partial \Gamma_n^{(i)}}$ leads to the linear laws

$$J_n^{(i)} = -\frac{L_n^{(ii)}}{T}\frac{\partial \mu_n^{(i)}}{\partial \Gamma_n^{(i)}}, \tag{2-4}$$

where, $L_n^{(ii)}$ are Onsager coefficients. Using the fact that these coefficients are proportional to $p_n^{(i)} \equiv p_n(\Gamma_n^{(i)}, t)$ [44], we have $L_n^{(ii)} = \frac{D_i}{R} p_n^{(i)}$, where D_i is a diffusivity along the i^{th} coordinate and R is the constant of gases. For $i = 1$, Eq.(2-4) gives the sequential self-assembly flux, for $i = 2$ the disassembly flux, for $i = 3$ the second-order activation flux and for $i = 4$ the rotational flux of the structures, as shown in Figure **2-3**.

The chemical potential for the NESA process defined in the $\mathbf{\Gamma}_n$-space is given by

$$\mu_n^{(i)}(\Gamma_n^{(i)}, t) = RT\ln(\psi_n^{(i)} p_n^{(i)}) + \phi_n^{(i)}(\Gamma_n^{(i)}). \tag{2-5}$$

Here the probability density $p_n^{(i)}$ depends only on $\Gamma_n^{(i)}$. $\phi_n^{(i)}(\Gamma_n^{(i)})$ is the potential barrier and $\psi_n^{(i)}$ an activity coefficient. The diffusivity through the θ_n coordinate and the rotational flux are computed from the internal energy of rotation taken from [45]. The diffusion and the energy of rotation are functions of the length of the linear structure n (see Annex D).

Introducing the chemical potential (Eq.(2-5)) in the current given by Eq.(2-4), and using the continuity equation (Eq.(2-1)), we obtain the Fokker-Planck equation for first-order structures,

$$\frac{\partial p_n(\mathbf{\Gamma}_n, t)}{\partial t} = \sum_{i=1}^{4} D_i \frac{\partial}{\partial \Gamma_n^{(i)}}\left[\frac{\partial p_n^{(i)}}{\partial \Gamma_n^{(i)}} + p_n^{(i)}\frac{\partial \ln \psi_n^{(i)}}{\partial \Gamma_n^{(i)}} + \frac{p_n^{(i)}}{k_B T}\frac{\partial \phi_n^{(i)}}{\partial \Gamma_n^{(i)}}\right] \tag{2-6}$$

where $n = 1, \ldots, N-1$. For $\gamma_{N-1} = 1$, the structure is composed of N BB, the maximum number of BB that can be assembled.

2.3.2. Second-order structures

Second-order structures composed of n building blocks are described in terms of the probability density $q_n(\boldsymbol{\gamma}_n, \boldsymbol{\gamma}'_n, t)/N$, whose evolution is governed by a kinetic equation similar to Eq.(2-6). Due to the fact that assembly and disassembly of second-order structures are non-sequential processes in which a second-order structure composed of n BB can be induced to assembly $N-n$ different structures, and can be disassembly in n ways, the corresponding reaction coordinates for assembly and disassembly are vectors: $\boldsymbol{\gamma}_n \in \mathbb{R}^{N-n}$, and $\boldsymbol{\gamma}'_n \in \mathbb{R}^n$. Notice that this kind of structures are not characterized by an orientation because the agglomerate does not have a characteristic axis and therefore the rotation is much more limited than in the case of first-order structures. Further, the activation coordinate is not considered because there are not higher order structures. Proceeding as we did in the case of the first-order structures, but considering the vectorial nature, we obtain the FPE for the second-order structures

$$\frac{\partial q_n(\boldsymbol{\Gamma}'_n, t)}{\partial t} = -\sum_{i=1}^{2} D_{s,i} \frac{\partial}{\partial \Gamma_n'^{(i)}} \cdot \left[\frac{\partial q_n^{(i)}}{\partial \Gamma_n'^{(i)}} + q_n^{(i)} \frac{\partial \ln \psi_n'^{(i)}}{\partial \Gamma_n'^{(i)}} + \frac{q_n^{(i)}}{k_B T} \frac{\partial \phi_n'^{(i)}}{\partial \Gamma_n'^{(i)}} \right] \tag{2-7}$$

Here $\boldsymbol{\Gamma}'_n \equiv [\boldsymbol{\gamma}_n, \boldsymbol{\gamma}'_n]$ and $D_{s,i}$ is the diffusivity along the i^{th} coordinate of the $\boldsymbol{\Gamma}'_n$-space. The flux in the $\boldsymbol{\Gamma}'_n$ space is denoted as $\boldsymbol{J}_n(\boldsymbol{\Gamma}'_n, t) \equiv [\boldsymbol{J}_n^{(\boldsymbol{\gamma})}, \boldsymbol{J}_n^{(\boldsymbol{\gamma}')}]$. We consider that $\phi'_{n,i}$ and $\psi'_{n,i}$ are the potential barrier and the activity coefficient for the second-order structures.

2.3.3. Activated building blocks

Building block activation is carried out in two steps, from DBC to $DBC-Me$ and from $DBC-Me$ to $DBC-ME_2$. The activation process takes place along the α_b coordinate where $b = 1,2$ corresponds to the b^{th} activation, in which for $\alpha_1 = 0$ represents the state for DBC, $\alpha_1 = 1$ the $DBC-Me$ and $\alpha_2 = 1$ the $DBC-Me_2$. Let $p_b'(\alpha_b, t)$ be the probability density to find the b^{th} activated state at α_b and time t. The FP equation for the pre-activated states is given by

$$\frac{\partial p_b'(\alpha_b, t)}{\partial t} = -D_{act} \frac{\partial}{\partial \alpha_b} \left[\frac{\partial p_b'}{\partial \alpha_b} + p_b' \frac{\partial \ln \psi_b}{\partial \alpha_b} + \frac{p_b'}{k_B T} \frac{\partial \phi_b}{\partial \alpha_b} \right] \tag{2-8}$$

Here D_{act} acts as a diffusivity along the activation coordinate which does not depend on b and ψ_b and ϕ_b are the activity coefficient and the potential barrier involved in the activation process. The fluxes are denoted by J_b', with $J_b'(1,t)$ the flux at state b induced by the activator to bring forth the activated state $b+1$.

2.3.4. Boundary conditions

In the proposed model, the boundary conditions (BC) of the FP equations are crucial to explain the formation of the different structures emerging in the gelation process. Inner BC couple first-order structures: A_n to A_{n+1} and outer BC couple first-order structures to second-order ones.

BC for pre-activated states

The outer BC at $\alpha_1 = 0$ considers the deactivated BB produced in disassembly processes:

$$\left.\frac{\partial p_1'}{\partial \alpha_1}\right|_{\alpha_1=0} = \sum_{n=1}^{N} J_n^{(\gamma')}(1,t) + \sum_{n=1}^{N}\sum_{y=1}^{n} y J_n^{(\gamma'_y)}(1,t) \tag{2-9}$$

in which $J_n^{(\gamma'_y)}$ at $\gamma'_y = 1$ represents the flux of disassembled second-order structures composed of $n-y$ BB and the flux of y deactivated BB produced in the disassembly. $J_n^{(\gamma')}(1,t)$ is the flux of first-order structures composed of $n-1$ BB produced by the disassembly of first-order structures composed of n BB.
On the other hand, since activated BB are consumed at each step of first-order self-assembly, the BC for $p_2'(1,t)$ is

$$\left.\frac{\partial p_2'}{\partial \alpha_2}\right|_{\alpha_2=1} = -\sum_{n=1}^{N-1} J_n^{(\gamma)}(0,t) \tag{2-10}$$

Inner BC for the activation step between α_1 and α_2 are

$$-\left.\frac{\partial p_1'}{\partial \alpha_1}\right|_{\alpha_1=1} = \left.\frac{\partial p_2'}{\partial \alpha_2}\right|_{\alpha_2=0} = J_1'(1,t) \tag{2-11}$$

in which the change of the probability density of $DBC-Me$ is equal to minus the change of the probability density of the state $DBC-Me$ that interacts with the activator to produce the activated BB ($DBC-Me_2$).

BC for first-order structures

First-order structures are coupled to the pre-activated states by means of the outer BC in which the BB available for assembling is the starting point to obtain the first-order structures composed of two BB:

$$\left.\frac{\partial p_1}{\partial \Gamma_1^{(\gamma)}}\right|_{\mathbf{\Gamma}_1=\mathbf{0}} = J_2'(1,t) \tag{2-12}$$

The FP equations for first-order structures are coupled through the inner BC in which assembly and disassembly processes have a main role. Considering the different couplings, the BC for the first-order structures at $\mathbf{\Gamma}_n = \mathbf{0}$ are:

$$\begin{aligned}\left.\frac{\partial p_n}{\partial \Gamma_n^{(\gamma)}}\right|_{\mathbf{\Gamma}_n=\mathbf{0}} = \left.\frac{\partial p_n}{\partial \Gamma_n^{(\gamma')}}\right|_{\mathbf{\Gamma}_n=\mathbf{0}} = \left.\frac{\partial p_n}{\partial \Gamma_n^{(\lambda)}}\right|_{\mathbf{\Gamma}_n=\mathbf{0}} = \left.\frac{\partial p_n}{\partial \Gamma_n^{(\theta)}}\right|_{\mathbf{\Gamma}_n=\mathbf{0}} \\ = J_{n-1}^{(\gamma)}(1,t) + J_{n+1}^{(\gamma')}(1,t) + J_n^{(\theta)}(\pi,t)\end{aligned} \tag{2-13}$$

The BC at $\Gamma_n^{(i)} = 1$ are given by :

$$\left.\frac{\partial p_n}{\partial \Gamma_n^{(\gamma)}}\right|_{\Gamma_n^{(\gamma)}=1} = -J_n^{(\gamma)}(1,t) \tag{2-14}$$

$$\left.\frac{\partial p_n}{\partial \Gamma_n^{(\lambda)}}\right|_{\Gamma_n^{(\lambda)}=1} = -J_n^{(\lambda)}(1,t) \tag{2-15}$$

$$\left.\frac{\partial p_n}{\partial \Gamma_n^{(\theta)}}\right|_{\Gamma_n^{(\theta)}=\pi} = -J_n^{(\theta)}(\pi,t) \tag{2-16}$$

The formation kinetics of first and second-order structures are coupled through the λ_n reaction coordinate since it is through this coordinate that the first-order structure yields a second-order structure. The current $J_n^{(\lambda)}$ corresponds to the rate at which first-order structures disappear to form second-order structures and is equal to the rate of formation of second-order structures at $\lambda = 1$. One has

$$\left.\frac{\partial p_n}{\partial \Gamma_n^{(\gamma')}}\right|_{\Gamma_n^{(\gamma')}=1} = -J_n^{(\gamma')}(1,t) \tag{2-17}$$

For first-order structures with $n = N-1$, at $\gamma_n = 1$, the flux $J_n^{(\gamma)}$ vanishes because the assembly of another block to the structure is not possible.

BC for second-order structures

The BC at $\boldsymbol{\Gamma}'_n$ must be specified for each component of the second-order assembly coordinate ($\boldsymbol{\gamma}_n$) and the second-order disassembly coordinate ($\boldsymbol{\gamma}'_n$). They depend mainly on the assembly and disassembly fluxes producing second-order structures composed of n BB and also on the activation flux of first-order structures ($J_n^{(\lambda)}$):

$$\begin{aligned}
&\left.\frac{\partial q_n}{\partial \Gamma_n'^{(\gamma_1)}}\right|_{\boldsymbol{\Gamma}'_n=\mathbf{0}} = \ldots = \left.\frac{\partial q_n}{\partial \Gamma_n'^{(\gamma_m)}}\right|_{\boldsymbol{\Gamma}'_n=\mathbf{0}} = \ldots = \left.\frac{\partial q_n}{\partial \Gamma_n'^{(\gamma_{\lfloor n/2\rfloor})}}\right|_{\boldsymbol{\Gamma}'_n=\mathbf{0}} = \\
&\left.\frac{\partial q_n}{\partial \Gamma_n'^{(\gamma'_N)}}\right|_{\boldsymbol{\Gamma}'_n=\mathbf{0}} = \ldots = \left.\frac{\partial q_n}{\partial \Gamma_n'^{(\gamma'_y)}}\right|_{\boldsymbol{\Gamma}'_n=\mathbf{0}} = \ldots = \left.\frac{\partial q_n}{\partial \Gamma_n'^{(\gamma'_{n+1})}}\right|_{\boldsymbol{\Gamma}'_n=\mathbf{0}} = \\
&J_n^{(\lambda)}(1,t) + \sum_{m=1}^{\lfloor n/2\rfloor} J_m^{(\gamma_n)}(1,t) + \sum_{y=n+1}^{N} J_y^{(\gamma'_n)}(1,t)
\end{aligned} \tag{2-18}$$

The BC at $\Gamma_n'^{(i_j)} = 1$ are given by:

$$\left.\frac{\partial q_n}{\partial \Gamma_n'^{(\gamma_m)}}\right|_{\Gamma_n^{(\gamma_m)}=1} = -J_n^{(\gamma_m)}(1,t) \tag{2-19}$$

$$\left.\frac{\partial q_n}{\partial \Gamma_n^{(\gamma'_y)}}\right|_{\Gamma_n^{(\gamma'_y)}=1} = -J_n^{(\gamma'_y)}(1,t) \tag{2-20}$$

Table **2-1** summarizes the main features of the kinetic model proposed to describe the gelation process.

Tab. 2-1.: Summary of the kinetic model

	b^{th} pre-acticated state	First-order structure (n BB)	Second-order structure (n BB)
Reaction coordinates	α_b	$\boldsymbol{\Gamma}_n \equiv [\gamma_n, \gamma'_n, \lambda_n, \theta_n]$	$\boldsymbol{\Gamma}'_n \equiv [\boldsymbol{\gamma}_n, \boldsymbol{\gamma}'_n]$
Rates	J'_b	$J_n^{(\gamma)}$,$J_n^{(\gamma')}$,$J_n^{(\lambda)}$,$J_n^{(\theta)}$	$\boldsymbol{J}_n^{(\boldsymbol{\gamma})}$, $\boldsymbol{J}_n^{(\boldsymbol{\gamma}')}$
Potentials	$\phi_b(\alpha_b)$	$\phi_n^{(\gamma)}$,$\phi_n^{(\gamma')}$,$\phi_n^{(\lambda)}$,$\phi_n^{(\theta)}$	$\phi_n'^{(\boldsymbol{\gamma})}(\boldsymbol{\gamma})$,$\phi_n'^{(\boldsymbol{\gamma}')}(\boldsymbol{\gamma}')$
Parameters	D_{act}	D_1, D_2, D_3	$D_{s,1}, D_{s,2}$
FP Equation	Eq. 2-8	Eq. 2-6	Eq. 2-7
Main inner B.C.	Eq. 2-11	Eq. 2-13	Eq. 2-18
Main outer B.C.	Eqs. 2-9, 2-10	Eqs. 2-14-2-16	Eqs. 2-19, 2-20

2.4. Methods: mesoscopic thermodynamics and internal variables

Integrating over the γ_n, γ'_n, λ_n coordinates and over $\boldsymbol{\gamma}_n$,$\boldsymbol{\gamma}'_n$, and α_b, i.e. performing a coarse graining of the description that reduces the coordinates to only the orientation, we obtain the probabilities which are proportional to the concentrations of the components when the system is sufficiently dilute. The resulting probabilities are: $p'_b(t)$ corresponding to the BB blocks in their pre-activate states, $p_n(\theta_n,t)$ corresponding to the first-order structures and $q_n(t)$ corresponding to the second-order structure. We then have: $p_n(t) \propto C_n^{(1)}(t)$ (first-order structure concentration), $q_n(t) \propto C_n^{(2)}(t)$ (second-order structure concentration) and $p'_0(t) \propto C_{DBC}$ (DBC concentration), $p'_1(t) \propto C_{DBC-Me}$ ($DBC-Me$ concentration) and $p'_2(t) \propto C_{DBC-Me_2}$ ($DBC-Me_2$ concentration). Considering the initial conditions:

$$p'_0(0) = 1, \tag{2-21}$$

and

$$p'_1(0) = p'_2(0) = p_n(\theta_n,0) = q_n(0) = 0, \quad \forall\theta_n, \quad \forall n > 1, \tag{2-22}$$

the initial concentration of DBC ($C_{DBC}(0) = 100mM$) is the constant of proportionality between the probabilities and the concentrations of each structure. For instance for first-order structures, the concentration is: $C_n^{(1)}(t) = C_{DBC}(0)\int_{\theta_n} p_n(\theta_n,t)d\theta_n$. For the activated states, the measurable concentrations are: $C_{DBC}(t) = C_{DBC}(0)p'_0(t)$, $C_{DBC-Me}(t) = C_{DBC}(0)p'_1(t)$ and $C_{DBC-Me_2}(t) = C_{DBC}(0)p'_2(0)$.

To solve the kinetic equations (2-6)-(2-8), we need to know the diffusivities along the reaction coordinates involved in the activation, assembly, and disassembly processes. These values are related to the kinetic constants of the reactions [44]. The estimation of these quantities is performed by minimizing the error between the results of the model and the experimental data restricted to physical limits of the diffusivities for each process. The estimated values are shown in the Annex D. The numerically estimated diffusivity for self-assembly is higher than for disassembly which means that the self-assembly reaction rate is higher than that for the disassembly enabling the existence of NESA structures. We have found that the diffusivity for first order processes is larger than that for second order processes. This result can be explained from the fact that first- order structures are simpler and their formation needs of less energy, moreover they are more unstable. The rotational diffusivity for first-order structures D_4 has been computed from Eq.(9.17) of [45] in which D_4 is multiplied by a factor that depends on the surrounding structures (see the Annex D). These parameters are estimated under the experimental conditions considered in [16]. With respect to the parameters D_{act}, D_1 and $D_{s,1}$, we expect that they depend on temperature [16], similarly to D_4. Moreover, we presume that D_2 and $D_{s,2}$ increase if the pH decreases because hydrolysis is favored at lower pH values [16]. To prove these behaviors, further experiments and modeling should be carried out at different values of pH and temperature.

Details on how to model the potential barriers, including the standard chemical potentials included in the barriers, are given in the Annex D. Furthermore, we can compute the OH^- added from the fluxes (Eq.(2-4), following the mechanism described in Figure **2-2**. Finally, considering that the maximum number of BB that can integrate a structure is $N = 56$, we obtain the numerical solution of the kinetic equations by using a finite-volume method programmed in MATLAB ®. The solution of the kinetic equations for larger values of N does not entail a significantly better comparison with the experimental results and is computationally more costly.

2.5. Results and discussion

In Figure **2-4**, we compare the results of our model with the experimental gelation data [16] in which an activator is added to the system at $t = 0$ and at $t = 400$ hours. It is observed the presence of two stages, from $t = 0$ to $t = 400$ hours and from $t = 400$ to $t = 900$ hours.

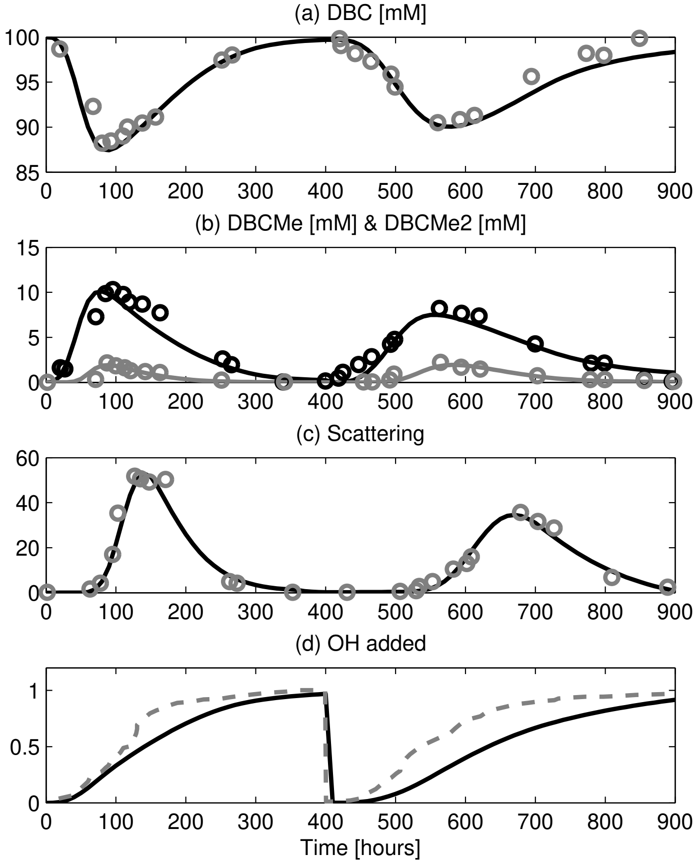

Fig. 2-4.: Concentration and Dynamic Light Scattering (DLS) results vs. time $[h]$. Experimental data taken from [16] are represented by hollow circles and dashed lines, whereas solid lines correspond to the results of our model. (a) DBC concentration $[mM]$. (b) $DBC-Me$ and $DBC-Me_2$ concentration $[mM]$. (c) Quantitative measurement of aggregation by DLS in counts per second. (d) OH^- added $[mmol]$.

In the first stage, Figure **2-4**(a) shows how the number of deactivated BB (DBC) decreases up to reaching a concentration around $87mM$ at $t = 95h$ and subsequently increases until its initial concentration of $100mM$ at $t = 399h$. Figure **2-4**(b) shows how the first activated state of the BB ($DBCMe$) has a maximum in concentration (10,2mM) at $t = 95h$ coinciding with the time at which the minimum of DBC is found. The experimental data for $DBCMe$ show a minimum concentration at $t = 100h$. This is because in our numerical results, the activated BB ($DBC-Me_2$) emerges smoothly contrary to what happens in the experiments where $DBC-Me_2$ emerges sharply at $t = 95h$.

Figure **2-4**(c) shows the numerical results reproducing the Dynamic Light Scattering (DLS) measurements (taken from [16]) which considers the dynamics of all the intermediate structures in the system and their size (more information about the DLS can be found in the Annex D). Numerical results present two maxima (almost imperceptible) at $t = 140h$ and $t = 145h$, contrary to experimental results where the maxima take place at $t = 127h$ and $t = 170h$. The presence of two maxima instead of only one is due to the fact that disassembly rates are quite different for big and small structures since the latter have less stable assembled blocks with a higher chemical potential. As a consequence, at certain times there is a pronounced disassembly of the smaller structures but not of the bigger ones. This fact is detected in the DLS experiments by the presence of the local minimum between the two maxima. The presence of the maxima means that bigger structures appear considerably later in relationship to a maximum concentration of activated BB since several intermediates small-size structures emerge sequentially, as we assumed. The small difference between the maxima in the numerical results is possible because a value for the maximum length of the fibers lower than the one of the experiments was used which considerably reduces the amount of possible intermediate structures thus leading to a small difference in the disassembly rates. Figure **2-4**(c) shows how our numerical results reproduce the behavior of the gelation mechanism.

Notice that first and second stages exhibit different dynamics due to the accumulation of the secondary product ($MeOH$) which affects the equilibrium and kinetics of the activation process. The maxima and minima values for the concentration predicted by our model take place $10h$ earlier than the ones observed experimentally, as shown in Figure **2-4**(a) and Figure **2-4**(b). This small shift only represents an error of 1 % in the prediction and could probably be due to the inaccuracy of the value of the activity coefficient of $MeOH$ at relatively high concentrations.

In Figure **2-4**(c), we show how the numerical results agree with the tendency related to the emergence of bigger self-assembled structures measured in the DLS. This confirms that the proposed model efficiently considers those intermediate self-assembled structures which come up in the real system in a sequential and non-sequential way. The figure shows a good agreement of our results with the experiments, with an error of less than 3 % in Figure **2-4**(a) and of about 8 % in Figure **2-4**(c). The errors become smaller when increasing N in the numerical solutions because in this case we take more intermediate structures into consideration.

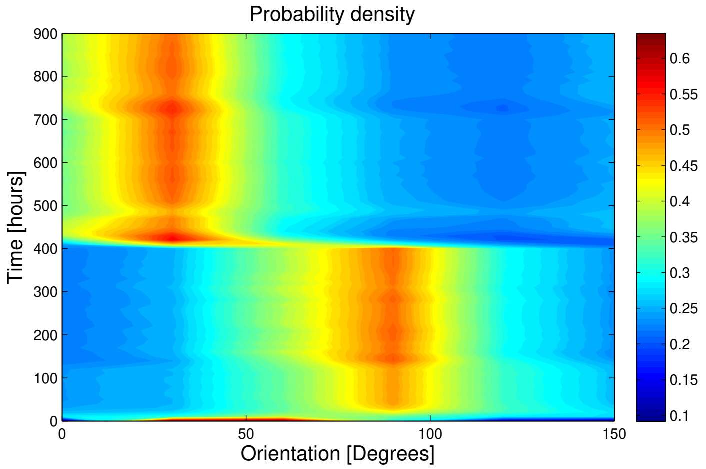

Fig. 2-5.: Colormap for the time evolution of the probability distribution of the spatial orientation of first-order self-assembled structures. At $t = 400h$ the gelation process is re-initiated.

The evolution over time of the probability distribution of the spatial orientation of the most probable linear fibers is shown in the colormap of Figure **2-5**. After adding the activator at 400 hours, gelation is re-initiated with a dramatic change in the most probable orientation of linear fibers, from 90 to 30 degrees. This change is caused by the complete hydrolysis (disassembly) of the gel.

Deactivation of the BB drives the system to its equilibrium state which occurs at $t \approx 400h$. Further addition of activator makes the assembly process begin again from a random configuration yielding a different more likely orientation of the fibers.

Figure **2-5** allows us to understand the meso-architecture of the NESA structure. Thus, for instance, by knowing the probability distribution of each kind of structure, it is possible to relate it to porosity, an important structural property of gels. This result constitutes the starting point to study microscopic configurations of NESA structures.

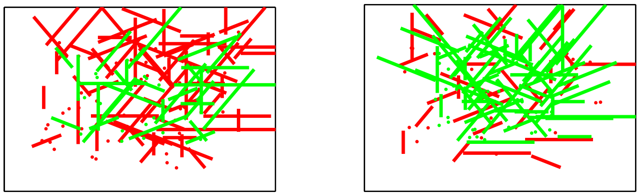
(a) 100 hours (b) 200 hours

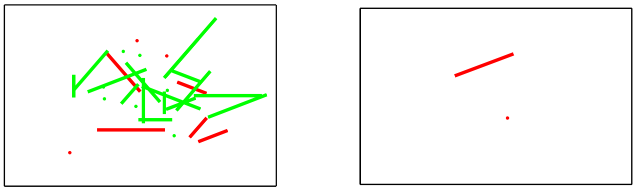
(c) 300 hours (d) 500 hours

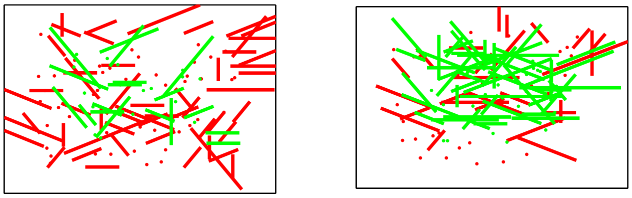
(e) 600 hours (f) 700 hours

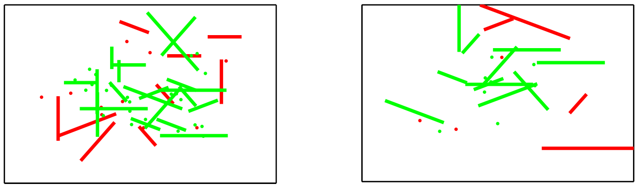
(g) 800 hours (h) 900 hours

Fig. 2-6.: Snapshots of the gelation process taken every 100 hours. Green bars represent the aggregated fibers whereas the red bars indicate the non-aggregated fibers.

In Figure **2-6**, we show snapshots of the gelation process obtained at different times. We observe that at times between 100 and 200 hours, and around 700 hours, the size and number of the structures composing the gel reaches a maximum value which corresponds to the maxima of the DLS measurements shown in Figure

2-4(c). Green bars represent the agglomerated fibers (second-order structures) and red bars correspond the first-order structures (non-aggregated fibers). Red points represent some activated BB and small first-order structures. For more information about the snapshots, see the Annex D.

2.6. Conclusions: The dynamic evolution of mesoscopic NESA structures

The results obtained indicate not only that the proposed model reproduces the main features of gelation experiments with great accuracy (see Figure **2-4**) but also contributes to new insights in the dynamic evolution of NESA structures. The model we have proposed enables us to rationalize how a transient organization in the system involving intermediate aggregation states precedes the appearance of a more complex structure: the gel (see Figure **2-6**). Further, the model allows for the description of the evolution of the internal architecture of the structures at the meso-scale (see Figure **2-5**).

Currently, there is a great deal of interest in the control of hydrogel structures (their micro-architecture and porosity) for medical applications [46, 47, 48, 49, 50, 51] as well as in the synthesis of self-assembled particles for technological purposes [23, 52, 53]. The approach presented in this chapter -mechanism, formalism and mathematical model- can be used to contribute to a better understanding of these processes (control of hydrogels and synthesis of advanced materials) because they start from basic components (BB) and share a common origin: activation, self-assembly, and disassembly.

Finally, our formalism enables us to understand deeply the kinetics of the self-assembly processes by means of a robust mathematical model which can be solved by using a simple numerical scheme. Our model could be extended to take into account the effect of external fields and gradients.

Bibliography

[1] Andrés Arango-Restrepo, J Miguel Rubi, and Daniel Barragán. Understanding gelation as a nonequilibrium self-assembly process. *J. Phys. Chem. B*, 122(18):4937–4945, 2018.

[2] Marcin Fialkowski, Kyle J M Bishop, Rafal Klajn, Stoyan K Smoukov, Christopher J Campbell, and Bartosz A Grzybowski. Principles and Implementations of Dissipative (Dynamic) Self-Assembly. *J.Phys. Chem. B*, 110:2482–2496, 2006.

[3] Konstantin V Tretiakov, Igal Szleifer, and Bartosz A Grzybowski. The Rate of Energy Dissipation Determines Probabilities of Non- equilibrium Assemblies. *Angew. Chem. int. Ed*, 52:10304–10308, 2013.

[4] Ilya Prigogine and G Nicolis. *Self organization in non equilibrium systems*. John wiley & sons, 1 edition, 1977.

[5] Mazen Al-Ghoul and Byung Chan Eu. Hyperbolic reaction-diffusion equations and irreversible thermodynamics: II. Two-dimensional patterns and dissipation of energy and matter. *Physica D: Nonlinear Phenomena*, 97:531–562, 1996.

[6] Susan A. P. van Rossum, Marta Tena-Solsona, Jan H. van Esch, Rienk Eelkema, and Job Boekhoven. Dissipative out-of-equilibrium assembly of man-made supramolecular materials. *Chem. Soc. Rev.*, 46:5519–5535, 2017.

[7] Alessandro Sorrenti, Jorge Leira-Iglesias, Albert J Markvoort, Tom FA de Greef, and Thomas M Hermans. Non-equilibrium supramolecular polymerization. *Chem. Soc. Rev.*, 2017.

[8] Job Boekhoven. *Multicomponent and Dissipative Self-Assembly Approaches: toward functional materials*. PhD thesis, Delft University of Technology, 2012.

[9] D Krishna Kumar and Jonathan W Steed. Supramolecular gel phase crystallization: orthogonal self-assembly under non-equilibrium conditions. *Chem. Soc. Rev.*, 43(7):2080–2088, 2014.

[10] Andrés Arango-Restrepo, Daniel Barragán, and J Miguel Rubi. Nonequilibrium self-assembly induced liesegang rings in a non-isothermal system. *PCCP*, 20(7):4699–4707, 2018.

[11] Job Boekhoven, Wouter E Hendriksen, Ger JM Koper, Rienk Eelkema, and Jan H van Esch. Transient assembly of active materials fueled by a chemical reaction. *Science*, 349(6252):1075–1079, 2015.

[12] Leroy Cronin, Anne De Wit, Ivria J Dolobo, Bruno Escribano, Raymond E Goldstein, Florence Haudin, David E H Jones, Alan L Mackay, Jerzy Maselko, Jason J Pagano, J Pantaleone, Michael J Russell, C Ignacio Sainz-d, Oliver Steinbock, David A Stone, Yoshifumi Tanimoto, and Noreen L Thomas. From chemical gardens to chemobrionics From Chemical Gardens to Chemobrionics. *Chem. Rev*, 115:8652–8703, 2015.

[13] FJ Ndlec, Thomas Surrey, Anthony C Maggs, and Stanislas Leibler. Self-organization of microtubules and motors. *Nature*, 389(6648):305–308, 1997.

[14] Cyril Papaseit, Nathalie Pochon, and James Tabony. Microtubule self-organization is gravity-dependent. *PNAS*, 97(15):4–8, 2000.

[15] Thomas Surrey, Francois Nédélec, Stanislas Leibler, and Eric Karsenti. Physical Properties Determining Self-Organization of Motors and Microtubules. *Science*, 292:1167–1171, 2001.

[16] Job Boekhoven, Aurelie M. Brizard, Krishna N. K. Kowlgi, Ger J. M. Koper, Rienk Eelkema, and Jan H. van Esch. Dissipative Self-Assembly of a Molecular Gelator by Using a Chemical Fuel. *Angew. Chem.*, 122(28):4935–4938, 2010.

[17] Arshad Desai and Timothy J Mitchison. Microtubule Polymeriztion Dynamics. *Annu. Rev. Cell Dev. Biol.*, 13:83–117, 1997.

[18] Andrew R Hirst, Sangita Roy, Meenakshi Arora, Apurba K Das, Nigel Hodson, Paul Murray, Stephen Marshall, Nadeem Javid, Jan Sefcik, Job Boekhoven, Jan H Van Esch, Stefano Santabarbara, Neil T Hunt, and Rein V Ulijn. Biocatalytic Induction of Supramolecular Order. *Nat. Chem*, 2(12):1089–1094, 2010.

[19] Job Boekhoven, Jos M Poolman, Chandan Maity, Feng Li, Lars Van Der Mee, Christophe B Minkenberg, Eduardo Mendes, Jan H Van Esch, and Rienk Eelkema. Catalytic Control Over Supramolecular Gel Formation. *Nat. Chem*, 5(5):433–437, 2013.

[20] Linda N Lucas, Jan van Esch, Richard M Kellogg, and Ben L Feringa. Photocontrolled self-assembly of molecular switches. *Chem. Commun.*, (8):759–760, 2001.

[21] Jaap J.D De Jong. Light-Driven Dynamic Pattern Formation. *Angew. Chem. int. Ed*, 44:2373–2376, 2005.

[22] Rafal Klajn, Kyle J M Bishop, and Bartosz A Grzybowski. Light-controlled self-assembly of reversible and irreversible nanoparticle suprastructures. *PNAS*, 104(25):10305–10309, 2007.

[23] Prateek K. Jha, Vladimir Kuzovkov, Bartosz A. Grzybowski, and Monica Olvera de la Cruz. Dynamic self-assembly of photo-switchable nanoparticles. *Soft Matter*, 8(1):227–234, 2012.

[24] Jorge Leira-Iglesias, Alessandro Sorrenti, Akihiro Sato, Peter A Dunne, and Thomas M Hermans. Supramolecular pathway selection of perylenediimides mediated by chemical fuels. *Chem. Commun.*, 52(58):9009–9012, 2016.

[25] AK Dambenieks, PHQ Vu, and TM Fyles. Dissipative assembly of a membrane transport system. *Chem. Sci.*, 5(9):3396–3403, 2014.

[26] Bartosz A Grzybowski, Howard A Stone, and George M Whitesides. Dynamic self-assembly of magnetized, millimetre-sized objects rotating at a liquid–air interface. *Nature*, 405(6790):1033, 2000.

[27] C. Suryanarayana. *Non-Equilibrium Processing of Materials*. Elsevier, 1 edition, 1999.

[28] Stephen Mann. Self-assembly and transformation of hybrid nano-objects and nanostructures under equilibrium and non-equilibrium conditions. *Nat. Mater.*, 8(10):781–792, 2009.

[29] Martin McCullagh, Tatiana Prytkova, Stefano Tonzani, Nicolas D. Winter, and George C. Schatz. Modeling self-assembly processes driven by nonbonded interactions in soft material. *J. Phys. Chem. B*, 112(34):10388–10398, 2008.

[30] Martin Kröger. Simple models for complex nonequilibrium fluids. *Phys. Rep.*, 390(6):453–551, 2004.

[31] Katsuyo Thornton, John Ågren, and PW Voorhees. Modelling the evolution of phase boundaries in solids at the meso-and nano-scales. *Acta Mater.*, 51(19):5675–5710, 2003.

[32] C Reichhardt and CJ Olson Reichhardt. Dynamical ordering and directional locking for particles moving over quasicrystalline substrates. *Phys. Rev. Lett.*, 106(6):060603, 2011.

[33] Scott H Northrup, Stuart A Allison, and J Andrew McCammon. Brownian dynamics simulation of diffusion-influenced bimolecular reactions. *J. Chem. Phys*, 80(4):1517–1524, 1984.

[34] Bartosz A Grzybowski, Krzysztof Fitzner, Jan Paczesny, and Steve Granick. From dynamic self-assembly to networked chemical systems. *Chem. Soc. Rev.*, 46(18):5647–5678, 2017.

[35] Rashmi C Desai and Raymond Kapral. *Dynamics of Self-organized and Self-assembled Structures*. Cambridge University Press, 1 edition, 2009.

[36] D Reguera, JM Rubi, and JMG Vilar. The mesoscopic dynamics of thermodynamic systems. *J. Phys. Chem. B*, 109(46):21502–21515, 2005.

[37] José MG Vilar and J M Rubi. Thermodynamics “beyond” local equilibrium. *PNAS*, 98(20):11081–11084, 2001.

[38] Goutam Palui and Arindam Banerjee. Fluorescent gel from a self-assembling new chromophoric moiety containing azobenzene based tetraamide. *J. Phys. Chem. B*, 112(33):10107–10115, 2008.

[39] Gianfranco Ercolani. A model for self-assembly in solution. *J. Phys. Chem. B*, 107(21):5052–5057, 2003.

[40] G. J M Koper, J. Boekhoven, W. E. Hendriksen, J. H. Van Esch, R. Eelkema, I. Pagonabarraga, J. M. Rubí, and D. Bedeaux. The Lost Work In Dissipative Self-Assembly. *Int. J. Thermophys.*, 34(7):1229–1238, 2013.

[41] Jin Zhang, Haiqiao Wang, Xiaoyang Li, Shasha Song, Aixin Song, and Jingcheng Hao. Two gelation mechanisms of deoxycholate with inorganic additives: Hydrogen bonding and electrostatic interactions. *J. Phys. Chem. B*, 120(27):6812–6818, 2016.

[42] Yan Qiao, Yiyang Lin, Zhiyi Yang, Huanfa Chen, Shaofei Zhang, Yun Yan, and Jianbin Huang. Unique temperature-dependent supramolecular self-assembly: From hierarchical 1d nanostructures to super hydrogel. *J. Phys. Chem. B*, 114(36):11725–11730, 2010.

[43] S. Kjelstrup, J M Rubi, I. Pagonabarraga, and D Bedeaux. Mesoscopic Non-Equilibrium Thermodynamics Analysis of Molecular Motors. *Phys. Chem. Chem. Phys.*, 15:19405–19414, 2013.

[44] I Pagonabarraga, A Pérez-Madrid, and JM Rubi. Fluctuating hydrodynamics approach to chemical reactions. *Physica A*, 237(1-2):205–219, 1997.

[45] M.Doi and S.E.Edwards. *The Theory of Polymer Dynamics*. Oxford University Press, 1 edition, 1986.

[46] Allan S Hoffman. Hydrogels for Biomedical Applications. *Adv. Drug Deliv. Rev.*, 64:18–23, 2012.

[47] Nasim Annabi, Jason W Nichol, D Ph, Xia Zhong, and Chengdong Ji. Controlling the Porosity and Microarchitecture of Hydrogels for Tissue Engineering. *J. Tissue Eng.*, 16(4):371–383, 2010.

[48] Zulma A. Jiménez and Ryo Yoshida. Temperature Driven Self-Assembly of a Zwitterionic Block Copolymer That Exhibits Triple Thermoresponsivity and pH Sensitivity. *Macromolecules*, 48(13):4599–4606, 2015.

[49] Jinxing Jiang and Kenji Sakurai. Formation of Ultrathin Liesegang Patterns. *Langmuir*, 32(36):9126–9134, 2016.

[50] Yukikazu Takeoka and Masayoshi Watanabe. Tuning Structural Color Changes of Porous Thermosensitive Gels Through Quantitative Adjustment of the Cross-Linker in Pre-Gel Solutions. *Langmuir*, 19(22):9104–9106, 2003.

[51] Marta Tena-Solsona, Benedikt Rieß, Raphael K Grötsch, Franziska C Löhrer, Caren Wanzke, Benjamin Käsdorf, Andreas R Bausch, Peter Müller-Buschbaum, Oliver Lieleg, and Job Boekhoven. Non-equilibrium dissipative supramolecular materials with a tunable lifetime. *Nat. Commun.*, 8:15895, 2017.

[52] P. K. Kundu, D. Samanta, R. Leizrowice, B. Margulis, H. Zhao, M Börner, T Udayabhaskararao, Debasish Manna, and Rafal Klajn. Light-Controlled Self-Assembly of Non-Photoresponsive Nanoparticles. *Nat. Chem.*, 7(8):646–652, 2015.

[53] Keitaro Sou, Li Yan Chan, and Chi-lik Ken Lee. Photo-Switchable and Self-Erasable Fluorescent Nanoprobe. *J. Photochem. Photobiol. A. chem.*, 332:25–31, 2016.

3. Nonequilibrium self-assembly induced Liesegang rings in a non-isothermal system

We propose a model to show the formation of Liesegang rings under non-isothermal conditions. The model formulates reaction-diffusion equations for all components intervening in the process together with an evolution equation for the temperature. The reactive parts in these equations follow from the analysis of the non-equilibrium self-assembly (NESA) process undergone by the meso-particles which make up the patterns. The solution of these equations enables us to know the concentration of each component, the spherical structures diameter, and the system's temperature as a function of time and radial position. The values found for the structures diameter and the rings position are in agreement with the experiments. The results for the system's temperature with peaks at the rings positions suggest that heat accumulates at these positions as a consequence of the dissipation inherent to the NESA process. Our model enables us to rationalize how from non-homogeneous initial conditions a transient self-organization process involving formation of self-assembled structures may produce macroscopic patterns. It can, in general, be used to analyze pattern formation due to diffusion-reaction-precipitation processes with potential applications in the design of advanced materials.

This chapter was published in *the Journal of Physical Chemistry Chemical Physics*, **20**, 4699-4707 , (2018). Ref.[1]

3.1. Introduction: Spatio-temporal patterns

Pattern formation and self-organising phenomena are ubiquitous in biology [2, 3, 4], chemistry [5], physics [6], and materials science [7]. A representative example of such phenomena is the periodic precipitation pattern discovered by *R. E. Liesegang* in 1896 [8, 9], known as Liesegang patterns, which consist of a number of concentric rings (in 2D) or bands (in 1D) resulting from the diffusion of ionic co-precipitate and periodic precipitation of an insoluble solid in a gel medium [10].

Different physico-chemical processes such as supersaturation, nucleation, particle growth, electro-migration and temperature effects are involved in the formation of these patterns [11]. The presence of these processes gives rise to the appearance of various types of structures such as the well-known bands with revert spacing [12], bands with secondary structures [13], fractals [14], spirals [15], and 3D helices [16]. In the last years, patterned systems have been used in modern micro- and nanotechnology [17, 18]. Their control and engineering constitute a crucial task for applications to those areas [19].

Precipitating systems own two necessary conditions for self-organization: to be out of equilibrium and to evolve according to a nonlinear kinetics [20]. These systems may develop intermediate dissipative structures before the emergence of the final spatial pattern [21]. Recently, synthesis based on nucleation and particle growth in a reaction-diffusion system taking place in a gel matrix has been recognized as an important method to produce self-assembled structures under non-equilibrium conditions [22, 23, 24, 25]. This synthesis brings about the formation of Liesegang patterns which are composed of mono-disperse nano and micro-structures whose size varies predictably from ring to ring [26, 27, 28]. These structures built up from fundamental components called building blocks (BB). Under far-from-equilibrium conditions in which the system is driven by a supersaturation gradient, solid forms may emerge [23]. The non-equilibrium nature of this process is highlighted by the occurrence of polymorphism and the appearance of both stable and metastable structures [29, 30, 31]. In the synthesis, two electrolytes act as fundamental components that trigger the self-assembly process, forming stable non-equilibrium self-assembly (NESA) structures. This method in which meso-structures of different sizes are obtained is known as bottom-up self-assembly [18].

In general, NESA structures [32, 33] which arise spontaneously from a set of disordered components may induce the appearance of spatio-temporal patterns which originate from the periodicity inherent to the kinetics of the process [18]. NESA structures dissipate matter and energy until they reach a stationary state (dissipative self-assembled structure [32]), a metastable state (non-dissipative self-assembled structure kinetically trapped [34]) or a stable states (non-dissipative equilibrium self-assembled structure) [23])[35, 36]. Thus NESA structures can be considered precursors of the self-organized structures being less complex than the self-organized ones because the lack of complex networks of feedback loops in the system [37, 36].

Upon bringing about variations of the environmental parameters, it is possible to obtain meso-particles with a well-defined size [26, 38] or surfaces with nano-patterns [39], thus providing a promising method for the formation of versatile self-assembled structures that can be used for practical applications in material science. For instance, the patterns' spatial features can be controlled externally by an external electric field [12, 40]. Pattern design can be controlled by temperature, ionic force and light intensity [39], gel quality and concentration [41] and charged and modified nano-particles [42].

For several decades, equilibrium thermodynamics has been used to account for the formation of stable self-assembled structures that may exhibit high complexity; however, the dynamical properties are poorly explained [23, 18, 33, 36]. Many of these self-organized structures, usually found in nature, present dynamic and adaptive properties and are therefore observed under far-from-equilibrium conditions [43, 18, 33, 36]. To elucidate the nature of the self-assembly mechanisms operating under these conditions it is of primary importance to characterize NESA structures. As mentioned above, we understand that the structures are built up from fundamental components, BB, and are sustained by mass and energy dissipation processes. [44, 45]. Whether the type of structure is stable or metastable depends on the parameters of the system and of the surroundings [36]. Understanding the nature of the dissipative processes involved in the assembly of BB is a key issue in the design of new materials [46, 47, 48, 49, 50, 51] for useful applications in medicine [52, 53], catalysis [54] and energy storage [18].

Liesegang patterns have been exhaustively studied because of their theoretical importance in chemistry [55] and potential applications to material science [39]. A classical explanation of the mechanism that triggers their formation is the existence of a chemical instability in an autocatalytic reaction followed by spatial diffusion and periodical precipitation of one of the components [56]. To discover the mechanisms leading to the formation of Liesegang patterns, several models have been proposed. Some of them are based on: the DLVO theory of stability of colloids [57], the Ostwald supersaturation model [58, 59], the reaction-diffusion equations coupled to dynamical competitive particle growth [60] and the Muller-Polezhaev model which incorporates supersaturation, nucleation, and kinetics of particle growth, and even dissolution coupled to diffusion [61, 40, 62]. There are also models based on the existence of solubility thresholds derived from the nano-particle charge-neutrality condition [42].

Most of these models are formulated mathematically by means of parabolic reaction-diffusion equations [20, 63, 12, 64] and by hyperbolic partial differential equation [21]. Some reaction-diffusion models may provide expressions for the entropy production which can be used to analyze the different structures formed and may evaluate the thermodynamic consistency of models and transitions between the structures. [21, 45, 65, 66].

Although the existence of Liesegang patterns has been known for more than hundred years, there is still no consensus about what is the underlying mechanism that gives rise to their formation [67, 20]. Current mechanisms consider the spatial diffusion-reaction-nucleation of the species involved in isothermal systems as the only key process triggering the pattern formation. However, systems that develop Liesegang patterns have been identified as self-organized systems. Differently, from the classical explanation, the emergence of NESA structures is a key factor for the appearance of the patterns. Thus, the role played by the BB in the emergence of the structures in non-isothermal systems is important to better understand the formation of the patterns.

In this chapter, we propose a new mechanism for the non-equilibrium self-assembly of mesoscopic structures which gives rise to the formation of Liesegang patterns from fundamental building blocks. We develop a mathematical model from the mesoscale to describe the two-dimensional Liesegang pattern formation under non-isothermal conditions. Specifically, the model proposed gives information about the size of the structures, the spatial distribution of the patterns, the particle concentration of the structures and the spatial distribution of the temperature. The model provides an expression of the entropy production rate and equivalently of the power dissipated in the formation of the patterns.

The chapter is organized as follows. In Section 2, we describe the NESA mechanism leading to the formation of Liesegang patterns. In section 3, we present the dynamical model for the evolution of a structure composed of BB which consists of a set of kinetic equations able to explain the non-periodical agglomeration of the structures that precede the appearance of the rings. We also analyze the energy balance which reveals the non-isothermal nature of the process. In Section 4, we present the numerical solutions for the concentrations, position and size of the structures in each ring of the pattern and their temperature. Finally, in Section 5, we present our main conclusions.

3.2. Mechanism: bottom-up self-assembly of Liesegang rings

In some reaction-diffusion processes taking place in a gelatin matrix (to avoid convection effects), periodical precipitation of a suspension of insoluble solids gives rise to the appearance of Liesegang patterns, as illustrated in Fig.**3-1**. The pattern formation mechanism runs as follows. When the membrane separating both electrolytes (represented by the cylinder surface) is removed, the activator (E) diffuses in the gelatin matrix and reacts with the fundamental component (B) to produce a more energetic component. The product of the reaction interacts strongly with itself producing a small and soluble component. This component is thermodynamically unstable so it tends to separate from the solution forming a non-soluble component (nuclei). When the concentration of the non-soluble component reaches a threshold value, agglomeration starts producing clusters that precipitate or remain suspended in the gel. Since as a consequence of the agglomeration, the nuclei concentration decreases, precipitation ceases and the nuclei grow again until they reach a critical size. Thus the whole process starts again until one of the electrolytes is completely consumed.

3.2.1. Classical mechanism based only on chemical processes

In the system studied [26], potassium dichromate ($K_2Cr_2O_7$) (inner salt) and silver nitrate ($AgNO_3$) (outer salt) are the soluble salts that trigger the formation of the non-soluble salt: silver chromate (Ag_2CrO_4). The classical chemical mechanism considers the dissolution of the salts in the aqueous media, the hydrolysis of the cations, and the production of insoluble salts:

$$\mathrm{AgNO_{3(aq)}} \rightleftharpoons \mathrm{Ag^+} + \mathrm{NO_{3(aq)}}^-$$

$$\mathrm{K_2Cr_2O_{7(aq)}} \rightleftharpoons 2\,\mathrm{K^+} + \mathrm{Cr_2O_{7(aq)}}^{2-}$$

$$\mathrm{Cr_2O_{7(aq)}}^{2-} + \mathrm{H_2O} \rightleftharpoons 2\,\mathrm{CrO_{4(aq)}}^{2-} + 2\,\mathrm{H^+}$$

$$\mathrm{CrO_{4(aq)}}^{2-} + 2\,\mathrm{Ag^+} \rightleftharpoons \mathrm{Ag_2CrO_{4(s)}}$$

$$\mathrm{Cr_2O_{7(aq)}}^{2-} + 2\,\mathrm{Ag^+} \rightleftharpoons \mathrm{Ag_2Cr_2O_{7(s)}}$$

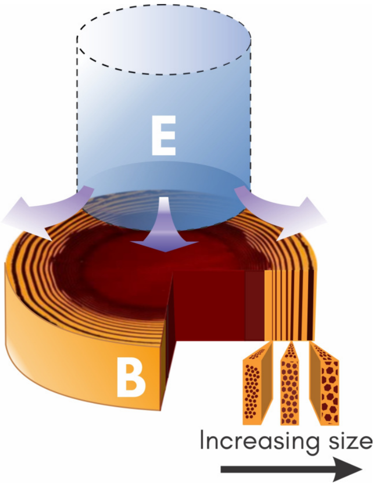

Fig. 3-1.: Illustration of the experimental setup and sketch of the spatial patterns consisting of quasi-periodic precipitation rings. Electrolyte E diffuses into the matrix and interacts with electrolyte B to trigger the bottom-up self-assembly of meso-structures leading to the Liesegang patterns. Structures size increases as a function of the radial position. Adapted from commons.wikimedia.org with license CC-BY-SA-3.0.

Here the equilibrium between dichromate $Cr_2O^{2-}_{7(aq)}$ and chromate $CrO^{2-}_{4(aq)}$ is displaced favoring the formation of $CrO^{2-}_{4(aq)}$ due to the $NaOH$ added. Considering the analytical value of the chromate/dichromate equilibrium constant close to 10^{-15} [68], with an initial dichromate concentration of $0,010M$ [26] at a given pH of 8, it is possible to determine that the fraction of dichromate in equilibrium is less than $0,01\,\%$.
This classic mechanism does not consider the formation of intermediate components between the chromate/silver ions and the silver chromate solid. The existence of intermediates is related to the presence aqueous silver chromate, to small interaction between this aqueous component and to nucleation and stabilized growth of the non-soluble silver chromate by silver ions.

3.2.2. Mechanism for the formation of NESA structures composing the Liesegang rings

NESA processes involve two fundamental ingredients: activation that enables the self-assembly of the fundamental components [37] and the presence of two opposed forces [33] that trigger the assembly and disassembly mechanisms. Further, NESA processes originate different types of hierarchical structures that differ in their geometry, micro-architecture or whether precursors are present or not. In the studied system [26], we identify two kinds of structures: first and second order structures and two sub-processes: activation and self-assembly causing the structure formation. We do not consider dis-assembly because we assume that there is not re-dissolution of the solids.

Specifically, in the experiments [26] that we want to reproduce, the outer electrolyte is silver ion (Ag^+), the inner electrolyte is chromate (CrO_4^{2-}), and the solid product is silver chromate (Ag_2CrO_4). We denote Ag^+ by E (the activator), CrO_4^{2-} by B (the disactivated building block), $Ag_2CrO_{4(aq)}$ by A (the activated building block), $(Ag_2CrO_4)_{n(aq)}$ by A_n (first order structure), $(Ag_2CrO_4)_{n(s)}$ by G (second order building block) and $lAg^+((Ag_2CrO_4)_{n(s)})_m$ by G_m (second order structure). The different steps in the NESA mechanism are: first-order activation (process 1, chemical reaction), first-order self-assembly (process 2, physical interaction/pre-nucleation), second-order activation (process 3, phase change), and second-order self-assembly (process 4, aggregation). They can be expressed as:

(1) $\mathrm{2E+B \rightleftharpoons A}$

(2) $\mathrm{nA \rightleftharpoons A_n}$

(3) $\mathrm{A_n \rightleftharpoons G}$

(4) $\mathrm{mG} + l\mathrm{E} \longrightarrow \mathrm{G_m}$

Notice that in the formation of first-order structures, we have not considered more intermediate steps in which the activated building blocks may add up sequentially to form structures made up by a number of blocks smaller than n. This approximation is also made for the formation of the second-order structures. However, m depends on the concentration of the E component.

3.3. The model

The model we propose is based on the mesoscopic nonequilibrium thermodynamic formalism in which the kinetics of activation processes follow from the entropy production and is then subjected to the second law [69]. The different states of the system can be parametrized by a reaction coordinate $\mathbf{\Gamma}$ and their probability is given by $p(\mathbf{\Gamma},t)$ where $\mathbf{\Gamma} \equiv [\boldsymbol{r}, \boldsymbol{\gamma}]$ is a vector of a phase space which may in general depend on position $\boldsymbol{r}$.

3.3.1. Mass balance

The state of the i^{th} component in the system at time t is described by the probability distribution $p_i(\mathbf{\Gamma},t)$. The distribution is defined in an ensemble of systems in a landscape large enough to carried out a thermodynamic analysis. The continuity equation for the probability in the $\mathbf{\Gamma}$-space is given by,

$$\frac{\partial p_i(\mathbf{\Gamma},t)}{\partial t} = -\nabla_{\mathbf{\Gamma}} \cdot \boldsymbol{J}_i(\mathbf{\Gamma},t), \tag{3-1}$$

where $\boldsymbol{J}_i$ is a flux for the i^{th} component defined in $\mathbf{\Gamma}$-space. Assuming uncoupling processes among the sub-spaces describing the NESA processes (γ_j), the continuity equation is now rewritten as:

$$\frac{\partial p_i(\mathbf{\Gamma},t)}{\partial t} = -\nabla_{\boldsymbol{r}} \cdot \boldsymbol{J}_i^{(\boldsymbol{r})}(\boldsymbol{r},t) - \sum_{j=1}^{4} \frac{\partial}{\partial \gamma_j} J_{i,j}^{(\boldsymbol{\gamma})}(\boldsymbol{r},\gamma_j,t), \tag{3-2}$$

Here the spatial diffusive flux, $\boldsymbol{J}_i^{(\boldsymbol{r})}$, only depends on the spatial coordinate and time. The flux for the i^{th} component in the j^{th} process ($j = 1,...,4$), $J_{i,j}^{(\boldsymbol{\gamma})}$ depends on the spatial coordinate ($\boldsymbol{r}$), the internal coordinate of the j^{th} process and on time.

Carrying out a coarse-graining approach to eliminate the $\boldsymbol{\gamma}$-coordinate, we obtain the continuity equation in terms of position and time,

$$\frac{\partial p_i(\boldsymbol{r},t)}{\partial t} = -\nabla_{\boldsymbol{r}} \cdot \boldsymbol{J}_i^{(\boldsymbol{r})}(\boldsymbol{r},t) - \sum_{j=1}^{4} \left[J_{i,j}^{(\boldsymbol{\gamma})}(\boldsymbol{r},1,t) - J_{i,j}^{(\boldsymbol{\gamma})}(\boldsymbol{r},0,t) \right], \tag{3-3}$$

Here $J_{i,j}^{(\boldsymbol{\gamma})}(\boldsymbol{r},0,t)$ is the flux of the component i consumed in the j^{th} process, while $J_{i,j}^{(\boldsymbol{\gamma})}(\boldsymbol{r},1,t)$ is the flux of the component i produced in the j^{th} process.

In the absence of interactions, the concentration C_i can be related to the probability through $C_i = C_0 p_i$, where C_0 is the initial concentration of the reactive. The spatial diffusive flux can be expressed as $\boldsymbol{J}_i^{(d)} = C_0 \boldsymbol{J}_{i,j}^{\boldsymbol{\gamma}}$, and the reaction rate per component as $\dot{r}_{i,j}(\boldsymbol{r},t) = C_0 \left[J_{i,j}^{(\boldsymbol{\gamma})}(\boldsymbol{r},1,t) - J_{i,j}^{(\boldsymbol{\gamma})}(\boldsymbol{r},0,t) \right]$. Thus multiplying Eq.(3-3) by C_0 and using the previous relations, we obtain the mass-balance equation for the concentration of the i^{th} component

$$\frac{\partial C_i(r,t)}{\partial t} = -\nabla_{\boldsymbol{r}} \cdot J_i^{(d)}(\boldsymbol{r},t) - \sum_{j=1}^{4} \dot{r}_{i,j}(\boldsymbol{r},t). \tag{3-4}$$

Considering an homogeneous gel matrix used to avoid convective effects and angular difussion, we obtain the balance equation for the components intervening in the NESA process for the formation of macroscopic patterns

$$\frac{\partial C_i(r,t)}{\partial t} = -\frac{1}{r}\frac{\partial}{\partial r} r J_i^{(d)}(r,t) - \sum_{j=1}^{4} \dot{r}_{i,j}(r,t), \tag{3-5}$$

The diffusive flux is given by $J_i^{(d)}(r,t) = -D_{eff}\frac{\partial C_i}{\partial r}$ where D_{eff} is an effective diffusion coefficient.

The expressions for the rates $\dot{r}_{i,j}$ are computed in the quasi-stationary regime [70] in which they only depend on position and time. They include Arrhenius factors ($k_j(T) = \hat{k}_j \exp(E_a/RT)$) [69, 71]. The rates can describe processes (or reactions) which do not fulfill the law of mass action because of the presence of activity coefficients in the original kinetic expressions. The obtained rates for the NESA for the formation of the structures composing the Liesegang patterns are given by:

$$R_1 = k_1^{+}(T) C_B C_E^2 - k_1^{-}(T) C_A, \tag{3-6}$$

$$R_2 = k_2^{+}(T) C_A^2 - k_2^{-}(T) C_{A_n}, \tag{3-7}$$

$$R_3 = k_3^{+}(T) C_{A_n}^2 - k_3^{-}(T) C_G \tag{3-8}$$

$$R_4 = \begin{cases} k_4(T) C_G C_{G_m}^2 & \text{if} \quad C_G < C_{lim} \\ k_4(T) C_G C_{G_m}^2 + k_4(T) C_E C_G (C_G - C_{lim}) & \text{if} \quad C_G \geq C_{lim} \end{cases} \tag{3-9}$$

The first-order activation rate given in (Eq. 3-6) is a kinetic expression of first order in the building block concentration (C_B) and second order in the activator (C_C). Since we are not considering the formation of intermediate structures with a number of blocks less than n, we approach the first-order self-assembly rate

(Eq. 3-7), as a kinetic of second order in the activated building block concentration (C_A). The second-order activation rate (Eq. 3-8) is a first-order kinetic expression in the first-order structure concentration (C_{A_n}). In the process, the solid nuclei may emerge even in the regions between bands (more information about the presence of these particles is given in the Annex D).

With respect to the aggregation process rate in (Eq. 3-9), there exists a threshold value for the precursor concentration (C_G), auto-catalytic effects and stabilizing effects due to an excess of the activator (the electrolyte E). Below the threshold concentration, an auto-catalytic effect of the second-order structure is expected since the structure tends to minimize the surface area to become more stable interacting with itself; the precursor (G) can be viewed as a building block of the second-order structure. Therefore, under the threshold concentration, we find a second-order kinetics for the second-order structure concentration (C_{G_m}) and a first-order one for the precursor (C_G). For a precursor concentration (C_G) higher than the threshold value, we obtain the same kinetic contribution as the one obtained below that limit. An additional contribution comes up due to the stabilization effect related to the excess of electrolyte. The electrolyte (E) contributes to first-order in the kinetics and the precursor (G) has a second-order contribution since the agglomeration involves two components. Finally, from Eqs. 3-6-3-9, we can write the $\dot{r}_{i,j}$ fluxes using the stoichiometry of the processes 1-4 (see Annex D).

Notice that the probability (concentration) is not conserved because the fluxes are not zero at the boundaries of the $\boldsymbol{\gamma}$ coordinates, i.e the total concentration is not constant. However, the concentration of the building blocks (C_{BB}) is conserved and can be expressed as:

$$C_{BB} = C_B + C_A + nC_{A_n} + nC_G + mnC_{G_m} \tag{3-10}$$

3.3.2. Energy Balance

As the rates depend on temperature and the processes (chemical reactions, nucleation, phase change and agglomeration) are exothermic or endothermic, we must consider the energy conservation equation

$$\frac{\partial e(r,t)}{\partial t} = -\frac{1}{r}\frac{\partial}{\partial r} rJ_e(r,t), \tag{3-11}$$

with J_e the energy flux fulfilling the relation $J_e = -k_{eff}\frac{\partial T(r,t)}{\partial r}$, where k_{eff} is an effective thermal conductivity and T the temperature. In a diluted reactive media with sufficiently small changes in temperature, the energy $e(r,t)$ per volume unit can be written as $e(r,t) \approx \sum_i C_i h_i$, where the molar specific enthalpy h_i is the sum of the standard formation enthalpy (h_i^0) and the enthalpy related to the heat capacity ($c_{P,i}$), $h_i \approx h_i^0 + c_{P,i}(T - T_{ref})$, with T_{ref} a reference temperature. Using the last relation for the energy flux, the enthalpy, Eq.3-3 and the process rates ($\dot{r}_{i,j}$), we can rewrite the energy conservation Eq. 3-11 in the form

$$\sum_i C_i c_{P,i} \frac{\partial T(r,t)}{\partial t} = -\frac{1}{r}\frac{\partial}{\partial r} rJ_e(r,t) + \sum_i h_i \frac{1}{r}\frac{\partial}{\partial r} rJ_{d,i}(r,t) - \sum_{j=1}^{4} \Delta h_j R_j, \tag{3-12}$$

where Δh_j is the reaction heat of the process. The first term on the right-hand side of Eq.3-12 is related to heat diffusion, the second takes into account the energy flux due to concentration gradients and the last term comes from the heat generated (or consumed) in exothermic (or endothermic) processes.

3.3.3. Initial Conditions

The equations of the model, the evolution equations for the concentrations of the different components Eq.3-3 and for the temperature Eq. 3-12, must be solved with homogeneous Neumann boundary conditions in $r \in [0 \quad L]$ (isolated system) and initial conditions given by

$$C_E(r,0) = \begin{cases} C_{E,0} & \text{if} \quad r \leq r_{lim} \\ 0 & \text{if} \quad r < r_{lim} \end{cases} \tag{3-13}$$

$$C_B(r,0) = \begin{cases} C_0 & \text{if} \quad r > r_{lim} \\ 0 & \text{if} \quad r \leq r_{lim} \end{cases} \tag{3-14}$$

$$C_{w,0} = 1000 C_0, \forall r \tag{3-15}$$

$$C_i(0,r) = 0, \quad \text{for} \quad i = A, A_n, G, G_m \, \forall r \tag{3-16}$$

where C_w is the water concentration and r_{lim} is the initial position of the membrane separating both electrolytes. The initial condition for the temperature is $T(0,r) = T_0 \; \forall r$, with $T_0 = 298{,}15 \; K$.

3.3.4. Structure size

As previously mentioned, the excess in the electrolyte concentration stabilizes the second-order structure that is considered spherical. Then we assume that a low concentration in the electrolyte causes growth of the structure in order to diminish its surface while a high electrolyte concentration neutralizes the growth of the structure. Therefore, the structure diameter d is a function of the electrolyte concentration $C_E(r,t)$. We assume that the change in the structure growth relative to the change in the activator concentration C_E is inversely proportional to the electrolyte concentration,

$$\frac{\Delta d}{\Delta C_E} \propto -1/C_E \tag{3-17}$$

Taking the limit of very small changes in which the fraction in Eq.3-17 becomes a derivative, and integrating from the limit where the membrane was placed (r_{lim}) until r, we obtain the relation between the structure diameter and the electrolyte concentration C_E:

$$d(r,t) = d_0 + \omega \ln(C_E(r_{lim},0)/C_E(r,t)), \quad \forall r > r_{lim}, \tag{3-18}$$

where ω is a constant that accounts for the dispersion in the size of the structures. For very small values of ω, the structures in each pattern (ring) have a common size d_0. Notice that the diameter is also a function of time because growth is affected by the electrolyte concentration which depends on space and time. This fact also contributes to the dispersion in the diameter distribution.

The number of building blocks (m) making up the second-order structure (G_m) follows from comparing the mass of the structure with the mass of a block. This is given by

$$m = \varepsilon^3 \frac{4\rho_{G_m}\pi(d/2)^3/3}{M_G} \tag{3-19}$$

Here ε is the packing factor, considered of the order of 0.6, M_G is the mass of a building block and ρ_{G_m} is the molar density of the structure .

3.3.5. Physical properties

The values of thermal conductivity, heat capacity and density are similar to those for water and aqueous solution at 37,5^oC. Table **3-1** shows the spatial diffusivity for each component in the aqueous-gel medium used for the numerical solution. Diffusivities are assumed to be constant because the small changes in the temperature. Diffusivities are in the range of $1x10^{-9}m^2/s$-$4x10^{-8}m^2/s$.

Tab. 3-1.: Estimated values for diffusivities $[m^2/s]$ for each component

$D_C x10^{10}$	$D_B x10^{10}$	$D_A x10^{10}$	$D_{A_n} x10^{10}$	$D_G x10^{10}$	$D_{G_m} x10^{10}$
400	100	100	10	10	0

The standard reaction heat, the estimated activation energy, the forward kinetic constant and the change of the standard chemical potential for each process used for the numerical solution are presented in Table **3-2**:

Tab. 3-2.: Estimated values for all set of physicochemical parameters

	process 1	process 2	process 3	process 4
$\hat{k}_j^+/100$	$1[m^9/mol^2s]$	$1[m^6/mols]$	$1[m^6/mols]$	$2{,}2*10^{11}[m^9/mol^2s]$
$\Delta h_j^0/RT$	$-7{,}6$	-384	$-0{,}1$	$-7{,}6*10^4$
$E_{a,j}/RT$	20	2	2	10
$\Delta\mu_j^0/RT$	5	140	0	14000

with the inverse process constant ($\hat{k}_j^-$) defined as: $\hat{k}_j^- = \exp(-\Delta\mu_j^0/RT)$. In Table **3-2**, the values of the kinetic constants considers the fact that the collision frequency for reactantsïn the process 4 (effective çrash”between nuclei) must be higher than the frequencies of the other processes because the big size and low concentration of the reactants. The estimated values for the reaction heat and standard free energy change of the process are computed from the formation enthalpy and standard free energy of the compounds, respectively. Finally, the values of activation energies are estimated according to the covalent-ionic nature of processes. Thus, the activation energy of process 1 (activation) owns the highest value because there are covalent bonds formation, whilst the physical processes (2,3 and 4) are generally quickly with reaction rates governed by the ions diffusion, in which the activation energy tends to be small.

The parameters included in Table **3-1** and Table **3-2** control the form of the final patterns, the average size of the structures and the size distribution. The relations among diffusivities, between diffusivities and kinetic constants have an impact on the ring separation and position of the first ring. Specifically, the relation between the salts diffusivity and their activation kinetic constants is key to predict the form of the final patterns. Furthermore, the Ag^+ diffusivity and the kinetic constants for processes 1 and 4 significantly affects the average size and the size distribution of the structures due to the activator distribution in the system. High diffusivity and small kinetic constants favor the formation of structures with a uniform size, but under these conditions the number of structures could probably decrease because the lack of enough activated BB to trigger the self-assembly in specific zones, creating a diffuse zone of precipitates/agglomerates. Additionally, the reaction heat and activation energies affect directly the temperature profile and indirectly the rates of the processes. In the next section, we compare the isothermal case in which the reaction heat is negligible with the non-isothermal case treated with our model and show how temperature variations affect the final patterns, size and size distribution of the structures.

3.3.6. Entropy production rate

The entropy production rate per unit of volume (σ_s) results from the diffusion and reaction processes. According to mesoscopic non-equilibrium thermodynamics [69], it is given by

$$\sigma_s = \frac{1}{T}\left[D_{eff}\left(\frac{\partial C_i}{\partial r}\right)^2 + \sum_j R_4^2/k_j^+(T)\right] \tag{3-20}$$

The entropy production coming from the heat conduction process (σ_v) is given by [72]

$$\sigma_v = \frac{\kappa_{eff}}{T^2}\left(\frac{\partial T}{\partial r}\right)^2 \tag{3-21}$$

with κ_{eff} an effective thermal conductivity of the system. Thus, the total entropy production rate per unit of volume (σ) is

$$\sigma = \sigma_s + \sigma_v. \tag{3-22}$$

3.4. Results and Discussion

We have numerically solved Eq.(3-5) for each component and Eq.(3-12) by means of a finite-volume method written in MATLAB ®. In Fig. **3-2**, we represent the ring distribution obtained from our model at time t_p for which the second-order structure formation rate tends to zero ($R_4 \to 0$). This time is smaller than the time needed to reach a homogeneous temperature; a homogeneous concentration is not achieved because there is not re-dissolution. In Fig. **3-2**, we show the numerical results obtained for the concentration that reproduce the experimental micro-graph (Fig.**3-1**).

To obtain the numerical solution, we also estimated the relevant parameters of our model. For the second-order structure diameter given in Eq.(3-18), we found $\omega = 16{,}5nm$ and $d_0 = 200nm$. We also estimated the stoichiometric coefficients n and l, finding $n = 140$ and $l = 1400$. For the kinetic constants, we found that k_4^+ must be $(m_0 n)^2$ times larger than k_1^+ (Table **3-2**). This relation follows from the fact that the second-order structure concentration (C_{G_m}) is, at least $m_0 n$ times smaller than the disactivated building block concentration (C_B). The rates R_1 and R_4 are of the same order, otherwise the balance between activation and self-assembly rate would be broken and only a diffuse zone (patternless) could be observed. We found that the value for the threshold concentration (C_{lim}) is around $0{,}01 C_{B,0}$. Finally to reproduce the spatial patterns, the activator

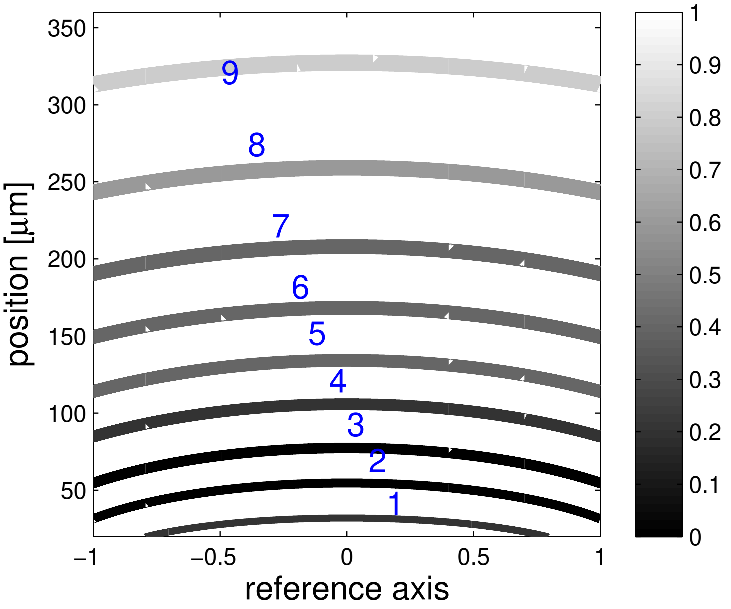

Fig. 3-2.: Model results. Ring distribution obtained from our model at time t_p. The darker colour corresponds to the highest concentration of precipitated structures while the lighter color indicates absence of structure. Rings are numbered in blue starting from the first visible one outside the diffusive zone, as in [26].

(C) diffusivity must be four times larger than the disactivated building block (B) diffusivity.

In Fig. **3-3**, we compare the results of our model with experimental data. Fig. **3-3**(a) shows a non-periodical ring distribution in which the separation between the rings increases with the distance from the membrane. This figure also shows the behaviour of the structure diameter, in which this quantity and its standard deviation as a function of position tends to increase. This is because both quantities are inversely proportional to C_E which decreases with position due to the fact that it is progressively consumed (see Annex D). The numerical results for the ring distribution and structure's diameter show a very good agreement with the experiments [26] with an error related to ring position of 6,4 %, and error related to structures' diameter of 4,9 %. This fact supports the assumptions made about the model: an absence of convection, constant physical properties of the medium, and a NESA kinetics that induces the formation of the structures composing the patterns. The small discrepancies of the results obtained in bands $5-7$ are probably due to the presence of inhomogeneities in the gel matrix around these rings which have not been considered in the model.

Fig. **3-3**(b) shows the results found from the isothermal model which does not consider the energy balance given in Eq. 3-12 and uses the same physical parameters (diffusivities and kinetic constants) as the ones considered in the proposed model, against experimental data. Fig. **3-3**(b) shows that the isothermal model does not reproduce the experiments accurately since it predicts the appearance of fewer rings in the system (red numbers), specifically 8 rings instead of 9 (the experimental data are numbered in blue). For the first 8 rings, the error related to ring positions is 10,1 % and the error in the structures' diameter is 6,3 %. These errors are approximately 60 % and 30 % bigger than the error found for the non-isothermal model, for ring positions

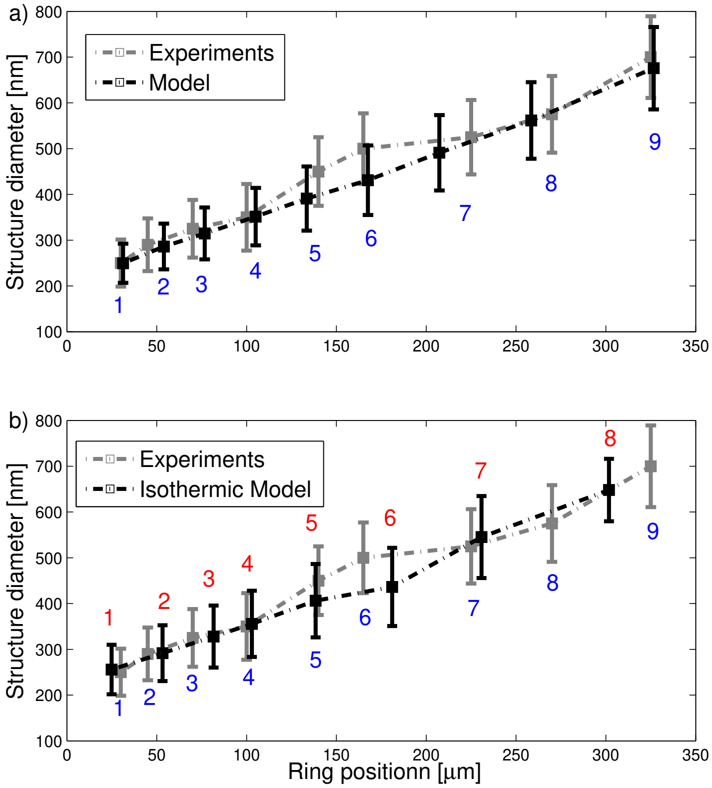

Fig. 3-3.: (a) Model results and experimental data for the structure diameter at the ring positions (numbered in blue from 1-9). The error in the estimated position is 6,4 %, and the error in the estimated structure's diameter is 4,9 %. (b) Isothermal-model results and experimental data for the structure diameter at the ring positions (numbered in red from 1-8). The error in the estimated position is 10,1 %, and the error in the estimated structure's diameter is 6,3 %. Grey squares denote the experimental data taken from [26]; black squares stand for our results. The dashed line connects the results obtained for the different rings.

and structure's diameter respectively. Notice that the separation between consecutive rings increases more for the isothermal-model (Fig. **3-3**(b)) than for the non-isothermal model Fig. **3-3**(a). This is so because in the non-isothermal model an increment of the temperature leads to an enhancement of the reaction rates, causing that the agglomerates reach quickly the threshold concentration to trigger the structure formation.

Notice that if the diffusivity of the activator (Ag^+) is lower, close to the diffusivity value of the disactivated BB precursor (CrO_4^{2-}), the separation between the bands decreases, and the isothermal model may reproduce the number of rings observed experimentally. Nevertheless, if the difference between diffusivities is small the diffuse zone (zone with non-soluble solids before the first ring shown [26]) becomes considerably smaller, contrary to what is observed in the experiments [26]. Furthermore, we could expect that the diffusivity of both components differs considerably because of its difference in charge and size. Therefore, the isothermal (Fig. **3-3**(b)) and the non-isothermal (Fig. **3-3**(a)) model results show that temperature differences in the system may affect significantly the formation of the rings.

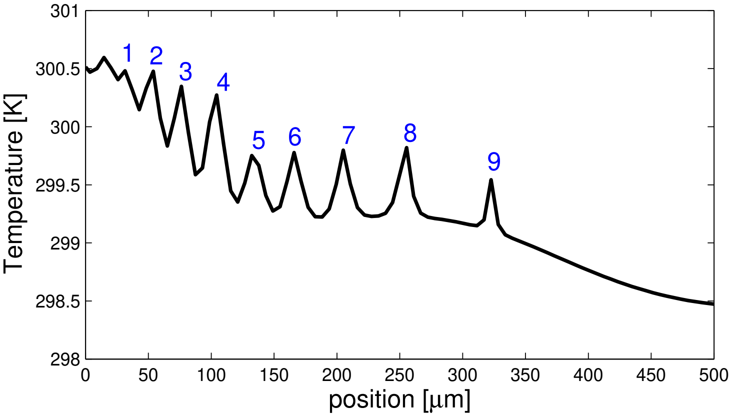

Fig. 3-4.: Temperature [K] vs. position [μm] at time t_p. Position zero (r^*) corresponds to the point where the membrane was placed ($r = r_{lim}$). Temperature peaks coincide with ring positions numbered from 1-9.

Our model also allows us to compute temperature variations in the system. Although they are found to be small, of about 2^oC, temperature gradients are large due to the smallness of the system, approximately $400K/m$. These gradients may give rise to changes in the rates and to structural changes in the gel that induce inhomogeneities [73].

In Fig. **3-4**, we show the temperature profile for times larger than t_p, at which agglomeration has ceased. Temperature shows a patchy behaviour with maxima located at the ring positions because it is at these positions where heat generation by non-adiabatic processes (chemical reactions, phase change, agglomeration) becomes more intense and heat accumulates before diffusing. The maxima decrease as the distance from the membrane dividing both electrolytes because at these positions, the concentrations and rates and consequently the kinetic activity and the resulting heat generation, have diminished.

3.5. Conclusions: From molecules to macroscopic patterns via dissipation

In this chapter, we have proposed a model to explain the formation of Liesegang patterns. The model involves two fundamental processes which trigger the formation of the structures: building block activation and self-assembly. We have not considered disassembly processes because in the case we study, redisolution of the structures is not significant. The model proposes that NESA processes yield different types of hierarchical structures that differ in their precursors and micro-architecture. We have identified two types of structures: first and second-order structures which correspond to the soluble nuclei (or the solid nuclei precursor) and to the solid agglomerate. The entropy production rate (Eq. 3-22) can be used for a thermodynamic description of the pattern formation.

The results obtained show not only that the proposed model reproduces the main characteristics of Liesegang rings with high accuracy (see Fig. **3-2**, and Fig. **3-3**), but also provides new insights into the dynamical evolution of NESA structures. Our model enables us to rationalize how from non-homogeneous initial conditions, a transient organization process involving the formation of self-assembled structures may give rise to macroscopic spatial patterns. Moreover, our model shows a patchy behaviour for the temperature (see Fig. **3-4**) with maxima at the ring positions because of the heat released by the NESA processes at these positions, especially in the case of a phase transition (process 3)[74] and crystal growth (process 4) [75].

Although we have discussed in particular the case of Liesegang pattern formation brought about by NESA process, our model could also be applied to describe NESA processes producing mesoparticles and other spatial patterns. For instance, the redisolution of solids in Liesegang patterns which leads to the formation of different patterns such as lenses[10] or spots[76], may be understood as a NESA systems in which activation of BB and assembly and disassembly processes may take place.

Currently in material science, there is a high interest in the design and control of structures to yield mesoparticles at a well-defined size [26]. Conversely, the control of the size of gold nanoparticles allows for then regulation of the catalytic activity of a reactive system [54]. Recently, optical sensors, known as plasmonic nanosensors, based on metal nano-particle arrays and single nanoparticles have shown a high potential as analytical tools in chemistry [77], where more stable and uniform nano-particles (in shape and size) may improve the sensing. Additionally, efforts have been made to develop novel synthesis methods based on the bottom-up approach to produce organic nanomaterials with well-defined shapes for potential medical applications [52, 53]. Pattern features and particle size modifications can be controlled by electric fields and thermal gradients. The approach presented in this chapter describing how activation, self-assembly and disassembly process may transform BB into precursors and subsequently into self-assembled structures can contribute to a better understanding of pattern formation processes in natural and synthetic systems.

Bibliography

[1] Andrés Arango-Restrepo, Daniel Barragán, and J Miguel Rubi. Nonequilibrium self-assembly induced liesegang rings in a non-isothermal system. *PCCP*, 20(7):4699–4707, 2018.

[2] JA Scott Kelso. *Dynamic patterns: The self-organization of brain and behavior*. MIT press, 1997.

[3] Donald S Coffey. Self-organization, complexity and chaos: the new biology for medicine. *Nature medicine*, 4(8):882–885, 1998.

[4] Scott Camazine. *Self-organization in biological systems*. Princeton University Press, 2003.

[5] VI Elokhin, AV Matveev, and VV Gorodetskii. Self-oscillations and chemical waves in co oxidation on pt and pd: Kinetic monte carlo models. *Kinetics and Catalysis*, 50(1):40–47, 2009.

[6] M. C. Cross and P. C. Hohenberg. Pattern Formation Outside of Equilibrium. *Rev. Mod. Phys.*, 65(3):851–1112, 1993.

[7] Marek Orlik. Self-organization in nonlinear dynamical systems and its relation to the materials science. *Journal of Solid State Electrochemistry*, 13(2):245–261, 2009.

[8] Raphael Ed Liesegang. Die achate. In *Silicate*, pages 186–190. Springer, 1914.

[9] Harry W Morse and George W Pierce. Diffusion and supersaturation in gelatine. *Physical Review (Series I)*, 17(3):129, 1903.

[10] Rabih F. Sultan. Propagating fronts in periodic precipitation systems with redissolution. *PCCP*, 4(8):1253–1261, 2002.

[11] Samar Sadek, Rabih Sultan, and I Lagzi. Precipitation patterns in reaction-diffusion systems. *Research Signpost, Trivandrum*, page 1, 2010.

[12] István Lagzi. Formation of Liesegang patterns in an electric field Â´. *Phys. Chem. Chem. Phys.*, 4:1268–1270, 2002.

[13] Stoyan K. Smoukov, István Lagzi, and Bartosz A. Grzybowski. Independence of Primary and Secondary Structures in Periodic Precipitation Patterns. *J. Phys. Chem. Lett.*, 2(4):345–349, 2011.

[14] Lara Mandalian and Rabih Sultan. Fractal structures in pbf 2/pb (no 3) 2 precipitate systems. *Collection of Czechoslovak chemical communications*, 67(12):1729–1742, 2002.

[15] András Volford, Ferenc Izsák, Mátyás Ripszám, and István Lagzi. Pattern formation and self-organization in a simple precipitation system. *Langmuir*, 23(3):961–4, 2007.

[16] RV Suganthi, EK Girija, S Narayana Kalkura, HK Varma, and A Rajaram. Self-assembled right handed helical ribbons of the bone mineral hydroxyapatite. *Journal of Materials Science: Materials in Medicine*, 20(1):131, 2009.

[17] IT Bensemann, M Fialkowski, and BA Grzybowski. Wet stamping of microscale periodic precipitation patterns. *The Journal of Physical Chemistry B*, 109(7):2774–2778, 2005.

[18] Bartosz A Grzybowski, Kyle J M Bishop, Christopher J Campbell, Marcin Fialkowski, and Stoyan K Smoukov. Micro- and nanotechnology via reaction-diffusion. *Soft Matter*, 1:114–128, 2005.

[19] István Lagzi. Controlling and engineering precipitation patterns. *Langmuir*, 28(7):3350–3354, 2012.

[20] Rabih Sultan and Peter Ortoleva. Periodic and aperiodic macroscopic patterning in two precipitate post-nucleation systems. *Physica D: Nonlinear Phenomena*, 63(1-2):202–212, 1993.

[21] Mazen Al-Ghoul. Generalized hydrodynamics of reaction-diffusion systems and dissipative structures. *Philos. Trans. Royal Soc. A*, 362(1821):1567–81, 2004.

[22] Hideki Nabika, Mami Sato, and Kei Unoura. Liesegang patterns engineered by a chemical reaction assisted by complex formation. *Langmuir*, 30(18):5047–5051, 2014.

[23] D Krishna Kumar and Jonathan W Steed. Supramolecular gel phase crystallization: orthogonal self-assembly under non-equilibrium conditions. *Chem. Soc. Rev.*, 43(7):2080–2088, 2014.

[24] Rita Tóth, Roché M. Walliser, István Lagzi, Florent Boudoire, Marcel Düggelin, Artur Braun, Catherine E. Housecroft, and Edwin C. Constable. Probing the mystery of Liesegang band formation: revealing the origin of self-organized dual-frequency micro and nanoparticle arrays. *Soft Matter*, 12(40):8367–8374, 2016.

[25] Roché M Walliser, Rita Tóth, István Lagzi, Daniel Mathys, Laurent Marot, Artur Braun, Catherine E Housecroft, and Edwin C Constable. Understanding the formation of aligned, linear arrays of Ag nanoparticles. *RSC Adv.*, 1(c):28388–28392, 2016.

[26] Roché M. Walliser, Florent Boudoire, Eszter Orosz, Rita Tóth, Artur Braun, Edwin C. Constable, Zoltán Rácz, and István Lagzi. Growth of Nanoparticles and Microparticles by Controlled Reaction-Diffusion Processes. *Langmuir*, 31(5):1828–1834, 2015.

[27] Hazar El-Batlouni, Houssam El-Rassy, and Mazen Al-Ghoul. Cosynthesis, coexistence, and self-organization of α-and β-cobalt hydroxide based on diffusion and reaction in organic gels. *The Journal of Physical Chemistry A*, 112(34):7755–7757, 2008.

[28] L. Mandalian, M. Fahs, M. Al-Ghoul, and R. Sultan. Morphology, particle size distribution, and composition in one- and two-salt metal oxinate Liesegang patterns. *J. Phys. Chem. B*, 108(4):1507–1514, 2004.

[29] Mazen Al-Ghoul, Manal Ammar, and Rabih O Al-Kaysi. Band propagation, scaling laws and phase transition in a precipitate system. I: Experimental study. *J. Phys. Chem. A*, 116(18):4427, 2012.

[30] Wolfgang Beckmann. *Crystallization: basic concepts and industrial applications*. John Wiley \& Sons, 2013.

[31] Mahmoud M Ayass, Andrew Abi Mansour, and Mazen Al-Ghoul. Alternating metastable/stable pattern in the mercuric iodide crystal formation outside the ostwald rule of stages. *J. Phys. Chem. A*, 118(36):7725–31, 2014.

[32] Konstantin V Tretiakov, Igal Szleifer, and Bartosz A Grzybowski. The Rate of Energy Dissipation Determines Probabilities of Non- equilibrium Assemblies. *Angew. Chem. int. Ed*, 52:10304–10308, 2013.

[33] Marcin Fialkowski, Kyle J M Bishop, Rafal Klajn, Stoyan K Smoukov, Christopher J Campbell, and Bartosz A Grzybowski. Principles and Implementations of Dissipative (Dynamic) Self-Assembly. *J.Phys. Chem. B*, 110:2482–2496, 2006.

[34] Susan A. P. van Rossum, Marta Tena-Solsona, Jan H. van Esch, Rienk Eelkema, and Job Boekhoven. Dissipative out-of-equilibrium assembly of man-made supramolecular materials. *Chem. Soc. Rev.*, 46:5519–5535, 2017.

[35] Alessandro Sorrenti, Jorge Leira-Iglesias, Albert J Markvoort, Tom FA de Greef, and Thomas M Hermans. Non-equilibrium supramolecular polymerization. *Chem. Soc. Rev.*, 2017.

[36] Job Boekhoven. *Multicomponent and Dissipative Self-Assembly Approaches: toward functional materials*. PhD thesis, Delft University of Technology, 2012.

[37] Job Boekhoven, Aurelie M. Brizard, Krishna N. K. Kowlgi, Ger J. M. Koper, Rienk Eelkema, and Jan H. van Esch. Dissipative Self-Assembly of a Molecular Gelator by Using a Chemical Fuel. *Angew. Chem.*, 122(28):4935–4938, 2010.

[38] Jinxing Jiang and Kenji Sakurai. Formation of Ultrathin Liesegang Patterns. *Langmuir*, 32(36):9126–9134, 2016.

[39] Ferenc Molnár, Ferenc Izsák, and István Lagzi. Design of equidistant and revert type precipitation patterns in reaction-diffusion systems. *Phys. Chem. Chem. Phys.*, 10(17):2368–73, 2008.

[40] M. Al-Ghoul and R. Sultan. Front propagation in patterned precipitation. 2. Electric effects in precipitation-dissolution patterning schemes. *J. Phys. Chem. A*, 107(2):1095–1101, 2003.

[41] István Lagzi and Daishin Ueyama. Pattern transition between periodic Liesegang pattern and crystal growth regime in reaction-diffusion systems. *Chem. Phys. Lett.*, 468(4-6):188–192, 2009.

[42] István Lagzi, Bartlomiej Kowalczyk, and Bartosz a. Grzybowski. Liesegang rings engineered from charged nanoparticles. *J. Am. Chem. Soc.*, 132(1):58–60, 2010.

[43] J.D. Halley and D.A Winkler. Consistent Concepts of Self-organization and Self-assembly. *Complexity*, 14(2):10–17, 2008.

[44] Ilya Prigogine and G Nicolis. *Self organization in non equilibrium systems*. John wiley & sons, 1 edition, 1977.

[45] Mazen Al-ghoul and Byung Chan Eu. Hyperbolic reaction-diffusion equations and irreversible thermodynamics. *Physica D*, 90:119–153, 1996.

[46] Andrew R Hirst, Sangita Roy, Meenakshi Arora, Apurba K Das, Nigel Hodson, Paul Murray, Stephen Marshall, Nadeem Javid, Jan Sefcik, Job Boekhoven, Jan H Van Esch, Stefano Santabarbara, Neil T Hunt, and Rein V Ulijn. Biocatalytic Induction of Supramolecular Order. *Nat. Chem*, 2(12):1089–1094, 2010.

[47] Job Boekhoven, Jos M Poolman, Chandan Maity, Feng Li, Lars Van Der Mee, Christophe B Minkenberg, Eduardo Mendes, Jan H Van Esch, and Rienk Eelkema. Catalytic Control Over Supramolecular Gel Formation. *Nat. Chem*, 5(5):433–437, 2013.

[48] Linda N Lucas, Jan van Esch, Richard M Kellogg, and Ben L Feringa. Photocontrolled self-assembly of molecular switches. *Chem. Commun.*, (8):759–760, 2001.

[49] Jaap J.D De Jong. Light-Driven Dynamic Pattern Formation. *Angew. Chem. int. Ed*, 44:2373–2376, 2005.

[50] Rafal Klajn, Kyle J M Bishop, and Bartosz A Grzybowski. Light-controlled self-assembly of reversible and irreversible nanoparticle suprastructures. *PNAS*, 104(25):10305–10309, 2007.

[51] Prateek K. Jha, Vladimir Kuzovkov, Bartosz A. Grzybowski, and Monica Olvera de la Cruz. Dynamic self-assembly of photo-switchable nanoparticles. *Soft Matter*, 8(1):227–234, 2012.

[52] Larken E Euliss, Julie A Dupont, Stephanie Gratton, Joseph Desimone, James D Martin, and Stephanie Gratton. Imparting size , shape , and composition control of materials for nanomedicine. *Chem. Soc. Rev.*, 35:1095–1104, 2006.

[53] Andrew Z Wang, Robert Langer, and Omid C Farokhzad. Nanoparticle Delivery of Cancer Drugs. *Annu. Rev. Med*, 63:185–198, 2012.

[54] Yanhu Wei, Dow Chemical, Shuangbing Han, Dow Corning, and Shuangbing Han. Photoswitchable Catalysis Mediated by Dynamic Aggregation of Nanoparticles. *J. Am. Chem. Soc.*, 132:11018–11020, 2010.

[55] Stefan C. Müller and John Ross. Spatial structure formation in precipitation reactions. *Journal of Physical Chemistry A*, 107(39):7997–8008, 2003.

[56] Michele Flicker, John Ross, Michele Flickert, and John Ross. Mechanism of chemical instability for periodic phenomena *. *The Journal of Chemical Physics*, 60(9):3458–3465, 1974.

[57] N Kanniah. Revert and Direct Liesegang Phenomenon of Silver Iodide : Factors Influencing the Transition Point Liesegang Rings. *J. Colloid Interface Sci.*, 94(2), 1983.

[58] Wolfgang Ostwald. Zur theorie der liesegang'schen ringe. *Kolloid-Zeitschrift*, 36(1):380–390, 1925.

[59] A Büki, É Kárpáti-Smidróczki, and M Zrínyi. Computer simulation of regular liesegang structures. *The Journal of chemical physics*, 103(23):10387–10392, 1995.

[60] Mazen Al-Ghoul and Tarek Ghaddar. Theoretical modeling of front propagation of cds nanoparticles in a gel. In *Journal of Nano Research*, volume 11, pages 19–24. Trans Tech Publ, 2010.

[61] M. Al-Ghoul and R Sultan. Front Propagation in Patterned Precipitation. 1. Simulation of a Migrating Co(OH) 2 Liesegang Pattern. *J. Phys. Chem. A*, 105(34):8053–8058, 2001.

[62] Maysam Msharrafieh, Mazen Al-Ghoul, Hazar Batlouni, and Rabih Sultan. Front propagation in patterned precipitation. 3. Composition variations in two-precipitate stratum dynamics. *The journal of physical chemistry. A*, 111(30):6967–76, 2007.

[63] Zoltan Racz. Formation of Liesegang patterns. *Physica A*, 274(1-2):50–59, 1999.

[64] István Lagzi. Simulation of liesegang patterns: Effect of reversible complex formation of precipitate. *The Journal of Physical Chemistry B*, 107(49):13750–13753, 2003.

[65] Mazen Al-Ghoul and Byung Chan Eu. Hyperbolic reaction-diffusion equations and irreversible thermodynamics: II. Two-dimensional patterns and dissipation of energy and matter. *Physica D: Nonlinear Phenomena*, 97:531–562, 1996.

[66] Mazen Al-Ghoul and Byung Chan Eu. Hyperbolic Reactionâˆ'Diffusion Equations, Patterns, and Phase Speeds for the Brusselator. *The Journal of Physical Chemistry*, 100(49):18900–18910, 1996.

[67] Carlos Rodriguez-navarro, Olga Cazalla, Kerstin Elert, and Eduardo Sebastian. Liesegang pattern development in carbonating traditional lime mortars. *Proc. Math. Phys. Eng. Sci.*, pages 2261–2273, 2002.

[68] JACK A Smith and CR Metz. Spectrophotometric determination of the chromate-dichromate equilibrium constant. *Proceedings of the Indiana Academy of Science*, 80:159–163, 1970.

[69] D Reguera, JM Rubi, and JMG Vilar. The mesoscopic dynamics of thermodynamic systems. *J. Phys. Chem. B*, 109(46):21502–21515, 2005.

[70] Ignacio Pagonabarraga and J. M. Rubi. Fluctuating hydrodynamics approach to chemical reactions. *Physica A*, 237:205–219, 1997.

[71] G. J M Koper, J. Boekhoven, W. E. Hendriksen, J. H. Van Esch, R. Eelkema, I. Pagonabarraga, J. M. Rubí, and D. Bedeaux. The Lost Work In Dissipative Self-Assembly. *Int. J. Thermophys.*, 34(7):1229–1238, 2013.

[72] Sybren Ruurds De Groot and Peter Mazur. *Non-equilibrium thermodynamics*. Dover Publications Inc., 1985.

[73] Yukikazu Takeoka and Masayoshi Watanabe. Tuning Structural Color Changes of Porous Thermosensitive Gels Through Quantitative Adjustment of the Cross-Linker in Pre-Gel Solutions. *Langmuir*, 19(22):9104–9106, 2003.

[74] F Elif Genceli Güner, Johan Wåhlin, Mogens Hinge, and Signe Kjelstrup. The temperature jump at a growing ice–water interface. *Chemical Physics Letters*, 622:15–19, 2015.

[75] F Elif Genceli, Marcos Rodriguez Pascual, Signe Kjelstrup, and Geert-Jan Witkamp. Coupled heat and mass transfer during crystallization of mgso4· 7h2o on a cooled surface. *Crystal Growth and Design*, 9(3):1318–1326, 2009.

[76] Malak Dayeh, Manal Ammar, and Mazen Al-Ghoul. Transition from rings to spots in a precipitation reaction–diffusion system. *RSC Advances*, 4(104):60034–60038, 2014.

[77] Jeffrey N Anker, W Paige Hall, Olga Lyandres, Nilam C Shah, Jing Zhao, and Richard P Van Duyne. Biosensing with plasmonic nanosensors. *Nat. Mater.*, 7:442–453, 2008.

PART II. Non-equilibrium self-assembly from dissipation

4. Modelling non-equilibrium self-assembly from dissipation

Non-equilibrium self-assembly is ubiquitous in physico-chemical and biological systems, and manifests itself at different scales, ranging from the molecular to the cosmological. The formation of microtubules, gels, cells and living beings among many others takes place through self-assembly under nonequilibrium conditions. We propose a general thermodynamic non-equilibrium model to understand the formation of assembled structures such as gels and Liesegang patterns and at the same time able to describe the kinetics and the energetics of the structure formation process. The model is supported for a global mechanism to obtain self-assembled structures from building blocks via activation, deactivation, assembly, and disassembly processes. It is proposed that the resulting structures can be characterised by a structural parameter. Our model may contribute to a better understanding of non-equilibrium self-assembly processes and give deeper insight as to how to obtain a specific structural architecture to materials, such as hydrogels which are of great importance in the design of advanced devices and novel materials.

This chapter was published in *the Journal of Molecular Physics*, **118**, e1761036, (2020). Ref.[1]

4.1. Introduction: Self-assembly process

Self-assembly (SA) is the process through which a disordered set of constituents interact with one another to form organised structures [2]. These constituents, the building blocks (BB), are the smallest discrete entities required in order to build a structure and they can be as small as atoms or as large as planets [3]. Understanding the molecular nature of the BB as to their chemical identity, geometry and charge is crucial to determine the architecture of emerging structures and the nature of the processes involved in the synthesis of materials[4].

Self-assembly leads to the formation of stationary, kinetically trapped or even to equilibrium structures. As a non equilibrium process, self-assembly carries with it entropy production and thus energy dissipation[5]. How energy dissipation may account for the emergence of ordered structures from a set of disordered components, and how the formation of the structures is governed by the laws of thermodynamics [6, 7] remains a question yet to be answered.

Currently, there is a great deal of interest in the understanding and manipulation of non-equilibrium self-assembly (NESA) structures such as hydrogels for medical applications [8, 9, 10, 11, 12, 13, 14, 15, 16] and self-assembled particles for technological applications [17, 18, 19]. In material science, there is considerable interest in obtaining structures with a given nano-, meso-, and micro-architecture in gel media [20]. Therefore, the structural architecture of the gel, as well as its porosity and its capacity of re-configuration under the action of external forces, are key to determining the type of emerging structures [21, 22].

The lack of a general thermodynamic framework for the description of self-assembled structures under non-equilibrium conditions has promoted the development of computational approaches. These approaches, however, are not always easy to implement since the number of particles needed to explain the formation of the structures is usually very large [23, 24, 25, 26, 27]. Kinetic models based on balance equations [28], hydrodynamic equations [29], and mesoscopic non-equilibrium thermodynamic formalism [30, 31, 32] provide ways to understand the dynamics of the formation of NESA structures. Thermodynamic approaches based on information and Gibbs entropies have also been proposed to characterise and understand NESA processes and their resulting assembled structures [33, 34, 35, 36].

In this chapter, we propose a general formalism to compute the entropy production at meso-scale, and to prove that self-assembled structures emerge at particular values of this quantity. We show that the formation kinetics of self-assembled materials can be described through the evolution of a structural parameter able to characterise the intermediate states of the process. This proposal may contribute to a better understanding of the kinetics of NESA processes, and may be useful to design specific structural architectures such as in hydrogels important in the synthesis of advanced materials mediated by Liesegang banding.

4.2. Methods: Mechanism and model

4.2.1. Mechanism

The formation of physico-chemical and biological non-equilibrium self-assembled structures involves activation [37, 38, 39], assembly and disassembly processes [40, 41, 42]. Molecular activation of the BB through a chemical substance provides the energy necessary to trigger the self-assembly process. BB and intermediate structures can also become activated when concentration, temperature or size of the structure surpass a certain threshold value, by phase-changes, by light [39] or by applying a rotating magnetic field [23].

Structure formation kinetics can be modelled by the evolution in time of a reaction Γ-coordinate from the initially disordered state to the final assembled structure. The sequence of intermediate structures parametrized by the Γ-coordinate form a unique trajectory leading to the final structure. The architecture of the structures can be characterised by a set of structural parameters η such as sphericity, radius of gyration, maximum length, porosity, average orientation and inter-connectivity among others. The entropy production, and therefore the energy dissipation, are both functions of the independent parameters η and Γ [43]. Furthermore, in our thermodynamic formalism, the relation between structural parameter and entropy production is bijective.
Fig.**4-1** shows a sketch of the gelation and Liesegang banding mechanisms. In the rows, we represent initial (Fig.**4-1**(a)), intermediate (Fig.**4-1**(b)) and final (Fig.**4-1**(c)) states. The columns show two possible final states of both processes. Gelation is triggered by chemical activation of the BB which is followed by the formation of single fibers. These fibers are subsequently activated by van der Waals interactions bringing about a fiber aggregate, the gel. For Liesegang banding, the process begins with the formation of nucleus which aggregates to form the solid particles of variable size integrating the Liesegang bands. A thorough description of both processes can be found in [32] and [42].

For gelation (see first and second columns in Fig. **4-1**) the structural parameter N is the maximum length of the fibers composing the gel. In Fig.**4-1**(b), we observe that for $N = N_1$ intermediate fibers are longer than those for $N = N_2$. Fig.**4-1**(c) shows that a more interconnected and low-porosity gel emerges when the value of the structural parameter is N_1. For Liesegang banding, the structural parameter ω accounts for the homogeneity in the size of solid particles composing the different rings. In Fig.**4-1**(b), we observe how at $\omega = \omega_1$, the variation in size of the structures is more significant than at $\omega = \omega_2$. We can thereby see in Fig.**4-1**(c) that rings are more homogeneous at ω_2 than at ω_1.

4.2.2. Thermodynamic model

Entropy production in NESA processes

The formation of NESA structures is a dissipative process that consumes energy and matter. The entropy production rate is a measure of the amount of energy dissipated and may give information about the kinetics of the process and the type of structures formed.

We consider that the state of the system is characterised by the probability distribution $p(\Gamma, t; \eta)$ and that at

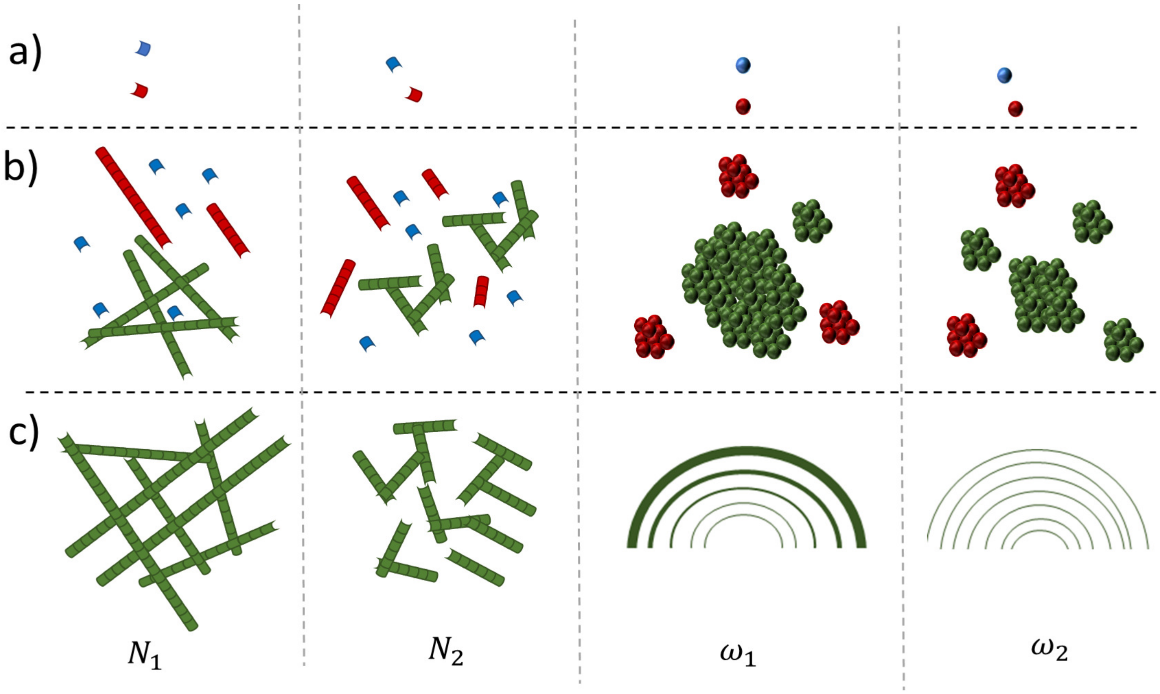

Fig. 4-1.: Sketch of the formation of NESA structures. The values of the structural parameters N_1 and N_2 correspond to two different maximum lengths of the fibers giving rise to different porosities of the gel while ω_1 and ω_2 account for the homogeneity of the sizes of the structures composing the different Liesegang rings. The process follows a unique spatio-temporal trajectory with different intermediate structures. a) Deactivated (blue) and activated (red) BB. b) Intermediate structures: fibers (red cylinders), agglomerated fibers (green fibers), nuclei (red BB agglomerated), solid particle (green agglomerated nuclei). c) Final NESA structures: two typical gel structures and two typical Liesegang ring configurations.

time t the system has a configuration Γ [44, 31] for a given value of the parameter η. The final structural architecture can be determined from the knowledge of the entropy production of the assembly process in terms of the structural parameter η. Entropy variations in the process δS are given by

$$\delta S(t;\eta) = -\frac{1}{T}\int_{\Gamma}\mu(\Gamma,t;\eta)\delta p(\Gamma,t;\eta)d\Gamma \tag{4-1}$$

with μ the chemical potential of the system. To compute the entropy production rate σ associated to the formation of a structure, we take the time derivative of Eq.(4-1) and use the probability conservation law $\frac{\partial p}{\partial t} = -\nabla_{\Gamma}\cdot\vec{J}$ in which $\vec{J}$ is the probability current defined in the space of the reaction Γ-coordinate. We then obtain

$$\sigma(t;\eta) = -\frac{1}{T}\int_{\Gamma}\vec{J}(\Gamma,t;\eta)\cdot\nabla_{\Gamma}\mu(\Gamma,t;\eta)d\Gamma \tag{4-2}$$

where we have used the fact that the current at the surface of the $\Gamma-$coordinate vanishes. Considering that the components of the reaction coordinate are independent and normalised to one [45], the entropy production rate is found to be

$$\sigma(t;\eta) = -\frac{1}{T}\sum_j \int_0^1 J_j(\Gamma_j,t;\eta)\frac{\partial \mu_j(\Gamma_j,t;\eta)}{\partial \Gamma_j}d\Gamma_j \tag{4-3}$$

If we now neglect cross-couplings between currents and their conjugate chemical potential derivatives [32] because it is not possible, for instance, that a building block be assembled and disassembled simultaneously in the same structure, we obtain the current J_j in terms of its conjugated thermodynamic force

$$J_j(\Gamma_j,t;\eta) = -\frac{L_j}{T}\left(\frac{\partial \mu_j(\Gamma_j,t;\eta)}{\partial \Gamma_j}\right)_{\Gamma_{i\neq j}} \tag{4-4}$$

where $L_j = D_j p/R$ is an Onsager coefficient, with D_j a diffusion coefficient in process j. This expression can be used in the continuity equation to obtain the mass balance for each constituent of the system.

Kinetic equations

We consider that the state of the i^{th} constituent in the system at time t is described by the probability distribution $p_i(\boldsymbol{r},\boldsymbol{\Gamma}_i,t)$, where $\boldsymbol{r}$ is the position vector and k the number of uncoupled processes involved in the formation of the structures ($\Gamma_{i,j}$). The continuity equation is expressed as

$$\frac{\partial p_i(\boldsymbol{r},\boldsymbol{\Gamma}_i,t;\eta)}{\partial t} = -\nabla_{\boldsymbol{r}}\cdot \boldsymbol{J}_i^{(\boldsymbol{r})}(\boldsymbol{r},t) - \sum_{j=1}^{k}\frac{\partial}{\partial \Gamma_{i,j}}J_{i,j}(\boldsymbol{r},\Gamma_{i,j},t;\eta), \tag{4-5}$$

where $\boldsymbol{J}_i^{(\boldsymbol{r})}$ is the diffusion current and $J_{i,j}$ the flux of the i^{th} constituent in the j^{th} process. Performing a coarse-graining description that eliminates the $\boldsymbol{\Gamma}_i$-coordinate [42], we then obtain the continuity equation in terms of position and time

$$\frac{\partial p_i(\boldsymbol{r},t;\eta)}{\partial t} = -\nabla_{\boldsymbol{r}}\cdot \boldsymbol{J}_i^{(\boldsymbol{r})}(\boldsymbol{r},t) - \sum_{j=1}\upsilon_{ij}\dot{r}_j(\boldsymbol{r},t;\eta). \tag{4-6}$$

Here $\dot{r}_j$ is the rate of the NESA process j involving the constituent i and υ is a stoichiometric coefficient. At this point, we highlight the fact that the processes along the coordinates Γ_i take place through energetic barriers. The shape of these depends on the standard chemical potential of the states, the activation energy of each sub-process and on the nature of the intermediate states (metastable and unstable) of the particular NESA process [46, 42].

When the activation energies are sufficiently high, the sub-processes along the Γ_i coordinates are quasi-stationary, i.e. the rate does not depend on the reaction coordinate [45]. In this case, we can obtain the expression for the rate in terms of the fugacity difference $\Delta_j\mathfrak{z}$ between the initial and the final states,

$$\dot{r}_j(t;\eta) = \frac{D_j}{\int_0^1 \exp(-\phi(\Gamma_j)/RT)))d\Gamma_j}\Delta_j\mathfrak{z}(t;\eta) \tag{4-7}$$

in which $\mathfrak{z} = exp(\mu/RT)$ is the fugacity and $\phi(\Gamma_j)$ the potential barrier. The rate can also be written as $\Delta_j\mathfrak{z} \approx \exp(\mu_r^0/RT)c_r - \exp(\mu_p^0/RT)c_p$, with c_r and c_p the reactant and product concentrations [47] in accordance with the law of mass action.

4.3. Results and Discussions

In this section, we will apply our non-equilibrium self-assembly model to two particular situations: gelation and Liesegang banding processes [41, 20]. The model is based on the analysis of the dissipation in the process and in the fact that structures emerge at particular values of the entropy production.

In Fig. **4-2**, we show how the entropy and the energy of the structures vary along the self-assembly process studied. For gelation, Fig. **4-2**(a), we observe that the most interconnected and then the less porous gel emerges at high values of the entropy produced and low values of the entropy and energy. For Liesegang banding, Fig. **4-2** (b), the most uniform (same thickness) Liesegang bands appear at high values of the entropy produced but, unlike gelation, at high values of energy and entropy.

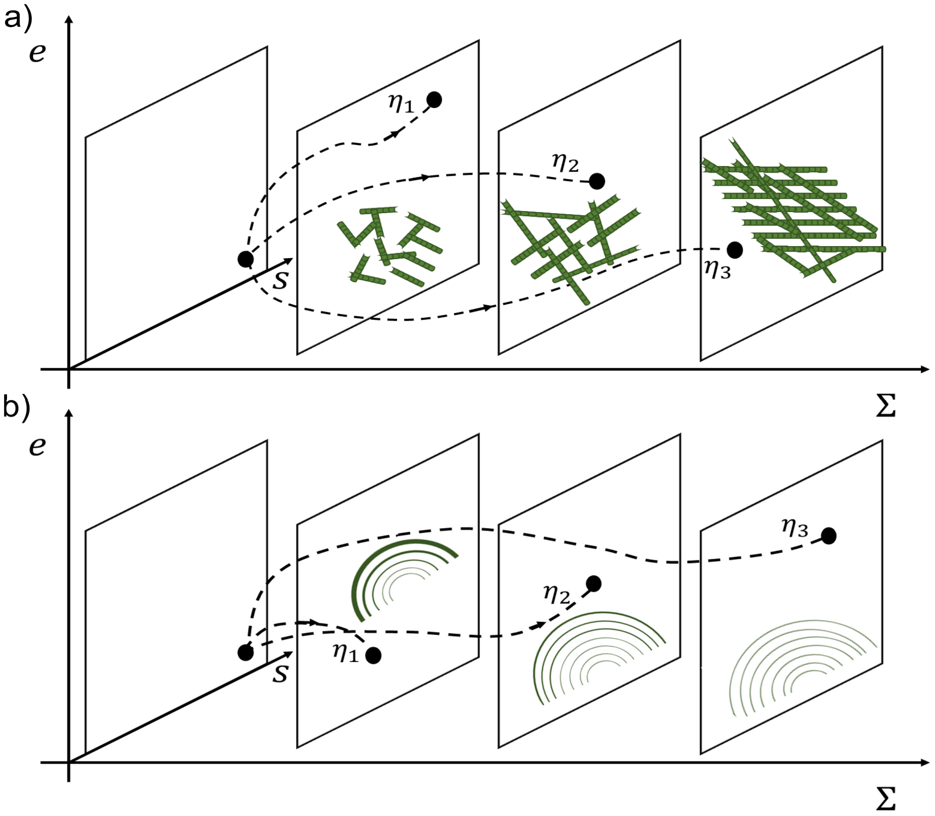

Fig. 4-2.: Sketch for energetics of NESA structures for three typical formation pathways of the structural parameter η. Black points represent the values of the specific energy (e) and entropy (s) of the structure for a given value of the total entropy produced (Σ) in the formation process. Dashed lines illustrate the possible trajectories followed by the system in the formation of each structure reaching a specific $e-s$ planes for 3 values of the total entropy produced. Each plane characterises: a) gel architecture having different inter-connectivity and porosity; b) Liesegang rings for different structure size distributions.

For gelation, we have solved Eq.4-6 by considering Eq.4-7 and while neglecting the spatial diffusion term for all the possible constituents of the system. To calculate the concentrations c_i (or probabilities p_i) and from these thereby obtain the specific energy $e(N)$, specific entropy $s(N)$ and entropy production $\sigma(N)$, we have solved the resulting system of differential equations numerically. The specific entropy has been computed from the expression $s(N) = -R\sum_i^N p_i(N)\ln p_i(N)$, with R the gas constant while the specific energy has been obtained from $e(N) = \sum_i^N p_i(N)\mu_i^0 + Pv(N)$ where the specific volume of the system $v(N)$ depends on the degree of inter-connectivity of the fibers and with μ_i^0 as the standard chemical potential of the constituent i.The inter-connectivity of gel fibers is closely related to porosity which depends on concentration and on the size and average orientation of the fibers [32]. The total entropy produced in gelation (Σ_g) is the integral over time of the entropy production rate $\sigma(N)$:

$$\Sigma_g(N) = \int_0^\infty \sigma(t;N)dt \tag{4-8}$$

For Liesegang banding, we use Eq.4-6 (and Eq.4-7) for each component to describe the reaction-diffusion phenomena taking place in the formation of the rings. To calculate the concentrations c_i or probabilities p_i, we have numerically solved the corresponding system of differential equations, and thereby obtaining the specific energy defined as $e(\omega) \approx \sum_i p_i(\omega)h_i^0 + 4\pi\gamma r_p(\omega)^2$ and the specific entropy defined as $s(\omega) = -R\sum_i p_i(\omega)\ln p_i(\omega)$, where h_i^0 is the standard specific enthalpy and r_p the average particle radius integrating the rings (depending on the structural parameter ω, $r_p(\omega)$). We have also computed the total entropy produced, in Liesegang processes ($\Sigma_L(\omega)$):

$$\Sigma_L(\omega) = \int_0^\infty \int_{\boldsymbol{r}} \sigma(\boldsymbol{r},t;N)d\boldsymbol{r}dt \tag{4-9}$$

In Fig. **4-3**, we present the total entropy produced, computed from Eq.(4-8) and Eq.(4-9), as a function of the structural parameters. The dashed line shows a tendency of the numerical results (black dots) obtained from Eq.(4-6) for each constituent. To better visualise the self-assembly process, we include insets for two values of the structural parameter, N_2 and N_1. It is observed that the intricate micro-structure of the gel emerges at high values of the structural parameter. In Fig. **4-3**(b), the continuous line represents the numerical results obtained from Eq.(4-6). The insets illustrate the form of the structures for two values of ω_1 and ω_2. At low values of ω more homogeneous bands appear that have the same thickness. The gray filled circle represents an experimental result obtained in Ref.[20].

Gelation and Liesegang banding can take place simultaneously as has been shown for example in the case in which the gel is deformed by the action of mechanical stresses while Liesegang patterns form in the gel [48]. Currently, there is a great deal of interest in the control of micro-architecture and porosity of hydrogel structures for medical applications [8, 9, 10, 11, 12, 13], and to the synthesis of self-assembled particles for technological purposes [17, 18, 19]. In Liesegang ring formation, the BB and intermediate structures diffuse, react and agglomerate in a gel medium wherein the nature and the architecture play a key role in formation kinetics. Gelation thus determines the formation of Liesegang rings and their shape. How to model the movement of the constituents, intermediate structures, and other components through the gel under the action of a driven force such as a chemical potential difference, a temperature gradient or an electric field still remains an open problem. The model has to integrate the architecture of the gel with that of the formed structures to describe the motion of the components through the gel medium.

The model presented here accounts for the transformation of BB into precursors and subsequently into

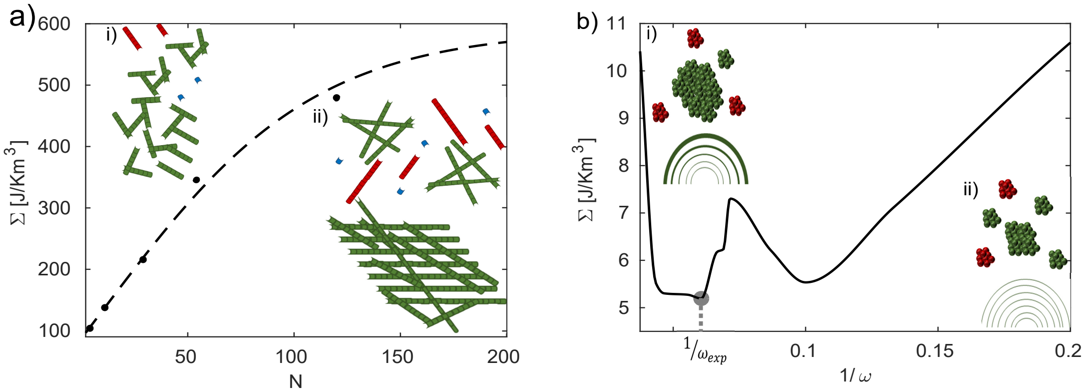

Fig. 4-3.: Total entropy Σ produced as a function of the structural parameter. a) Σ in gelation computed from Eq.4-3. Black dots stand for numerical results for the system of differential equations, resulting from considering Eq.4-6 for each constituent.Dashed line gives the tendency of the numerical results. Each dot represents a result for a value of N. Insets i) and ii) illustrate the intermediate and gel structure for N_2 and N_1 respectively. b) Σ in Liesegang ring formation computed from Eq.4-3. The continuous black line represents our numerical results for the system of differential equations describing the dynamic evolution of the concentration of the constituents in the system (Eq.4-6). This line is elaborated by solving the model for several values of ω. The grey filled circle is the estimated experimental result for the structural parameter obtained in Ref. [20].

self-assembled structures can contribute to a better understanding of the self-assembly kinetics in natural and synthetic systems frequently found in biology and biomedicine as well as in advanced materials. The connection found between the entropy produced and the type of structures formed may provide an answer to the important question of why a set of disordered units may give rise to a determined self-assembled structure.

Bibliography

[1] A. Arango-Restrepo, Daniel Barragán, and J. Miguel Rubi. Modelling non-equilibrium self-assembly from dissipation. *Molecular Physics*, 118(9-10):e1761036, 2020.

[2] Bartosz A Grzybowski, Christopher E Wilmer, Jiwon Kim, Kevin P Browne, and Kyle J.M Bishop. Self-assembly : from crystals to cells. *Soft Matter*, 5:1110–1128, 2009.

[3] George M Whitesides and Bartosz Grzybowski. Self-assembly at all scales. *Science*, 295(5564):2418–2421, 2002.

[4] Stephen Mann. Self-assembly and transformation of hybrid nano-objects and nanostructures under equilibrium and non-equilibrium conditions. *Nat. Mater.*, 8(10):781–792, 2009.

[5] Susan A. P. van Rossum, Marta Tena-Solsona, Jan H. van Esch, Rienk Eelkema, and Job Boekhoven. Dissipative out-of-equilibrium assembly of man-made supramolecular materials. *Chem. Soc. Rev.*, 46:5519–5535, 2017.

[6] Marcin Fialkowski, Kyle J M Bishop, Rafal Klajn, Stoyan K Smoukov, Christopher J Campbell, and Bartosz A Grzybowski. Principles and Implementations of Dissipative (Dynamic) Self-Assembly. *J.Phys. Chem. B*, 110:2482–2496, 2006.

[7] Rashmi C Desai and Raymond Kapral. *Dynamics of Self-organized and Self-assembled Structures*. Cambridge University Press, 1 edition, 2009.

[8] Allan S Hoffman. Hydrogels for Biomedical Applications. *Adv. Drug Deliv. Rev.*, 64:18–23, 2012.

[9] Nasim Annabi, Jason W Nichol, D Ph, Xia Zhong, and Chengdong Ji. Controlling the Porosity and Microarchitecture of Hydrogels for Tissue Engineering. *J. Tissue Eng.*, 16(4):371–383, 2010.

[10] Zulma A. Jiménez and Ryo Yoshida. Temperature Driven Self-Assembly of a Zwitterionic Block Copolymer That Exhibits Triple Thermoresponsivity and pH Sensitivity. *Macromolecules*, 48(13):4599–4606, 2015.

[11] Jinxing Jiang and Kenji Sakurai. Formation of Ultrathin Liesegang Patterns. *Langmuir*, 32(36):9126–9134, 2016.

[12] Yukikazu Takeoka and Masayoshi Watanabe. Tuning Structural Color Changes of Porous Thermosensitive Gels Through Quantitative Adjustment of the Cross-Linker in Pre-Gel Solutions. *Langmuir*, 19(22):9104–9106, 2003.

[13] Marta Tena-Solsona, Benedikt Rieß, Raphael K Grötsch, Franziska C Löhrer, Caren Wanzke, Benjamin Käsdorf, Andreas R Bausch, Peter Müller-Buschbaum, Oliver Lieleg, and Job Boekhoven. Non-equilibrium dissipative supramolecular materials with a tunable lifetime. *Nat. Commun.*, 8:15895, 2017.

[14] Yiming Wang, Robin M de Kruijff, Matija Lovrak, Xuhong Guo, Rienk Eelkema, and Jan H van Esch. Access to metastable gel states using seeded self-assembly of low molecular weight gelators. *Angew. Chem. Int. Ed.*, 2018.

[15] Alison M Douglas, Alexandros A Fragkopoulos, Michelle K Gaines, L Andrew Lyon, Alberto Fernandez-Nieves, and Thomas H Barker. Dynamic assembly of ultrasoft colloidal networks enables cell invasion within restrictive fibrillar polymers. *Proc. Natl. Acad. Sci.*, 114(5):885–890, 2017.

[16] Jeffrey C Gaulding, Michael H Smith, John S Hyatt, Alberto Fernandez-Nieves, and L Andrew Lyon. Reversible inter-and intra-microgel cross-linking using disulfides. *Macromolecules*, 45(1):39–45, 2011.

[17] Prateek K. Jha, Vladimir Kuzovkov, Bartosz A. Grzybowski, and Monica Olvera de la Cruz. Dynamic self-assembly of photo-switchable nanoparticles. *Soft Matter*, 8(1):227–234, 2012.

[18] P. K. Kundu, D. Samanta, R. Leizrowice, B. Margulis, H. Zhao, M Börner, T Udayabhaskararao, Debasish Manna, and Rafal Klajn. Light-Controlled Self-Assembly of Non-Photoresponsive Nanoparticles. *Nat. Chem.*, 7(8):646–652, 2015.

[19] Keitaro Sou, Li Yan Chan, and Chi-lik Ken Lee. Photo-Switchable and Self-Erasable Fluorescent Nanoprobe. *J. Photochem. Photobiol. A. chem.*, 332:25–31, 2016.

[20] Roché M. Walliser, Florent Boudoire, Eszter Orosz, Rita Tóth, Artur Braun, Edwin C. Constable, Zoltán Rácz, and István Lagzi. Growth of Nanoparticles and Microparticles by Controlled Reaction-Diffusion Processes. *Langmuir*, 31(5):1828–1834, 2015.

[21] Janane Rahbani, Ali R. Behzad, Niveen M. Khashab, and Mazen Al-Ghoul. Characterization of internal structure of hydrated agar and gelatin matrices by cryo-sem. *Electrophoresis*, 34(3):405–408, 2013.

[22] Li Chen, Qinjun Kang, Ya-Ling He, and Wen-Quan Tao. Mesoscopic study of the effects of gel concentration and materials on the formation of precipitation patterns. *Langmuir*, 28(32):11745–11754, 2012.

[23] Bartosz A Grzybowski, Howard A Stone, and George M Whitesides. Dynamic self-assembly of magnetized, millimetre-sized objects rotating at a liquid–air interface. *Nature*, 405(6790):1033, 2000.

[24] Martin McCullagh, Tatiana Prytkova, Stefano Tonzani, Nicolas D. Winter, and George C. Schatz. Modeling self-assembly processes driven by nonbonded interactions in soft material. *J. Phys. Chem. B*, 112(34):10388–10398, 2008.

[25] C Reichhardt and CJ Olson Reichhardt. Dynamical ordering and directional locking for particles moving over quasicrystalline substrates. *Phys. Rev. Lett.*, 106(6):060603, 2011.

[26] Helgi I Ingólfsson, Cesar A Lopez, Jaakko J Uusitalo, Djurre H de Jong, Srinivasa M Gopal, Xavier Periole, and Siewert J Marrink. The power of coarse graining in biomolecular simulations. *Wiley Interdiscip. Rev. Comput. Mol. Sci.*, 4(3):225–248, 2014.

[27] Mario Tagliazucchi, Emily A Weiss, and Igal Szleifer. Dissipative self-assembly of particles interacting through time-oscillatory potentials. *Proc. Natl. Acad. Sci.*, 111(27):9751–9756, 2014.

[28] Mazen Al-Ghoul and Byung Chan Eu. Hyperbolic reaction-diffusion equations and irreversible thermodynamics: II. Two-dimensional patterns and dissipation of energy and matter. *Physica D: Nonlinear Phenomena*, 97:531–562, 1996.

[29] Konstantin V Tretiakov, Igal Szleifer, and Bartosz A Grzybowski. The Rate of Energy Dissipation Determines Probabilities of Non- equilibrium Assemblies. *Angew. Chem. int. Ed*, 52:10304–10308, 2013.

[30] Masao Doi. Onsager's variational principle in soft matter. *J. Phys.: Condens. Matter*, 23(28):284118, 2011.

[31] D Reguera, JM Rubi, and JMG Vilar. The mesoscopic dynamics of thermodynamic systems. *J. Phys. Chem. B*, 109(46):21502–21515, 2005.

[32] Andrés Arango-Restrepo, J Miguel Rubi, and Daniel Barragán. Understanding gelation as a nonequilibrium self-assembly process. *J. Phys. Chem. B*, 122(18):4937–4945, 2018.

[33] Roderick C Dewar, Charles H Lineweaver, and Robert K Niven. *Beyond the Second Law: Entropy Production and Non-equilibrium Systems.* Springer-Verlag Berlin Heidelberg, 1 edition, 2014.

[34] Jason R Green, Anthony B Costa, Bartosz A Grzybowski, and Igal Szleifer. Relationship between dynamical entropy and energy dissipation far from thermodynamic equilibrium. *Proc. Natl. Acad. Sci.*, 110(41):16339–16343, 2013.

[35] Ilya Prigogine and G Nicolis. *Self organization in non equilibrium systems*. John wiley & sons, 1 edition, 1977.

[36] Y. Kawazura and Z. Yoshida. Entropy production rate in a flux-driven self-organizing system. *Phys. Rev. E: Stat. Phys., Plasmas, Fluids, - Statistical, Nonlinear, and Soft Matter Physics*, 82(6):1–8, 2010.

[37] Soumen De and Rafal Klajn. Dissipative Self-Assembly Driven by the Consumption of Chemical Fuels. *Adv. Mater.*, 1706750:1706750, 2018.

[38] Jaap J.D De Jong. Light-Driven Dynamic Pattern Formation. *Angew. Chem. int. Ed*, 44:2373–2376, 2005.

[39] Linda N Lucas, Jan van Esch, Richard M Kellogg, and Ben L Feringa. Photocontrolled self-assembly of molecular switches. *Chem. Commun.*, (8):759–760, 2001.

[40] Helmut Cölfen and Stephen Mann. Higher-Order Organization by Mesoscale Self-Assembly and Transformation of Hybrid Nanostructures. *Angew. Chem. int. Ed*, 42(21):2350–2365, 2003.

[41] Job Boekhoven, Aurelie M. Brizard, Krishna N. K. Kowlgi, Ger J. M. Koper, Rienk Eelkema, and Jan H. van Esch. Dissipative Self-Assembly of a Molecular Gelator by Using a Chemical Fuel. *Angew. Chem.*, 122(28):4935–4938, 2010.

[42] Andrés Arango-Restrepo, Daniel Barragán, and J Miguel Rubi. Nonequilibrium self-assembly induced liesegang rings in a non-isothermal system. *PCCP*, 20(7):4699–4707, 2018.

[43] Andrés Arango-Restrepo, J. Miguel Rubi, and Daniel Barragán. The role of energy and matter dissipation in determining the architecture of self-assembled structures. *The Journal of Physical Chemistry B*, 123(27):5902–5908, 2019.

[44] José MG Vilar and J M Rubi. Thermodynamics "beyond" local equilibrium. *PNAS*, 98(20):11081–11084, 2001.

[45] I Pagonabarraga, A Pérez-Madrid, and JM Rubi. Fluctuating hydrodynamics approach to chemical reactions. *Physica A*, 237(1-2):205–219, 1997.

[46] A Arango-Restrepo, J.M Rubi, and D Barragán. Kinetics and energetics of chemical reactions through intermediate states. *Physica A*, 509:86–96, 2018.

[47] JM Rubi, D Bedeaux, S Kjelstrup, and I Pagonabarraga. Chemical cycle kinetics: removing the limitation of linearity of a non-equilibrium thermodynamic description. *Int. J. Thermophys.*, 34(7):1214–1228, 2013.

[48] Job Boekhoven, Wouter E Hendriksen, Ger JM Koper, Rienk Eelkema, and Jan H van Esch. Transient assembly of active materials fueled by a chemical reaction. *Science*, 349(6252):1075–1079, 2015.

5. The role of energy and matter dissipation in determining the architecture of self-assembled structures

We show how the architecture of self-assembled structures can be determined from the knowledge of the energy and matter dissipation inherent to its formation. When the amount of dissipation quantified by the total entropy produced in the process is represented in terms of parameters which describe the shape of the assembled structures, its extremes correspond to structures found in experimental situations such as in gelation and Liesegang ring formation. It is found that only a small amount of extra energy is needed to yield smooth changes in the form of the assembled structures. The connection found between the entropy produced and the type of structures formed may constitute a selection criterion which shows why a set of disordered units may gives rise to a determined self-assembled structure.

This chapter was published in *the Journal of Physical Chemistry B*, **123**, 5902-5908, (2019). Ref.[1]

5.1. Introduction: Structural parameters and trajectories

There is currently growing evidence that the type of non-equilibrium self-assembled (NESA) structures formed largely depends on the conditions under which the process takes place and that the final state of the system seems to correspond to basins of the free energy landscape [2, 3, 4, 5]. Nevertheless, NESA processes dissipate matter and energy [6, 7, 8, 9, 10] and tend to minimize the free energy by forming structures thus increasing order and consequently decreasing entropy. Due to the second law, entropy must then be produced and released to the environment. In equilibrium processes, the formed structures lie at the minima of the free energy. Outside equilibrium, this is not necessarily so due to the existence of dissipation. For instance, microtubules and microtubule-based structures are dynamically assembled under non-equilibrium conditions and their free energy is not necessarily a minimum. These structures, however, may result from the optimization of kinetic or structural parameters [11, 12, 13]. Specifically, it is found that the ratio between two kinetic parameters describing the assembly of an active gel dictates the form of the final structure and as a consequence the functionality of the gel [14]. The entropy produced in the response of the active gel could give us information about the optimal value of the ratio of the kinetic parameter.

What is the amount of energy dissipated in the formation of a non-equilibrium self-assembled (NESA) structure from a set of disordered elements? And how is the formation of these structures governed by the laws of thermodynamics? In the lack of a non-equilibrium potential that can constitute a structure selection mechanism, as occurs in equilibrium [8], we wonder why under specified conditions a determined structure appears and not another. A satisfactory answer to these important questions has not yet been found.

Some studies have shown that in the transition between disordered to ordered states where self-assembled structures may emerge, the entropy production rate reaches a maximum value (as occurs in ecosystems or in enzymatic kinetics) [15, 16, 17, 18], a minimum value (as happens in the formation of spatiotemporal structures or self-healing surfaces) [19, 20, 21, 22] or even both extremes (as observed in flux-driven systems) [23, 24]. In all these situations, the extreme values are obtained by considering that fluxes and thermodynamic forces are the relevant variables of the system. The use of only fluxes and forces, however, does not provide a complete characterization of the assembled structures in which the architecture is a key factor for the knowledge of the structural properties. A parameter must then be proposed to characterize the architecture of the structures and to quantify the energy dissipated in their assembly. In the case of self-assembled polymorphic structures [10], it was found that the amount of energy and matter dissipated may play an important role in its formation.

In this chapter, we show that self-assembled structures emerge when the total entropy produced as a function of a structural parameter accounting for the geometry of the structures reaches extreme values. We illustrate this fact in two particular self-assembly processes: gelation and Liesegang ring banding. It is found that only a small amount of extra energy is needed to yield smooth changes in the form of the assembled structures. The chapter is organized as follows. In section 2, we present a general expression for the entropy production. In section 3, we obtain the entropy production rate of gelation and Liesegang ring banding processes as a function of their corresponding structural parameters. In section 4, we establish the relation between the type of structure and the dissipation in the processes mentioned. Finally, in section 5 present our main conclusions.

5.2. Theory

5.2.1. Entropy produced in NESA processes

The formation of NESA structures consumes energy and matter. The entropy production rate is a measure of the amount of energy dissipated and, as we will show in this chapter, may give information about the type of NESA structures formed.

Self-assembly has been described as an activated process taking place along reaction coordinates Γ [7] parametrizing the transformation from the disordered to the assembled state. The state of the system is described by means of the probability $P(\Gamma,t)$ such that activation occurs at time t and at a determined value of Γ of the reaction coordinates [25, 26]. Although Γ characterizes the degree of advancement of the activated process, it cannot account for the final architecture of the structure which depends on the free energy landscape. To describe the final form of the structure we introduce the structural parameter η. Variations of the Gibbs entropy in the process δS are then given by

$$\delta S(t;\eta) = -\frac{1}{T}\int_{\Gamma} \mu(\Gamma,t;\eta)\delta P(\Gamma,t;\eta)d\Gamma \tag{5-1}$$

with μ the chemical potential and where we have neglected irreversible changes in the solvent. The entropy depends on the conformations of the assembled structures whose architecture is characterized by a set of the structural parameters η such as sphericity, radius of gyration, maximum length, porosity, average component orientation or component interconnectivity among others.

To compute the entropy production rate σ associated to the formation of a structure, we take the time derivative of eq.(5-1) and use the probability conservation law $\frac{\partial P}{\partial t} = -\nabla_{\Gamma}\cdot \vec{J}_{\Gamma}$ in which $\vec{J}_{\Gamma}$ is the flux in the space of the internal coordinates Γ. We then obtain

$$\sigma(t;\eta) = -\frac{1}{T}\int_{\Gamma} \vec{J}_{\Gamma}(\Gamma,t;\eta)\cdot\nabla_{\Gamma}\mu(\Gamma,t;\eta)d\Gamma \tag{5-2}$$

in which we have used the fact that the fluxes at the surface of the Γ space vanish.

Considering that the reaction coordinates are independent and normalized to one, Γ [27], the entropy production rate can thus be expressed as

$$\sigma(t;\eta) = -\frac{1}{T}\sum_{j}\int_{0}^{1} J_j(\Gamma_j,t;\eta)\frac{\partial\mu_j(\Gamma_j,t;\eta)}{\partial\Gamma_j}d\Gamma_j \tag{5-3}$$

Neglecting cross effects since there are disjoint processes [7], i.e, it is not that a new building block assembled and disassembled simultaneously to the same structure, and from the entropy production expression we obtain the flux J_j in terms of its conjugated thermodynamic force, the corresponding chemical potential gradient

$$J_j(\Gamma_j,t;\eta) = -\frac{L_j}{T}\frac{\partial\mu_j(\Gamma_j,t;\eta)}{\partial\Gamma_j} \tag{5-4}$$

where $L_j = D_jP/R$ is an Onsager coefficient, with D_j a diffusion coefficient. For high activation energies, the process is quasi-stationary, i.e. the flux does not depend on the reaction coordinate [27]. In this case we can obtain the expression for the flux in terms of the fugacity difference $\Delta_j \mathfrak{z}$ between the initial and the final states,

$$J_j(t;\eta) = \frac{D_j}{\int_0^1 \exp(-\phi(\Gamma_j)/RT)))d\Gamma_j} \Delta_j \mathfrak{z}(t;\eta) \tag{5-5}$$

in which $\mathfrak{z} = exp(\mu/RT)$ is the fugacity and $\phi(\Gamma_j)$ the potential barrier in the Γ_j coordinate. This expression for the flux, also written as $\Delta_j \mathfrak{z} \approx \exp(\mu_r^0/RT)C_r - \exp(\mu_p^0/RT)C_p$, with C_r and C_p the reactant and product concentrations [28], is in accordance with the law of mass action. Using the flux J_j we obtain the more compact expression

$$\sigma(t;\eta) = R\sum_j k_j(\Delta_j \mathfrak{z}(t;\eta))^2 \tag{5-6}$$

where k_j is the kinetic constant of the process in units of s^{-1}.

If in addition, heat and mass transfer take place in the system, the entropy production rate in terms of the forces is given by

$$\sigma(\vec{r},t;\eta) = \frac{\lambda}{T^2}[\nabla T]^2 + \sum_k \mathscr{D}_k \left[\nabla\left(\frac{\mu_k(\eta)}{T}\right)\right]^2 + R\sum_j k_j(\Delta_j \mathfrak{z}(\eta))^2 \tag{5-7}$$

Here λ is the thermal conductivity and $\mathscr{D}_k$ the diffusion coefficient of the specie k.

The total entropy produced in the process Σ depending on the structural parameter is given by

$$\Sigma(\eta) = \int_0^\tau \int_{\vec{r}} \sigma(\vec{r},t;\eta)d\vec{r}dt \tag{5-8}$$

where τ is a characteristic time of the process. The work done on the system to form the structures is the lost work $W_l(\eta) = T\Sigma(\eta)$ which can be computed from the total entropy produced. The knowledge of this quantity is basic to compute the energetic performance.

Fig.**5-1** shows a typical form of the Σ landscape as a function of the sphericity defined as

$$\eta_{sph} = \frac{l_a l_b l_c}{max(l_a,l_b,l_c)^3} \tag{5-9}$$

which characterizes the shape of the formed structure and where (l_a,l_b,l_c) are the lengths of the three main axes of the structure. In general, structures emerge at different values of the total entropy produced. We expect that Bi-dimensional structures emerge at low values of η and Σ while more complex structures appear at higher values of these quantities because these last ones require more processes to be assembled.

5.2.2. Entropy production in the study cases

In this Section, we will use eq.(5-7) to obtain the expressions of the entropy production rate in gelation and Liesegang ring banding as a function of the structural parameters.

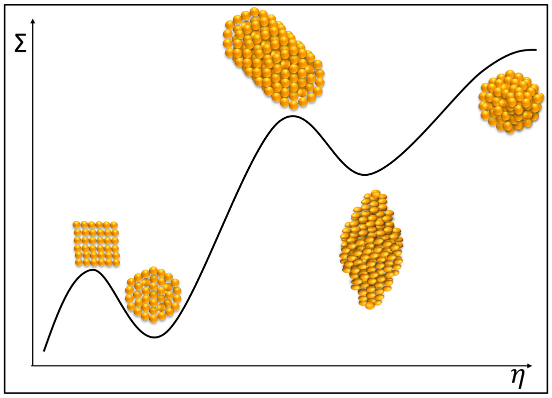

Fig. 5-1.: Sketch of the entropy production Σ landscape of NESA structures as a function of the structural parameter η which in this case corresponds to the sphericity of the structure defined in eq. (5-9). Two-dimensional structures emerge at low values of Σ and η whereas three-dimensional structures assembled from 2-D structures which require more steps in their formation appear at higher values of Σ and η.

Gelation

As a first example, we will compute the entropy production associated to the formation of a fibrous network (gel) that uses a chemical fuel as an activator in an isothermal media [29]. In the process, the fuel activates the building blocks (BB) which assemble into fibers subsequently forming an agglomerate, the gel. As shown in Fig. **5-2**, the whole process consists of activation, assembly and disassembly of BB, fibers and agglomerates which constitute zeroth- first- and second order structures, respectively [7]. In the process, an amount of activator is added at $t = 0\ hr$ and $t = 400\ hr$. This semi-continuous feeding of activator promotes the assembly of intermediate dissipative structures [29, 9, 5] but not the assembly of stationary structures. The experiments show the presence of two maxima in the concentration of agglomerated fibers that appear when the assembly and disassembly rates are equal and when the assembled BB reach the lowest possible energy which correspond to the case of the largest fibers.

A model to describe the gelation kinetics was proposed in ref.[7]. In Fig.**5-2**, we present a sketch of the gelation mechanism showing the involved structures and the processes taking place (assembly, disassembly, activation and rotation).

The model describes the kinetics of the different steps of the process as diffusion in a potential barrier along reaction coordinates [26, 25]. The coordinates can be identified from the knowledge of the internal architecture of the structures. The form of the potential barrier depends on the number of BB composing the fibers (n) and of the maximum amount of BB that can be assembled in a fiber(N).

From the scheme presented in Fig.**5-2**, we write the entropy production for the gelation process σ_g as:

$$\sigma_g(t;N) = \sum_{i=1}^{2} \sigma_{0,i} + \sum_{n=2}^{N} \sum_{i=1}^{4} \sigma_{1,i}^{(n)} + \sum_{n=2}^{\infty} \left[\sum_{m=2}^{\infty} \sigma_{2,1}^{(n,m)} + \sum_{y=1}^{n-1} \sigma_{2,2}^{(n,n-y)} \right] \tag{5-10}$$

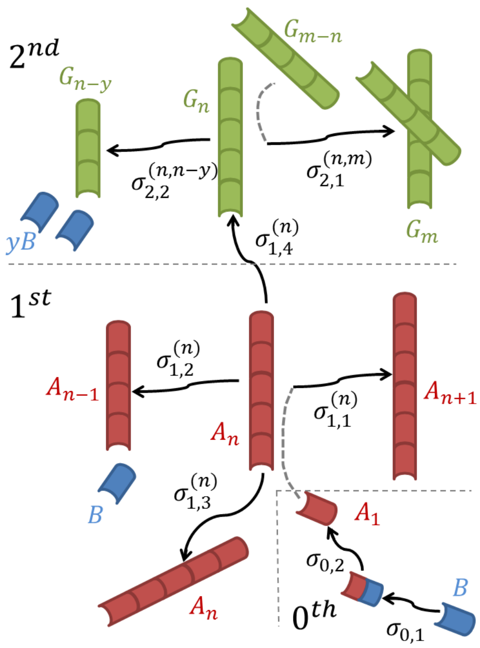

Fig. 5-2.: Gelation sketch. Zeroth-order structures B (BB represented by blue blocks) are activated (A_1) in two steps with the corresponding entropy productions $\sigma_{0,1}$ and $\sigma_{0,2}$. First-order structures: fibers represented by red cylinders, composed of n BB (A_n) may interact with an activated BB becoming a fiber with $n+1$ BB (A_{n+1}), release a disassemble BB yielding a fiber with $n-1$ BB (A_{n-1}) and rotate or become activated giving rise to a second-order structure with n BB (G_n). The corresponding entropy productions of these processes are: $\sigma_{1,1}^{(n)}, \sigma_{1,2}^{(n)}, \sigma_{1,3}^{(n)}$ and $\sigma_{1,4}^{(n)}$, respectively. Second-order structures: the agglomerated fibers represented by overlapping green cylinders, can be formed by adding a second-order structure with $m-n$ BB (G_{m-n}) to G_n to produce an agglomerate with m BB (G_m). The structure may also disassemble giving rise to G_{n-y}. The entropy productions are $\sigma_{2,1}^{(n,m)}$ and $\sigma_{2,2}^{(n,n-y)}$, respectively, with $m = 2, 3, ...$ and $y = 1, 2, ..., n-1$.

Using eq.(5-6), we can write the entropy production as a function of the fugacities of the structures which can be obtained from the probabilities obtained from the Fokker-Planck equation (eq. (2-6))

$$\sigma_g(t;N)/R = \sum_{i=1}^{2} k_{0,i}(\Delta_i \mathfrak{z})^2 + \sum_{n=2}^{N}\sum_{i=1}^{4} k_{1,i}(\Delta_i \mathfrak{z}(n,N))^2 + \sum_{n=2}^{\infty}\left[\sum_{m=2}^{\infty} k_{2,m}(\Delta_m \mathfrak{z}(n,N))^2 + \sum_{y=1}^{n-1} k_{2,y}(\Delta_y \mathfrak{z}(n,N))^2\right] \tag{5-11}$$

in which the kinetic constants depend on the shape of the potential barrier of each activated process.

Liesegang ring formation

A representative example of pattern formation and self-organization is the periodic precipitation pattern discovered by *R. E. Liesegang* in 1896 [30, 31], known as Liesegang patterns. These consist of a number of concentric rings (in 2D) or bands (in 1D) resulting from the diffusion of an ionic co-precipitate and periodic precipitation of an insoluble solid in a gel medium [32], as illustrated in Fig. **5-3**.

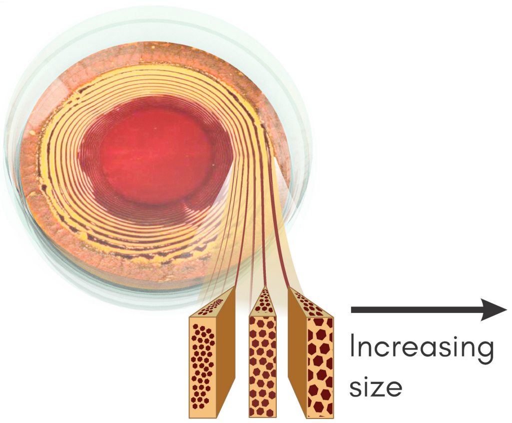

Fig. 5-3.: Liesegang rings composed of NESA structures. The size of the structures increases as the radius of the ring increases. Adapted from commons.wikimedia.org with license CC-BY-SA-3.0.

Processes such as reaction-diffusion, supersaturation, nucleation, particle growth, electro-migration and temperature effects are involved in the formation of these patterns [33]. Synthesis based on nucleation and particle growth in a reaction-diffusion system taking place in a gel matrix has been recognized as an important method to produce self-assembled structures under non-equilibrium conditions [34, 35]. This synthesis brings about the formation of Liesegang patterns which are composed of mono-disperse nano and micro-structures whose size varies predictably from ring to ring [36]. The non-equilibrium nature of this process is highlighted by the occurrence of polymorphism and the appearance of both stable and metastable structures [37, 38]. In the synthesis, two electrolytes act as fundamental components that trigger the self-assembly process, forming stable assembled structures from NESA structures. This method in which meso-structures of different sizes are obtained is known as bottom-up self-assembly [39].

A mechanism for the formation of Liesegang patterns from fundamental BB, based on NESA mechanism and mesoscopic thermodynamics [25, 26], was proposed in ref. [6]. The different steps in the mechanism are: activation of the fundamental constituent (BB), pre-nucleation of the aqueous activated BB, nucleation, and aggregation/growth of the solid nucleus. The model provides information about the size of the structures, the spatial distribution of the patterns, the particle concentration of the structures and the spatial distribution of the temperature.

The knowledge of the structure size composing the rings is crucial to describe the dynamics of the process and to relate the structural parameter to the entropy production. In the proposed mechanism, an excess of electrolyte concentration stabilizes the final structure that is considered spherical. It is assumed that a low concentration in the electrolyte causes growth of the structure in order to diminish its surface while a high electrolyte concentration neutralizes its growth [6]. Additionally, we suppose that the ratio between the variations of the diameter of the structure and the electrolyte concentration is directly proportional to a sensibility parameter ω in the form:

$$\frac{\Delta d}{\Delta C_E} = -\omega / C_E \tag{5-12}$$

Then, the structure diameter d is a function of the electrolyte concentration $C_E(r,t)$ and is given by

$$d(r,t) = d_0 + \omega \ln(C_E(r_{lim},0)/C_E(r,t)), \quad \forall r > r_{lim}, \tag{5-13}$$

where d_0 is the diameter of the structures in a uniform distribution and r_{lim} indicates the position of the inner boundary. J_i, because the number of building blocks (m) required to the formation of the NESA structures depends on the structure's size. This quantity is given by

$$m = \varepsilon^3 \frac{4\rho_s \pi (d/2)^3/3}{M_s} \tag{5-14}$$

with ε the packing factor, approximately 0.6, M_0 the mass of a building block and ρ_s the molar density of the structure. $1/\omega$ will play the role of the structural parameter. Small values of this parameter correspond to a large dispersion of sizes while higher values indicate uniform size distribution.

To compute the entropy production rate of the process, we use eq.(5-7) and consider a 2D radial geometry in a diluted media where four NESA sub-processes take place. We then obtain:

$$\sigma_L(r,t;\omega) = \frac{\kappa}{T^2}\left(\frac{\partial T}{\partial r}\right)^2 + \sum_k \frac{\mathscr{D}_k}{T}\left(\frac{\partial C_k}{\partial r}\right)^2 + \frac{1}{T}\sum_{i=1}^{4} J_i^2(\omega)/k^+ \tag{5-15}$$

with k_i^+ the forward kinetic constant of the i^{th} sub-process. The entropy production then follows by solving eq.(3-5) of the appendix for each component and eq.(3-12) for the temperature.

5.3. Results and Discussion

In this Section, we will proceed to analyze the behavior of the entropy production and its implications in the formation of self-assembled structures in two particular cases: gelation and Liesegang ring formation.

5.3.1. Analysis of the entropy production in gelation

The knowledge of the entropy production rate enables us to differentiate the various steps taking place in a gelation process. This quantity can be obtained from the kinetics of the process by numerically solving the Fokker-Plank equations describing the temporal evolution of the concentrations of the different structures. From these concentrations we can obtain the corresponding fugacity of the structures. Details about the formulation of these equations have been given in ref. [7]. In the Appendix, we summarize the main steps of the kinetics of the process. By using these results in eq.(5-11), we compute the entropy production rate for the gelation process shown in Fig.**5-4**. Growth of fibers and their subsequent agglomeration is the dominant process in the zones 1 seen in Fig. **5-4**(a) and (b) while in the zones 2 disassembly dominates producing more entropy than in the assembly stage. In Fig.**5-4**, we also observe that in the second stage of the experiment (after 400 *hr*) the curve has a different form. This is because the assembly process is re-initiated at different initial conditions. We find that by increasing N, the form of both peaks of zones 1 and 2 is different. This is due to the fact that there is a greater diversity of structures and a more efficient assembly of the fibers since the difference between the heights of the peaks of both zones is higher. Peaks at $N = 54$ are higher than at

$N = 29$, consequently the total entropy produced is larger in the former case.

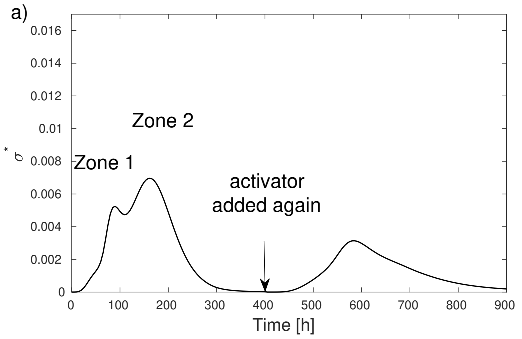

Fig. 5-4.: Entropy production rate $\sigma^* = \sigma/C_0R$ $[1/s]$ in gelation computed for two different values of N, with R as the universal constant of gases and C_0 the initial concentration of deactivated BB. The first stage of the experiment takes place for times between 0 and 400 *hr*. Zones 1 and 2 correspond to times between 0 and 110 *hr* and between 110 and 400 *hr*, respectively. The second stage of the experiment occurs at times between 400 and 900 *hr*. a) σ^* for $N = 29$. b) σ^* for $N = 54$.

In Fig.**5-5**(a), we represent the total entropy produced Σ obtained from eq.(5-8). Dots represent the numerical results that are connected by the dashed line. We observe that at low values of N it increases linearly whereas a nonlinear dependence appears at higher values of N. Consequently, at low values of N the total entropy produced per maximum number of BB assembled is approximately constant. At larger values of N, the linear behavior breaks down and Σ does not increase significantly. This fact is more clearly illustrated in Fig.**5-5**(b) which represents the derivative of Σ with respect to N. For a very large value of N, the derivative tends to zero meaning that the growth of long fibers has a low energetic cost.

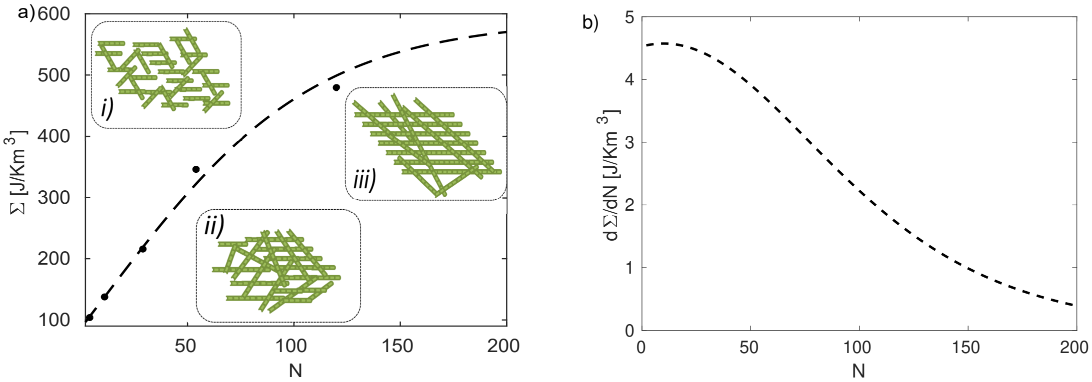

Fig. 5-5.: a) Total entropy produced Σ as a function of N. b) Derivative of Σ with respect N in the gelation process. Black dots represent our numerical results from the model presented in ref. [7], connected by the dashed line. The insets *i*), *ii*) and *iii*) illustrate the gel structure for $N = 29$, $N = 54$ and $N = 120$, respectively.

Since typical values of the maximum number of assembled BB in a fiber are $N \approx 10^4$ [29], we thus conclude that the structures are characterized by a maximum value of the total entropy produced as a function of N. Moreover, the architecture is such that a slight alteration on the assembled structure leads to a minimum change on the energetic cost.

The value of the maximum number of BB per fiber N characterizes the type of self-assembled structures. The insets i), ii) and iii) in Fig.**5-5** represent assembled gel structures for $N = 29$, $N = 54$ and $N = 120$. Notice that larger values of N yield more interconnected aggregated fibers. In the case of gelation, N does not depend on external conditions but only on the nature of the BB. From the result $d\Sigma/dN \geq 0$, we then conclude that an increase of N, implying an increase of Σ, favors the agglomeration of the fibers thus yielding more hierarchical structures.

5.3.2. Analysis of entropy production in Liesegang ring formation

We have numerically solved the system of partial differential equations presented in [6] to obtain the evolution in space and time of the temperature and concentration of the components. Details on the formulation of these equations are presented in the Appendix. From these results, and by using the entropy production rate given in eq.(5-15), we compute the total entropy produced as a function of the structural parameter $1/\omega$. Results for Σ and $d\Sigma/d(1/\omega)$ are shown in Fig.**5-6** where the grey filled circle corresponds to experimental results presented in ref.[36].

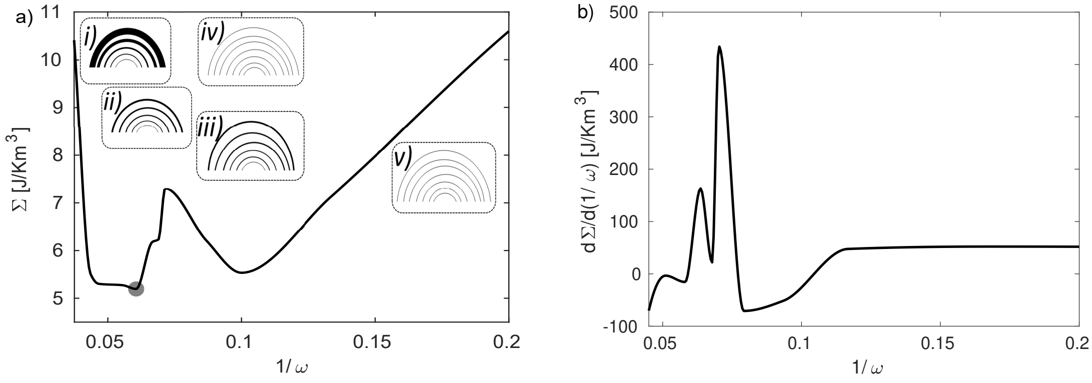

Fig. 5-6.: a) Total entropy produced Σ as a function of the structural parameter $1/\omega$. b) Derivative of Σ with respect to $1/\omega$ in Liesegang ring banding. Continuous black line represents our numerical results from the model presented in ref.[6]. The grey filled circle is the experimental result obtained in ref.[36]. Insets *i*), *ii*), *iii*), *iv*) and *v*) illustrate the Liesegang rings for $1/\omega$ equal to 0,040, 0,058 (global minimum), 0,066 (local maximum), 0,1 (local minimum) and 0,2 respectively.

Fig. **5-6**(a) shows that the entropy produced is a non-monotonous function of $1/\omega$. It shows two minima and one maximum value and a linear behavior starting at $1/\omega > 0{,}1$. This last behavior differs from that observed at lower values of $1/\omega$ and shows the existence of a transition towards more homogeneous Liesegang rings with a constant variation of the energetic cost in relation to the parameter $1/\omega$, as is clearly observed in Fig.**5-6**(b). The non-monotonous behavior found for $1/\omega < 0{,}1$ is a consequence of the fluctuation in the number of rings formed. The number of rings increases because the amount of mass needed to form a ring decreases as a function of $1/\omega$, but the spatial distance between rings increases impairing the emergence of new rings. This feedback generates fluctuations in the number of rings for $1/\omega < 0{,}1$. In Fig.**5-6**(a), the grey filled circle found in the experiments is very close to the global minimum of the total entropy produced for and intermediate value of $1/\omega$. This fact shows that the system evolves towards a structure which minimizes the lost work in its formation. The structure thus adopts an architecture such that the work lost in changing the configuration is almost negligible.

The insets in Fig.**5-6**(a) show the Liesegang patterns obtained for a specific values of $1/\omega$ representing the structure's size distribution. Darker rings correspond to structures with higher average sizes. Notice that larger $1/\omega$ yields a more homogeneous size distribution along the rings. The structural parameter $1/\omega$ depends on the nature of each component of the system and on external and initial conditions. In this process, there is no clear increment in the hierarchical order of the structures; for this reason, the total entropy produced does not necessarily increase as a function of the structural parameter. This behavior is the opposite of the case of gelation where the entropy production is maximum due to the increase of the hierarchical order of the structures.

5.4. Conclusions: Extreme values of dissipation and increment of the order

We have shown that the knowledge of the entropy generated in a non-equilibrium self-assembly process determines the architecture of structures formed when they can be characterized by a structural parameter. We have analyzed this feature in two particular situations: a gelation process and the formation of Liesegang rings. We have shown that the structures observed in these systems are found at extreme values of the entropy produced when represented as a function of the structural parameter. Gel structures correspond to maximum values of the total entropy produced while for Liesegang rings, the entropy produced is a minimum.

We have found that processes leading to a marked increment in the hierarchical order of the structures are characterized by the highest possible value of lost work as a function of the structural parameter. For instance, gelation processes dissipate the maximum amount of available free energy to increase the hierarchical order. On the other hand, Liesegang ring banding which does not show a significant increment in the hierarchical order, the energetic cost is minimized.

The connection found between the entropy produced in an self-assembly process and the type of emerging structures shed light on the thermodynamic basis of self-assembling and on the existence of a non-equilibrium thermodynamic principle able to analyze the evolution of systems towards complexity.

Bibliography

[1] Andrés Arango-Restrepo, J. Miguel Rubi, and Daniel Barragán. The role of energy and matter dissipation in determining the architecture of self-assembled structures. *The Journal of Physical Chemistry*

B, 123(27):5902–5908, 2019.

[2] Baiyong Ding, Ying Li, Meng Qin, Yin Ding, Yi Cao, and Wei Wang. Two approaches for the engineering of homogeneous small-molecule hydrogels. *Soft Matter*, 9(18):4672–4680, 2013.

[3] Ying Li and Yi Cao. The physical chemistry for the self-assembly of peptide hydrogels. *Chin. J. Polym. Sci.*, pages 1–13, 2017.

[4] Marta Tena-Solsona, Benedikt Rieß, Raphael K Grötsch, Franziska C Löhrer, Caren Wanzke, Benjamin Käsdorf, Andreas R Bausch, Peter Müller-Buschbaum, Oliver Lieleg, and Job Boekhoven. Non-equilibrium dissipative supramolecular materials with a tunable lifetime. *Nat. Commun.*, 8:15895, 2017.

[5] Susan A. P. van Rossum, Marta Tena-Solsona, Jan H. van Esch, Rienk Eelkema, and Job Boekhoven. Dissipative out-of-equilibrium assembly of man-made supramolecular materials. *Chem. Soc. Rev.*, 46:5519–5535, 2017.

[6] Andrés Arango-Restrepo, Daniel Barragán, and J Miguel Rubi. Nonequilibrium self-assembly induced liesegang rings in a non-isothermal system. *PCCP*, 20(7):4699–4707, 2018.

[7] Andrés Arango-Restrepo, J Miguel Rubi, and Daniel Barragán. Understanding gelation as a nonequilibrium self-assembly process. *J. Phys. Chem. B*, 122(18):4937–4945, 2018.

[8] Marcin Fialkowski, Kyle J M Bishop, Rafal Klajn, Stoyan K Smoukov, Christopher J Campbell, and Bartosz A Grzybowski. Principles and Implementations of Dissipative (Dynamic) Self-Assembly. *J.Phys. Chem. B*, 110:2482–2496, 2006.

[9] G. J M Koper, J. Boekhoven, W. E. Hendriksen, J. H. Van Esch, R. Eelkema, I. Pagonabarraga, J. M. Rubí, and D. Bedeaux. The Lost Work In Dissipative Self-Assembly. *Int. J. Thermophys.*, 34(7):1229–1238, 2013.

[10] Konstantin V Tretiakov, Igal Szleifer, and Bartosz A Grzybowski. The Rate of Energy Dissipation Determines Probabilities of Non- equilibrium Assemblies. *Angew. Chem. int. Ed*, 52:10304–10308, 2013.

[11] Arshad Desai and Timothy J Mitchison. Microtubule Polymeriztion Dynamics. *Annu. Rev. Cell Dev. Biol.*, 13:83–117, 1997.

[12] Torsten Wittmann, Anthony Hyman, and Arshad Desai. The spindle: a dynamic assembly of microtubules and motors. *Nat. Cell Biol.*, 3(1):E28, 2001.

[13] Thomas Surrey, Francois Nédélec, Stanislas Leibler, and Eric Karsenti. Physical Properties Determining Self-Organization of Motors and Microtubules. *Science*, 292:1167–1171, 2001.

[14] D. A. Head, W. J. Briels, and Gerhard Gompper. Nonequilibrium structure and dynamics in a microscopic model of thin-film active gels. *Phys. Rev. E*, 89:032705, Mar 2014.

[15] Roderick C Dewar, Charles H Lineweaver, and Robert K Niven. *Beyond the Second Law: Entropy Production and Non-equilibrium Systems.* Springer-Verlag Berlin Heidelberg, 1 edition, 2014.

[16] Roderick Dewar. Information theory explanation of the fluctuation theorem, maximum entropy production and self-organized criticality in non-equilibrium stationary states. *J. Phys. A: Math. Gen.*, 36(3):631, 2003.

[17] Robert K. Niven. Steady state of a dissipative flow-controlled system and the maximum entropy production principle. *Phys. Rev. E: Stat. Phys., Plasmas, Fluids, - Statistical, Nonlinear, and Soft Matter Physics*, 80(2):1–15, 2009.

[18] R. K. Niven. Minimization of a free-energy-like potential for non-equilibrium flow systems at steady state. *Philos. Trans. Royal Soc. B*, 365(1545):1323–1331, 2010.

[19] Ilya Prigogine and G Nicolis. *Self organization in non equilibrium systems.* John wiley & sons, 1 edition, 1977.

[20] Mikhail Nosonovsky and George G Adams. Vibration and stability of frictional sliding of two elastic bodies with a wavy contact interface. *Journal of applied mechanics*, 71(2):154–161, 2004.

[21] Michael Nosonovsky and Bharat Bhushan. Thermodynamics of surface degradation, self-organization and self-healing for biomimetic surfaces. *Philos. Trans. Royal Soc. A*, 367(1893):1607–1627, 2009.

[22] Michael Nosonovsky and Bharat Bhushan. Surface self-organization: From wear to self-healing in biological and technical surfaces. *Appl. Surf. Sci.*, 256(12):3982–3987, 2010.

[23] Y. Kawazura and Z. Yoshida. Entropy production rate in a flux-driven self-organizing system. *Phys. Rev. E: Stat. Phys., Plasmas, Fluids, - Statistical, Nonlinear, and Soft Matter Physics*, 82(6):1–8, 2010.

[24] Yohei Kawazura and Zensho Yoshida. Comparison of entropy production rates in two different types of self-organized flows: Bénard convection and zonal flow. *Phys. Plasmas*, 19(1):012305, 2012.

[25] José MG Vilar and J M Rubi. Thermodynamics "beyond" local equilibrium. *PNAS*, 98(20):11081–11084, 2001.

[26] D Reguera, JM Rubi, and JMG Vilar. The mesoscopic dynamics of thermodynamic systems. *J. Phys. Chem. B*, 109(46):21502–21515, 2005.

[27] I Pagonabarraga, A Pérez-Madrid, and JM Rubi. Fluctuating hydrodynamics approach to chemical reactions. *Physica A*, 237(1-2):205–219, 1997.

[28] JM Rubi, D Bedeaux, S Kjelstrup, and I Pagonabarraga. Chemical cycle kinetics: removing the limitation of linearity of a non-equilibrium thermodynamic description. *Int. J. Thermophys.*, 34(7):1214–1228, 2013.

[29] Job Boekhoven, Aurelie M. Brizard, Krishna N. K. Kowlgi, Ger J. M. Koper, Rienk Eelkema, and Jan H. van Esch. Dissipative Self-Assembly of a Molecular Gelator by Using a Chemical Fuel. *Angew. Chem.*, 122(28):4935–4938, 2010.

[30] Raphael Ed Liesegang. Die achate. In *Silicate*, pages 186–190. Springer, 1914.

[31] Harry W Morse and George W Pierce. Diffusion and supersaturation in gelatine. *Physical Review (Series I)*, 17(3):129, 1903.

[32] Rabih F. Sultan. Propagating fronts in periodic precipitation systems with redissolution. *PCCP*, 4(8):1253–1261, 2002.

[33] Samar Sadek and Rabih Sultan. Liesegang patterns in nature: a diverse scenery across the sciences, a review paper. In I Lagzi, editor, *Precipitation patterns in reaction-diffusion systems*, pages 1–43. Research Signpost, Trivandrum, 2010.

[34] Hideki Nabika, Mami Sato, and Kei Unoura. Liesegang patterns engineered by a chemical reaction assisted by complex formation. *Langmuir*, 30(18):5047–5051, 2014.

[35] D Krishna Kumar and Jonathan W Steed. Supramolecular gel phase crystallization: orthogonal self-assembly under non-equilibrium conditions. *Chem. Soc. Rev.*, 43(7):2080–2088, 2014.

[36] Roché M. Walliser, Florent Boudoire, Eszter Orosz, Rita Tóth, Artur Braun, Edwin C. Constable, Zoltán Rácz, and István Lagzi. Growth of Nanoparticles and Microparticles by Controlled Reaction-Diffusion Processes. *Langmuir*, 31(5):1828–1834, 2015.

[37] Mazen Al-Ghoul, Manal Ammar, and Rabih O Al-Kaysi. Band propagation, scaling laws and phase transition in a precipitate system. I: Experimental study. *J. Phys. Chem. A*, 116(18):4427, 2012.

[38] MM Ayass, I Lagzi, and M Al-Ghoul. Three-dimensional superdiffusive chemical waves in a precipitation system. *Phys. Chem. Chem. Phys.*, 16(45):24656–24660, 2014.

[39] Bartosz A Grzybowski, Kyle J M Bishop, Christopher J Campbell, Marcin Fialkowski, and Stoyan K Smoukov. Micro- and nanotechnology via reaction-diffusion. *Soft Matter*, 1:114–128, 2005.

6. A Criterion for the Formation of Nonequilibrium Self-Assembled Structures

Is there a criterion able to determine the type of structures formed in a non-equilibrium self-assembly process? This important question has a clear answer when the process takes place under equilibrium conditions: structures emerge at minimum values of the free energy. Experiments, however, have shown that when self-assembly takes place outside equilibrium they do not appear at those free energy minima but rather at optimal values of structural parameters. On the basis of these observations, we propose a selection criterion for which structures come up at the minima of a non-equilibrium free energy that takes into account the energy needed to change their configuration. The criterion is able to predict the formation and configuration of structures such as Liesegang rings and patterns in magnetic colloids and could constitute a powerful tool to understand the synthesis of advanced materials, enantiomers, and nanoparticles.

This chapter was published in *the Journal of Physical Chemistry B*, **125**, 1838-1845, (2021). Ref.[1]

6.1. Introduction: Variational principles and non-equilibrium potentials

Being able to understand and to control the formation of self-assembled structures from a disorderly set of building blocks (BB) is a basic issue in the implementation of adaptive and reconfigurable materials [2], in the synthesis of hydrogels [3], the design of engineered tissues [4], the use of nano-particles in medicine [5], and the production of enantiopure drugs [6], to mention just a few. This knowledge could also provide a deeper insight into the origin of life [7].

The search for a general criterion to predict the evolution of dissipative systems has been the subject of numerous investigations over the years. As early as 1931, Onsager proposed a variational principle in terms of a potential, the dissipation function [8]. Years later, Graham analyzed the question of why there exist systems far from thermodynamic equilibrium whose stationary states may be described by a non-equilibrium potential which can be interpreted as a natural generalization of thermodynamic functions [9]. Subsequently, Prigogine formulated his minimum entropy production principle as a criterion to explain self-organization processes [10]. In the same line as Graham, Maes found a potential for non-equilibrium steady-states as a function of the energy dissipated in the process which is not necessarily a minimum [11]. On the contrary, Dewar proposed his maximum entropy production principle (from Shannon entropy) to describe self-organization processes [12]. More recently, Doi showed that from Onsager's principle one can derive nonlinear evolution equations [13]. All these criteria account for the emergence of non-equilibrium steady-states and the appearance of self-organization in terms of *state variables* but they do not predict the formation of self-assembled structures characterized by *structural parameters*, as observed in the experiments.

In equilibrium self-assembly, structures emerge at minimum values of the free energy ΔG_{rev}, the energy needed to form a structure in the absence of dissipation. The probability of finding the structure is thus given by the canonical distribution: $p_{eq} \propto \exp(-\Delta G_{rev}/k_B T)$, with k_B the Boltzmann constant and T the temperature. This criterion predicts the appearance of structures in equilibrium but is no longer valid when self-assembly takes place outside equilibrium. Experiments show that a great diversity of structures arise at specific values of structural parameters characterizing the structures. For instance, hydrogels appear at optimal values of the maximum size of the fibers forming them [14, 15]. Crystallized structures emerge at particular values of the sphericity [16] or of the density [17] while chiral molecules and proteins do it at typical values of the orientation of a functional group [18, 19, 20]. The parameters characterizing the formation of microtubule-based structures are the average distance between structures and the ratio between kinetic constants [21, 22, 23]. Some other examples to which we will pay more attention later are Liesegang banding, where the parameter is the distance between bands [24, 25], and magneto-hydrodynamic assemblies that can be characterized by the number of particles located at a central region of the structure [26]. These results foster the search for an effective potential able to predict the formation of structures under non-equilibrium conditions in the same way as free energy does in equilibrium processes. Based on the form of this potential, we will propose a criterion for the formation of nonequilibrium self-assembled structures.

The chapter is organized as follows. In ”Non-equilibrium self-assembly kinetics”, we formulate the kinetics of the process and obtain the probability of the formation of a structure. In Çriterion for the formation of structures", we propose the selection criterion and illustrate its use for crystallization. In Results and discussions", we apply our formalism to the cases of Liesegang rings and pattern formation in magnetic colloids. In the last Section, we present our main conclusions.

6.2. Methods

6.2.1. Non-equilibrium self-assembly kinetics

We consider the formation of multiple forms B_i ($i = 1, ..., M$) of a structure B (polymorphs) from a precursor A via nonequilibrium self-assembly processes taking place at constant temperature, volume and pressure:

$$\mathrm{A} \longleftrightarrow \mathrm{B_i}$$

Experiments show that polymorphs emerge at certain values η_i of a parameter that characterises the formed structures [15, 17, 19, 20, 21, 25, 26]. The process, illustrated in Fig.**6-1**(a), can be modelled by the evolution of the state of the system in a potential $\Phi(\gamma, \eta)$, with γ and η reaction coordinates (normalized to one), as shown in Fig.**6-1**(b). In the energy landscape, the wells, separated by potential barriers, identify different compounds involved in the processes. The precursor A corresponds to the state $\gamma = 0$ and the polymorphs B_i to $\gamma = 1$, for all values of η.

Probability conservation along the path leading to B_i implies that ρ fulfills the continuity equation

$$\frac{\partial \rho(\gamma, \eta_i, t)}{\partial t} = -\frac{\partial J_i}{\partial \gamma} \tag{6-1}$$

where J_i is the probability current. The energy per unit of volume ρe along the trajectory is

$$\frac{\partial \rho e}{\partial t} = -\frac{\partial J_{e,i}}{\partial \gamma} \tag{6-2}$$

where $J_{e,i}$ is the energy current. The irreversible entropy change in the formation of the i^{th} polymorph is given by

$$\delta_{irr} s(\eta_i, t) = -\frac{1}{T} \int_0^1 (\mu \delta\rho - \delta\rho e)_{\eta_i} d\gamma \tag{6-3}$$

with μ the chemical potential. Taking the time derivative of Eq.(6-3), using Eqs.(6-1)-(6-2) and the form of the energy current: $J_{e,i} = -J_i \partial E_c / \partial \gamma$ [27], where E_c is the energy that the system needs to overcome the barrier in η in order to change the configuration of a polymorph, with $-\partial E_c / \partial \gamma$ its associated force F, the entropy production rate for the formation of the i^{th} polymorph is

$$\sigma(\eta_i, t) = -\frac{1}{T} \int_0^1 \left(-\mu \frac{\partial J_i}{\partial \gamma} - J_i F \right)_{\eta_i} d\gamma. \tag{6-4}$$

In the case of a single polymorph, E_c vanishes, therefore the entropy production rate reduces to that of a single chemical reaction [28].

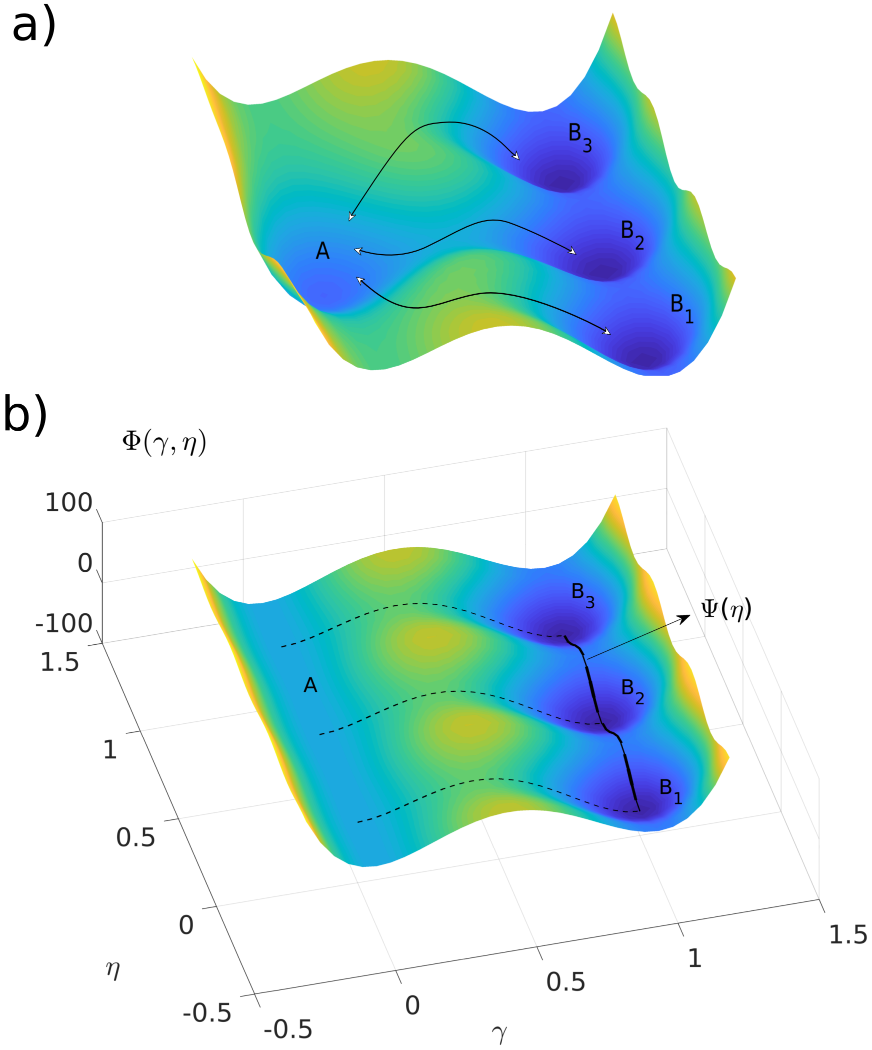

Fig. 6-1.: Kinetics of the polymorph formation process in the space of reaction coordinates. a) Formation of three possible structures (B_1, B_2, B_3) from the precursor A. b) Potential barrier Φ as a function of the reaction coordinates γ and η . The continuous black line represents the potential for $\gamma = 1$, Ψ, at the end of the process when polymorphs are formed. The dashed black lines are the trajectories leading from the precursor to the polymorphs parametrized by the coordinate γ.

Integrating this expression by parts, we obtain the local entropy production rate

$$\sigma(\gamma,\eta_i,t) = -\frac{1}{T}J_i\left(\frac{\partial\mu_{eff}}{\partial\gamma}\right)_{\eta_i} \tag{6-5}$$

where $\mu_{eff} = \mu + E_c$ is an effective chemical potential which considers the formation of multiple polymorphs. The total entropy produced in the formation of a structure at time t is

$$\Sigma(\eta_i,t) = \int_0^t\int_0^1 \sigma(\gamma,\eta_i,t^{'})d\gamma dt^{'} \tag{6-6}$$

The Goudy-Stodola theorem, relates the energy dissipated E_d with the entropy produced Σ as: $E_d = T\Sigma$ [29]. The formation of structures from building blocks is an irreversible process that includes activation, mass diffusion and heat conduction. All these processes and not only heat exchange from the reservoir produce entropy.

The chemical potential μ along the trajectory is the sum of ideal and excess parts: $\mu = \mu^{id} + \mu^{ex}$. The ideal chemical potential is: $\mu^{id} = \mu_0 + k_BT\ln\rho$ with μ_0 the standard chemical potential along the trajectory. The excess chemical potential is: $\mu^{ex} = k_BT\ln f + E_d$ with f the activity coefficient and E_d the energy dissipated per mol used to overcome the potential barrier. The effective chemical potential can be re-written as

$$\mu_{eff} = k_BT\ln\rho + \Phi \tag{6-7}$$

with Φ an effective potential barrier that takes into account the non-ideal nature of the process

$$\Phi = \Phi_{rev} + T\Sigma + E_c, \tag{6-8}$$

where we have used the relation $E_d = T\Sigma$ which corresponds to the energy needed to overcome the potential barrier in γ that is dissipated in the process. The reversible part of the potential, $\Phi_{rev} = \mu_0 + k_BT\ln f$, is the equilibrium free energy per mol. From the local entropy production rate (Eq.(6-5)), we obtain the expression of the current [30]

$$J_i(\gamma,\eta_i,t) = -\frac{D_\gamma}{k_BT}\rho\frac{\partial\mu_{eff}}{\partial\gamma} \tag{6-9}$$

where D_γ is the diffusivity in γ-space which can also be written as

$$J_i(\gamma,\eta_i,t) = -D_\gamma e^{-\beta\Phi}\frac{\partial e^{\beta\mu_{eff}}}{\partial\gamma} \tag{6-10}$$

with $\beta = (k_BT)^{-1}$. In order to study the kinetics of the formation of the structures, we perform a coarse-graining of the description eliminating the γ coordinate so that the probability distribution is given by $p(\eta_i,t) = \int_0^1\rho(\gamma,\eta_i,t)d\gamma$. The continuity equation for the probability p is obtained by integrating Eq.(6-1) in γ

$$\frac{dp(\eta_i,t)}{dt} = -J_i(\eta_i,t) \tag{6-11}$$

while the kinetic equation for the precursor A is

$$\frac{dp_0(t)}{dt} = \sum_{i=1}^{M} J_i(\eta_i, t) \tag{6-12}$$

where $\sum_i p(\eta_i,t) + p_0(t) = 1$ to fulfill probability conservation in (γ,η)- space. Assuming that the process is quasi-stationary [30], fast enough so that the current does not depend on γ, and integrating Eq.(6-10) in γ, we obtain the quasi-stationary flux as a combination of two (forward and backward) Arrhenius factors

$$J_i(\eta_i,t) = \frac{D_\gamma}{\int_0^1 e^{\beta\Phi} d\gamma} \left(e^{\beta\mu_{eff}(1,\eta_i,t)} - e^{\beta\mu_{eff}(0,\eta_i,t)} \right) \tag{6-13}$$

This expression, consistent with the law of mass action, shows that the current is a nonlinear function of the chemical potential difference (affinity). We then conclude that that the theory presented, within the framework of mesoscopic non-equilibrium thermodynamics [28], is not restricted to the linear domain proper of non-equilibrium thermodynamics [27].

Eqs.(6-11) and (6-13) describe the kinetics of the formation of polymorph B_i. The stationary probability is thus given by

$$p(\eta) = p(\eta_0) e^{-\beta\Delta\Psi(\eta)} \tag{6-14}$$

with $\Delta\Psi = \Psi - \Psi_0$, where $\Psi(\eta_i,t) \equiv \Phi(1,\eta_i,t)$ and $\Psi_0 \equiv \Phi(0,\eta,t)$.
In the case of formation of two polymorphs, B_1 and B_2, characterized by the coordinates η_1 and η_2, the relation between the stationary probabilities is

$$\frac{p(\eta_1)}{p(\eta_2)} = \exp(-\beta(\Delta\Psi(\eta_1) - \Delta\Psi(\eta_2))) \tag{6-15}$$

This relation explains the experimental feature that outside equilibrium some structures may emerge with a higher probability which has been observed in the formation of enantiomers [18] and magneto-hydrodynamic patterns [26]. In equilibrium, the probabilities coincide since the potential reaches the same value for all values of η.

6.2.2. Criterion for the Formation of Structures

Studies carried out in ecological, enzymatic and gelation processes show that ordered states and self-assembled structures emerge when the energy dissipation reaches a maximum value as a function of input fluxes, kinetic constants and fiber sizes [31, 32, 33]. On the contrary, in the formation of spatio-temporal structures, self-healing surfaces, Liesegang rings and magneto-hydrodynamic assemblies, the energy dissipation shows a minimum as a function of stationary fluxes, external perturbation, scale factors, and central particles[10, 34, 33, 26]. The fact that systems evolves making efficient use of available resources [35, 36], enables us to assume that an extreme value of the energy dissipated, at which $T\partial\Sigma/\partial\eta|_{\eta*} = 0$, is the signature of an optimal design of the structures. Smooth changes in the configuration of the structures can thus be induced by a small amount of energy dissipated [33].

Since E_c is the energy needed to overcome the barrier in η to change the configuration of a polymorph, close to η^* we have $E_c = T|\Sigma(\eta) - \Sigma(\eta^*)|$ which corresponds to the energy needed to reach the optimal configuration. Expansion of $\Sigma(\eta)$ around η^* gives

$$\Sigma(\eta) \approx \Sigma(\eta*,t) + \frac{1}{2}\left(\frac{\partial^2\Sigma}{\partial\eta^2}\right)_{\eta*}(\eta - \eta*)^2 \tag{6-16}$$

and

$$\frac{\partial\Sigma}{\partial\eta} \approx \left(\frac{\partial^2\Sigma}{\partial\eta^2}\right)_{\eta*}(\eta - \eta*) \tag{6-17}$$

Combining both relations and substituting the resulting expression for $\Sigma(\eta)$ into E_c close to η^*, we obtain

$$E_c \approx \frac{T}{2}\left(\frac{\partial\Sigma}{\partial\eta}\right)^2 \Bigg/ \left|\left(\frac{\partial^2\Sigma}{\partial\eta^2}\right)_{\eta*}\right| \tag{6-18}$$

this expression is analogous to the conformational temperature for systems of interacting particles in quasi-equilibrium [37].

The emergence of the structures leads to energy changes summarized in the effective potential (Eq.(6-8)). By using Eq.(6-8) and Eq.(6-18), the change in the effective potential is given by

$$\Delta\Psi \approx \Delta\Psi_{rev} + T\Sigma + \frac{T}{2}\frac{(\Sigma')^2}{|\Sigma''(\eta^*)|} \tag{6-19}$$

This result can now be used in Eq.(6-14) to obtain the probability to find a structure which explains why structures appear at specific values of the parameter η and not necessarily at the minima of the equilibrium free energy. Our criterion then states that the most likely structure emerges at the minimum of the effective potential change $\Delta\Psi$.

An identical expression of the potential follows from the optimization process of the energy required to form a structure in which the presence of dissipation is introduced as a constraint to the kinetics. Details of this optimization process are presented in the Annex D.

An example of application of the criterion established is crystallization. Crystal structures, represented in Fig.**6-2**, are characterized by sphericity η which is a measure of how different its form is from that of a sphere. It is defined as the ratio between the surface area of a sphere whose volume V is the same as the volume of the formed structure and the surface area of the structure A, i.e., $\eta \equiv \pi^{1/3}(6V)^{2/3}/A$ [38]. Non-spherical crystals and non-racemic mixtures of chiral non-spherical crystals [18] having different values of the sphericity are observed in a crystallization process when the metastable phase moves under the influence of a shear stress [16, 28]. Characterization of the agglomerates and crystals only in terms of their number of constituents cannot account for the formation of different polymorphs which can be distinguished from each other by their different sphericities.

In Fig.**6-2**(a), we illustrate the evolution of the shape of a crystal, through different polymorphs, in terms of the sphericity. In Fig.**6-2**(b), we represent the probability distribution of the structures fulfilling Eq.(6-14)

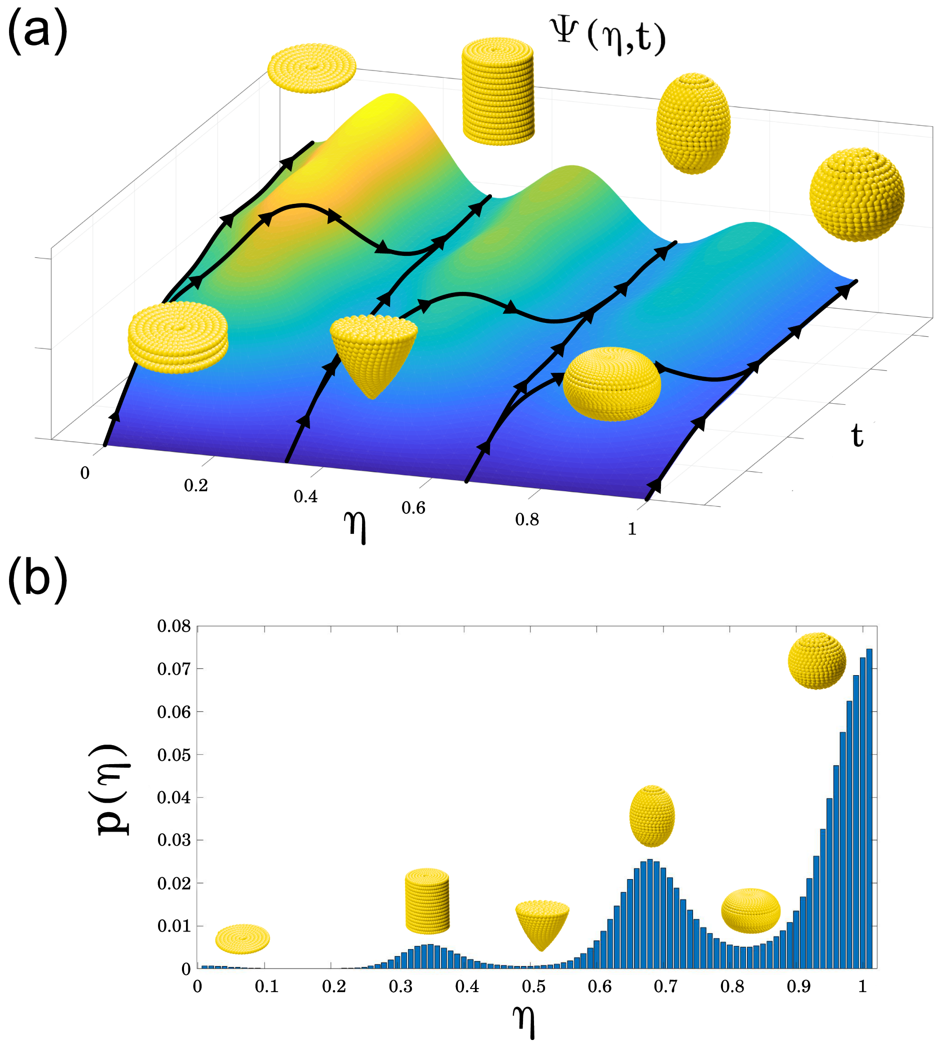

Fig. 6-2.: Sketch of : a) A typical form of the potential energy landscape $\Psi(\eta,t)$ showing the existence of different polymorphs (yellow structures), varying from 2-D disks ($\eta \to 0$) to spheres ($\eta \to 1$). Dashed lines show the trajectories that the shape of a structure performs in η-space. The potential increases in time due to its dependence on the entropy produced at time t, see Eq.(6-19). b) The long-term probability as a function of the structural parameter $p(\eta)$. The probability is higher when the potential is lower, see Eq.(6-14). This typical behavior has been found in the cases of Liesegang rings and pattern formation in suspensions of colloidal magnetic particles.

which corresponds to the stationary solution of Eq.(6-11). In the figure, we illustrate that the formation of disks ($0 < \eta < 1/5$) appearing at high values of Ψ is less likely than that of spheres ($\eta \to 1$) for which the potential is smaller. Finally, we highlight that structural parameters characterizing the structures must be distinguished from order parameters which measure the degree of order of systems undergoing phase transitions [39, 40].

6.3. Results and Discussion

6.3.1. Liesegang rings

A representative example of pattern formation and self-organization in NESA processes is the periodic precipitation pattern discovered by *R. E. Liesegang* in 1896 [41, 42]. This consists of a number of concentric rings (in 2D) or bands (in 1D) resulting from the diffusion of an ionic co-precipitate and the periodic precipitation of an insoluble solid in a gel medium [43], as illustrated in Fig.**6-3**(a)-(d). The process gives rise to the formation of polymorphic stable or metastable structures [44, 45]. It is induced by the existence of heterogeneous initial conditions in which the main ion, the inner ion, is located at the center of the system (for a 2D system) and is separated from the outer ion by means of a membrane. At $t = 0$, the membrane is taken out and the diffusion-reaction-precipitation phenomenon is triggered. A more detailed explanation of the phenomenon and the values of the relevant physico-chemical parameters are given in Ref.[24].

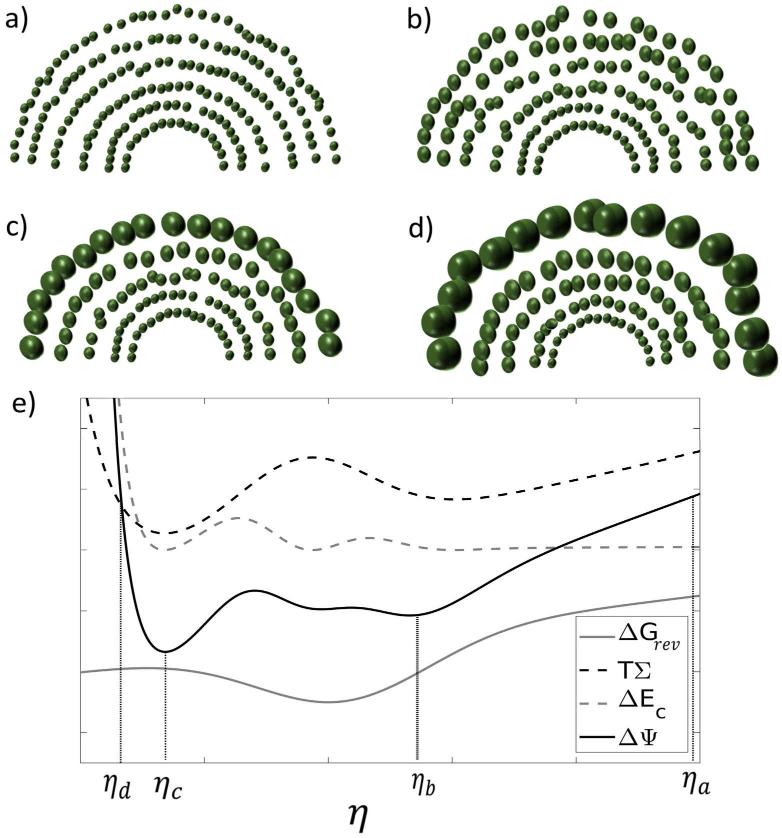

Fig. 6-3.: Polymorphs of Liesegang rings and potential $\Delta\Psi$ as a function of particle size variation. (a)-(d) Liesegang rings are characterized by η_a, η_b, η_c and η_d. Low values of η, such as η_d, correspond to high variations of the particle size from ring to ring while at higher $\eta's$, η_a, those variations are smaller.(e) Effective potential $\Delta\Psi$ (Eq.(6-19)), dissipated energy $T\Sigma$, reversible free energy change ΔG_{rev} (both from Ref. [33]) and configurational energy ΔE_c (Eq.(6-18)). The global minimum of $\Delta\Psi$ does not coincide with the minimum of ΔG_{rev} but appears at η_c which represents the same structure as that found in the experiments [25].

The structural parameter η is, in this case, the variation of the particle size from ring-to-ring which affects the chemical potential and the stoichiometry of the process and thus modifies the reaction rates and the energy dissipation. In our study, we have solved the model for different values of η. In this case, the potential follows from $\Delta\Psi_{rev} \equiv \Delta G_{rev}$ (free energy change per mol) and Σ which can be obtained from the formation dynamics of the Liesegang rings by solving numerically the system of partial differential equations for each component of the system (see Appendices). The reversible free energy change is: $n\Delta G_{rev}(\eta) = \sum_i n_i(\eta) h_i^0 + 4n_s \pi\gamma r_p(\omega)^2 - RT\sum_i n_i(\eta)\ln n_i(\eta)/n_T$ [24], where h_i^0 is the standard specific enthalpy, n_i the number of moles of component $i-th$, n the total number of moles and r_p the average particle radius conforming the rings which depend on the variation in particle size from ring to ring. The total entropy produced per mol is: $\Sigma(\eta) = \int_0^\infty \int_r \sigma(r,t;\eta) drdt$, where r is the radial coordinate and σ the entropy production rate per mol of the BB.

In Fig.**6-3**(e), we show how the potential varies with the structural parameter. We observe that the global minimum of $\Delta\Psi$ does not coincides with the global minimum of ΔG_{rev} due to the presence of dissipation. The value of η that minimizes $\Delta\Psi$, denoted by η_c agrees with that of the structural parameter obtained in the experiments [25]. The values of the parameter at which one observes sharp, slight and no variation of the average particle size from ring to ring are denoted by η_d, η_b and η_a, respectively.

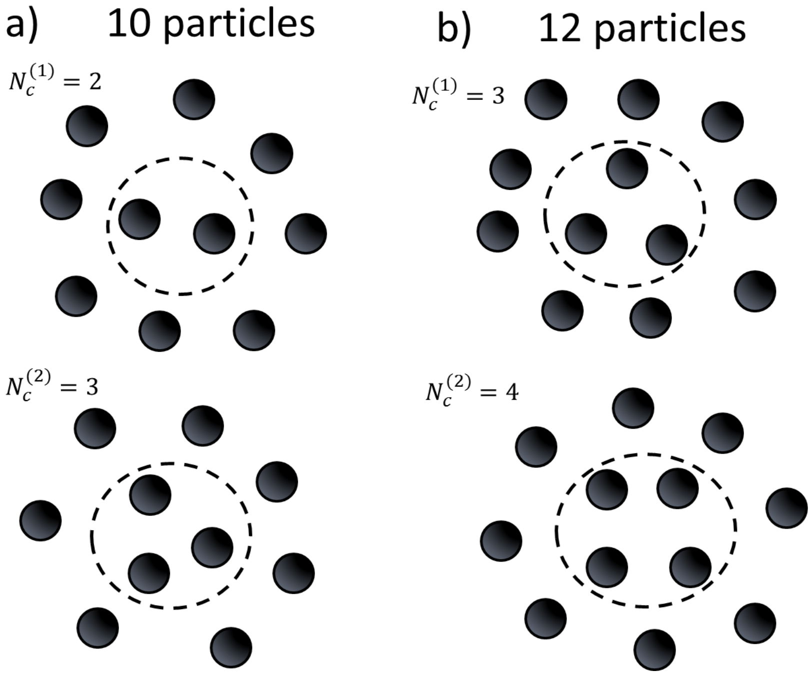

Fig. 6-4.: Steady-state polymorphs observed in experiments with colloidal magnetic particles [26]. Circles denote the regions where central particles are located. (a) For $N = 10$, one observes two structures with number of central particles N_c: $N_c^{(1)} = 2$ and $N_c^{(2)} = 3$. (b) For $N = 12$, the numbers of central particles are $N_c^{(1)} = 3$ and $N_c^{(2)} = 4$.

6.3.2. Patterns in magnetic colloids

In this second case, we consider a set of small magnetic particles suspended on a liquid-air interface under the influence of a magnetic field generated by a rotating magnet [46]. The movement of the particles perturbs the fluid's state of rest giving rise to the formation of a hydrodynamic pattern which in turn induces the assembly of the particles that orbit around the axis of the magnet (Fig.**6-4**). The energy supplied by the rotating magnet is dissipated in the fluid due to its viscous nature.

We will apply our formalism to compute the probability of predicting the type of structures emerging in the magneto-hydrodynamic system described. Experiments [26] were performed at different values of the Reynolds number *Re* and at two different numbers of particles *N*. One observes the existence of two polymorphs that differ in the number of particles N_c in the central region of the system (see Fig.**6-4**). Both *Re* and N_c characterize the structures. The experiments [26] show the existence of only two possible values of N_c.

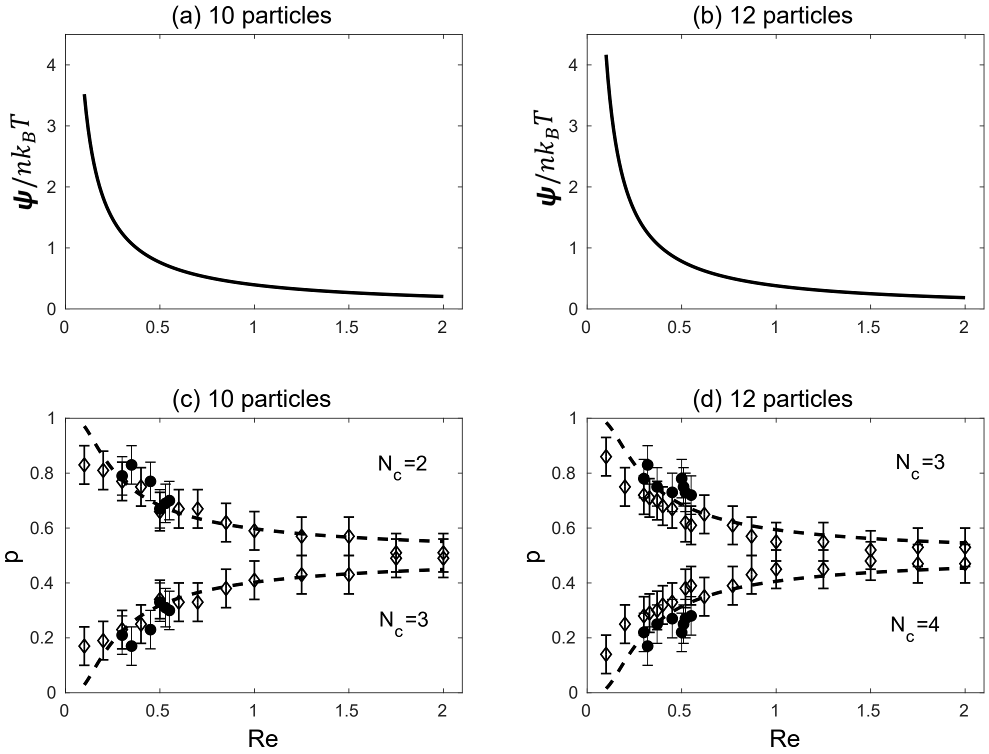

Fig. 6-5.: Potential and probability for different numbers of particles, particles in the central region and Reynolds numbers. Experimental data are represented by filled symbols and simulation results by hollow symbols[26]. Dashed lines stand for predictions of our model. In (a) and (b), we represent the difference between the potentials of both polymorphs, $\Psi = \Psi_{Nc^{(2)}} - \Psi_{Nc^{(1)}}$. Figures (c) and (d) show the probability for each polymorph.

Since the change of the free energy for both configurations and different *Re* is equal because composition and fluid-particle interaction do not depend on these variables, by using Eq.(6-19) with $\Delta\Psi_{rev} = 0$, the potential for each polymorph Ψ_{N_c} as a function of Re is

$$\Psi_{N_c}(Re) = T\Sigma_{N_c}(Re) + \frac{T}{2}\frac{\left(\Sigma'_{N_c}(Re)\right)^2}{\Sigma''_{N_c}(Re^*)} \tag{6-20}$$

with $T\Sigma_{N_c}(Re)$ the energy dissipated in each configuration due to viscous effects [26] and Re^* the Reynolds number that maximizes dissipation. The probability of finding a structure characterized by a value of N_c as a function of Re is given by

$$p_{N_c}(Re) = k_0 \exp\left(\frac{-\Psi_{N_c}(Re)}{k_B T}\right). \tag{6-21}$$

where k_0 is a normalization constant obtained from the condition : $\sum_{N_c} p_{N_c}(Re) = 1$. In Figs.**6-5**(c) and (d), we show the probability for structures with $N = 10$ and $N = 12$ particles as a function of the Reynolds number. As follows from the figure, our results show very good agreement with experiments [26] with errors of 4,7 % and 5,8 %, respectively.

In the figure, we observe that in the cases of 10 and 12 particles, the configurations corresponding to the polymorph with $N_c^{(2)}$ are the most dissipative and thus the less likely, as follows from Eq.(6-20). For high values of Re, dissipation increases and is similar for both polymorphs, thus making the probability of observing them also similar.

6.4. Conclusions: The criterion and the dissipation

In summary, we have proposed a criterion that accounts for the formation of self-assembled structures under nonequilibrium conditions. It establishes that the structures emerge at the minima of an effective potential (eq.(6-19)) that takes into account the energy needed to change their configuration, with a probability given by eq.(6-14). The selection criterion is based on experimental observations in which self-assembled structures emerge at particular values of some structural parameters that characterize the structures and not at the minima of the free energy, as occurs when the process takes place under equilibrium conditions. It has been validated in two cases of current interest: Liesegang patterns and pattern formation in suspensions of colloidal magnetic particles. In both cases, we find that the most likely polymorphs found in the experiments are precisely those which minimize the potential proposed.

The framework presented could systematically be used to predict the formation of polymorphs which are crucial to identify transient states in protein-folding, to understand why certain organic enantiomers are predominant [47], to improve the computer-aided drug-design [48], and, in general, to analyze the synthesis of crystals, hydrogels, reconfigurable materials, man-made tissues and nanoparticles.

Bibliography

[1] Andrés Arango-Restrepo, Daniel Barragán, and J. Miguel Rubi. A criterion for the formation of nonequilibrium self-assembled structures. *The Journal of Physical Chemistry B*, 125(7):1838–1845, 2021.

[2] Susan A. P. van Rossum, Marta Tena-Solsona, Jan H. van Esch, Rienk Eelkema, and Job Boekhoven.

Dissipative out-of-equilibrium assembly of man-made supramolecular materials. *Chem. Soc. Rev.*, 46:5519–5535, 2017.

[3] Allan S Hoffman. Hydrogels for Biomedical Applications. *Adv. Drug Deliv. Rev.*, 64:18–23, 2012.

[4] Karoly Jakab and et al. Tissue engineering by self-assembly of cells printed into topologically defined structures. *Tissue Engineering Part A*, 14(3):413–421, 2008.

[5] Andrew Z Wang, Robert Langer, and Omid C Farokhzad. Nanoparticle Delivery of Cancer Drugs. *Annu. Rev. Med*, 63:185–198, 2012.

[6] Maria C Nunez, M Eugenia Garcia-Rubino, Ana Conejo-Garcia, Olga Cruz-Lopez, Maria Kimatrai, Miguel A Gallo, Antonio Espinosa, and Joaquin M Campos. Homochiral drugs: a demanding tendency of the pharmaceutical industry. *Current medicinal chemistry*, 16(16):2064–2074, 2009.

[7] Editorial. Self-assembling life. *Nat. Nanotechnol.*, 11:909, 2016.

[8] Lars Onsager. Reciprocal relations in irreversible processes. i. *Phys. Rev.*, 37:405–426, Feb 1931.

[9] R Graham and H Haken. Generalized thermodynamic potential for markoff systems in detailed balance and far from thermal equilibrium. *Zeitschrift für Physik A Hadrons and nuclei*, 243(3):289–302, 1971.

[10] Ilya Prigogine and G Nicolis. *Self organization in non equilibrium systems*. John wiley & sons, 1 edition, 1977.

[11] Christian Maes and Karel Netocny. Minimum entropy production principle from a dynamical fluctuation law. *Journal of Mathematical Physics*, 48(5):053306, 2007.

[12] Roderick Dewar. Information theory explanation of the fluctuation theorem, maximum entropy production and self-organized criticality in non-equilibrium stationary states. *J. Phys. A: Math. Gen.*, 36(3):631, 2003.

[13] Masao Doi. Onsager's variational principle in soft matter. *Journal of Physics: Condensed Matter*, 23(28):284118, jun 2011.

[14] Andrés Arango-Restrepo, J Miguel Rubi, and Daniel Barragán. Understanding gelation as a nonequilibrium self-assembly process. *J. Phys. Chem. B*, 122(18):4937–4945, 2018.

[15] Job Boekhoven, Aurelie M. Brizard, Krishna N. K. Kowlgi, Ger J. M. Koper, Rienk Eelkema, and Jan H. van Esch. Dissipative Self-Assembly of a Molecular Gelator by Using a Chemical Fuel. *Angew. Chem.*, 122(28):4935–4938, 2010.

[16] David Reguera and J. M. Rubi. Homogeneous nucleation in inhomogeneous media. ii. nucleation in a shear flow. *The Journal of Chemical Physics*, 119(18):9888–9893, 2003.

[17] Sarah L. Price. From crystal structure prediction to polymorph prediction: interpreting the crystal energy landscape. *Phys. Chem. Chem. Phys.*, 10:1996–2009, 2008.

[18] Dilip K. Kondepudi, Rebecca J. Kaufman, and Nolini Singh. Chiral symmetry breaking in sodium chlorate crystallizaton. *Science*, 250(4983):975–976, 1990.

[19] Tsuneomi Kawasaki, Naoya Takamatsu, Shohei Aiba, and Yuji Tokunaga. Spontaneous formation and amplification of an enantioenriched α-amino nitrile: a chiral precursor for strecker amino acid synthesis. *Chem. Commun.*, 51:14377–14380, 2015.

[20] Fumika Suzuki, Takamasa Momose, and S. Y. Buhmann. Stern-gerlach separator of chiral enantiomers based on the casimir-polder potential. *Phys. Rev. A*, 99:012513, Jan 2019.

[21] Thomas Surrey, François Nédélec, Stanislas Leibler, and Eric Karsenti. Physical properties determining self-organization of motors and microtubules. *Science*, 292(5519):1167–1171, 2001.

[22] Torsten Wittmann, Anthony Hyman, and Arshad Desai. The spindle: a dynamic assembly of microtubules and motors. *Nat. Cell Biol.*, 3(1):E28, 2001.

[23] D. A. Head, W. J. Briels, and Gerhard Gompper. Nonequilibrium structure and dynamics in a microscopic model of thin-film active gels. *Phys. Rev. E*, 89:032705, Mar 2014.

[24] Andrés Arango-Restrepo, Daniel Barragán, and J Miguel Rubi. Nonequilibrium self-assembly induced liesegang rings in a non-isothermal system. *PCCP*, 20(7):4699–4707, 2018.

[25] Roché M. Walliser, Florent Boudoire, Eszter Orosz, Rita Tóth, Artur Braun, Edwin C. Constable, Zoltán Rácz, and István Lagzi. Growth of Nanoparticles and Microparticles by Controlled Reaction-Diffusion Processes. *Langmuir*, 31(5):1828–1834, 2015.

[26] Konstantin V Tretiakov, Igal Szleifer, and Bartosz A Grzybowski. The Rate of Energy Dissipation Determines Probabilities of Non- equilibrium Assemblies. *Angew. Chem. int. Ed*, 52:10304–10308, 2013.

[27] Sybren Ruurds De Groot and Peter Mazur. *Non-equilibrium thermodynamics*. Dover Publications Inc., 1985.

[28] D Reguera, JM Rubi, and JMG Vilar. The mesoscopic dynamics of thermodynamic systems. *J. Phys. Chem. B*, 109(46):21502–21515, 2005.

[29] Adrian Bejan, George Tsatsaronis, and Michael Moran. *Thermal Design and Optimization*. John Wiley and Sons, New York, 1996.

[30] I Pagonabarraga, A Pérez-Madrid, and JM Rubi. Fluctuating hydrodynamics approach to chemical reactions. *Physica A*, 237(1-2):205–219, 1997.

[31] Roderick C Dewar, Charles H Lineweaver, and Robert K Niven. *Beyond the Second Law: Entropy Production and Non-equilibrium Systems.* Springer-Verlag Berlin Heidelberg, 1 edition, 2014.

[32] R. K. Niven. Minimization of a free-energy-like potential for non-equilibrium flow systems at steady state. *Philos. Trans. Royal Soc. B*, 365(1545):1323–1331, 2010.

[33] Andrés Arango-Restrepo, J. Miguel Rubi, and Daniel Barragán. The role of energy and matter dissipation in determining the architecture of self-assembled structures. *The Journal of Physical Chemistry B*, 123(27):5902–5908, 2019.

[34] Michael Nosonovsky and Bharat Bhushan. Surface self-organization: From wear to self-healing in biological and technical surfaces. *Appl. Surf. Sci.*, 256(12):3982–3987, 2010.

[35] Marc-Olivier Coppens. A nature-inspired approach to reactor and catalysis engineering. *Curr. Opin. Chem. Eng.*, 1(3):281 – 289, 2012.

[36] Elisa Magnanelli, Simon Birger Byremo Solberg, and Signe Kjelstrup. Nature-inspired geometrical design of a chemical reactor. *Chem. Eng. Res. Des.*, 152:20 – 29, 2019.

[37] Jerome Delhommelle and Denis J. Evans. Configurational temperature profile in confined fluids. i. atomic fluid. *The Journal of Chemical Physics*, 114(14):6229–6235, 2001.

[38] Hakon Wadell. Volume, shape, and roundness of quartz particles. *The Journal of Geology*, 43(3):250–280, 1935.

[39] Ricard V. Solé and Susanna C. Manrubia. Extinction and self-organized criticality in a model of large-scale evolution. *Phys. Rev. E*, 54:R42–R45, Jul 1996.

[40] Ken Sekimoto. Evolution of the domain structure during the nucleation-and-growth process with non-conserved order parameter. *Physica A: Statistical Mechanics and its Applications*, 135(2):328 – 346, 1986.

[41] Raphael Ed Liesegang. Die achate. In *Silicate*, pages 186–190. Springer, 1914.

[42] Harry W Morse and George W Pierce. Diffusion and supersaturation in gelatine. *Physical Review (Series I)*, 17(3):129, 1903.

[43] Rabih F Sultan. Propagating fronts in periodic precipitation systems with redissolution. *Phys. Chem. Chem. Phys.*, 4(8):1253–1261, 2002.

[44] Mazen Al-Ghoul, Manal Ammar, and Rabih O Al-Kaysi. Band propagation, scaling laws and phase transition in a precipitate system. I: Experimental study. *J. Phys. Chem. A*, 116(18):4427, 2012.

[45] MM Ayass, I Lagzi, and M Al-Ghoul. Three-dimensional superdiffusive chemical waves in a precipitation system. *Phys. Chem. Chem. Phys.*, 16(45):24656–24660, 2014.

[46] Konstantin V. Tretiakov, Kyle J. M. Bishop, and Bartosz a. Grzybowski. The dependence between forces and dissipation rates mediating dynamic self-assembly. *Soft Matter*, 5(6):1279, 2009.

[47] Dilip Kondepudi, Bruce Kay, and James Dixon. End-directed evolution and the emergence of energy-seeking behavior in a complex system. *Phys. Rev. E: Stat. Phys., Plasmas, Fluids, - Statistical, Nonlinear, and Soft Matter Physics*, 91(5):1–5, 2015.

[48] Mohammad H Baig, Khurshid Ahmad, Gulam Rabbani, Mohd Danishuddin, and Inho Choi. Computer aided drug design and its application to the development of potential drugs for neurodegenerative disorders. *Current Neuropharmacology*, 16(6):740–748, 2018.

PART III. Meso-Structures and Non-Equilibrium Processes

7. Non-equilibrium self-assembly and energy dissipation induces chiral symmetry breaking

Crystallisation has been understood as an out-of-equilibrium self-assembly process that produces entropy. This is a special chapter in which we present our own experiments showing that energy dissipation plays an important role not only in the assembly process but also in the function of the assembled structures, in particular a function related to optical activity, crucial for understanding self-organisation and the origin of life. In this chapter, we want to quantify the effect of different initial conditions and external forces on the excess of crystalline enantiomers (by measuring the chiral symmetry breaking in the system).

Spontaneous mirror symmetry breaking is observed in a wide variety of systems on very different scales ranging from subatomic to cosmological. Systems exhibiting the formation of optical enantiomers have been studied to understand how they emerge, however, the mechanism and kinetics proposed do not explain why are they formed. We conducted experiments on the formation of salt crystals under non-equilibrium conditions, measuring for the first time the optical rotation angle of enantiomeric crystals in solution as a function of time during their formation. The enantiomer excess found is explained by the differences in the energies of the intermediate states of the enantiomers which have to be equal to the irreversible energy dissipated per salt mole in the processes. The non-equilibrium thermodynamics analysis proposed allows us to unveil why the existence of enantiomeric excesses in some salt crystals and amino acids might constitute a powerful tool to understand the emergence and amplification of the symmetry breaking taking place in molecules, proteins and crystals.

This chapter is based on a paper in preparation.

7.1. Introduction: Chiral symmetry-breaking

The fact that two or more theoretically equi-probable resulting states are not obtained in the expected proportions is known as chiral symmetry breaking which may occur on a wide variety of scales, being observed in elementary particles, simple organic molecules, amino acids, DNA, RNA, proteins and salt crystals [1, 2, 3, 4]. As the resulting states have the same energy, a thermodynamic treatment based on the study of quasi-equilibrium processes cannot explain the symmetry breaking in a system. In order to understand the phenomenon and investigate its potential intensification, several kinetic models have been proposed [4]. Such models with its corresponding simplifications run the risk of leading to incomplete, if not simply erroneous, interpretations of system thermodynamics [5].

Experiments have shown that the action of external factors such as polarised light [6], shearing [7, 8], temperature gradients [9] and in general external forces can give rise to a disproportion in the concentrations of the isomers (enantiomers) or even hinder their formation [1, 10]. Studying the role played by the presence of external forces in the thermodynamics and kinetics of enantiomer formation under non-equilibrium conditions is therefore of vital importance for understanding the mechanism of chiral symmetry breaking. The basic research we propose may have a technological impact in for example the production of efficient and safe medicines [10, 11, 12], the use of liquid crystals in biosensors and microlasers,[12], the control of self-assembly for the production of advanced materials [13] and in providing a deeper understanding of the emergence of life [14, 3].

Energy dissipation (from entropy production) takes place on all levels and it may shade light to understand why symmetry is broken to enable the emergence of homochiral structures (enantiomers), as the precursors of self-assembled and -organised structures. The emergence of biological self-organised structures comes from the directed and selective self-assembly of homochiral constituents in which energy dissipation and autocatalytic networks must be present [15, 16, 17, 18, 19, 5]. At the mesoscopic scale, it is well known that the formation of self-assembled structures entails dissipation [16, 17, 20, 21] whereas, at molecular scale, the emergence of enantiomers from chiral molecules requires symmetry breaking [22].

The mirror images of a chiral compound: Levorotatory (L) and Dextrorotatory (D) optical enantiomers, have the same energy but opposite optical rotation angles for polarized light. The crystallisation process of $NaClO_3$ has been the subject of much interest in recent years [4, 10, 2]. Experiments consisting of evaporating the solvent to obtain $NaClO_3$ crystals [7], performed by stirring the sample, showed the existence of a disproportion in the concentrations of both enantiomeric crystals of $NaClO_3$. When these experiments were performed without stirring, the concentrations of both enantiomers were found to be similar. Evaporation experiments also showed a dispropotion of enantiomers in the absence of stirring but at low supersaturation of salt [10]. These experiments clearly showed symmetry breaking in enantiomer formation when the process takes place outside of equilibrium. However, previous works aim to measure the enantiomeric excess only at the final of the crystallisation process, losing the information of the transient state and therefore lacking in relating the magnitude of the forces (temperature gradients, over-saturation) and the enantiomeric excess as a function of time. On the other hand, when considering the transient measurements, samples are taken, thus isolating the crystals and losing the connection with the forces present in the system [4, 10]. Therefore, it is important to consider the transient dynamics of the crystallization process and measure the populations

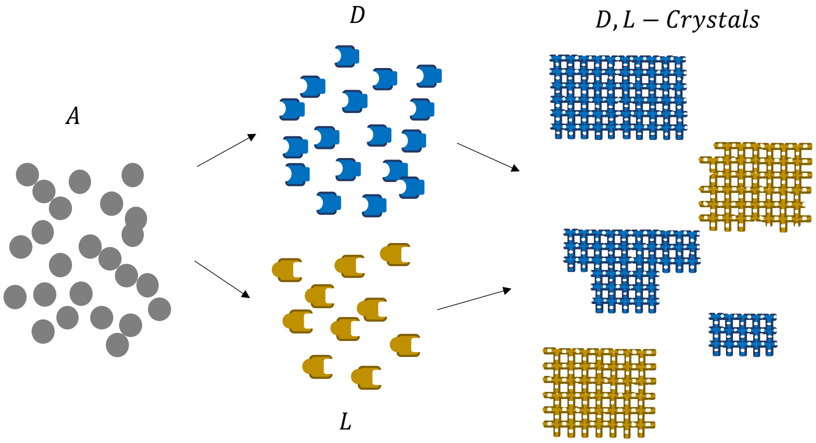

Fig. 7-1.: Cartoon of the chiral symmetry breaking from an achiral compound A (grey circles), which transforms into the chiral compounds D and L (blue and golden puzzle pieces respectively) leading to the formation of D and L crystals (blue and golden puzzles respectively).

in situ to be able to understand the role of the energy dissipation in chiral symmetry breaking.

In Fig.**7-1** we present a cartoon of the chiral symmetry breaking in which chiral structures, such as crystals, are built. From an achiral compound A, can be obtained chiral blocks or pieces D and L, in 1:1 proportion (non-dissipative processes) or in disproportion (symmetry breaking in dissipative processes) showing enantiomeric excess. Chiral blocks assemble sequentially or by agglomeration to form chiral structures, like puzzle pieces make up a puzzle or as solid compounds make up a crystal.

In this chapter, we show, by means of a non-equilibrium thermodynamic model, that the energy required to break the symmetry, and therefore leading to an enantiomeric crystal excess observed from the experiments, must be equal to the energy released in each stage of the crystallisation process. This energy increases the free energy barrier of one of the enantiomeric crystals and, consequently, decreases the formation rate of the enantiomer, thus explaining the enantiomeric excess. In the experiments performed, we have measured for the first time the enantiomeric excess of $NaClO_3$ along the crystallisation process of this substance, for different non-equilibrium conditions. The non-equilibrium thermodynamics model proposed provides the value of the energy dissipation responsible of the increase of the energy barrier and, therefore, of the enantiomeric excess percentage. We have found that the enantiomeric excess becomes more important when the actuating forces, temperature and fugacity differences, increase and therefore when energy dissipation, measured in terms of the entropy production rate, is larger. This result clearly shows the important role played by dissipation in the enantiomer formation process.

7.2. Dissipation at chiral symmetry breaking

Under equilibrium conditions, the formation process of L and D enantiomers leads to equivalent final populations since their free energies are identical. This is not the case when the process takes place outside of equilibrium, with the consequent dissipation of energy, where an excess of one enantiomer over the other is observed. This excess has been attributed to a disparity in the activation energies of the two enantiomers [2, 23, 4] which causes different formation rates. In order to explain the reason of such a disparity, we analysed the formation of $NaClO_3$ enantiomeric crystals. By measuring the optical rotation angle of the solution throughout the crystallization process and modelling the different kinetic mechanisms that take place, we show that the occurrence of an enantiomeric excess originates from the energy released in each step of the crystallisation. This energy is absorbed by the intermediary state of one of the enantiomers thus increasing the free-energy barrier and reducing its formation rate. Such intermediary reaches a more energetic excited state, and therefore more unstable since around the compound there are inhomogeneities (gradients) and other unstable intermediaries that induce a variation in the energy levels of the intermediary. It is important to notice that the first excited intermediary, of one enantiomer, contributes to inducing the transition to the excited intermediary state of the same enantiomer. Which enantiomer intermediary is initially excited is a process of stochastic nature in agreement with previous works [7].

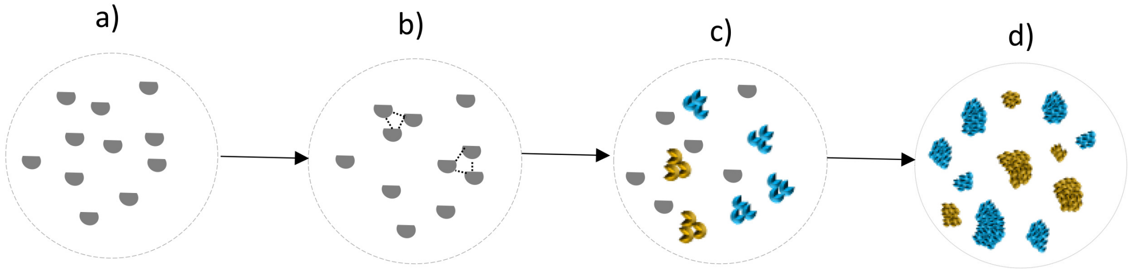

Fig. 7-2.: Enantiomer formation process. The circles zoom up a small portion of the system of 10nm (a,b,c) and 0,1mm (d) in size. The system is initially an under-saturated mixture ($\Delta z < 0$) of salt, denoted by grey dots, and glycerine a). The heat transfer to the surroundings causes the temperature of the system to decrease leading to stage b) characterised by an increase in the interaction between the salt compound (black dashed lines) thus reaching saturation ($\Delta z = 0$). For $\Delta z > 0$, small nuclei of both enantiomers are formed (L- and D-nuclei represented by gold and blue dots respectively) in the process of phase-change in which one of the enantiomers is dominant, as represented in stage c). Finally, crystal emergence takes place leading the system to a state of chemical and thermal equilibrium d) in which $\Delta z = 0$ and $\Delta T = 0$, with an enantiomeric excess.

In Fig.**7-2**, we illustrate the different stages of the crystallization process in which the two driving forces, temperature difference ΔT between the system and its surrounding and fugacity difference Δz between the solid and liquid phases reach different values. Initially (Fig.**7-2**(a)), the system is an under-saturated mixture of salt and glycerine, with $\Delta z < 0$ and a maximum value of ΔT. When the mixture comes into contact with its surroundings, it cools down to saturation point at which $\Delta z = 0$ while the salt in the aqueous phase forms small clusters that maximise Δz (Fig.**7-2**(b)). Thus, a fraction of the aqueous salt undergoes a phase change that favours the formation of nuclei of one enantiomer over the other, reaching a state in which $\Delta z > 0$ and $\Delta T > 0$ (Fig.**7-2**(c)). Once the nuclei of the first enantiomer are formed, crystals emerge and grow and eventually redissolve bringing the system to a final state characterised by a non-racemic mixture of enantiomeric crystals in which $\Delta z = 0$ and $\Delta T = 0$ (Fig.**7-2**(d)).

To analyse the kinetics and energetics of the enantiomer formation process, we will consider that the transformation of an achiral compound A, the aqueous component, into L- or D-enantiomeric crystals takes

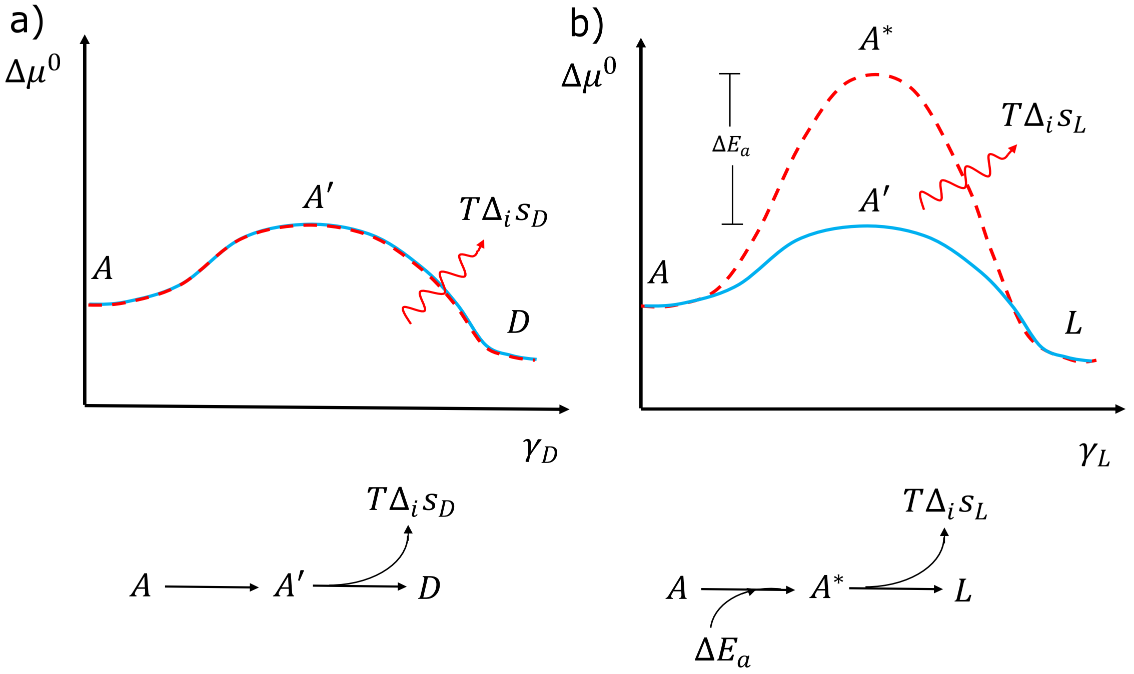

Fig. 7-3.: Free-energy landscapes in the formation of D (a) and L (b) enantiomers as a function of the reaction coordinates γ_L and γ_D. When the process takes place in equilibrium, where $\Delta z = 0$ and $\Delta_i s = 0$, the formation of both enantiomers from the achiral compound A takes place through the same state A prime. In this case, the barriers are represented by the continuous blue lines. Outside equilibrium, for $\Delta z > 0$ and $\Delta_i s > 0$, the energy $T\Delta_i s_D$ released in the formation of enantiomer D contributes to increase the barrier of enantiomer L by an amount $\Delta E_a = T\Delta_i s_T$ (with $\Delta_i s_T$ the total energy dissipated per salt mole) which reduces the formation rate of the L compound and breaks the symmetry. In this case, the landscape corresponds to the dashed red lines. The energy dissipated in the formation of a L-enantiomer is $T\Delta_i s_L$ whereas for a D-enantiomer is $T\Delta_i s_D$. This illustration corresponds to a crystallisation process in which the first excited intermediary corresponded to one of the L-enantiomer and so, the whole process is conditioned to the excitement only of L-intermediaries.

place across a standard free energy potential barrier, as illustrated in Fig.**7-3**(a). In non-dissipative quasi-equilibrium processes, in which $\Delta z \approx 0$, the state on top of the barrier $A^{'}$ is common to both enantiomers, as the blue lines of Fig.**7-3** show. Since there is no irreversible change of the entropy, $\Delta_i s = 0$, the entropy change per mole is simply the reversible change $\Delta_r s$. The formation of both enantiomers thus takes place along the same free-energy barrier which results in a racemic (1:1) mixture [7].

Outside equilibrium (Fig. **7-3**), when $\Delta z \neq 0$ and $\Delta T \neq 0$, the entropy change per salt mole is $\Delta s = \Delta_r s + \Delta_i s$, where the irreversible part contains contributions of both enantiomers: $\Delta_i s = \Delta_i s_L + \Delta_i s_D$. The energy dissipated in the formation of the D enantiomer is thus $T\Delta_i s_D$ (Fig. **7-3**(a)) whereas that for the L enantiomer is $T\Delta_i s_L$(Fig. **7-3**(b)). The figures illustrates the fact that the formation process of both enantiomers takes place across two different free energy barriers that have different transition states ($A^{'}$ and A^*) whose energy difference is $\Delta E_a = T\Delta_i s_T$, with $\Delta_i s_T$ the total entropy produced per mole. This disparity in barrier height leads to different enantiomer formation rates, which explains the excess of one enantiomer over the other

[2, 23, 4].

The total entropy produced consists of the entropy produced in the formation of the enantiomers $\Delta_i s$ and those corresponding to the remaining irreversible processes taking place in the system such as heat transfer, crystal emergence, crystal growth, precipitation and diffusion. In the Theory Section, we compute the entropy production rate σ of all irreversible processes and from it the total entropy production given through the expression: $\Delta_i s_T = \int \sigma dt/N$, where $N = N_L + N_D$ is the number of moles of solid salt, and N_L and N_D the number of moles of salt composing L- and D nuclei and crystals.

The model we propose (see Theory Section) computes the number of moles N_L and N_D and from them the enantiomeric excess defined as

$$\%e.e. = \frac{|N_L - N_D|}{N} 100\% \tag{7-1}$$

and the optical rotation angle

$$\alpha = \alpha_0 (N_L(h) - N_D(h))/N_0 \tag{7-2}$$

with $\alpha_0 = 50^o$ a reference angle, N_0 the initial amount of salt molecules and h the height of the test tube at which measurements were taken. Comparison of the model results with measurements of the rotation angle will be performed in the Results Section.

7.3. Experimental set up

A critical decision was to choose glycerol as the solvent, as we needed high dielectric and thermal properties, low evaporation, high viscosity and a refractive index close to that of crystals to avoid high light scattering. The initial step of the experiment was to mix given amounts of salt and solvent in our test tube (a cylindrical quartz cuvette with an inner diameter of 20 mm) and then heat from the bottom of the mixture to ensure complete dissolution at a constant temperature. The absence of optical activity was verified once the maximum temperature was reached. Once the salt has dissolved and only the homogeneous phase is present and the temperature is constant, we started the experiment by turning off the heater and letting the system cool down. We started measuring the optical activity and the temperature of the system until a steady state was reached and no considerable changes in optical activity were recorded. The height at which the measurements were made varied according to the initial salt/solvent ratio and the cooling conditions to avoid high scattering or low optical activity. In the enhanced cooling cases and for $w_s/w_g = 0{,}36$ in natural cooling, the measurement height was $h = H/3$, where H is the height of the test tube. For the remainig natural cooling cases, the height was $h = H/4$.

The polarimeter used is a home-built Mueller matrix polarimeter that incorporates four photoelastic modulators (4-PEM polarimeter) which allowed us to determine with high sensitivity the time-varying enantiomeric excess of the $NaClO_3$ solution. The instrument, described in detail in [24], was operated in transmission using a 405 nm laser diode (5W) as the light source. As the photoelastic modulators operate at high frequency ($\sim$ 50 kHz), this instrument can measure the 16 Mueller matrix elements of the sample simultaneously and at fast acquisition rates. In our experiments, a Mueller matrix was measured every $\sim$ 1s during the several hours that each of the experiments lasted. A scheme of our experimental setup is shown in Fig. **7-4**.

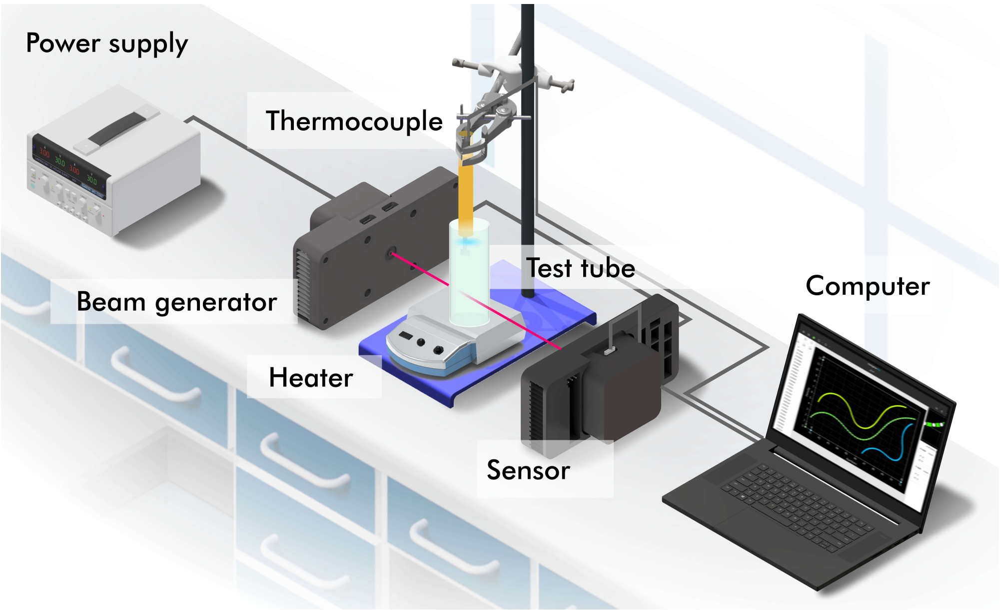

Fig. 7-4.: Experiment set up. Devices and equipment: Power supply, laser, polarization state generator (beam generator), thermocouple, test tube, heater, polarization state analyzer (sensor), detector and computer. The power supply provides the energy to the laser and the polarization state generator and polarization state analyzer so that there is a fine control of the transformation of polarization of light after passing through the solution in the test tube. All polarization data is transferred and stored in a computer. To manually measure the average temperature of the solution, a thermocouple is used which is placed over the laser beam to avoid interference.

The solution was contained in a cylindrical fused quartz cell with a path length of 20 mm. When the salt was completely dissolved a clear solution was observed and the measured Mueller matrix was the 4×4 identity matrix, indicating that there was no optical rotation (or any other optical effect) . However, as the salt began to precipitate the solution became progressively hazy, until at some point Tyndall scattering became evident. Scattering could also be identified from the Mueller matrix measured by the appearance of depolarisation, as the scattered photons tend to randomise their polarisation.

The measured Mueller matrices were analysed using the differential [25] formalism, which is well suited for the study of polarized light transmitted in turbid media. This method assumes that the polarisation properties of the medium have a uniform distribution along the optical path. The Mueller differential formalism can be introduced through the equation

$$\frac{d\mathbf{M}}{dz} = \mathbf{m}\mathbf{M}, \tag{7-3}$$

where the so-called differential matrix $\mathbf{m}$ relates the Mueller matrix of the homogeneous anisotropic medium to its spatial derivative along the direction of light propagation (z). A generally depolarizing Mueller matrix, satisfying Eq. (7-3) is $\mathbf{M} = e^{\mathbf{m}d} = e^{\mathbf{L}}$, where d is the optical pathlength and $\mathbf{L} = \ln\mathbf{M}$ the accumulated differential Mueller matrix. The optical rotation of this depolarizing medium is then determined as:

$$\alpha[^\circ] = \frac{180(l_{12} - l_{21})}{4\pi}, \tag{7-4}$$

where l_{ij} are the elements of **L**. Apart from optical rotation and depolarization, no other polarimetric effect (e.g. linear birefringence) were observed in the samples.

7.4. Model: kinetics and energetics of enantiomeric crystal formation

The model we propose describes the kinetics and energetics of enantiomeric crystal formation process which involves the solvent (glycerol) whose concentration remains practically constant, the dissolved salt and the solid salt in L- and D-configurations.

7.4.1. Salt phase change

In the first stage of the process, the dissolved salt form small nuclei that are the precursors of solid salt L- and D-nuclei. This process takes place along a reaction coordinate γ and is illustrated in Fig.**7-3**(b). The molar fraction of the salt that remains in aqueous state x evolves in time according to the reaction-diffusion equation

$$\frac{\partial x}{\partial t} = -\dot{r}_L - \dot{r}_D + D\frac{\partial^2 x}{\partial y^2} \tag{7-5}$$

where y is the coordinate along the axis of the test tube, D the diffusion coefficient, and $\dot{r}_L$ and $\dot{r}_D$ the phase change rates from dissolved salt to solid salt in L- and D- configurations, respectively.

The emergence rates of the nuclei precursors of the crystals, $\dot{r}_L$ and $\dot{r}_D$, are proportional to the fugacity difference between solid and liquid phases or oversaturation forces Δz_L and Δz_D. The L-rate is given by

$$\dot{r}_L = ke^{-\frac{E_{a,L}}{k_B T}}\Delta z_L \tag{7-6}$$

where k is a kinetic constant, and $E_{a,L} = E^0_{a,L} + \Delta E_a$ the activation energy with $E^0_{a,L}$ the activation energy of a quasi-equilibrium process. The forces depend on the free energy of the salt in aqueous and solid states, as well as on the molar fractions of the salt in both states and configurations. The L-oversaturation force is given by

$$\Delta z_L = e^{\frac{\mu_A}{k_B T}} - e^{\frac{\mu_L}{k_B T}} \tag{7-7}$$

where the chemical potentials are $\mu_A = \mu^0_A + k_B T \ln x f$ and $\mu_L = \mu^0_L + k_B T \ln x_L f_L$, with f and f_L being fugacity coefficients accounting for the non-ideality of the salt-solvent mixture, and x_L is the molar fraction of the salt in L-configuration.

For high salt concentrations, f is linear in x and must be zero for $x < x_s$, with x_s the saturation molar fraction, since under this condition there is no phase change. The activity coefficient is thus given by $f = f_0\Theta(x - x_s)$, with f_0 a constant, which implies that the oversaturation force behaves as $\Delta z_L \propto x^2$ and therefore so do $\dot{r}_L$ and $\dot{r}_D$. This behaviour is typical of an autocatalytic process, such as THE O A? IN the crystal formation process [7, 2]. To define f_L, we use the Gibbs-Duhem equation

$$x d\mu_A + x_L d\mu_L + x_D d\mu_D = 0 \tag{7-8}$$

in which x_D is the molar fraction of the salt in D-configuration. The molar fractions fulfil the relation $x + x_L + x_D = x_0$, with x_0 the initial molar fraction of the aqueous phase.

The solid phase is composed of the small nuclei and the L- and D-crystals. The corresponding reaction-diffusion equation for the molar fraction of salt conforming the solid L-nuclei is given by

$$\frac{\partial x_L}{\partial t} = \dot{r}_L - \dot{r}_L^{(c)} + D\frac{\partial^2 x_L}{\partial y^2} \tag{7-9}$$

where $\dot{r}_L^{(c)}$ is the rate at which L-nuclei transforms into L-crystals. An analogous equation holds for the evolution of x_D. The energy dissipation rate of the phase change is according to non-equilibrium thermodynamics given by [26, 27]

$$T\sigma_{ph}(y,t) = -(\dot{r}_L \Delta z_L + \dot{r}_D \Delta z_D) \tag{7-10}$$

where we have neglected the contribution of diffusion since it is much smaller than that of the phase change.

7.4.2. Crystallisation kinetics

Self-assembly of solid nuclei leads to the formation of L- and D-crystals which may also dissolve and precipitate because their density is different from that of the solvent. Whether precipitation occurs or not depends on the size of the crystal a_L and on the molar fraction of salt molecules n_L making up L-crystals. The mass flux of such molecules is $J_L^{(c)} = -D\partial n_L/\partial y - k_p \Delta\rho_c g a_L^3 n_L$, where the drift term is due to the buoyancy force [28], with k_p a precipitation constant [29], $\Delta\rho_c$ the difference between the molar density of the crystal and the solvent, and g the gravity force. The corresponding balance equation is thus

$$\frac{\partial n_L}{\partial t} = \dot{r}_L^{(c)} + \frac{\partial}{\partial y}\left(D\frac{\partial n_L}{\partial y} + k_p a_L^3 n_L\right) \tag{7-11}$$

The number of molecules forming a L-crystal is $N_L = N_0 n_L$, with N_0 the initial number of salt molecules. An analogous equation holds for N_D.

To find the crystal formation rate $\dot{r}_L^{(c)}$, we will describe the process in terms of the probability $p(l,t)$ of finding a crystal of size l at time t [30] which obeys the conservation law

$$\frac{\partial p}{\partial t} = -\frac{\partial J}{\partial l} \tag{7-12}$$

where J is the crystallization current in l-space [30]

$$J = -\frac{D_l}{k_B T} p \frac{\partial \mu}{\partial l} \tag{7-13}$$

with D_l a diffusivity in l-space and $\mu = k_BT \ln f^{(c)}p/(f^{(c)}p)_{eq} + \phi$ the chemical potential, with ϕ the energy required to form a crystal of size l and $f^{(c)}$ a fugacity coefficient. This energy consists of volume and surface contributions and is given by $\phi = -(\Delta\mu^0/v_p)l^3 + \Gamma l^2$, where v_p is the specific volume of the crystal and Γ the specific surface energy per unit of area[30]. The crystal growth rate at $l = a_0$, with a_0 the nuclei size, has to be equal to the rate at which crystals emerge, i.e., $\dot{r}_L^{(c)} = J(a_0)$. By knowing the amount of salt x_L necessary to make up L-crystals, and the actual amount of salt in the L-crystals n_L, we can obtain $J(a_0)$. Thus, by evaluating Eq.(7-13) at $l = a_0$ we obtain the rate of crystal formation

$$\dot{r}_L^{(c)} = -\frac{k_l a_0}{k_BT} \left.\frac{\partial\phi}{\partial l}\right|_{l=a_0} \Delta_c z \tag{7-14}$$

in which the fugacity difference between the L-crystal and the L-nuclei is $\Delta_c z = x_L^2 + x_L n_L - a_0 n_L^2/a_L$, where the first term x_L^2 accounts for crystal emergence from auto-catalysis or agglomeration of the nuclei whereas the second $x_L n_L$ results from absorption of nuclei on the crystals and the third corresponds to the inverse process in which smaller sizes favour the re-dissolution of the crystals in the solvent [2]. The rate of crystal formation $\dot{r}_D^{(c)}$ can be computed in a similar way.

By multiplying Eq. 7-12 by l and integrating in l, we obtain the evolution equation of the average L-crystal size a_L[30]

$$\frac{da_L}{dt} = -\frac{D_l l_0^2}{k_BT}\left(\frac{\partial\phi_L}{\partial a_L}\right) n_L \tag{7-15}$$

with $\phi_L = \phi(a_L)$, and $a_L = \int_{a_0}^{\infty} l p dl$. An analogous evolution equation can be written for D-crystals.

The entropy production rate of the crystal growth process σ_g is expressed as a sum of products between fluxes (J) and forces ($\frac{\partial\mu}{\partial l}$) [28]. The resulting expression of the entropy production rate considering the growing process of both enantiomeric crystals is

$$T\sigma_g(y,t) = -\int_{l_0}^{\infty} J(l_L)\frac{\partial\mu(l_L)}{\partial l_L}dl_L - \int_{l_0}^{\infty} J(l_D)\frac{\partial\mu(l_D)}{\partial l_D}dl_D \tag{7-16}$$

Analogously, the entropy production rate due to precipitation is

$$T\sigma_p(y,t) = -J_L^{(c)}\left(\frac{\partial n_L}{\partial y} + \Delta\rho_c g a_L^3 n_L\right) - J_D^{(c)}\left(\frac{\partial n_D}{\partial y} + \Delta\rho_c a_D^3 g n_D\right) \tag{7-17}$$

7.4.3. Heat transfer

The heat that the system exchanges with the environment which is at constant temperature T_s causes the temperature varies according to the equation

$$c_0 c_p \frac{\partial T}{\partial t} = \frac{2U}{d}(T_s - T) + \kappa\frac{\partial^2 T}{\partial y^2} \tag{7-18}$$

where c_p is the specific heat of the mixture at constant pressure, U the convective heat transfer coefficient, c_0 the total molar concentration, d the test tube diameter, and κ the thermal conductivity. The corresponding

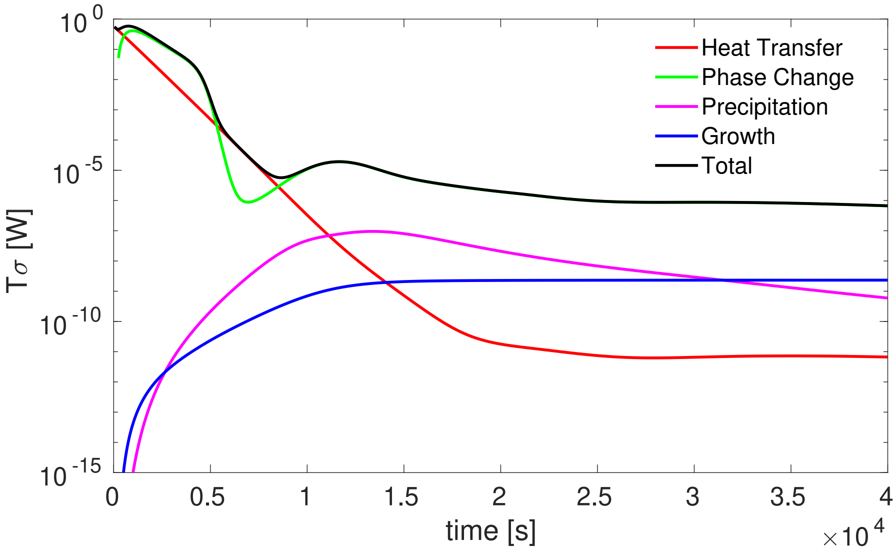

Fig. 7-5.: Time-dependent energy dissipation rate of the different irreversible processes occurring in crystal formation. The dissipation associated with phase change contributes most to the total dissipation while that due to heat exchange is significant in the initial states of the process.The dissipation for the other processes is much smaller than the above by orders of magnitude.

entropy production is [28]

$$\sigma_T(y,t) = \frac{\kappa}{T^2}\left(\frac{\partial T}{\partial y}\right)^2 \tag{7-19}$$

The different contributions to the energy dissipation rate in the crystallisation process obtained from Eqs.7-10,7-16,7-17,7-19 are represented in Fig. **7-5**. We observe that heat transfer and nuclei formation are the most dissipative processes and that the supersaturation gradient is the main driving force for crystal formation [31, 32, 33], as it causes the most dissipation. This conclusion is reached in all the cases studied.

7.5. Results and discussion

In the NaClO$_3$ crystallisation experiments, we measured the optical rotation angle of the solution throughout the process, for two cooling protocols and different salt concentration values, i.e. for different values of the over-saturation force with the purpose of exploring different values of the energy dissipation. The salt-solvent concentration ratio values considered, in grams of solute per grams of solvent, were: $w_s/w_g = 0{,}235$, $w_s/w_g = 0{,}32$, and $w_s/w_g = 0{,}36$, in the case of natural cooling, when the boundaries of the system are in contact only with the surrounding air, and $w_s/w_g = 0{,}235$, $w_s/w_g = 0{,}30$, and $w_s/w_g = 0{,}36$, for enhanced cooling, when the boundaries are in contact with water which has a higher cooling rate. These values have been chosen so that, under the conditions in which the experiments are carried out, we warranty that a fraction of the salt will be in solid phase when the temperature reaches room temperature. This is fulfil since the equilibrium solubility at room temperature in glycerine (the solvent) is $(w_s/w_g)_s = 0{,}23$ [34].

We have solved numerically Eqs. 7-5, 7-9, 7-11, 7-15 and 7-18 by using the finite-difference method in MATLAB®. In this way, we obtain the molar fractions of dissolved salt x, of salt of L- and D-nuclei x_L and x_D, of salt in L- and D-crystals n_L and n_D, and the average size of L- and D-crystals a_L and a_D, as well as the temperature T, all these quantities as a function of position and time. We thus define $N_L = N_0 n_L$ and $N_D = N_0 n_D$ which are used to compute the enantiomeric excess and optical rotation angle, as shown in Eqs. 7-1-7-2. The evolution equations of the molar fractions contain the expression of the free-energy barrier ΔE_a through the rates. The behaviour of these quantities is thus affected by dissipation. From Eqs.7-10,7-16,7-17,7-19, we then compute the entropy production rate σ as the sum of the entropy production rates of phase-change, growth, precipitation and heat exchange. Temperature and average crystal size are found in AppendixE as well as the physical-chemical values used.

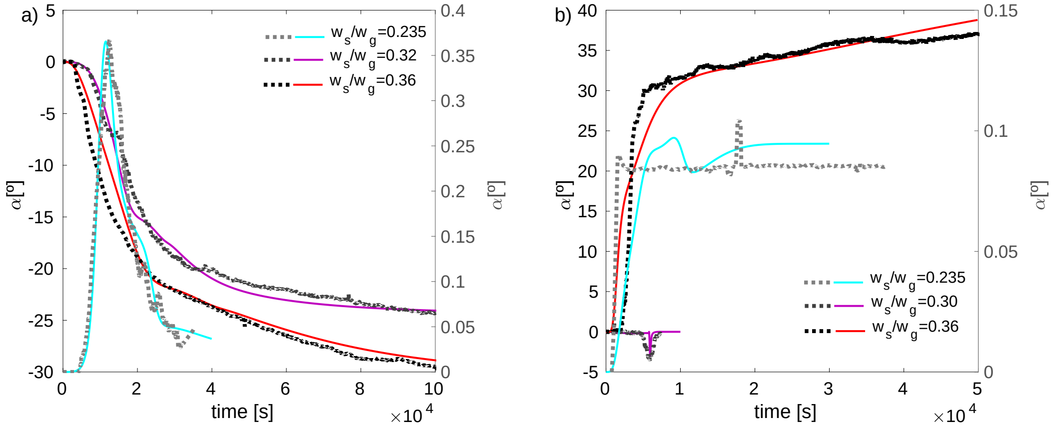

Fig. 7-6.: Optical rotation angle of the solution. a) Case of natural cooling with air. b) Case of enhanced cooling with air and water. Dotted lines represent experimental data whereas continuous lines stand for model results. The right y-axes show the results for the salt/solvent ratio $w_s/w_g = 0{,}235$ whereas the left y-axes correspond to the cases $w_s/w_g > 0{,}235$.

Fig.**7-6** depicts the evolution over time of the optical rotation angle obtained from the model and the experiments which indicates that in the 50 % of the cases analysed L-crystals are predominant (in accordance with the random dominance of enantiomeric excess [7]), as three out of six cooling conditions give a negative value of the optical rotation angle. Fig.**7-6**(a) shows that for $w_s/w_g = 0{,}235$ the angle reaches a maximum value and then decreases due to the precipitation of crystals that went out of the measurement range of the laser beam. For the remaining values of w_s/w_g, the magnitude of the angle increases as the phase changes and crystal growth occurs. We see that the optical rotation angle takes higher values as w_s/w_g increases. In Fig. **7-6**(b), we observe that in the case $w_s/w_g = 0{,}30$ the angle reaches a minimum value due to crystal precipitation. For $w_s/w_g = 0{,}235$, the angles are one to two orders of magnitude smaller than those obtained for the other salt-solvent concentration ratios.

In Fig.**7-7**, we represent the energy dissipation rate of: i) heat transfer with the environment due to a temperature difference; ii) solid nuclei formation driven by the over-saturation force; iii) crystal growth caused by surface and volume energy differences. For both cooling protocols, a peak appears in the early stages, when the supersaturation strength reaches a maximum value. For $w_s/w_g = 0{,}235$, the maximum contribution to

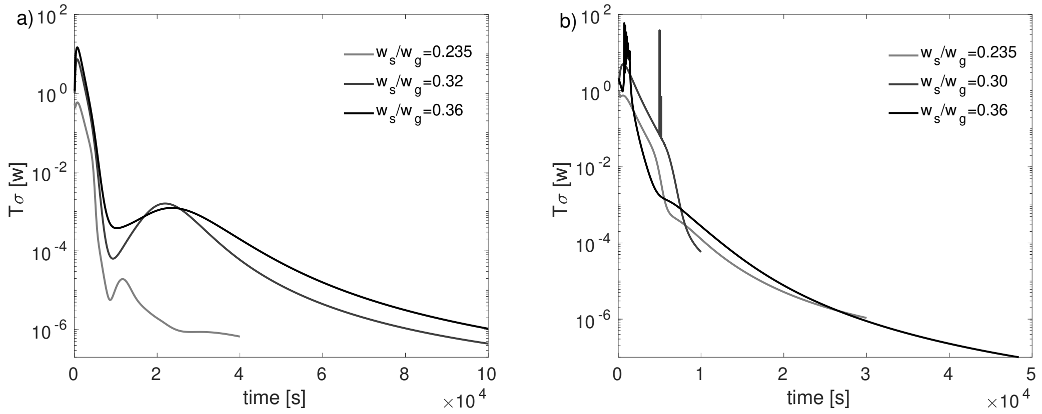

Fig. 7-7.: Time-dependent energy dissipation rate for: a) natural cooling, and b) enhanced cooling.

the peak comes from heat transfer as the number of nuclei is still low. Fig.**7-7**(a) shows the presence of two peaks and one minimum whereas in Fig.**7-7**(b) there is only one peak for each salt/solvent concentration ratio. We also observe that for enhanced cooling the peaks are slightly higher than those for natural cooling which is a consequence of the fact that in the former case the energy barrier is higher and consequently the barrier crossing rate diminishes which leads to an increase of the enantiomer population difference, as shown in Fig.**7-8**.

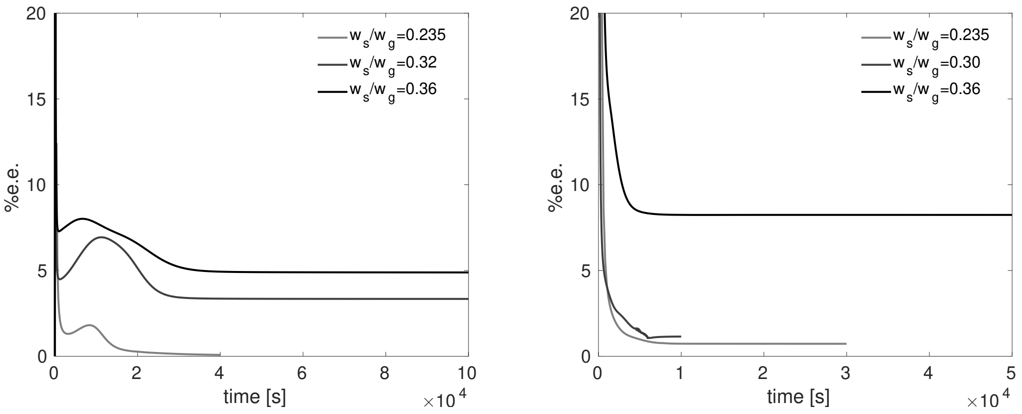

Fig. 7-8.: Enantiomeric excess percentage as a function of time for: a) natural cooling, and b) enhanced cooling.

In Fig.**7-8**, we plot the enantiomeric excess percentage as a function of time. In Fig.**7-8**(a), we observe the occurrence of maxima at times similar to those at which the energy dissipation rate is minimal, reported in Fig.**7-7**(a). Fig.**7-8** (b) shows that the maxima of the enantiomeric excess disappear when cooling is enhanced which is a consequence of the lack of a minimum in the energy dissipation rate in Fig.**7-7**(b). The minimum values of $T\sigma$ are found when the dissipation due to phase change decreases and heat exchange becomes the most dissipative process, as can be observed in Fig.**7-5**. Thus, as the energy barrier of one of the enantiomers increases, the rate of phase change decreases which promotes a higher e.e.

The figure also shows that the enantiomeric excess increases with w_s/w_g. This is due to the fact that the oversaturation force increases thus leading to a higher energy dissipation rate, as shown in Fig.(**7-7**). Moreover, for both cooling protocols, the percentage of enantiomeric excess reaches a constant value although some crystal growth and redissolution still occurs. The final e.e. percentage value is higher in the case of enhanced cooling, as the energy dissipation rate is initially higher. Therefore, the early excess of one of the enantiomers, with a lower redissolution rate, causes the enantiomeric crystals to persist over time.

Chiral symmetry breaking in $NaClO_3$ crystal formation is a consequence of the absorbed dissipated energy as a free-energy that increases the free-energy barrier of one of the enantiomers, leading to uneven rates of emergence of the L- and D- enantiomeric crystals and thus to an excess of one of the enantiomers. Our model describes the dynamical behaviour of the fraction of enantiomeric crystals from which we can estimate the optical rotation angle of the system with very good agreement with our measurements of this quantity as a function of time. The model also allows us to estimate the energy dissipated in the process as well as the enantiomeric excess.

By means of the experiments and the proposed model, we found that the required energy (energy change in one of the enantiomeric intermediates) to induce the measured enantiomeric excess is equal to the energy dissipated per solid salt mole. From our results, we identified not only that one of the intermediates must absorb the dissipated energy as free energy, but also that we could consider the connection between physical chemistry and quantum chemistry out of equilibrium by calculating the allowed amount of energy absorbed by the intermediate as well as the value of the fugacity coefficients as a function of the dissipated energy. For future work, it might be interesting to explore the possibility that the non-ideal interactions of the components affecting the kinetics, due to variations in fugacity from non-equilibrium conditions, are related to the energy levels of the molecules and thus to quantum effects, meaning that non-equilibrium thermodynamics could shed a light on connecting quantum phenomena with mesoscopic dynamics.

Bibliography

[1] Thomas Buhse, José-Manuel Cruz, MarÃa E. Noble-Terán, David Hochberg, Josep M. Ribó, Joaquim Crusats, and Jean-Claude Micheau. Spontaneous deracemizations. *Chemical Reviews*, 121(4):2147–2229, 2021. PMID: 33464058.

[2] Josep M. Ribó, David Hochberg, Joaquim Crusats, Zoubir El-Hachemi, and Albert Moyano. Spontaneous mirror symmetry breaking and origin of biological homochirality. *Journal of The Royal Society Interface*, 14(137):20170699, 2017.

[3] Hans Kuhn. Origin of life - symmetry breaking in the universe: Emergence of homochirality. *Current Opinion in Colloid & Interface Science*, 13(1):3–11, 2008. Molecular Recognition and Chirality in Amphiphilic Assemblies.

[4] Dilip K. Kondepudi and Kouichi Asakura. Chiral autocatalysis, spontaneous symmetry breaking, and stochastic behavior. *Accounts of Chemical Research*, 34(12):946–954, 2001. PMID: 11747412.

[5] Josep M Ribó and David Hochberg. Spontaneous mirror symmetry breaking: An entropy production survey of the racemate instability and the emergence of stable scalemic stationary states. *Physical Chemistry Chemical Physics*, 22(25):14013–14025, 2020.

[6] AS Garay. Origin and role of optical isomery in life. *Nature*, 219(5152):338–340, 1968.

[7] Dilip K Kondepudi, Rebecca J Kaufman, and Nolini Singh. Chiral symmetry breaking in sodium chlorate crystallizaton. *Science*, 250(4983):975–976, 1990.

[8] Hiromasa Niinomi, Teruki Sugiyama, Miho Tagawa, Shunta Harada, Toru Ujihara, Satoshi Uda, Katsuhiko Miyamoto, and Takashige Omatsu. In situ observation of chiral symmetry breaking in naclo3 chiral crystallization realized by thermoplasmonic micro-stirring. *Crystal Growth & Design*, 18(8):4230–4239, 2018.

[9] Josep M. Ribó, Joaquim Crusats, Zoubir El-Hachemi, Albert Moyano, Celia Blanco, and David Hochberg. Spontaneous mirror symmetry breaking in the limited enantioselective autocatalysis model: Abyssal hydrothermal vents as scenario for the emergence of chirality in prebiotic chemistry. *Astrobiology*, 13(2):132–142, 2013. PMID: 23379530.

[10] Marian Szurgot. *Crystallization and Materials Science of Modern Artificial and Natural Crystals*, chapter Parity Violation in Unstirred Crystallization from Achiral Solutions. InTech, Rijeka, Croatia, 2012.

[11] Maria C. Nunez, M. E. Garcia-Rubino, Ana Conejo-Garcia, Olga Cruz-Lopez, Maria Kimatrai, Miguel A. Gallo, Antonio Espinosa, and Joaquin M. Campos. Homochiral drugs: A demanding tendency of the pharmaceutical industry. *Current Medicinal Chemistry*, 16(16):2064–2074, 2009.

[12] Joonwoo Jeong, Zoey S. Davidson, Peter J. Collings, Tom C. Lubensky, and A. G. Yodh. Chiral symmetry breaking and surface faceting in chromonic liquid crystal droplets with giant elastic anisotropy. *Proceedings of the National Academy of Sciences*, 111(5):1742–1747, 2014.

[13] Hai-Tao Feng, Chenchen Liu, Qiyao Li, Haoke Zhang, Jacky W. Y. Lam, and Ben Zhong Tang. Structure, assembly, and function of (latent)-chiral aiegens. *ACS Materials Letters*, 1(1):192–202, 2019.

[14] F.C. Frank. On spontaneous asymmetric synthesis. *Biochimica et Biophysica Acta*, 11:459–463, 1953.

[15] Stuart A Kauffman et al. *The origins of order: Self-organization and selection in evolution*. Oxford University Press, USA, 1993.

[16] Marta Tena-Solsona, Caren Wanzke, Benedikt Riess, Andreas R Bausch, and Job Boekhoven. Self-selection of dissipative assemblies driven by primitive chemical reaction networks. *Nature communications*, 9(1):1–8, 2018.

[17] A. Arango-Restrepo, D. Barragán, and J. M. Rubi. Self-assembling outside equilibrium: emergence of structures mediated by dissipation. *Phys. Chem. Chem. Phys.*, 21:17475–17493, 2019.

[18] Bas GP van Ravensteijn, Ilja K Voets, Willem K Kegel, and Rienk Eelkema. Out-of-equilibrium colloidal assembly driven by chemical reaction networks. *Langmuir*, 36(36):10639–10656, 2020.

[19] David Hochberg and Josep M. Ribó. Entropic analysis of mirror symmetry breaking in chiral hypercycles. *Life*, 9(1), 2019.

[20] Andrés Arango-Restrepo, J. Miguel Rubi, and Daniel Barragán. The role of energy and matter dissipation in determining the architecture of self-assembled structures. *The Journal of Physical Chemistry B*, 123(27):5902–5908, 2019.

[21] Andrés Arango-Restrepo, Daniel Barragán, and J. Miguel Rubi. A criterion for the formation of nonequilibrium self-assembled structures. *The Journal of Physical Chemistry B*, 125(7):1838–1845, 2021. PMID: 33566612.

[22] Josep M. Ribó. Chirality: The backbone of chemistry as a natural science. *Symmetry*, 12(12), 2020.

[23] Mikhail Rekharsky and Yoshihisa Inoue. Chiral recognition thermodynamics of β-cyclodextrin:the thermodynamic origin of enantioselectivity and the enthalpy-entropy compensation effect. *Journal of the American Chemical Society*, 122(18):4418–4435, 2000.

[24] Oriol Arteaga, John Freudenthal, Baoliang Wang, and Bart Kahr. Mueller matrix polarimetry with four photoelastic modulators: theory and calibration. *Applied optics*, 51(28):6805–6817, 2012.

[25] Oriol Arteaga. Historical revision of the differential stokes–mueller formalism: discussion. *JOSA A*, 34(3):410–414, 2017.

[26] Andrés Arango-Restrepo, J. Miguel Rubi, and Daniel Barragán. Understanding gelation as a nonequilibrium self-assembly process. *The Journal of Physical Chemistry B*, 122(18):4937–4945, 2018. PMID: 29664639.

[27] Andrés Arango-Restrepo, Daniel Barragán, and J. Miguel Rubi. Nonequilibrium self-assembly induced liesegang rings in a non-isothermal system. *Phys. Chem. Chem. Phys.*, 20:4699–4707, 2018.

[28] Sybren Ruurds De Groot and Peter Mazur. *Non-equilibrium thermodynamics*. Dover Publications Inc., 1985.

[29] A. Mersmann. Crystallization and precipitation. *Chemical Engineering and Processing: Process Intensification*, 38(4):345–353, 1999.

[30] I Santamaria-Holek, A Gadomski, and J M Rubi. *Journal of Physics: Condensed Matter*, 23(23):235101, may 2011.

[31] M. Szurgot. Chiral symmetry breaking in unstirred crystallization. *Crystal Research and Technology*, 47(1):109–114, 2012.

[32] Mark Barrett, Mairtin McNamara, HongXun Hao, Paul Barrett, and Brian Glennon. Supersaturation tracking for the development, optimization and control of crystallization processes. *Chemical Engineering Research and Design*, 88(8):1108–1119, 2010.

[33] Hiroshi Takiyama. Supersaturation operation for quality control of crystalline particles in solution crystallization. *Advanced Powder Technology*, 23(3):273–278, 2012.

[34] Atherton Seidell et al. *Solubilities of inorganic and metal organic compounds*. van Nostrand, 1940.

8. Enhancing carrier flux for efficient drug delivery in cancer tissues

In this chapter we consider the non-equilibrium phenomena that take place in a tissue due to the action of external forces. We have understood the tissue as a self-organised structure that has a dynamical response under the action of ultrasound and nanoparticles carrying medicaments. The model and the results presented here are the starting point for analysing a tissue as a self-organised structure dissipating energy as we will show in the next chapter.

Ultrasound focused toward tumours in the presence of circulating microbubbles improves the delivery of drug-loaded nanoparticles and therapeutic outcomes, however, the efficacy varies among the different properties and conditions of the tumours. Therefore, there is a need to optimise the ultrasound parameters and determine the properties of the tumour tissue, important for the successful delivery of nanoparticles. Here, we propose a mesoscopic model considering the presence of entropic forces to explain the ultrasound-enhanced transport of nanoparticles across the capillary wall and through the interstitium of tumours. The nanoparticles move through channels of variable shape whose irregularities can be assimilated to barriers of entropic nature that the nanoparticles must overcome to reach their targets. The model assumes that focused ultrasound and circulating microbubbles cause the capillary wall to oscillate thereby changing the width of transcapillary and interstitial channels. Our analysis provides values for the penetration distances of nanoparticles into the interstitium that are in agreement with experimental results. We found that the penetration increased significantly with increasing acoustic intensity as well as tissue elasticity, which means softer and more deformable tissue (Young modulus lower than 50kPa). Whereas porosity of the tissue and pulse repetition frequency of the ultrasound had less impact on the penetration length. We also considered that nanoparticles can be absorbed into cells and to extracellular matrix constituents, finding that the penetration length is increased when there is a low absorbance coefficient of the nanoparticles compared to their diffusion coefficient (close to 0,2). The model can be used to predict which tumour types in terms of elasticity will successfully deliver nanoparticles into the interstitium. It can also be used to predict the penetration distance into the interstitium of nanoparticles with various sizes and the ultrasound intensity needed for the efficient distribution of the nanoparticles.

This chapter was published in *Biophysical Journal*, **120**(23), 5255-5266, (2021). Ref.[1]

8.1. Introduction

A major problem of using nanoparticles (NP's) in cancer treatment is their low and heterogenous uptake in tumour cells. A meta-analysis reported that only 0,7 % of injected NP's accumulated in the tumours [2]. NP's that are injected intravenously encounter several barriers on their way to the cancer cells in the tumour. Tumour vasculature is characterized by a chaotic morphology with shunts, looped vessels and disorganized interconnections which lead to a heterogenous spatial distribution [3]. The abnormal tumour vessels also result in hyperpermeable tumour vessels which together with the lack of functional lymphatic capillaries have resulted in the concept of the enhanced permeability and retention effect [4]. This effect is heterogenous both within tumours and among tumour types [5], and recently Sindhwani et al [6] revealed that transcellular extravasation occurred more frequently than paracellular through gaps. The NP's successfully extravasating across the capillary wall, need to penetrate through the interstitial space between the tumour and the stromal cells. This interstitium consists of a network of collagen fibers embedded in a hydrophilic gel of glycosaminoglycans.The high interstitial fluid pressure in tumours, which can be as high as the microvascular pressure, eliminates the transcapillary pressure gradient as well as pressure gradients within the tumour, thus diffusion becomes the major transport mechanism [7, 8]. However, diffusion of NP's is an extremely slow process. Furthermore, the cells and collagen network form steric hindrance and the negatively charged gel of glycosaminoglycans interact with NP's and might absorb them [9].

Research on the impact of the collagen network on glycosaminoglycans [10] has reported that collagen limit macromolecules transport. An increase in the amount of collagen resulted in increased stiffness and resistance to diffusion through the extracellular matrix. Higher amounts of glycosaminoglycan were found to reduce the hydraulic conductivity which determines the interstitial flow through the pore network in the extracellular matrix, while the hydraulic conductivity is less influenced by the amount of collagen [11, 12]. The steric exclusion of NP's in the interstitium can be quantified by the available volume fraction, which is reported to be heterogenous within the tumour and among tumours [13]. Altogether, these impediments for the successful delivery of drug-loaded NP's, which have been reviewed by Rakesh Jain's group [14], suggest that administration of NP's should be combined with another treatment to improves transport.

Ultrasound (US) focused toward the tumour in the presence of intravascular microbubbles has been shown preclinically [15, 16, 17, 18] as well as in clinical trials [19] to improve the delivery and therapeutic outcome of drug-loaded NP's and small molecular drugs. Application of US triggers acoustic radiation, acoustic streaming and cavitation which this last one is the dominant process. At low acoustic pressures, microbubble oscillations are isotropic and mostly linear and are referred to as stable cavitation. Increasing the acoustic pressure, will result in non-linear oscillations and the microbubbles will collapse in a violent process called inertial cavitation. The oscillations of microbubbles result in microstreaming in the surrounding fluid and in shear stress on the boundaries in the proximity of the microbubbles [20, 21]. Oscillating microbubbles in contact with the capillary wall have been studied by high speed imaging and it has been reported that they induce oscillations in the capillary [22, 23] thereby changing its radius and introducing gaps between the endothelial cells. Furthermore, when the microbubbles undergo inertial cavitation, jet streams are formed that can generate pores in the plasma membrane of endothelial cells, and induce formation of gaps between the endothelial cells [24, 20]. It is not clear, however, how the action of the oscillating microbubbles improves the transport of NP's through the interstitium. A correlation between enhanced drug uptake and disruption of collagen fibers in tumours in mice exposed to US and microbubbles has been reported [25]. Hancock et al. [26] found that high-intensity US (with no microbubbles) increased the penetration of NP's through the interstitium in calf mice muscle, and gaps between the muscle fibers were observed. They suggested that these gaps were due to shear strain induced by acoustic radiation force [26]. Transmission electron microscopy of murine brain tissue demonstrated that the electrostatically charged extracellular space interconnecting cells, were enlarged after exposure to US and microbubbles, especially in the perivascular regions and to a less extent within the parenchyma, and diffusion of NP's was increased [27]. Furthermore, MRI analyses of brain tissue revealed increased interstitial flow velocity and improved the transport of NP's in the brain parenchyma [28]. The behavior of microbubbles and their role in drug delivery have been extensively described in three recent review articles [29, 30, 31].

To optimize US-mediated delivery of NP's and drugs, it is essential to understand the underlying mechanisms and determine which parameters are most critical for the successful delivery of therapeutic agents. Successful delivery of NP's depends on very many parameters such as the US exposure parameters (frequency, acoustic power, pulse length, pulse repetition frequency and overall exposure time), properties of the NP's (size, charge, shape, surface coating, material) and tissue properties (porosity, elasticity, viscosity). Experimentally, it is not possible to control all these parameters and determine their impact. Experimentally it is not possible to control all these parameters and determine the impact of the individual parameters. Thus, mathematical models and simulations of penetration of NP's into the tumour interstitium combined with experimental verification are an important approach.

The aim of the present work is to establish a model to predict which US parameters and tissue properties are most important to enhance transport for successful delivery of NP's across the capillary wall and through the interstitium.The study focuses on the transport of NP's because the time scale on which delivery occurs is much shorter than the response time of the cells to the drug and of the collective phenomena that can take place in a set of cells. The model considers that variations in the microstructure of the cancer tissue, produced by US, which lead to changes in the space accessible to the NP's, generate entropic forces. These forces drive the NP's through the tissue to the cancer cells where drugs are delivered. The model takes into account the parameters of the US and the properties of the cancer tissue to establish optimal scenarios for improving the efficacy of cancer therapies.

8.2. Methods

Entropic barriers

The movement of NP's towards the cancer cells takes place through pores in the tumour interstitium, which can be viewed as channels (see Fig.**8-1**(a)-(b)). Constrictions hampering the motion of the NP's are modelled by potential barriers to be overcome to proceed (see Fig.**8-1**(c)). These barriers which originate from variations in the space available to the particles along their trajectories and therefore from entropy variations are given by $\phi = k_B T \ln(A_h(r)/A_0)$ where A_h is the cross-sectional area of the channel which quantifies its tortuosity, A_0 a reference area, k_B Boltzmann's constant and T the temperature [32].

The presence of the barriers gives rise to a force $F = -\partial\phi/\partial r$ (continuous line in Fig.**8-1**, (c)-(d)respectively)

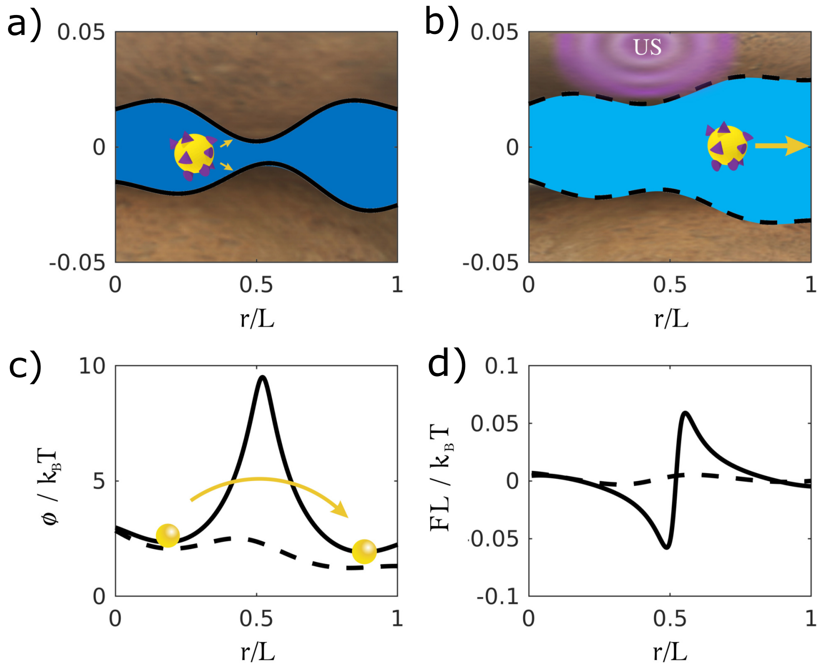

Fig. 8-1.: Sketch of an entropic barrier and its associated force acting on the NP's along a channel of length L. a) The presence of a constriction prevents the NP's from advancing through a channel. b) Application of US widens the channel allowing the NP to advance towards the targets. c) Entropic potential ϕ[33] before (continuous line) and after (dashed line) application of US. d) Associated force $F = -\partial\phi/\partial r$ which changes from negative to positive after application of US.

acting on the NP's that may help them to reach a target. Fig. **8-1** (b) shows how application of US deforms a channel, lowering the barrier (dashed line in Fig.**8-1**, (c)) and changing the sign of the induced force (dashed line in Fig.**8-1**, (d)), from negative (when nanoparticles approach a constriction) to positive (when they move towards an overture).

The presence of oscillations in the barrier and other oscillating forces may trigger the phenomenon known as entropic stochastic resonance which for a given frequency the transport of particles may be improved [34]. For this reason, in the model, we propose in the next subsection the pulse repetition frequency f in the time scale of the oscillation of the channels.

8.2.1. Model

In the model, we describe the flux of NP's in a small volume element exposed to focused US. Figure **8-2**(a) depicts the network of capillaries in cancerous tissue. The volume of interest is represented as a yellow cylinder centered around a part of a capillary surrounded by cancerous tissue. Figure **8-2**(b) shows a close-up of that volume containing the capillary, the capillary wall made up of endothelial cells and the cancer cells. In Fig.**8-2**(c), we show a cross-section of the cylinder with the interstitial space between cancer cells forming channels through which NP's may flow. We model NP's transport through the capillary wall and the interstitium in a time scale of the order of seconds since the pulse repetition frequency f varies between 0,1 and 0,5 Hz. The experiments show that for these frequencies NP's, transport takes places between 15

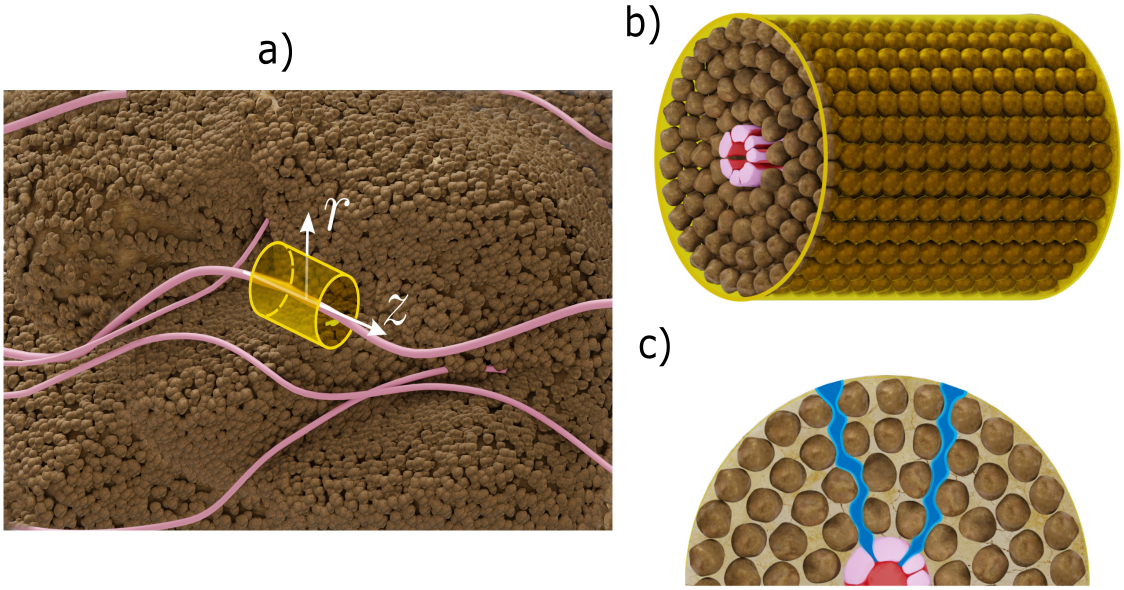

Fig. 8-2.: Illustration of the studied system. (a) Capillaries are shown in red colour while our volume of interest, the yellow cylinder, is centred on a part of the capillary. Blood flow, carrying NP's and microbubbles, takes place in the z-direction in the capillary while the movement of the NP's through the capillary wall to the surrounding cells occurs in the radial direction r. (b) 3D view: Inner red cylinder represents the blood vessel, the concentric magenta cylinder-like corresponds to the blood vessel wall composed of endothelial cells and a 2D collagen network, and the set of color brown spheres-like represents the cancer cells which together with the collagen network, as well as the glycosaminoglycans, compose the interstitium and cancer cells system. (c) Frontal view of the system: NP move through the blue-colored channels.

and 30 seconds [35].

System I: Capillary wall

Fig.**8-3** illustrates the shape of a symmetric channel through the capillary wall whose width varies with position and time due to the effect of the US. The width $h_I(r,t)$ is modelled by the sinusoidal function given in Eq.8-12. The flux of NP in the radial direction is denoted by J.

In the capillary wall, NP's may proceed through the free space between the endothelial cells, or through the interior of them. Particles moving along the channels experience an entropic force that results from variations of the channel shape induced by US. The essential driving force is thus the chemical potential gradient which incorporates the effect of the entropic force [36, 33, 37, 38, 39, 32, 40, 41]. In Appendix B can be found more information about entropic barriers and transport through interstices.

Following [33, 40], we analyse the motion of NP's along r and y (see Fig.**8-3**), from $r = R$ to $r = R + R_I$, where R_I is the thickness of the capillary wall, a constant, and R the capillary radius given in Eq.8-10. The

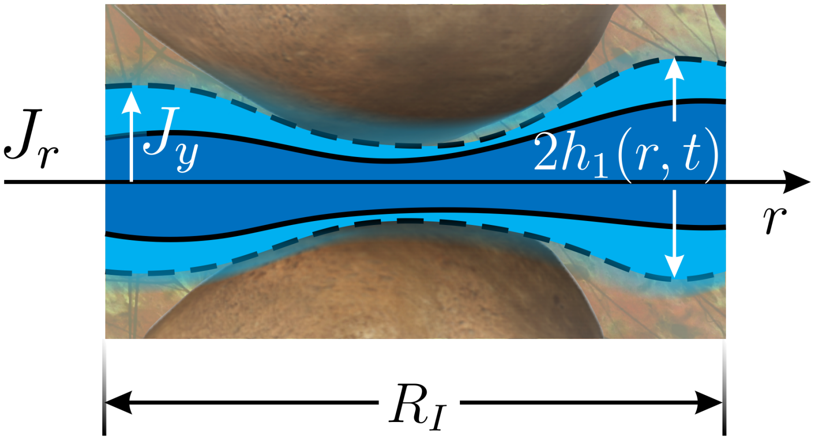

Fig. 8-3.: Blood vessel wall: Endothelial cells and collagen. The thickness of the wall is given by R_I while the proposed channel width h_I (Eq.8-12) is given by the dashed black line (proposed in the Methods as a function of the US pulse repetition frequency, Eq.8-10). The black continuous line illustrates the symmetric channel in the basal case (without US). Blue zones illustrate the free space for the movement of the NP's while the brown zone corresponds to the space occupied by the endothelial cells and the collagen network of the basal membrane.

molar balance of NP's in a channel is given by

$$\left(\frac{\partial x}{\partial t}+\frac{x}{V_I}\frac{\partial V_I}{\partial t}\right)+v\frac{\partial x}{\partial r}=-\frac{\partial J^I}{\partial r}-\frac{\partial J_y}{\partial y} \tag{8-1}$$

where we have assumed that the fluid is incompressible (with a constant density). Here x is the molar fraction of the NP's and J^I their flux, both depending on r and time t. absorption of the NP's on the wall of the channels takes place in y- direction, and J_y is the absorption flux. The volume of the system V_I, a function of h_I, may change because the blood vessel volume varies while R_I is assumed to be constant. The velocity of NP's v generated by the first US pulse is constant along the channel but may depend on the basal radius of the capillary, R_0, and on the acoustic intensity.

The boundary conditions for the flux of NP's are $J^I(R,y,t)=J^0(t)$ and $J^I(R+R_I,y,t)=J^{II}(R+R_I,y,t)$, where $J^{II}(R+R_I,y,t)$ is the flux into the interstitium and cancer cells, defined in next subsection. For the absorption process, we consider $J_y(r,0,t)=0$ and $J_y(r,h_I,t)=J_{I,a}$, where $J_{I,a}$ is the flux of NP's absorbed onto the capillary wall.

The diffusion flux J^I is given by [40]

$$J^I(r,t)=-\frac{D}{k_BT}x\frac{\partial\mu^I}{\partial r} \tag{8-2}$$

Here $D(r,t)$ is a diffusion coefficient which depends on position and time due to the tortuosity and periodic motion of the channels. It is given by $D=D_0/[1+(\frac{\partial h_I}{\partial r})^2]^{1/2}$ [37], with D_0 the diffusion coefficient of the NP's not affected by constrictions. The form of this coefficient is crucial to validate the one-dimensional treatment of the process described by Eqs.(8-1)-(8-2) [33] . In the presence of the entropic barriers, the chemical potential is given by

$$\mu^I(r,t) = k_BT\ln x(r,t) + \phi(r,t) \tag{8-3}$$

where $\phi = k_BT\ln\left(\frac{\pi(h_I(r,t)-R_{NP})^2}{\pi R_I^2}\right)$[42], since $A_h = \pi(h_I(r,t)-R_{NP})^2$ with R_{NP} the radius of a NP and $A_0 = \pi R_I^2$. The form of this potential shows that the tortuosity of the channels gives rise to a non-ideal behaviour where $\frac{\pi(h_I(r,t)-R_{NP})^2}{\pi R_I^2}$ plays the role of an activity coefficient.

System II: Interstitium and cancer cells

NP's move through the channels of the interstitium (see Fig.**8-2**(b)-(c)) which delimit channels and are absorbed into the cancer cells where drugs are finally delivered. To simplify our analysis, we assume that the channels are approximately symmetric with respect to their main transport axis and do not bifurcate which is a consequence of the nature of the matrix structure and of a sufficiently high US pulse intensity resulting in a dominant transport in the radial direction. Fig.**8-4** shows a sketch of a channel in the interstitium surrounded by cells. The channels have width h_{II} (for more details see Methods, Eq.8-15).

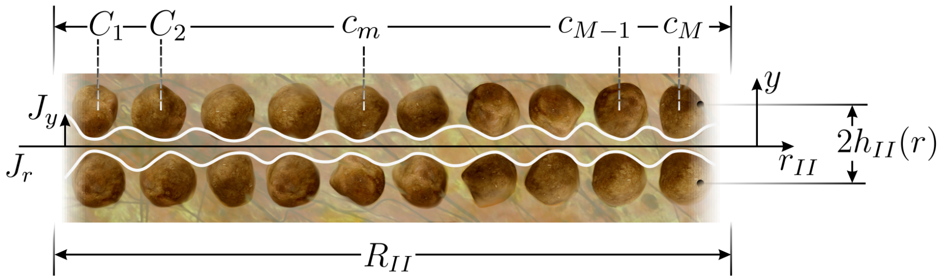

Fig. 8-4.: Channel in the instertitium surrounded by cells. The maximum length of the subsystem is given by R_{II}. The proposed channel width h_{II} (Eq.8-15) is given by the white continuous line. Each dark brown object represents cancer cells. The arrangement of the cells is idealised as a belt of sequential and ordered cells forming a symmetric channel, where the maximum number of sequential cells in the radial direction is M.

The molar balance of NP's includes diffusion and absorption and is given by

$$\left(\frac{\partial x}{\partial t} + \frac{x}{V_{II}}\frac{\partial V_{II}}{\partial t}\right) + v\frac{\partial x}{\partial r} = -\frac{\partial J^{II}}{\partial r} - \frac{\partial J_a}{\partial y} \tag{8-4}$$

Here J_a is the absorption flux and J^{II} is the flux in r direction. Boundary conditions are: $J_a(r,0,t) = 0$, $J_a(r,h_{II},t) = J_c(r,t)$, with J_c the absorbed molar flux into the cells, $J^I(R+R_I,y,t) = J^{II}(R+R_I,y,t)$. We assume that the molar fraction of NP's far from the capillary is zero. The boundary conditions make Eq.(8-1) and Eq.(8-4) coupled.

The corresponding flux is given by an equation similar to Eq.(8-2) where the local diffusion coefficient has the same form as the one for system I: $D(r,t) = D_0/(1+(\frac{\partial h_{II}}{\partial r})^2)^{1/2}$ [33] . The chemical potential is in this case

$$\mu^{II}(r,t) = k_B T \ln x(r,t) + k_B T \ln \left(\frac{h_{II}(r,t) - R_{NP}}{R_I} \right)^2 \tag{8-5}$$

where the second term on the right-hand side represents the contribution of the entropic barrier resulting from variations of the cross-sectional area of the channels. The absorption flux in Eq.(8-4) is proportional to the mole fraction gradient

$$J_a(r,t) = -D \frac{\partial x}{\partial y}. \tag{8-6}$$

The molar balance in the cells is given by

$$\frac{\partial x^c}{\partial t} = J_c + J_d \tag{8-7}$$

where x^c is the mole fraction of the NP's in the cells and $J_d(r,t)$ the drug delivery flux. The absorption flux is proportional to the difference of mole fractions of the NP's in the channel and in the cells

$$J_c(r,t) = -D_a \frac{x^c - x}{h_{II}(r,t)} \tag{8-8}$$

where D_a is an absorption coefficient. Finally, to obtain the drug delivery rate, we view the delivery process as a first-order reaction in which the NP's are decomposed into NP's and drugs. Therefore, the drug delivery fluxJ_d is given by

$$J_d(r,t) = -kx^c \tag{8-9}$$

where k is a kinetic constant.

8.2.2. Ultrasound-induced changes of the tissue microstructure

To complete the model, we need to know the capillary radius R, the capillary wall channel width h_I and the width of the channel in the interstitium h_{II}. To assess how the entropic forces contribute to the total force which also includes the chemical potential gradient, we need to estimate the minimum opening of the channels.

US pulses and the circulating microbubbles induce variations in R over time [20]. The frequency of the US is thousand times higher than the pulse repetition frequency f which implies that $R(t)$ depends basically on f. The variation of the capillary radius is assumed to be of the form

$$R(t) = A|\sin(ft)| + R_0 \tag{8-10}$$

where R_0 is the basal radius of the blood vessel.
During exposure to US, the pulse repetition frequency considered varies between 0,1 and 0,5 Hz. We have estimated the amplitude A from the energy given to the system by the US pulses. The amount of energy needed to expand the capillary a distance A is $E_e = k_e A^2/2$ where k_e is the elastic constant of the medium which is a function of the Young modulus $Y \equiv k_e L_0/A$, where L_0 is the basal length of the system and A is the area where the force is applied [43]. We next assume that the energy given by US is proportional to MI:

$E_{\mathrm{US}} = C_0$ MI where the constant $C_0 = 10^{-14}$J can be estimated from experiments [35]. By equating E_e with E_{US}, we thus find

$$A = \sqrt{\frac{2C_0\mathrm{MI}}{k_e}} \tag{8-11}$$

Typical values of MI in the experiments are 0.2, 0.4 and 0.8 and the elastic constant used in the model is in the range $10^{-4}[N/m] \leq k_e \leq 10^{-3}[N/m]$, corresponding to $1[kPa] \leq Y \leq 120[kPa]$ [44, 45].

The width of the channel in the capillary wall system (see Fig.**8-3**) as a function of time and position is modelled by

$$h_I = A_I\left(\sin\left(\pi\frac{r}{R_I} - \frac{\pi}{2}\right) + 1\right)|\sin(ft)| + H_{0,I} \tag{8-12}$$

with A_I an amplitude and $H_{0,I}$ the radius of the channel at the side facing the capillary. We consider that $H_{0,I}$ increases with R when the blood vessel wall expands and assume that $H_{0,I}$ has the form

$$H_{0,I}(t) = h_0\left(\frac{R(t)}{R_0}\right)^{\alpha} \tag{8-13}$$

with h_0 the radius of the inlet aperture in the capillary in the basal state, and where the exponent α fall within the interval $2-3$, where the lower limit indicates that the aperture is proportional to the capillary area whereas in the upper limit it is proportional to the capillary volume.

The amplitude A_I is expressed as a function of the medium porosity ϕ through the relation $\phi \equiv \frac{1}{\pi R_I^3}\int_0^{R_I} \pi h_I^2 dr$ where the reference volume containing one channel is a cylinder of radius and length R_I. One obtains:

$$A_I = \sqrt{(2/3)\phi R_I^2 - (2/9)h_0^2} - (2/3)h_0. \tag{8-14}$$

Channels in the interstitium (see Fig.**8-4**) have radius h_{II}. The impact of the US in the channels in the interstitium decreases with the distance from the power source (the capillary)[46]. The proposed width of the interstitial channel is thus assumed to be of the form:

$$h_{II} = A_{II}\left(\sin\left(\frac{2l\pi r}{R_{II}} - \frac{\pi}{2}\right) + 1\right)\left(1 + \frac{|\sin(ft)|R_{II}}{R_{II} + r}\right) + H_{0,II} \tag{8-15}$$

with A_{II} the amplitude and $H_{0,II}$ the minimum radius of the interstitial space. We assume that the minimum amplitude depends on R through H_0, while in the basal state it takes the average value of the interstitium width [44], therefore $H_{0,II} = \beta h_0 + H_0$, with β a coefficient which must be between 5 to 10.

The amplitude A_{II} was computed by using the porosity of the interstitium of the carcinogenic tissue $\phi^* = \frac{1}{\pi R_I^2 R_{II}}\int_0^{R_{II}} \pi h_{II}^2 dr$, where the reference volume containing one channel is a cylinder of radius R_I and length R_{II}. The amplitude is then

$$A_{II} = \sqrt{(2/3)\phi^* R_{II} R_I} \tag{8-16}$$

which has been obtained by considering that $\phi^* R_{II} R_I \gg h_0$.

8.2.3. Experimental testing

The flux of NP's through the capillary wall and in the interstitium was compared with the experimental results reported in [35]. Transport of NP's was imaged in real-time during US exposure using intravital multiphoton microscopy. Tumours were growing in dorsal window chambers in athymic mice. The US transducer was placed in a water-filled cone 45^o relative to the image plane to minimise reflections from the window chamber and reduce standing waves. The US transducer was aligned with the objective to expose the tissue in the field of view to US. Microbubbles and NP's were injected intravenously immediately before the US was turned on. The characteristics of US exposure were: US frequency of 1 MHz, MI= 0,2, 0,4, 0,8, pulse repetition frequency $f = 0{,}1$ and 0,5 Hz, pulse length of 10 ms, and total US exposure time of 5 minutes. The behaviour of fluorescence-labeled NP's was recorded continuously during the US exposure and where the penetration of the NP's took place in a time range of 15 to 30 seconds from the initial extravasation.

8.2.4. Solution procedure

Once we specified the value of the tissue parameters and therefore the shape of the channels, we solved the coupled Eqs. (8-1) and (8-4) for the molar fraction of the NP's by using the finite differences method in MATLAB 2017b. The existence of a stable and unique solution was guaranteed by considering space and time steps such that: $\Delta t < \Delta r^2$, with $\Delta r = 5 \times 10^{-8}$m. The penetration length was computed as $\Delta L = r^* - R_0$, where r^* is such that $x(r^*) = x_0 \times 10^{-6}$, a very small and virtually undetectable value experimentally, with x_0 the initial molar fraction of NP's.

8.3. Results

The model provides the essential kinetics of NP's transport across the capillary wall and through the interstitium, estimating how far the NP's can reach to act on the malignant cells, depending on the characteristics of the US, the properties of the tissue and the nature of the NP's.

8.3.1. Validation of the model

We have compared the penetration length ΔL obtained from our model with the experimental results from [35]. This quantity is defined as the maximum distance that the NP's can reach measured from the capillary. To obtain it, we solve numerically the coupled Eqs. (8-1) and (8-4) and calculate the distance at which the molar fraction vanishes. The comparison is performed for different values of the mechanical index MI[1] used to indicate stable or inertial cavitation [48]. Other input data of the model, cf. Materials and Methods Section, are the geometry of the microstructure of the capillary wall and the interstitium, as well as the physico-chemical properties of the medium and of NP's. Their values and the literature sources are presented in Table **8-1**.

Results for ΔL are shown in Fig.**8-5** for different values of MI which can be tuned by varying the capillary radius and the initial velocity. In the figure, one can observe the presence of noise in the experimental data

---

[1] MI= $\Delta P_{neg}/f_{US}^{0,5}$[47] where the negative pressure ΔP_{neg}, given in kPa, is the pressure difference inside and outside a bubble.

Tab. 8-1.: Structural and physico-chemical parameters of the model

Parameter	Maximum	Minimum	Default
NP diffusivity, $D_0[\mu m^2/s]$ [49]	6	5,7	6
NP radius, $R_{NP}[nm]$[35]	-	-	80
Vessel basal radius, $R_0[\mu m]$[50]	25	4	10
Inlet aperture$^{(*)}$, $h_0[nm]$[50]	90	50	80
Porosity, ϕ	0,5	1×10^{-4}	5×10^{-2}
Young Modulus, $Y[kPa]$[45]	120	1	11
Cell diameter, $l[\mu m]$[35]	–	–	10

(*) Inlet aperture in the capillary wall [50]. Note: values for R_I and R_{II} are $10\mu m$ and $200\mu m$, respectively. Mechanical index (MI) and pulse repetition frequency f (US parameters) range from 0 to 0,8 and from 0,1 Hz to 0,5 Hz, respectively.

which can be attributed to different possible values for the capillary basal radius R_0 and velocity v. The basal capillary radius and the initial particle velocity vary with the microstructure geometry ranging from $4\mu m$ to $20\mu m$ and up to $30\mu m/s$, respectively [35]. Default values for the tuned parameters appear on the right column of Table **8-1**.

The relative importance of the different contributions to the flux equations was analysed in terms of the Péclet number, which describes the ratio between advective and diffusive transport: Pe $\equiv vl/D$, with l the cell diameter introduced in Table **8-1**, and the dimensionless number $\Sigma \equiv 2\gamma^{1/2}/\delta$ accounting for entropic barrier effects, with $\delta \equiv h_0/R_0$ and $\gamma \equiv \text{máx}(dh/dr)$ [40]. In some experimental situations such as in flow through tissues [11] and biological membranes [51], the fluid velocity v is very small. According to previous results for similar systems [52, 14], the velocity can only be up to $100\mu m/s$. In our case, at initial times Pe ≈ 100 and $\Sigma \approx 10$ while the Reynolds number is Re $\approx 10^{-4}$. Therefore, convection is negligible while the entropic barrier effect is up to one order of magnitude more than the effect of diffusion.

In Fig. **8-5**, we observe that increasing MI leads to larger penetration lengths of the NP's. These values of MI correspond to significant variations of the cross-sectional area of the channels. The penetration length was analysed with respect to the basal capillary radius and the initial velocity of the nanoparticles. The penetration length seemed to be longest when NPs extravasted from capillaries with intermediate radii. A positive correlation was found between penetration length and initial velocity. The values of these quantities lead us to identify the following regimes:

i) A pure diffusion regime, observed in most of the curves of Fig.**8-5**(a) where ΔL grows slowly until it reaches a maximum value. This maximum (steady-state) value is mainly characterised by the average cross-sectional area. In this regime, the velocity v and the entropic effect are negligible (Pe$\leq 0{,}1$).

ii) A biased diffusion regime [38] observed in Fig.**8-5**(b), in which ΔL keeps growing faster than in the pure diffusion case reaching quickly a maximum value. In this case, the effect of diffusion is enhanced by the entropic force while the inertial contribution relates to the existence of an initial velocity v of the NP can be present without being dominant (Pe≤ 1).

iii) A regime in which the initial convection combines with biased diffusion. This case is observed in Fig.**8-5**(c) where the initial inertial effect is evidenced by the pronounced linear increase of ΔL caused by the first

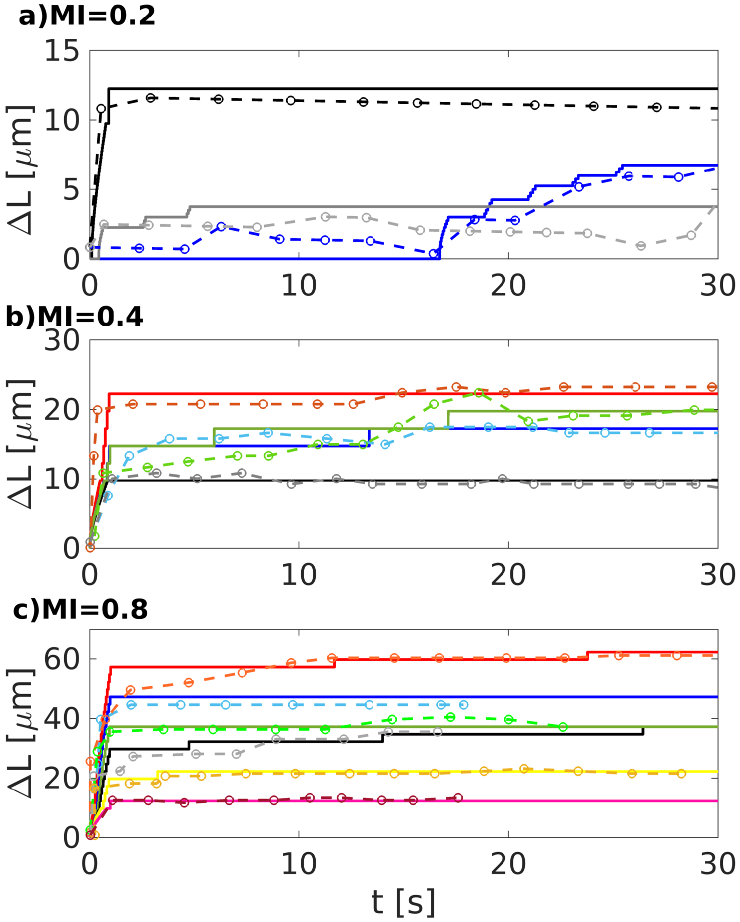

Fig. 8-5.: Penetration length of the NP's ΔL $[\mu m]$ as a function of time around a mice capillary. Each line represents the extravasation of one or a set of NP's. Model results, obtained for geometric parameters and default values given in Table **8-1**, correspond to continuous lines whereas experimental data correspond to dashed lines [35] for mechanical indices MI = 0.2, (a) 0,4 (b) and 0.8 (c). The basal radius of the capillaries are represented by different colours and for which is estimated the initial velocity from the model; (a) black lines: $R_0 = 8$ μm and $v_0 = 6{,}19$ μm/s, grey lines: $R_0 = 13$ μm and $v_0 = 0$, and blue lines: $R_0 = 20$ μm and $v_0 = 0$; (b) Black lines: $R_0 = 4$ μm and $v_0 = 4{,}75$ μm/s, red lines: $R_0 = 6{,}5$ mum and $v_0 = 8{,}6$ μm/s, blue line: $R_0 = 11{,}5$ μm and $v_0 = 6$ μm/s, green lines: $R_0 = 12{,}5$ μm and $v_0 = 6{,}9$ μm/s; (c) Black lines:$R_0 = 4$ μm and $v_0 = 14$ μm/s, green and yellow lines correspond to $R_0 = 7$ μm with $v_0 = 15{,}7$ and $v_0 = 8{,}125$ μm/s respectively, blue and red lines correspond to $R_0 = 7{,}5$ μm with $v_0 = 11{,}4$ and $v_0 = 20{,}5$ μm/s respectively, magenta lines: $R_0 = 9$ μm and $v_0 = 5$ μm/s. For all the model results, the pulse repetition frequency (f) is kept constant at a value of 0,1 Hz as in the experiments. Highest error percentage between experimental and theoretical curves is around 3,25 %.

US pulse that triggers extravasation across the capillaries. In this case, ΔL does not change considerably after this initial period (of about two seconds) in which convection dominates (Pe$\approx$ 100).

8.3.2. Model predictions

The model provides values of the penetration length of the NP's and can be used to analyse how sensitive it is to US settings (Fig.**8-6**), medium properties (Fig.**8-7**) and transport properties of the NP's (Fig.**8-8**). This allows the identification of optimal scenarios for more efficient drug delivery.

Fig.**8-6** shows that the penetration length increases almost linearly with MI, whereas such a monotonic behaviour is not observed in terms of the pulse repetition frequency, f [35]. It is also found that variations of f has a little impact on ΔL while this quantity is highly sensitive to variations of MI. For the range of MIs considered, the resulting variation in the amplitude of the capillary radius R (cf. Eq.8-11) goes from 1 to 4 μm.

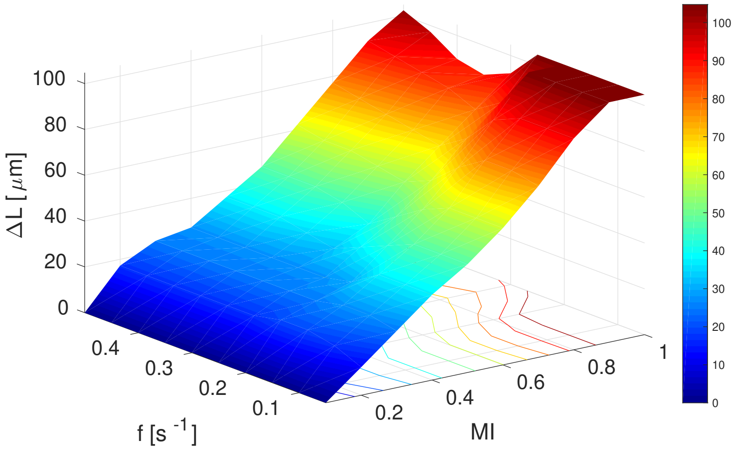

Fig. 8-6.: Dependence of the penetration length (in μm) on the Mechanical Index (MI) and pulse repetition frequency f in s^{-1}. For this range of MI values, the amplitude of the oscillations of the capillary radius R (Eq.8-11) varies from 1 to 4 μm. The parameters MI and f are involved in h_I and h_{II}, as shown in the Methods. Default values for porosity, elastic constant, capillary radius, minimum aperture, and diffusivities used to obtain the results are given in Table **8-1**. The velocity is $10\mu m/s$.

Fig. **8-7** shows the role of the tissue elasticity which depends on the Young modulus. Penetration of NP's is more efficient when the medium is easily deformable, i.e., with a small elastic constant k_e that facilitates the widening of the capillaries. The results obtained also show that the average width of channels may increase up to 45 %. The role of porosity is of minor importance, compared to that of elasticity.

Fig. **8-8** shows the role of absorption of NP's into cells and to constituents in the interstitium. We observe that ΔL becomes larger at small values of the ratio between absorption and diffusion coefficients in which case only a few NP's are absorbed.

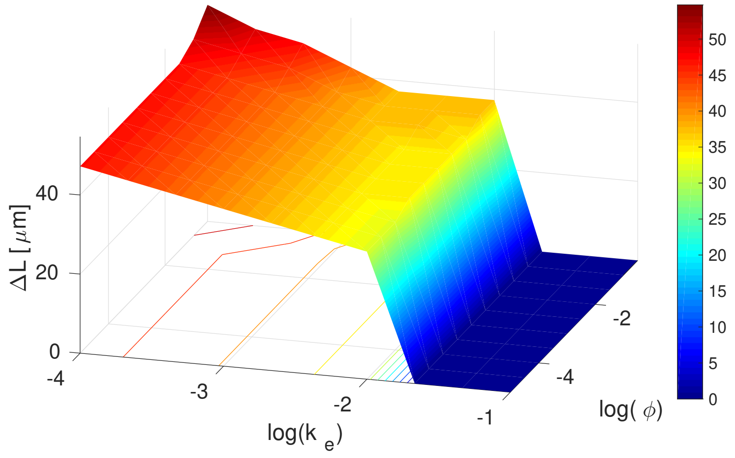

Fig. 8-7.: Penetration length as a function of the logarithm of the porosity and elasticity (in N/m). The parameters ϕ and k_e are involved in h_I and h_{II}, as shown in the Methods. Default values for capillary radius, minimum aperture and diffusivities used to obtain the results are given in Table **8-1**. The velocity is $10\mu m/s$, MI$=$ 0,4, and $f = 0{,}5$ Hz.

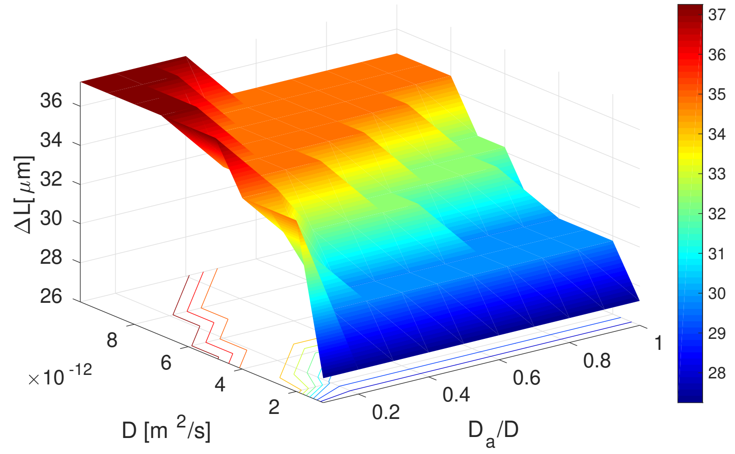

Fig. 8-8.: Dependence of the penetration length on the diffusivity D in m^2/s and on the ratio between absorptivity D_a and diffusivity. Default values for porosity, elastic constant, capillary radius, minimum aperture and diffusivities used to obtain the results are given in Table **8-1**. Velocity is $10\mu m/s$, MI$=$ 0,4, and $f = 0{,}5 s^{-1}$.

8.4. Discussion

The model considers that the oscillating microbubbles cause the capillary wall to oscillate, thereby changing the width of both transcapillary and interstitial channels, thus inducing the emergence of entropic forces. A basic feature that our model describes is that by applying US with a MI in the range $0{,}2 - 0{,}8$, the radius of the capillary changed from 4 to 45 % with respect to the basal radius. This is supported by high-speed imaging of oscillating microbubbles which demonstrated that capillaries expand their radius up to 40 % during microbubble expansion [22, 23, 46].

The model included two US parameters, MI and pulse repetition frequency, as presented in Fig.**8-6**. The pulse repetition frequency in the range of 0,1 to 0,5 Hz had little impact on the penetration of NP's. In a clinical situation, the time between the US pulses should be longer than the perfusion time of microbubbles to allow new microbubbles to enter the US target volume [53]. However, the model does not take into account the blood flow and perfusion time of microbubbles and we assume always available microbubbles in the capillary which may give more sensitivity to f in the predictions for ΔL.

Using our model and introducing the Peclet number, we revealed different transport mechanisms for the three MIs applied. At MI= 0,2, the NP's are driven by a purely diffusive process, whereas at MI= 0,4 the diffusion is biased. The highest acoustic intensity applied, MI= 0,8, caused instantaneous convection. Previous studies have shown that the acoustic radiation force does not move NP's directly by Stokes drag, but through acoustic streaming [54, 55], and can cause NP's to be displaced up to 100 μm from the capillary wall [55]. The average maximum penetration of NP's with a radius of 80 nm using MI= 0,8, was approximately 60 μm, thus reaching a substantial part of the tumour cells as the intercapillary distance is reported to vary between 100-300 μm, depending on tumour type [56, 57] and NP's can penetrate in both directions from the capillary. US at MI= 0,8 and microbubbles are shown to displace smaller NP's deeper into the interstitium [58]. The model can be used to predict which MI is needed to deliver NP's of different sizes to all tumour cells. The acoustic intensity applied should deliver NP's efficiently, and avoid severe tissue damage and haemorrhage, thus it is important to know the optimal MI, not exposing the tumours to unnecessary acoustic intensities.

As observed in our analysis, Fig.**8-7**, elasticity is an important parameter to consider in future studies. Shear wave elasticity imaging of pancreatic tumours in mice reported an inverse correlation between shear modulus and uptake of a small molecular fluorescent drug [59], demonstrating the importance of tissue elasticity for successful drug delivery. This might be particularly important for pancreatic tumours, very stiff tumours, due to extensive desmoplasia. The microenvironment and mechanical properties of pancreatic tumours, as well as other tumours, also depends on solid stress and the high interstitial fluid pressure [60]. Solid stress depends on tumour stiffness, activated cancer fibroblasts and the amount of collagen and hyaluronan [14]. Recently US and microbubbles were reported to reduce solid stress and solid stress deformation, but not Young modulus, in two xenografts with low and high Young modulus, respectively, and the reduced solid stress correlated with improved delivery of NP's [61].

Elasticity was found to have a larger impact than tissue porosity on NP's transport. Tissue elasticity depends on collagen and negatively charged glycosaminoglycans and hyaluronan which will attach cations and water, causing swelling of the tissue [14]. Softer tissue being more easily deformed was found to increase penetration of NP's further into the interstitium than stiffer tissue, thus proposing changes in the extracellular matrix and tissue elasticity might be a strategy for improving the delivery of NP's. US and oscillating microbubbles have been reported to change tumour stiffness as published by Bezer et al. [62] where was reported that the deformation of gel phantoms and the displacement of the gel decreased as the gel stiffness increased.

Porosities ranging from 0,5 to 10^{-5} had a very small impact on the penetration of NP's, suggesting that the width of the channels is larger than the diameter of the NP's. Although the overall porosity is low, the width of the individual channels in our model is sufficient for NP's to move. Ultrasound and microbubbles cause the width of the channels to change periodically, which might push NP's forward. Although we found that the impact of the porosity in the transport is small, it has been proposed that increasing the available volume in tumour tissue, for instance by changing the structure of the extracellular matrix, the delivery of drugs can be improved [63].

The model includes the absorptive flux and predicts the impact of NP's absorbing to the extracellular matrix constituents and to cells, as evidenced in Fig.**8-8** as a function of the diffusion coefficient as well as the ratio between diffusion and absorption coefficients. Absorption reduces the available NP's and our model showed that the ratio between the absorptive coefficient D_a and the diffusion coefficient D need to be small to obtain a deep penetration of NP's into the interstitium, while increasing the diffusion coefficient increased the penetration distance. In accordance with our results, previous findings elucidate that NP's can be absorbed to the surface of cells in the tumour and to extracellular matrix constituents primarily through electrostatic interactions [9]. Notice that NP's adhering to cell surfaces can also trigger cellular uptake.

The model is set in the mesoscale which describes accurately the experimental results and the resulting analysis are in agreement with previous works while we set the first step to consider entropic forces to predict the penetration of NP's into the interstitium. The model can be extended to consider effects after US-exposure. There is an interesting paper combining modelling and intravital microscopy to image penetration of drugs in brain metastasis exposed to US and microbubbles, where an increment in the penetration of drugs into the brain metastasis was demonstrated. By integrating the experimental results with a pharmacokinetic model of drug transport, Arvantis et al. found that US and microbubbles increased the hydraulic conductivity rather than the diffusion coefficient [64]. The next step in our model might be to also include how hydraulic conductivity impacts the delivery of NP's as well a longer time scale to consider more interesting phenomena as for instance the re-organisation of the media while the medicament acts on the carcinogenic tissue.

8.5. Conclusions

The role of the tumour-tissue microstructure in the drug transport during US treatment is key to understand how to improve US-mediated drug delivery. The model proposed can be used to study how drug delivery varies among different tumours and also to predict which type of cancer can benefit from ultrasound-mediated delivery of therapeutic agents. We found in our model predictions that tumour tissues exhibiting high elasticity might be the most favoured for drug transport mediated by ultrasound. Whereas a low ratio between absorption and diffusion coefficient of NP's seems to enhance the transport of NP's in the tumour. We also conclude that pulse repetition frequency as well as porosity does not affect considerable the NP's transport. The model could also bring information about the value of the parameters (MI, f, the initial molar fraction of NP's) that optimise resources and minimise the damage to the patient.

Bibliography

[1] Andrés Arango-Restrepo, J. Miguel Rubi, Signe Kjelstrup, Bjørn Atle J. Angelsen, and Catharina de Lange Davies. Enhancing carrier flux for efficient drug delivery in cancer tissues. *Biophysical Journal*, 120(23):5255–5266, 2021.

[2] Stefan Wilhelm, Anthony J Tavares, Qin Dai, Seiichi Ohta, Julie Audet, Harold F Dvorak, and Warren CW Chan. Analysis of nanoparticle delivery to tumours. *Nature reviews materials*, 1(5):1–12, 2016.

[3] Rakesh K Jain. Determinants of tumor blood flow: a review. *Cancer Res.*, 48(10):2641–2658, 1988.

[4] H Maeda, J Wu, T Sawa, Y Matsumura, and K Hori. Tumor vascular permeability and the epr effect in macromolecular therapeutics: a review. *J. Control. Release*, 65(1):271 – 284, 2000.

[5] Hiroshi Maeda. Toward a full understanding of the epr effect in primary and metastatic tumors as well as issues related to its heterogeneity. *Advanced drug delivery reviews*, 91:3–6, 2015.

[6] Shrey Sindhwani and et al. The entry of nanoparticles into solid tumours. *Nature materials*, 19(5):566–575, 2020.

[7] Yves Boucher and Rakesh K. Jain. Microvascular pressure is the principal driving force for interstitial hypertension in solid tumors: Implications for vascular collapse. *Cancer Research*, 52(18):5110–5114, 1992.

[8] L Eikenes, M Tari, I Tufto, Ø S Bruland, and C de Lange Davies. Hyaluronidase induces a transcapillary pressure gradient and improves the distribution and uptake of liposomal doxorubicin (caelyxâ„¢) in human osteosarcoma xenografts. *Br. J. Cancer*, 93(1):81–88, 2005.

[9] Triantafyllos Stylianopoulos, Ming-Zher Poh, Numpon Insin, Moungi G. Bawendi, Dai Fukumura, Lance L. Munn, and Rakesh K. Jain. Diffusion of particles in the extracellular matrix: The effect of repulsive electrostatic interactions. *Biophys. J.*, 99(5):1342 – 1349, 2010.

[10] Paolo A. Netti, David A. Berk, Melody A. Swartz, Alan J. Grodzinsky, and Rakesh K. Jain. Role of extracellular matrix assembly in interstitial transport in solid tumors. *Cancer Res.*, 60(9):2497–2503, 2000.

[11] Edward A. Swabb, James Wei, and Pietro M. Gullino. Diffusion and convection in normal and neoplastic tissues. *Cancer Res.*, 34(10):2814–2822, 1974.

[12] L.J. Liu and M. Schlesinger. Interstitial hydraulic conductivity and interstitial fluid pressure for avascular or poorly vascularized tumors. *Journal of Theoretical Biology*, 380:1–8, 2015.

[13] Ava Krol, Julie Maresca, Mark W. Dewhirst, and Fan Yuan. Available volume fraction of macromolecules in the extravascular space of a fibrosarcoma: Implications for drug delivery. *Cancer Res.*, 59(16):4136–4141, 1999.

[14] Triantafyllos Stylianopoulos, Lance L. Munn, and Rakesh K. Jain. Reengineering the physical microenvironment of tumors to improve drug delivery and efficacy: From mathematical modeling to bench to bedside. *Trends Cancer*, 4(4):292 – 319, 2018. Special Issue: Physical Sciences in Oncology.

[15] Annemieke van Wamel, Per Christian Sontum, Andrew Healey, Svein Kvaale, Nigel Bush, Jeffrey Bamber, and Catharina de Lange Davies. Acoustic cluster therapy (act) enhances the therapeutic efficacy of paclitaxel and abraxaneÂ® for treatment of human prostate adenocarcinoma in mice. *J. Control. Release*, 236:15 – 21, 2016.

[16] Sofie Snipstad and et al. Ultrasound improves the delivery and therapeutic effect of nanoparticle-stabilized microbubbles in breast cancer xenografts. *Ultrasound Med. Biol.*, 43(11):2651 – 2669, 2017.

[17] Chung-Yin Lin, Jia-Rong Li, Hsiao-Ching Tseng, Ming-Fang Wu, and Win-Li Lin. Enhancement of focused ultrasound with microbubbles on the treatments of anticancer nanodrug in mouse tumors. *Nanomedicine*, 8(6):900–907, 2012.

[18] Spiros Kotopoulis, Anthony Delalande, Mihaela Popa, Veronika Mamaeva, Georg Dimcevski, Odd Helge Gilja, Michiel Postema, Bjørn Tore Gjertsen, and Emmet McCormack. Sonoporation-enhanced chemotherapy significantly reduces primary tumour burden in an orthotopic pancreatic cancer xenograft. *Mol. Imaging Biol.*, 16(1):53–62, 2014.

[19] Georg Dimcevski and et al. A human clinical trial using ultrasound and microbubbles to enhance gemcitabine treatment of inoperable pancreatic cancer. *J. Control. Release*, 243:172 – 181, 2016.

[20] Victor Frenkel. Ultrasound mediated delivery of drugs and genes to solid tumors. *Adv. Drug Deliv. Rev.*, 60(10):1193 – 1208, 2008. Ultrasound in Drug and Gene Delivery.

[21] Sofie Snipstad, Einar Sulheim, Catharina de Lange Davies, Chrit Moonen, Gert Storm, Fabian Kiessling, Ruth Schmid, and Twan Lammers. Sonopermeation to improve drug delivery to tumors: from fundamental understanding to clinical translation. *Expert Opin. Drug Deliv.*, 15(12):1249–1261, 2018.

[22] Hong Chen, Wayne Kreider, Andrew A. Brayman, Michael R. Bailey, and Thomas J. Matula. Blood vessel deformations on microsecond time scales by ultrasonic cavitation. *Phys. Rev. Lett.*, 106:034301, Jan 2011.

[23] Li Chen, Qinjun Kang, Ya-Ling He, and Wen-Quan Tao. Mesoscopic study of the effects of gel concentration and materials on the formation of precipitation patterns. *Langmuir*, 28(32):11745–11754, 2012.

[24] Sophie Hernot and Alexander L. Klibanov. Microbubbles in ultrasound-triggered drug and gene delivery. *Adv. Drug. Deliv. Rev.*, 60(10):1153–1166, 2008. Ultrasound in Drug and Gene Delivery.

[25] Tong Li and et al. Pulsed high-intensity focused ultrasound enhances delivery of doxorubicin in a preclinical model of pancreatic cancer. *Cancer Res*, 75(18):3738–3746, 2015.

[26] Hilary A. Hancock, Lauren H. Smith, Julian Cuesta, Amir K. Durrani, Mary Angstadt, Mark L. Palmeri, Eitan Kimmel, and Victor Frenkel. Investigations into pulsed high-intensity focused ultrasound-enhanced delivery: Preliminary evidence for a novel mechanism. *Ultrasound Med. Biol.*, 35(10):1722–1736, 2009.

[27] David S. Hersh, Ben A. Nguyen, Jimena G. Dancy, Arjun R. Adapa, Jeffrey A. Winkles, Graeme F. Woodworth, Anthony J. Kim, and Victor Frenkel. Pulsed ultrasound expands the extracellular and perivascular spaces of the brain. *Brain Res.*, 1646:543–550, 2016.

[28] Colleen T Curley and et al. Augmentation of brain tumor interstitial flow via focused ultrasound promotes brain-penetrating nanoparticle dispersion and transfection. *Science adv.*, 6(18):eaay1344, 2020.

[29] Klazina Kooiman, Silke Roovers, Simone A.G. Langeveld, Robert T. Kleven, Heleen Dewitte, Meaghan A. O'Reilly, Jean-Michel Escoffre, Ayache Bouakaz, Martin D. Verweij, Kullervo Hynynen, Ine Lentacker, Eleanor Stride, and Christy K. Holland. Ultrasound-responsive cavitation nuclei for therapy and drug delivery. *Ultrasound Med. Biol.*, 46(6):1296–1325, 2020.

[30] Michel Versluis, Eleanor Stride, Guillaume Lajoinie, Benjamin Dollet, and Tim Segers. Ultrasound contrast agent modeling: A review. *Ultrasound Med. Biol.*, 46(9):2117–2144, 2020.

[31] Sofie Snipstad, Krister Vikedal, Matilde Maardalen, Anna Kurbatskaya, Einar Sulheim, and Catharina de Lange Davies. Ultrasound and microbubbles to beat barriers in tumors: improving delivery of nanomedicine. *Advanced Drug Delivery Reviews*, page 113847, 2021.

[32] J. Miguel Rubi. Entropic diffusion in confined soft-matter and biological systems. *EPL (Europhysics Letters)*, 127(1):10001, aug 2019.

[33] D. Reguera and J. M. Rubí. Kinetic equations for diffusion in the presence of entropic barriers. *Phys. Rev. E*, 64:061106, Nov 2001.

[34] Poornachandra Sekhar Burada, Gerhard Schmid, David Reguera, Mendeli H Vainstein, JM Rubi, and Peter Hänggi. Entropic stochastic resonance. *Phys. Rev. Lett.*, 101(13):130602, 2008.

[35] Petros T. Yemane and et al. Effect of ultrasound on the vasculature and extravasation of nanoscale particles imaged in real time. *Ultrasound Med. Biol.*, 45(11):3028–3041, 2019.

[36] P. Reimann, C. Van den Broeck, H. Linke, P. Hänggi, J. M. Rubi, and A. Pérez-Madrid. Giant acceleration of free diffusion by use of tilted periodic potentials. *Phys. Rev. Lett.*, 87:010602, Jun 2001.

[37] David Reguera, Gerhard Schmid, Poornachandra Sekhar Burada, J M Rubi, Peter Reimann, and Peter Hanggi. Entropic transport: Kinetics, scaling, and control mechanisms. *Phys. Rev. Lett.*, 96(13):130603, 2006.

[38] P. S. Burada, G. Schmid, D. Reguera, J. M. Rubí, and P. Hänggi. Biased diffusion in confined media: Test of the fick-jacobs approximation and validity criteria. *Phys. Rev. E*, 75:051111, May 2007.

[39] Yoshua Chávez, Marco-Vinicio Vázquez, and Leonardo Dagdug. Unbiased diffusion through a linear porous media with periodic entropy barriers: a tube formed by contacting ellipses. *J. Chem.*, 2015, 2015.

[40] A. Arango-Restrepo and J. M. Rubi. Entropic transport in a crowded medium. *J. Chem. Phys.*, 153(3):034108, 2020.

[41] Alexander M. Berezhkovskii, Leonardo Dagdug, and Sergey M. Bezrukov. Peculiarities of the mean transition path time dependence on the barrier height in entropy potentials. *J. Phys. Chem. B*, 124(12):2305–2310, 2020.

[42] D Reguera and J M Rubi. Engineering tube shapes to control confined transport. *Eur. Phys. J.*, 223(14):3079–3093, 2014.

[43] Cornelis Storm, Jennifer J Pastore, Fred C MacKintosh, Tom C Lubensky, and Paul A Janmey. Nonlinear elasticity in biological gels. *Nature*, 435(7039):191–194, 2005.

[44] Fu-Shi Quan and Kyung Sook Kim. Medical applications of the intrinsic mechanical properties of single cells. *Acta Biochim. Biophys. Sin.*, 48(10):865–871, 09 2016.

[45] Alireza Nabavizadeh and et al. Noninvasive young's modulus visualization of fibrosis progression and delineation of pancreatic ductal adenocarcinoma (pdac) tumors using harmonic motion elastography (hme) in vivo. *Theranostics*, 10(10):4614, 2020.

[46] Charles F. Caskey, Susanne M. Stieger, Shengping Qin, Paul A. Dayton, and Katherine W. Ferrara. Direct observations of ultrasound microbubble contrast agent interaction with the microvessel wall. *J. Acoust. Soc. Am.*, 122(2):1191–1200, 2007.

[47] Christy K. Holland and Robert E. Apfel. Thresholds for transient cavitation produced by pulsed ultrasound in a controlled nuclei environment. *J. Acoust. Soc. Am.*, 88(5):2059–2069, 1990.

[48] Robert E Apfel and Christy K Holland. Gauging the likelihood of cavitation from short-pulse, low-duty cycle diagnostic ultrasound. *Ultrasound Med. Biol.*, 17(2):179–185, 1991.

[49] Alain Pluen, Paolo A. Netti, Rakesh K. Jain, and David A. Berk. Diffusion of macromolecules in agarose gels: Comparison of linear and globular configurations. *Biophys. J.*, 77(1):542 – 552, 1999.

[50] Jack L Cronenwett and K Wayne Johnston. *Rutherford's vascular surgery e-book*. Elsevier Health Sciences, 2014.

[51] Bengt O. Hedbys and Saiichi Mishima. Flow of water in the corneal stroma. *Exp. Eye Res.*, 1(3):262 – 275, 1962.

[52] S R Chary and R K Jain. Direct measurement of interstitial convection and diffusion of albumin in normal and neoplastic tissues by fluorescence photobleaching. *Proc. Natl. Acad. Sci.*, 86(14):5385–5389, 1989.

[53] Arsenii V. Telichko, Huaijun Wang, Sunitha Bachawal, Sukumar U. Kumar, Jagathesh C. Bose, Ramasamy Paulmurugan, and Jeremy J. Dahl. Therapeutic ultrasound parameter optimization for drug delivery applied to a murine model of hepatocellular carcinoma. *Ultrasound Med. Biol.*, 47(2):309–322, 2021.

[54] Mia Kvaale Løvmo and et al. Effect of acoustic radiation force on displacement of nanoparticles in collagen gels. *IEEE Transactions on Ultrasonics, Ferroelectrics, and Frequency Control*, 68(3):416–431, 2021.

[55] Mercy Afadzi and et al. Effect of acoustic radiation force on the distribution of nanoparticles in solid tumors. *IEEE Transactions on Ultrasonics, Ferroelectrics, and Frequency Control*, 68(3):432–445, 2021.

[56] Hassan K. Awwad, Mervat El Aggar, Nadia Mocktar, and Mohsin Barsoum. Intercapillary distance measurement as an indicator of hypoxia in carcinoma of the cervix uteri. *International Journal of Radiation Oncology*Biology*Physics*, 12(8):1329–1333, 1986.

[57] Yoshihiko Yoshii and Kohei Sugiyama. Intercapillary distance in the proliferating area of human glioma. *Cancer research*, 48(10):2938–2941, 1988.

[58] Petros Tesfamichael Yemane. *Ultrasound for the delivery of a nanocarrier across biological barriers in tumors: impact of cavitation and acoustic radiation force*. PhD thesis, NTNU, 2020.

[59] Eugene J. et al. Koay. A visually apparent and quantifiable ct imaging feature identifies biophysical subtypes of pancreatic ductal adenocarcinoma. *Clin. Cancer Res.*, 24(23):5883–5894, 2018.

[60] Hadi T. Nia, Lance L. Munn, and Rakesh K. Jain. Mapping physical tumor microenvironment and drug delivery. *Clin. Cancer Res.*, 25(7):2024–2026, 2019.

[61] Einar Sulheim, Ingunn Hanson, Sofie Snipstad, Krister Vikedal, Yrr MÃ¸rch, Yves Boucher, and Catharina de Lange Davies. Sonopermeation with nanoparticle-stabilized microbubbles reduces solid stress and improves nanomedicine delivery to tumors. *Adv. Ther.*, page 2100147, 2021.

[62] James H. Bezer, Hasan Koruk, Christopher J. Rowlands, and James J. Choi. Elastic deformation of soft tissue-mimicking materials using a single microbubble and acoustic radiation force. *Ultrasound Med. Biol.*, 46(12):3327–3338, 2020.

[63] Fan Yuan, Ave Krol, and Sheng Tong. Available space and extracellular transport of macromolecules: effects of pore size and connectedness. *Ann Biomed Eng*, 29(12):1150–1158, 2001.

[64] Costas D. Arvanitis and et al. Mechanisms of enhanced drug delivery in brain metastases with focused ultrasound-induced blood–tumor barrier disruption. *Proc. Natl. Acad. Sci. U.S.A*, 115(37):E8717–E8726, 2018.

9. Energy dissipation unveils the transition from healthy to carcinogenic tissues

This chapter studies the energetic response of a tissue characterised by the Young modulus under the action of a chemical and mechanical external forces.

Tissues are self-organised structures that self-assembled from basic building blocks, having a wide and efficient dynamic response under external stimuli to keep their function. Tumours can also be seen as self-organised or self-assembled structures that have a high rate of self-replication and high robustness under the action of external forces/stimuli as a change in the diet (substrates concentration changes), chemotherapy, radiotherapy, ozone-therapy, ultrasound among others. By solving the question of what is the value and the behaviour of the energy dissipated for different types (micro-structures) of carcinogenic tissue (pancreatic adenocarcinoma), we may unveil thermodynamic criteria for the structural configuration of such self-organised systems. Therefore, we present a non-equilibrium thermodynamic analysis of the energy dissipated in the pancreatic adenocarcinoma under the effect of a mechanical external force and a chemical external force. We compute the energy dissipated in tissue as a function of a set of parameters that define the micro-structure (elasticity and porosity), from healthy to rigid pancreatic adenocarcinoma. We found that healthy tissues tend to minimise the energy dissipated (being energetically efficient) while average pancreatic adenocarcinoma tend to maximise the energy dissipated (having a robust and quick mechanical response). As a consequence, we estimate from our criteria that healthy tissues are 1000 times more probable than average carcinogenic tissues, which is in accordance with the statistics of the world health organisation (WHO).

This chapter is based on a manuscript in preparation.

9.1. Introduction: Probability and thermodynamics of cancer

According to the World Health Organization, in 2020, about 10 million people suffered complications from cancer (i.e., 0.13 % of the world population) [1]. Statistical projections show that by 2030 this percentage could be twice[2]. It is therefore critical to consider new approaches to understand the emergence and sustainability of carcinogenic tissues to reveal the most probable properties and thus apply the most suitable treatment [3]. Understanding the proportion of the emergence of the different cancer stages may bring us hints of how cancer evolves from a thermodynamics perspective [4, 5, 6, 7, 8, 9, 10, 11].

Since not only genetics and biochemistry have been shedding a light on the problem of cancer but also physical sciences, mainly in the transition from healthy to cancer states [6], thermodynamics might unveil the rules and principles on cancer emergence and growth from the protein-protein to the cell-cell interaction level [7] [8, 9]. Furthermore, from early studies, it was concluded that a formal physical theory on cancer is required, with particular emphasis on thermodynamics [10]. Entropy production rate has been an important non-equilibrium quantity to explain theoretically different phenomena in carcinogenic tissues along with different scales which might bring information about strategies to improve current treatments or even new treatments [5, 4, 11, 12].

Self-organised (SO) and self-assembled (SA) structures under non-equilibrium conditions are known by having an advanced dynamical response under external stimuli [13, 14]. As mentioned by *Erwin Schrodinger* in *What is life?* [15], life exists due to the ordering of its fundamental components at expense of the dissipation of energy to the surroundings, or as stated by *Illya Prigogine*, due to the energy dissipation coming from the non-equilibrium phenomena taking place in the system (living being) [16]. The dissipation came from the existence of gradients triggering in fluxes of heat, mass as well as chemical reactions. The formation of SO structures has been analysed theoretically and experimentally showing that their configuration coincides with processes maximising or minimising the total energy dissipated [17, 18, 19, 20], being cancer a clear example [21]. Therefore, structures in a minimum energy dissipation regimen are associated with thermodynamically efficient SA/SO structures while structures in a maximum energy dissipation regimen are associated with an efficient dynamical response under external stimuli, both cases are highly important and observed in biological, physical, and chemical systems [22].

Carcinogenic tissues can be understood as the result of a set of cells with highly self-replication rates and able to modify group (structure) parameters to survive [23]. In cancer treatments, these tissues are exposed to external forces to disassemble the structure by getting rid of the fundamental blocks (cancer cells)[24]. These treatments trigger non-equilibrium condition for which the SO structure (carcinogenic tissue) reacts and dissipate energy [25, 26] as a function of the mechanical properties of the tissue. Values of these mechanical properties bring us information bout the stage of cancer, as well as the invasive potentials [27, 28]. The idea that changes in cellular and extra-cellular mechanical properties can promote the growth of cancer has been studied [29], in which the connection between the mechanics and biochemical aspects is a powerful tool to develop therapies and diagnosis [30].

We can attempt, from a thermodynamic framework, to relate this invasive potential with the energy dissipated in a given stage of cancer (values of the mechanical parameters), as a non-equilibrium phase transitions

[6]. Nevertheless, tissues are systems under non-equilibrium conditions and we must emphasise that only the use of the classical Gibbs free energy does not bring enough information about the probability to observe a state (mechanical property value).

In this study, we analyse the case of carcinogenic tissues (pancreatic adenocarcinoma) to unveil why carcinogenic structures have adapted mechanically, with certain porosity and elasticity, using a non-equilibrium thermodynamic approach. From a previously proposed model, we compute the total energy dissipated for different possible carcinogenic structures under the action of a mechanical and chemical external force working as a cancer treatment. From our results, we relate the most dissipating configurations with reported data on pancreatic adenocarcinoma. These results then are useful to estimate model parameters by knowing that carcinogenic tissues are configured to maximise energy dissipation. Furthermore, we can justify why some mechanical property values are not found in nature since their probability, computed from the thermodynamic criterion, is extremely small. Finally, from the present work, we can understand more the energetic reason why carcinogenic tissues, in different cancer stages, adopts given values of porosity and elasticity, key properties to consider in treatments. The criterion might open a possibility to compute the probability of cancer stage transitions from historical data of individual organs and mechanical properties.

9.2. Methods

9.2.1. Energy dissipation

The action of the external forces and the response of the tissue triggers the emergence of phenomena dissipating energy. Through the entropy production rate we are able to quantify such dissipation.

The entropy production rate (σ) results from the forces acting over the TAs and over the tissue. Diffusion of the NPs under the action of the mechanical external force as well as the adsorption and deactivation of the NPs are the phenomena producing entropy. Additionally, the stretching-deformation of the tissue is a process leading to a considerable entropy production. According to non-equilibrium thermodynamics [31, 32], the resulting entropy production rate from the NPs movement is given by

$$\sigma_c(r,t;\eta) = -\frac{1}{T}\left[J\frac{\partial \mu}{\partial r} + J_c\Delta x(r,t) + J_d x_c(r,t)\right] \tag{9-1}$$

where η is a vector containing the porosity and Young modulus of the tissue.

To compute the entropy production from the stretching-deformation, we assume that the external mechanical force is written as $F = C_0\Delta P\sin\omega t$. From linear non-equilibrium thermodynamics [31], the flux or velocity of stretching is $J_m = -\kappa F$, being κ the permitivity of the stretching process which we define as $\kappa = \Lambda^{-1}\sqrt{Y/\rho}/\lambda$ with Λ the attenuation coefficient in J/m^3, λ the characteristic length (cell diameter) and ρ the tissue density. Therefore, the entropy production rate from the stretching-deformation is given by:

$$\sigma_m(r,t;\eta) = \kappa C_0^2(\Delta P\sin\omega t)^2 \tag{9-2}$$

The entropy production rate due to the external chemical and mechanical force is the sum of both contributions $\sigma = \sigma_c + \sigma_m$. The total entropy produced as a function of the porosity and Young modulus is written as:

$$\Sigma(\eta) = \int_0^\infty \int_0^\infty \sigma(r,t;\eta) dr dt \tag{9-3}$$

in which the total energy dissipated is defined as $E_d(\eta) = T\Sigma(\eta)$.

9.2.2. Non-equilibrium criteria

In the case of self-assembled and self-organised structures, a criterion has been proposed [33] to understand the ”why.ºf the emergence and maintenance of such structures under non-equilibrium conditions as well as to explain the probability of observation does not necessarily follow classical equilibrium thermodynamics probabilities.

The thermodynamic information of a self-assembled or self-organised structure can be summarised in the effective potential defined from the energy dissipated during the response process for a given pair of values of elasticity and porosity

$$\Delta\Psi \approx \Delta\Psi_{rev} + T\Sigma + \frac{T}{2}\frac{(\partial_Y \Sigma)^2}{|\partial_{YY}\Sigma(Y^*,\phi^*)|} + \frac{T}{2}\frac{\left(\partial_\phi \Sigma\right)^2}{|\partial_{\phi\phi}\Sigma(Y^*,\phi^*)|} \tag{9-4}$$

in which $\Delta\Psi_{rev} \equiv \Delta G_{rev}$, i.e., to the free energy change at equilibrium conditions. The values Y^* and ϕ^* correspond to the ones where $\nabla\Sigma = 0$. In the case of healthy and carcinogenic tissues, characterised by both elasticity and porosity represented by the vector η_1 and η_2 respectively, the ratio between the probabilities is

$$\frac{p(\eta_1)}{p(\eta_2)} = \exp(-\beta(\Delta\Psi(\eta_1) - \Delta\Psi(\eta_2))) \tag{9-5}$$

9.2.3. Current and transition probability

From the solution $p(\eta)$ we can estimate the dimensionless probability current of one state at a given η_1 going to the state (or configuration) η_2. It is defined as:

$$J_{\eta_1 \to \eta_2} = -\left(\left.\frac{\partial p}{\partial \eta}\right|_{\eta_1} + \frac{p(\eta_1)}{nk_B T} \left.\frac{\partial \Delta\Psi}{\partial \eta}\right|_{\eta_1} \right) \tag{9-6}$$

This current brings information about the evolution of the states under small perturbations. Thus we can know, from a given state, how favoured the transition to another state is. Negative fluxes indicate a non-favoured transition whereas high positive fluxes show a favoured process where most of the possible events tend to the change of state, the transition. Furthermore, from the derivative of the flux, we know from conservation equation [33] that a derivative equal to zero (maximum or minimum of the current) means a dynamically stable state and therefore a point where the change of probability density is also null, i.e., there is no transition. Additionally, a region with a negative derivative indicates accumulation or, in other words, a region where the states converge whereas a positive value means that the probability is in constant change and the transition is favoured.

Current is also useful to define and delimit the different stages in the evolution of a tissue as a function of mechanical properties, in this case, Youngâ€™s modulus. In the definition, we consider that a stable region is delimited by a clear change in the sign of the flux from negative to positive since at that point there is a divergence of fluxes and a transition should be unlikely. The opposite is not true, a change from positive to negative means convergence. That point might be defined as kinetically trapped but not necessarily delimits a stage. Limits of the stages must be given by critical points in the current and its derivative since at these points there is a change in the energetics and thermodynamics of the response of the system under external perturbations.

We can estimate the transition probability from a simple analysis. First, we compute the average fluxes along two stages

$$\langle J \rangle_{s_i \to s_{i+1}} = \int_{Y_i}^{Y_{i+1}} J(Y) dY \tag{9-7}$$

next, we consider four conditions for the transition probability as a function of the average flux:

i) for an average flux equal to zero, the transition probability should be 0.5 since on average the events happening toward are equal to the event happening backwards. ii) for average flux much greater than 0, the transition tend to 1. iii) for average flux much lower than 0, the transition tend to 0. iv) Transition should depend also on the average value of the derivative of the flux along the stages.

The function fulfilling these requirements is an hyperbolic tangent:

$$P_{s_i \to s_{i+1}} = \frac{1}{2}\left(1 + \tanh(\mathscr{C}_i \langle J \rangle_{s_i \to s_{i+1}})\right) \tag{9-8}$$

with $\mathscr{C}$ a constant depending on the average derivative of the current at the i^{th} stage. Finally, the conditional probability of being in the stage i (for $i > 1$) is:

$$P_i^c = \prod_{j=2}^{j=i} P_{s_{j-1} \to s_j} \tag{9-9}$$

where the probability of staying at the initial stage is

$$P_1^c = 1 - P_{s_1 \to s_2} \tag{9-10}$$

9.3. Results

To obtain the results we use the model and results of the previous chapter and we solve Eqs.9-2-9-10 for different values of the Young modulus and porosity. From Fig.**9-1** we observe that the average pancreatic adenocarcinoma maximize (locally) the energy dissipation while healthy tissues minimize it in accordance with experimental results (Carcinogenic and Healthy tissue dashed regions). Carcinogenic tissues then dissipate as much energy as possible as a response under external stimuli (attack) to keep their configuration (nature). This is in accordance with cancer dynamics in which self-replication and self-healing are the main phenomena taking place to avoid states very close to the thermodynamic equilibrium (death). Contrary, healthy tissues have a smooth response under the external force due to external stimuli is not sensed as an attack, and the biological function is not compromised. This, in accordance with the efficient use of energy in healthy organisms.

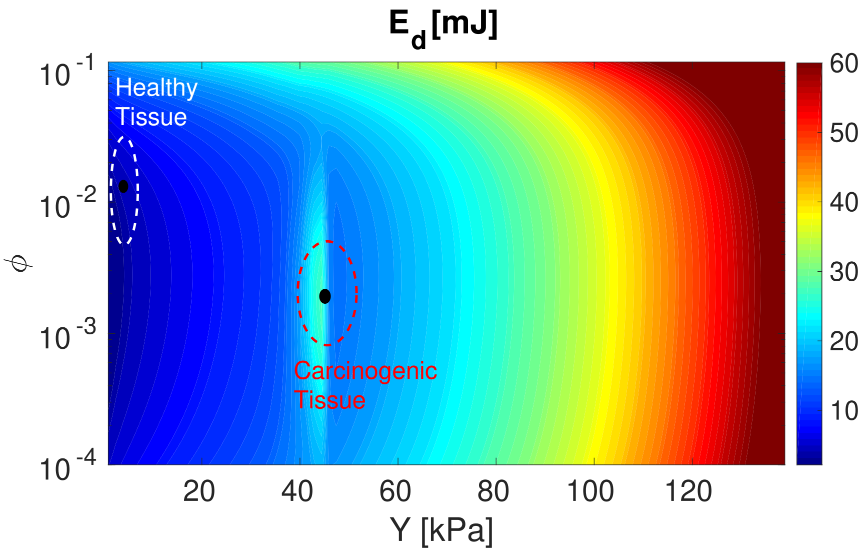

Fig. 9-1.: The energy dissipated in *mJ* per gram of tissue under the effect of an external force as a function of Young’s modulus and porosity. Values from our model are given by the colourmap. Healthy tissue and Carcinogenic Tissue regions correspond to pancreatic adenocarcinoma experimental data [34, 35].

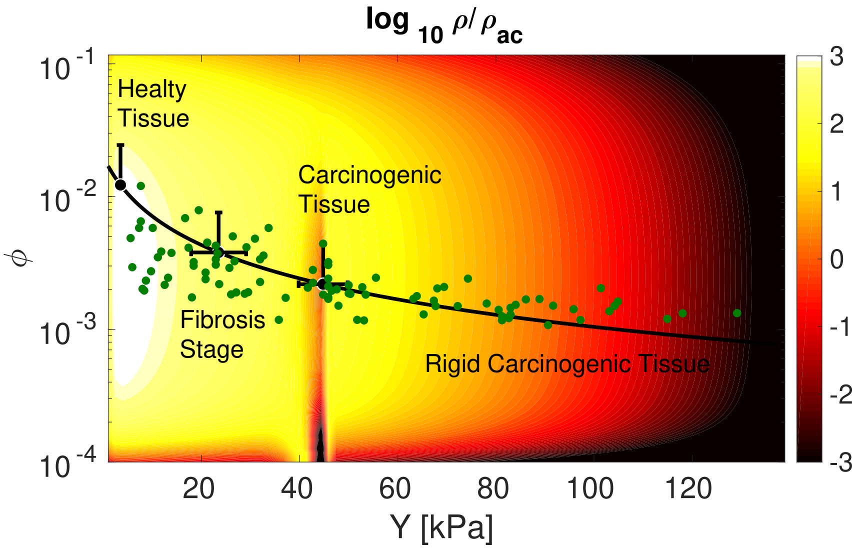

Fig. 9-2.: Probability density as a function of Young’s modulus and porosity. Values from our model are given by the colourmap. Green points correspond to pancreatic adenocarcinoma experimental data [34, 35] whereas the continuous black line corresponds to the tendency for the experimental data.

In Fig.**9-2** we observe that there are limits for which is extremely rare to find a structure having low porosity or high youngâ€™s modulus. Different experimental measures (green points) follow a tendency (black line)

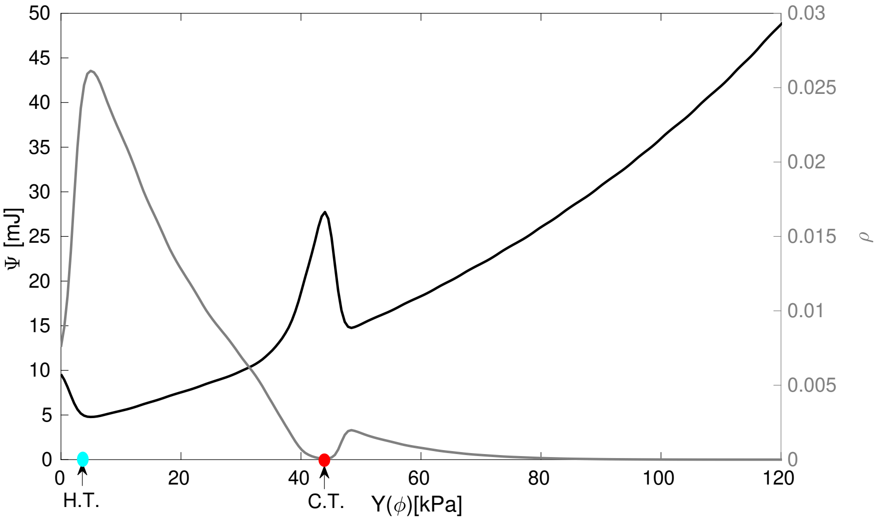

Fig. 9-3.: Ψ (black line) and ρ (grey line) as a function of Y. Blue and red point corresponds to the value of Y for the average healthy and carcinogenic tissues respectively. Right axis shows the values for the probability density ρ.

such that the probability estimation from the model tends to enclose the experimental data in the expected region. Regarding the healthy tissues, they are four orders of magnitude more probable to find than an average pancreatic adenocarcinoma. Rigid carcinogenic tissues seem to be a configuration that all carcinogenic tissues tend to reach due to is a likely probable configuration.

From the experimental trend of elasticity and porosity (Fig.**9-2**), we can obtain the dissipated energy E_d, the effective potential *Psi* and the probability density *rho* using our model (see previous chapter) and thermodynamic criterion as a function of elasticity, see Fig.**9-3**. It illustrates that the average pancreatic adenocarcinoma and healthy tissue are at the extreme point of the effective potential. The relative probability shows that, for example, of all possible configurations of pancreatic adenocarcinoma (as a function of porosity), the probability of observing healthy tissue is 1000 times greater than the probability of observing pancreatic adenocarcinoma. However, it should be noted that this is a probability density as a function of elasticity, not total probability. From the probability density, we can calculate the probability of being in a stage (defined from two values of Y), however, this probability considers the stages as independent entities but we know that they are related and one stage depends on the previous one. To actually calculate the probability of being in a given stage, we must calculate the conditional probability of the transition probability to jump from one stage to the next.

In Fig.**9-4**, we present the probability current and its derivative with respect to Young's modulus. The cyan region corresponds to the healthy tissue measurements (healthy stage) while the blue region corresponds to the transition from healthy to fibrous tissue which we call the initial fibrosis stage. The green region represents the fibrous tissue data (fibrosis stage), while the white regions correspond to extremely improbable Young's modulus values in a pancreas. In the red region, we find the carcinogenic stage which represents the majority of cancer measurements, while the magenta region represents the advanced carcino-

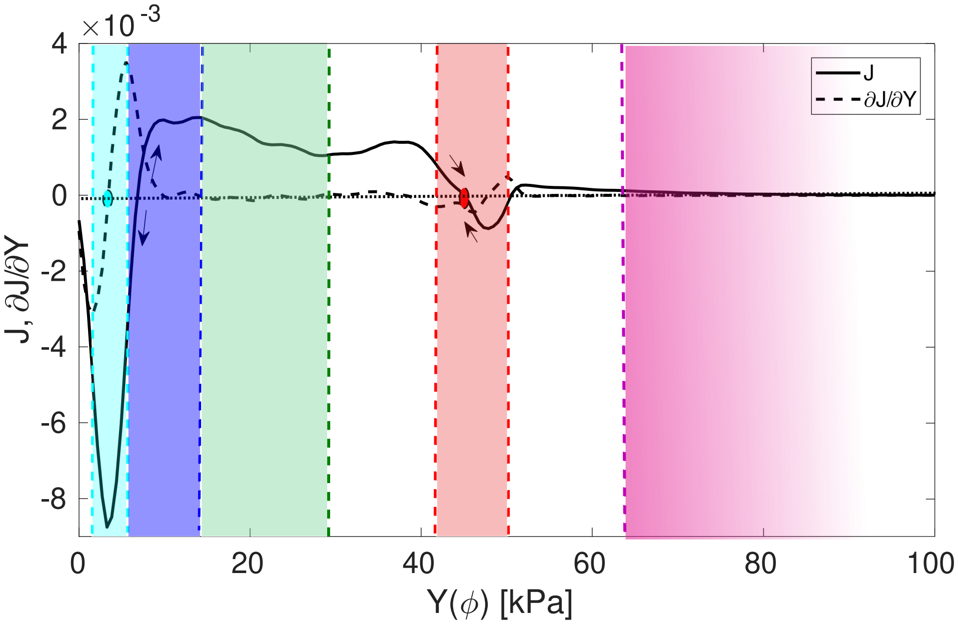

Fig. 9-4.: Probability current J and its derivative $\partial J/\partial Y$ as a function of Yong modulus Y. Cian, blue, green, red and magenta region corresponds to healthy, initial fibrosis, fibrosis, carcinogenic and advanced carcinogenic stages. White regions represent unlikely configurations (values of Y) for the pancreas. Blue and red points represent the average healthy and carcinogenic tissues.

genic stage. We note that the healthy and fibrosis stage correspond to $\partial J/\partial Y = 0$, i.e. a dynamically stable point/state. Around the transition from the healthy stage to initial fibrosis, there is a change in the sign of the J-probability current (from negative to positive), where we expect a low probability of jumping from one stage to the other. The fibrosis and transition stages have a positive current, which means that the transit through these stages is short, high probability of transition and favours the cancer stage once the jump from healthy to initial fibrosis is made. Furthermore, in the cancer stage we find a convergence as the current sign changes from positive to negative, which means that there is a configuration to which the system will tend once the initial barrier is overcome (from healthy to fibrosis in this case). Finally, the transition from cancer to advanced cancer tends to be slow as the current tends to zero, probably because the flux tends to be positive and where the advanced and rigid cancer stage appears to be dynamically stable because the derivative is approximately zero.

It is from this information that we can calculate the transition probability and, therefore, the corresponding conditional probability. In Fig.**9-5** we show the transition probability (left side) and the conditional stage probability (right side). We observe a very low probability of jumping from a healthy stage to initial fibrosis (as expected from the current probability analysis). The transition probabilities tend to be 1 for all other cases (except when jumping from cancer to transitional stage), i.e., once healthy tissue reaches an initial fibrosis stage, the spontaneous process will be to reach a cancerous stage. Let us keep in mind that the energetic analysis is based on mechanical and chemical forces acting on a tissue, so the increase in stiffness (Young's modulus) seems to be favored once a critical point (initial fibrosis) is reached. The conditional probability results emphasize the fact that beyond fibrosis stages, the probability of observation is low, around 25 in

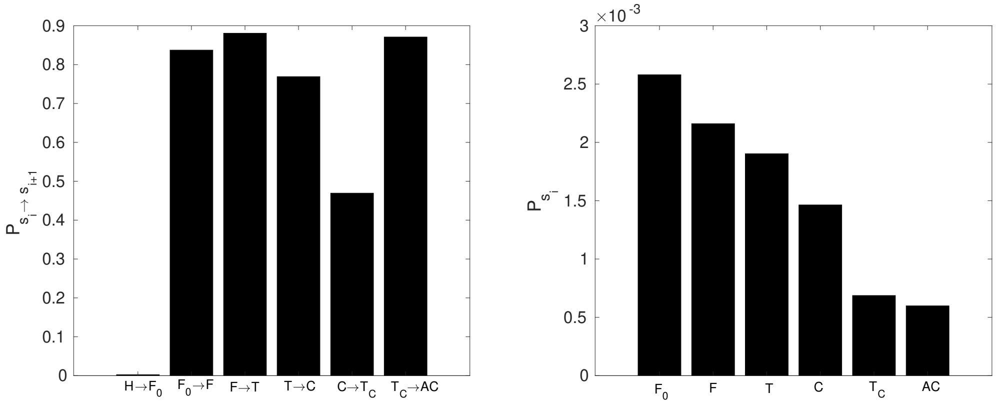

Fig. 9-5.: Transition probability and conditional stage probability. In the left side is shown the transition probability from healthy to initial fibrosis ($H \to F_0$), initial fibrosis to fibrosis ($F_0 \to F$), fibrosis to transition stage ($F \to T$), transition stage to cancer ($T \to C$), cancer to carcinogenic transition stage ($C \to T_C$) and from carcinogenic transition stage to advanced/rigid cancer ($T_C \to AC$). In the right side is drawn the conditional stage probability for the initial fibrosis F_0, fibrosis F, transition T, cancer C, carcinogenic transition T_C and Advanced cancer stage AC.

10000. Specifically, we found that the probability of observing pancreatic tissue in the cancer stage is about 1/1000, which is according to the data provided by WHO.

9.4. Discussion: From thermodynamics to treatments

Considering that healthy tissues and pancreatic adenocarcinoma are found in the minimum and maximum energy dissipated configurations, we use the model to estimate the tissue configuration as a function of two structural parameters (α accounting for the sensitivity of the change of the minimum radius of the capillary as a function of the external force and the fenestrian radius, the minimum radius of the capillary). This criterion is then useful to define parameters that can not be easily measurable and to validate theoretical models as we show here (See Methods). It also may be used to characterise different stages of cancer as a function of structural parameters.

We can justify the existence of pancreatic adenocarcinoma from a thermodynamical point of view. We reproduce the probability of observing average pancreatic adenocarcinoma from our criterion. We understand the tissue as a self-organised system that evolves in an inner space, in this case, given by the porosity and elasticity, in which we have recognised the different stages of a tissue as a function of structural properties and we related the probability of observation with the energy dissipated under the effect of an external force or perturbation to perform a non-equilibrium thermodynamical analysis.

This thermodynamic perspective when analysing the pancreatic adenocarcinoma as a self-organised structure allows us to understand from a general formalism the different possible stages of cancer and, therefore, contributes to understanding how cancer evolves. Cancer could be understood as a self-organised structure in an organism looking for higher robustness and adaptability in shorter times. They can deal with external inputs and release as much energy as possible, in an irreversible way, to then reach a pseudo-steady state where no energy (mechanical or chemical) from the external source is stored to avoid changes in the key parameters of the structure, i.e. cancer dissipates to do not lose its adaptable nature.

Carcinogenic tissues seem to be a highly dissipative structure and for that reason using treatments to increase dissipation is not the best strategy. Future treatments should consider external agents that interact with the carcinogenic tissue inducing low energy dissipation such as chemical drugs that do not show high free energy changes, i.e., chemical reactions close to the equilibrium and low drug concentrations. This comment is, of course, from a purely thermodynamical point of view and from our study case in pancreatic adenocarcinoma.

The probability current is an important variable not only to calculate theoretically the transition probability (without simulations), but also to define the stages or regimes of self-assembled and self-organized structures. From the current probability and from the thermodynamic point of view, we could predict the evolution of a cancer (from the initial stage) using a model and patient data (Young's Modulus of healthy and unhealthy affected tissue). Therefore, a predictive model could be used in the future to give more accurate estimates of the evolution of a cancer. This would be an important tool to know not only the level of cancer intensity but also the level of treatment required.

From a more complete model, we can capture much better the behaviour of the energy dissipated and thus a more detailed and precise analysis of the stages probabilities, structure evolution and future treatments outlook. Future work might be done while considering different metabolic routes when analysing dissipation to corroborate our findings.

Bibliography

[1] Health World Organization. Cancer, 2022.

[2] Health World Organization. Population, 2022.

[3] Andrés Arango-Restrepo, J. Miguel Rubi, Signe Kjelstrup, Bjørn Atle J. Angelsen, and Catharina de Lange Davies. Enhancing carrier flux for efficient drug delivery in cancer tissues. *Biophysical Journal*, 120(23):5255–5266, 2021.

[4] Umberto Lucia, Antonio Ponzetto, and Thomas S. Deisboeck. A thermodynamic approach to the "mitosis/apoptosis" ratio in cancer. *Physica A: Statistical Mechanics and its Applications*, 436:246–255, 2015.

[5] Umberto Lucia. Thermodynamics and cancer stationary states. *Physica A: Statistical Mechanics and its Applications*, 392(17):3648–3653, 2013.

[6] Paul CW Davies, Lloyd Demetrius, and Jack A Tuszynski. Cancer as a dynamical phase transition. *Theoretical Biology and Medical Modelling*, 8(1):1–16, 2011.

[7] Edward A Rietman, John Platig, Jack A Tuszynski, and Giannoula Lakka Klement. Thermodynamic measures of cancer: Gibbs free energy and entropy of protein–protein interactions. *Journal of biological physics*, 42(3):339–350, 2016.

[8] Mostafa Sadeghi Ghuchani. Thermodynamic modeling of the competition between cancer and normal cells. *Journal of Non-Equilibrium Thermodynamics*, 45(1):19–25, 2020.

[9] Edward A. Rietman and Jack A. Tuszynski. *Thermodynamics and Cancer Dormancy: A Perspective*, pages 61–79. Springer International Publishing, Cham, 2017.

[10] Hiroaki Kitano. Cancer as a robust system: implications for anticancer therapy. *Nature Reviews Cancer*, 4(3):227–235, 2004.

[11] Umberto et al. Lucia. Constructal thermodynamics combined with infrared experiments to evaluate temperature differences in cells. *Scientific Reports*, 5(1):1–10, 2015.

[12] Umberto Lucia, Antonio Ponzetto, and Thomas S Deisboeck. Constructal approach to cell membranes transport: Amending the “norton-simon” hypothesis for cancer treatment. *Scientific Reports*, 6(1):1–14, 2016.

[13] Helmut Cölfen and Stephen Mann. Higher-order organization by mesoscale self-assembly and transformation of hybrid nanostructures. *Angew. Chem. Int. Ed.*, 42(21):2350–2365, 2003.

[14] Marcin Fialkowski, Kyle J M Bishop, Rafal Klajn, Stoyan K Smoukov, Christopher J Campbell, and Bartosz A Grzybowski. Principles and Implementations of Dissipative (Dynamic) Self-Assembly. *J.Phys. Chem. B*, 110:2482–2496, 2006.

[15] Erwin Schrodinger. *What is life*, volume 90. Cambridge: Cambridge University Press, 1944.

[16] Ilya Prigogine and G Nicolis. *Self organization in non equilibrium systems*. John wiley & sons, 1 edition, 1977.

[17] Roderick C Dewar, Charles H Lineweaver, and Robert K Niven. *Beyond the Second Law: Entropy Production and Non-equilibrium Systems.* Springer-Verlag Berlin Heidelberg, 1 edition, 2014.

[18] Michael Nosonovsky and Bharat Bhushan. Surface self-organization: From wear to self-healing in biological and technical surfaces. *Appl. Surf. Sci.*, 256(12):3982–3987, 2010.

[19] Y. Kawazura and Z. Yoshida. Entropy production rate in a flux-driven self-organizing system. *Phys. Rev. E: Stat. Phys., Plasmas, Fluids, - Statistical, Nonlinear, and Soft Matter Physics*, 82(6):1–8, 2010.

[20] Elisa Magnanelli, Ã˜ivind Wilhelmsen, Mario Acquarone, Lars P. Folkow, and Signe Kjelstrup. The nasal geometry of the reindeer gives energy-efficient respiration. *Journal of Non-Equilibrium Thermodynamics*, 42(1):59–78, 2017.

[21] Anthonie W.J. Muller. Cancer is an adaptation that selects in animals against energy dissipation. *Medical Hypotheses*, 104:104–115, 2017.

[22] Andrés Arango-Restrepo, J. Miguel Rubi, and Daniel Barragán. The role of energy and matter dissipation in determining the architecture of self-assembled structures. *The Journal of Physical Chemistry B*, 123(27):5902–5908, 2019. PMID: 31194550.

[23] A. Agosti, S. Marchesi, G. Scita, and P. Ciarletta. Modelling cancer cell budding in-vitro as a self-organised, non-equilibrium growth process. *Journal of Theoretical Biology*, 492:110203, 2020.

[24] Alexander O Goushcha, Tatiana O Hushcha, Leonid N Christophorov, Michael Goldsby, et al. Self-organization and coherency in biology and medicine. *Open Journal of Biophysics*, 4(04):119, 2014.

[25] Liao-fu Luo. Entropy production in a cell and reversal of entropy flow as an anticancer therapy. *Frontiers of Physics in China*, 4(1):122–136, 2009.

[26] S. Suresh, J. Spatz, J.P. Mills, A. Micoulet, M. Dao, C.T. Lim, M. Beil, and T. Seufferlein. Reprint of: Connections between single-cell biomechanics and human disease states: gastrointestinal cancer and malaria. *Acta Biomaterialia*, 23:S3–S15, 2015.

[27] Janine T Erler and Valerie M Weaver. Three-dimensional context regulation of metastasis. *Clinical & experimental metastasis*, 26(1):35–49, 2009.

[28] Kandice R. Levental et al. Matrix crosslinking forces tumor progression by enhancing integrin signaling. *Cell*, 139(5):891–906, 2009.

[29] Parag Katira, Roger Bonnecaze, and Muhammad Zaman. Modeling the mechanics of cancer: Effect of changes in cellular and extra-cellular mechanical properties. *Frontiers in Oncology*, 3, 2013.

[30] Subra Suresh. Biomechanics and biophysics of cancer cells. *Acta Biomaterialia*, 3(4):413–438, 2007.

[31] Sybren Ruurds De Groot and Peter Mazur. *Non-equilibrium thermodynamics*. Dover Publications Inc., 1985.

[32] D Reguera, JM Rubi, and JMG Vilar. The mesoscopic dynamics of thermodynamic systems. *J. Phys. Chem. B*, 109(46):21502–21515, 2005.

[33] Andrés Arango-Restrepo, Daniel Barragán, and J. Miguel Rubi. A criterion for the formation of nonequilibrium self-assembled structures. *The Journal of Physical Chemistry B*, 125(7):1838–1845, 2021. PMID: 33566612.

[34] Alireza Nabavizadeh and et al. Noninvasive young's modulus visualization of fibrosis progression and delineation of pancreatic ductal adenocarcinoma (pdac) tumors using harmonic motion elastography (hme) in vivo. *Theranostics*, 10(10):4614, 2020.

[35] Phuong et al. Vincent. High-resolution *Ex Vivo* elastography to characterize tumor stromal heterogeneity in situ in pancreatic adenocarcinoma. *IEEE Transactions on Biomedical Engineering*, 67(9):2490–2496, 2020.

10. A Thermodynamic Framework for Stretching Processes in Fibre Materials

In this chapter, we study the dynamical response of a set of organised fibbers exposed to a constant external force. We can deal with such a structure as an assembled structure in which its dynamical response and critical points are characterised by the energy dissipation in the elongation-breaking process.

A fibre breakage process involves heat exchange with the medium and energy dissipation in form of heat, sound and light, among others. A purely mechanical treatment is therefore in general not enough to provide a complete description of the process. We have proposed a thermodynamic framework which allow us to identify new alarming signals before the breaking of the whole set of fibres. The occurrence of a maximum of the reversible heat, a minimum of the derivative of the dissipated energy or a minimum in the stretching velocity as a function of the stretch can prevent us from an imminent breakage of the fibres which depends on the nature of the fibres material and on the load applied. The proposed conceptual framework can be used to analyse how dissipation and thermal fluctuations affect the stretching process of fibres in systems as diverse as single-molecules, textile and muscular fibres and composite materials.

This chapter was published in *Frontiers in Physics*, **9**, (2021). Ref.[1]

10.1. Introduction

When external load/stretch is applied on a fibre materials composed of elements with different strength threshold, weaker elements fail first. As the surviving elements have to support the load, stress (load per element) increases and that can trigger more element-failure. With continuous loading/stretching, at some point the system collapses completely, i.e, external load/stretch is above the strength of the whole system at that point. Such a system-collapse is known as "catastrophic failure" for that system.

There are several physics-based approaches [2, 3, 4] that can model such a scenario. Fibre bundle model (FBM) is one of those models and FBM has become a useful tool for studying fracture and failure [5, 6, 7] of composite materials under different loading conditions. The simplicity of the model allows to achieve analytic solutions [6, 8] to an extent that is not possible in any of the fracture models studied so far. For these reasons, FBM is widely used as a model of breakdown that extends beyond disordered solids. In fact, fibre bundle model was first introduced by a textile engineer [5]. Later, physicists took interest in it, mainly to explore the failure dynamics and avalanche phenomena in this model [9, 10, 11]. Furthermore, it has been used as a model for other geophysical phenomena, such as snow avalanche [12], landslides [13, 14], biological materials [15] or even earthquakes [16].

Although stretching processes in FBM have been analysed extensively [2, 3, 4, 5, 6, 7], mainly by physics community, a concrete thermodynamic description for the stretching process is still lacking in this field. In the efforts to unveil the stretching-failure phenomena, thermodynamics seems to be an important tool because it allows incorporating variables such as temperature, entropy, reversible heat, entropy production rate, and energy dissipation to thus unify stretching-failure dynamics and energy analysis. Especially where surface effects, heat release and sound emission, due to energy dissipation, are present when dealing with the stretching-failure of fibrous materials.

In this manuscript, we intend to develop a thermodynamic framework to analyse not only the energetics of the stretching-failure phenomena but also the dynamics by means of non-equilibrium thermodynamics formalism at all scales, from a single molecule to a macro-structure. We believe that our thermodynamic framework could carry over to other problem areas, eventually also outside the physical sciences such as molecular biology and nanotechnology.

We arrange the article as follows: After the Introduction (section 1) we give a short background of studies on stretching of FBM in section 2. In several subsections of section 2, we discuss strength and stability in FBM, energy variations during stretching, and warning signs of catastrophic failure. In section 3 we introduce a proper thermodynamic framework of the stretching process and analyse the mesoscopic regime and small-fluctuation regime. All the simulation results are presented in section 4 including dynamics and energetics, Fokker-Plank approach, and role of fluctuations on the stretching process. We make some conclusions at the end (section 5).

10.2. Background: Stretching of a Fibre Bundle

In 1926, F. T. Peirce introduced the fibre Bundle Model [5] to study the strength of cotton yarns in connection with textile engineering. Some static behaviour of such a bundle (with equal load sharing by all the surviving fibres, following a failure) was discussed by Daniels in 1945 [17] and the model was brought to the attention of physicists in 1989 by Sornette [18].

In this model, a large number of parallel Hookean springs or fibres are clamped between two horizontal platforms; the upper one (rigid) helps hanging the bundle while the load hangs from the lower one. The springs or fibres are assumed to have different breaking strengths. Once the load per fibre exceeds a fibre's own threshold, it fails and can not carry load any more. The load/stress it carried is now transferred to the surviving fibres. If the lower platform deforms under loading, fibres closer to the just-failed fibre will absorb more of the load compared to those further away and this is called local-load-sharing (LLS) scheme [19]. On the other hand, if the lower platform is rigid, the load is equally distributed to all the surviving fibres. This is called the equal-load-sharing (ELS) scheme. Intermediate range load redistribution are also studied (see e.g., [20]).

10.2.1. Strength and Stability in FBM

Let us consider a fibre bundle model having N parallel fibres placed between two stiff bars (Fig.**10-1**). Under a external force, the system responds linearly with a elastic force. The dimensionless elastic force F_e for a given dimensionless stretch value x (ranging from 0 to 1) is $F_e = \kappa x$, where κ is the dimensionless spring constant $\kappa = k_e L_m / F$ with k_e as the elastic constant of the material, L_m the maximum stretching length and F the external force (applied load). If the stretch x exceeds this threshold, the fibre fails irreversibly. In the equal-load-sharing (ELS) model, the bars are stiff and the applied load F is shared equally by the intact fibres.

Fibre strength distribution

The strength thresholds of the fibres are drawn from a probability density $p(x)$. The corresponding cumulative probability is given by

$$P(x) = \int_0^x p(y)dy. \tag{10-1}$$

from which we can obtain the number of non broken fibres as a function of the average deformation of the set of fibres x:

$$n(x) = N(1 - P(x)) \tag{10-2}$$

The fraction of broken fibres, or damage, is then given by $m(x) = 1 - n(x)/N$. For a uniform distribution one has $p(x) = 1$, $P(x) = x$ and $n(x) = N(1-x)$.

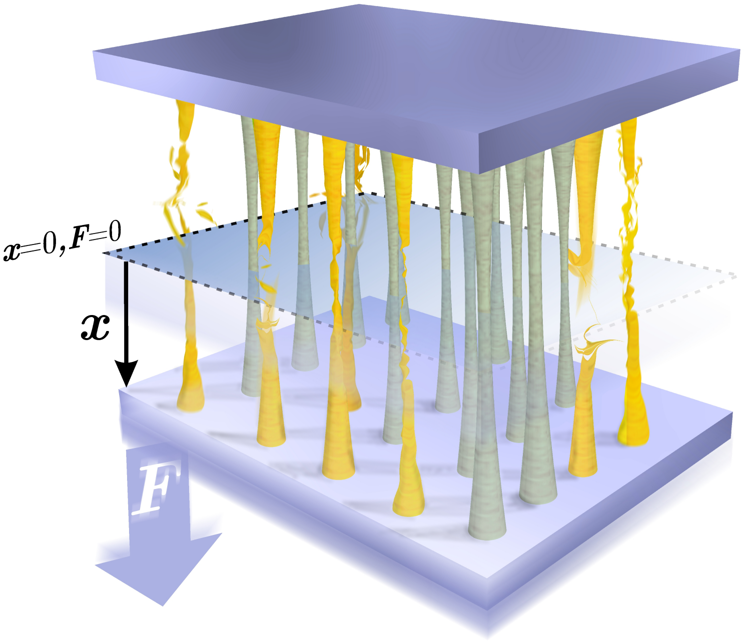

Fig. 10-1.: Illustration of the system. Under the application of a constant external force F, the set of fibres stretch a length x, however, due to they have different strength thresholds, some of them break (yellow fibres) resulting in the increment of load for the non-broken fibres (grey fibres)

The critical/failure strength

The bundle exhibits an elastic force

$$F_e(x) = N(1 - P(x))\kappa x. \tag{10-3}$$

The normalised elastic force (F_e/N) versus the average stretch x is represented in Figure **10-2** for a uniform probability distribution.

The elastic force-maximum is the strength of the bundle and the corresponding stretch value (x_c) is the critical stretch beyond which the bundle collapses. Two distinct regimes of the system can be recognised: one stable, for $0 < x \leq x_c$, and another unstable, for $x > x_c$.

The critical stretch value follows from the condition $dF_e/dx = 0$.In the case of a uniform threshold distribution, using the corresponding values of $p(x_c)$ and $P(x_c)$ we obtain $x_c = 1/2$.

10.2.2. Energies in FBM during stretching

When N is large, one can express the elastic E_e and the breaking E_b energies in terms of the stretch x as

$$E_e(x) = \frac{N\kappa}{2}\, x^2 \,(1 - P(x)) \tag{10-4}$$

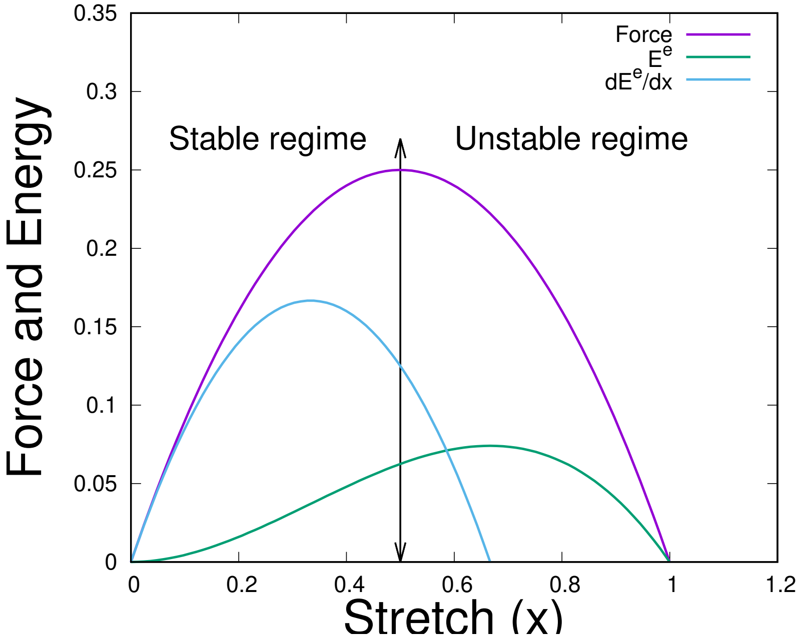

Fig. 10-2.: Force and energy against stretch x for a uniform distribution of the fibre strengths in the bundle, i.e, for $p(x) = 1$.

and

$$E_b(x) = \frac{N\kappa}{2} \int_0^x dy \left[p(y)y^2\right] \tag{10-5}$$

For a uniform distribution within the range $(0,1)$, setting $p(x) = 1$ and $P(x) = x$ in Eqns. (10-4), (10-5), we get $E_e(x) = \frac{N\kappa}{2} x^2(1-x)$ and $E_b(x) = \frac{N\kappa}{6} x^3$. Clearly, breaking energy increases steadily with the stretch but elastic energy reaches a maximum (see Fig.**10-2**).

10.2.3. The warning signal of a catastrophic failure

The elastic energy reaches a maximum values which falls in the unstable region of Fig. **10-2**, after the critical value of the extension. Its knowledge is thus not useful to predict the catastrophic failure point of the system. However, the maximum value x_{max} of dE_e/dx appears before x_c (see Fig. **10-2**). To obtain the relation between x_{max} and x_c we take the derivative of dE_e/dx, with respect x, in which for a uniform distribution, the solution of $d^2E_e(x)/dx^2 = 0$ gives

$$x_{max} = \frac{2}{3} x_c \tag{10-6}$$

The rate of change of the elastic energy thus shows a peak before the failure comes [21].

10.3. Thermodynamics of Stretching processes

The stretching-failure of fibres/materials are seen at a small scale, for example during stretching of molecules in biological objects [22]. Similar stretching-failure phenomena are also observed on a much bigger scale, like in the case of bridges made of long cables [23]. The observation in Ref. [21] that elastic energy variation could be a useful indicator of upcoming stretching-induced failure motivates us to construct a proper thermodynamics framework for such stretching-failure phenomenon. For this purpose, we are going to introduce some new concepts like thermal bath, irreversible energy dissipation, entropy production, etc., and we believe that such a framework will help to explore some new features of stretching-failure behaviour in general. In this Section, we will compute the energy dissipated and the heat released in the stretching process and show that dissipation provides a warning signal of the failure.

10.3.1. Energetics

Due to the load F, the system experiences an external work W which affects the elastic and breaking energies and the entropy S as well. Energy conservation can thus be formulated as

$$W = \Delta E_e + \Delta E_b + T\Delta S. \tag{10-7}$$

where $T\Delta S$ is the heat released Q_r in the process and ΔE_d the energy dissipated, with T the temperature. All the terms in this equations are measured in units of FL_mN. The elastic energy of the fibres as a function of the elongation results from the elastic energy per fibre times the number of unbroken fibres (Eq.10-2):

$$\Delta E_e(x) = \frac{n(x)}{N}\varphi(x) \tag{10-8}$$

where $\varphi(x) = \frac{\kappa}{2}x^2$. The breaking energy results from the elastic energy which transforms into kinetic and surface energy. An infinitesimal change of this energy is related to the infinitesimal change of the damage through $dE_b(x) = \varphi(x)dm(x)$. Therefore, its total change is:

$$\Delta E_b(x) = \int_0^x \varphi(z)\left(\frac{\partial m(z)}{\partial z}\right)dz. \tag{10-9}$$

The work done by the external force is the sum of the work done on each fibre:

$$W(x) = \frac{1}{FN}\sum_{i=1}^{n(x)} w_i(x) \approx \frac{1}{FN}\int_0^n w(x)dn', \tag{10-10}$$

where the work per fibre w is:

$$w_i(x) = -\int_0^x \frac{F}{n(y)}dy. \tag{10-11}$$

Changes in the entropy in the stretching process are expressed as

$$\Delta S = \Delta_r S + \Delta_i S \tag{10-12}$$

where $\Delta_r S$ is the entropy supplied to the system by its surroundings and $\Delta_i S$ the entropy produced in the process. The second law of thermodynamics states that $\Delta_i S \geq 0$, where the zero value holds for reversible stretching (at quasi-equilibrium). The entropy supplied can be positive or negative; the sign depends on the interaction of the system with its surroundings [24]. For a closed system that may exchange heat with the surroundings it is given by the Carnot-Clausius expression

$$\Delta_r S = \frac{Q_r}{T}, \tag{10-13}$$

where Q_r is the reversible or compensated heat, supplied for the surroundings and T the temperature of the environment. The irreversible change of the entropy, or the total entropy produced, at average elongation x is given by

$$\Delta_i S = \int_0^t \frac{n(x)}{N} \sigma dt' \tag{10-14}$$

where σ is the entropy production rate. The Goudy-Stodola theorem relates the total energy dissipated ΔE_d to the entropy produced $\Delta_i S$[25]:

$$\Delta E_d = T \Delta_i S \tag{10-15}$$

At this point, it is important to distinguish between reversible heat Q_r and dissipated energy E_d. The former is the energy in form of heat supplied from or towards the surroundings in order to keep the temperature of the system constant. This quantity can be measured, for instance, by using a calorimeter. The latter is the free energy lost that can be transferred as heat, sound, or light, to mention just a few forms of energy. The energy dissipated is thus not necessarily related to a measurable heat flux or to a measurable temperature change in the neighbourhood of the system. This is the reason why reversible heat is frequently referred on the literature as measurable heat [24].

10.3.2. Mesoscopic non-equilibrium thermodynamics

When the fibres are immersed in a heat bath, their length can fluctuate. The effect of these fluctuations is negligible when the energy of the fibres is much greater than the thermal energy $k_B T$ which is the limit of validity of a purely mechanical treatment. For smaller system energies, the fluctuations become increasingly important. This is the case, for example, in the stretching of DNA [26]. Here, we analyse the dynamics of the elongation fluctuations and compute the entropy production rate and the energy dissipated in the process.

The probability density $\rho(x,t)$ to find a fibre with length x at dimensionless time t fulfils the continuity equation

$$\frac{\partial \rho(x,t)}{\partial t} = -\frac{\partial J(x,t)}{\partial x} \tag{10-16}$$

ensuing from probability conservation. In this equation, J is the probability current which vanishes at the boundaries ($x = 0$ and $x = 1$). The entropy production rate σ of the stretching process follows from mesoscopic non-equilibrium thermodynamics [27]:

$$\sigma(t) = -\frac{1}{T} \int_0^1 J(x,t) \frac{\partial \mu(x,t)}{\partial x} dx \tag{10-17}$$

By coupling linearly the flux J and its conjugated thermodynamic force (chemical potential gradient $\partial\mu/\partial x$), we obtain the dimensionless current

$$J(x,t) = -\rho(x,t)\frac{\partial\mu(x,t)}{\partial x} \tag{10-18}$$

which corresponds to Fick's diffusion law written in dimensionless form where $t = t^{'}D/L_m^2$ is the dimensionless time and D the diffusivity [27]. The chemical potential is related to the free energy of the system through $\mu(x,t) = \left(\frac{\partial G}{\partial n}\right)_{T,P}$ which in turns is given by

$$\Delta G = \Delta H - T\Delta_r S = \int_0^n \int_0^x \frac{1}{n(y)}dydn - n(x)\frac{\varphi(x)}{N} + \frac{k_B T}{FL_m}n(x)\ln\rho(x) \tag{10-19}$$

with H the enthalpy to which the elongation work and the elastic (potential) energy contribute. From now on, we will use the dimensionless force per fibre $f = FL_m/k_B T$. Taking the derivative of the Gibbs free energy with respect to the number of non-broken fibres n and considering Eq.10-2, we obtain the chemical potential

$$\mu(x,t) = \int_0^x \frac{1}{n(y)}dy - \varphi(x) + \frac{1}{f}\ln\rho. \tag{10-20}$$

For large values of f, the entropic contribution is very small. Notice that the signs of the enthalpic terms have been changed because the external work is done in the direction of the movement while the elastic force has the opposed direction.

Substituting Eq.(10-20) in Eq.(10-18) and the resulting flux in Eq.(10-16), we obtain the Fokker-Planck equation describing the evolution of the probability distribution

$$\frac{\partial\rho(x,t)}{\partial t} = \frac{\partial}{\partial x}\left(N\frac{\rho(x,t)}{n(x)} - \rho(x,t)\frac{\partial\varphi(x)}{\partial x} + \frac{1}{f}\frac{\partial\rho(x,t)}{\partial x}\right) \tag{10-21}$$

The average elongation of the fibres corresponds to the first moment of the probability density ρ, solution of this equation:

$$\bar{x}(t) = \int_0^1 x\rho(x,t)dx \tag{10-22}$$

Taking the time derivative of Eq.(10-22) and using the conservation law (Eq.(10-16)), we obtain

$$\dot{\bar{x}}(t) = \int_0^1 J(x,t)dx \tag{10-23}$$

from which we can interpret J as the local stretching velocity.

10.3.3. Small fluctuations regime

When fluctuations are very small, the variance of the probability distribution takes very small values and therefore we could approximate $\rho(x,t)$ by a delta function centred on $\bar{x}$: $\delta(x-\bar{x}(t))$. By combining Eq.(10-

18) and Eq.(10-20) and substituting $\rho(x,t)$ by the delta function, we obtain

$$J(x,t) = \delta(x-\bar{x}(t))\left(\frac{1}{f}+\frac{N}{n(x)}-\kappa x\right) \tag{10-24}$$

where we have used the definition of φ. Integrating now Eq.(10-24) in x, we obtain the stretching velocity

$$\dot{\bar{x}}(t) = \frac{1}{f}+\frac{N}{n(\bar{x})}-\kappa\bar{x} \tag{10-25}$$

where the first term on the right side is the entropic contribution, the second results from the presence of the load and the third is due to the elastic force which opposes to the elongation of the fibres. For very small fluctuations, the entropy production rate Eq.(10-17) is: $\sigma(t) = \dot{\bar{x}}^2$. Using this result into Eq.10-14, and the equality $\dot{\bar{x}} = d\bar{x}/dt$, we obtain the irreversible entropy change

$$\Delta_i S(\bar{x}) = \int_0^{\bar{x}} \frac{n(\bar{x})}{N}\dot{\bar{x}}d\bar{x} \tag{10-26}$$

10.4. Results and Discussion

In this Section, we obtain analytic expressions and numerical results for the dynamics and energetics of the stretching process assuming a uniform distribution of the strength thresholds of the fibres, $P(x) = x$. In order to simplify the notation, from now on x will stand for the average value $\bar{x}$.

10.4.1. Dynamics and energetics for small fluctuations

Dynamics

The average stretching velocity for a uniform distribution is obtained from Eq.(10-25) which is now written as

$$\dot{x}(t) = \frac{1}{f}+\frac{1}{1-x}-\kappa x \tag{10-27}$$

Its derivative with respect to the elongation given by

$$\frac{d\dot{x}(t)}{dx} = \frac{1}{(1-x)^2}-\kappa \tag{10-28}$$

has a minimum around $x = 1-\sqrt{1/\kappa}$, for $\kappa \geq 1$, indicating that for large enough values of κ, the stretching velocity exhibits a non-monotonic behaviour. By integrating Eq.(10-27), we obtain the expression relating t and x:

$$t = -\frac{1}{2\kappa}\ln(1-\kappa x(1-x)) - \frac{1}{\sqrt{(4-\kappa)\kappa}}\left[\tan^{-1}\left(\frac{\sqrt{\kappa}(1-2x)}{\sqrt{4-\kappa}}\right) - \tan^{-1}\left(\frac{\sqrt{\kappa}}{\sqrt{4-\kappa}}\right)\right], \tag{10-29}$$

For $\kappa \geq 4$, this equation diverges or is imaginary which indicates that the process is not possible. From this relation, we can anticipate the asymptotic form of x through the behaviour of the inverse tangent.

Energetics

From the dynamic of the process, we can compute the work, the energies and the heat involved. The work follows from Eq.(10-10) and Eq.(10-11):

$$W = -x(\ln x - 1), \tag{10-30}$$

The breaking energy, computed from Eq.(10-9) is:

$$\Delta E_b = \frac{\kappa}{6} x^3 \tag{10-31}$$

As expected, the breaking energy increases as the elongation increases. From Eq.(10-8), the elastic energy change is:

$$\Delta E_e = \frac{\kappa}{2}(1-x)x^2, \tag{10-32}$$

and its derivative

$$\frac{d\Delta E_e}{dx} = \frac{\kappa}{2} x(2-3x) \tag{10-33}$$

From these expressions, we observe that the maximum of ΔE_e is located at $x = 2/3$ whereas the maximum of $\frac{d\Delta E_e}{dx}$ is found at $x = 1/3$. Through these values, we can analyse the different stages of the process. At $x = 1/3$, the system loses its capacity to store energy and the process enters a metastable regime. At $x = x_c$, the capacity to respond effectively to the action of the external load decreases and the process enters an unstable state. Finally, at $x = 2/3$, the system cannot store more energy in form of elastic energy and falls into an imminent failure regime.

On the other hand, the energy dissipated (Eq.(10-15)) is:

$$\Delta E_d \approx \frac{x}{f}\left(1 - \frac{x}{2}\right) + x - \frac{\kappa}{12}(4-3x)x^3 \tag{10-34}$$

which decreases when κ increases because at a large elastic constant more elastic energy can be stored to be subsequently transformed into kinetic energy after the breaking of the fibres. The first derivative of the energy dissipated, given by:

$$\frac{d\Delta E_d}{dx} \approx \frac{1}{f}(1-x) + 1 - \kappa(1-x)x^2 \tag{10-35}$$

must be positive, according to the second law which imposes that $0 \leq \kappa \leq 13/2$, for $f \gg 1$. Combining this restriction with that inherent to Eq.(10-29), we conclude that the stretching process is feasible for $0 \leq \kappa \leq 4$. Analysing the derivative of the dissipated energy, we find that it has a minimum at $x \approx 2/3$, located close to the maximum of the elastic energy. The dissipated energy may thus give us information about the transition to the imminent failure regime.

Finally, the reversible heat Q_r is obtained by using Eq.(10-7):

$$Q_r = W - \Delta E_d - \Delta E_e - \Delta E_b \tag{10-36}$$

Its derivative with respect to the elongation

$$\frac{dQ_r}{dx} = -\ln x - \frac{1}{f}(1-x) - 1 - \kappa x(1-x)^2. \tag{10-37}$$

shows that the maximum of Q_r depends on κ and is given by:

$$x^* \approx (368 - 54\kappa + 4\kappa^2)/1000 \tag{10-38}$$

From this expression, one can see that for $\kappa \geq 3/4$ the maximum of Q_r lies before the maximum of the derivative of the elastic energy. This result indicates that by measuring the maximum of the reversible heat (the point at which the process becomes exothermic $dQ_r/dx < 0$), we can know beforehand what is the state at which the system reaches the metastable regime. For $0 \leq \kappa \leq 3/4$, the maximum lies in between $x = 1/3$ and $x = 0{,}368$, i.e. in the metastable region.

Another way to find alarming signals is to calculate the intersection point of the curves $d\Delta E_e/dx$ and dQ_r/dx, x^*, which can be obtained from Eq.10-37 and Eq.10-33, for $f \gg 1$:

$$x^* \approx (368 - 118\kappa + 24\kappa^2 - 2\kappa^3)/1000, \tag{10-39}$$

For $1/3 \leq \kappa \leq 4$, this point is located at the metastable regime. Thus, by measuring the heat released and computing the elastic energy, we can estimate the value of elongation just before the system enters the metastable region. Finally, from Eq.(10-28) we see that the minimum of the stretching velocity is located before the maximum of the change of the elastic energy ($x = 1/3$), for $1 \leq \kappa \leq 9/4$ whereas for $9/4 \leq x \leq 4$ it is situated in the metastable regime, before the process reaches the unstable stage.

10.4.2. Fokker-Planck approach

To analyse the dynamic and the energetics of the process in the case in which fluctuations are not necessarily small, we will use the Fokker-Planck equation (Eq.(10-21)) from which we can obtain the average elongation of the fibres and the energy dissipated. We have solved this equation by implementing the finite difference method in the software MATLAB 2017b. The results for ρ, represented in Fig.**10-3**, show a Gaussian-like behaviour. We can observe that as the process progresses the solution displaces to the right. In the inset, we represent the variance for $f \gg 1$, which increases linearly with the elongation of the fibres. The small value of the variance indicates that the assumption of small fluctuations is justified in this case.

By using Eq.(10-22) and Eq.(10-2), we compute the average elongation and the number of non-broken fibres which are represented in Fig.**10-4**. Both quantities exhibit a quasi-linear behaviour and an asymptotic behaviour close to the breaking point. This comes from the fact that by decreasing the number of non-broken fibres, the force exerted per fibre increases thus triggering an accumulative effect, typical of catastrophic events. The inset of the figure shows a non-monotonic behaviour of the damage rate evidencing the competition between the elastic and external forces in the stretching process in which finally the load force per fibre becomes much higher and the rate increases exponentially.

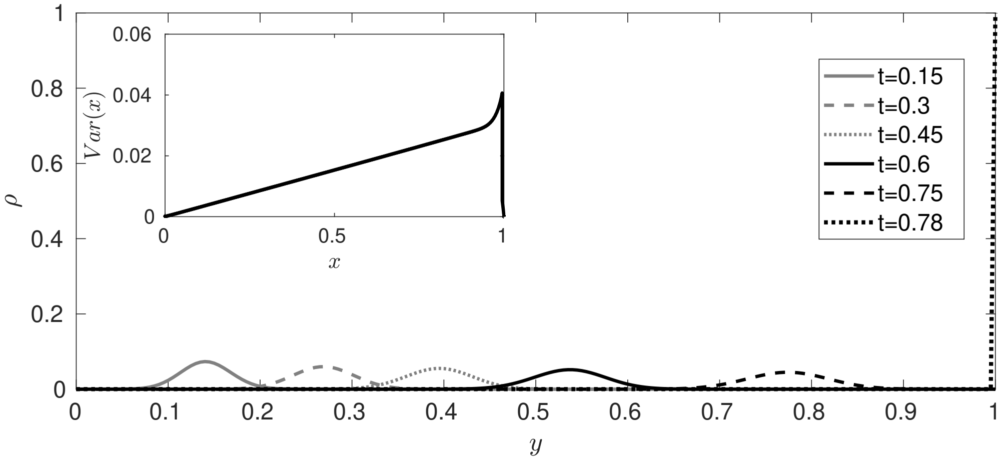

Fig. 10-3.: Probability density as a function of the elongation y at different times, for $\kappa = 2$. Gaussian-like solutions displace to the right because of the action of the external force. The inset shows the variance of the probability distribution as a function of the average elongation of the set of fibres x. The variance increases linearly, then non-linearly and finally it decays to zero.

The stretching velocity $\dot{x}$ follows from the dynamics of x. By taking the derivative of $\dot{x}$ with respect to x, we obtain the change of the stretching velocity as a function of the average elongation. In Fig.**10-5**, we show the behaviour of both quantities for $\kappa = 2$. We observe the existence of a minimum of the stretching velocity around $x = 0{,}29$ which appears before the system reaches the maximum change of the elastic energy (the transition towards the metastable regime).

From the dynamics of the process, we can calculate the energy dissipated by using Eq.(10-17) and Eqs.(10-14)-(10-15). Fig.**10-6** shows the energetics of the process. As predicted from the analytical results, we observe a maximum of the elastic energy and of the reversible heat. Furthermore, the maximum of Q_r is located around $x = 0{,}366$, independently of the values of κ. Additionally, the net reversible heat at the end of the process ($Q_r(x = 1)$) is zero which shows that the stretching process is endothermic at small deformations and exothermic at larger deformations. The irreversible heat released results in measurable changes in the temperature of the environment.

The derivatives of the different energies with respect to x are represented in Fig.**10-7**. Before the imminent failure regime, the behaviour of the temporal derivatives coincides with that of the spatial derivatives due to the fact that in this regime x is linear in time, as follows from Eq.(10-29). The results obtained confirm that the derivative of the elastic energy has a maximum at $x = 1/3$ and its primitive a maximum at $x = 2/3$ while the derivative of the breaking energy always grows. They also confirm that both derivatives take the same value at $x = 1/2$. The derivative of the reversible heat always decreases which indicates that the net flux of reversible heat is much higher at the beginning of the process. The curve of this derivative intersects that of the derivative of the elastic energy around $x = 1/5$, for $\kappa = 2$, while for lower values of κ the intersection point moves to the right, being $\kappa = 1/2$ the highest value of κ at which the crossing takes place before the process reaches the metastable regime.

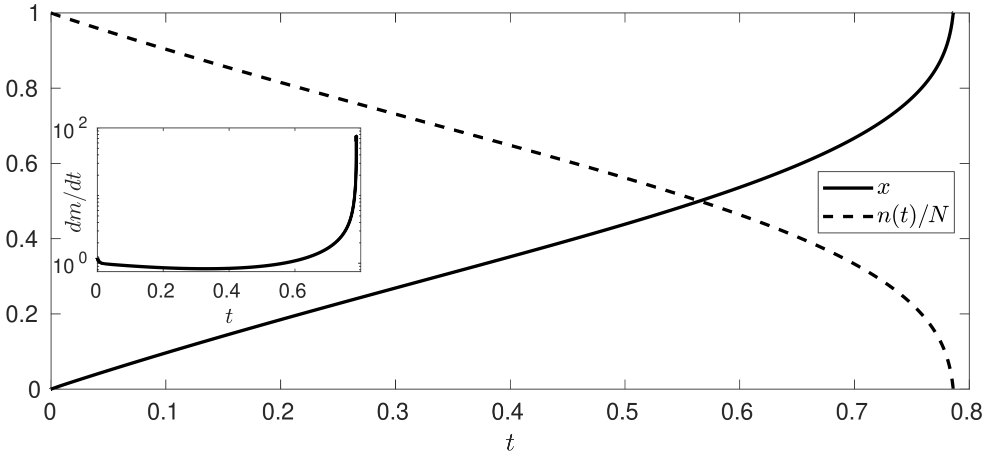

Fig. 10-4.: Average elongation of the set of fibres x (continuous line) and fraction of non-broken fibres n/N (dashed line) as a function of time t, for $\kappa = 2$. The inset represents the rate of damage to the fibre bundle which exhibits a non-monotonic behaviour thus evidencing the competition between elastic and external forces in the stretching process.

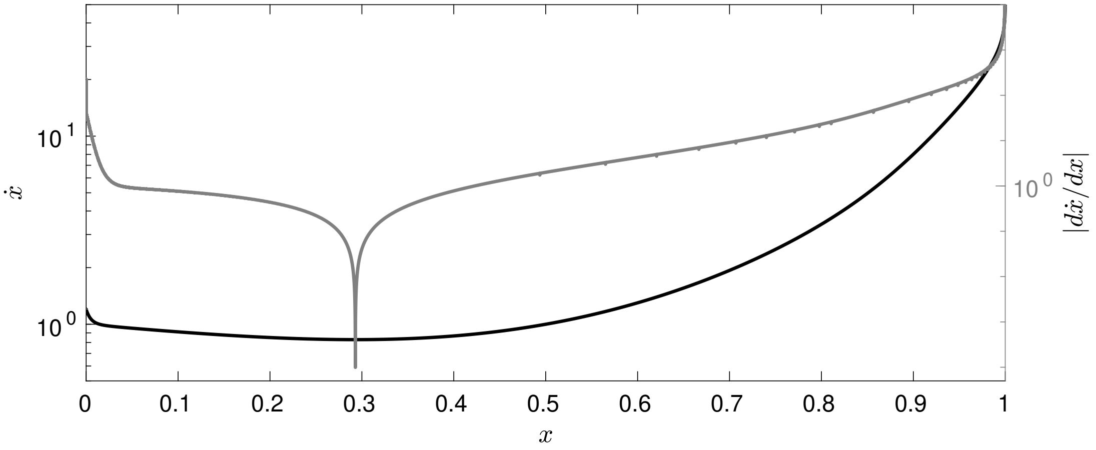

Fig. 10-5.: Stretching velocity $\dot{x}$ (left grid, black continuous line) and absolute value of $d\dot{x}/dx$ (right grid, grey continuous line) as a function of the average elongation x, for $\kappa = 2$ represented in in logarithmic scale.

From Fig.**10-7**, we also confirm the fact that the derivative of the dissipated energy is always positive, in accordance with the second law of thermodynamics. Interestingly, the minimum of this derivative is found around $x = 1/2$ (independently of the value of κ) which the same value at which the derivatives of the elastic and breaking energy coincide.

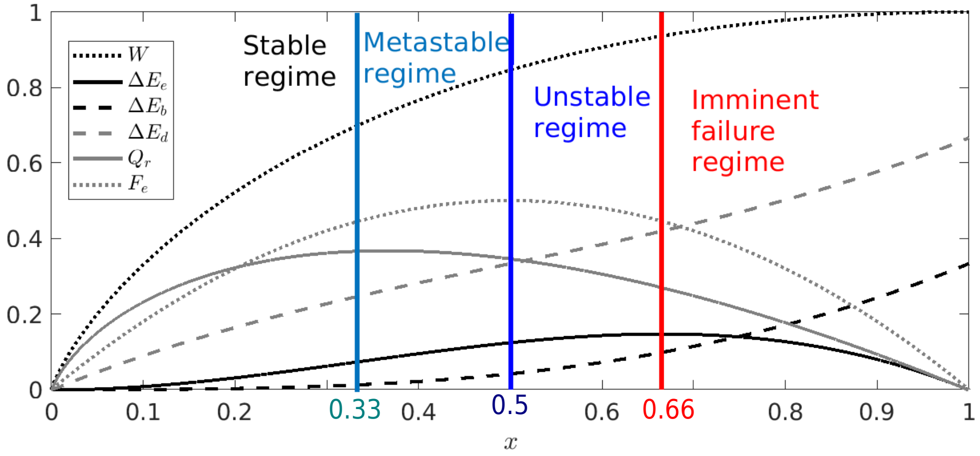

Fig. 10-6.: Energetics as the stretching progress, for $\kappa = 2$. The work done W (dotted black line) is computed from Eq.10-10, the elastic energy ΔE_e (continuous black line) is computed from Eq.10-8, the breaking energy ΔE_b (dashed black line) is computed from Eq.10-9, the dissipated energy ΔE_d (dashed grey line) is computed from Eq.10-14 and Eq.10-17, and the reversible heat Q_r (continuous grey line) is computed from Eq.10-7 and Eq.10-12. Metastable regime threshold (light blue line) is located at $x = 1/3$, unstable regime threshold (blue line) is located at $x = 1/2$ while the imminent failure threshold (red line) is located at $x = 2/3$.

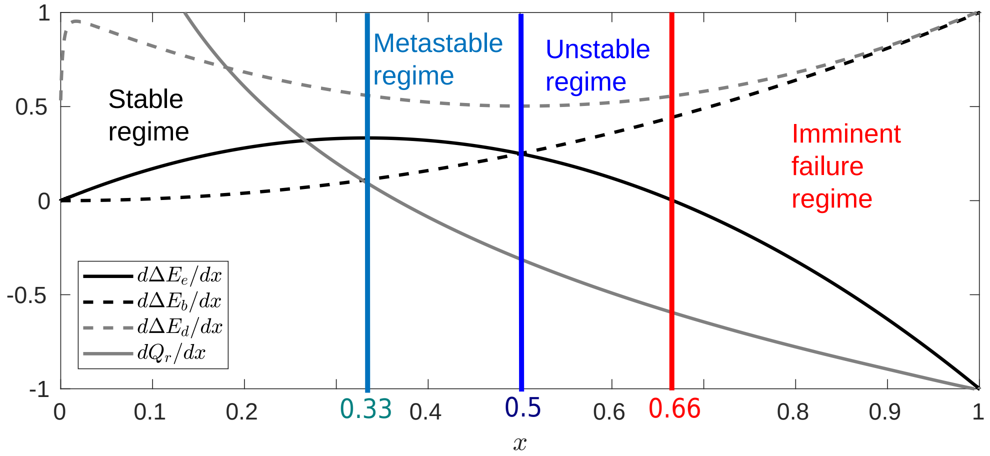

Fig. 10-7.: Derivatives for the energies of the stretching process as a function of the average elongation x, for $\kappa = 2$. $d\Delta E_e/dx$: continuous black line; $d\Delta E_b/dx$: dashed black lines; $d\Delta E_d/dx$: dashed grey line; and dQ_r/dx: continuous grey line. Metastable regime transition: light blue line at $x = 1/3$; unstable regime transition: blue line at $x = 1/2$; and imminent failure regime transition: red line at $x = 2/3$.

10.4.3. Role of the fluctuations in the stretching process

The role that fluctuations play in the process can be estimated by comparing the value of the relevant quantities when we use the small fluctuations approach or when we adopt a Fokker-Planck description for the same value of κ. Fig. **10-8** shows the change of the stretching velocity with position. In particular, for $\kappa = 2$ the location of the minimum of this quantity computed from both approaches is the same, meaning that close to the minimum the system is practically insensitive to the presence of fluctuations. However, for small elongations the velocities are slightly different while at the imminent failure regime they differ considerably due to the presence of fluctuations.

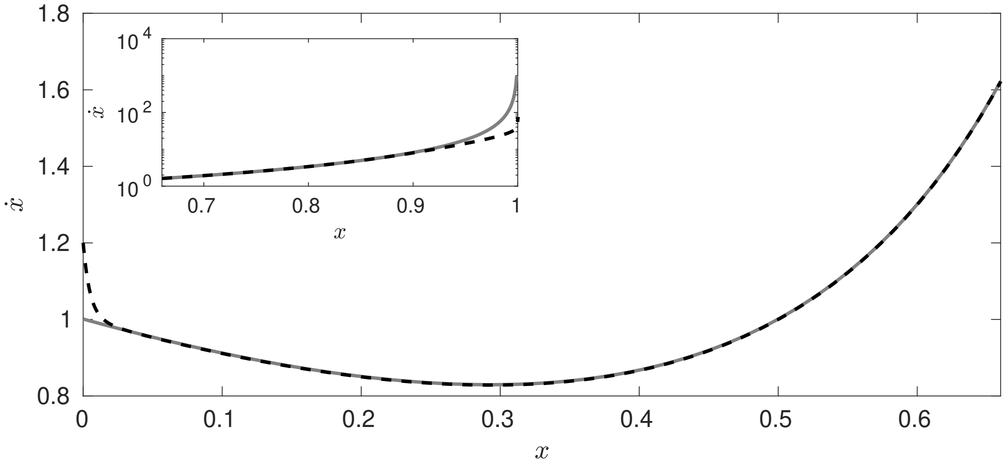

Fig. 10-8.: Results for the stretching velocity $\dot{x}$ as a function of the average elongation x before the imminent failure regime, for $\kappa = 2$. The inset shows $\dot{x}$ in the imminent failure regime. The continuous grey line is obtained by assuming small fluctuations while the dashed black line shows the behaviour of that quantity for larger fluctuations obtained from the numerical solution of the Fokker-Planck equation.

As shown in Fig.**10-9**, energy dissipation and reversible heat are affected by fluctuations at all stages of the process. The dissipated energy is overestimated in the approach of small fluctuations whereas the reversible net heat ($Q_r(x = 1)$) is very sensitive to fluctuations, as concluded from the fact that this quantity is different in both approaches.

Figs.**10-8**-**10-9** show that the small fluctuations approach adequately describes the dynamics but not the energetics. The high accuracy in the dynamics is due to the almost Gaussian nature of the probability with a sufficiently small variance which is represented in Fig.**10-3**. The observed disparity in the reversible heat and energy dissipated lies in the approximation used. Additionally, the small deviation of the stretching velocity are accumulated thus affecting the energy dissipated in the case of small fluctuation. Differences between both approaches become even more patent at smaller values of κ and f when the effect of the fluctuations is less important.

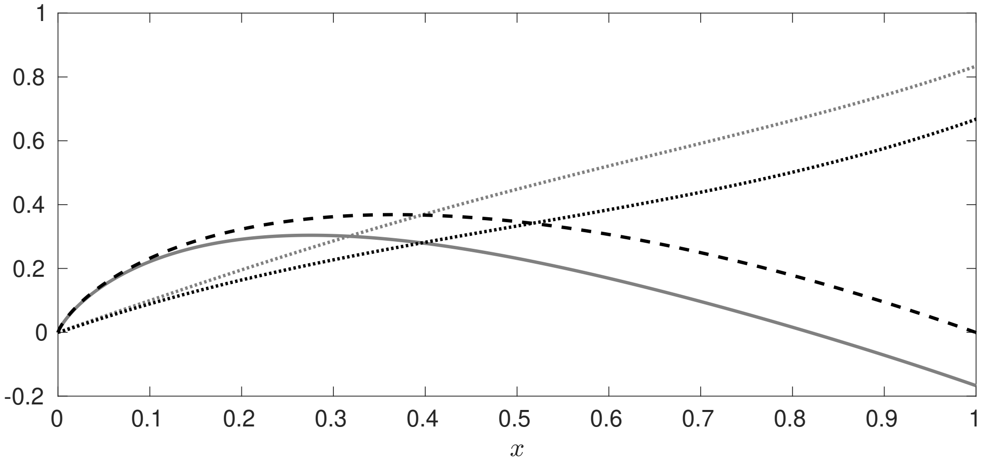

Fig. 10-9.: Dissipated energy and reversible heat as a function of the average elongation x, for $\kappa = 2$. Results for ΔE_d and Q_r obtained when fluctuations are small are represented, respectively, by dotted and continuous grey lines. The same quantities for larger fluctuations, computed from the Fokker-Planck equation, correspond to the dotted and dashed black lines, respectively.

10.5. Conclusions

We have proposed a thermodynamic framework that analyses the role played by dissipation in a fibre stretching process, describes its different stages and obtains new alarming signals before the whole set of fibres break. Our thermodynamic framework has identified relevant regimes (metastable, unstable and imminent-failure) as well as provided new transition indicators in terms of stretching velocity variation and entropy production rate which is an important quantity to measure the energy-efficiency of processes [28]. Specifically, we have shown that the maximum of the reversible heat may emerge before the process enters into the unstable regime. For some values of κ and small fluctuations, this maximum is located in the stable regime. In the same line, we found that the minimum of the entropy production rate is located around the transition to the unstable regime, and that for small fluctuations, this minimum defines the starting of the imminent failure regime for all values of κ. We have also proved that when the heat release flux is equal to the entropy production rate, in this intersection, the system is close to the transition towards the metastable regime. Similarly, we found that the minimum of the stretching velocity is always located in the stable zone but the exact location strongly depends on the value of κ.

Under this approach, a more general analysis of the stretching process as a function of $\kappa = k_e L_m / F$ could be performed to investigate the effect of the relation between force and elastic constant on the dynamics. Additionally, for a small system with a low number of fibres, the approach can be applied to investigate biological stretching-failure processes such as fibre muscle elongations and biochemical stretching as in DNA chains. Finally, as the stretching process releases heat and dissipates energy, we can have considerable temperature changes which can influence the individual failure of elements [29, 30, 31]. Further work is therefore needed on this issue.

Bibliography

[1] A. Arango-Restrepo, J. M. Rubi, and Srutarshi Pradhan. A thermodynamic framework for stretching processes in fiber materials. *Frontiers in Physics*, 9, 2021.

[2] Bikas K Chakrabarti and Lucien-Gilles Benguigui. *Statistical physics of fracture and breakdown in disordered systems*. Number 55. Oxford University Press, 1997.

[3] Hans J Herrmann and Stéphane Roux. *Statistical models for the fracture of disordered media*. Elsevier, 1990.

[4] Soumyajyoti Biswas, Purusattam Ray, and Bikas K Chakrabarti. *Statistical physics of fracture, breakdown, and earthquake: effects of disorder and heterogeneity*. John Wiley & Sons, 2015.

[5] Frederick Thomas Peirce. Tensile tests for cotton yarns:the weakest link theorems on the strength of long and of composite specimens. *J. Textile Inst*, 17:T355–368, 1926.

[6] Srutarshi Pradhan, Alex Hansen, and Bikas K. Chakrabarti. Failure processes in elastic fiber bundles. *Rev. Mod. Phys.*, 82:499–555, Mar 2010.

[7] Alex Hansen, Per Christian Hemmer, and Srutarshi Pradhan. *The fiber bundle model: modeling failure in materials*. John Wiley & Sons, 2015.

[8] Srutarshi Pradhan and Bikas K. Chakrabarti. Precursors of catastrophe in the bak-tang-wiesenfeld, manna, and random-fiber-bundle models of failure. *Phys. Rev. E*, 65:016113, Dec 2001.

[9] Per C. Hemmer and Alex Hansen. The Distribution of Simultaneous Fiber Failures in Fiber Bundles. *Journal of Applied Mechanics*, 59(4):909–914, 12 1992.

[10] Srutarshi Pradhan, Alex Hansen, and Per C. Hemmer. Crossover behavior in burst avalanches: Signature of imminent failure. *Phys. Rev. Lett.*, 95:125501, Sep 2005.

[11] Srutarshi Pradhan and Per C. Hemmer. Relaxation dynamics in strained fiber bundles. *Phys. Rev. E*, 75:056112, May 2007.

[12] Ingrid Reiweger, JÃ¼rg Schweizer, JÃ¼rg Dual, and Hans JÃ¼rgen Herrmann. Modelling snow failure with a fibre bundle model. *Journal of Glaciology*, 55(194):997â€“1002, 2009.

[13] D. Cohen, P. Lehmann, and D. Or. Fiber bundle model for multiscale modeling of hydromechanical triggering of shallow landslides. *Water Resources Research*, 45(10), 2009.

[14] Natasha Pollen and Andrew Simon. Estimating the mechanical effects of riparian vegetation on stream bank stability using a fiber bundle model. *Water Resources Research*, 41(7), 2005.

[15] Nicola M. Pugno, Federico Bosia, and Tamer Abdalrahman. Hierarchical fiber bundle model to investigate the complex architectures of biological materials. *Phys. Rev. E*, 85:011903, Jan 2012.

[16] Didier Sornette. Mean-field solution of a block-spring model of earthquakes. *Journal de Physique I*, 2(11):2089–2096, 1992.

[17] Henry Ellis Daniels and Harold Jeffreys. The statistical theory of the strength of bundles of threads. i. *Proceedings of the Royal Society of London. Series A. Mathematical and Physical Sciences*, 183(995):405–435, 1945.

[18] D Sornette. Elasticity and failure of a set of elements loaded in parallel. *Journal of Physics A: Mathematical and General*, 22(6):L243–L250, mar 1989.

[19] D.Gary Harlow and S.Leigh Phoenix. Approximations for the strength distribution and size effect in an idealized lattice model of material breakdown. *Journal of the Mechanics and Physics of Solids*, 39(2):173 – 200, 1991.

[20] Raul Cruz Hidalgo, Yamir Moreno, Ferenc Kun, and Hans J. Herrmann. Fracture model with variable range of interaction. *Phys. Rev. E*, 65:046148, Apr 2002.

[21] Srutarshi Pradhan, Jonas T. Kjellstadli, and Alex Hansen. Variation of elastic energy shows reliable signal of upcoming catastrophic failure. *Frontiers in Physics*, 7:106, 2019.

[22] Eivind Bering, Signe Kjelstrup, Dick Bedeaux, J. Miguel Rubi, and Astrid S. de Wijn. Entropy production beyond the thermodynamic limit from single-molecule stretching simulations. *The Journal of Physical Chemistry B*, 124(40):8909–8917, 2020.

[23] Dongsheng Li, Jinping Ou, Chengming Lan, and Hui Li. Monitoring and failure analysis of corroded bridge cables under fatigue loading using acoustic emission sensors. *Sensors*, 12(4):3901–3915, 2012.

[24] Sybren Ruurds De Groot and Peter Mazur. *Non-equilibrium thermodynamics*. Dover Publications Inc., 1985.

[25] Adrian Bejan, George Tsatsaronis, and Michael Moran. *Thermal Design and Optimization*. John Wiley and Sons, New York, 1996.

[26] J. M. Rubi, D. Bedeaux, and S. Kjelstrup. Thermodynamics for single-molecule stretching experiments. *The Journal of Physical Chemistry B*, 110(25):12733–12737, 2006. PMID: 16800609.

[27] D Reguera, JM Rubi, and JMG Vilar. The mesoscopic dynamics of thermodynamic systems. *J. Phys. Chem. B*, 109(46):21502–21515, 2005.

[28] Signe Kjelstrup, Dick Bedeaux, Eivind Johannessen, and Joachim Gross. *Non-Equilibrium Thermodynamics for Engineers*. WORLD SCIENTIFIC, 2nd edition, 2017.

[29] Stéphane Roux. Thermally activated breakdown in the fiber-bundle model. *Phys. Rev. E*, 62:6164–6169, Nov 2000.

[30] Srutarshi Pradhan and Bikas K. Chakrabarti. Failure due to fatigue in fiber bundles and solids. *Phys. Rev. E*, 67:046124, Apr 2003.

[31] Srutarshi Pradhan, Anjan Kumar Chandra, and Bikas K. Chakrabarti. Noise-induced rupture process: Phase boundary and scaling of waiting time distribution. *Phys. Rev. E*, 88:012123, Jul 2013.

11. Enzymatic evolution driven by entropy production

An enzyme is a complex self-organised structure that has been evolving to specialise and increase its efficiency. The questions we ask are: thermodynamic or kinetic efficiency? are there limits in the kinetic and thermodynamic efficiency?.

We show that the structural evolution of enzymes is largely influenced by the entropy produced in the enzymatic process. We have computed this quantity for the case in which the process has unstable and metastable intermediate states. By assuming that the kinetics takes place along a potential barrier, we have found that the behaviour of the total entropy produced is a non-monotonic function of the intermediate state energy. By diminishing the number of metastable intermediate states, the total entropy produced decreases and consequently the enzyme kinetics and the thermodynamic efficiency are enhanced. Minimising locally the total entropy produced for an enzymatic process with metastable intermediate states, the kinetics and the thermodynamic efficiency are raised. In contrast, in the absence of metastable intermediate states, a maximum of the entropy produced results in an improvement of the kinetic performance although the thermodynamic efficiency diminishes. Our results show that the enzymatic evolution proceeds not only to enhance the kinetics but also to optimise the total entropy produced.

11.1. Introduction: Kinetics and thermodynamics of enzymatic processes

Enzymes are the devices responsible for all the energy conversions in the cell. They are very elaborately adapted for this function and as catalysts they have the capacity to accelerate the rate of biochemical reactions [1]. It has been shown that enzyme performance depends on their structure, reactivity, catalytic efficiency and activation energy. However the thermodynamic efficiency of the enzyme activity is related to the kinetic performance is currently an open problem.

The description of enzymatic mechanisms demands the use of a very intricate standard free-energy landscape containing multiple minima and transition states [2]. However, there is experimental evidence [3] showing that enzymatic processes take place along just one path (see Fig.**11-1**). For instance, processes mediated by adenylate kinase (AdK) arise along only one possible path having multiple intermediate conformations that may facilitate a rapid transition [4]. It has been argued that relatively small free-energy differences between conformations could improve the fine control of transitions by environmental perturbations and signaling [5]. Additionally, a recent study of the enzyme mechanisms has shown that on average each reaction undergoes 4.3 steps and involves 2.7 intermediates [6].

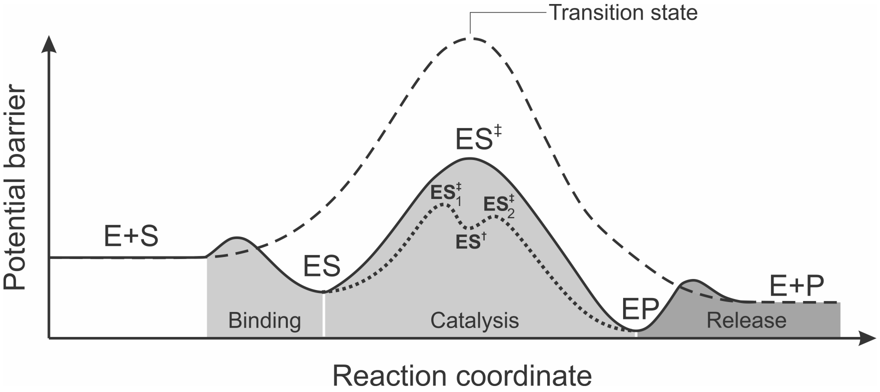

Fig. 11-1.: Potential barrier for a general enzymatic process: Free energy landscape for a complete enzymatic process; substrate binding $E+S \rightleftharpoons ES$, catalysis $ES \rightleftharpoons EP$, product release $EP \rightleftharpoons E+P$. Dashed line corresponds to a non-enzymatic process $S \rightleftharpoons P$. The catalysis takes place in the catalytic step in which we can find the transition states. The intermediate states that can be unstable ($ES^{\ddagger}$,$ES_1^{\ddagger}$ and $ES_2^{\ddagger}$) or metastable ($ES^{\dagger}$).

The catalytic nature of the enzyme has been related to an electrostatic stabilization of the transition state during the enzymatic process, as shown in the catalysis zone in Fig.**11-1**. This electrostatic effect can be seen as a combination of the reduction in both the energy of the transition state and in the reorganization energy [7]. The active sites are pre-organized in a geometry which minimizes conformational reorganization and maintains an optimal stabilization for the transition state in each step during catalysis [8, 9]. For instance, theoretical results for serine esterases show that these perform multiple steps minimizing the conformational rearrangements to avoid energetic conflicts following a ”minimally frustrated”path or a minimum energy path.[10, 7].

How proteins and enzymes evolve remains as an open question [11]. Average enzymes exhibit moderate catalytic efficiencies [12] because maximal rates may not evolve in cases that can be associated with weaker selection pressures [13]. Also, it seems likely that the catalytic efficiency of some enzymes toward their natural substrates could be increased in many cases by natural or laboratory evolution [12]. Evolutionary pressures play a key role in shaping enzyme parameters (related to potential barrier); that is, maximal rates have not evolved in cases where a particular enzymatic rate is not expected to be under stringent selection [12]. Initially, it is proposed that enzymes have evolved firstly to optimize the speed of the actual breaking-bonding chemical processes, optimizing the potential barrier for the diffusion through transition states to finally tune the rates [7, 14]. However, evolutionary pressures have their limits and cannot enhance the kinetics of an enzyme at its optimum or ad infinitum [12].

Enzyme evolution seems to be globally driven by physiological conditions to improve reaction rates by means of changes in the structure to stabilize the transition states thus decreasing activation energies and modifying the number of metastable intermediates. However, most of the enzymes are far from optimal kinetic conditions not only due to evolutionary aspects and physical-chemical constraints because of thermodynamic restrictions. There is no clear evidence of the fact that improving reaction rates leads to an improvement of thermodynamic efficiency of catalytic processes. As far as we know, enzymes must be stable in order to conserve their structure and locally unstable in order to function. Therefore, there is a debate about which trajectory an enzyme should take to evolve structurally and why these trajectories are taken. In that sense, thermodynamically, the evolution of the enzyme could be conditioned to decrease or increase the entropy produced in the catalytic step of the process.

Our purpose in this chapter is to analyze the transition between enzyme-subtract and enzyme-product states (the catalytic step of the enzymatic process of Fig.**11-1**). As the enzyme activity takes place at the mesoscopic level [15], the enzymatic processes is modeled by a diffusion through a potential barrier whose intermediate states are parametrized by means of a reaction coordinate, in which the shape of the potential barrier is related to the structural changes of the enzyme [16]. Therefore, we use the Mesoscopic Non-Equilibrium Thermodynamics (MNET) [17, 8] formalism to quantify the entropy produced in the transit/diffusion through the potential barrier and thus obtain the reaction rates defined in the space of the reaction coordinate[17]. By modelling the potential barrier with and without local minima, we compute the entropy production. Here, we present how the enzyme evolution could be directed towards an optimization of the total entropy produced as a function of the activation energy restricted to the relaxation time.

11.2. Methods

MNET provides a general framework for the study of small-scale far from equilibrium systems which unify thermodynamic and kinetics aspects [17, 8, 18]. Activated processes such as chemical reactions, adsorption [19], electro-chemistry [20], unzipping RNA [21], active transport [15] and biochemical cycles [22] that take place in physico-chemical and biological systems, can be viewed as processes that proceed along an internal coordinate that parameterizes the different molecular configurations. Considering that the catalytic efficiency of enzymes depends on their structures [23], we will adopt a molecular perspective to analyze the process through the MNET formalism. Moreover, we will consider that the rearrangement of the enzyme active site in a process determines the activation energy and the reaction rate [24].

11.2.1. Conservation equation and entropy production

In the process, an enzyme-substrate complex transforms into an enzyme-product complex in a homogeneous close system under isothermal conditions. The transformation takes place along the reaction coordinate γ defined from 0 to 1. The evolution of the probability density to find the complex in the state γ at time t is governed by the continuity equation:

$$\frac{\partial p(\gamma,t;E_a)}{\partial t} = -\frac{\partial}{\partial \gamma} J(\gamma,t;E_a) \tag{11-1}$$

Here, J is the current along the reaction coordinate and E_a the activation energy. Assuming local equilibrium along the γ-coordinate, we use the Gibbs relation and the continuity equation (Eq.(11-1)) to obtain the entropy production of the enzymatic process at the mesoscale [17]:

$$\sigma(\gamma,t;E_a) = -\frac{1}{T} J(\gamma,t;E_a) \frac{\partial \mu(\gamma,t;E_a)}{\partial \gamma}, \tag{11-2}$$

where μ the chemical potential. From the entropy production (Eq.(11-2)), we can write the linear law for the current, given by

$$J(\gamma,t;E_a) = -\frac{L(\gamma,t)}{T}\frac{\partial \mu(\gamma,t;E_a)}{\partial \gamma}, \tag{11-3}$$

whith L an Onsager coefficient which is in general a function of the state of the enzyme and the time. Using the fact that the Onsager coefficient is in very good approximation proportional to $p(\gamma,t;E_a)$, we introduce the constant diffusion coefficient $\mathscr{D}$ through the expression:

$$L(\gamma,t;E_a) = \frac{\mathscr{D}}{k_B}p(\gamma,t;E_a). \tag{11-4}$$

The chemical potential along the γ-coordinate is given by

$$\mu(\gamma,t;E_a) = k_B T \ln p(\gamma,t;E_a) + \phi(\gamma;E_a) \tag{11-5}$$

where ϕ is the potential barrier of enthalpic nature through which the diffusion process takes place along the γ-coordinate. This barrier is a function of the activation energy and is intimately related to the enzyme structure. By inserting the expression of the current (Eq.(11-3)) into the continuity equation (Eq.(11-1)), we obtain the Fokker-Plank type kinetic equation:

$$\frac{\partial p(\gamma,t;E_a)}{\partial t} = \mathscr{D}\left[\frac{\partial^2 p(\gamma,t;E_a)}{\partial \gamma^2} + \frac{1}{k_B T}\frac{\partial}{\partial \gamma}\left(p(\gamma,t;E_a)\frac{\partial \phi(\gamma;E_a)}{\partial \gamma}\right)\right] \tag{11-6}$$

By solving this equation, we can compute the entropy production rate and from this, the total entropy produced in the process

$$\Delta S_P(E_a) = \int_0^{t_R}\int_0^1 \sigma(\gamma,t;E_a)d\gamma dt \tag{11-7}$$

where t_R is the relaxation time of the process. To study the thermodynamic efficiency, in the following sections we will analyze the lost work defined as $W_L = T\Delta S_P(E_a)$.

The diffusivity through the potential barrier $\mathscr{D}$ is the only kinetic parameter of the model. This parameter depends neither on the activation energy nor on the shape of the potential barrier and it will be used to construct a dimensionless time: $\tau = t\mathscr{D}$. As we will show in the results section, for the fastest processes (with activation energy $\propto 1k_BT$) the dimensionless time is around 1. Considering the time reported in [25], the diffusivity could take a reference value of $10^{14}s^{-1}$.

11.2.2. Modeling potential barriers

Enzymes can be modified artificially by changing the potential barrier landscape of the enzymatic process. For instance, although triose phosphate isomerase is considered an advanced and perfect enzyme, its structure was modified by changing the activation energy of the enzymatic process thus altering the reaction rate. These modifications of the energy landscape having an impact on the kinetics of the process could be the next step in the kinetic evolution of the enzyme[26]. In this section, we present particular forms of the energetic barriers and in the results section we analyze the lost work as a function of the parameters shaping the barrier. In Appendix A canbe found more details about the proposal of the barriers and how to define them.

Two particular forms of the barriers are shown in Fig. **11-2**(a) and their modifications are depicted in Fig.**11-2**(b)-(d). Barriers with an unstable intermediate are shown in Fig.**11-2**(b) for different activation energies. Barriers with a metastable intermediate are shown in Figs **11-2**(c)-(d) for different intermediate energies and transition-state energies. These barriers will be used in our numerical calculations to study enzymatic reactions taking place in a closed system. Notice that in Figs. **11-2**(c)-(d) the difference between the maxima ($\Delta E_a = E_{ES_1^\dagger} - E_{ES_2^\dagger}$) which is related to the activation energy is fixed. The proposed potential barriers are bistable and tristable functions modelled by polynomials. They must fulfill some thermodynamics conditions. For instance, at $\gamma = 0$ and $\gamma = 1$ the values of the potential coincide with the standard chemical potential of the *ES* and *EP* states. Moreover, barriers representing a process with only unstable states there is only one maximum corresponding to the transition state. For those with a metastable intermediate state there are two maxima and one minimum representing the transition state and the metastable state. Finally, the macroscopic equilibrium relations must be fulfilled.

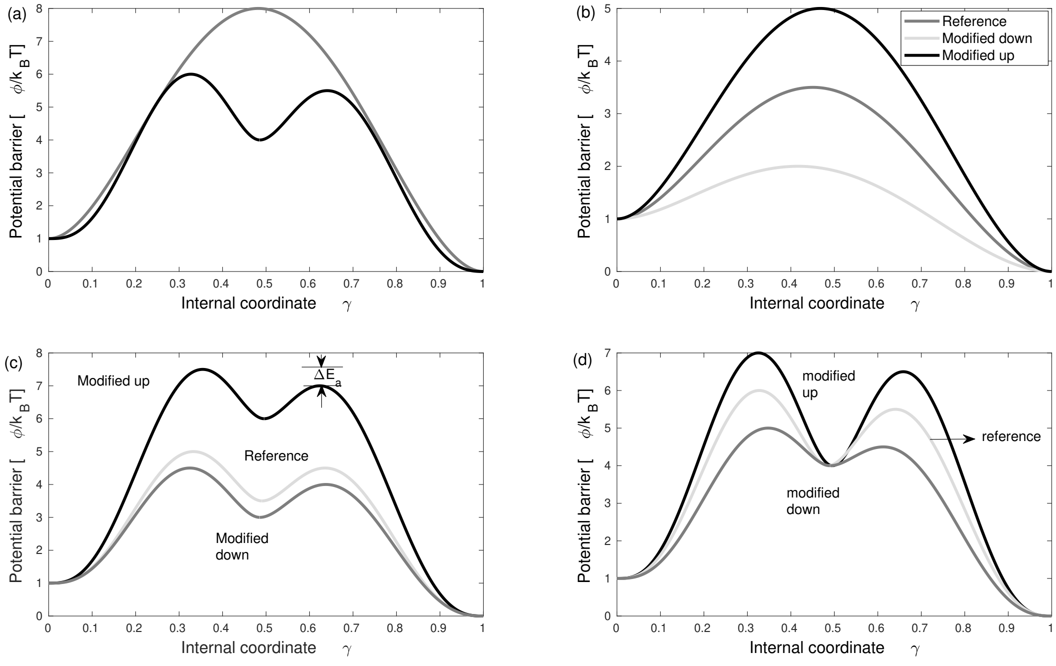

Fig. 11-2.: Potential barrier $\phi(\gamma)$ as a function of the reaction coordinate γ for metastable and unstable intermediates. Potential barrier for: (a) an unstable intermediate state (gray line) and a metastable intermediate state (black line) in an enzymatic process ES $\rightleftharpoons$ EP.(b) an enzymatic process with unstable intermediate state for three activation energies due to modifications or mutations. (c) a metastable intermediate state for three intermediate energies due to modifications or mutations, for ΔE_a fixed.(d) a metastable intermediate state for fixed intermediate energy but different activation energies due to modifications or mutations, for ΔE_a fixed.

Enzymes might mutate to enhance their functions. We have recognized two kind of barriers in which enzymatic processes takes place. The way potential barriers are modified, shown in Fig. **11-2**, may mimic the enzyme mutation process. Fig.**11-3** exemplifies a scenario where the enzyme through mutations could change the energy of the intermediate states in the catalytic process. The proposed mutation factor ζ depends on the activation energy and on the changes of the potential barrier with the energy of the intermediate states. An energy landscape (in terms of the barriers) as a function of the mutation factor (characterizing possible mutation paths) and the reaction coordinate is given by,

$$\phi(\gamma,\zeta) = \begin{cases} \phi_1(\gamma) & \text{in} \quad \text{Fig.}\mathbf{11\text{-}2}\text{(b)} \quad \text{if} \quad 0 \geq \zeta < 0{,}35 \\ \phi_2(\gamma) & \text{in} \quad \text{Fig.}\mathbf{11\text{-}2}\text{(c)} \quad \text{if} \quad 0{,}35 \geq \zeta < 0{,}6 \\ \phi_3(\gamma) & \text{in} \quad \text{Fig.}\mathbf{11\text{-}2}\text{(d)} \quad \text{if} \quad 0{,}6 \geq \zeta \leq 1, \end{cases} \tag{11-8}$$

The mutation factor helps us exemplify a hypothetical landscape of barriers in an enzymatic process. Notice that there are more possible ways to change the energy of the intermediate and transition states and therefore the shape of the potential barrier. Nevertheless, here we illustrate some representative cases as a first approximation.

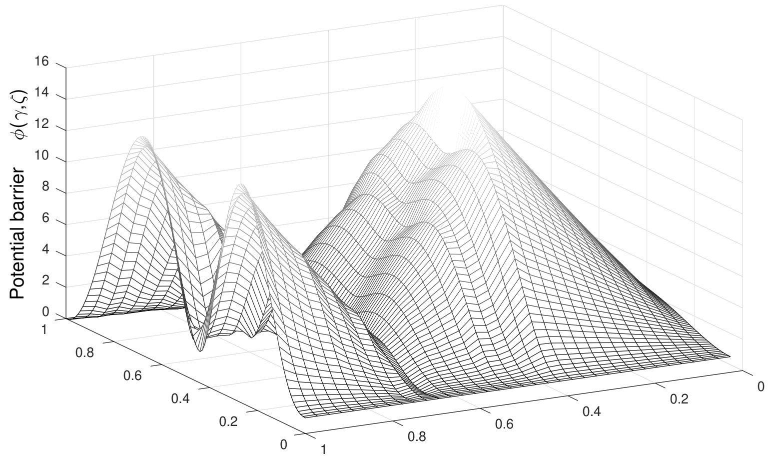

Fig. 11-3.: Potential barrier $\phi(\gamma)$ as a function of the reaction coordinate γ and of the mutation factor ζ. Sketch of a generic potential barrier representing different possible energetic configurations of the enzymes related to their structural configuration and parametrized by ζ.

Why nature uses mutations to increase or decrease the energy of intermediate states (or the activation energies) is as of yet unanswered. We hypothesize that not only kinetics but also energetic issues are involved in enzymatic mutations. Under this perspective, the lost work related to the more energetic states in an enzymatic process (transition states), is key to understanding how evolution could enhance enzyme kinetics.

11.3. Results and Discussion

The entropy production rate calculated by using the potential barrier shown by the gray line in Fig. **11-2**(a) is plotted as a function of dimensionless time in Fig. **11-4**. The curves correspond to different values of the activation energy. The relaxation times t_{Ri} are indicated by arrows, and are proportional to the activation potential energy ($\phi^* - \phi(0)/k_B T$). A decrease of the activation potential energy, however, leads to an increase of the enzymatic reaction rates and to an increment of the initial entropy production. In this sense, an eventual kinetic principle that predicts infinite rates will also predict an infinite entropy production, which seems to be meaningless. Since the dynamics of the enzyme can be characterized by the entropy generation and the relaxation time, the total entropy produced is in general a non-trivial function of the activation energy and can give us information about which are the most efficient configurations of the enzyme.

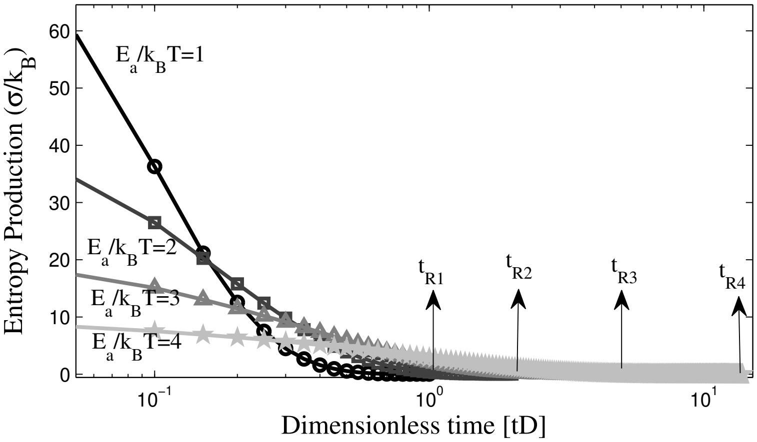

Fig. 11-4.: Entropy production $\sigma(E_a)$ as a function of the dimensionless time ($t\mathscr{D}$) for different activation energies, for processes with unstable intermediates. The dimensionless time axis is presented in logarithmic scale.

Integrating the entropy production over γ and over time for the cases shown in Fig. **11-4**, we find that lost work always decreases for increments of the activation potential energy and of the relaxation time of the process (Fig. **11-5**, black dashed line). One could then infer that for a given process a maximization of the lost work (or a minimization of the thermodynamic efficiency) results in an enhancement of the kinetics and a minimization of the relaxation time. This case will be considered as the reference scenario. Nevertheless, a more complex behavior of enzymatic processes with metastable intermediate states can be found in two ways.

First, by changing the shape of the potential barrier, as shown in Fig. **11-2**(c), and by computing the lost work for different values of the activation potential energy of the metastable state (ES), in which ΔE_a is fixed, we obtained the lost work shown by the gray dashed line in Fig. **11-5**. Lost work exhibits a local minimum (in this case around $5k_BT$) and when it approaches this value, it starts to decrease until it converges with the value found in the reference scenario (a process with only unstable intermediates). This could be plausible because for high intermediate energy, the condition to overcome the barrier is similar to that of

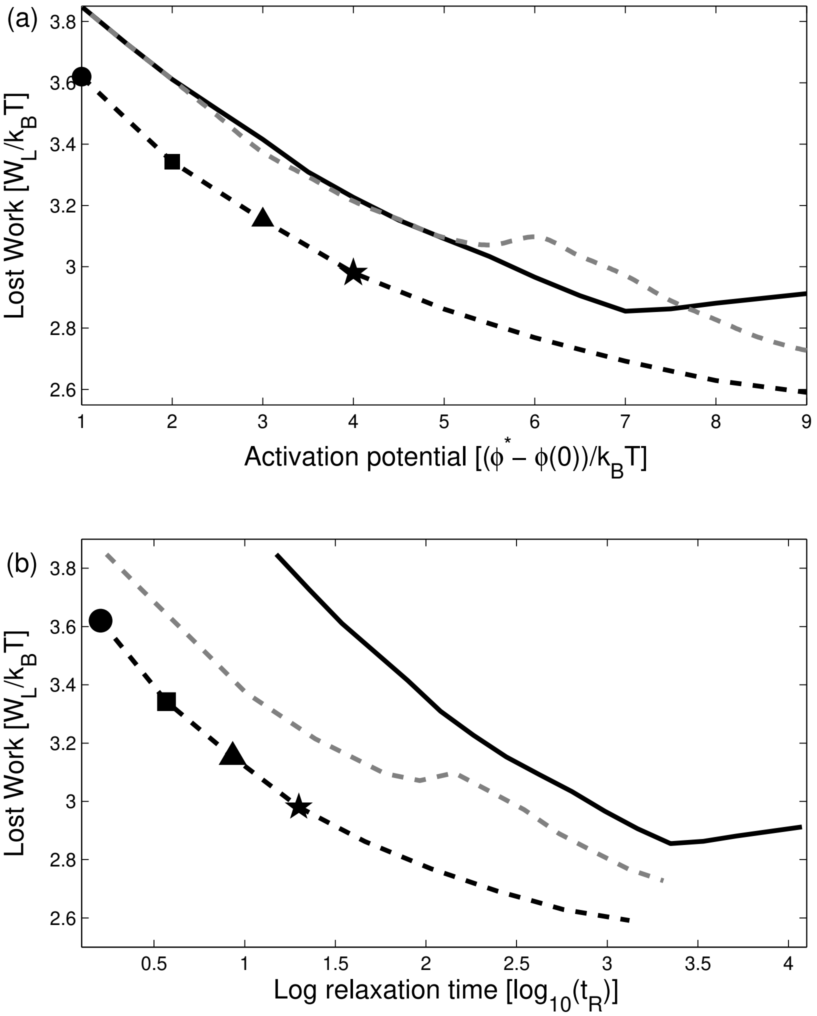

Fig. 11-5.: (a) Lost work as a function of the activation potential energy for enzymatic process. (b) Lost work as a function of the relaxation time of the process. Integration over time for each data ($E_a/k_BT = 1;2;3;4$) shown in Fig.**11-4** gives us lost work as a function of the activation energy (or relaxation time) for a process only with unstable intermediate states (black dashed line), as shown in Fig.**11-2**(b). Lost work for a process with metastable intermediates states: intermediate state energy is fixed (black continuous line) forming a deep well in the potential barrier for ΔE_a fixed, as shown in Fig.**11-2**(d); intermediate state energy increases proportional to the first activation energy (gray dashed line), for ΔE_a fixed, as shown in Fig.**11-2**(c).

the case shown in Fig.**11-2**(b) for high intermediate energies. Moreover, the relaxation times are similar to those of the reference scenario because the energies of transition states and the metastable intermediate are alike. Therefore, the process cannot be divided into two subprocesses, as in the case shown in Fig. **11-2**(d), giving rise to a slowing down of the kinetics.

In a second way, by changing the shape of the potential barrier, as shown in Fig. **11-2**(d) for different energy values of the transition states ($ES_1^\ddagger$ and $ES_2^\ddagger$), we obtained the lost work shown by the black continuous line in Fig. **11-5**. In Fig. **11-5**(a), there is a local minimum (in this case around $7k_BT$) and from this value the lost work increases. Notice that for higher values of the activation potential, the height of the two peaks (transition states energies) and the depth of the well in the potential barrier increases. In this case, the probability density around the metastable state at the beginning of the process is low and consequently goes up considerably, increasing the rate of jumps over the second wall of the potential barrier. This increases the relaxation time and gives rise to the appearance of two stages in the enzymatic process, contrary to what happens at low values of the transition states as shown in Fig. **11-2**(c). Therefore, depending on the value of the activation potential, we can observe one-stage or two-stages processes. The minimum observed in Fig. **11-5** reveals the presence of a transition between both types of processes.

From Fig.**11-5** we conclude that in the most efficient processes taking place in a system with a metastable intermediate state, the energy is similar to that of the transition states to avoid deep wells in the potential barrier. One can thus expect that if the enzymatic process involves a metastable intermediate state (as in Fig. **11-2**(c)(d)), the enzyme could evolve towards structures such that the intermediate state involved have an energy similar to that of the transition states in order to decrease the presence of subprocesses that may impair the thermodynamic and kinetic efficiencies.

Additionally from Fig.**11-5** we conclude that a given process with metastable intermediate does not necessarily maximize the lost work to enhance the kinetics. It is found that in the surrounding of the local minimum, kinetics and energetics of the process could be simultaneously improved. Therefore, by decreasing lost work we obtain an enhancement of the kinetics. One can thus expect that if the enzymatic process involves a metastable intermediate, the enzyme could evolve towards a structural configuration such that the process has an activation potential energy that ensures a local minimum in lost work.

Notice that the lost work for an enzymatic process with a metastable intermediate (Fig. **11-2**(c)-(d)) is larger than for a process with unstable intermediates (Fig. **11-2**(b)). This is because of the presence of two (or more) sub-processes involved to overcome the potential barrier. Therefore, an additional scenario could exist in which the enzyme may evolve towards a more efficient structural configuration. Thus enzymes catalyzing processes with metastable intermediates could increase the energy of these intermediates and shift the potential barrier to the ones shown in Fig. **11-2**(b), thereby avoiding sub-processes. In this scenario, once the enzymatic processes avoids the metastable intermediate state, the enzyme may evolve towards a configuration in which the activation energy decreases in order to maximize the lost work, as indicated in Fig. **11-5**.

11.4. Conclusions

In this chapter, we have shown how enzyme evolution is conditioned to an optimization of the total entropy produced as a function of the activation energy. We have found that the shape of the potential barrier determines the thermodynamic efficiency of the activated processes because lost work depends on the nature of the intermediate state.

An increase of the reaction rate and of the thermodynamic efficiency can be induced by decreasing the number of intermediates states or by decreasing the energetic difference between intermediate and transition states. This conclusion is in accordance with the observation that some enzymes minimized the number and height of the peaks of the energetic barriers between consecutive conformations [10]. Moreover, our conclusion is in accordance with a minimum energetic path concept (”minimally frustrated”path)[7].

In the framework of the transition state theory, the efficiency of an enzyme has been related to the number of conformational changes that it must undergo to return to its original state. From this perspective, if the energy related to the conformation changes is minimized, higher reaction rates could be obtained [27]. In the context of the present work, however, if the energy related to conformational changes is minimized, lost work is minimized as well since it entails a decrease of the energetic barriers, thus avoiding metastable intermediates. Therefore, the energy related to conformational changes is not minimized to improve the kinetics (as claimed in the literature [27]) but rather to optimize the thermodynamic performance of enzymatic process.

Our results support the idea that enzymatic process have on average 2.7 intermediates per reaction [6] and not just one or even no intermediate at all. This is because the structural configuration of the enzyme is determined by a local minimum in lost work of the enzymatic process as a function of the activation potential energy. In this scenario, an enhancement of the kinetics around the minimum leads to a decrease of the lost work and consequently to an improvement of the thermodynamic efficiency, thus favoring the enzyme’s structural stability and the catalytic activity.

The fact that central metabolism enzymes are more efficient than secondary metabolism enzymes could be explained from a thermodynamic point of view. This is because the evolutionary pressures [12, 28] may be related to a high probability of modifications in the enzyme structure which could changes the activation energies. This forces these enzymes to evolve either towards a local minimum of lost work thus enhancing their kinetic and thermodynamic efficiency, or towards a maximum of lost work to improve only their kinetics.

The model presented here might be used to analyze the effect of temperature and pH (considered as the mutation factors) over kinetics through the modification of the shape of the potential barrier upon variations of those quantities.

Bibliography

[1] Trevor Palmer and Philip L Bonner. *Enzymes: biochemistry, biotechnology, clinical chemistry*. Elsevier, 2007.

[2] Stephen J Benkovic, Gordon G Hammes, and Sharon Hammes-schiffer. Free-Energy Landscape of Enzyme Catalysis. *Biochemistry*, 47:3317–3321, 2008.

[3] Liskin Swint-kruse and Harvey F Fisher. Enzymatic reaction sequences as coupled multiple traces on a multidimensional landscape. *Trends Biochem. Sci.*, 33(3):104–112, 2008.

[4] Dechang Li, Ming S Liu, and Baohua Ji. Mapping the dynamics landscape of conformational transitions in enzyme: the adenylate kinase case. *Biophysical journal*, 109(3):647–660, 2015.

[5] Davit A Potoyan, Pavel I Zhuravlev, and Garegin A Papoian. Computing free energy of a large-scale allosteric transition in adenylate kinase using all atom explicit solvent simulations. *J. Phys. Chem. B*, 116(5):1709–1715, 2012.

[6] Gemma L Holliday, Daniel E Almonacid, John BO Mitchell, and Janet M Thornton. The chemistry of protein catalysis. *J. Mol. Biol.*, 372(5):1261–1277, 2007.

[7] A.J.T. Smith, R. Muller, M. D. Toscano, P Kast, H W Hellinga, D Hilvert, and K N Houk. Structural Reorganization and Preorganization in Enzyme Active Sites: Comparisons of Experimental and Theoretically Ideal Active Site Geometries in the Multistep Serine Esterase Reaction Cycle. *J. Am. Chem. Soc.*, 130(10):15361–15373, 2008.

[8] Jordi Villà and Arieh Warshel. Energetics and dynamics of enzymatic reactions. *J. Phys. Chem. B*, 105(33):7887–7907, 2001.

[9] Suwipa Saen-Oon, Sara Quaytman-Machleder, Vern L Schramm, and Steven D Schwartz. Atomic detail of chemical transformation at the transition state of an enzymatic reaction. *PNAS*, 105(43):16543–16548, 2008.

[10] David D Boehr, Dan McElheny, H Jane Dyson, and Peter E Wright. The dynamic energy landscape of dihydrofolate reductase catalysis. *science*, 313(5793):1638–1642, 2006.

[11] Amir Aharoni, Leonid Gaidukov, Olga Khersonsky, Stephen McQ Gould, Cintia Roodveldt, and Dan S Tawfik. The 'evolvability' of promiscuous protein functions. *Nat. Genet.*, 37(1):73–76, 2004.

[12] Arren Bar-even, Elad Noor, Yonatan Savir, Wolfram Liebermeister, Dan Davidi, Dan S Tawfik, Ron Milo, Dan S Taw, and Ron Milo. The Moderately Efficient Enzyme : Evolutionary and Physicochemical. *Biochemistry*, 50:4402–4410, 2011.

[13] G. G. B. Tcherkez, G. D. Farquhar, and T. J. Andrews. Despite slow catalysis and confused substrate specificity, all ribulose bisphosphate carboxylases may be nearly perfectly optimized. *PNAS*, 103(19):7246–7251, 2006.

[14] Monika Fuxreiter and Arieh Warshel. Origin of the catalytic power of acetylcholinesterase: Computer simulation studies. *J. Am. Chem. Soc.*, 120(1):183–194, 1998.

[15] Signe Kjelstrup, J Miguel Rubi, and Dick Bedeaux. Energy dissipation in slipping biological pumps. *PCCP*, 7(23):4009–18, 2005.

[16] Moisés Santillán. Dynamic Stability and Thermodynamic Characterization in an Enzymatic Reaction at the Single Molecule Level. *Physica A*, 390(21-22):4038–4044, 2011.

[17] D Reguera, JM Rubi, and JMG Vilar. The mesoscopic dynamics of thermodynamic systems. *J. Phys. Chem. B*, 109(46):21502–21515, 2005.

[18] J Miguel Rubi. Mesoscopic thermodynamics for the dynamics of small-scale systems. *Entropy*, 17(10):7201–7212, 2015.

[19] I Pagonabarraga and JM Rubi. Derivation of the langmuir adsorption equation from non-equilibrium thermodynamics. *Physica A*, 188(4):553–567, 1992.

[20] JM Rubi and Signe Kjelstrup. Mesoscopic nonequilibrium thermodynamics gives the same thermodynamic basis to butler- volmer and nernst equations. *J. Phys. Chem. B*, 107(48):13471–13477, 2003.

[21] JM Rubi, D Bedeaux, and S Kjelstrup. Unifying thermodynamic and kinetic descriptions of single-molecule processes: Rna unfolding under tension. *J. Phys. Chem. B*, 111(32):9598–9602, 2007.

[22] Anders Lervik, Dick Bedeaux, and Signe Kjelstrup. Kinetic and mesoscopic non-equilibrium description of the ca2+ pump: a comparison. *Eur. Biophys. J.*, 41(5):437–448, 2012.

[23] Richard Wolfenden. Transition State Analog Inhibitors and Enzyme Catalysis. *Annu.Rev.Biophys.Bioeng.*, 5:271–306, 1976.

[24] a Kohen and J P Klinman. Enzyme catalysis: Beyond classical paradigms. *Acc. Chem. Res*, 31(7):397–404, 1998.

[25] Steven D Schwartz and Vern L Schramm. Enzymatic transition states and dynamic motion in barrier crossing. *Nat. Chem. Biol.*, 5(8):551–558, 2009.

[26] Jeremy R Knowles and W John Albery. Perfection in enzyme catalysis: the energetics of triosephosphate isomerase. *Acc. Chem. Res.*, 10(4):105–111, 1977.

[27] Sandeep Kumar Pfizer, Chung Jung, and Tsai Leidos. Transition-state Ensemble in Enzyme Catalysis : Possibility , Reality , or Necessity ? *J.theor.Biol*, (2013):383–397, 2000.

[28] Alan Fersht. *Structure and mechanism in protein science: a guide to enzyme catalysis and protein folding*. Macmillan, 1999.

12. Role of interfacial entropy in the particle-size dependence of thermophoretic mobility

Surfactants are organised in different ways on the surface of particles and droplets, affecting thermodynamic state variables as well as transport properties. In this chapter, we analyse how the organisation and distribution of surfactant molecules affect the response of a droplet under an external force (temperature gradient).

We show that changes in the surface tension of a particle due to the presence of non-ionic surfactants and impurities, which alter the interfacial entropy, have an impact on the value of the thermophoretic mobility. We have found the existence of different behaviors of this quantity in terms of particle size which can be summarized through a power law. For particles which are small enough, the thermophoretic mobility is a constant whereas for larger particles it is linear in the particle radius. These results show the important role of the interfacial entropic effects on the behavior of the thermophoretic mobility.

This chapter was published in *the Physical Review Letters*, **125**, 045901, (2020). Ref.[1]

12.1. Introduction: Thermophoresis

Particles movement induced by temperature gradients [2] known as the Soret effect has been the subject of many experimental and theoretical studies in recent years [3, 4, 5, 6] due to its importance in areas as diverse as soft condensed matter, biophysics, microgravity and nanoscience. Thermophoresis may for example be used for the control of colloids and macromolecules[7] and to implement effective particle separation methods [8] and focusing techniques [9]. Studies on thermophoresis have also shown their importance in the deposition of micro- and nano-particles [10] in laminar [11] and turbulent [12] pipe flows, removing and collecting aerosol particles [13] and in biotechnological applications [14, 15].

Crucial to the study of the motion of the particles is the knowledge of the thermophoretic mobility $\mathscr{D}_T$, the proportionality factor between the thermophoretic velocity $\vec{v}_T$ and the temperature gradient ∇T: $\vec{v}_T = -\mathscr{D}_T \nabla T$, and whether it depends on the particle size or not. There is no general consensus on this question [16]. Experiments performed with polystyrene solid particles of sizes between $40nm$ and $2\mu m$ in Tris buffer solution, show a linear dependence of the thermophoretic mobility on the particle radius a [17] whereas others made with n-alkane liquid particles in water/surfactant ranging from 5 to $16nm$ support the fact that the mobility does not depend on the particle radius [18, 19]. An experiment carried out with latex particles in a solution containing tetrabutylammonium perchlorate with particle radius ranging from 100 to $400nm$ [20], supported by simulation results of rigid particles with radius in the interval 36 to $154nm$ [21] shows a decreasing behavior of the thermophoretic mobility as a function of the particle radius. These different behaviors of $\mathscr{D}_T$ may be due to the fact that more than just a single driving force determines the thermophoretic force in experimental systems, each with a different size dependence. The thermophoretic force may result from the temperature response of the core-material of the particles relative to that of the solvent, the possible presence of electrical double layers and from the distribution of surfactant and fluid molecules at the interface which affects the interfacial entropy. To analyze the origin and the role of the interfacial entropic effects in thermophoresis is the main objective of this Letter.

The thermophoretic velocity can be obtained from hydrodynamics by computing the force exerted by the solvent on a particle moving with a given velocity in the presence of a temperature gradient. [22, 23, 24, 25]. The force contains a thermophoretic contribution proportional to the temperature gradient [26]. A general expression valid when the particle is a drop, a bubble or a solid particle with a monolayer of adsorbed solvent [27, 28, 29] (see Appendix C) was given in [24]: $\vec{F} = -\mu^{-1}\vec{u} + \mathscr{D}_T \mu^{-1} \nabla T$ where μ is the mobility. Under the hydrodynamic approach, $\mathscr{D}_T$ is proportional to the derivative of the surface tension with respect to the temperature $\gamma_T \equiv d\gamma/dT$ and to the particle radius (a) and is a function of the viscosities and thermal conductivities of the inner and outer fluids.

In our analysis, we show how the distribution of the non-ionic solvent and surfactant molecules adsorbed at the interface may depend on the size of the particle. Since this distribution affects the interfacial entropy, it may bring about a dependence of the surface tension and consequently of the γ_T factor on particle size. We thus find that for sufficiently large particles, the ratio between the numbers of fluid and surfactant molecules on the particle surface does not depend on the radius (a). Therefore, γ_T does not depend on a and so the thermophoretic mobility is a linear function of a. On the contrary, for small particles that ratio may depend on the radius of the particle due to entropic effects which lead to a different behaviour of γ_T as a function of a.

12.2. Surface tension derivative

To show how the distribution of fluid and surfactant molecules at the interface affects the thermophoretic velocity, we will consider the stationary movement of a drop immersed in a fluid subjected to a temperature gradient. Both the fluid inside the drop and the surrounding fluid are assumed to be multicomponent, incompressible and Newtonian. Quantities inside and outside the drop and at the interface will be denoted by the sub-indexes i, o and s, respectively.

To compute γ_T, we use the Gibbs-Duhem relations for the inner (i) and outer (o) fluids and the interface (s) to obtain:

$$-Ad\gamma = S^{(s)}dT + N_1^{(s)}d\mu_1^{(s)} + N_2^{(s)}d\mu_2^{(s)} \tag{12-1}$$

$$-V^{(\beta)}dp^{(\beta)} = S^{(\beta)}dT + N_1^{(\beta)}d\mu_1^{(\beta)} + N_2^{(\beta)}d\mu_2^{(\beta)} \tag{12-2}$$

The fluids in each subsystem have two components indicated by sub-indexes 1 and 2. In Eq.(12-2), $\beta = i, o$. Moreover, A is the surface area of the particle, N the number of molecules, μ the chemical potential, V the volume and S the entropy.

We consider equipotential systems for which $d\mu_1^{(\beta)} = -d\mu_2^{(\beta)}$ and rewrite the number of molecules of the j-component as $N_j^{(\beta)} = N^{(\beta)}x_j^{(\beta)}$, with $x_j^{(\beta)}$ the molar fraction in the sub-system β. Moreover, we assume that the radius of the particle is constant and use $d(p^{(i)} - p^{(o)}) = 2d(\gamma/a)$ obtained from the Young-Laplace equation for a constant particle radius. These assumptions together with equilibrium conditions ($d\mu_j^{(i)} = d\mu_j^{(s)} = d\mu_j^{(o)}$), leads to

$$\gamma_T = -\rho_a \frac{\left[s^{(s)} - \delta x^{(s)}\left(\frac{\Delta(\rho s)}{\Delta(\delta(\rho x))}\right)\right]}{1 + \frac{2}{a}\frac{\delta x^{(s)}}{\Delta(\delta(\rho x))}\rho_a} \tag{12-3}$$

Here $\rho_a \equiv N/A$ is the interfacial density, $s^{(s)}$ the interfacial entropy per mol, $\delta y^{(\beta)} \equiv y_1^{(\beta)} - y_2^{(\beta)}$ in which y could be a thermodynamic variable (x,s,ρ among others), $\Delta(\rho s) \equiv (\rho s)_i - (\rho s)_o$, with ρ the molar density, and $\Delta(\delta\rho x) \equiv (\delta(\rho x))_i - (\delta(\rho x))_o$. Defining $s^* \equiv s^{(s)} - \delta x^{(s)}\left(\frac{\Delta(\rho s)}{\Delta(\delta(\rho x))}\right)$ as the surface entropy considering the difference in the changes of the chemical potential of the components with temperature and introducing a Tolman-like length [30] $\delta = \frac{\delta x^{(s)}}{\Delta(\delta(\rho x))}\rho_a$, we obtain

$$\gamma_T = -\rho_a \frac{s^*}{\left(1 + \frac{2\delta}{a}\right)} \tag{12-4}$$

From this expression, we conclude that when the size and number of surfactant molecules increases, the number of configurations available for the molecules of the fluid decreases and therefore the interfacial entropy decreases and so does γ_T. For a one-component system ($x^\beta = 1$) forming two phases (bubble in liquid/drop in vapor), for which $\delta x^{(s)} = 1$ and $\Delta(\delta(\rho x)) = \rho^i - \rho^o$, i.e, $\delta = \rho_a/(\rho^i - \rho^o)$, the length δ converges to the Tolman's length [30].

The analysis of how surface tension depends on the radius of the particle was performed in [30] for only one component by assuming that ρ_a and the temperature are constant. In general, however, we could expect a non-uniform distribution of the solvent molecules with the particle size in the interfacial region, mainly in small enough droplets. We can thus express the interface density as

$$\rho_a = \rho_a^{(\infty)}\Omega(a) \tag{12-5}$$

where $\rho_a^{(\infty)} \equiv N^{(\infty)}/A$ is the surface density at a sufficiently large particle radius and $\Omega(a)$ is a function accounting for finite-size effects in the surface density that we have to determine.

Considering an ideal interface for which $s^* = s_1^* x_1^{(s)} + s_2^* x_2^{(s)}$ and large enough particles, we then obtain

$$\gamma_T^{\infty} = -s^*\rho_a^{(\infty)} = x_1^{(s)}\gamma_{T,1}^{(\infty)} + x_2^{(s)}\gamma_{T,2}^{(\infty)} \tag{12-6}$$

in which $\gamma_{T,1}^{(\infty)}$ and $\gamma_{T,2}^{(\infty)}$ are usually reported in the literature for pure liquids and large systems [31]. Finally, the general expression for γ_T in an ideal system in which the size of the particle does not change with the temperature, is given by:

$$\gamma_T = \Omega(a)\frac{\gamma_T^{(\infty)}}{\left(1+2\frac{\delta}{a}\right)} \tag{12-7}$$

When this expression is integrated in temperature, one obtains a generalization of Tolman's formula for the surface tension valid for multicomponent systems and by taking finite-size effects into account [30].

For a non-ideal interface, the surface tension derivative with respect to the temperature for large systems is in this case given by

$$\hat{\gamma}_T^{(\infty)} = \gamma_T^{(\infty)} + f(x_j^{(s)}, T) \tag{12-8}$$

where the term f is a non-ideal surface entropy that may in general depend on the interfacial molar fractions and temperature. It considers the changes in the surface entropy caused by surfactants or impurities adsorbed on the interface.

For a non-constant particle radius and by performing an analogous procedure to the one above, we can then arrive at general expression for γ_T in which is non-ideal interactions are also considered:

$$\gamma_T = \frac{\Omega(a)}{\left(1+2\frac{\delta}{a}\right)}\left(\hat{\gamma}_T^{(\infty)} + \frac{2\delta}{3a}\gamma k_v\right) \tag{12-9}$$

where $k_v = \frac{1}{v_o}\frac{dv_o}{dT}$ is the thermal compressibility coefficient.

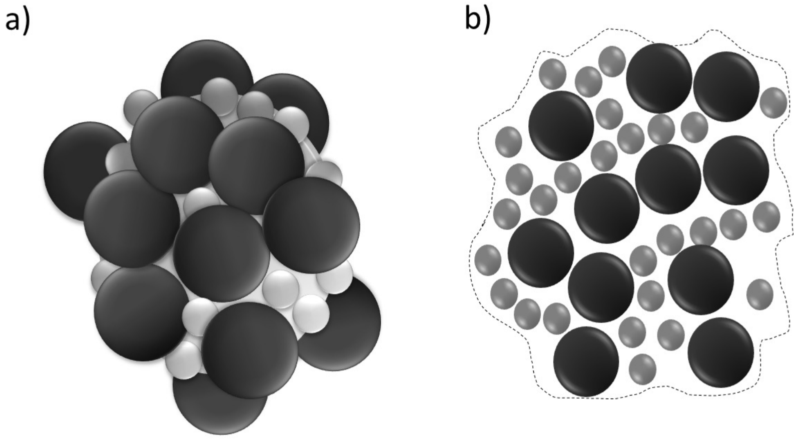

Fig. 12-1.: (a) Fluid (gray) and surfactant (black) molecule distribution in the interface of a spherical particle of radius a. (b) Distribution of fluid and surfactant molecules in a spot of the interface.

12.3. The role of the interfacial distribution

To compute $\Omega(a)$, we first find the number N of fluid molecules at the interface whose available space is affected by the presence of impurities and surfactants (see Fig. **12-1**). The area of the particle surface occupied by the N fluid molecules is $N\pi r_0^2/\phi$, where r_0 is the radius of a molecule and ϕ the packing factor of the interface. Values of ϕ fall in the interval $0{,}34 \leq \phi \leq 0{,}5$ [32]. For a liquid interface like ours, we chose the lowest value, $\phi \approx 0{,}34$. Analogously, the surface area occupied by the surfactant molecules is $N^{'}\pi r_s^2/\phi$ where $N^{'}$ is their number and r_s their radius. The surface area covered by both fluid and surfactant molecules is then $M = (\pi/\phi)Nr_0^2(1+(r_s/r_0)^2N^{'}/N)$, where the ratio between surfactant and fluid molecules depends on the surface molar fraction of surfactant in the interface ($x_3^{(s)}$), $N^{'}/N = x_3^{(s)}/(1-x_3^{(s)})$.

To obtain the number of solvent molecules on the surface, we use the constraint $M < 4\pi a^2$ in the previous expression of the area covered by fluid and surfactant molecules M. The value of N is then given by the floor function

$$N = \left\lfloor \frac{(4\phi)(a/r_0)^2}{(1+g(a))} \right\rfloor \tag{12-10}$$

where the quantity $g(a) \equiv (r_s/r_0)^2N^{'}/N$ compares the areas of the particle surface covered by fluid molecules and surfactant.

In Fig.**12-2**(a), we plot the total number of molecules on the interface ($N_t \equiv N+N^{'}$) for the cases $N^{'}/N$ constant and $N^{'}/N$ linear in a. Both behaviors lead to a constant $\mathscr{D}_T$ and to a $\mathscr{D}_T$ linear in a. Curves intersect at a value of the particle radius a_0, below which the total number of particles is higher for the case $N^{'}/N \sim a$ than when $N^{'}/N \sim$ const. Contrarily, above a_0 only the opposite is true. Fig. **12-2**(b) shows that the area not covered by particles ψ is larger in the first case at values of the radius $a < 13nm$. A linear dependence of $N^{'}/N$ on a and equivalently a linear dependence of $g(a)$ on a is thus entropically more favorable for $a \leq a_0$ where a_0 is a threshold radius at which the ratio between the number of molecules of surfactant and the fluid

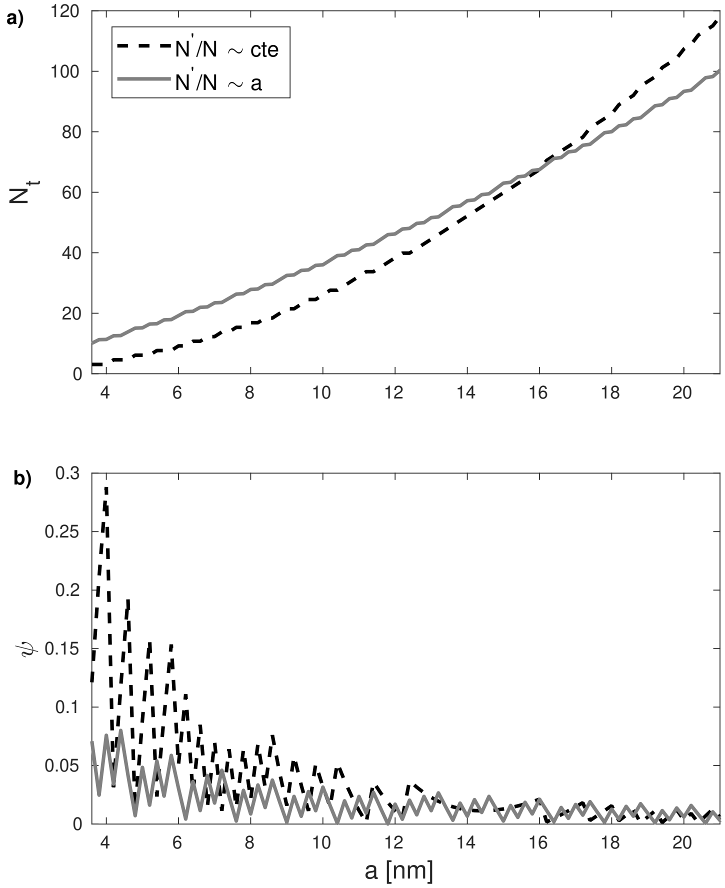

Fig. 12-2.: (a) Total number of molecules on the surface $N_t = N + N^{'}$ for different particle radii $a[nm]$. (b) fraction of the particle-free area $\psi \equiv 1 - M/4\pi a^2$. The black dashed line corresponds to a constant value of $N^{'}/N$ and the gray continuous line to a linear dependence of $N^{'}/N$ on the particle radii a. Both behaviors lead to a constant $\mathscr{D}_T$ and to a $\mathscr{D}_T$ linear in a.

in the interface becomes constant. Notice that the factor $g(a)$ can be expressed as

$$g(a) = g(a_0)\left[\Theta(a - a_0) + (a/a_0)\Theta(a_0 - a)\right] \tag{12-11}$$

where

$$g(a_0) = \left(\frac{r_s}{r_0}\right)^2 \left(\frac{N'}{N}\right)_{(a_0)} \tag{12-12}$$

For a monolayer composed by only fluid molecules, the number of molecules on the interface is approximately $N^{(\infty)} = \pi\phi(a/r_0)^2$. Therefore, by considering Eq.(12-5), for which $\Omega(a) = N/N^{(\infty)}$ and using Eq.(12-10), the finite-size effects in the surface density can thus be evaluated through the relation

$$\Omega(a) = \frac{1}{\pi\phi(a/r_0)^2}\left\lfloor \frac{4\phi(a/r_0)^2}{1 + g(a)} \right\rfloor \tag{12-13}$$

Using the representation of the floor function in Fourier series [33], we approximate the surface density as $\Omega(a) \approx 4/\pi(1+g(a)) - 1/N_\infty + \sum_k sin(8N^{(\infty)}/1+g(a))/\pi k N^{(\infty)}$. For $N^{(\infty)} \gg 1$, we can approximate $\Omega \approx 4/\pi(1+g(a))$. This behaviour explicitly shows how the presence of surfactant molecules on the surface mediated by steric and excluded volume effects affects the distribution of fluid molecules and thus the surface tension.

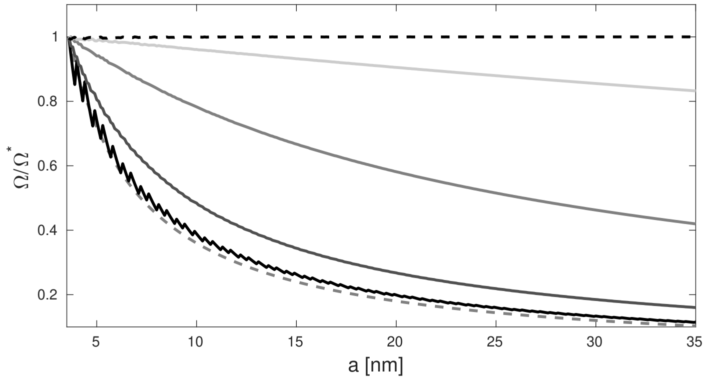

Fig. 12-3.: Function Ω/Ω^* versus particle radius a where Ω^* denotes the maximum value of Ω. Continuous black, dark gray, gray and light gray lines correspond to $r_s/r_0 = 12, 6, 3, 1{,}5$ respectively, whereas the dashed black line is the result for $x_3^{(s)} = 0$. As a reference, The dashed gray line decreasing as $1/a$ serves as a reference.

In Fig.**12-3**, we show the behavior of $\Omega(a)$ for a monolayer interface with $r_0 = 0{,}32nm$ and threshold radii $a_0 = 32nm$ for different values of the ratio r_s/r_0. To illustrate the behavior of this function, we use the approximation $x_3^{(s)} \approx \Phi(r_s/r_0)$ where Φ is the volume fraction of the surfactant in the solution, with $\Phi \approx 0{,}029$ [19]. From the figure, we observe the power law behaviour $\Omega \sim 1/a^\alpha$ with $0 < \alpha < 1$. In particular, $\Omega \sim 1/a$ for $r_s/r_0 = 12$ and the curve exhibits sharp behavior due to the discrete nature of N inherent to the floor function of Eq.(12-10). By decreasing r_s/r_0, Ω tends to a constant.

12.4. Study case

To further verify the validity of our model, we will consider the case of a non-electrolytic system of n-alkane-water with a non-ionic surfactant studied in [34, 19] and compare the results of our model with the experimental data [19]. We will assume that the molecular radius, surfactant fraction and behavior with the temperature is the same for each n-alkane [19]. Moreover, based on the experimental result that the thermophoretic mobility is proportional to the temperature [35, 36], we will assume that the function f accounting for the non-ideal behavior of the interface is linear in the temperature. In order to consider the surface entropy change by adsorption of surfactant molecules, f must also be proportional to the surface area covered by the surfactant, $g(a)$. To account for changes in the direction of the thermophoretic velocity reported in [19] at a certain transition temperature T_t, we write $f(T) = k_f g(a)(T - T_t)$ where k_f is a fitting parameter.

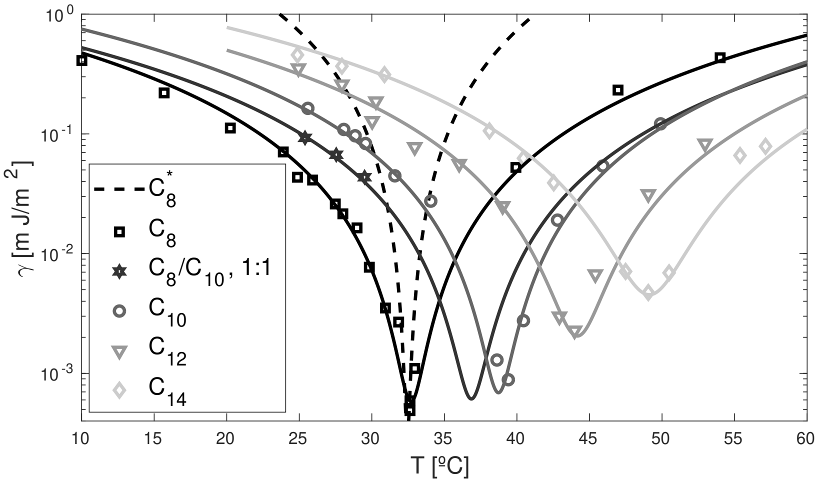

Fig. 12-4.: Surface tension versus temperature for different hydrocarbons (n-octane C_8, equi-molar mixture of n-octane/n-decane C_8/C_{10}, n-decane C_{10}, n-dodecane C_{12} and n-butadecane C_{14}) components in a surfactant water system. The continuous lines represent model results and geometric forms show experimental data. C_8^* corresponds to the case N/A constant.

To obtain the surface tension, we integrate Eq. (12-9) in the temperature for $r_s = 12r_0$ and $a_0 = 16nm$ and use k_f to fit the experimental data [19, 37]. The values of k_f for each n-alkane fall between 2,5 to 5,4 $[mJ/m^2K^2]$. Fig. **12-4** shows the behavior of γ as a function of T, evidencing an accurate matching of model results and experimental data for each n-alkane. The dashed black curve gives the surface tension for a constant value of N/A [30] which does not reproduce the experimental data for n-octane. This feature supports our contention that N/A must be a function of particle size.

The thermophoretic mobility can be obtained from hydrodynamics [24] and is proportional to γ_T in the form

$$\mathscr{D}_T = -\frac{2a\gamma_T}{\eta_0}\frac{1}{(2+\lambda_i/\lambda_o)(2+3\eta_i/\eta_o)} \tag{12-14}$$

where $\eta_{i,o}$ and $\lambda_{i,o}$ are the viscosities and thermal conductivities of the inner i and outer o fluids. Our analysis of γ_T then leads us to know how the thermophoretic mobility behaves in accordance with the size of the particle.This expression does not consider the thermodynamic properties of the core material that may have an impact on the total mobility, as happens in the case of Janus particles that exhibit an internal mass gradient [38, 39].

In Fig. **12-5**(a), we show the behavior of γ_T as a function of the particle size for the family of the n-alkanes studied in [19], evaluated at $T = 27^oC$. Since the n-alkanes have similar physico-chemical properties, we plot γ_T for the family of n-alkanes, inferring the behavior: $\gamma_T \propto 1/a$. In the figure, we also compare the results obtained from our model with experiments [19]. The thermophoretic mobility as a function of the particle size is shown in Fig. **12-5**(b). We observe that it varies smoothly around the constant value $3{,}54\mu m^2/Ks$, as commented in Refs. [19, 18]. These variations could be a consequence of the small size of the particles [40] in whose case a continuous variation of their surface area is not necessarily followed by a constant change

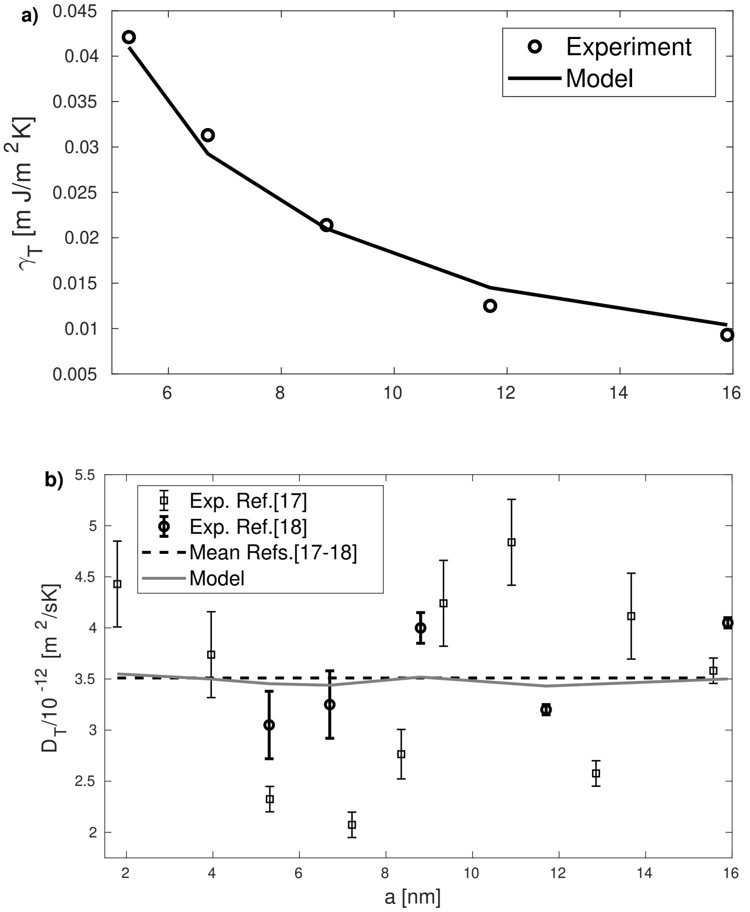

Fig. 12-5.: (a) γ_T factor versus particle radii $a[nm]$. Here $\gamma_T \propto 1/a$. (b) Thermophoretic mobility $\mathscr{D}_T$ versus particle radius for $T = 27^oC$. The continuous line corresponds to model results and the symbols to experimental data from [19, 18].

of their covered area, as illustrated in Fib 2(b).

In this range of particle sizes, one can question the validity of a purely thermodynamic treatment due to a greater importance of fluctuations at those scales [41] and to the possible existence of a strong coupling between particle and bath that may modify the thermal response of the particle [42]. To estimate what is the impact of these factors on the thermophoresis phenomenon is currently an unsolved problem.

By using Eq.(12-14) and considering the behavior of Ω shown in Fig.**12-3** and Eq.(12-9), we infer the power law for the thermophoretic mobility $\mathscr{D}_T \propto a^{1-\alpha}$ in which the exponent α depends on how the surfactant molecules are distributed on the particle surface. The value $\alpha = 0$ corresponds to a size-independent distribution which results in a linear behavior of $\mathscr{D}_T$ with the particle radius, similar to the one observed in Ref. [17] for charged particles. Interfacial entropic effects could in this case contribute to the thermal response of the particle. It has been indicated that this linear behavior is not reproduced by means of a pure hydrodynamic treatment for charged particles [43]. When $\alpha = 1$ the fraction of covered area by the surfactant on the interface increases linearly with the radius and consequently $\mathscr{D}_T$ does not depend on the size of the particle, as observed experimentally in [18, 19]. In the case in which $\alpha > 1$, $\mathscr{D}_T$ decreases with the particle radius, as observed in the experiments presented in [21, 20]. Finally, for long enough polymers it has been observed that $\mathscr{D}_T$ does not depend on their length [44]. This result can be explained from our theory if we model the unrolled polymer as a set of bonded spheres having the same radius. Since the radius is small we conclude that the effective $\mathscr{D}_T$ is a constant.

12.5. Conclusions

In summary, we have shown that the presence of fluid and surfactant molecules adsorbed on the particle surface modifies the interfacial entropy and in turn the surface tension. This feature has an impact on the thermophoretic mobility which in general fulfills a power law in the particle radius. We have found the tendency that for particles which are small enough the thermophoretic mobility is a constant whereas for larger particles it is linear in the radius. Our results show how and under what conditions interfacial entropic effects play a relevant role in the behavior of thermophoretic mobility.

Bibliography

[1] A. Arango-Restrepo and J. M. Rubi. Role of interfacial entropy in the particle-size dependence of thermophoretic mobility. *Phys. Rev. Lett.*, 125:045901, Jul 2020.

[2] Roberto Piazza, Sara Iacopini, and Benedetta Triulzi. Thermophoresis as a probe of particle-solvent interactions: The case of protein solutions. *Phys. Chem. Chem. Phys.*, 6(7):1616–1622, 2004.

[3] Werner Koehler and Konstantin I Morozov. The soret effect in liquid mixtures-a review. *J. Non-Equilib. Thermodyn.*, 41(3):151–197, 2016.

[4] MA Rahman and MZ Saghir. Thermodiffusion or soret effect: Historical review. *Int. J. Heat Mass Transf.*, 73:693–705, 2014.

[5] R Piazza and A Parola. Thermophoresis in colloidal suspensions. *J. Phys. Condens. Matter*, 20(15):153102, 2008.

[6] Jean K Platten. The soret effect: a review of recent experimental results. *Int. Appl. Mech.*, 73(1):5–15, 2006.

[7] Øivind Wilhelmsen, Dick Bedeaux, and David Reguera. Tolman length and rigidity constants of the lennard-jones fluid. *J. Chem. Phys.*, 142:171103, 2015.

[8] Fathi A Messaud, Ron D Sanderson, J Ray Runyon, Tino Otte, Harald Pasch, and S Kim Ratanathanawongs Williams. An overview on field-flow fractionation techniques and their applications in the separation and characterization of polymers. *Prog. Polym. Sci.*, 34(4):351–368, 2009.

[9] David Ross and Laurie E Locascio. Microfluidic temperature gradient focusing. *Anal. Chem.*, 74(11):2556–2564, 2002.

[10] Iman Zahmatkesh. On the importance of thermophoresis and brownian diffusion for the deposition of micro-and nanoparticles. *Int. Commun. Heat Mass*, 35(3):369–375, 2008.

[11] Chuen Jinn Tsai, Jyh Shyan Lin, Shankar G. Aggarwal, and Da Ren Chen. Thermophoretic deposition of particles in laminar and turbulent tube flows. *Aerosol Sci. Technol.*, (38):131–139, 2004.

[12] Byung Uk Lee, Du Sub Byun, Gwi-Nam Bae, and Jin-Ha Lee. Thermophoretic deposition of ultrafine particles in a turbulent pipe flow: Simulation of ultrafine particle behaviour in an automobile exhaust pipe. *J. Aerosol Sci.*, 37(12):1788 – 1796, 2006.

[13] Huan J. Keh and Chang L. Ou. Thermophoresis of aerosol spheroids. *Aerosol Sci. Technol.*, (38):675–684, 2004.

[14] Dieter Braun and Albert Libchaber. Thermal force approach to molecular evolution. *Phys. Biol.*, 1(1):P1–P8, feb 2004.

[15] G. Kucsko, P. C. Maurer, N. Y. Yao, M. Kubo, H. J. Noh, P. K. Lo, H. Park, and M. D. Lukin. Nanometre-scale thermometry in a living cell. *Nature*, 500:54–58, 2013.

[16] Roberto Piazza. Thermophoresis: moving particles with thermal gradients. *Soft Matter*, 4:1740–1744, 2008.

[17] Stefan Duhr and Dieter Braun. Thermophoretic depletion follows boltzmann distribution. *Phys. Rev. Lett.*, 96:168301, Apr 2006.

[18] Daniele Vigolo, Giovanni Brambilla, and Roberto Piazza. Thermophoresis of microemulsion droplets: Size dependence of the soret effect. *Phys. Rev. E*, 75:040401, Apr 2007.

[19] Philipp Naumann, Sascha Datta, Thomas Sottmann, Bastian Arlt, Henrich Frielinghaus, and Simone Wiegand. Isothermal behavior of the soret effect in nonionic microemulsions: Size variation by using different n-alkanes. *J. Phys. Chem. B*, 118(12):3451–3460, 2014.

[20] Paul M. Shiundu, P.Stephen Williams, and J.Calvin Giddings. Magnitude and direction of thermal diffusion of colloidal particles measured by thermal field-flow fractionation. *J. Colloid Interface Sci.*, 266(2):366 – 376, 2003.

[21] Jennifer Kreft and Yeng-Long Chen. Thermal diffusion by brownian-motion-induced fluid stress. *Phys. Rev. E*, 76:021912, Aug 2007.

[22] R Shankar Subramanian. The stokes force on a droplet in an unbounded fluid medium due to capillary effects. *J. Fluid Mech.*, 153:389–400, 1985.

[23] Francisco E Torres and Eric Herbolzheimer. Temperature gradients and drag effects produced by convection of interfacial internal energy around bubbles. *Phys. Fluids A*, 5(3):537–549, 1993.

[24] J. Bafaluy, I. Pagonabarraga, J.M. Rubi, and D. Bedeaux. Thermocapillary motion of a drop in a fluid under external gradients. faxÃ©n theorem. *Phys. A*, 213(3):277 – 292, 1995.

[25] Z Khattari, P Steffen, and Th M Fischer. Migration of a droplet in a liquid: effect of insoluble surfactants and thermal gradient. *J. Phys. Condens. Matter*, 14(19):4823, 2002.

[26] Sybren Ruurds De Groot and Peter Mazur. *Non-equilibrium thermodynamics*. Dover Publications Inc., 1985.

[27] Pei Tillman and J M Hill. Determination of nanolayer thickness for a nanofluid. *Int. J. Heat Mass Transf.*, 34(4):399–407, 2007.

[28] X F Zhou and L Gao. Thermal conductivity of nanofluids: Effects of graded nanolayers and mutual interaction. *J. Appl. Phys.*, 100(8):083503, 2008.

[29] Andrés Arango-Restrepo and J. Miguel Rubi. The soret coefficient from the faxén theorem for a particle moving in a fluid under a temperature gradient. *Eur. Phys. J. E*, 42(5):55, May 2019.

[30] Richard C. Tolman. The effect of droplet size on surface tension. *J. Chem. Phys*, 17(3):333–337, 1949.

[31] Bruce E Poling, J M Prausnitz, and John P O apos Connell. Properties of Gases and Liquids. In *Experimental Thermal and Fluid Science*. 2007.

[32] Luc Alberts. *Initial porosity of random packing: Computer simulation of grain rearrangement*. PhD thesis, 2005.

[33] Edward Charles Titchmarsh. *The theory of the Riemann zeta-function*. Oxford University Press, 1986.

[34] Philipp Naumann, Nils Becker, Sascha Datta, Thomas Sottmann, and Simone Wiegand. Soret coefficient in nonionic microemulsions: concentration and structure dependence. *J. Phys. Chem. B*, 117(18):5614–5622, 2013.

[35] Marco Braibanti, Daniele Vigolo, and Roberto Piazza. Does thermophoretic mobility depend on particle size? *Phys. Rev. Lett.*, 100:108303, Mar 2008.

[36] Yuki Kishikawa, Haruka Shinohara, Kousaku Maeda, Yoshiyuki Nakamura, Simone Wiegand, and Rio Kita. Temperature dependence of thermal diffusion for aqueous solutions of monosaccharides, oligosaccharides, and polysaccharides. *Phys. Chem. Chem. Phys.*, 14:10147–10153, 2012.

[37] T. Sottmann and R. Strey. Ultralow interfacial tensions in water-n-alkane-surfactant systems. *J. Chem. Phys*, 106:8606, 1997.

[38] Juan D. Olarte-Plata and Fernando Bresme. Orientation of janus particles under thermal fields: The role of internal mass anisotropy. *J. Chem. Phys.*, 152(20):204902, 2020.

[39] Juan D Olarte-Plata and Fernando Bresme. Theoretical description of the thermomolecular orientation of anisotropic colloids. *Phys. Chem. Chem. Phys.*, 21(3):1131–1140, 2019.

[40] Ailo Aasen, David Reguera, and Øivind Wilhelmsen. Curvature corrections remove the inconsistencies of binary classical nucleation theory. *Phys. Rev. Lett.*, 124:045701, Jan 2020.

[41] D Reguera, JM Rubi, and JMG Vilar. The mesoscopic dynamics of thermodynamic systems. *J. Phys. Chem. B*, 109(46):21502–21515, 2005.

[42] Rodrigo de Miguel and J. Miguel Rubí. Negative thermophoretic force in the strong coupling regime. *Phys. Rev. Lett.*, 123:200602, 2019.

[43] Alois Würger. Hydrodynamic boundary effects on thermophoresis of confined colloids. *Phys. Rev. Lett.*, 116:138302, 2016.

[44] Mingcheng Yang and Marisol Ripoll. Driving forces and polymer hydrodynamics in the soret effect. *J. Phys. Condens. Matter*, 24(19):195101, apr 2012.

Conclusions and Perspectives

Conclusions

In part I, we have presented a kinetic and thermodynamic description of non-equilibrium self-assembly processes that explains the formation of structures and their functionalities occurring at different scales. It is based on the formulation of Fokker Planck equations for the probability distribution as a function of reaction coordinates and structural parameters characterising the processes and the structures. The solution of such equations provides the dynamic evolution of the structures as well as the entropy produced in the process.

We have studied in particular the formation of gels and Liesegang patterns, as well as structures formed by magnetic colloids and enantiomeric crystals that provide insight into the formation of e.g. microtubules, cells, tissues, nanoparticles, synthetic vesicles and tissues among others. The main results obtained are the following:

- By considering the different steps of the self-assembly process: activation, assembly and disassembly, we have reproduced the experimental results for the gelation dynamics [1] (Figure **2-4**) and the Liesegang rings formation as well as their final spatial distribution [2] (Figs. **3-2** and **3-3**).
- We rationalise how a transient organisation in the system, involving intermediate aggregation states, precedes the appearance of a more complex structure: the gel (Figure **2-6**). Moreover, we showed how from non-homogeneous initial conditions, a transient organisation process involving the formation of self-assembled structures, give rise to macroscopic spatial patterns: macroscopic Liesegang rings (Fig. **3-2**).
- We obtained the evolution of the internal architecture of the structures at the meso-scale (Figure **2-5**, for the probability density of the orientation of the fibbers) as well as the patchy behaviour for the temperature (Fig. **3-4**) when the structures emerge.
- Our formalism accounts for the kinetics of self-assembly processes by means of a mathematical model that can be solved numerically. It could be extended to account for the effect of external fields and gradients. Although we have applied it to specific cases, it could also be applied to NESA processes that produce mesoparticles and other spatial patterns.

In part II, we have shown that the knowledge of the entropy generated in a non-equilibrium self-assembly process determines the architecture of the structures when they can be characterised by a structural parameter. This feature was analysed in two particular cases: gelation and formation of Liesegang rings.

- We have shown that the structures observed in these systems emerge at extreme values of the entropy produced when represented as a function of the structural parameter. Gel structures correspond to maximum values of the total entropy produced while Liesegang rings to minimum values.
- We have found that processes leading to a higher hierarchical order of the structures are characterised by the greatest possible value of lost work as a function of the structural parameter. For instance, gelation processes dissipate the maximum amount of available free energy to increase the hierarchical order. On the contrary, for Liesegang ring banding which does not entails a significant increment of the hierarchical order, the energetic cost is minimum.
- We have proposed a criterion that accounts for the formation and selection of self-assembled structures under nonequilibrium conditions. It establishes that the structures emerge at the minima of an effective potential (eq.(6-19)) that takes into account the energy needed to change their configurations, with a probability given by eq.(6-14). The criterion has been validated in two cases: Liesegang patterns and pattern formation in suspensions of colloidal magnetic particles. In both cases, we find that the most likely polymorphs found in the experiments are precisely those which minimize the potential proposed.

In part III, we have analysed the response of various self-organised systems to external forces. The main conclusions are the following:

- We found that the energy required to induce crystal symmetry breaking, quantified by the measured enantiomeric excess, is equal to the energy dissipated per solid salt mole. Furthermore, we concluded that one of the intermediate states absorbs the dissipated energy as free energy in accordance to our experiments.
- We have shown that healthy and carcinogenic tissues are characterised by particular values of structural parameters: Young modulus and porosity, which minimise and maximise, respectively, the energy dissipated by the tissue when exposed to mechanical and chemical external forces.
- The analysis of pancreatic adenocarcinoma as a self-organised structure has allowed PRECISAR to understand in a general formalism the different possible stages of the cancer and therefore its evolution.
- We have proposed a thermodynamic framework that analyses the role of dissipation in a fibre stretching process, describing its different stages and obtaining new alarm signals before the fibre bundle breaks. We have shown the existence of metastable, unstable and imminent-failure regimes and provided new transition indicators in terms of stretching velocity variation and entropy production rate which is an important quantity to measure the energy-efficiency of the processes.
- We have shown how enzyme evolution is conditioned to an optimization of the total entropy produced as a function of the activation energy. We have found that the shape of the potential barrier determines the thermodynamic efficiency of the activated processes because lost work depends on the nature of

the intermediate state.

- The distribution and organisation of surfactant molecules on the surface of a droplet, which depends on the droplet size, dictates the value of the interfacial entropy. We showed how and under what conditions interfacial entropic effects play a relevant role in the behavior of thermophoretic mobility.

Our findings support the existence of an effective potential that describes the formation of non-equilibrium self-assembled structures from a dynamic and thermodynamic perspective.

Perspectives

The conceptual framework presented can in general be used to describe the kinetics of non-equilibrium self-assembly processes. The results obtained offer the following perspectives:

- *Synthesis and study of the mechanical properties of the gels* . The proposed gelation model could be used to study the mechanical properties of the gel under external stress as a function of a structural parameter. It could also be used to estimate the optimal conditions for the control of the assembly of hydrogels with possible medical applications as mentioned in Ref. [3, 4, 5, 6, 7, 8].
- *Particle synthesis*. We could explore the controlled synthesis of nanoparticles of defined size as a function of initial conditions and external gradients, a useful topic in the synthesis of drug-carrying nanoparticles. [9, 10].
- *Prediction of structures*. The proposed self-assembly criterion could be used to predict the formation of polymorphs, which are crucial for identifying transient states in protein folding, in order to understand why certain organic enantiomers are predominant [11]. The results could improve computer-aided drug design [12], and be used to analyse the synthesis of crystals, hydrogels, reconfigurable materials, artificial tissues and nanoparticles.
- *Symmetry-Breaking amplified by shear rates*. We could analyse the influence of hydrodynamic effects in the crystals formation, enantiomeric excess and energy dissipation. To this purpose we could perform experiments in presence of stirring.
- *Estimation of the fugacity under non-equilibrium conditions*. From the crystallization model proposed we could compute the fugacity coefficients to investigate the importance of non-ideal effects coming from the non-equilibrium nature of the process.
- *Non-equilibrium thermodynamics analysis of cancer progression based on metabolic pathways*. An energetic analysis could shed light on the effect of the concentration of different molecules on cancer progression in order to propose food-based treatments based on bioenergetics.
- *Configuration of Saturn's rings*. Planetary rings are structures whose formation is not yet well understood[13]. The explanation of why different types of rings can be observed is an open question whose answer

could be related to the formation of spatio-temporal patterns [14]. We could use our approach to understand the formation and stability of Saturn's rings by considering them as a out-of-equilibrium self-assembled structure.

- *Dissipation in the fibber bundled model*. From the fibber bundle model proposed, we could analyse not only the energy coming into play but also the dynamics at all scales, from single molecule to macrostructure, under non-isothermal conditions. Our thermodynamic framework could be transferred to other problem areas of catastrophic events, eventually also outside the physical sciences, such as molecular biology and nanotechnology.

- *Self-assembly of Janus particles*. We could use our formalism to study the different structures formed through self-assembly of Janus particles and to analyse the role played by dissipation.

We hope that the results obtained in this thesis can constitute a reference framework for the development of new models and experimental studies capable of revealing new properties of self-organised systems that dissipate matter and energy.

Bibliography

[1] Job Boekhoven, Aurelie M. Brizard, Krishna N. K. Kowlgi, Ger J. M. Koper, Rienk Eelkema, and Jan H. van Esch. Dissipative Self-Assembly of a Molecular Gelator by Using a Chemical Fuel. *Angew. Chem.*, 122(28):4935–4938, 2010.

[2] Roché M. Walliser, Florent Boudoire, Eszter Orosz, Rita Tóth, Artur Braun, Edwin C. Constable, Zoltán Rácz, and István Lagzi. Growth of Nanoparticles and Microparticles by Controlled Reaction-Diffusion Processes. *Langmuir*, 31(5):1828–1834, 2015.

[3] Allan S Hoffman. Hydrogels for Biomedical Applications. *Adv. Drug Deliv. Rev.*, 64:18–23, 2012.

[4] Nasim Annabi, Jason W Nichol, D Ph, Xia Zhong, and Chengdong Ji. Controlling the Porosity and Microarchitecture of Hydrogels for Tissue Engineering. *J. Tissue Eng.*, 16(4):371–383, 2010.

[5] Zulma A. Jiménez and Ryo Yoshida. Temperature Driven Self-Assembly of a Zwitterionic Block Copolymer That Exhibits Triple Thermoresponsivity and pH Sensitivity. *Macromolecules*, 48(13):4599–4606, 2015.

[6] Jinxing Jiang and Kenji Sakurai. Formation of Ultrathin Liesegang Patterns. *Langmuir*, 32(36):9126–9134, 2016.

[7] Yukikazu Takeoka and Masayoshi Watanabe. Tuning Structural Color Changes of Porous Thermosensitive Gels Through Quantitative Adjustment of the Cross-Linker in Pre-Gel Solutions. *Langmuir*, 19(22):9104–9106, 2003.

[8] Marta Tena-Solsona, Benedikt Rieß, Raphael K Grötsch, Franziska C Löhrer, Caren Wanzke, Benjamin Käsdorf, Andreas R Bausch, Peter Müller-Buschbaum, Oliver Lieleg, and Job Boekhoven. Non-equilibrium dissipative supramolecular materials with a tunable lifetime. *Nat. Commun.*, 8:15895, 2017.

[9] Larken E Euliss, Julie A Dupont, Stephanie Gratton, Joseph Desimone, James D Martin, and Stephanie Gratton. Imparting size , shape , and composition control of materials for nanomedicine. *Chem. Soc. Rev.*, 35:1095–1104, 2006.

[10] Andrew Z Wang, Robert Langer, and Omid C Farokhzad. Nanoparticle Delivery of Cancer Drugs. *Annu. Rev. Med*, 63:185–198, 2012.

[11] Dilip Kondepudi, Bruce Kay, and James Dixon. End-directed evolution and the emergence of energy-seeking behavior in a complex system. *Phys. Rev. E: Stat. Phys., Plasmas, Fluids, - Statistical, Nonlinear, and Soft Matter Physics*, 91(5):1–5, 2015.

[12] Mohammad H Baig, Khurshid Ahmad, Gulam Rabbani, Mohd Danishuddin, and Inho Choi. Computer aided drug design and its application to the development of potential drugs for neurodegenerative disorders. *Current Neuropharmacology*, 16(6):740–748, 2018.

[13] Michele Dougherty, Larry Esposito, and Stamatios Krimigis. *Saturn from Cassini-Huygens*. Springer Science & Business Media, 1 edition, 2009.

[14] Marcin Fialkowski, Kyle J M Bishop, Rafal Klajn, Stoyan K Smoukov, Christopher J Campbell, and Bartosz A Grzybowski. Principles and Implementations of Dissipative (Dynamic) Self-Assembly. *J.Phys. Chem. B*, 110:2482–2496, 2006.

A. Appendix: Kinetics and energetics of chemical reactions through intermediate states

We analyze the kinetics and the energetics of chemical reactions passing through an intermediate state. Two approaches are adopted. The first one is a mesoscopic description in which the state of the reaction undergoes a diffusion process in a tristable potential along a reaction coordinate which parametrizes different molecular configurations in the reaction pathway. The second consists of a two-level system model. We show that the reaction flux and the energy dissipated (lost work) depend significantly on the mean life of the intermediate state. It is found that the values of these quantities obtained through both approaches differ especially at early stages, in the presence of high chemical potential differences for low energies of the intermediate state. The analysis presented unifies kinetics and energetics of chemical reactions steps and can be applied to explain the mechanism of enzymatic and organic reactions, RNA and protein folding and sorption processes.

This Appendix was published in *the Journal of Physica A: Statistical Mechanics and its Applications*, **509**, 86-96, (2018). Ref.[1]

A.1. Introduction

The activation pathway of many activated processes [2, 3, 4] exhibits the presence of multiple intermediate states [5, 6, 7, 8]. These states reveal the existence of metastable molecular structures [9, 10] some of which are very short-lived and can hardly be detected by the experiments whereas others may persist for longer times [11, 12, 13]. Intermediate states are present in processes such as chemisorption [14], protein folding [15, 16, 17], RNA folding [18], organic reactions [6, 19] and enzymatic kinetics [20, 21, 22, 23, 24] to mention just a few.

The existence of intermediate states may significantly affect the activation kinetics. In desorption from chemisorbed layers [14], the presence of weakly-bound intermediate states, promoted by the existence of a second layer, determines the desorption kinetics [25] which depend on the activation energies and on the presence of multiple binding states [26]. In protein folding processes, as in the folding of the 71-residue (mainly α-helical FF domain from human HYPA/FBP11), intermediate states are observed, being even more stable than the denatured ones [8], i.e, in a denaturation processes, the intermediate states are more stables than the initial unfolded state. Multiple intermediate conformational states arise in enzymatic reactions such as the one taking takes place in adenylate kinase (AdK) in which the energy barriers separating the open and closed states of the enzyme are low enough to facilitate rapid transitions among the intermediate states. [27, 11].

Intermediate conformations in the activation pathway can be detected by the energy dissipated in the form of heat which can be measured by calorimetric techniques such the differential scanning calorimetry [28], successfully used to identify protein conformations changes in second order transitions [29, 30]. The heat dissipated is related to the entropy production rate whose global value results from local contributions along the reaction pathway which depend on the form of the free-energy landscape built by the presence of such states. Obtaining the entropy production by means of non-equilibrium thermodynamic methods is then of primary importance to evaluate structural changes in the system [31, 32, 33].

The traditional way to analyze the kinetics of chemical and biochemical processes is based on the law of mass action (LMA) [34, 35] which assumes that the relative change of a substance in the reaction is proportional to the time elapsed and to the amount of substances. The LMA proposes a description of the kinetics of the reaction but it does not account for the dissipation inherent to the process. It was proposed that dissipation could be obtained from non-equilibrium thermodynamics [36] (NET). This theory, however, provides linear laws between fluxes and forces and can only describe the reaction close to equilibrium, at low values of the affinity, in which case reaction rate and affinity are proportional to each other. This is the reason why kinetics and dissipation have been treated in the past independently.

The possibility of a systematic use of the method of NET to describe the nonlinear reaction kinetics was discussed in [2], for a single unimolecular reaction. In the mesoscopic non-equilibrium thermodynamics (MNET) theory [37, 38], the chemical reaction is viewed as a diffusion process in a free-energy potential [39] through a reaction coordinate which parametrizes the different molecular configurations along the activation pathway. The coarse-graining description, based on the probabilities defined in Eq. (7)-(9), leads to the LMA [2]. This approach is simpler but its accuracy must be carefully analyzed. This will be one of the objectives of the Appendix.

The formulation of MNET theory extends the applicability of thermodynamic concepts deep into mesoscopic and irreversible regimes showing how the probabilistic interpretation of thermodynamics together with probability conservation laws can be used to obtain Fokker-Planck equations for the relevant degrees of freedom. It may also describe the interplay of chemical reactions with other transport processes such as mass diffusion or heat transport [40]. In this way one can describe nonlinear processes such as chemisorption [41], nucleation [4, 42, 43], thermal emission [44], evaporation and condensation [45], electro-chemistry [46], unzipping RNA [47], active transport [48] and biochemical cycles [24] taking place in physico-chemical and living systems.

Our purpose in this Appendix is to analyze how the presence of intermediate states in the reaction pathway may affect the kinetics and the energetics of the process. Since the form of the potential barrier is unknown [48, 49, 47, 24, 40], we propose a method to shape the potential barrier by imposing thermodynamic restrictions. The form of the barrier is used in the Fokker-Planck equation to obtain the probability distribution from which we compute the average reaction flux and the entropy production. The results obtained by means of this mesoscopic approach will be compared with those resulting from the quasi-stationary approach used in the derivation of the law of mass action. We will also compute the lost work for both approaches to understand the role played by dissipation in the kinetics of the process.

The Appendix is organised as follows. In Section 2, we briefly review the mesoscopic nonequilibrium thermodynamics approach [2, 38, 37]. Section 3 is devoted to introducing a model of the potential barrier based on thermodynamic restrictions. In Section 4, we compare the average values of the current and of the energy dissipated in the process for both approaches and set up conditions under which the quasi-stationary approach may be valid. Finally, in the last section, we summarize our main results.

A.2. Mesoscopic non-equilibrium thermodynamic approach

To analyse the chemical kinetics in the presence of intermediate states, we will consider the case of two consecutive reversible first-order chemical reactions

$$\mathrm{A} \underset{\mathrm{k_1}^-}{\overset{\mathrm{k_1}^+}{\rightleftharpoons}} \mathrm{B} \underset{\mathrm{k_2}^-}{\overset{\mathrm{k_2}^+}{\rightleftharpoons}} \mathrm{C}$$

in which a reactant A transforms into the product C passing through an intermediate state B which can be either unstable or metastable. Here k_1^+ and k_1^- are the forward and backward kinetic constants for the first reaction respectively and k_2^+ and k_2^- the kinetic constants for the second reaction. We assume that the reactions take place in an homogeneous, isothermal and closed system. An example of this reaction scheme is a biochemical reaction in which an enzymatic complex enzyme-substrate (A) produces the complex enzyme-product (C) in the presence of an intermediate state (B) [50].

We assume that the reactions take place along the dimensionless reaction coordinate γ defined from 0 to 1 which parametrizes the states of the reactions. We assign to these states the probability density $p(\gamma,t)$. Its conservation is formulated locally through the continuity equation

$$\frac{\partial p(\gamma,t)}{\partial t} = -\frac{\partial}{\partial \gamma} J(\gamma,t) \tag{A-1}$$

where J is the probability current. The expression of the current follows by considering local equilibrium in the space of the reaction-coordinate. This assumption, that can be justified when there is a great disparity between the relaxation times of particle velocities and of conformational changes of the reaction complex, allows us to compute the entropy production proper of a diffusion process through a potential barrier [37, 38]

$$\sigma(\gamma,t) = -\frac{1}{T} J(\gamma,t) \frac{\partial \mu(\gamma,t)}{\partial \gamma}, \tag{A-2}$$

Here μ is the chemical potential and T is the temperature. From this expression, we can infer the linear law for the current

$$J(\gamma,t) = -\frac{L(\gamma,t)}{T} \frac{\partial \mu(\gamma,t)}{\partial \gamma}, \tag{A-3}$$

where L is an Onsager coefficient which is in general a function of the γ-coordinate. Using the fact that the coefficient is in first approximation proportional to $p(\gamma,t)$ and introducing the constant diffusion coefficient $\mathscr{D}$, measured in s^{-1}, one has

$$L(\gamma,t) = \frac{\mathscr{D}}{k_B} p(\gamma,t). \tag{A-4}$$

The chemical potential along the γ-coordinate in a non-ideal system is given by

$$\mu(\gamma,t) = k_B T \ln \psi(\gamma) p(\gamma,t) + \phi(\gamma) \tag{A-5}$$

Here ϕ is the potential barrier of enthalpic nature and ψ an activity coefficient characterizing the non-ideal behavior. For an ideal system $\psi(\gamma) = 1$, inserting the expression of the current (Eq.(A-3)) into Eq.(A-1), we obtain the Fokker-Plank equation

$$\frac{\partial p(\gamma,t)}{\partial t} = \mathscr{D} \left[\frac{\partial^2 p(\gamma,t)}{\partial \gamma^2} + \frac{1}{k_B T} \frac{\partial}{\partial \gamma} \left(p(\gamma,t) \frac{\partial \phi(\gamma)}{\partial \gamma} \right) \right], \tag{A-6}$$

whose solution is subjected to the initial condition $p(0,0) = \delta(0)$ and to Neumann boundary conditions.

In a coarse-graining description, we define the macroscopic probability for each component from the probability density p obtained from Eq. (A-6):

$$P_A(t) = \int_0^{\gamma_{AB}} p(\gamma,t) d\gamma, \tag{A-7}$$

$$P_B(t) = \int_{\gamma_{AB}}^{\gamma_{BC}} p(\gamma,t) d\gamma \tag{A-8}$$

$$P_C(t) = \int_{\gamma_{BC}}^{1} p(\gamma,t) d\gamma \tag{A-9}$$

The integration limit γ_{AB} represents the state at which A completely becomes B while γ_{BC} stands for the state at which B completely becomes C.

A.3. Modelling the potential barriers

To obtain the solution of the Fokker-Planck equation, we need to know the form of the potential barrier. We will analyze two particular cases of potential barriers one with an unstable intermediate and another with a metastable intermediate. For the case of unstable intermediate state B, the kinetics reduces to that of a two-state system, A and C and can then be described by a bistable potential. On the contrary, if the state B is metastable we have to consider the transitions to and from this state and the potential must be tristable.

A.3.1. Bistable potential

We first consider the reaction

$$\mathrm{A} \underset{\mathrm{k}^-}{\overset{\mathrm{k}^+}{\rightleftharpoons}} \mathrm{C}$$

The potential barrier for this case is modeled by a bistable potential whose minima located at $\gamma = 0$ and $\gamma = 1$ correspond to the reactants and products and the maximum at γ^* is the transition state (B). The form of the barrier must fulfill some thermodynamic requirements. Stability of the initial and final states of the reaction imposes two conditions on the first derivative of the potential. Three more conditions come from the values of the standard chemical potentials and the activation energy at $\gamma = 0$, $\gamma = 1$ and $\gamma = \gamma^*$, respectively. Moreover, since the potential barrier is related to the equilibrium probability distribution, the values of the coordinate such that $\gamma < \gamma^*$ denote the state A and those for which $\gamma \geq \gamma^*$ correspond to the state C.
For the potential barrier, we thus propose a fifth-order polynomial with two minima and a maximum in the interval [0,1]. The polynomial includes six parameters whose values follow from the seven thermodynamic restrictions which as a matter of fact reduce to six since the location of the transition state is unknown. The potential barrier is then given by

$$\phi(\gamma) = \sum_{i=0}^{5} c_i \gamma^i \tag{A-10}$$

where the constrains are

$$\phi(0) = \mu_A^0; \quad \phi(1) = \mu_C^0; \quad \phi(\gamma^*) = \text{máx}(\phi(\gamma)) - \mu_A^0 = \varepsilon;$$

$$\left.\frac{d\phi(\gamma)}{d\gamma}\right|_{\gamma=0} = \left.\frac{d\phi(\gamma)}{d\gamma}\right|_{\gamma=1} = \left.\frac{d\phi(\gamma)}{d\gamma}\right|_{\gamma=\gamma^*} = 0;$$

$$\exp((\mu_A^0 - \mu_C^0)/RT) = \frac{P_{C,eq}}{P_{A,eq}} = \frac{\int_{\gamma^*}^{1} \exp(-\phi(\gamma)/RT)d\gamma}{\int_0^{\gamma^*} \exp(-\phi(\gamma)/RT)d\gamma}$$

This system of equations enables one to determine γ^*, and $c_i, i = 0, 1, .., 5$. For instance, for $(\mu_A^0 - \mu_C^0)/RT = 1$ and $\varepsilon/RT = 5$, we obtain the potential barrier shown in Figure.**D-1**.

A.3.2. Tristable potential

We now consider the situation in which the reaction takes place through an intermediate component and corresponds to the one given in the previous section. The potential barrier is now modelled by a tristable

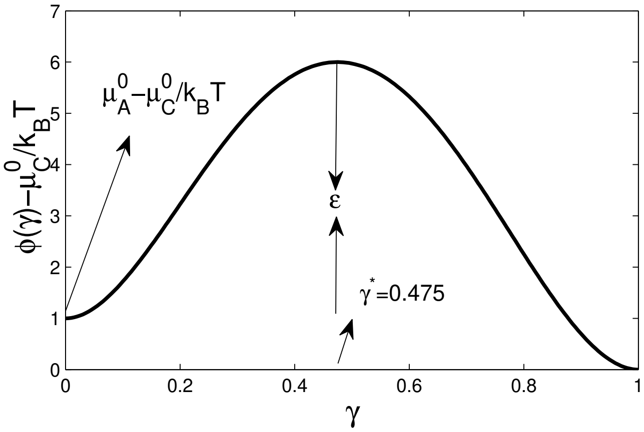

Fig. A-1.: Bistable potential $\phi(\gamma)/k_BT$ modelling a process with an unstable intermediate.

potential whose minima are located at $\gamma=0$, $\gamma=1$ and γ^* which corresponds to the reactant (A), product (C) and intermediate (B), respectively. Further, the potential barrier is described by two maxima at γ_{AB} and γ_{BC} which represent the transition states between A, B and C respectively. The form of the barrier is subjected to thermodynamics constraints. Stability at A, B and C imposes three conditions on the first derivative of the potential. Five more restrictions come from the values of the standard chemical potentials at $\gamma=0$ for A, $\gamma=1$ for C, at $\gamma=\gamma^*$ for B and transition state energy at $\gamma=\gamma_{AB}$ and $\gamma=\gamma_{BC}$. Moreover, since the potential barrier is related to the equilibrium probability distribution, values of $\gamma\in[0, \quad \gamma_{AB}]$ denote state A, $\gamma\in[\gamma_{AB}, \quad ,\gamma_{BC}]$ correspond to state B and $\gamma\in[\gamma_{BC}, \quad 1]$ to state C.

For the potential barrier, we thus propose a stepwise function composed of two fifth-order polynomials which are continuous at $\gamma=\gamma^*$ and whose derivative exists at $\gamma=\gamma^*$. Each polynomial includes six parameters whose values follow from the seven thermodynamic restrictions which as a matter of fact reduce to six since as in the case of the bistable potential the location of the transition state is unknown. The potential barrier is then given by

$$\phi(\gamma)=\begin{cases}\phi^-(\gamma) & 0\le\gamma\le\gamma^*\\ \phi^+(\gamma) & \gamma^*\le\gamma\le 1\end{cases}$$

where the constrains for $\phi^-(\gamma)$ are:

$$\phi^-(0)=\mu_A^0;\quad \phi^-(\gamma^*)=\mu_B^0;\quad \phi^-(\gamma_{AB})=\mu_A^0+\varepsilon^-;$$

$$\left.\frac{d\phi^-(\gamma)}{d\gamma}\right|_{\gamma=0}=\left.\frac{d\phi^-(\gamma)}{d\gamma}\right|_{\gamma=\gamma_{AB}}=\left.\frac{d\phi^-(\gamma)}{d\gamma}\right|_{\gamma=\gamma^*}=0;$$

$$\exp((\mu_A^0-\mu_B^0)/RT)=\frac{P_{B,eq}}{P_{A,eq}}=\frac{\int_{\gamma_{AB}}^{\gamma^*}\exp(-\phi^-(\gamma)/RT)d\gamma+\int_{\gamma^*}^{\gamma_{BC}}\exp(-\phi^+(\gamma)/RT)d\gamma}{\int_0^{\gamma_{AB}}\exp(-\phi^-(\gamma)/RT)d\gamma}$$

and those for $\phi^+(\gamma)$ are:

$$\phi(\gamma^*)=\mu_B^0;\quad \phi(1)=\mu_C^0;\quad \phi(\gamma_{BC})=\mu_B^0+\varepsilon^+;$$

$$\left.\frac{d\phi^+(\gamma)}{d\gamma}\right|_{\gamma=1} = \left.\frac{d\phi^+(\gamma)}{d\gamma}\right|_{\gamma=\gamma_{BC}} = \left.\frac{d\phi^+(\gamma)}{d\gamma}\right|_{\gamma=\gamma^*} = 0;$$

$$\exp((\mu_A^0 - \mu_C^0)/RT) = \frac{P_{C,eq}}{P_{A,eq}} = \frac{\int_{\gamma_{BC}}^{1} \exp(-\phi^+(\gamma)/RT)d\gamma}{\int_0^{\gamma_{AB}} \exp(-\phi^-(\gamma)/RT)d\gamma}$$

For instance, for $(\mu_A^0 - \mu_C^0)/RT = 1$, $\mu_B^0/RT = 4$, $\varepsilon^-/RT = 7$ and $\varepsilon^+/RT = 2$, we obtain the tristable potential barrier shown in Figure **A-2**.

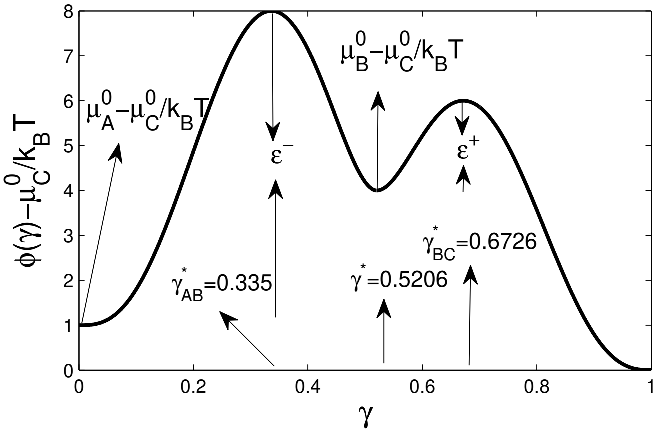

Fig. A-2.: Tristable potential $\phi(\gamma)/k_BT$ modelling a process with a metastable intermediate.

A.3.3. Multistable potential barrier

Complex reaction schemes, non-elementary reactions and non-unimolecular reactions can be expressed as superposition of simultaneous and sequential first-order reactions. We consider the case of a chemical reaction scheme composed of Y consecutive first-order processes, in which in the y^{th} process, the component $A^{(x)}$ transforms into component $A^{(x+z-1)}$. The process is modelled by a potential barrier with z stable and metastable states with $x = 1, \ldots. Z-1$ and $z = x+1, \ldots, Z$, being Z the maximum number of stable and metastable states involved in the reaction mechanism. The y^{th} process is

$$\mathrm{A}^{(\mathrm{x})} \underset{\mathrm{k}_\mathrm{x}^-}{\overset{\mathrm{k}_\mathrm{x}^+}{\rightleftharpoons}} \mathrm{A}^{(\mathrm{x+1})} \underset{\mathrm{k}_\mathrm{x+1}^-}{\overset{\mathrm{k}_\mathrm{x+1}^+}{\rightleftharpoons}} \ldots \underset{\mathrm{k}_\mathrm{x+z-2}^-}{\overset{\mathrm{k}_\mathrm{x+z-2}^+}{\rightleftharpoons}} \mathrm{A}^{(\mathrm{x+z-1})}$$

The cases of bistable and tristable processes studied previously correspond to $Y = 1$, $x = 1$ and $z = 2$ (bistable) and $z = 3$ (tristable). Now, considering that the y^{th} process is parametrized by the γ_y coordinate, the y^{th} potential barrier ($\phi_y(\gamma_y)$) is a piecewise function composed of $z-1$ pieces. Therefore, the multistable potential barrier for the y^{th} sequential process is given by

$$\phi_y(\gamma_y) = \left\{ \phi_y^{(j)}(\gamma_y) \quad if \quad \gamma_{y,j-1} \le \gamma_y \le \gamma_{y,j} \quad \forall j \,|\, j = 1, \ldots, z_y - 1. \quad \gamma_{y,0} = 0 \quad \wedge \quad \gamma_{y,z_y-1} = 1 \right.$$

Here, $\gamma_{y,j}$ is the position of the j^{th} state of the sequential process.

A.4. Quasi-stationary approach

A.4.1. Fluxes

When the potential barrier is high enough, the reaction reaches a quasi-stationary state in which J may depend on time but is practically constant along the reaction coordinate γ. This case was analyzed in detail in [2] for unimolecular reactions, showing that the reaction flux is given by the LMA which follows by integrating Eq. (A-3) over γ. If the process contains more than two stable or metastable states, this integration must be performed in the two zones of the potential barrier. One obtains

$$J(t) = \begin{cases} J_{AB}(t) = \frac{-\mathscr{D}}{\int_0^{\gamma^*} \exp(\phi(\gamma)/RT)d\gamma}\left[\exp(\mu(\gamma^*)/RT) - \exp(\mu(0)/RT)\right], & 0 \leq \gamma \leq \gamma^* \\ J_{BC}(t) = \frac{-\mathscr{D}}{\int_{\gamma^*}^{1} \exp(\phi(\gamma)/RT)d\gamma}\left[\exp(\mu(1)/RT) - \exp(\mu(\gamma^*)/RT)\right], & \gamma^* < \gamma \leq 1 \end{cases} \tag{A-11}$$

The fluxes for both reactions can be rewritten in terms of probabilities and reaction rates as

$$J_{AB}(t) = k_1^+ P_A - k_1^- P_B, \tag{A-12}$$

$$J_{BC}(t) = k_2^+ P_B - k_2^+ P_C, \tag{A-13}$$

where the reaction constants depend on the potential barrier and $\mathscr{D}$

$$k_1^+ = \frac{\mathscr{D}}{\int_0^{\gamma^*} \exp(\phi(\gamma)/RT)d\gamma} \exp(\mu_A^0/RT)$$

$$k_1^- = \frac{\mathscr{D}}{\int_0^{\gamma^*} \exp(\phi(\gamma)/RT)d\gamma} \exp(\mu_B^0/RT)$$

$$k_2^+ = \frac{\mathscr{D}}{\int_{\gamma^*}^{1} \exp(\phi(\gamma)/RT)d\gamma} \exp(\mu_B^0/RT)$$

$$k_2^- = \frac{\mathscr{D}}{\int_{\gamma^*}^{1} \exp(\phi(\gamma)/RT)d\gamma} \exp(\mu_C^0/RT)$$

We have considered that in first approximation the diffusivity coefficient is constant along the reaction coordinate and has then a common value for both reactions. This approximation is valid when the potential is sufficiently smooth as frequently occurs in many reactions. The probability conservation laws of the components A, B, and C are

$$\frac{dP_{qs,A}}{dt} = -J_{AB}(t), \tag{A-14}$$

$$\frac{dP_{qs,B}}{dt} = J_{AB}(t) - J_{BC}(t), \tag{A-15}$$

$$\frac{dP_{qs,C}}{dt} = J_{BC}(t), \tag{A-16}$$

If the quasi-stationary approach successfully describes the reactive process, the probabilities P_{qs} in Eqs. (A-

14),(A-15) and (A-16) should converge to the probabilities in Eqs. (A-7),(A-8) and (A-9) that can be found by solving the Fokker-Planck equation.

To define the entropy production rate in the quasi-stationary approach (σ_{qs}) for the coupled reactions, notice that in Eq. (A-11) the driving force is the fugacity difference ($\Delta\exp(\mu/RT)$). Therefore, in this approach the entropy production rate is written in terms of flux-force pairs [36]. Rewriting the force as a function of the flux using Eqs. (A-12), (A-13), we obtain the expression for $\sigma_{qs}(t)$,

$$\sigma_{qs}(t) = \frac{R}{\mathscr{D}}\left[J_{AB}(t)^2\int_0^{\gamma^*}\exp(\phi(\gamma)/RT)d\gamma + J_{BC}(t)^2\int_{\gamma^*}^1\exp(\phi(\gamma)/RT)d\gamma\right] \tag{A-17}$$

A.4.2. Testing the quasi-stationary approximation

Once the potential is built up, we can analyze the validity of the quasi-stationary approximation for processes having a unstable or a metastable intermediate state B by computing the probabilities and the lost work as a function of the intermediate state E_B.

To evaluate the error made when using the quasi-stationary approximation, we introduce the distance $\delta(E_B)$ in the probability space through the expression

$$\delta(E_B)^2 = \frac{1}{t_R}\int_0^{t_R}(P(t;E_B) - P_{qs}(t;E_B))^2 dt \tag{A-18}$$

from which we may construct a variance or a norm. Here t_R is the relaxation time of the process defined as the time at which the probability in the quasi-stationary approach reaches the 99,95 % of the equilibrium value

$$\frac{P_{qs,C}(t_R;E_B)}{P^{eq}_{qs,C}(t_R;E_B)} = 0{,}9995. \tag{A-19}$$

In the case of a metastable intermediate case, $P \equiv [P_A, P_B, P_C]$ and $P_{qs} \equiv [P_{qs,A}, P_{qs,B}, P_{qs,C}]$. When the intermediate state is unstable, $P \equiv [P_A, P_C]$, and $P_{qs} \equiv [P_{qs,A}, P_{qs,C}]$.

A.4.3. Lost work

The reaction kinetics entails dissipation that can be quantified by means of the lost work related to the entropy production [36]. This quantity can give us information about the energetic efficiency of the process and the consistency of the kinetic models proposed. The lost work computed from the mesoscopic approach is defined as

$$W_L(E_B) = T\int_0^{\infty}\int_0^1 \sigma(\gamma,t)d\gamma dt \tag{A-20}$$

whereas the lost work corresponding to the quasi-stationary approach is

$$W_L^{(qs)}(E_B) = T\int_0^1 \sigma_{qs}(t)d\gamma \tag{A-21}$$

These two quantities can be computed from the knowledge of the probability distributions.

A.5. Results

A.5.1. Mesoscopic approach

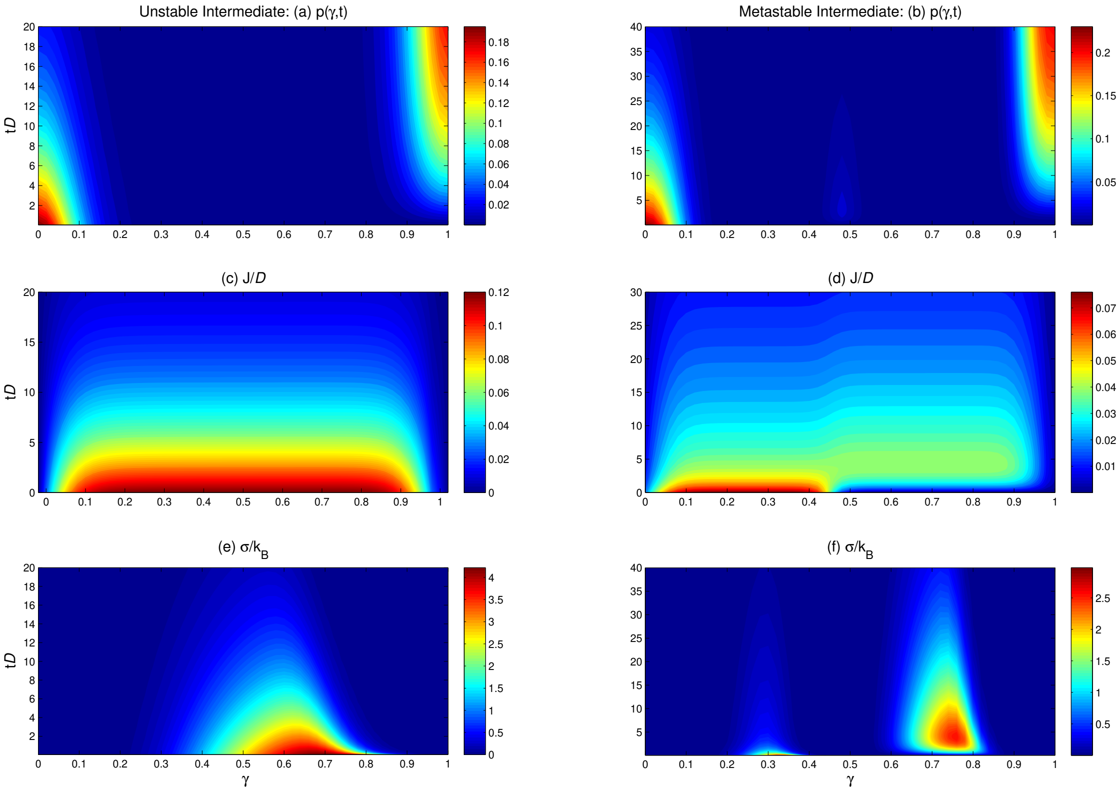

Fig. A-3.: Results obtained from the mesoscopic approach **as a function of the dimensionless time** $t\mathscr{D}$. (a) probability density, (c) flux, and (e) entropy production rate, as a function of the reaction coordinate and time for a process with an unstable intermediate. (b) probability density, (d) flux, and (f) entropy production rate, as a function of the reaction coordinate and time for a process with a metastable intermediate. In the potential barriers is used $\mu_A^0 - \mu_C^0 = 4k_BT$. For the unstable case, $E_B = 10k_BT$. For the metastable case, $E_B = 5k_BT$, $\varepsilon^- = 7k_BT$, and $\varepsilon^+ = 5k_BT$.

We have numerically solved the Fokker-Planck equation (Eq. (A-6)) by means of a finite-volume method written in MATLAB®[51] to obtain the probability density and from it the reaction flux and the entropy production rate for processes with unstable and stable intermediate states. The results are presented in Fig. **A-3**, as a function of the dimensionless time $\tau = t\mathscr{D}$. The difference between the standard chemical potentials for component A and C is $4k_BT$, the value of the energy of the intermediate is $10k_BT$ for the bistable case, for the tristable case is $5k_BT$ and the transition state energies are $12k_BT$ and $10k_BT$, respectively.

The relatively low values used for the potential barrier parameters illustrate particular situations in which the quasi-stationary approach is less accurate because of a low energetic potential. These low energetic barriers are frequently found in processes such as conformational movements of organic compounds and proteins, ion exchange (in zeolites), intermolecular interactions and hydrogen bonds[52, 53, 54, 55, 56] and in some physico-chemical processes [57, 58, 59, 55, 56].

The Figs. **A-3** (a) and (b) show the temporal evolution of the probability density in the cases of unstable and mestastable intermediates, respectively. We can observe how the density of states decreases with time near $\gamma = 0$ and increases at $\gamma = 1$, as could be expected. In Figure **A-3**(b), at early stages there is an slight increment of the density of the state around $\gamma = 0{,}45$ due to the existence of the metastable intermediate. This increase could be more visible if the metastable state had a lower energy.

The Figs. **A-3**(c) and (d) show the evolution over time of the flux for both cases. We can observe how the fluxes decrease with time. Fig. **A-3**(c) shows a constant flux for a specific time and reaction coordinate in between $\gamma = 0{,}15$ and $\gamma = 0{,}85$. Nevertheless, this flux is not quasi-stationary because it depends on γ for dimensionless times $t\mathscr{D}$ smaller than 20. Fig. **A-3**(d) shows a similar behavior with the presence of two different zones. This confirms the fact that in the quasi-stationary approach there are two fluxes describing the process. Again the flux is not completely constant in γ and differs from the one obtained in the mesoscopic approach.

Fig. **A-3**(e) and (f) present the temporal evolution of the entropy production rate for both cases. We can observe how the entropy production rate decreases over time until it vanishes in thermodynamic equilibrium. Fig. **A-3**(e) shows a displacement of the maximum over time because the probability distribution changes around this region, not because the flux is constant in this region. The maximum is always located at the right side of the unstable state B which is found at $\gamma = 0{,}41$. The entropy production is higher at γ values such that the first derivative of $\phi(\gamma)$ is negative and its second derivative is also negative. Fig. **A-3**(f) shows maxima of the entropy production, the first around $\gamma = 0{,}3$ and the second around $\gamma = 0{,}78$, corresponding to both subprocesses, A to B and B to C. Notice that the entropy production of the second subprocess does not appear at very early stages due to the fact that the flux in this zone vanishes. Further, as in Fig. **A-3**(e), the entropy production is larger at γ values such that the first derivative of $\phi(\gamma)$ is negative and its second derivative is also negative.

A.5.2. Accuracy of the quasi-stationary approach

To compare the results obtained by means of both approaches, we have solved Eqs.(A-14-A-16) and (A-6) for different values of (E_B) and used Eqs. (A-7-A-9) to compute the coarse-graining probabilities and Eq.(A-18) to compute the error.

As it is shown in Figs. **A-3**(c) and (d), the fluxes depend on γ especially at early times of the process. This fact causes significant deviations of the quasi-stationary approach from the mesoscopic description, as becomes manifest in Fig. **A-4**(a). These differences are more pronounced at low energies of the intermediate state. For instance, in the case of an unstable intermediate the deviation is higher than 100 % for early stages.

In Fig. **A-4**(b), we show the computed average deviation for processes with unstable and metastable intermediate states as a function of its energy. We can see that the average deviation decreases when one increments the energy of the intermediate state because when increasing the energy barriers, the process slows down and the flux becomes homogeneous in γ.

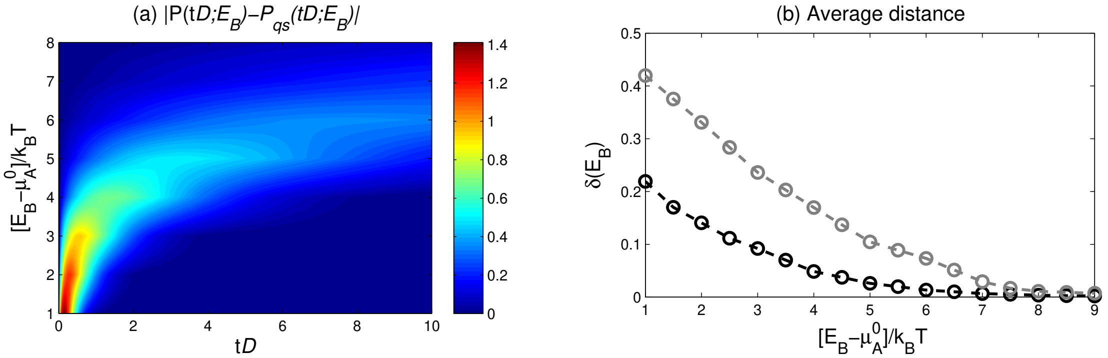

Fig. A-4.: Deviation and average deviation as a function of the intermediate energy. (a) $|P(t;E_B)-P_{qs}(t;E_B)|$ as a function of $t\mathscr{D}$ and E_B. (b) $\delta(E_B)$ as a function of E_B. Black empty circles represent the average deviation computed in the case of an unstable intermediate whereas grey circles stand for the case of a metastable intermediate. In the potential barrier, we have taken $\mu_A^0-\mu_C^0=k_BT$. For the metastable case, we have considered $\varepsilon^-=E_B+2k_BT$, and $\varepsilon^+=E_B+k_BT$.

Notice that the average deviation is smaller than 1 % for intermediate states with energy larger than 6,5k_BT and 8,5k_BT. The deviation is smaller than 10 % if the energy of the intermediate state is higher than 3k_BT and 5,5k_BT. For these energies, however, we find instantaneous deviations $\delta(t;E_B)$ of around 100 % and 60 %. Even for the unstable case shown in Fig. **A-4**(a), for an energy around 8k_BT the instantaneous deviation between both approaches for early stages is of 20 %. This confirms the fact that the largest difference between both approaches takes place at early stages of the processes.

A.5.3. Lost work

In Fig. **A-5**, we compare the lost work computed from Eqs. (A-20) and (A-21) for processes having unstable and metastable intermediate states. For both approaches, we obtain that the lost work decreases as the energy of the intermediate state E_B increases. Considering that $\mu_A^0-\mu_C^0=k_BT$ and using the initial condition $p(0,0)=\delta(0)$, we found that in the quasi-stationary approach the lost work converges to k_BT. For these processes (with unstable and metastable intermediate) the available free energy is completely dissipated in the process. To the contrary, in the mesocopic approach the lost work tends to $\exp((\mu_A^0-\mu_C^0))/k_BT)$ which is higher than the available energy. Therefore the system takes energy from the thermal fluctuations of the environment to cross the potential barrier thus explaining the higher dissipation observed in this case.

The quasi-stationary approach underestimates the value of the lost work. The origin of this discrepancy lies in the different nature of the kinetics of both approaches. In the mesoscopic approach, the state of the system undergoes by a diffusion process whereas the quasi-stationary approach is obtained by a coarse-graining of the diffusion kinetics that only considers the initial and final states thus ignoring the possibility of different paths connecting both states. This fact leads to an underestimation of the flux computed from the quasi-stationary approach, especially at early times of the process (see Fig. **A-4**) which implies a decrease of the entropy production and of the lost work. The lost work computed from the mesoscopic approach is larger than the one computed from the quasi-stationary approach for different values of $\Delta\mu^0=\mu_A^0-\mu_C^0$. The difference is, at least ek_BT:

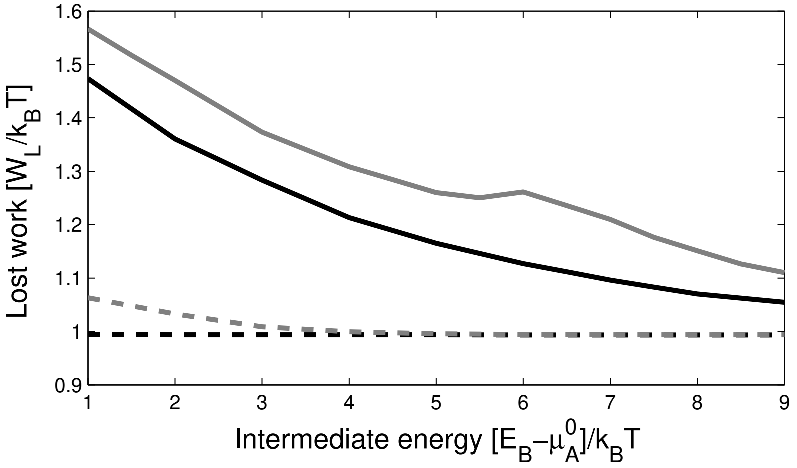

Fig. A-5.: The lost work W_L as a function of the intermediate energy E_B. The continuous line stands for the mesoscopic approach and the dashed lines for the quasi-stationary approach. The lost work for a process with an unstable intermediate is represented by a black line and that for a process with a metastable intermediate is represented by a gray line. To more clearly illustrate the behaviour, we have plotted the lost work for the mesoscopic approach as $W_L/\exp((\mu_A^0-\mu_C^0)/k_BT)$.

$$W_L(\Delta\mu^0) \geq W_L^{(qs)}(\Delta\mu^0) + ek_BT \tag{A-22}$$

This quantity has been computed analytically by using the quasi-stationary approach. In the mesoscopic approach, the lost work has been estimated as the sum of two contributions corresponding to the transit along the left and right hand sides of the barrier.

In Fig. **A-5**, we observe that for the mesoscopic approach with a metastable intermediate state (grey continuous line), the lost work is not a monotonous function of E_B since it exhibits a local minimum around $E_B = 6{,}5k_BT$. The minimum does not appear in the case of the quasi-stationary approach. The existence of the minimum is the signature of an increase of the thermodynamic and kinetic efficiencies of the process.

From this figure, one observes that when increasing the energy of the intermediate state, a reaction with an unstable intermediate and a sequential process with a metastable intermediate dissipate the same amount of energy.

A.6. Conclusions

In this Appendix, we have analyzed the relevance that the presence of intermediate states in the activation pathway has on reaction kinetics and on energy dissipation.The main results obtained are the following:

The probability density for the case of a metastable intermediate presents a slight accumulation around the gamma value where the metastable state is located (see Fig. **A-3**(b)). The fluxes and the entropy production show a non-monotonic behavior along the reaction coordinate γ (see Fig. **A-3**(d),(f)) while for the case of an unstable intermediate we found a monotonic behavior in γ and t (see Fig. **A-3**(c),(e)).

Our results show that at early stages the reaction flux strongly depends on the reaction coordinate (see Fig. **A-3**(c) and (d)) contrary to the assumption of the quasi-stationary approximation made to derive the LMA in which it is only a function of time [60]). When the height of the barrier increases the average deviation defined in Eq. A-18 decreases (see Fig. **A-4**(b)) and the quasi-stationary approximation becomes valid [2].

The lost work computed from the mesoscopic (Eq. A-2) and quasi-stationary (Eq. A-17) approaches are different. Their values obtained for processes with unstable and metastable states converge for high energies of the intermediate state. However, we have found that in both approaches this quantity depends on $\Delta\mu^0$ and it differs in a factor of approximately ek_BT. Furthermore, in processes with a metastable intermediate, the lost work computed from the mesoscopic approach shows a local minimum which runs contrary to its behavior in the quasi-stationary approach. The presence of this minimum is related to an increase in the efficiency of the process.

The results found for the reaction flux and the entropy production show that the presence of intermediate states may play an important role in the kinetics and energetics of enzymatic and organic reactions, RNA and protein folding and chemisorption processes. The mesoscopic approach presented thus provides a general framework to study the chemical kinetics of these processes.

Bibliography

[1] A Arango-Restrepo, J.M Rubi, and D Barragán. Kinetics and energetics of chemical reactions through intermediate states. *Physica A*, 509:86–96, 2018.

[2] Ignacio Pagonabarraga and J. M. Rubi. Fluctuating hydrodynamics approach to chemical reactions. *Physica A*, 237:205–219, 1997.

[3] David Reguera, J M Rubi, and A Pérez-Madrid. Fokker–planck equations for nucleation processes revisited. *Physica A: Statistical Mechanics and its Applications*, 259(1):10–23, 1998.

[4] D Reguera, JM Rubi, and A Pérez-Madrid. Kramers-type picture for crystal nucleation. *J. Chem. Phys.*, 109(14):5987–5993, 1998.

[5] Diwakar Shukla, Yilin Meng, Benoît Roux, and Vijay S Pande. Activation pathway of src kinase reveals intermediate states as novel targets for drug design. *Nature communications*, 5:3397, 2014.

[6] AW Castleman and KHa Bowen. Clusters: Structure, energetics, and dynamics of intermediate states of matter. *The Journal of Physical Chemistry*, 100(31):12911–12944, 1996.

[7] Peter L Privalov. Intermediate states in protein folding. *Journal of molecular biology*, 258(5):707–725, 1996.

[8] Per Jemth, Stefano Gianni, Ryan Day, Bin Li, Christopher M Johnson, Valerie Daggett, and Alan R Fersht. Demonstration of a low-energy on-pathway intermediate in a fast-folding protein by kinetics, protein engineering, and simulation. *Proceedings of the National Academy of Sciences of the United States of America*, 101(17):6450–6455, 2004.

[9] Gregory R Bowman and Vijay S Pande. Correction for Bowman et al., Protein folded states are kinetic hubs. *Proceedings of the National Academy of Sciences*, 107(38):16749–16749, 2010.

[10] Frank Noé and Stefan Fischer. Transition networks for modeling the kinetics of conformational change in macromolecules. *Current opinion in structural biology*, 18(2):154–162, 2008.

[11] Steven D Schwartz and Vern L Schramm. Enzymatic transition states and dynamic motion in barrier crossing. *Nature chemical biology*, 5(8):551–558, 2009.

[12] Andrew J Baldwin and Lewis E Kay. Nmr spectroscopy brings invisible protein states into focus. *Nature chemical biology*, 5(11):808–814, 2009.

[13] Jie-rong Huang, Timothy D Craggs, John Christodoulou, and Sophie E Jackson. Stable intermediate states and high energy barriers in the unfolding of gfp. *Journal of molecular biology*, 370(2):356–371, 2007.

[14] A Cassuto and David A King. Rate expressions for adsorption and desorption kinetics with precursor states and lateral interactions. *Surface Science*, 102(2-3):388–404, 1981.

[15] Anthony L Fink. Compact intermediate states in protein folding. *Annual review of biophysics and biomolecular structure*, 24(1):495–522, 1995.

[16] Kazuo Fujiwara, Munehito Arai, Akio Shimizu, Masamichi Ikeguchi, Kunihiro Kuwajima, and Shintaro Sugai. Folding- unfolding equilibrium and kinetics of equine beta-lactoglobulin: Equivalence between the equilibrium molten globule state and a burst-phase folding intermediate. *Biochemistry*, 38(14):4455–4463, 1999.

[17] Gayathri Swaminath, Yang Xiang, Tae Weon Lee, Jacqueline Steenhuis, Charles Parnot, and Brian K Kobilka. Sequential binding of agonists to the beta2 adrenoceptor kinetic evidence for intermediate conformational states. *Journal of Biological Chemistry*, 279(1):686–691, 2004.

[18] Shi-Jie Chen. Rna folding: conformational statistics, folding kinetics, and ion electrostatics. *Annu. Rev. Biophys.*, 37:197–214, 2008.

[19] John E McMurry. *Organic chemistry*. Cengage Learning, 2015.

[20] Mary K Campbell and Shawn O Farrell. Biochemistry, brooks. *Cole, Belmont, CA*, 2011.

[21] Qi Chen, Ramon Groote, Holger Schönherr, and G Julius Vancso. Probing single enzyme kinetics in real-time. *Chemical Society Reviews*, 38(9):2671–2683, 2009.

[22] Gemma L Holliday, Daniel E Almonacid, John BO Mitchell, and Janet M Thornton. The chemistry of protein catalysis. *J. Mol. Biol.*, 372(5):1261–1277, 2007.

[23] Adam JT Smith, Roger MuÌˆller, Miguel D Toscano, Peter Kast, Homme W Hellinga, Donald Hilvert, and KN Houk. Structural reorganization and preorganization in enzyme active sites: comparisons of experimental and theoretically ideal active site geometries in the multistep serine esterase reaction cycle. *Journal of the American Chemical Society*, 130(46):15361–15373, 2008.

[24] Anders Lervik, Dick Bedeaux, and Signe Kjelstrup. Kinetic and mesoscopic non-equilibrium description of the ca2+ pump: a comparison. *Eur. Biophys. J.*, 41(5):437–448, 2012.

[25] David A King. The influence of weakly bound intermediate states on thermal desorption kinetics. *Surface Science*, 64(1):43–51, 1977.

[26] R Gorte and LD Schmidt. Desorption kinetics with precursor intermediates. *Surface Science*, 76(2):559–573, 1978.

[27] Dechang Li, Ming S Liu, and Baohua Ji. Mapping the dynamics landscape of conformational transitions in enzyme: the adenylate kinase case. *Biophysical journal*, 109(3):647–660, 2015.

[28] M. J. O'Neill and E. S. Watson. Differential microcalorimeter, August 2 1966. US Patent 3,263,484.

[29] Julian M Sturtevant. Biochemical applications of differential scanning calorimetry. *Annual review of physical chemistry*, 38(1):463–488, 1987.

[30] L Feng and JD Andrade. Protein adsorption on low-temperature isotropic carbon: I. protein conformational change probed by differential scanning calorimetry. *Journal of Biomedical Materials Research Part A*, 28(6):735–743, 1994.

[31] Terell L. Hill. *Free Energy Transduction and Biochemical Cycle Kinetics*. 1989.

[32] Xavier Turon, Orlando J Rojas, and Randall S Deinhammer. Enzymatic kinetics of cellulose hydrolysis: a qcm-d study. *Langmuir*, 24(8):3880–3887, 2008.

[33] Jeffrey K. Weber, Diwakar Shukla, and Vijay S. Pande. Heat dissipation guides activation in signaling proteins. *PNAS*, 112(33):10377–10382, 2015.

[34] Waage P Guldberg. Videnskabs-selskabet i christiana, 1864.

[35] Miloslav Pekar. Thermodynamics and foundations of mass-action kinetics. *Progress in Reaction Kinetics and Mechanism*, 30(1-2):3–113, 2005.

[36] Sybren Ruurds De Groot and Peter Mazur. *Non-equilibrium thermodynamics*. Dover Publications Inc., 1985.

[37] D Reguera, JM Rubi, and JMG Vilar. The mesoscopic dynamics of thermodynamic systems. *J. Phys. Chem. B*, 109(46):21502–21515, 2005.

[38] José MG Vilar and J M Rubi. Thermodynamics “beyond” local equilibrium. *PNAS*, 98(20):11081–11084, 2001.

[39] Hendrik Anthony Kramers. Brownian motion in a field of force and the diffusion model of chemical reactions. *Physica*, 7(4):284–304, 1940.

[40] D Bedeaux, I Pagonabarraga, J M Ortiz De Zárate, JV Sengers, and S Kjelstrup. Mesoscopic nonequilibrium thermodynamics of non-isothermal reaction-diffusion. *Physical Chemistry Chemical Physics*, 12(39):12780–12793, 2010.

[41] I Pagonabarraga and JM Rubi. Derivation of the langmuir adsorption equation from non-equilibrium thermodynamics. *Physica A*, 188(4):553–567, 1992.

[42] David Reguera and J M Rubi. Homogeneous nucleation in inhomogeneous media. i. nucleation in a temperature gradient. *The Journal of chemical physics*, 119(18):9877–9887, 2003.

[43] David Reguera and JM Rubi. Homogeneous nucleation in inhomogeneous media. ii. nucleation in a shear flow. *J. Chem. Phys.*, 119(18):9888–9893, 2003.

[44] G Gomila, A Pérez-Madrid, and JM Rubi. Non-equilibrium thermodynamics of thermionic emission processes in abrupt semiconductor junctions, including the effects of surface states. *Physica A*, 233(1-2):208–220, 1996.

[45] D Bedeaux, S Kjelstrup, and JM Rubi. Nonequilibrium translational effects in evaporation and condensation. *J. Chem. Phys.*, 119(17):9163–9170, 2003.

[46] JM Rubi and Signe Kjelstrup. Mesoscopic nonequilibrium thermodynamics gives the same thermodynamic basis to butler- volmer and nernst equations. *J. Phys. Chem. B*, 107(48):13471–13477, 2003.

[47] JM Rubi, D Bedeaux, and S Kjelstrup. Unifying thermodynamic and kinetic descriptions of single-molecule processes: Rna unfolding under tension. *J. Phys. Chem. B*, 111(32):9598–9602, 2007.

[48] Signe Kjelstrup, J Miguel Rubi, and Dick Bedeaux. Energy dissipation in slipping biological pumps. *PCCP*, 7(23):4009–18, 2005.

[49] G. J M Koper, J. Boekhoven, W. E. Hendriksen, J. H. Van Esch, R. Eelkema, I. Pagonabarraga, J. M. Rubí, and D. Bedeaux. The Lost Work In Dissipative Self-Assembly. *Int. J. Thermophys.*, 34(7):1229–1238, 2013.

[50] Leonor Menten and MI Michaelis. Die kinetik der invertinwirkung. *Biochem Z*, 49:333–369, 1913.

[51] Inc MathWorks. *MATLAB: the language of technical computing. Desktop tools and development environment, version 7*, volume 9. MathWorks, 2005.

[52] Vassilis J. Inglezakis and Antonis A. Zorpas. Heat of adsorption, adsorption energy and activation energy in adsorption and ion exchange systems. *Desalination and Water Treatment*, 39(1-3):149–157, 2012.

[53] Mohamed Ahmed Mahmoud. Kinetics and thermodynamics of U(VI) ions from aqueous solution using oxide nanopowder. *Process Safety and Environmental Protection*, 102(2):44–53, 2016.

[54] Athi N Naganathan, Urmi Doshi, and Victor Muñoz. Protein folding kinetics: Barrier effects in chemical and thermal denaturation experiments. *Journal of the American Chemical Society*, 129(17):5673–5682, 2007.

[55] Sheila S. Jaswal, Stephanie M.E. Truhlar, Ken A. Dill, and David A. Agard. Comprehensive analysis of protein folding activation thermodynamics reveals a universal behavior violated by kinetically stable proteases. *Journal of Molecular Biology*, 347(2):355–366, 2005.

[56] Francesco Mallamace, Carmelo Corsaro, Domenico Mallamace, Sebastiano Vasi, Cirino Vasi, Piero Baglioni, Sergey V. Buldyrev, Sow-Hsin Chen, and H. Eugene Stanley. Energy landscape in protein folding and unfolding. *Proceedings of the National Academy of Sciences*, 113(12):3159–3163, 2016.

[57] Ayman D. Allian, Kazuhiro Takanabe, Kyle L. Fujdala, Xianghong Hao, Timothy J. Truex, Juan Cai, Corneliu Buda, Matthew Neurock, and Enrique Iglesia. Chemisorption of CO and mechanism of CO oxidation on supported platinum nanoclusters. *Journal of the American Chemical Society*, 133(12):4498–4517, 2011.

[58] Toribio F. Otero, J. J. Ruiz, L. Camacho, R. Rodríguez-Amaro, J. G. Martinez, R. Z. Pytel, S. R. Lafontaine, P. A. Wieringa, and I. W. Hunter. Reactions driving conformational movements (molecular motors) in gels: conformational and structural chemical kinetics. *Phys. Chem. Chem. Phys.*, 19(3):1718–1730, 2017.

[59] RC Bansal, FJ Vastola, and PL Walker Jr. Kinetics of chemisorption of oxygen on diamond. *Carbon*, 10(4):443–448, 1972.

[60] Andrés Arango-Restrepo and J M.iguel Rubi. Non-isothermal activation kinetics. *CMST*, 23(3):155–163, 2017.

B. Appendix: Entropic transport in a crowded medium

To know how liquid matter moves through a crowded medium due to the action of a force constitutes currently a problem of great practical importance, present in cases as diverse as the transport of particles through a cell membrane and through a particulate porous medium. To calculate the mass flow through the system, we present an approach that emulates the texture of the medium by using entropic barriers that particles must overcome in order to move. The model reproduces the scaling behavior of the velocity with the force found in many systems in order to show how the scaling exponent depends on the micro-structure of the medium. Our model offers a new perspective able to characterize the flow of matter through the medium, and may be useful in studies of nano-fluids, oil recovery, soil drainage, tissue engineering and drug delivery.

This Appendix was published in *the Journal of Chemical Physics*, **153**,034108, (2020). Ref.[1]

B.1. Introduction

To know how liquid matter moves through the interstices of a crowded medium composed of a random distribution of obstacles is a basic problem usually found in transport through cellular and synthetic membranes and tissues, soils and in porous media in general [2, 3, 4, 5, 6, 7, 8]. What the mass flux through the medium induced by an external driving force is, and how it depends on the micro-structure of the medium are fundamental questions in many physico-chemical and biological processes as well as in technological applications.

The flow through the medium exhibits a wide variety of behaviors to the application of a driving force. Experiments performed with different liquid phases and crowded media such as in synthetic polymer membranes, aquaporin-based cell membranes, tissues and particulate solid media [9, 10, 11], show that in general the velocity of the fluid v scales as: $v \propto (\Delta P)^{\alpha}$ where ΔP is the imposed pressure difference and α a scaling exponent. The linear case $\alpha = 1$ corresponds to Darcy's law [12]: $v = \frac{k}{\eta}\Delta P$ where k and η are the permeability and viscosity respectively assumed constant whereas $\alpha \neq 1$ characterizes non-Darcy regimes [13].

Lattice Boltzmann simulations of a pore network [14] and non-equilibrium thermodynamics models [15, 16] have been used to reproduce steady-state flows, and to show the existence of non-Darcy regimes. For crowded media modeled by channels of a constant cross-sectional area, stochastic models have been proposed to compute the velocity of tagged particles [17, 3]. Flow through a crowded medium has also been analyzed under the perspective of random walks in which fluctuations are not of thermal origin but generated by the randomness of the channel distribution [18, 19, 20]. Averages of the different quantities are thus calculated over a statistical ensemble characterized by a probability distribution. It was shown in Refs. [18] that if the porous medium is isotropic and homogeneous the probability is a Gaussian, and the resulting average velocity is linear in the pressure drop, thus fulfilling Darcy's law.

The complex micro-structure of crowded media results in an irregular landscape of empty spaces through which particles may move leading to an inhomogeneous distribution of micro-states, and consequently to a position-dependent entropy. These entropy variations induce entropic forces that may hamper (in the case of constrictions in the pores) or promote (in the case of apertures) the motion of the particles [21, 22, 23]. It has been shown that the presence of these forces play an important role in diffusion through an ordered distribution of solid particles mimicking a crowded medium [24, 25].

In this Appendix, we show that modeling local variations of the geometry of the medium by entropic barriers enables us to know the impact of the micro-structure of the medium on the flow of matter through it induced by a driving force. Our model allows us to reproduce the scaling behavior of the velocity in terms of the force observed in the experiments performed in very different systems.

The Appendix is organized as follows. In Section II, we describe the crowded medium micro-structure and present the entropic barriers model from which we can compute the velocity that in general fulfills a scaling low in terms of the applied force. In Section III, we compare our results with experiments. Finally, in Section IV, we present our main conclusions.

B.2. Model

B.2.1. Crowded medium micro-structure

Let us consider a cube-shaped piece of material of side R and length L whose internal structure can be modeled by a set of N channels uniformly distributed, as shown in Fig.**B-1**(a), through which a suspension of tagged particles may flow under the action of an applied force F.

The micro-structure of a crowded medium is usually given through statistical properties of the distribution of lengths and widths of the pores or sizes of the particles constituting the medium. In Refs.[25, 24] the interstices of a porous medium composed of solid spheres are modeled by periodic channels. This periodicity results from the fact that the medium is composed of a large number of objects and voids which sequentially alternate.

We will assume that the shape of the channel is modeled by a periodic function or by a random function (see Fig.**B-2**). Periodicity requires that the radius of the n channel r_n fulfills the relation: $r_n(x) = r_n(x+l_n)$ where l_n is the period. To simplify our analysis of the particle transport, we have modeled the channels by simple relationships between r_n and l_n, with l_n randomly distributed. We will show that this choice reproduces different behaviors observed experimentally.

The volume occupied by the N channels is $V_p = \sum_{n=1}^{N} V_n$, with $V_n = L/l_n \int_0^{l_n} \pi r_n(x)^2 dx$. We assume that the length of the periods is randomly distributed. For sufficiently large numbers of channels, the volume can be expressed as

$$V_p = N \int_{l_0}^{L} \frac{L}{l_n} \left(\int_0^{l_n} \pi r_n(x;l_n)^2 dx \right) \rho(l_n) dl_n \tag{B-1}$$

where $\rho(l_n)$ is the period probability distribution and l_0 the minimum period. To consider variations along different length scales in the sizes of the objects, and of the free spaces constituting the crowded medium and thus in the period l_n, we suppose that the length of the periods follows a log-normal distribution [26]:

$$\rho(l_n) = \frac{1}{l_n \sigma \sqrt{2\pi}} \exp\left(- \left(\frac{\ln(l_n/l)}{\sqrt{2}\sigma} \right)^2 \right) \tag{B-2}$$

where $\ln(l)$ is the mean and σ the standard deviation. The fluctuating area of the pores in a cross-section at position x, $A(x) \equiv \pi \sum_{n=1}^{N} r_n^2(x)$, where r_n is a sinusoidal function, is represented in Fig.**B-1**(b).

The expression for the volume V_p in terms of the dimensionless variables $\hat{x} \equiv x/l_n$ and $\hat{r} \equiv r_n/l_n$ is

$$V_p = NL \int_{l_0}^{L} l_n^2 \left(\int_0^1 \pi \hat{r}(\hat{x})^2 d\hat{x} \right) \rho(l_n) dl_n \tag{B-3}$$

Since $\hat{r}$ does not depend on l_n, the integrals can be solved separately to obtain

$$V_p = NLl^2 \xi \exp(2\sigma^2) \tag{B-4}$$

for $L \gg l$ and $l_0 \ll l$, where $\xi \equiv \pi \overline{\hat{r}^2}$ (with $\overline{\hat{r}^2} \equiv \int_0^1 \hat{r}(\hat{x})^2 d\hat{x}$) is the average cross-sectional area of the

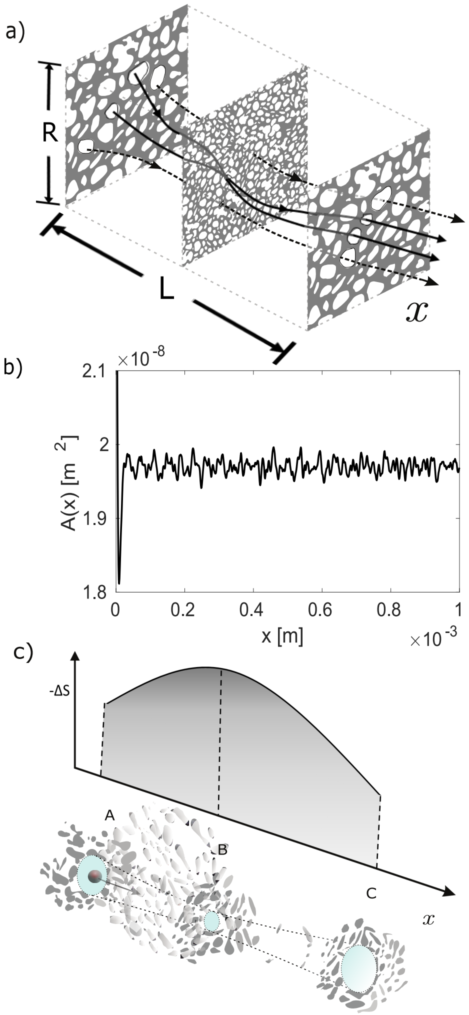

Fig. B-1.: Microstructure of a crowded medium and its characterization by means of entropic barriers. a) Cross sections at different positions. Continuous and dashed lines represent paths that intersect and do not intersect, respectively. The average trajectory of a particle in parallel and unconnected channels is represented by dashed lines while continuous lines represent the trajectory in connected channels. b) Area occupied by the channels as a function of x. c) Shape of a channel and its associated entropic barrier from position A to C $\Delta S(x) = k_B \ln(a_n/l_n^2)$ with $a_n \equiv \pi r_n(x)^2$ the cross-sectional area. The maximum height of the barrier takes place at B where the constriction is more pronounced.

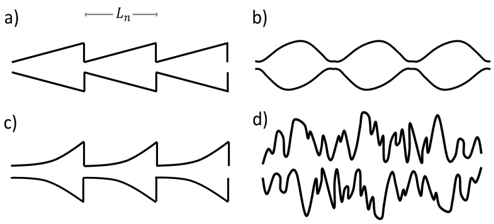

Fig. B-2.: Micro-structure of the channels. (a) Conical: $r_n/l_n = mx/l_n + b$. (b) Sinusoidal: $r_n/l_n = m\sin(2\pi x/l_n) + b$. (c) Exponential: $r_n/l_n = b\exp(mx/l_n)$. (d) Random. The structures are characterized by the parameters m and b. Negative values of m describe a shrink of the linear and exponential channels

channel. By considering that on average $\sqrt{N}$ channels can be aligned in a strip of length R and that the separation among those channels is proportional to the lineal porosity ($\varepsilon^{1/3}$), we have $R = \sqrt{N} l \hat{r} \varepsilon^{-1/3}$ and then: $N = (R/l)^2 \varepsilon^{2/3}/\bar{\hat{r}}^2$. Substituting this relation in V_p, considering the porosity $\varepsilon \equiv V_p/R^2 L$ and solving for ξ, we obtain an expression for the dimensionless cross-sectional area as a function of the medium geometry

$$\xi = \varepsilon^{1/3} \bar{\hat{r}}^2 \exp(-2\sigma^2) \tag{B-5}$$

where $max(d\bar{r}/d\hat{x})^2 = \gamma$, with $\gamma \ll 1$ [27]. The expressions for ξ and γ are used to find the constants b y m linking the shape of the channel with the crowded media architecture. For instance, for an exponential channel (Fig.**B-2**(c)) we have that: $\xi = \pi b^2(\exp(2m) - 1)/2m$, and $\gamma = (mb)^2 \exp(2m)$ for $m > 0$ or $\gamma = (mb)^2$ for $m < 0$.

B.2.2. Kinetics

To analyze the transport of the fluid through the medium, we will adopt the stochastic approach proposed in [18, 19] for which small volume elements of the fluid containing many molecules, or fluid particles, move affected by the randomness of the medium. Transport of these particles is thus described by means of a probability distribution which obeys a kinetic equation of the Fokker-Planck type. In the case of crowded medium being isotropic and homogeneous, the probability is a Gaussian, similarly to the case of Brownian motion in which randomness is due to thermal fluctuations.

We will first compute the velocity of the fluid particles through a single channel of non-constant cross-sectional area and subsequently average the result over a random distribution of sizes of the channels. When the corrugated channel is sufficiently narrow, the particle probability distribution equilibrates much faster in the transverse directions than along the transport direction, reaching a local equilibrium distribution. One can thus perform a coarse-graining description in which the motion is practically 1-d and the particles proceed through entropic barriers resulting from the irregularities in the shape of the channel [21, 27] driven by an external force [23]. The probability distribution $p(x,t)$ obeys the Fick-Jacobs equation.

$$\frac{\partial p(x,t)}{\partial t} + v\frac{\partial p}{\partial x} = \frac{\partial}{\partial x}\left(D\frac{\partial p}{\partial x} + \frac{Dp}{k_B T}\frac{\partial G}{\partial x}\right) \tag{B-6}$$

where v is the velocity of the fluid and D a local diffusion coefficient accounting for an effective diffusion mediated by the presence of variations of the cross-sectional area of the channel through its local slope. Its expression resulting from the coarse-graining description was given in [21]. In our case one has: $D(x) = D_0\left(1+(d\bar{\hat{r}}/d\hat{x})^2\right)^{-1/2}$, with D_0 the diffusion coefficient in absence of entropic barriers [28]. It has been shown [21] that the introduction of a spatially-dependent diffusion coefficient $D(x)$ in Eq. (6) improves the results of the transport coefficient [21, 23]. The free energy is given by $G = H - TS$, where $H = \frac{M}{2}v^2 + \int F dx$ is the enthalpy, with M the mass of the moving particles, and S the entropy which is nonconstant (see Fig.**B-1**(c)) due to the irregularities in the shape of the channels: $S(\hat{x}) = k_B \ln(\pi\hat{r}^2(\hat{x}))$. Variations of the entropy through the medium gives rise to the presence of entropic forces [21].

The Fick-Jacobs equation is strictly valid for sufficiently small slopes of the channels, $\gamma \ll 1$. However, its validity extends to higher values of γ with a very small error in the mobility of the particles with respect to Brownian dynamics simulation results [27].

The relative importance of the different terms of Eq.(B-6) can be analyzed by expressing it in dimensionless form. To this purpose, we introduce the Péclet number, $Pe \equiv vl/D$, the dimensionless force $f \equiv Fl/k_BT$, the dimensionless number $I \equiv l^3\rho v^2/k_BT$, comparing kinetic energy with thermal energy and the dimensionless number $\Sigma \equiv 2\gamma^{1/2}/\delta$ accounting for entropic effects, with $\delta \equiv min(\hat{r})$. In many experimental situations such as flow though porous media with low porosity [9, 10], tissues [29] and biological membranes [30] among others, the velocity of the fluid is very small, of the order of $1-100nm/s$, the characteristic lengths vary from 0,1 to $100\mu m$ and $D_0 \approx 10^{-11}m^2/s$. We then conclude that Reynolds numbers are $Re \approx 10^{-7}$, $Pe \approx 10^{-2}$, $I \approx 10^{-9}$, $f \approx 10$ and $\Sigma \approx 20$. Therefore, in these cases external and entropic forces dominate over the remaining contributions to the kinetics which makes that Eq.(B-6) reduces to

$$\frac{\partial p(x,t)}{\partial t} = \frac{\partial}{\partial x}\left(D\frac{\partial p}{\partial x} + \frac{Dp}{k_BT}\frac{\partial G}{\partial x}\right) \tag{B-7}$$

The average of the dimensionless velocity can be computed from the distribution of mean-first passage times [23] or through the calculation of the particle diffusion current [27] of Eq.(B-7), arriving at the same result:

$$\langle\dot{\hat{x}}\rangle = \frac{1-exp(-f)}{\int_0^1 d\hat{x}\exp(-\hat{G}(\hat{x}))\int_{\hat{x}}^{\hat{x}+1} d\hat{z}\hat{D}(\hat{z})^{-1}\exp(\hat{G}(\hat{z}))} \tag{B-8}$$

where $\hat{z} \equiv z/l_n$, and $\hat{G}(\hat{x}) = -f\hat{x} - TS(\hat{x})$ is the dimensionless free energy.

In Fig.**B-3**, we show how $\langle\dot{x}\rangle$ behaves as a function of the force f for the exponential channel in Fig. **B-2**. A linear behavior is observed for sufficiently small and high values of f whereas at intermediate values of the force and small enough values of ξ, the behavior is nonlinear. To compute the average particle velocity in an exponential channel, we use the relation $r_n/l_n = b\exp(mx/l_n)$ in Eq.(B-8) and perform a series expansion of $\hat{D}$ for small values of $|m|$, obtaining:

$$\langle\dot{\hat{x}}\rangle \approx \frac{(1-\exp(-f))(f+2m)}{(1-\exp(-(f+2m)))} \tag{B-9}$$

where $|m| = (\gamma/2\xi)^{1/3}$. From this expression, we conclude that for high enough values of f, the linear behavior is shifted to the right in the amount of $2|m|$, as observed in the experiments of fluid flow through sand and clay [9]. There exists a threshold value of the force f_0 that separates two regimes, one in which the velocity is practically zero (diffusion dominates) and other in which the force causes a significant increment in the particle velocity (biased diffusion dominates), in agreement with the experiments performed in sand and clay [31, 32].

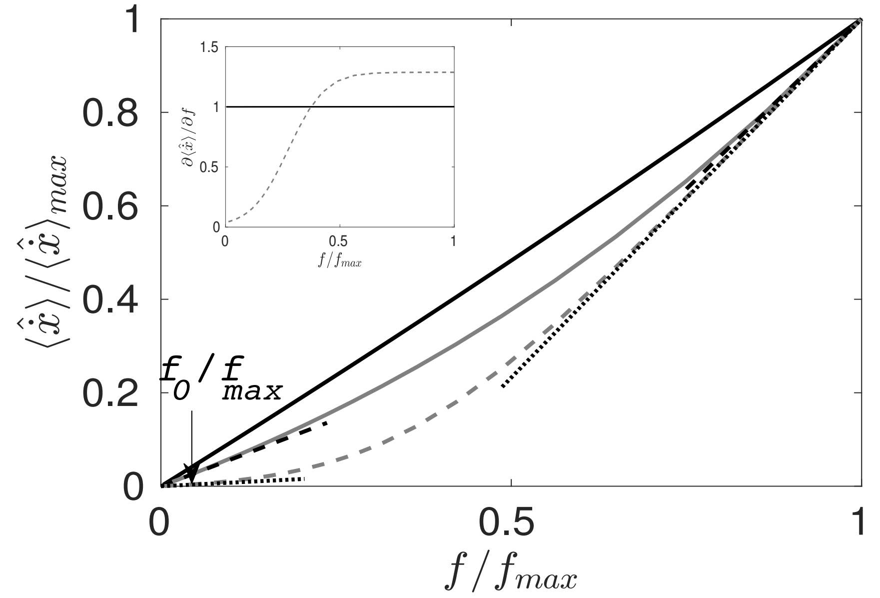

Fig. B-3.: Normalized dimensionless particle velocity $\langle\hat{x}\rangle/\langle\hat{x}\rangle_{max}$ for the exponential channel of Fig. **B-2** as a function of the normalized external force f/f_{max} for different values of ξ, with $f_{max} = 2\gamma/\xi$. Continuous black, gray and dashed gray lines correspond to ξ equal to $1{,}0 \times 10^{-2}$, $2{,}1 \times 10^{-3}$, $4{,}2 \times 10^{-4}$, respectively. Black dashed and dotted lines denote the linear regime. In the non-linear regime $\langle\hat{x}\rangle \propto f^{\alpha}$. For $\xi = 2{,}1 \times 10^{-3}$ and $\xi = 4{,}2 \times 10^{-4}$, we obtain α equal to 1,5 and 2, respectively. In the inset, we represent the differential mobility $\partial\langle\hat{x}\rangle/\partial f$ for $\xi = 1{,}0 \times 10^{-2}$ (continuous black line) and for $\xi = 4{,}2 \times 10^{-4}$ (dashed gray line).

The total flux through a medium composed of parallel channels can be computed as in the case of an electrical current passing through a set of parallel conductors subjected to a common potential difference. The total flow Q is the sum over the N channels of the flow along each channel $Q_n = \xi l_n^2 v_n$. The average velocity through the medium $v_= \equiv Q/N\xi l^2$ is then given by

$$v_= \equiv \frac{1}{N}\sum_{n=1}^{N} v_n \left(\frac{l_n}{l}\right)^2 \tag{B-10}$$

where $v_n = \frac{D_0}{l_n}\langle\hat{x}\rangle$. In the case of intersecting channels, similar to a series circuit in which the inverse of the total flow $1/Q$ is the sum over the N channels of the inverse of the flow through each channel $1/Q_n$, we obtain the expression for the average velocity through the medium:

$$\frac{1}{v_{\neq}}\frac{1}{N} \equiv \sum_{n=1}^{N} \frac{1}{v_n}\left(\frac{l}{l_n}\right)^2 \tag{B-11}$$

By considering that the crowded medium is composed of a large number of channels whose periods are distributed according with the log-normal distribution (Eq.(B-2)), the average velocity of the particles flowing through the medium is

$$v_{=,\neq} \equiv \left[\int_0^\infty \left(v_n\left(\frac{l_n}{l}\right)^2\right)^{\pm 1} \rho(l_n)dl_n\right]^{\pm 1} \tag{B-12}$$

where the plus symbol in the exponent stands for unconnected channels and the minus for interconnected channels. By performing the integral of this expression, one obtains

$$v_{=,\neq} = \frac{D_0}{l}\langle\hat{x}\rangle \exp(\pm\sigma^2/2) \tag{B-13}$$

From this expression, we conclude that the average velocity in a medium constituted by unconnected channels increases with σ^2 since a high disorder entails wider channels while just the opposite behavior occurs for connected channels.

When the distribution of periods is a normal distribution, one gets: $v \approx \frac{D_{0,eff}}{l}\langle\hat{x}\rangle\left(1+\frac{\sigma}{l}\sqrt{\frac{2}{\pi}}\exp(-(\frac{l}{\sigma})^2)\right)^{\pm 1}$ which increases or decreases more smoothly with σ than in the case of a log-normal distribution. We then conclude that the period distribution related to the pore-size distribution, affects the magnitude of the velocity but not its behavior with the force, in accordance with Ref. [33].

The case of a homogeneous and isotropic random medium considered in [18] can be analyzed by means of our model. For a fixed value of the period of the channels, the standard deviation σ vanishes and Eq.B-13 gives $v = \frac{D_{0,eff}}{l}\langle\hat{x}\rangle$. If in addition the cross-sectional area of the channel is constant, Eq. B-8 reduces to $\langle\hat{x}\rangle = 1-\exp(-f))$ which for $f \ll 1$, leads to a Darcy-like behavior of the average velocity in terms of an external pressure difference: $v = \frac{k}{\eta}\Delta P$, with $k = r^2/6\pi a$ and a the effective radius of the particle, according to Ref.[18]. Darcy's behavior for the velocity can also be reproduced from our model at high values of ξ, i.e. high porosity and large standard deviation of the size distribution of the objects composing the medium (fibers, proteins, solid particles, etc.). A linear behavior of the velocity in terms of temperature and chemical potential gradients, considered as driving forces, has also been found in the flow through synthetic polymer membranes [34], cell membranes composed by aquaporins [35] and in chemotaxis in solid particulate media [36].

For a range of values of the force used in the experiments, model results obtained from Eq. (B-13) can also be represented by the power law:

$$v(f) \propto f^{\alpha} \tag{B-14}$$

where the exponent α follows by fitting the results of the velocity obtained from Eq. (B-13) with the power law Eq. (B-14). Experimentally, α usually varies between $3/4$ and $5/2$. The exponent is mainly affected by the parameter ξ which depends on the microstructure of the medium. The scaling law proposed is useful to quantify deviations from the linear behavior given by Darcy's law.

B.3. Results

To test the validity of our model, we have applied it to the cases of: i) water and heavy oil flowing through a solid particulate medium composed of sand and/or clay particles, ii) serum flow through hepatoma tissue (carcinogenic tumor) and subcutaneous tissue, iii) ringer solution and paraffin oil flowing through a synovial membrane, and iv) water flowing through a corneal membrane, where experimental results are available. In all these cases the flow is induced by a pressure gradient that can be osmotic, intra-articular or imposed. Comparison with experiments is made by tuning ξ, the average period l which is related to the average size of the constituents making up the medium (solid particles in particulate medium, proteins in biological membranes and interstices in tissues) and the standard deviation σ. Values of these parameters are given in Table **B-1** for both, unconnected and connected channels.

Tab. B-1.: Representative parameter values for the analyzed media*

Medium	α	$\xi \times 10^{-6}$	$l_{\neq}[\mu m]$	$l_{=}[\mu m]$	$\sigma^2_{\neq}$	$\sigma^2_{=}$
[a]Sand	0.93	3.5	100	240	2.0	0.2
[b]Clay$_A$	1.40	33	55	130	1.7	1.1
[b]Clay$_B$	1.60	69	7.2	54.0	1.3	1.7
[b]Sand	1.74	176	10	12.7	0.6	0.2
[c]Hepatoma	0.85	11	7.5	1.01	2.5	1.7
[c]Subcutaneous	1.88	62	3.4	0.29	2.2	1.4
[d]synovial	2.45	123	2.5	0.39	1.9	2.1
[e]synovial	0.75	11	8.4	1.02	1.9	1.9
[b]Cornea$_C$	0.93	1100	0.4	0.03	0.6	2.0
[b]Cornea$_D$	0.79	340	0.5	0.05	1.0	2.1

[a] Heavy oil in, [b] Water in, [c] Serum in,[d] Ringer solution in, [e] Paraffin oil in, A : Standard clay,B : Artificial clay, C,D : relative hydration of the cornea 3,7 and 3,2, respectively. $_{\neq}$ connected and $_{=}$ unconnected set of channels. *.

In the study cases, the force F acting on the tagged particles is given by the product between the pressure difference ΔP and the average cross-sectional area $l^2\xi$. The dimensionless force $f = Fl/k_BT$ given previously becomes

$$f = \frac{l^3 \xi \Delta P}{k_B T} \tag{B-15}$$

with $\Delta P = L\nabla P$. Here we can recognize the term $l^3\Delta P$ as the energy change at constant volume due to pressure changes.

By considering periodic exponential channels, we compute from Eq.(B-8) the average velocity through a single channel. We then substitute the result into Eq.(B-13) to obtain the average velocity across the medium as a function of the force which is related to the pressure difference through Eq.(B-15).

In Figs. **B-4** and **B-5**, we have represented the velocity as a function of ∇P obtained from our model for the cases mentioned above and found a very good agreement with the experimental data. In the figures, we illustrate how our model reproduces the experimental behavior of the velocity by fitting the parameter ξ which represents the average cross-sectional area of the channels. The average channel period $l_{\neq,=}$ and the standard deviation $\sigma_{\neq,=}$ of the channel period distribution are used to scale the velocity and the pressure gradient.

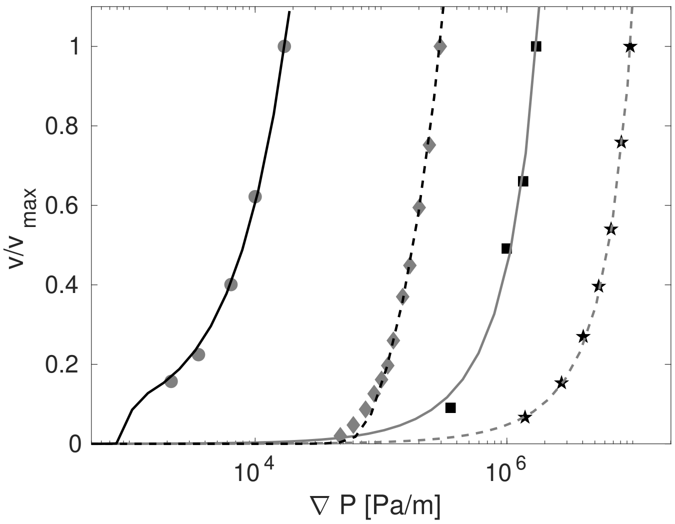

Fig. B-4.: Normalized velocity v/v_{max} versus pressure gradient ∇P. Black and gray continuous lines correspond to the model results for heavy oil and water through sand, respectively. Black and gray dashed lines represent the model results for water through standard and artificial clay. Filled circles, diamonds, squares and stars denote the experimental data obtained in Refs. [9, 10]. The values of the exponent α are 0,93, 1,4, 1,6 and 1,74, respectively. The maximum velocities reached v_{max} are 2,5, 32, 600 and 700 nm/s, respectively.

For high enough experimental values of the applied force, the velocity fulfills the scaling law $v \propto (\Delta P)^{\alpha}$ where the exponent α depends on the micro-structure of the medium (in accordance with Ref. [38]) through ξ and therefore on the distribution of entropic barriers. The scaling law, and in particular the values of the exponent α, summarizes the model results for the range of pressure gradients used in the experiments. In the cases analyzed, we have found that α varies between $3/4$ and $5/2$. Notice that for low forces, the velocity is constant and tends to zero because diffusion and capillary effects dominate the kinetics.

As concluded from Table **B-1**, α increases as ξ increases or equivalently when the height of the entropic barriers diminishes thereby facilitating the transit of particles through the channels. Moreover, the exponent increases as the average length of l decreases and the standard deviation of the distribution σ increases, in the case of inter-connected channels, or decreases for unconnected channels. We can then conclude that when the medium is modeled by a set of connected channels and consists of big constituents (large l) whose sizes vary along several length scales (large σ), the entropic barriers are high (low ξ) enough to hamper the motion of the particles. This behavior is also found for unconnected channels and big constituents whose sizes do not vary significantly (small σ).

In Table **B-1**, we can see the difference between the values of l and σ for unconnected and connected channels configurations. The average length of the unconnected channels $l_=$ is more sensitive to the nature of the medium than the average length of the connected channels $l_{\neq}$. In the case of sand and clay media, $l_=$ and $\sigma^2_{\neq}$ are larger than $l_{\neq}$ and $\sigma^2_{=}$, respectively. Just the opposite is true for tissues and biological membranes. From the estimated values of $\sigma_=$ and $\sigma_{\neq}$ presented in Table **B-1**, we may conclude that sand and clay media

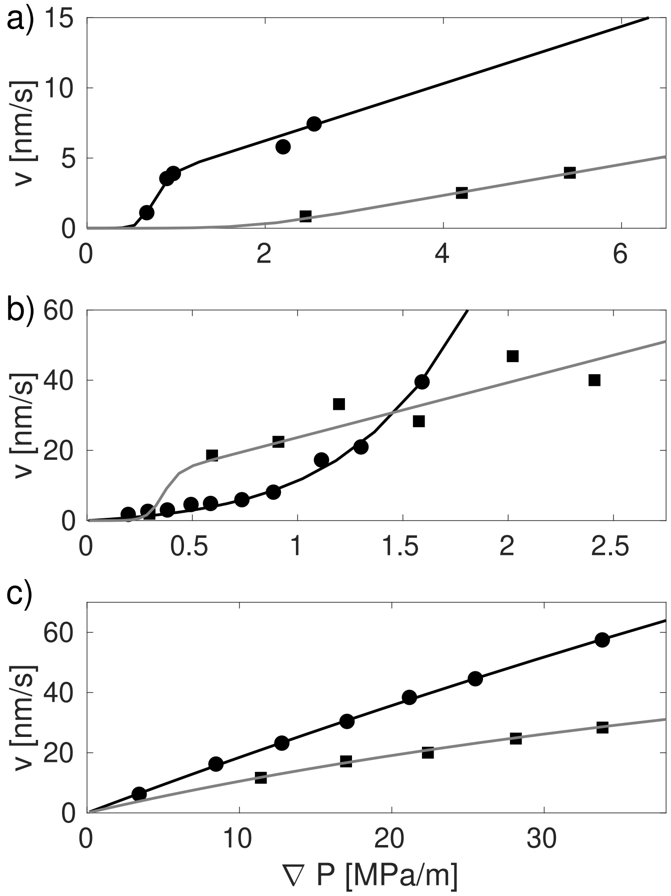

Fig. B-5.: Velocity v versus pressure gradient ∇P through tissues and biological membranes. Continuous lines correspond to the model results whereas symbols stand for experimental data. a) Serum flow through hepatoma tissue (filled dark circles) and subcutaneous tissue (filled dark squares) [29]. The exponents are $\alpha = 0{,}85, 1{,}88$. b) Ringer solution (filled dark circles) and paraffin oil (filled dark squares) flowing through a synovial membrane [37]. The values of α are 2,45 and 0,75. The velocity of the ringer solution is scaled by a factor of 10. c) Water flowing through a corneal membrane for a relative hydration of 3,7 (filled dark circles) and 3,2 (filled dark squares) [30]. In this case, $\alpha = 0{,}93, 0{,}79$.

are mainly composed of connected channels, with $l > 1\mu m$ in agreement with the experiments of Ref.[9], while biological membranes are mainly made up of unconnected channels, with $l < 1\mu m$ in agreement with the experiments of Refs.[30, 29].

How sensitive the exponent α is to variations of ξ and thus to the heights of the barriers can be analyzed from the data presented in Table **B-1**. For clay media (A and B) and corneal membranes (C and D) the ratio of the corresponding values of ξ is approximately 3 which leads to a small difference among the exponents, of about 0,2. To the contrary, for sand media (a and b), tissues(Hepatoma and Subcutaneous tissues), and synovial membranes (d and e) that ratio is larger than 5 which results in differences of the exponent larger than 0,8. Finally, by considering an exponential channel (Fig.**B-2**(c)), we find that: i) $\alpha < 1$ corresponds to $m < 0$, the case where the cross-sectional area of the channels decreases in the direction of the flow and then suddenly increases; ii) $\alpha \geq 1$ corresponds to $m > 0$, the case in which the media consists of channels with increasing cross-sectional area in the direction of the flow and with a sharp narrowing. Furthermore, a linear relationship between velocity and applied force is observed in Figs.**B-3**-**B-4**-**B-5** for low and high values of the force, whereas at intermediate values of the force the velocity follows a power law characterized by the α exponent.

B.4. Conclusions

In summary, we have proposed a model that analyzes how matter moves through a crowded medium upon application of a driving force. The medium consists of a large number of periodic channels whose periods are randomly distributed following a log-normal probability distribution, typical of systems with a great multiplicity of length scales, as is the case of a crowded medium. The complexity of the medium is emulated by means of entropic barriers that particles must surmount to proceed. This description significantly simplifies the analysis of liquid matter transport through the medium. We have shown that the average velocity depends on the applied force through the power law: $v \propto f^{\alpha}$, observed in many different experimental situations. The exponent of the law is sensitive to the micro-structure of the medium.

The analysis presented could also be extended to the case in which the medium is composed of the two types of channels discussed: connected and unconnected.

Our model constitutes a general proposal to describe the flux of matter through a crowded media generated by an applied force that can be used in the study of synthetic and cellular membranes, tissues and porous media [35, 11] driven by external forces such as pressure [6, 7, 9, 10], temperature [34] and chemical potential gradients[36, 39, 40].

Bibliography

[1] A. Arango-Restrepo and J. M. Rubi. Entropic transport in a crowded medium. *J. Chem. Phys.*, 153(3):034108, 2020.

[2] O. Bénichou, P. Illien, G. Oshanin, A. Sarracino, and R. Voituriez. Microscopic theory for negative differential mobility in crowded environments. *Phys. Rev. Lett.*, 113:268002, Dec 2014.

[3] O. Bénichou, P. Illien, G. Oshanin, A. Sarracino, and R. Voituriez. Nonlinear response and emerging nonequilibrium microstructures for biased diffusion in confined crowded environments. *Phys. Rev. E*, 93:032128, Mar 2016.

[4] Markus Spanner, Felix Höfling, Sebastian C. Kapfer, Klaus R. Mecke, Gerd E. Schröder-Turk, and Thomas Franosch. Splitting of the universality class of anomalous transport in crowded media. *Phys. Rev. Lett.*, 116:060601, 2016.

[5] Patrick Huber. Soft matter in hard confinement: phase transition thermodynamics, structure, texture, diffusion and flow in nanoporous media. *J. Phys. Condens. Matter*, 27(10):103102, feb 2015.

[6] D Mandal. Hydrodynamics of particles in liquid-solid packed fluidized bed. *Powder Technol.*, 276:18–25, 2015.

[7] P Kundu, V Kumar, and IM Mishra. Numerical modeling of turbulent flow through isotropic porous media. *Int. J. Heat Mass Transf.*, 75:40–57, 2014.

[8] T. Bhattacharjee and S.S. Datta. Bacterial hopping and trapping in porous media. *Nat. Commun.*, 10(1):2075, 2019.

[9] Dale Swartzendruber. Non-darcy flow behavior in liquid-saturated porous media. *J. Geophys. Res.*, 67(13):5205–5213, 1962.

[10] Mark G Bernadiner and Angelos L Protopapas. Progress on the theory of flow in geologic media with threshold gradient. *J. Environ. Sci. Health A*, 29(1):249–275, 1994.

[11] J R Levick. Flow through interstitium and other fibrous matrices. *Q. J. Exp. Physiol.*, 72(4):409–437, 1987.

[12] Henry Darcy. *Les Fontaines publiques de la ville de Dijon.* V. Dalamont, 1856.

[13] Morteza Dejam, Hassan Hassanzadeh, and Zhangxin Chen. Pre-darcy flow in porous media. *Water Resour. Res.*, 53(10):8187–8210, 2017.

[14] Santanu Sinha, Magnus Aa. Gjennestad, Morten Vassvik, Mathias Winkler, Alex Hansen, and Eirik G. FlekkÃ¸y. Rheology of high-capillary number two-phase flow in porous media. *Front. Phys.*, 7:65, 2019.

[15] Isha Savani, Dick Bedeaux, Signe Kjelstrup, Morten Vassvik, Santanu Sinha, and Alex Hansen. Ensemble distribution for immiscible two-phase flow in porous media. *Phys. Rev. E*, 95:023116, Feb 2017.

[16] Alex Hansen, Santanu Sinha, Dick Bedeaux, Signe Kjelstrup, Magnus Aa. Gjennestad, and Morten Vassvik. Relations between seepage velocities in immiscible, incompressible two-phase flow in porous media. *Transport Porous Med*, 125(3):565–587, Dec 2018.

[17] R. Kusters and C. Storm. Dynamic phase separation of confined driven particles. *EPL (Europhysics Letters)*, 118(5):58004, jun 2017.

[18] Adrian E. Scheidegger. Statistical hydrodynamics in porous media. *J. Appl. Phys.*, 25(8):994–1001, 1954.

[19] PG Saffman. A theory of dispersion in a porous medium. *J. Fluid Mech.*, 6(3):321–349, 1959.

[20] Ekaterina Stalgorova and Tayfun Babadagli. Modeling miscible injection in fractured porous media using random walk simulation. *Chem. Eng. Sci.*, 74:93 – 104, 2012.

[21] David Reguera and J M Rubi. Kinetic equations for diffusion in the presence of entropic barriers. *Phys. Rev. E*, 64(6):061106, 2001.

[22] J. Miguel Rubi. Entropic diffusion in confined soft-matter and biological systems. *EPL (Europhysics Letters)*, 127(1):10001, aug 2019.

[23] David Reguera, Gerhard Schmid, Poornachandra Sekhar Burada, J M Rubi, Peter Reimann, and Peter Hanggi. Entropic transport: Kinetics, scaling, and control mechanisms. *Phys. Rev. Lett.*, 96(13):130603, 2006.

[24] Marco-Vinicio Vazquez, Alexander M. Berezhkovskii, and Leonardo Dagdug. Diffusion in linear porous media with periodic entropy barriers: A tube formed by contacting spheres. *J. Chem. Phys.*, 129(4):046101, 2008.

[25] Yoshua Chávez, Marco-Vinicio Vázquez, and Leonardo Dagdug. Unbiased diffusion through a linear porous media with periodic entropy barriers: a tube formed by contacting ellipses. *J. Chem.*, 2015, 2015.

[26] Eckhard Limpert, Werner A. Stahel, and Markus Abbt. Log-normal distributions across the sciences: Keys and clues: On the charms of statistics, and how mechanical models resembling gambling machines offer a link to a handy way to characterize log-normal distributions, which can provide deeper insight into variability and probability-normal or log-normal: That is the question. *BioScience*, 51(5):341–352, 05 2001.

[27] Poornachandra Sekhar Burada, Gerhard Schmid, David Reguera, J M Rubi, and Peter Hanggi. Biased diffusion in confined media: Test of the fick-jacobs approximation and validity criteria. *Phys. Rev. E*, 75(5):051111, 2007.

[28] A Díaz-Guilera, JM Rubí, and D Bedeaux. Renormalization of the diffusion coefficient in a fluid in elongational flow. *Physica A*, 154(2):257–270, 1989.

[29] Edward A. Swabb, James Wei, and Pietro M. Gullino. Diffusion and convection in normal and neoplastic tissues. *Cancer Res.*, 34(10):2814–2822, 1974.

[30] Bengt O. Hedbys and Saiichi Mishima. Flow of water in the corneal stroma. *Exp. Eye Res.*, 1(3):262 – 275, 1962.

[31] R E Hayes, A Afacan, and B Boulanger. An equation of motion for an incompressible newtonian fluid in a packed bed. *Transport Porous Med.*, 18(2):185–198, 1995.

[32] Stephen Whitaker. The equations of motion in porous media. *Chem. Eng. Sci.*, 21(3):291–300, 1966.

[33] Karen Alim, Shima Parsa, David A. Weitz, and Michael P. Brenner. Local pore size correlations determine flow distributions in porous media. *Phys. Rev. Lett.*, 119:144501, Oct 2017.

[34] Soowhan Kim and M. M. Mench. Investigation of temperature-driven water transport in polymer electrolyte fuel cell: Thermo-osmosis in membranes. *J. Membr. Sci.*, 328(1):113 – 120, 2009.

[35] Fangqiang Zhu, Emad Tajkhorshid, and Klaus Schulten. Pressure-induced water transport in membrane channels studied by molecular dynamics. *Biophys. J.*, 83(1):154 – 160, 2002.

[36] Kirk E. Nelson and Timothy R. Ginn. Theoretical investigation of bacterial chemotaxis in porous media. *Langmuir*, 17(18):5636–5645, 2001.

[37] J R Levick. The influence of hydrostatic pressure on trans-synovial fluid movement and on capsular expansion in the rabbit knee. *J. Physiol.*, 289(1):69–82, 1979.

[38] F. Zami-Pierre, R. de Loubens, M. Quintard, and Y. Davit. Transition in the flow of power-law fluids through isotropic porous media. *Phys. Rev. Lett.*, 117:074502, Aug 2016.

[39] Roseanne M. Ford and Ronald W. Harvey. Role of chemotaxis in the transport of bacteria through saturated porous media. *Adv. Water Res.*, 30(6):1608 – 1617, 2007.

[40] J W Barton and R M Ford. Determination of effective transport coefficients for bacterial migration in sand columns. *Appl. Environ. Microbiol.*, 61(9):3329–3335, 1995.

C. Appendix: The Soret coefficient from the Faxén theorem for a particle moving in a fluid under a temperature gradient

We compute the Soret coefficient for a particle moving through a fluid subjected to a temperature gradient. The viscosity and thermal conductivity of the particle are in general different from those of the solvent and its surface tension may depend on temperature. We find that the Soret coefficient depends linearly on the derivative of the surface tension with respect to temperature and decreases in accordance with the ratios between viscosities and thermal conductivities of particle and solvent. Additionally, the Soret coefficient also depends on a parameter which gives the ratio between Marangoni and shear stresses, a dependence which results from the local stresses inducing a heat flux along the particle surface. Our results are compared to those obtained by using the Stokes value for the mobility in the calculation of the Soret coefficient and in the estimation of the radius of the particle. We show cases in which these differences may be important. The new expression of the Soret coefficient can systematically be used for a more accurate study of thermophoresis.

This Appendix was published in *the European Physical Journal E*, **42**, 55, (2019). Ref.[1]

C.1. Introduction

The motion of particles driven by a temperature gradient [2] known as Soret effect has been subject of many experimental and theoretical studies in recent years [3, 4, 5, 6] due to its importance in areas as diverse as soft condensed matter, biophysics, microgravity and nanoscience [7, 8, 9, 10, 11, 12, 13, 14], where the evaluation of the Soret coefficient is key in order to develop such applications [15].

The Soret coefficient can be obtained from hydrodynamics by computing the forces exerted on the moving particle. The force exerted on a spherical solid particle of radius a that moves through an isothermal fluid at rest with velocity $\vec{u}$ is given by the Stokes formula $\vec{F} = -\mu_0^{-1}\vec{u}$, where $\mu_0 = (6\pi a\eta_0)^{-1}$ is the mobility, with η_0 as the fluid viscosity. In the case in which the fluid itself moves with stationary velocity $\vec{u}_0(r)$, the value of the force is given by the Faxén theorem which for a solid particle and constant temperature is: $\vec{F} = -\mu_0^{-1}(\vec{u}-\vec{u}_0)$ [16]. In the presence of a temperature gradient ∇T_0, the force must contain a thermophoretic contribution proportional to the gradient [17] which is usually added to the friction force leading to $\vec{F} = -\mu_0^{-1}\vec{u} + D_{T,0}\mu_0^{-1}\nabla T_0$ where $D_{T,0}$ is a thermophoretic mobility. A more general expression of the Faxén theorem valid when the particle is not necessarily solid was given in [18]: $\vec{F} = -\mu^{-1}\vec{u} + D_T\mu^{-1}\nabla T_0$ where the mobility is now μ instead of the Stokes value μ_0 and the thermophoretic mobility is D_T. Under Faxén's approach, both mobility and thermophoretic mobility depend on the ratios of the viscosities α and thermal conductivities β between particle and solvent and on the derivative of the surface tension as a function of the temperature γ_T as well. As we will see throughout the Appendix, considering the Stokes mobility instead of the Faxén mobility leads in some cases to important differences in the estimation of the radius and the Soret coefficient of the particle through measurements of the diffusivity.

Based on the hydrodynamic model, we will compute the mobility, the thermophoretic mobility and the Soret coefficient of a particle as a function of the ratio of viscosities and thermal conductivities of a particle and a solvent. We will also analyze the role played by a temperature-dependent surface tension in the motion of the particle. These results will be used to estimate the differences between those coefficients when obtained by using the Stokes and Faxén expressions for the mobility.

The Appendix is organized as follows. In Section 2, we formulate the Faxén theorem giving the expression of the force exerted on a particle moving through a fluid subjected to a temperature gradient. From this, we infer the expressions of the mobility, the thermophoretic mobility and the Soret coefficient which depend on the viscosities and thermal conductivities of particle and solvent and on the heat generated at the surface of the particle due to its motion. Section 3 is devoted to analyze the behavior of both mobilities as a function of these quantities. In Section 4, we study the case of a solid particle as a limiting case of our theory. In Section 5, we analyze the case of n-octane-water/surfactant to compute the deviation of the diffusivity and the Soret coefficient from their values obtained by using the Stokes formula for the mobility. We also give the error percentage in the estimation of the particle radii and the Soret coefficient if the Stokes instead the Faxén value of the mobility is used. Finally, in section 6 we present our main conclusions.

C.2. Hydrodynamics of a particle in a temperature gradient

We consider the stationary movement of a solid or liquid particle of constant radius a immersed in a fluid at rest subjected to a temperature gradient. Both fluid inside the particle and solvent are assumed to be non-ionic, incompressible and Newtonian and have viscosities η_i and η_o and thermal conductivities λ_i and λ_o respectively. The interface between both fluids has surface tension γ which in general may depend on temperature and composition.

In the study of the dynamics of a particle immersed in a fluid, one is usually concerned with the calculation of the force exerted by the fluid on the particle. The problem has been formulated and solved focusing on different situations. A classical and vast literature on the subject exists [19, 20]. The knowledge of the force acting on the particle in terms of the unperturbed hydrodynamic fields, as given by the Faxén theorem [16], constitutes the starting point in the study of Brownian motion since it allows us to derive the Langevin equation as well as the fluctuation-dissipation theorem [21].

The nature of the interface affects the transport properties of the particle. Surface tension plays an important role in particle motion. Even in the absence of an imposed temperature gradient, the heat generated at the surface due to the local stresses induced by motion gives rise to a temperature difference between the front and the back of the particle (see fig.**C-1**). The dependence of the interfacial tension on temperature gives rise to thermocapillary effects [22, 23].

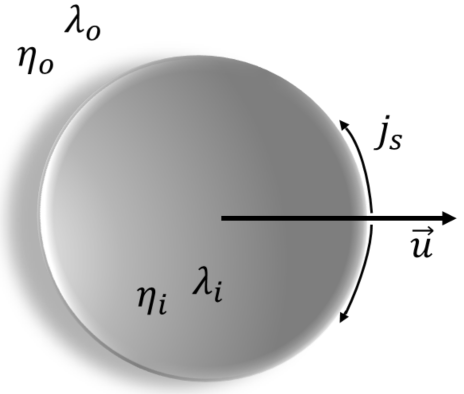

Fig. C-1.: Particle motion with velocity $\vec{u}$ induces local stresses at the interface which in turn cause a surface energy excess e_s and an interfacial heat current j_s. The induced heat current is $j_s \equiv (e_s - \gamma)\nabla_s \cdot \vec{u}$ where $\nabla_s = (\mathbf{1} - \vec{n}\vec{n}) \cdot \nabla$ is the surface gradient and $e_s - \gamma \approx \gamma_T T$ [24]. The heat flux thus has a discontinuity at the interface related to the heat generation due to the thermocapillary effect. Furthermore, velocity and temperature fields are coupled through the boundary condition (for details see [18]). The ratio between viscosities and thermal conductivities of particle (η_i,λ_i) and solvent (η_0,λ_0) plays an important role in the determination of the induced fields and therefore in the transport coefficients [18].

The total force exerted on a Brownian particle was derived in [18] for the general case of applied temperature and velocity gradients by solving the corresponding boundary value problem. Neglecting the solvent velocity, the force is

$$\begin{aligned}\vec{F} \quad &= \frac{2\pi\eta_0 a}{1+\alpha+2E/3(2+\beta)}\times \\ &\left[\frac{2a\gamma_T}{\eta_0(2+\beta)}\nabla T_0(0)-\left(\alpha+2+\frac{2E}{2+\beta}\right)\vec{u}\right]\end{aligned} \tag{C-1}$$

where $\nabla T_0(0)$ is the value of the temperature gradient in the absence of a particle computed at its centre. Comparing this expression to the force $\vec{F} = -\mu^{-1}\vec{u} + D_T\mu^{-1}\nabla T_0$, we then obtain the mobility and the thermophoretic mobility:

$$\mu = \frac{1}{4\pi a\eta_0}\left(\frac{1+\alpha+\frac{2}{3}\frac{E}{2+\beta}}{1+3\alpha/2+\frac{E}{2+\beta}}\right), \tag{C-2}$$

$$D_T = -\frac{a\gamma_T}{\eta_0}\frac{1}{(2+\beta)\left(1+3\alpha/2+\frac{E}{2+\beta}\right)} \tag{C-3}$$

where $\gamma_T = \partial\gamma/\partial T$ is usually a negative quantity, $\alpha = \eta_i/\eta_o$ is the ratio of viscosities and $\beta = \lambda_i/\lambda_o$ the ratio of conductivities of the particle and solvent. The case of a solid particle corresponds to $\alpha \to \infty$, however, due to the presence of an absorbed layer, α may take very high but not infinite values, as we will show in sect. B.4. The coefficient E quantifies the ratio of the Marangoni stress to the shear stress [25] and is given by

$$E = \frac{T\gamma_T^2}{\lambda_0\eta_0}. \tag{C-4}$$

The effect of the induced heat flux may be significant for low viscous liquids or for fluid-particle surface **tension** slightly dependent on the temperature. Since $E \propto \gamma_T^2$, for sufficiently small values of γ_T, surface tension effects are negligible. Typical values of E range from 10^{-5} to 4 [23].

Considering the effect of α, β and E on the mobility, the diffusivity of the particle is given by $D = k_B T\mu$. Without taking into account these effects, the diffusivity is given by the Stokes relation $D_0 = k_B T\mu_0$. Estimations of the radius of the particle are usually done [26, 27, 28, 29, 30, 31] by measurements of the diffusivity D_m, through the expression $a_0 = k_B T/6\pi\eta_0 D_m$. The value of the radius of the particle in our approach is then

$$a = \frac{k_B T}{4\pi\eta_0 D_m}\left(\frac{1+\alpha+\frac{2}{3}\frac{E}{2+\beta}}{1+3\alpha/2+\frac{E}{2+\beta}}\right), \tag{C-5}$$

This expression differs from the one obtained under the Stokes approach by a factor of $\left(\frac{3+3\alpha+\frac{2E}{2+\beta}}{2+3\alpha+\frac{2E}{2+\beta}}\right)$. The error percentage in the estimation of a (ε_a) is then

$$\varepsilon_a = \left(2+3\alpha+\frac{2E}{2+\beta}\right)^{-1} 100\,\% \tag{C-6}$$

For solvents of high viscosity, for γ approximately constant or for high values of β (metallic particles in common solvents), $E \to 0$ and one obtains a simplified expression for a:

$$a \approx \frac{k_B T}{4\pi\eta_0 D_m}\left(\frac{1+\alpha}{1+3\alpha/2}\right). \tag{C-7}$$

Taking into account the previous results, the Soret coefficient S_T is then given by

$$S_T = \frac{D_T}{D} = -\frac{4\pi\gamma_T a^2}{k_B T(2+\beta)(1+\alpha+\frac{2}{3}\frac{E}{2+\beta})} \tag{C-8}$$

The Soret coefficient obtained when one considers μ_0 instead of μ is

$$S_{T,0} = \frac{D_T}{D_0} = -\frac{6\pi a_0^2\gamma_T}{k_B T(2+\beta)\left(1+3\alpha/2+\frac{E}{2+\beta}\right)} \tag{C-9}$$

S_T differs from $S_{T,0}$ by a factor of $\left(\frac{2+3\alpha+\frac{2E}{2+\beta}}{3+3\alpha+\frac{2E}{2+\beta}}\right)$ which shows that they are approximately equal for sufficiently large values of α and in the absence of surface tension effects ($E \to 0$). The error percentage in the estimation of S_T (ε_{S_T}) is

$$\varepsilon_{S_T} = \left(3+3\alpha+\frac{2E}{2+\beta}\right)^{-1} 100\,\% \tag{C-10}$$

From this expression and eq.(C-6), we see that the error percentage may be significant for low values of α, as happens for bubbles. The error is less sensitive to changes of β because the effect of β is conditioned to values of E.

C.3. Mobility and thermophoretic mobility

In this Section, we will study the behavior of mobility and thermophoretic mobility as a function of the parameters α, β and E by using eqs.(C-2), (C-3). We will compare the mobility from the Faxén theorem μ (eq.(C-2)) and from the Stokes approach μ_0, through the ratio μ/μ_0.

In fig. **C-2** (a), we show that by decreasing E and α, and increasing β, the ratio μ/μ_0 increases. Alkane drops with low viscosity, metallic particles with high conductivity or non-polar solvents with low surface tension (weakly dependent on the temperature) are examples in which μ/μ_0 is significantly high. When the effect of Marangoni stresses is very small ($E \to 0$), the dependence of μ/μ_0 on β is negligible.

We show in fig. **C-2** (b) that a decrease in E, α and β leads to an increase of D_T. Additionally, surface tension very sensitive to temperature changes and solvents with low viscosity favor an enhancement of thermophoretic mobility. We can thus expect very high values of D_T for systems with nano-bubbles and low D_T for systems composed of metallic particles or systems with very low surface tension.

In fig. **C-2**, we observe that μ could deviate from μ_0 up to 50 % while D_T could increase or decrease about 10 times depending on the values of the α, β and E parameters. Differences of the physical properties of

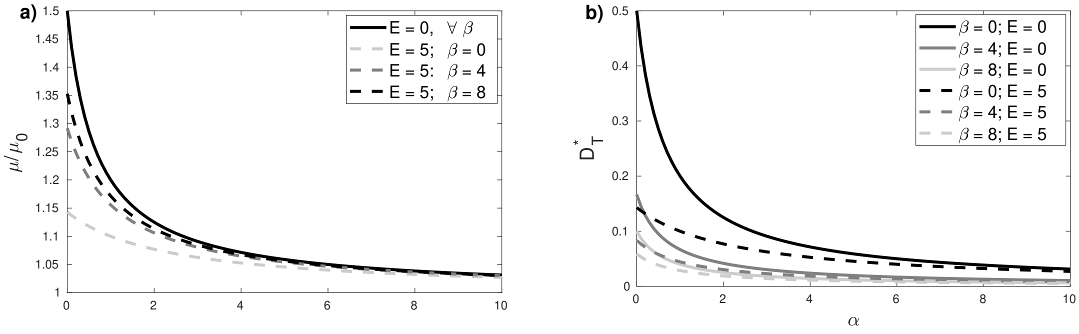

Fig. C-2.: Mobilities as a function of the transport properties ratios. a) μ/μ_0, b) $D_T^* \equiv -D_T/a\gamma_T$ for different values of viscosity ratio α, thermal conductivity ratio β and for the effect of the induced heat E.

particle and surrounding fluid are thus crucial to determine the particle radius and the Soret coefficient.

C.4. The case of solid particles

In this Section, we compare our results obtained from the Faxén theorem with those presented in Ref.[32] in which the steady Navier-Stokes and heat equations are solved by assuming the existence of a solid-like nanolayer. Our expression of the thermophoretic mobility depends on the ratio between particle and fluid viscosities (α) whereas in the solid-like nanolayer approach [32], this dependence is not considered.

In the hypothetical case of a solid particle without adsorbed components on the surface and negligible surface tension, $\alpha \to \infty$ and $E \to 0$, thus $\mu \to \mu_0$ and $D_T \to 0$. This case can be analyzed by means of the Faxén approach if we consider a monolayer of absorbed solvent on the particle surface [33, 34] with an effective viscosity.

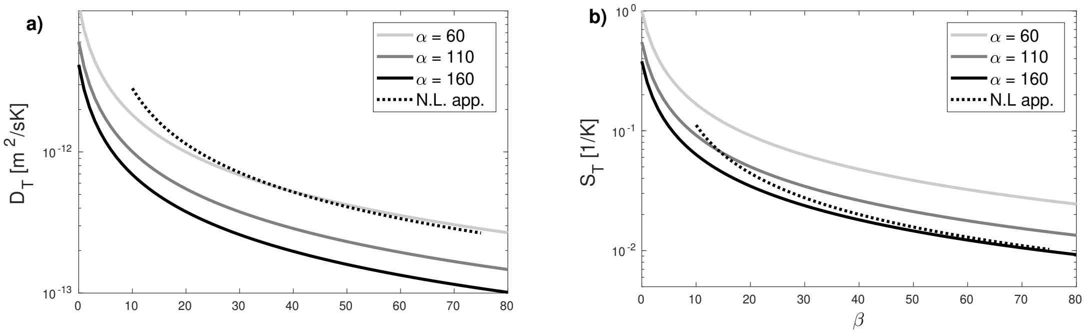

Fig. C-3.: Comparison between Faxén theorem results (continuous lines) and the solid-like nanolayer (dotted line) approaches for a solid particle in water. a) Thermophoretic mobility and b) Soret coefficient. Particle radius $a = 20\ nm$, T = 300,15K, $\gamma_T = 10^{-4} J/mK$, $\eta_o = 10^{-3} Pa \times s$, $E = 0{,}006$.

In fig. **C-3**, we show the results for D_T and S_T obtained from both approaches. . For both cases, D_T, as well as S_T, behave as $1/\beta$ for high β values which correspond to the case of metal nanoparticles in a fluid.

For D_T, the result given by the Faxén theorem matches with the solid-like nanolayer approach for $\alpha = 60$ while for S_T the ratio of viscosities must be approximately 160. The fact that this comparison requires two different effective viscosities reveals the uncertainty of the solid-like nanolayer approach. Furthermore, this approach cannot accurately predict the thermophoretic mobility and Soret coefficient for drops and bubbles because when $\beta \approx 3{,}4$ the solution diverges.

C.5. Study case

We have computed the mobilities and the Soret coefficient of a drop of n-octane in a solution of water/surfactant as a function of the temperature at which drops are stable. Implicitly, the variations in the temperature give rise to different values of α, β and E. Values for these coefficients are found to fall in the intervals $0{,}43-0{,}71$, $0{,}13-0{,}17$ and $0-2{,}5\ E-5$, respectively. These values correspond to: η_o in between $0{,}47-1{,}31$ mPa.s, η_i in $0{,}33-0{,}57$ mPa.s, λ_o in $0{,}57-0{,}66$ w/mK and λ_i in $0{,}089-0{,}1$ w/mK. Physical properties of drops and solvent have been inferred from those of pure substances by means of a mixing rule [35, 36]. Values of γ_T have been taken from [37]. We compare our results with the ones obtained with the Stokes approach.

For a n-octane drop, we show in fig. **C-4** the mobilities as a function of the temperature. In fig. **C-4**(a), we observe that both diffusivities differ because in D_0 the effect of the induced heat and the ratio between transport coefficients are not considered. In the figure, we also show the behavior of the thermophoretic mobility D_T computed from eq.(C-3). By using eq.(C-2) a slight non-linear increment of the diffusivity as a function of the temperature caused by the effect of α and β is observed. As one can see, D_T decreases with temperature and becomes negative at $T = 305{,}4\ K$ due to the fact that here the surface tension has a minimum and therefore the sign of its derivative changes [37]. The order of magnitude of D_T agrees with the experimental results presented in [26] for the interval $300K < T < 302K$, and furthermore, the value of D_T for $T = 300{,}15K$ approaches experimental results (black square in fig. **C-4** (a)) with an error lower than 10 %.

In fig. **C-4**(b), we show the behavior of the Soret coefficient as a function of the temperature obtained from eq.(C-8) and from eq.(C-9). Although S_T and $S_{T,0}$ are in good agreement in order of magnitude, S_T is closer than $S_{T,0}$ to the experimental data presented in [26] (black circle in fig. **C-4** (b)). S_T corresponds to a particle radius a and $S_{T,0}$ to a particle radius a_0. There is, however, a mismatch between both approaches caused by the effect of the ratios between viscosities and thermal conductivities of drops and solvent. In fig.**C-4**(c), we show (from eq.(C-6) and eq.(C-10)) the error percentage in the estimation of the radii of the drop and the Soret coefficient when using Stokes instead of Faxén approach. For the studied system, the errors are significant, of the order of 20 % and 30 %, because of the difference between viscosities of the drop interface and solvent/surfactant media.

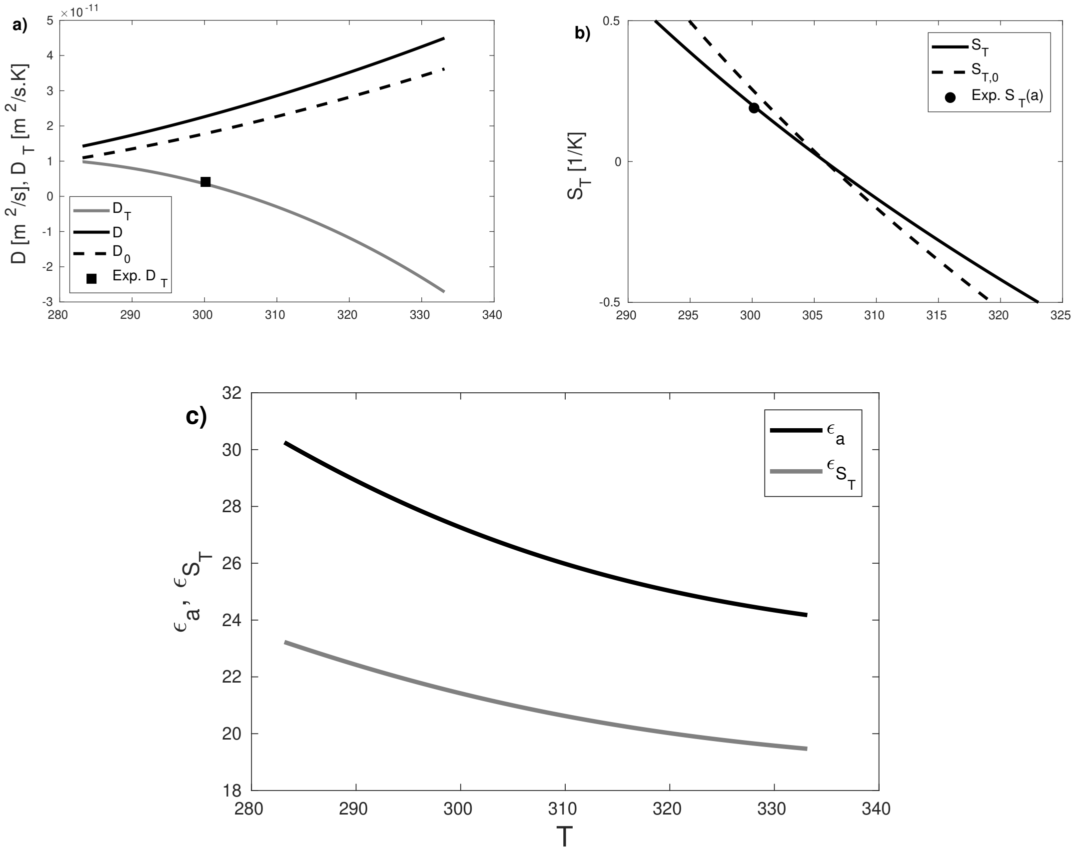

Fig. C-4.: Mobilities, Soret coefficient and error percentages as a function of temperature. a) Diffusivity computed from Faxém theorem D (continuous black line), Diffusivity computed from Stokes approach D (dashed black line), thermophoretic mobility D_T (continuous gray line) and experimental D_T (the black square)[26]. b) Soret Coefficient computed from Faxén theorem (continuous black line), Soret coefficient computed from Stokes approach (dashed black line) and experimental S_T (the black circle) [26] evaluated to the estimated particle radius a. c) Error percentages in the estimation of particle radii (black line) and Soret coefficient (gray line) by considering only the Stokes approach.

C.6. Conclusions

Mobility, thermophoretic mobility and Soret coefficient are affected significantly by the ratio between the viscosities and thermal conductivities of particle and solvent and by the heat generated at the surface of the particle resulting from the local stresses induced by its motion. Mobilities are highly influenced by these ratios especially for low values of the viscosity ratio (see fig.**C-2**), as happens in nano-bubbles. They decrease when the heat induced at the surface, seen through the coefficient E, increases (see fig.**C-2**) as happens for low viscosity and conductivity solvents such as simple alkanes and for temperatures close to the boiling point [23]. When the particle has a very high thermal conductivity compared to that of the solvent, as occurs in metal nanoparticles, the thermophoretic mobility and Soret coefficient decrease as $1/\beta$ (see fig.**C-3**).

The sign of the thermophoretic mobility and Soret coefficient is conditioned by the sign of the surface tension derivative with respect to the temperature γ_T, as shown in fig.**C-4**(a). For nano-drops of n-octane in water/surfactant, we find error percentages in the estimation of particle radii and Soret coefficient larger than 20% if the dependence of transport coefficients on α and β are omitted.

The results presented provide new and more accurate relationships for the estimation of the radius of the particle and the Soret coefficient from measurements of particle diffusivity.

Bibliography

[1] Andrés Arango-Restrepo and J. Miguel Rubi. The soret coefficient from the faxén theorem for a particle moving in a fluid under a temperature gradient. *Eur. Phys. J. E*, 42(5):55, May 2019.

[2] Roberto Piazza, Sara Iacopini, and Benedetta Triulzi. Thermophoresis as a probe of particle-solvent interactions: The case of protein solutions. *Phys. Chem. Chem. Phys.*, 6(7):1616–1622, 2004.

[3] Werner Koehler and Konstantin I Morozov. The soret effect in liquid mixtures-a review. *J. Non-Equilib. Thermodyn.*, 41(3):151–197, 2016.

[4] MA Rahman and MZ Saghir. Thermodiffusion or soret effect: Historical review. *Int. J. Heat Mass Transf.*, 73:693–705, 2014.

[5] R Piazza and A Parola. Thermophoresis in colloidal suspensions. *J. Phys. Condens. Matter*, 20(15):153102, 2008.

[6] Jean K Platten. The soret effect: a review of recent experimental results. *Int. Appl. Mech.*, 73(1):5–15, 2006.

[7] Øivind Wilhelmsen, Dick Bedeaux, and David Reguera. Tolman length and rigidity constants of the lennard-jones fluid. *J. Chem. Phys.*, 142:171103, 2015.

[8] David Ross and Laurie E Locascio. Microfluidic temperature gradient focusing. *Anal. Chem.*, 74(11):2556–2564, 2002.

[9] Iman Zahmatkesh. On the importance of thermophoresis and brownian diffusion for the deposition of micro-and nanoparticles. *Int. Commun. Heat Mass*, 35(3):369–375, 2008.

[10] Chuen Jinn Tsai, Jyh Shyan Lin, Shankar G. Aggarwal, and Da Ren Chen. Thermophoretic deposition of particles in laminar and turbulent tube flows. *Aerosol Sci. Technol.*, (38):131–139, 2004.

[11] Byung Uk Lee, Du Sub Byun, Gwi-Nam Bae, and Jin-Ha Lee. Thermophoretic deposition of ultrafine particles in a turbulent pipe flow: Simulation of ultrafine particle behaviour in an automobile exhaust pipe. *J. Aerosol Sci.*, 37(12):1788 – 1796, 2006.

[12] Huan J. Keh and Chang L. Ou. Thermophoresis of aerosol spheroids. *Aerosol Sci. Technol.*, (38):675–684, 2004.

[13] Dieter Braun and Albert Libchaber. Thermal force approach to molecular evolution. *Phys. Biol.*, 1(1):P1–P8, feb 2004.

[14] G. Kucsko, P. C. Maurer, N. Y. Yao, M. Kubo, H. J. Noh, P. K. Lo, H. Park, and M. D. Lukin. Nanometre-scale thermometry in a living cell. *Nature*, 500:54–58, 2013.

[15] Juan Olarte-Plata, J. Miguel Rubi, and Fernando Bresme. Thermophoretic torque in colloidal particles with mass asymmetry. *Phys. Rev. E*, 97:052607, May 2018.

[16] H Faxen. H. faxén, ark. mat., astron. fys. 18, 1 (1924). *Ark. Mat., Astron. Fys.*, 18:1, 1924.

[17] Sybren Ruurds De Groot and Peter Mazur. *Non-equilibrium thermodynamics*. Dover Publications Inc., 1985.

[18] J. Bafaluy, I. Pagonabarraga, J.M. Rubi, and D. Bedeaux. Thermocapillary motion of a drop in a fluid under external gradients. faxÃ©n theorem. *Phys. A*, 213(3):277 – 292, 1995.

[19] R Berker. Encyclopedia of physics, vol. vili/2. *Fluid Dynamics I*, 1, 1963.

[20] J Happel and H. Brenner. *Low Reynolds Number Hydrodynamics*. Kluwer, Dordrecht, 1991.

[21] Robert Zwanzig. Hydrodynamic fluctuations and stokes' law friction. *J. Res. Natl. Bur. Std.(US) B*, 68:143–145, 1964.

[22] R Shankar Subramanian. The stokes force on a droplet in an unbounded fluid medium due to capillary effects. *J. Fluid Mech.*, 153:389–400, 1985.

[23] Francisco E Torres and Eric Herbolzheimer. Temperature gradients and drag effects produced by convection of interfacial internal energy around bubbles. *Phys. Fluids A*, 5(3):537–549, 1993.

[24] Arthur W Adamson, Alice Petry Gast, et al. *Physical chemistry of surfaces*. Interscience publishers New York, 1967.

[25] JF Harper, DW Moore, and JRA Pearson. The effect of the variation of surface tension with temperature on the motion of bubbles and drops. *J. Fluid Mech.*, 27(2):361–366, 1967.

[26] Philipp Naumann, Sascha Datta, Thomas Sottmann, Bastian Arlt, Henrich Frielinghaus, and Simone Wiegand. Isothermal behavior of the soret effect in nonionic microemulsions: Size variation by using different n-alkanes. *J. Phys. Chem. B*, 118(12):3451–3460, 2014.

[27] Aernout van Veluwen, Hendrik NW Lekkerkerker, Cornelus G de Kruif, and Agienus Vrij. Brownian diffusivities of interacting colloidal particles measured by dynamic light scattering. *Faraday Discuss.*, 83:59–67, 1987.

[28] WI Goldburg. Dynamic light scattering. *Am. J. Phys.*, 67(12):1152–1160, 1999.

[29] B. J. Berne and R. Pecora. *Dynamic light scattering: with applications to chemistry, biology, and physics*. Mineola, NY: Dover Publications, 2000.

[30] R Pecora. Dynamic light scattering measurement of nanometer particles in liquids. *J. Nanopart. Res.*, 2(2):123–131, 2000.

[31] Puthusserickal A Hassan, Suman Rana, and Gunjan Verma. Making sense of brownian motion: colloid characterization by dynamic light scattering. *Langmuir*, 31(1):3–12, 2014.

[32] H. L. Fu and L. Gao. Effect of interfacial nanolayer on thermophoresis in nanofluids. *International Journal of Thermal Sciences*, 61:61–66, 2012.

[33] Pei Tillman and J M Hill. Determination of nanolayer thickness for a nanofluid. *Int. J. Heat Mass Transf.*, 34(4):399–407, 2007.

[34] X F Zhou and L Gao. Thermal conductivity of nanofluids: Effects of graded nanolayers and mutual interaction. *J. Appl. Phys.*, 100(8):083503, 2008.

[35] Bruce E Poling, J M Prausnitz, and John P O apos Connell. Properties of Gases and Liquids. In *Experimental Thermal and Fluid Science*. 2007.

[36] A. A.H. Pádua, J. M.N.A. Fareleira, J. C.G. Calado, and W. A. Wakeham. Density and viscosity measurements of 2,2,4-trimethylpentane (isooctane) from 198 K to 348 K and up to 100 MPa. *J. Chem. Eng. Data*, 41:1488–1494, 1996.

[37] T. Sottmann and R. Strey. Ultralow interfacial tensions in water-n-alkane-surfactant systems. *J. Chem. Phys*, 106:8606, 1997.

D. Appendix: Part I and II

D.1. Understanding Gelation as a Non-Equilibrium Self-Assembly Process

In this Appendix we give more details on the estimated diffusivities, the potential barriers used and on the Dynamic Light Scattering and snapshots building. We first estimate the diffusivities along each reaction coordinate. We show how to model a potential barrier as a function of the standard chemical potential and the rotation potential of a rigid fiber in presence of other fibers. We model the standard chemical potential per building block in a linear fiber to build the potential barrier of each process. We indicate how to reproduce the DLS experimental results. Finally, we present the potential barrier for each fundamental process and discuss briefly on the activity coefficient.

D.1.1. Diffusivities

The diffusivities used in the model have been estimated from available experimental data [1] by minimizing the discrepancies (Eq. D-1) between experimental concentrations ($C_i^{(exp)}$) and model concentrations (C_i):

$$min_{(\boldsymbol{D})} \quad Error(\boldsymbol{D}) = \int_{t=0}^{t=900h} \sum_{i=DBC,DBCMe,DBCMe_2} \left| C_i(t) - C_i(t)^{(exp)} \right| dt \tag{D-1}$$

with $\boldsymbol{D} = [D_{act}, \quad D_1, \quad D_2, \quad D_3, \quad D_{s,1}, \quad D_{s,2}]$. To carry out the optimization process, a simple algorithm based on iterations was written and performed in MATLAB ®. The values of the diffusivities, shown in the table below, are those that minimize the error. They are used to obtain the model results presented in Fig. **2-4**.

Tab. D-1.: Diffusivities for NESA process of gelation

Fundamental process	Process diffusivity	Diffusivity $[s^{-1}]$
First-order activation	D_{act}	$3{,}125 * 10^{-9}$
Second-order activation	D_3	$2{,}78 * 10^{-2}$
First-order self-assembly	D_1	$1{,}74 * 10^{3}$
Second-order self-assembly	$D_{s,1}$	$1{,}09 * 10^{-1}$
First-order disassembly	D_2	$6{,}1 * 10^{-1}$
Second-order disassembly	$D_{s,2}$	$2{,}12 * 10^{-5}$

The rotational diffusivity for first-order structures D_4 has been computed from Eq. (9.16) of [2] which is valid for isotropic systems. The obtained value is $2{,}4 s^{-1}$. Nevertheless, as gelation does not necessarily form isotropic intermediates, we have used the diffusivity presented in Eq.(9.17) of [2] in which D_4 is multiplied by a factor that depends on the form of the surrounding structures. We have considered that this factor is a random number, between zero and one, since initially the BB have a random orientation which evolves over time ending up in a preferred orientation that is very difficult to be determined.

D.1.2. The potential barrier

The potential barrier depends on the standard chemical potential of each structure and the activation energy of each process. The potential barrier is assumed to be a bistable function where the activation energy increases with the size of the fiber and decreases with the size of the agglomerates because of steric effects. The minima of the potential located at $\gamma = 0$ and $\gamma = 1$ correspond to the reactants and products and the maxima at γ^* to the transition state.

The form of the barrier is subjected to thermodynamic restrictions. Stability of the initial and final states of the reaction imposes two conditions on the first derivative of the potential. Three more restrictions come from the values of the standard chemical potentials and the activation energy at $\gamma = 0$, $\gamma = 1$ and $\gamma = \gamma^*$, respectively. Moreover, since the potential barrier is related to the equilibrium probability distribution, values of $\gamma < \gamma^*$ denote the state A and $\gamma \geq \gamma^*$ correspond to the state B.

For the potential barrier, we thus propose a fifth-order polynomial that have two minima and a maximum in the interval [0,1]. The polynomial includes six parameters whose values follow from the seven thermodynamic restrictions which as a matter of fact reduce to six since the location of the transition state is unknown. The thermodynamic conditions include the knowledge of the standard chemical potential of each structure. The potential barrier is then given by

$$\phi(\gamma) = \sum_{i=0}^{5} c_i \gamma^i \tag{D-2}$$

where the constrains are

$$\phi(0) = \mu_A^0; \quad \phi(1) = \mu_B^0; \quad \phi(\gamma^*) = \text{máx}(\phi(\gamma)) - \mu_A^0 = \varepsilon$$

$$\frac{d\phi(\gamma)}{d\gamma}\Big|_{\gamma=0} = \frac{d\phi(\gamma)}{d\gamma}\Big|_{\gamma=1} = \frac{d\phi(\gamma)}{d\gamma}\Big|_{\gamma=\gamma^*} = 0$$

$$\exp((\mu_A^0 - \mu_B^0)/RT) = \frac{P_{B,eq}}{P_{A,eq}} = \frac{\int_{\gamma^*}^{1} \exp(-\phi(\gamma)/RT)d\gamma}{\int_{0}^{\gamma^*} \exp(-\phi(\gamma)/RT)d\gamma}$$

This system of equations enables one to determine γ^* and $c_i, i = 0, 1, .., 5$. For instance, for $(\mu_A^0 - \mu_B^0)/RT = 1$ and $\varepsilon/RT = 5$, we obtain the potential barrier shown in Figure **A-1**. The value of the maximum increases if n increases in the assembly of linear fibers. Thus $\phi_n(\gamma_n^*) \propto \text{máx}(\phi_n(0), \phi_n(1)) + k_B T \sqrt{(n)}$.

Additionally, the potential energy of rotation for the structures is extracted from Eq.(10.23) of [2]

$$\phi_{n,4}(\theta_n) = k_B T \int d\theta_n \int d\theta^{'} p_n(\theta_n, t) P(\theta^{'}, t) \beta(\theta_n, \theta^{'}) \tag{D-3}$$

with v the number of structures per unit of volume. For rod-like polymers in two dimensions:

$$\beta(\theta_n, \theta^{'}) = 2a^3 n^2 \frac{v}{2} (\cos(\theta_n)\sin(\theta^{'}) - \cos(\theta^{'})\sin(\theta_n)) \tag{D-4}$$

where in the present case $a \approx 10$ nm which corresponds to the apparent length of the BB [3]. Finally, the function $P(\theta^{'}, t)$ takes into account the structures with orientation $\theta^{'}$ which interact with the structure

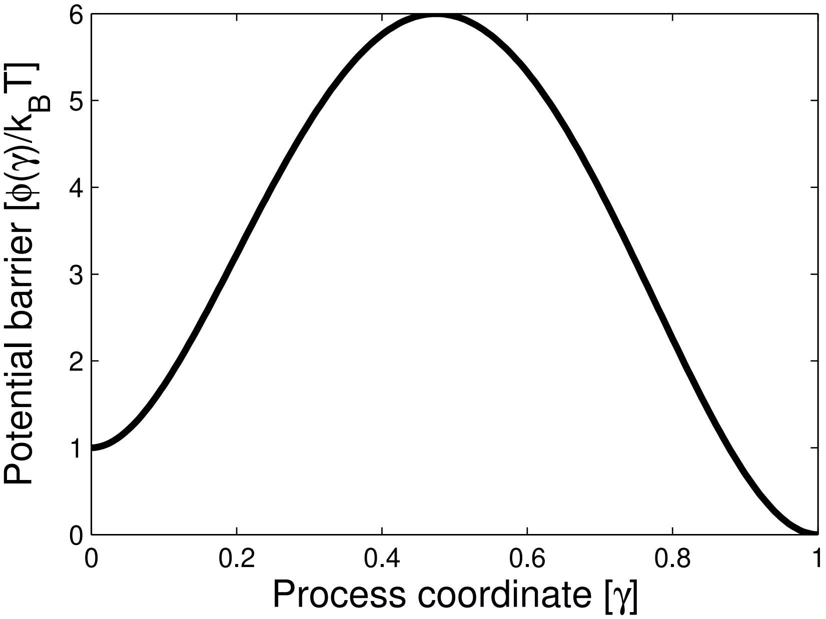

Fig. D-1.: Dimensionless potential barrier $[\phi(\gamma)/k_BT]$

composed of n blocks oriented an angle θ:

$$P(\theta',t) = \sum_n \frac{1}{n} p_n(\theta') \tag{D-5}$$

D.1.3. Standard chemical potential per building block

Single and agglomerated fibers are composed of BB. These blocks assemble spontaneously because the specific standard chemical potential per assembled block $\hat{\mu}_n^0$ decreases with the number of blocks ($\hat{\mu}_N^0 < \hat{\mu}_n^0$). This potential can be estimated by using the relation [4]

$$\frac{x_N}{N} = \left(\frac{x_1}{x_c}\right)^N \tag{D-6}$$

where x_1 and x_N are the concentrations of non-assembled and assembled BB respectively at minimum x_1 (critical point for large structures). For a given N, knowing x_1 and x_N (from experiments and the energy, respectively) we can estimate x_c, the critical concentration at equilibrium.
The increment of the standard chemical potential per BB ($\Delta\hat{\mu}^0$) as a function of N is given by:

$$\Delta\hat{\mu}^0 = \frac{RT}{N} \ln\left(\frac{N x_1^N}{x_N}\right), \tag{D-7}$$

This quantity is a monotonic function of N. Taking the first derivative of $\Delta\hat{\mu}^0$ with respect to N and using Eq. (D-6), we obtain

$$\frac{d\Delta\hat{\mu}^0}{dN} = -\frac{RT}{N}\left[\frac{\Delta\hat{\mu}^0}{RT} - \ln(x_1) - 1/N\right] \leq 0, \quad x_1 \leq 1, \tag{D-8}$$

There is a value $N = N^* \gg 1$, such that $\frac{\Delta\hat{\mu}^0}{RT} \approx \ln(x_1)$ and $\frac{d\Delta\hat{\mu}^0}{dN} = 0$, as a consequence $\Delta\hat{\mu}^0$ cannot decrease indefinitely. From this result, we conclude that structures such that $n > N^*$ have the same standard chemical potential. Therefore, structures having n assembled blocks, with $n > N^*$, have the same probability to be formed.

D.1.4. Standard chemical potential

Let μ_n^0 be the standard chemical potential for linear fibbers and $\Delta\mu_n^0 = \mu_n^0 + \mu_1^0 - \mu_{n+1}^0$ the standard driving force for the assembly of a linear fibber, with $n = 1, ...N$. Some requirements must be fulfilled in order that the standard chemical potential properly characterises the assembly of linear fibbers. First, μ_n^0 increases as the size of the structure increases because the assembly must have a limit. Second, the standard chemical potential per building block is related to the standard chemical potential of the structures. These conditions can be expressed as:

1. $d\mu_n^0/dn \geq 0, \forall n$
2. $d\Delta\mu_n^0/dn \leq 0, \forall n$
3. $\Delta\mu_{N-1}^0 = 0$
4. $\mu_1^0 = \hat{\mu}_1^0$
5. $\mu_N^0 = N\hat{\mu}_N^0$

A function fulfilling conditions 1 and 2 is:

$$\mu_n^0 = a_0 + a_1 \exp(a_2 n). \tag{D-9}$$

From conditions 3-5, we can compute a_0, a_1 and a_3.
Now let $\mu_{g,m}^0$ be the the standard chemical potential of the agglomerated fibers and $\Delta\mu_{g,m}^0 = \mu_{g,m}^0 + \mu_{g,n}^0 - \mu_{g,m+n}^0$ the standard driving force for fiber agglomeration, with $m = 1, ..., M = 2N$. As in the case of assembly of the linear fibers, the agglomeration process must fulfill some conditions which are similar to the previous ones except for the fact that the way in which $\mu_{g,m}^0$ increases is different. The requirements are now:

1. $d\mu_{g,m}^0/dm \geq 0, \forall m < N$
2. $d\mu_{g,m}^0/dm \leq 0, \forall m > N$
3. $d\mu_{g,m}^0/dm = 0, m = N$
4. $\mu_{g,1}^0 = \hat{\mu}_1^0$
5. $\mu_{g,N}^0 = N\hat{\mu}_N^0$

The function satisfying the first 3 conditions is:

$$\mu_m^0 = (a_3 m^2 + a_4 m + a_5)m, \tag{D-10}$$

where a_3, a_4 and a_5 are found from conditions 3-5, as well. From the standard chemical potential for each kind of structure, we can model the corresponding potential barrier.

D.1.5. Snapshots of the gelation process

We have represented the position of each fiber shown in Fig.**2-5** by a uniform random location. The number of fibers is proportional to the concentration of activated building blocks (first order structures composed of one block). The probability distribution for the orientation of the fibers is obtained by solving the Fokker-Planck system equations (see Fig. **2-5**).

D.1.6. Dynamic Light Scattering

To reproduce the Dynamic Light Scattering measurements, taken from [1], we use the fact that this quantity depends on the size of the second-order structure. Thus, we obtain the DLS results by computing the auto-correlation function of the average size for second-order structures obtained from the concentration of each structure as a function of time, solution of the system equations.

D.1.7. Potential barriers for each process

From the standard chemical potential and the potential barriers, we build the potential barrier for each process, as shown in Figure **D-2**. The .ªctivation energyïn each step depends on the steric effects and thermodynamic constraint as explained in the potential barrier section.
Notice that as each BB has two assembly centers, the activation takes place sequentially because the BB are symmetric. Therefore, the whole activation process is described by two reaction coordinates. In Figure **D-3**, we show the specific potential barriers.

D.1.8. Activity coefficient

We found that the activity coefficient for activation processes ψ_b depends on the concentration of the residue W which is $MeOH$, affecting significantly the first-order activation process. Thus $\psi_b = C_W^{1/2}$ because this component may affect the equilibrium state in the activation process. Otherwise, the activity coefficients for assembly and disassembly processes are approximately: $\psi_n = \phi_n' = 1$.

D.2. Nonequilibrium self-assembly induced Liesegang rings in a non-isothermal system

Abstract

we first present a scheme showing the formation of first-order structures. We express the fluxes $\dot{r}_{i,j}$ as a function of the rates R_j and give details on the derivation of the temperature evolution equation. Further, the pH and dichromate fraction is presented as a function of the dimensionless time and position, showing that the dichromate fraction is insignificant for the system conditions. We also present two figures displaying the position of the rings and the structure diameter, and a figure displaying the distribution of solid nuclei along the system. Finally, we show that the structures diameter dispersion is inversely proportional to the activator concentration C_E, thus supporting the fact that this dispersion increases with position.

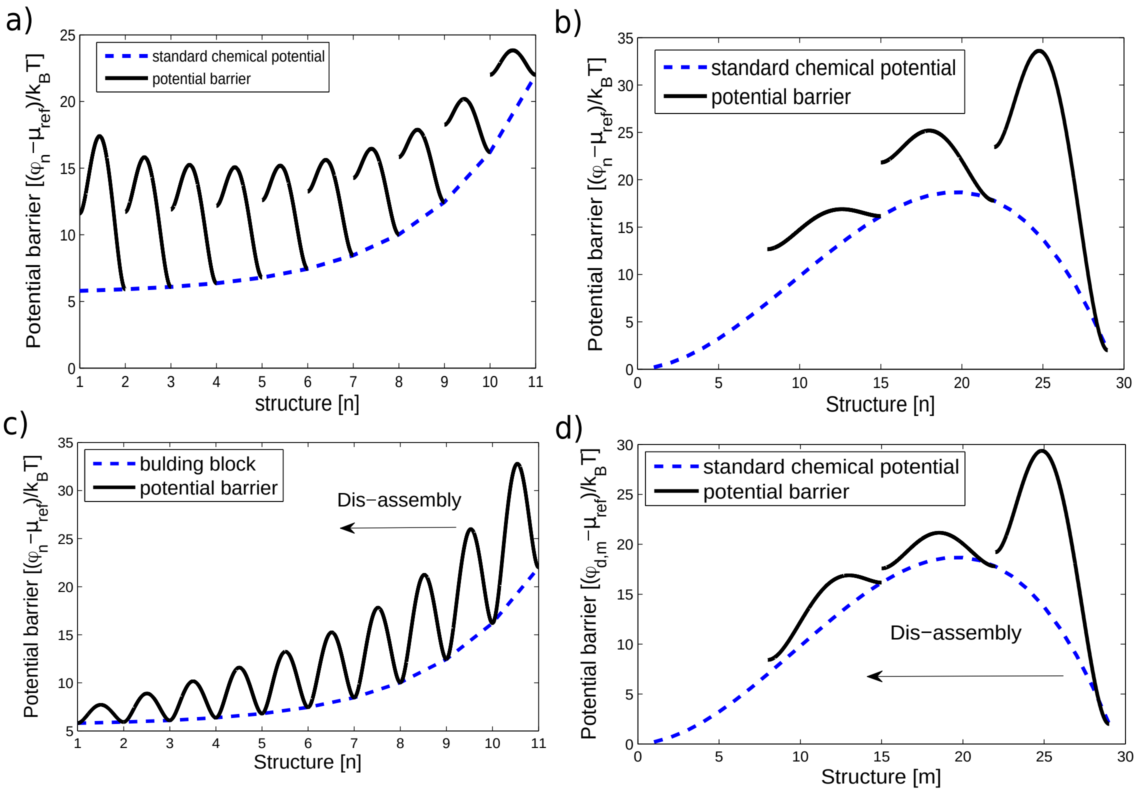

Fig. D-2.: Potential barriers for NESA processes. (a) First-order SA: Assembly of linear fibers. We show a process with ten steps, each one corresponding to the assembly of one BB. Each step is characterized by a potential barrier in which the activation energy and the standard chemical potential difference decreases with *n*. The effect of adding a BB is to increase the chemical potential in order that the process be spontaneous. (b) Second-order SA: Agglomeration. We show a second-order structure having 15,22 and 29 BB resulting from self-assembly of structures with 8,15 and 22 BB. In the last step, we found the highest activation energy expected because the size of the structure is not only limited thermodynamically but also kinetically. (c) First-order DA: Hydrolysis of linear fibers. The process represents the disassembly in ten steps of a structure composed of eleven BB. (d) Second-order DA: Aggregate hydrolysis. We show the second-order disassembly process for a structure with 29 BB. The process has 3 steps each one characterized by a potential barrier. The first step is not spontaneous, therefore we expect the appearance of metastable structures when some few BB become deactivated. However, if a large amount of BB are deactivated the process becomes spontaneous.

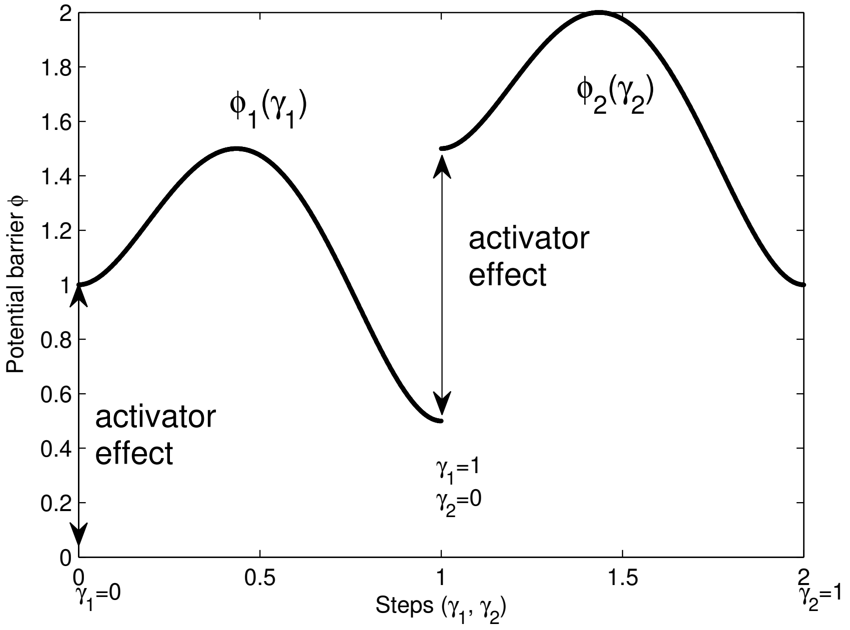

Fig. D-3.: Activation process for BB with two assembly centers. The effect of the activator is to increase the chemical potential in order to render the process spontaneous. Further, the activation energy increases with the number of activated assembly centers.

D.2.1. First-order structures formation

The mechanism for first-order self-assembly (process 2) is schematically expressed as:

$$\begin{gathered} \mathrm{A} + \mathrm{A} \rightleftharpoons \mathrm{A_2} \\ \mathrm{A_2} + \mathrm{A} \rightleftharpoons \mathrm{A_3} \\ . \\ . \\ . \\ \mathrm{A_{n\text{-}1}} + \mathrm{A} \rightleftharpoons \mathrm{A_n} \end{gathered}$$

In first-order structures formation, we have specified the intermediate steps in which the activated building blocks may add up sequentially to form structures composed of a number of blocks smaller than n, thus evidencing the presence of two reactants in the assembly process. The global process is expressed as:

$$\mathrm{nA} \rightleftharpoons \mathrm{A_n}$$

D.2.2. Fluxes in terms of the rates

From the kinetics (Eq.(3-6)-Eq.(3-9)) and using the stoichiometry of processes 1-4 (first and second-order activation and self-assembly), we can rewrite the fluxes $\dot{r}_{i,j}$ used in the mass and energy-balances. The $\dot{r}_{i,j}$ flux gives the rate at which the component i is transformed in the j^{th} process. Renaming components E, B, A, A_n, G and G_m by 1-6, we obtain

$$\sum_{j=1}^{4} \dot{r}_{1,j} = 2R_1 + lR_4 \tag{D-11}$$

$$\sum_{j=1}^{4} \dot{r}_{2,j} = R_1 \tag{D-12}$$

$$\sum_{j=1}^{4} \dot{r}_{3,j} = -R_1 + nR_2 \tag{D-13}$$

$$\sum_{j=1}^{4} \dot{r}_{4,j} = -R_2 + R_3 \tag{D-14}$$

$$\sum_{j=1}^{4} \dot{r}_{5,j} = -R_3 + mR_4 \tag{D-15}$$

$$\sum_{j=1}^{4} \dot{r}_{6,j} = -R_4 \tag{D-16}$$

D.2.3. Temperature equation

We first consider the diffusive energy flux $J_e = -k_{eff}\frac{\partial T(r,t)}{\partial r}$, where k_{eff} is an effective thermal conductivity and T the temperature.

In a diluted reactive media with small changes in temperature, the energy $e(r,t)$ per unit of volume can be written as $e(r,t) \approx \sum_i C_i h_i$. The change in the energy $e(r,t)$ is given by:

$$de(r,t) = \sum_i d(C_i h_i) = \sum_i C_i dh_i + h_i dC_i \tag{D-17}$$

where the molar specific enthalpy h_i is the sum of the standard formation enthalpy (h_i^0) and the enthalpy related to the heat capacity ($c_{P,i}$), $h_i \approx h_i^0 + c_{P,i}(T - T_{ref})$ with T_{ref} a reference temperature.
Dividing this equation by dt and inserting the mass conservation equation (Eq.(3-4)), we obtain

$$\frac{de(r,t)}{dt} = \sum_i C_i \frac{dT}{dt} + h_i \left(-\frac{\partial}{\partial r} rJ_{d,i}(r,t) - \sum_{j=1}^{4} \dot{r}_{i,j} \right) \tag{D-18}$$

This equation can also be expressed as

$$\frac{de(r,t)}{dt} = \sum_i C_i \frac{dT}{dt} - \sum_i \frac{\partial}{\partial r} rJ_{d,i}(r,t) - \sum_{j=1}^{4} \sum_i h_i \dot{r}_{i,j} \tag{D-19}$$

where $\sum_i h_i \dot{r}_{i,j} = -\Delta h_j R_j$ is the heat dissipation rate in the process. Therefore, the energy balance equation is

$$\frac{de(r,t)}{dt} = \sum_i C_i dT - \sum_i h_j \frac{\partial}{\partial r} rJ_{d,i}(r,t) + \sum_{j=1}^{4} \Delta h_j R_j \tag{S11}$$

Finally, inserting this expression (Eq.(S11)) into Eq.(3-11), we obtain the differential equation for the evolution in time of the temperature (Eq.(3-12)).

D.2.4. pH and Dichromate fraction

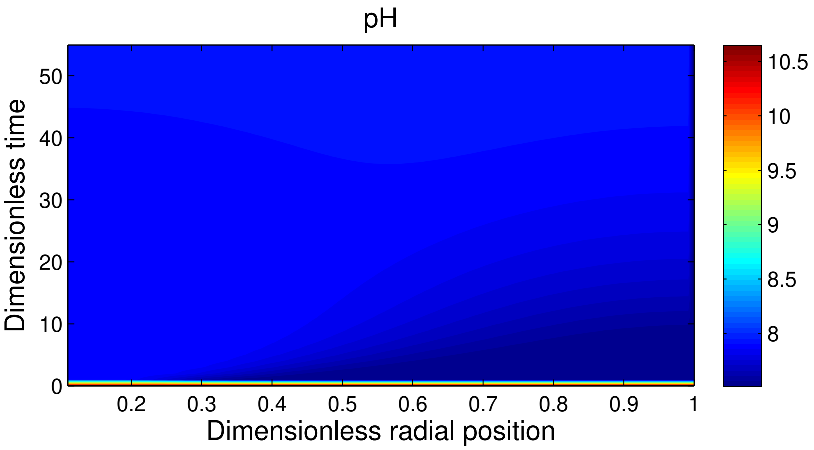

Fig. D-4.: pH against dimensionless time and position. pH values vary between 7.54 and 7.95 most of the time. pH higher than 8.5 is found for the earlier times of the process.

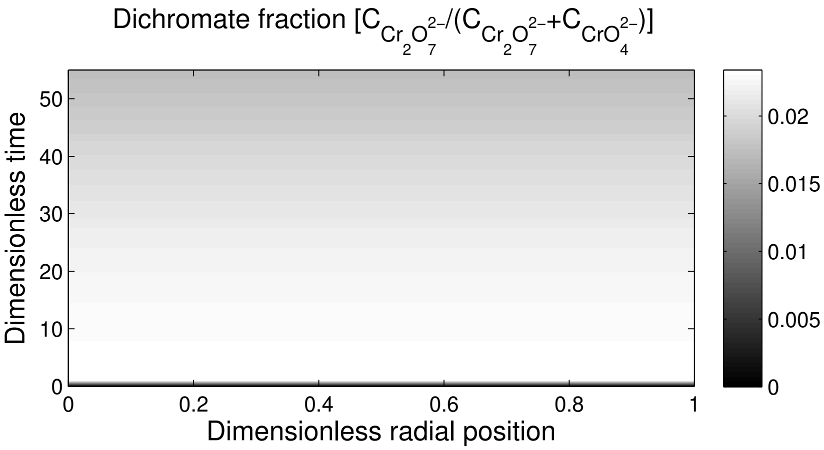

Fig. D-5.: Dichromate fraction vs. dimensionless time and position. Dichromate fraction is smaller than 0.022 in the whole system for every time.

D.2.5. Position of the Liesegang rings

D.2.6. Distribution of the Solid Nuclei along the system

It is possible to find solids in the region between rings. These solids correspond to the nuclei which are the precursors of the structures composing the patterns. In the Supp. Figure **D-8** is shown the concentration of the solid nuclei in the system. The blue numbers represent the position of the rings. Notice that the minima in the concentration of the solid nuclei correspond to the position in which emerges the rings.

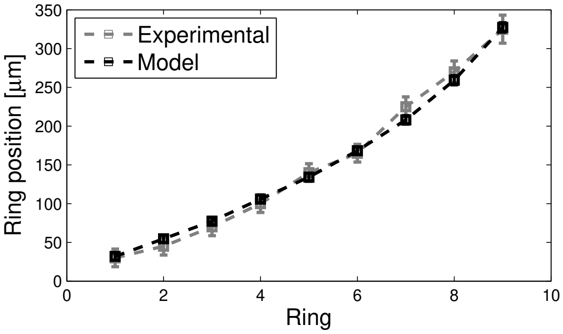

Fig. D-6.: Model results and experiments data for the ring position [μm] for each ring. The error percentage is approximately of 6,9 %. The dashed line connects the results obtained for the different rings. Grey squares represent experimental data taken from [5] whereas the black ones correspond to the results of the model.

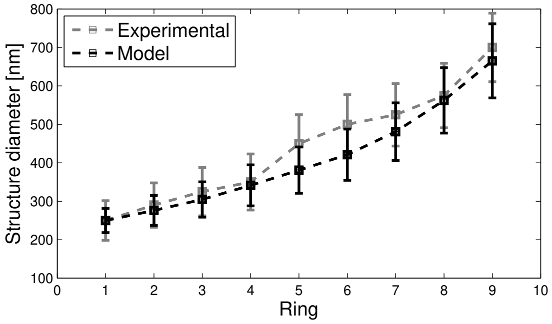

Fig. D-7.: Model results and experiments data for the structure diameter [nm] in each ring, with its standard deviation. The dashed line connects the results obtained for the different rings. The error is of approximately 6,7 %. Grey squares denote the experimental data taken from [5]; black squares stand for our results.

D.2.7. Diameter dispersion

A structure is formed when the agglomeration flux is positive ($R_4 > 0$). Its diameter is given by

$$d(r,t) = d_0 + \omega \ln(C_E(r_{lim},0)/C_E(r,t)), \quad \forall r > r_{lim}, |R_4(r,t) > 0, \tag{D-20}$$

In Fig.(**D-7**), we represent the average of the structure diameter

$$d(r) = \frac{1}{t_f(r)} \int_0^{t_p} d(r,t)dt, \tag{D-21}$$

where $t_f(r)$ is a time at which R_4 is greater than zero, at r. The variance for $d(r)$ is given by

$$\sigma_d^2(r) = \frac{1}{t_f(r)} \int_0^{t_p} (d(r,t) - d(r))^2 dt. \tag{D-22}$$

But here is hard to find a clear relation between σ_d and C_E. We assume that the standard deviation is proportional to the error Δd which is given by

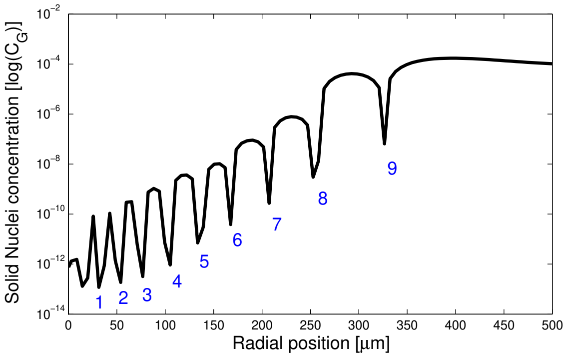

Fig. D-8.: Concentration of the solid nuclei as a function of the position. Blue number correspond to the position of each ring.

$$\Delta d(r) = \left|\frac{\partial d}{\partial C_E}\right| \Delta C_E, \tag{D-23}$$

Taking the derivative of d with respect to C_E from Eq.(3-18), and assuming that the error of C_E in a ring is proportional to the ring width (Δr_{ring}), we have

$$\Delta d(r) = \frac{\omega}{C_E}\Delta r_{ring}. \tag{D-24}$$

From the results of the model and the experimental data [5], we conclude that Δr_{ring} slightly increases from ring 1 to 5 and is almost constant from ring 6 to 9. Therefore, to know the value of the width of a ring is not enough to explain the increments of the diameter standard deviation. Nevertheless, C_E decreases in space and time because it is consumed, then when increasing time and distance C_E decreases which makes that the diameter standard deviation increases with distance.

D.3. A Criterion for the Formation of Nonequilibrium Self-Assembled Structures

An analogous method to obtain the potential by means of the optimization of the energy required to form a structure is presented.

The energy needed to form a structure (ΔE) for a given value of η is the sum of the energy change in the absence of dissipation and the energy dissipated in its formation, $\Delta E_d = T\Sigma$, where Σ is the entropy produced [6]:

$$\Delta E(\eta,t) = \Delta E_{rev}(\eta,t) + \Delta E_d(\eta,t) \tag{D-25}$$

The fact that nature evolves making efficient use of available resources [7, 8], enables us to assume that an extreme value of the energy dissipated, at which $\partial \Delta E_d / \partial \eta |_{\eta *} = 0$, is the signature of an optimal design of the structure. Close to η^*, the condition fulfilled is thus:

$$\left(\frac{d\Delta E_d(\eta)}{d\eta}\right)^2 \geq \psi(\eta) \tag{D-26}$$

where ψ is a residual function measuring deviations from the optimal structure.

To minimize the energy ΔE subjected to the restriction given in Eq.(D-26), we use the method of Lagrange multipliers. We then define the Lagrangian function

$$\mathscr{L} = \Delta E + \lambda \left(\left(\frac{d\Delta E_d(\eta)}{d\eta}\right)^2 - \psi(\eta) \right) \tag{D-27}$$

where λ is a Lagrange multiplier. Setting $\partial \mathscr{L}/\partial \eta = 0$, integrating over η and solving for $\lambda \psi \equiv \Psi$, we obtain

$$\Delta\Psi(\eta) = \Delta E(\eta) + \lambda \left(\frac{d\Delta E_d}{d\eta}\right)^2 \tag{D-28}$$

where the Lagrange multiplier is given by

$$\lambda = -2 \left(\frac{\partial^2 \Delta E_d}{\partial \eta^2}\right)^{-1} \Bigg|_{\eta^*} \tag{D-29}$$

One has $\lambda > 0$ since the derivative is computed around the maximum of E_d.

The potential obtained in Eq.(D-28) by means of the optimization method coincides with Eq. 6-19.

Bibliography

[1] Job Boekhoven, Aurelie M. Brizard, Krishna N. K. Kowlgi, Ger J. M. Koper, Rienk Eelkema, and Jan H. van Esch. Dissipative Self-Assembly of a Molecular Gelator by Using a Chemical Fuel. *Angew. Chem.*, 122(28):4935–4938, 2010.

[2] M.Doi and S.E.Edwards. *The Theory of Polymer Dynamics*. Oxford University Press, 1 edition, 1986.

[3] Dick Bedeaux, Signe Kjelstrup, and Jan Sengers. *Experimental Thermodynamics Volume X: Non-equilibrium Thermodynamics with Applications*. Royal Society of Chemistry, 2015.

[4] G. J M Koper, J. Boekhoven, W. E. Hendriksen, J. H. Van Esch, R. Eelkema, I. Pagonabarraga, J. M. Rubí, and D. Bedeaux. The Lost Work In Dissipative Self-Assembly. *Int. J. Thermophys.*, 34(7):1229–1238, 2013.

[5] Roché M. Walliser, Florent Boudoire, Eszter Orosz, Rita Tóth, Artur Braun, Edwin C. Constable, Zoltán Rácz, and István Lagzi. Growth of Nanoparticles and Microparticles by Controlled Reaction-Diffusion Processes. *Langmuir*, 31(5):1828–1834, 2015.

[6] A. Arango-Restrepo, D. Barragán, and J. M. Rubi. Self-assembling outside equilibrium: emergence of structures mediated by dissipation. *Phys. Chem. Chem. Phys.*, 21:17475–17493, 2019.

[7] Marc-Olivier Coppens. A nature-inspired approach to reactor and catalysis engineering. *Curr. Opin. Chem. Eng.*, 1(3):281 – 289, 2012.

[8] Elisa Magnanelli, Simon Birger Byremo Solberg, and Signe Kjelstrup. Nature-inspired geometrical design of a chemical reactor. *Chem. Eng. Res. Des.*, 152:20 – 29, 2019.

E. Appendix Part III: Energy dissipation induces and amplifies chiral symmetry breaking

E.1. Parameters

The characteristic dimensions of the system are presented in Table.**E-1**. The molecular radius of the salt is also presented.

Dimensions	d	H	h_0	l_0
Value $[m]$	$2{,}5\times10^{-2}$	$4{,}1\times10^{-2}$	$1{,}3\times10^{-2}$	$6{,}57\times10^{-10}$

Tab. E-1.: System dimensions.

The main transport coefficients are averaged for the temperature range between 20 and 120^oC are shown in Table.**E-2**

Trans. Coeff.	a	b	κ	U	k	k_l	K_p
Value	$12{,}04[Pa.s]$	$-0{,}1096[K^{-1}]$	$0{,}0571[w/mK]$	$15[w/m^2K]$	$10^{-2}[s^{-1}]$	$0{,}04-0{,}6[s^{-1}]$	$41-82[m^{-1}]$

Tab. E-2.: Transport coefficients. The viscosity is defined as $\eta = a\exp(b(T-273{,}15))$

The values of the physical-chemical properties are resumed in Table.**E-3**.

Physical properties	Glycerine	aqueous salt	solid salt L	solid salt D
$C_p[J/molK]$	249,96	104,6	104,6	104,6
$\mu^0[kJ/mol]$	$--$	$-262{,}67$	$-256{,}65$	$-256{,}65$
E_a/k_BT_a	$--$	$--$	≥ 2	≥ 2
$\delta[kg/m^3]$	1260	2540	2540	2540
$PM[g/mol]$	92	106,54	106,54	106,54

Tab. E-3.: Physical-chemical values.

Finally, the saturation of salt in a non-mixed medium is given by:

$$x_s = c_l + a_l\theta_l^b \tag{E-1}$$

with $\theta = (T-T_s)/Ts$ the dimensionless temperature $a_l = 1{,}956$, $b_l = 2{,}558$, $c_l = 0{,}144$ while the difusivity of the aqueous and solid salt molecules is:

$$D = \frac{k_BT}{6\pi\eta l_0} \tag{E-2}$$

E.2. Solid concentration

In Fig.**E-1** we present the results for the estimated dimensionless total solid concentration of the salt. In all cases, except for $w_s/w_g = 0{,}30$ under enhanced cooling, the solid concentration profiles have approximately a monotonic behaviour as typically found in damped and slightly under-damped systems or chemical reactions near first-order kinetics. In the case of $w_s/w_g = 0{,}30$ under enhanced cooling, the dropping of the solids concentration is explained by considering that through the measuring zone (height at which the measuring laser points) there are no solids due to the precipitation of the solids. The final value of the dimensionless total solid concentration increases as w_s/w_g increases or the measuring height decreases due to the concentration profile dropping exponentially as we go far from the bottom of the system. In Fig.**E-1**, measured salt concentration is lower for the case $w_s/w_g = 0{,}36$ than $w_s/w_g = 0{,}32$ due to for $w_s/w_g = 0{,}36$ the measurement was carried out at a higher height and in which we must remember that solid salt concentration decreases exponentially with the height. On the other hand, even if the model presents a high match with experimental results, the model should be tested for different heights by carrying the experiments at different heights and at the same concentration.

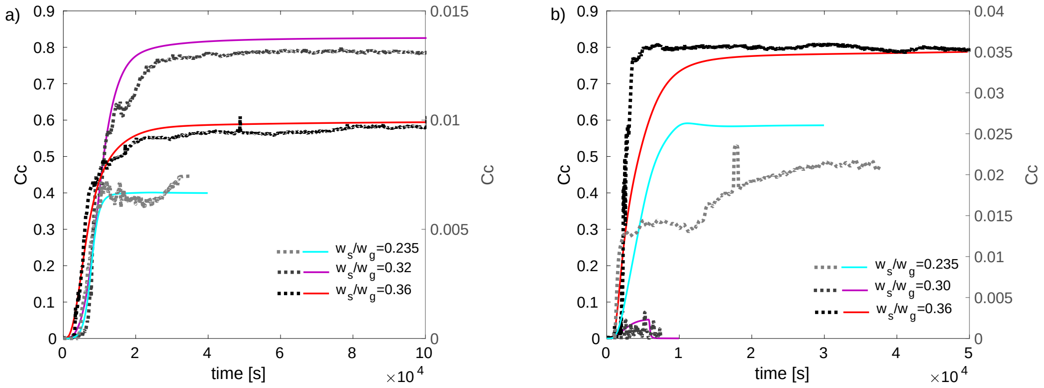

Fig. E-1.: Dimensionless solid concentration as a function of time. a) Behaviour for natural cooling (cooling with air), b) behaviour for enhanced cooling (cooling with air and water). Pointed lines correspond to experimental data whereas continuous lines to theoretical results. Right y-axes shows the results for initial salt mass w_s/w_g.

E.3. Average size and temperature

In Figs. **E-2** we present experimental data and model results for the case $w_s/w_g = 0{,}235$ under natural cooling conditions. The figure shows the cooling curve from which was estimated the global heat transfer coefficient in which we obtained an error percentage lower than 5 % between experimental data and model results.

Fig. **E-3** shows the dynamics for the growth of the crystals. This figure shows the average crystal size for both enantiomers. It is observed an exponential growth and a like-asymptotic limit for the size of the crystals since the time of the experiment is low compared with the diffusive time needed to grow a macroscopic

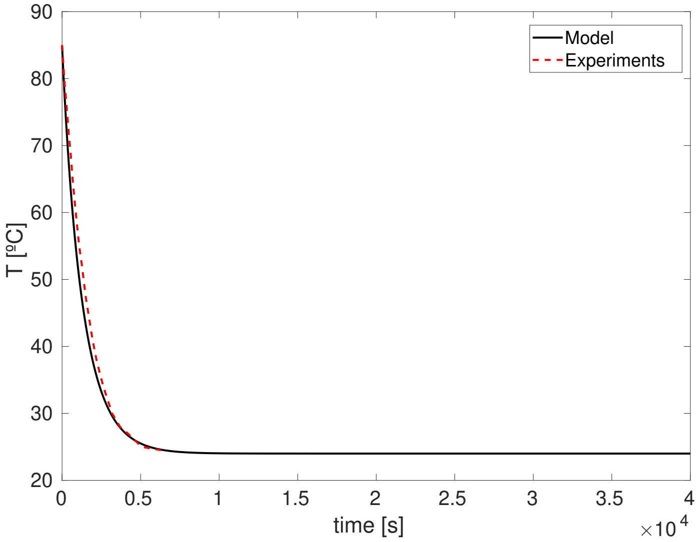

Fig. E-2.: Cooling dynamics. The experimental cooling curve is represented in a dashed red line. The cooling curve computed from the model corresponds to the continuous black line. Temperature measurement is carried out at a higher height in which the optical rotation angle is measured to avoid interference.

crystal of the size of the system. This process can take years in glycerine since diffusivity in glycerine at lab temperature is 1000 times higher than in water.

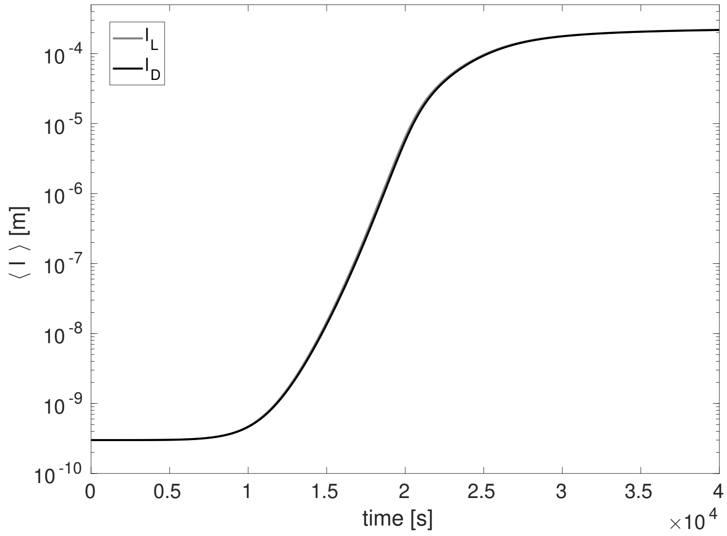

Fig. E-3.: Average crystal size dynamics. The average length for cubic crystals for both enantiomers. The light grey line corresponds to the Levogiro crystal whereas the black line to the Dextrogiro crystal.

E.4. Total energy dissipated

Finally, Fig.**E-4** shows the total energy dissipated in the process at time t. These theoretical results help to understand and prove that: 1) As we increase the value of w_s/w_g, the energy dissipated increases but this is not linear 2) The increments are different in both cases of cooling, in the case of enhanced cooling the energy dissipated is lower when $w_s/w_g = 0{,}36$. 3) Enhanced cooling leads to a lower energy dissipation in the crystal growing and emergence processes being related to higher enantiomeric excess compared to more thermodynamically inefficient processes.

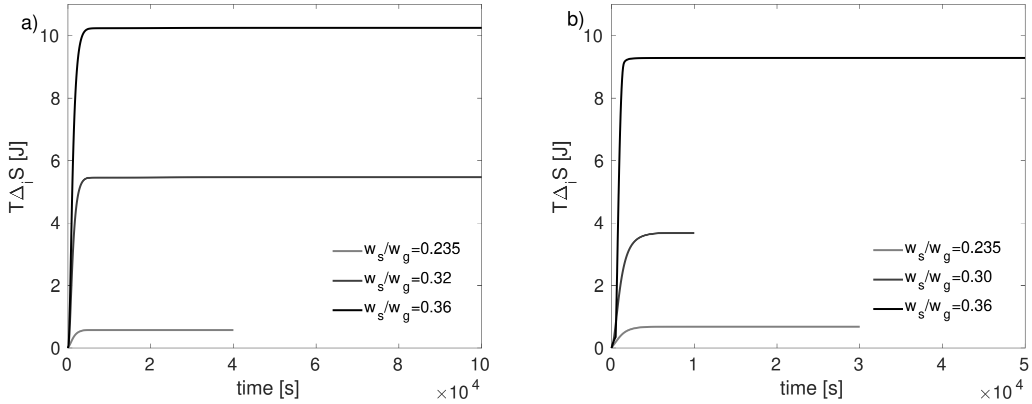

Fig. E-4.: Total energy dissipated as a function of time. a) Behaviour for natural cooling, b) behaviour for enhanced cooling

E.5. Activation energy change

We consider that the system only exchanges heat with the surroundings but not mass. We focus our analysis on the transition from achiral to chiral compound. In this transition, we have an intermediate state that may increase its free energy by absorbing a portion of the lost work coming from the entropy production. The free energy change in the system during the transition is given by the energy change of the process (from achiral to chiral) and the free energy change of the solvent (mainly by the decreasing of the internal energy due to heat exchange with the surroundings):

$$\Delta G_T = \Delta G_P^0 + \Delta G_S^0 \tag{E-3}$$

The free energy change from the chiral to intermediate state is:

$$\Delta G_{A-I} = \Delta H_{A-I}^0 - T\Delta S_{A-I}^0 + E_\Sigma \tag{E-4}$$

in which E_Σ is the absorbed energy coming from the entropy production. The free energy change from the intermediate to the chiral state is:

$$\Delta G_{I-C} = \Delta H_{I-C}^0 - T\Delta S_{I-C}^0 - T\Sigma_P \tag{E-5}$$

in which Σ_P is the entropy produced in the transition. The free energy change of the solvent during the transition is:

$$\Delta G_S = \Delta H_S^0 - T\Delta S_S^0 - T\Sigma_S \tag{E-6}$$

By adding these free energy changes, we obtain another relation for the free energy change of the system:

$$\Delta G_T = \Delta G_P^0 + \Delta G_S^0 + E_\Sigma - T\Sigma \tag{E-7}$$

where $\Sigma = \Sigma_P + \Sigma_S$. Comparing with Eq.E-3, we obtain that the total energy absorbed by the intermediate is

$$E_\Sigma = T\Sigma \tag{E-8}$$

Therefore the increment of the energy of the intermediary state per molecule is

$$\Delta E = T\frac{\Sigma}{N} \tag{E-9}$$